Rare Metal Technology

2024

Editors

Kerstin Forsberg

Takanari Ouchi

Gisele Azimi

Shafiq Alam

Neale R. Neelameggham

Alafara Abdullahi Baba

Hong Peng

Athanasios Karamalidis

TMS

Springer

The Minerals, Metals & Materials Series

Kerstin Forsberg · Takanari Ouchi · Gisele Azimi ·
Shafiq Alam · Neale R. Neelameggham ·
Alafara Abdullahi Baba · Hong Peng ·
Athanasios Karamalidis
Editors

Rare Metal Technology 2024

TMS

Ⓐ Springer

Editors
Kerstin Forsberg
KTH Royal Institute of Technology
Stockholm, Sweden

Gisele Azimi
University of Toronto
Toronto, ON, Canada

Neale R. Neelameggham
IND LLC
South Jordan, UT, USA

Hong Peng
University of Queensland
Brisbane, QLD, Australia

Takanari Ouchi
University of Tokyo
Tokyo, Japan

Shafiq Alam
University of Saskatchewan
Saskatoon, SK, Canada

Alafara Abdullahi Baba
University of Ilorin
Ilorin, Nigeria

Athanasios Karamalidis
Pennsylvania State University
University Park, PA, USA

Preface

Rare Metal Technology 2024 is the proceedings volume of the eleventh symposium on Rare Metal Extraction and Processing, which has been organized at the Annual TMS Meeting & Exhibition since 2014. The eleventh symposium was part of the 153rd TMS Annual Meeting & Exhibition, held at the Hyatt Regency Orlando in Orlando, Florida, USA from March 3rd to 7th, 2024 and was sponsored by the Hydrometallurgy and Electrometallurgy Committee of the TMS Extraction and Processing Division.

The aim of the Rare Metal Extraction and Processing symposium is to provide a forum for presentations and discussion of novel developments in rare metal extraction and processing from primary and secondary materials. Rare metals are less common or minor metals such as antimony, bismuth, barium, beryllium, boron, calcium, chromium, gallium, germanium, hafnium, indium, lithium, manganese, molybdenum, platinum group metals, rare earth metals, rhenium, scandium, selenium, sodium, strontium, tantalum, tellurium, titanium, and tungsten. These are metals that are produced in low-tonnage compared to high-tonnage metals such as iron, aluminum, copper, lead, tin, zinc, and silicon.

Rare metals are technology essential, and many are critical for the energy transition needed to achieve climate neutrality; this has led to an increasing demand for rare metals in recent years. At the same time, the grade of rare metals in ores is declining, resulting in increased energy and water consumption and carbon emissions in mining and extraction. Consequently, it is urgent to develop new sustainable, energy saving, and resource efficient processes and approaches for rare metal extraction and processing. The importance of the rare metals and their criticality has raised the interest for these metals in recent years, which is also reflected in the increasing number of participants in this symposium.

The chapters in this volume cover processing and extraction of rare metals from primary and secondary raw materials and include papers on process development and optimization within bio-, hydro-, and electro-metallurgy. Furthermore, various processing techniques for mineral beneficiation, extraction, separation, and purification of rare metals are covered.

I express my sincere gratitude to the co-organizers (co-editors) for their efforts to organize the symposium and edit the proceedings volume *Rare Metal Technology*

2024: Takanari Ouchi, Gisele Azimi, Shafiq Alam, Neale R. Neelameggham, Alafara Abdullahi Baba, Hong Peng, and Athanasios Karamalidis. In addition, on behalf of the organizers (editors), I would like to acknowledge the TMS staff, Kelly Markel, Matt Baker, Patricia Warren, Trudi Dunlap, and Colleen Madore for their assistance in assembling and publishing this proceedings book. Finally, we would like to thank all the authors, speakers, and participants of this symposium. Let's continue our efforts to create a good forum for sharing knowledge and discussions to advance the field of rare metal extraction and processing.

Kerstin Forsberg
Lead Organizer

Contents

Part II   Processing of Rare Earth Elements, Vanadium and Lithium

Part III   Biometallurgy and Flotation

Part V   Electrometallurgy and High Temperature Processes

Part VI   Poster Session

About the Editors

Kerstin Forsberg is a Professor in Chemical Engineering at KTH Royal Institute of Technology in Stockholm, Sweden. Her research is focused on separation processes, in particular crystallization. This knowledge is applied in collaborative projects concerning the recovery of resources from waste and to develop new innovative and more environmentally and economically sustainable processes. Forsberg is Head of the Division of Resource Recovery at KTH. She is also Deputy Director for the Research Platform for Industrial Transformation at KTH and director for the strategic partnership with IVL Swedish Environmental Research Institute. As a member of the Hydrometallurgy and Electrometallurgy Committee at The Minerals, Metals & Materials Society (TMS), Prof. Forsberg has contributed as a guest editor for *JOM* and by organizing technical symposia at TMS.

Takanari Ouchi is a lecturer at the Institute of Industrial Science at the University of Tokyo. He received his Doctor of Engineering in Nanoscience and Nanoengineering from Waseda University in 2011. In this tenure, he developed electrochemical deposition processes to fabricate metal nanostructures with both well-controlled crystallinity and uniformity at a single nanometer scale and demonstrated the applicability of these processes to the fabrication of bit-patterned magnetic recording media for future hard disk drives. After completing his doctoral degree, Dr. Ouchi joined the Massachusetts Institute of Technology (MIT), where he developed

liquid metal batteries, which is in principle a bidirectional electrolysis (electrorefining) cell, for application in grid scale energy storage. As a research scientist, he led a research group to systematically investigate the electrochemical properties of liquid metal electrodes in molten salt electrolytes and developed novel lithium, calcium, and sodium liquid metal batteries. Since he began working as a research associate at the University of Tokyo in 2017, he has developed new smelting and recycling processes for rare and precious metals using pyrometallurgical and electrometallurgical methods. Since August 2021, he has been appointed as a lecturer in the Department of Materials and Environmental Science, Institute of Industrial Science at the University of Tokyo. Dr. Ouchi has authored 32 peer-reviewed papers, including papers published in *Nature*, *Nature Energy*, and *Nature Communications*, nine conference proceedings, and seven review papers; he has also delivered over 100 talks at conferences. He has contributed to creating a vibrant field for metal extraction by organizing technical symposiums at The Minerals, Metals & Materials Society (TMS).

Gisele Azimi is a Professor in the Chemical Engineering and Applied Chemistry Department (cross appointed at Materials Science & Engineering) at the University of Toronto (U of T) and the Canada Research Chair (Tier 2) in Urban Mining Innovations. She is the director, and the first woman to hold the directorship, of the Ontario Centre for the Characterization of Advanced Materials (OCCAM) and she is the director of the Laboratory for Strategic Materials (LSM). The LSM was established to tackle the global challenges associated with the supply of strategic materials (through extraction and recycling), with wide applications, particularly in renewable energy and batteries. Dr. Azimi has been actively collaborating with Canadian industry and government. Dr. Azimi established the Laboratory for Strategic Materials with the mission of addressing the sustainability challenges associated with strategic materials such as rare earth elements (REEs), in terms of their production (supply) from primary or secondary resources (extraction or recycling, respectively) and utilization. On the supply side, she focuses on the extraction of REEs from conventional and unconventional

ores, process tailings, and electronic wastes. Through a multidisciplinary and innovative approach, which is the hallmark of her research group, she develops and enhances transformative processes over the entire spectrum of extraction, separation, and purification of strategic materials. Given the high costs and environmental challenges associated with extraction and processing of critical materials, she also develops technologies and products that alleviate reliance on them by replacing them with materials with similar properties that are abundant, less costly, and environmentally friendly. The national and international impact of her research is evident through the publications and citations of her original research by top international research groups. She has 85 journal papers published in internationally leading journals. She has delivered 43 invited, keynote, and plenary talks at universities and national and international conferences. Since joining U of T, she has filed 10 patent applications (2 patents granted so far). The relatively large number of patents that she holds further demonstrates the utility of her work. Since 2014, she has received 13 prestigious awards, including young researcher awards, for excellence in Research, Teaching, and Leadership, Canada Research Chair (Tier 2), Emerging Leaders of Chemical Engineering (CSChE), and The Young Leaders Award (The Minerals, Metals & Materials Society (TMS)).

Shafiq Alam is an Associate Professor at the University of Saskatchewan, Canada. He is an expert in the area of mining and mineral processing with profound experience in industrial operations, management, engineering, design, consulting, teaching, research, and professional services. As a productive researcher, Dr. Alam has secured 2 patents and has produced over 185 publications. He is the lead/co-editor of 15 books and an editorial board member of two mining and mineral processing journals named *Minerals* (an Open Access journal by MDPI) and *The International Journal of Mining, Materials and Metallurgical Engineering*. He is the winner of the 2015 Technology Award from the Extraction & Processing Division of The Minerals, Metals & Materials Society (TMS), USA.

With extensive relevant industry experience as a registered professional engineer, Dr. Alam has worked

on projects with many different mining industries. He is an Executive Committee Member of the Hydrometallurgy Section of the Canadian Institute of Mining, Metallurgy and Petroleum (CIM) where he held the Office of Secretary. During 2015–2017, he served as the Chair of the Hydrometallurgy and Electrometallurgy Committee of the Extraction & Processing Division (EPD) of TMS. Currently, he is the Secretary of the Recycling and Environmental Technologies Committee of TMS and is serving on the TMS-EPD Awards Committee. He is a lead/co-organizer of at least 19 Symposia at the International Conferences through CIM and TMS. Dr. Alam is one of the founding organizers of the Rare Metal Extraction & Processing Symposium at TMS and since 2014, he has been involved in organizing this symposium every year with great success. In the past, he was involved in organizing the International Nickel-Cobalt 2013 Symposium and TMS 2017 Honorary Symposium on Applications of Process Engineering Principles in Materials Processing, Energy and Environmental Technologies. Dr. Alam was also a co-organizer of the 9th and 10th International Symposia on Lead and Zinc Processing (PbZn 2020, PbZn 2023) held in California and China, respectively. He co-organized the Pressure Hydrometallurgy Symposium at the Conference of Metallurgists (COM 2023) organized by CIM, which was held in Toronto, Canada. In 2022, he was involved in co-organizing the 2022 Energy Technologies and CO_2 Management Symposium while in 2023 he was the lead-organizer of Rare Metal Technology Symposium. In addition to co-organizing the current 2024 Energy Technologies and CO_2 Management Symposium, Dr. Alam is also co-organizing the 2024 Rare Metal Extraction and Processing Symposium co-located with the TMS 2024 Annual Meeting and Exhibition in Orlando, Florida.

Neale R. Neelameggham IND LLC, is involved in international technology and management licensing for metals and chemicals, thiometallurgy, energy technologies, Agricoal, lithium-ion battery, energy efficient low cost OrangeH2, Netzero sooner with Maroon gas and Pink hydrogen, rare earth oxides, etc. He has more than 38 years of expertise in magnesium production and was involved in the process development of its startup company NL Magnesium to the present US Magnesium LLC, UT when he was instrumental in process development from the solar ponds to magnesium metal foundry. His expertise includes competitive magnesium processes worldwide. In 2016, Dr. Neelameggham and Brian Davis authored the ICE-JNME award winning paper "Twenty-First Century Global Anthropogenic Warming Convective Model." He is working on Agricoal® to greening arid soils, and at present energy efficient Orange hydrogen, and turbine generator electric car with hydrocarbons and steam. He authored *The Return of ManmadeCO2 to Earth: Ecochemistry.* Dr. Neelameggham holds 16 patents and applications and has published several technical papers. He has served in the Magnesium Committee of the TMS Light Metals Division (LMD) since its inception in 2000, chaired in 2005, and since 2007 has been a permanent advisor for the Magnesium Technology Symposium. He has been a member of the Reactive Metals Committee, Recycling Committee, Titanium Committee, and Program Committee for LMD and LMD council. Dr. Neelameggham was the Inaugural Chair, when in 2008, LMD and the TMS Extraction and Processing Division (EPD) created the Energy Committee and has been a Co-Editor of the Energy Technology Symposium through the present. He received the LMD Distinguished Service Award in 2010. As Chair of the Hydrometallurgy and Electrometallurgy Committee, he initiated the Rare Metal Technology Symposium in 2014 and has been a co-organizer to the present. He organized the 2018 TMS Symposium on Stored Renewable Energy in Coal and initiated Light Elements Technology in 2023.

Alafara Abdullahi Baba is Professor of Analytical/ Industrial and Materials Chemistry and Dean, Faculty of Physical Sciences, University of Ilorin, Nigeria. He holds a Ph.D. in Chemistry from the University of Ilorin (2008). His dissertation entitled "Recovery of Zinc and Lead from Sphalerite, Galena and Waste Materials by Hydrometallurgical Treatments" was judged the best in the area of Physical Sciences at the University of Ilorin, Nigeria in 2009. In addition, he was a Ph.D. project supervisor of the Best Postgraduate Student of the University of Ilorin in the 2021/2022 academic session. His area of research covers analytical, industrial, and materials chemistry in general with special interests in solid minerals and materials processing through hydrometallurgical routes; reactions in solution for metallurgical applications; preparation of phyllosilicates, porous, and bio-ceramic materials; ore beneficiation including indigenous barite processing for oil and gas applications with developing eco-friendly-cum-low energy synthetic routes for industrial, technological utilities, among others. Professor Alafara has been cited in many internationally acclaimed journals of high impact. As an academically inclined scholar with many distinct awards, several of his research breakthroughs of more than 150 publications have been presented at both national and international conferences and workshops for wider recognition. His University of Ilorin 198th Inaugural Lecture (2021) titled "Sustainable National Development: Mineral and Material Resources to the Rescue" affirmed the use of locally sourced minerals for industries, a condition for countries to save significant foreign earnings.

Professor Alafara has occupied various positions as a chairperson, secretary, and member of relevant academic and professional committees. He was Head, Department of Industrial Chemistry of the University of Ilorin between 2017–2020; Deputy Director, Central Research Laboratories (2014–2017); University of Ilorin Senate Representative for the Students' Disciplinary Committee (2019–2021); Secretary, Hydrometallurgy and Electrometallurgy Committee of the Extraction & Processing Division (2018–2021); Co-organizer of the Rare Metal Extraction & Processing Symposium and Lead Organizer, Energy Technologies & Carbon Dioxide Management Symposium (2021); Materials

Characterization - Education Committee; EPD and Best Awards Committee Representative; appointed EPD Council Education Representative (2021–Date), and guest editor for *JOM* (TMS, 2023–Date). He is also the current National President of the Materials Science and Technology Society of Nigeria and a Fellow of many professional societies including the Chemical Society of Nigeria and the Materials Science and Technology Society of Nigeria. He has supervised and is still supervising many undergraduate and postgraduate research works and is currently serving as an External Examiner to Postgraduate researchers in universities within and outside Nigeria.

Hong Peng is currently an Amplify Senior Lecturer at the School of Chemical Engineering, University of Queensland (UQ). He gained his Ph.D. degree in Chemical Engineering at UQ with the OZ Minerals Award for Excellent Thesis (2014). Dr. Peng has industry experience as a chemical engineer from the Olympic Dam site and Newcastle Technology Centre, BHP Billiton (2006-2009). He was the recipient of the 2020 TMS Young Leaders Professional Development Award. Dr. Peng's research focuses on the fundamental aspects of mineral processing, interfacial colloid science, crystal kinetics, and precipitation as well as molecular dynamics simulation. These projects are of interest to nanobubbles, mine tailings, zeolite, clay minerals, and metal resource recovery.

Athanasios Karamalidis is an Assistant Professor of Environmental Systems Engineering of the John and Willie Leone Family Department of Energy and Minerals Engineering of the Earth and Minerals Science College at The Pennsylvania State University. Previously, Dr. Karamalidis was an Associate Research Professor of Environmental Engineering at Carnegie Mellon University and an ORISE Faculty and Post-Doctoral Fellow specialized in geochemistry at the National Energy Technology Laboratory of the US Department of Energy. He is on the managing board and one of the managing members of SCORE consortium, a designated defense manufacturing community, for the acceleration of critical element commercialization in the

USA. His current academic and entrepreneurial activities focus on research and development of selective separation technologies for critical materials recovery from large volume industrial wastes, contributing to circular economy concepts. His work has been published in books, peer-reviewed international journals, conferences, seminars, patents, and other publications. He has served as a member of national committees for research and development, and as a reviewer/panelist for many federal agencies, including NSF, DOD, and DOE. He is member of various professional societies and held the position of Member of the Board of Directors and Secretary General of the Board of Directors of the Association of Greek Chemists for many years. As a member and Vice Chair of the Hydrometallurgy and Electrometallurgy Committee at The Minerals, Metals & Materials Society (TMS), Dr. Karamalidis has contributed as a guest editor for *JOM* and by organizing technical symposia at TMS.

Part I
Recycling

Recycling of Discarded Tantalum Capacitors for Metal Recovery

Shaila Mir and Nikhil Dhawan

Abstract The massive generation of electronic waste presents an opportunity for resource recycling. Discarded tantalum capacitors contain 30–35 wt.% tantalum, which is tightly encapsulated in an epoxy housing. Tantalum recycling is necessary due to scarcity, finite resources, and geopolitical constraints. Pyrolysis effectively degrades the epoxy resin and liberates the tantalum-rich sintered core from the outer resin. The manganese (MnO_2) was removed from the core using mild acid leaching to concentrate tantalum in the leach residue. Pyrolysis temperature (550–700 °C) influences the transformation of MnO_2 to lower oxides, thereby affecting its dissolution. The decomposed epoxy housing consists mainly of silica and silver, which is subjected to density separation. The metallic enrichment in the underflow fraction is limited due to finer silver particles. Nearly, 100 g capacitors can yield 34 g of Ta, equivalent to 0.28 tons of primary ore.

Keywords Capacitor · Tantalum · Pyrolysis · Recovery

Introduction

The rapid development of science and technology has increased the production of electronic waste (e-waste) [1]. Currently, the global quantity of e-waste generated is approximately 53.6 Mt, which is projected to increase to 74.7 Mt by 2030 [2]. Printed circuit boards (PCBs) are the core component of electronic products and makeup 4–7% of the total mass of e-waste [3, 4]. PCBs consist of metals (base, precious, and rare), polymers (epoxy resin), fiber-reinforced glass fibers, and toxic organic substances (brominated flame retardants, aromatic hydrocarbons) [5]. The informal processing involves the risk of release of toxic substances such as dioxins, furans

S. Mir (✉) · N. Dhawan
Materials Recycling Laboratory, Department of Metallurgical and Materials Engineering, Indian Institute of Technology, IIT-Roorkee, Roorkee, Uttarakhand 247667, India
e-mail: smir@mt.iitr.ac.in

N. Dhawan
e-mail: nikhil.dhawan@mt.iitr.ac.in

(dibenzo-p-dioxins and dibenzofurans PBDD/Fs), and effluents in the surroundings [6].

The recovery of base and precious metals from waste PCBs is often studied, while studies on the recovery of electronic components are limited. The composition of the electronic components is complex and consists of a rich and concentrated source of precious and rare metals. The unique properties of tantalum such as high electrical capacitance, low component volume, and high thermal stability make it an attractive choice for capacitor applications [7]. The single largest consumption of tantalum (42% of the annual production) is consumed in tantalum capacitors [8]. Naturally, Ta ore consists of complex (mixed oxides) minerals such as tantalite, columbite, and microlite containing 42–84% Ta (crustal abundance—1–2 ppm) in association with Nb (2–40%), which makes the extraction of Ta from ores difficult, and energy-intensive [9]. Moreover, the tantalum production is limited to fewer countries with a world production of ~ 2100 tons [10]. The scarcity of primary sources and geopolitical constraints on supply risk make it necessary to recycle secondary tantalum resources.

Tantalum capacitors consist of Ta metal anodes compressed into a sintered core which is coated with a layer of MnO_2 [11]. The cathode consists of a layer of Ag and graphite on the sintered anode, while the electrodes are tightly bound in an epoxy housing containing SiO_2 (for thermal durability), phenolic resin, and flame retardants, which make recycling difficult [12]. Therefore, the separation of the outer resin from metal values is important for recycling the valuable constituents. Pyrolysis is a promising technology for recycling organics compared to combustion with reduced emissions of hazardous constituents [13]. In this study, pyrolysis is used as a pre-concentration step for removing the outer resin from the inner core (consisting of Ta and Mn values). The effect of pyrolysis parameters on the separation of resin and core components is investigated. The effect of pyrolysis temperature on phase transformation and its effect on metal dissolution is studied. This study is aimed at the sequential separation of impurities (resin, SiO_2, Mn) and consequent enrichment of Ta values.

Materials and Methods

Tantalum capacitors were visually identified and manually removed from the discarded PCBs. The capacitors were subjected to pyrolysis treatment under an inert argon atmosphere for the decomposition of the outer resin. The effect of pyrolysis temperature (550–700 °C) and time (20–60 min) on resin decomposition was studied. The obtained pyrolyzed residue was mildly crushed and sieved. On sieving, the sintered core (SC) was separated in the coarser fraction (> 500 μm) while the outer epoxy resin was pulverized to obtain a homogenous fraction of < 212 μm. The SC was crushed and subjected to mild acidic leaching (1 M citric acid, S/L-1/25, 90 °C, 2 h) to separate Mn values in the leach solution and enrich Ta in the leach residue. Further, density-based separation using sink-float experiments was carried out to recover the metallic values from < 212 μm.

The thermal response of the capacitors was studied using thermo-gravimetric analysis (TGA) at a heating rate of 10 °C/min in the temperature range of 25–1200 °C under air and argon atmosphere. The underlying phases and associated transformations were identified using X-ray diffraction (XRD, Rigaku) at 2θ ranges of 10–100° with a scanning rate of 3°/min. The elemental composition of the samples was analyzed by an X-ray fluorescence spectrometer (XRF, Supermini 200 Rigaku Corporation, Japan). The morphology and compositional analysis were carried out using Scanning Electron Microscopy equipped with energy-dispersive X-ray Spectroscopy (SEM–EDS) (Fe-SEM, Zeiss EVO18). The elemental analysis of the leach solution was measured using microwave plasma atomic emission spectroscopy (MP-AES).

Results and Discussion

Feed Characterization

The Ta capacitors consist of Ta—34.0 wt.% (sintered core) Mn—10.9 wt.% (coated on sintered core), Si—33.4 wt.% (as a filler in outer epoxy housing), Ag—0.94 wt.% (cathode), Cu—4.4 wt.%, and Sn—1.1 wt.% values (from terminal components). The phase analysis of the capacitor revealed Ta, MnO_2, Ag, SiO_2, and minor fractions of Sn and Ag_2O (Fig. 1a). The SEM–EDS analysis of the crushed capacitors showed a strong association between the non-metal (C, Si) and metal (Mn, Ta) fractions (Fig. 1b). Since SC is a concentrated source of Ta, it is recommended to recover it separately from the epoxy resin component.
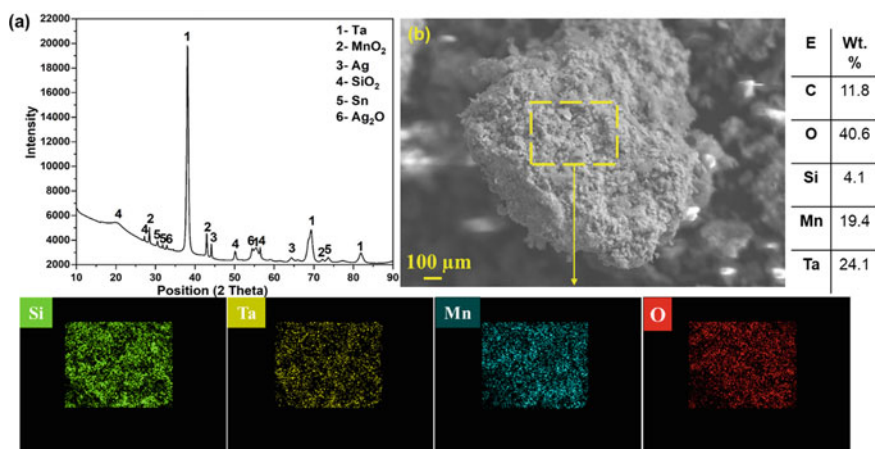
Fig. 1 a XRD and **b** SEM–EDS of crushed tantalum capacitors

Thermo-Gravimetric Analysis

Thermo-gravimetric analysis was performed to identify the temperature region corresponding to the degradation of the organic fraction, which is shown in Fig. 2a. No significant weight loss was observed up to 250 °C (region I); while there was a weight loss of around 5.5% in the range of 250–550 °C (region II). The weight loss in region I corresponds to the removal of water and light volatiles, while region II represents the rapid decomposition of halogenated epoxy resins [14] present in the housing of tantalum capacitors. Therefore, temperatures above 550 °C were chosen for conducting the pyrolysis experiments.

Using TG analysis and Coats-Redfern (C-R) method, the activation energy (E_a) and pre-exponential factor can be determined. In the equation, β is the heating rate (dT/dt (°C/ min)), and R is the universal constant (8.314 kJ /mol K). The value of n is selected using the least square method in which n with the highest correlation coefficient (R^2) of the fitted plot is chosen. The activation energy and pre-exponential factor are calculated from the slope ($-E_a/R$) and intercept of the plot. The highest R^2 is sought for n = 0.8, with the value of kinetic parameters E_a, A and R^2 obtained as 33.48 kJ/mol, 33 min^{-1}, and 0.993 respectively for the temperature range of ~ 250–550 °C [15].

Pre-Treatment: Structure Breakdown

Based on TG analysis, the temperature range of 550–700 °C is chosen for the pyrolysis process. The effect of pyrolysis temperature on the yield of pyrolysis products is shown in Fig. 2b. At lower temperatures (550 °C), the detachment of the sintered core and < 212 μm is not effectively attained. Therefore, misplacement of the products results in a slightly lower yield of the sintered core. Above 600 °C, no significant variation due to temperature is observed on the separation of the pyrolysis products (sintered core and $-212\,\mu$m). The effect of pyrolysis time (20–60 min) was found to have minimal effect on the pyrolysis responses (not shown) [15]. The product yield was similar (SC~44%, $-212\,\mu$m $\sim 32\%$) at 20 and 40 min of pyrolysis time.

The effect of pyrolysis temperature on the phase transformation is shown in Fig. 3a. As the pyrolysis temperature was increased, MnO_2 was transformed to lower oxides such as Mn_2O_3, Mn_3O_4, and MnO phases as shown in Eqs. 1–3. At 650 and 700 °C, the phases observed are similar (Ta, Mn_2O_3 and MnO). Therefore, 650 °C is chosen as an optimum pyrolysis temperature [15]. The preferential reduction of MnO_2 is advantageous as lower oxide states of manganese are readily acid-soluble and therefore, aids in downstream separation of Mn impurities. The SC consists of interlinked regions of Ta and Mn (Fig. 3b), which can effectively be separated by dissolving the acid-soluble Mn-oxide phases.

$$2\,MnO_2 = Mn_2O_3 + \frac{1}{2}O_2 \qquad\qquad (1)$$
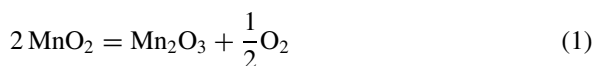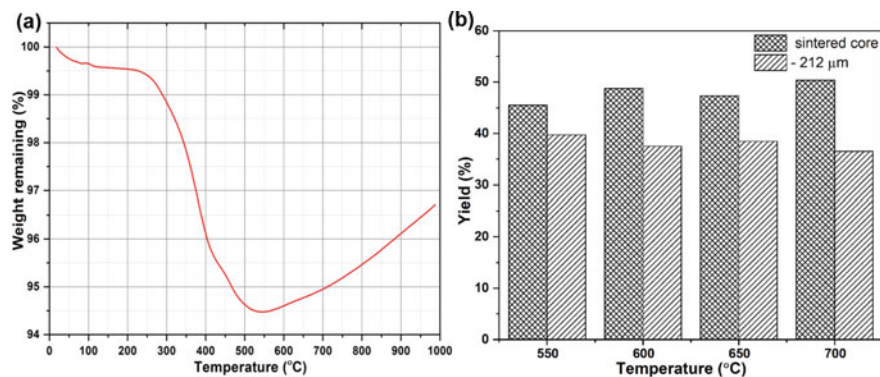
Fig. 2 a TG analysis. **b** Effect of pyrolysis temperature on yield (%) of pyrolyzed products

$$3\,Mn_2O_3 = 2\,Mn_3O_4 + \frac{1}{2}O_2 \tag{2}$$

$$Mn_3O_4 = 3\,MnO + \frac{1}{2}O_2 \tag{3}$$
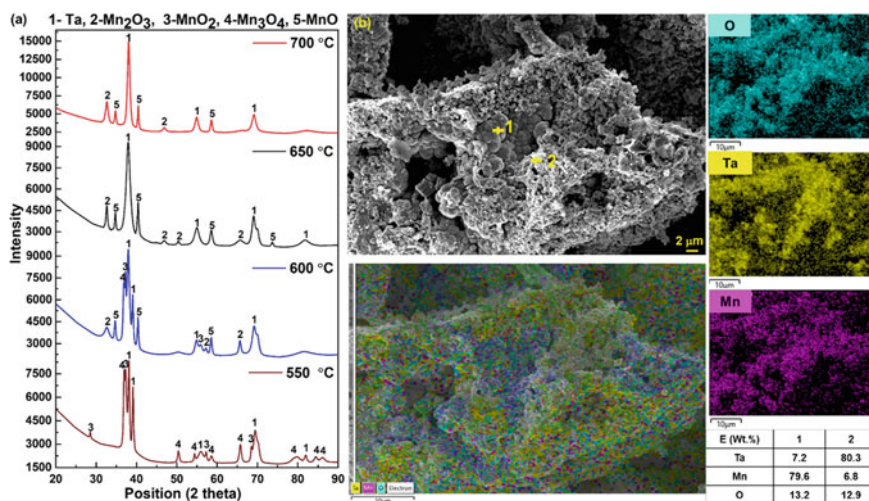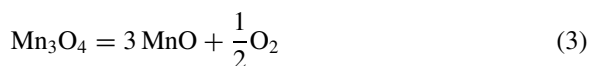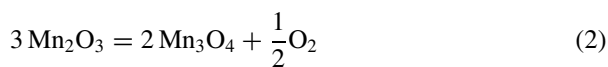
Fig. 3 a Effect of pyrolysis temperature on the reduction of Mn-oxide phases, **b** SEM–EDS and elemental mapping of the sintered core

Leaching of Manganese

The elemental analysis of the pyrolysis products (SC and $< 212\ \mu m$) is shown in Fig. 4a. The sintered core consists of Mn $\sim 17\%$ and Ta $\sim 73\%$ values, while the $< 212\ \mu m$ fraction consists majorly of Si (SiO_2)—78.3%, Mn—6.3%, Ta—5.3%, and Ag—2.4% values. The leaching (1M citric acid) of the SC recovered after pyrolysis is aimed at dissolving Mn values in the leach solution and consequently separating it from valuable Ta values. The pH of the solution was observed as 2.3–2.7, and according to the Eh–pH diagram (Fig. 4b), the dissolution of Mn as $+ 2$ ions is favorable under such conditions. The SEM–EDS analysis confirms the Ta-rich leach residue, consisting of 4.5% Mn (Fig. 4c). It is observed that with an increase in the pyrolysis temperature, the recovery of Ta increased from 81 to 94% (550–650 °C) and decreased slightly at 700 °C (91.5%). The minimal recovery of Mn ($< 8\%$), leads to the concentration and effective separation of Ta in leach residue with a recovery of $\sim 94.8\%$ and 96% purity.

E	Ta	Mn	O
Wt.%	74.9	4.5	20.6
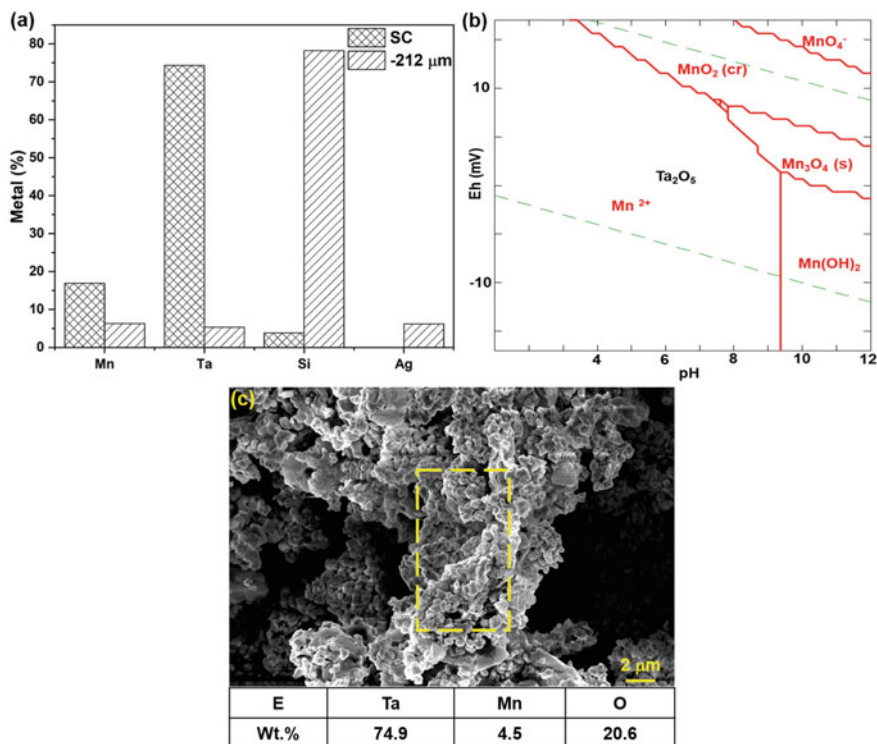
Fig. 4 **a** Elemental percentage of the pyrolysis products **b** Eh–pH diagram for Ta-Mn-H_2O system, **c** SEM analysis of the acid-leached residue
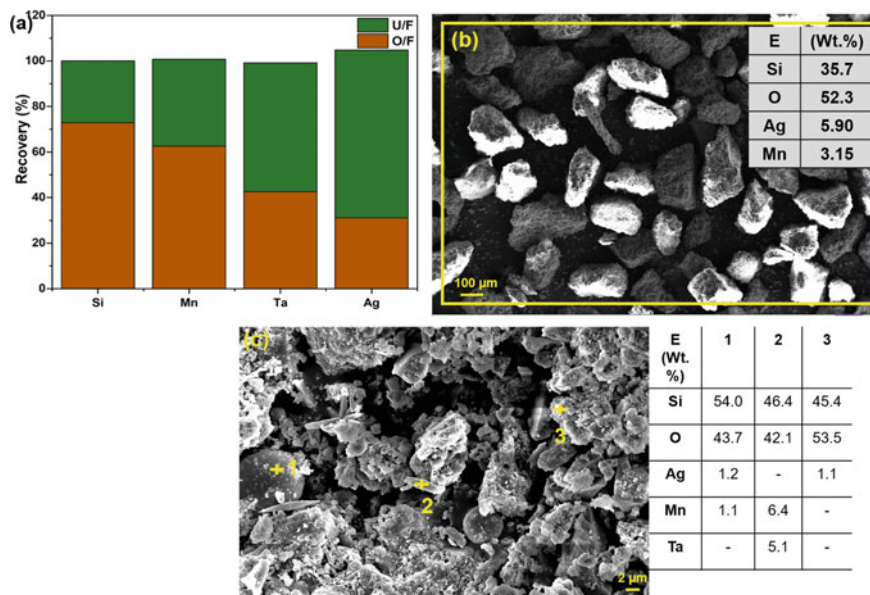
Fig. 5 **a** (%) Metal recovery in the overflow and underflow fractions. SEM/EDX analysis of **b** underflow product, **c** overflow product

Metal Recovery from Undersized Fraction

The $< 212\,\mu m$ fraction was subjected to density-based separation to separate heavier metals such as Ag (10.48 g/cm^3) from lighter SiO$_2$ (2.65 g/ cm^3). The metals (Ag and Ta values) are enriched in the underflow fraction with corresponding recovery of 73.7% and 56.6%, respectively, while 57.3% Si was recovered in the overflow fraction (Fig. 5a). The elemental mapping of the obtained underflow product is shown in Fig. 5b. A mixed morphology with variable particle sizes is revealed in the underflow fraction. The silver particles are finer, clustered, and dispersed throughout the matrix, and the association between various elements appears interlocked. The misplacement of Mn to the overflow fraction could be due to the finer particle morphology and adherence with lighter particles (Fig. 5c).

Mass Balance

It was calculated that processing 100 g of discarded Ta capacitors yields 32 g of Ta in the leach residue while 2.8 g of Mn is recovered from the leach solution [15]. Moreover, metallic values of ~ 2.4 g were recovered in the sink product of $< 212\,\mu m$. Pyrolysis and manual separation were found effective in the enrichment of Ta values

from 34 to 74% in the sintered core, while Ag values increased from 0.94 to 2.4% in the < 212 μm fraction.

Conclusions

In this study, end-of-life Ta capacitors are evaluated as a secondary source of Ta, Mn, and Ag. Pyrolysis as a pre-treatment was found efficient for the decomposition of the outer organic housing of Ta capacitors. The optimum pyrolysis parameters were chosen as 650 °C and 40 min based on the transformation of MnO_2 to lower oxides. It is observed that the pyrolysis products (a) sintered core consisted of Mn ~ 17% and Ta ~ 74.3% values, and (b) < 212 μm fraction consisted majorly of Si ~77.6%, Mn ~ 6.3%, Ta ~ 5.3%, and Ag ~ 2.4% values. During pyrolysis, the thermal transformation of MnO_2 was beneficial for subsequent separation of the Mn and Ta values. Leaching of the sintered core resulted in a higher Ta recovery of ~ 94% and minimal Mn recovery of ~ 6.3%. The sink-float test on −212 μm resulted in the separation of metallic values (Ag ~ 73.7% and Ta ~ 56.6%) in the underflow fraction, while 57.3% Si was recovered in the overflow fraction. It is deduced that 100 g of Ta capacitors can yield 34 g of Ta, which is equivalent to 0.28 tons of primary ore.

References

1. Khanna R, Saini R, Park M, Ellamparuthy G, Biswal SK, Mukherjee PS (2020) Factors influencing the release of potentially toxic elements (PTEs) during thermal processing of electronic waste. Waste Manag 105:414–424. https://doi.org/10.1016/j.wasman.2020.02.026. Epub 2020 Feb 29 PMID: 32126369
2. Forti V, Baldé CP, Kuehr R, Bel G (2020) The global E-waste monitor 2020: quantities, flows, and the circular economy potential. USA
3. Işıldar A, Rene ER, van Hullebusch ED, Lens PNL (2018) Electronic waste as a secondary source of critical metals: management and recovery technologies. Resour Conserv Recycl 135:296–312. https://doi.org/10.1016/j.resconrec.2017.07.031
4. Hao J, Wang Y, Wu Y, Guo F (2020) Metal recovery from waste printed circuit boards: a review for current status and perspectives. Resour Conserv Recycl 157. https://doi.org/10.1016/j.resconrec.2020.104787
5. Shen Y, Chen X, Ge X, Chen M (2018) Chemical pyrolysis of E-waste plastics: char characterization. J Environ Manage 214:94–103. https://doi.org/10.1016/j.jenvman.2018.02.096
6. Suresh SS, Bonda S, Mohanty S, Nayak SK (2018) A review on computer waste with its special insight to toxic elements, segregation and recycling techniques. Process Saf Environ Prot 116:477–493. https://doi.org/10.1016/j.psep.2018.03.003
7. Ueberschaar M, Otto SJ, Rotter VS (2017) Challenges for critical raw material recovery from WEEE—the case study of gallium. Waste Manag 60:534–545. https://doi.org/10.1016/j.wasman.2016.12.035

8. Kinsman LMM, Crevecoeur RAM, Singh-Morgan A, Ngwenya BT, Morrison CA, Love JB (2020) Tantalum recycling by solvent extraction: chloride is better than fluoride. Metals (Basel) 10:346. https://doi.org/10.3390/met10030346

9. Shikika A, Sethurajan M, Muvundja F, Mugumaoderha MC (2020) A review on extractive metallurgy of tantalum and niobium. Hydrometallurgy 198:105496. https://doi.org/10.1016/J.HYDROMET.2020.105496

10. United States Geological Survey (USGS) (2020) Mineral Commodity Summaries 2020

11. Habashi F (1997) In: Handbook of extractive metallurgy. vol 2(1). pp 737–752

12. Mineta K, Okabe TH (2005) Development of a recycling process for tantalum from capacitor scraps. J Phys Chem Solids 66:318–321. https://doi.org/10.1016/j.jpcs.2004.06.060

13. Jadhao PR, Ahmad E, Pant KK, Nigam DPK (2022) Advancements in the field of electronic waste recycling: critical assessment of chemical route for generation of energy and valuable products coupled with metal recovery. Sep Purif Technol 289:120773. https://doi.org/10.1016/J.SEPPUR.2022.120773

14. Yang J, Feng J, Li W, Chen X, Liu X, Ruan J, Qiu R, Xiong Y, Tian S (2019) A resource-utilization way of the waste printed circuit boards to prepare silicon carbide nanoparticles and their photocatalytic application. J Hazard Mater 373:640–648. https://doi.org/10.1016/j.jhazmat.2019.03.115

15. Mir S, Dhawan N (2022) Recycling of metallic values from discarded tantalum capacitors. Miner Process Extr Metall 132(2):87–98. https://doi.org/10.1080/25726641.2023.2177243

Novel Process for Tin Recovery from Waste Print Circuit Boards (WPCBs) by Selective Oxidation Roasting Under H$_2$O Atmosphere

Zijian Su, Bin Lei, Qiuyu Li, and Yuanbo Zhang

Abstract Waste printed circuit boards (WPCBs) are crucial secondary resources that contain a large number of valuable metals (Cu, Sn, Ti, Ni, Ag, Au, etc.), which have enormous recovery value. Current methods of extractive metallurgy have been principally focused on recovering copper and precious metals, with tin being largely overlooked. However, research has shown that the oxidation of tin to $SnO_{(g)}$ by $H_2O_{(g)}$ is a viable option. This study presents a new process for selectively recovering tin from WPCBs via oxidative roasting under $H_2O_{(g)}$ conditions. Thermodynamic analysis was used to investigate the transformation and regulation of metallic tin to gaseous SnO. It showed that tin could be highly selectively separated from WPCBs. The volatilization of Sn reaches 95.2% under optimal experimental conditions. In addition, copper and noble metals were enriched in the roasted residues and could be used for copper smelting.

Keywords WPCBs · Thermodynamic analysis · Selective recovery · Oxidation volatilization · SnO

Introduction

World tin ore reserves have been exhausted gradually during the past two decades. The exploitation of primary tin ores (mostly lean-grade ores of tin) was insufficient for refined tin production. Therefore, tin extraction from tin-containing secondary resources is becoming a research hotspot [1]. It was reported that the refined tin used for solder production accounted for 48% of the tin consumption in 2021, and the solder was mainly used in electronic products. Waste printed circuit boards (WPCBs) are typical electronic waste containing a large number of valuable metals (Cu, Sn,

Z. Su · B. Lei · Q. Li · Y. Zhang (✉)
School of Minerals Processing and Bioengineering, Central South University, Changsha 410083, China
e-mail: sintering@csu.edu.cn

Ag, Au, Ti, Ni, etc.), with Cu and Sn as the main ones, which have very high recycling values [1, 2].

In recent years, the hydrometallurgical process was commonly utilized to convert valuable metals in WPCBs, using inorganic acids, cyanides, thiourea thiosulfate, etc. However, these processes aimed to recover precious metals such as copper, gold, and silver, and a large amount of tin was lost in the leaching process. Additionally, the hydrometallurgical approach has drawbacks such as low processing capacity and excessive acid consumption [3–6].

The pyrometallurgical process was still essential for the comprehensive utilization of WPCBs, of which WPCBs were always used as primary Cu-bearing materials for copper smelting. Tin was partially reduced to the alloy phase, while most of the tin was easily combined with CaO or SiO_2 and lost in the smelting slag, making it difficult to separate and recover Sn [7, 8]. In addition, most studies have been devoted to the recovery of Cd, Zn, and Pb from pre-treated WPCBs, using vacuum distillation technology. Tin was difficult to achieve high-value utilization [9, 10].

Previous studies have shown that Sn can be converted to $SnO_{(g)}$ and volatilized at high temperatures by moderating the CO-CO_2 atmosphere [2, 11, 12]. Similarly, Sn was easily converted to $SnO_{(g)}$ in the H_2O-H_2 atmosphere. It was noteworthy that the saturation vapor pressure of $SnO_{(g)}$ was much higher than that of the metals Sn, SnO_2, Cu, Ag, Au, etc., the tin component could be converted to SnO and separated from WPCBs.

Based on the above studies, a new process for selective oxidative recovery of Sn from WPCBs under an $H_2O_{(g)}$ atmosphere was developed in this paper. The conversion and conditioning process from metallic tin to gaseous SnO in WPCBs was investigated using thermodynamic analysis, XRD, and ICP. The volatilization rate of tin under optimal conditions reached 95.2%. This work provided an efficient and clean pretreatment idea for the high-value utilization of WPCBs.

Materials and Methods

Materials

Pretreatment will significantly enhance the separation and recovery efficiency of WPCBs. The pyrolysis slag pyrolyzed at 450–550 °C was used in this study [13]. The XRD (Bruker D8 advance, Germany) analysis of the WPCBs pyrolysis slag in Fig. 1 showed that the sample mostly was Cu-Sn alloys and Sn monomers. Additionally, the diffraction peaks of the Cu monomers appeared weak, and no diffraction peaks of other impurities were found.

To further clarify the main chemical components of the pyrolysis slag of WPCBs, X-ray fluoroscopy (XRF, Axios mAX, PANalytical Co., Ltd., in Holland) was carried out as shown in Table 1. The results indicated that Cu and Sn were 38.37% and 15.46%, respectively. The impurity elements (including Si, Ca, and Al) were 27.65%,
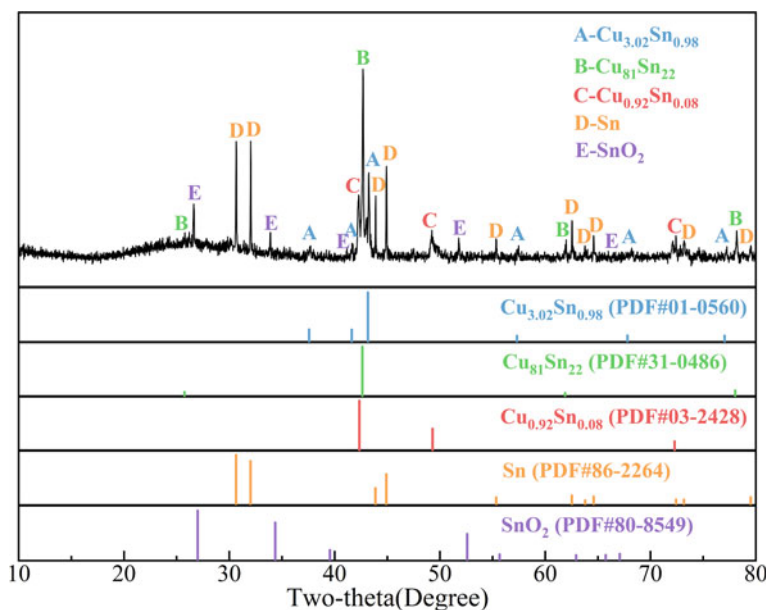
Fig. 1 XRD pattern of WPCBs after pyrolysis

Table 1 Chemical composition of WPCBs after pyrolysis

Cu/wt.%	Sn/wt.%	Si/wt.%	Ca/wt.%	Al/wt.%	Ag/g·t^{-1}	Au/g·t^{-1}
38.37	15.46	27.65	8.75	6.38	714.20	22.20

8.75%, and 6.38%, respectively. The precious metals Ag and Au were very low, less than 1000 ppm.

Materials

The experiments were carried out in a horizontal tube furnace. To investigate the effect of roasting parameters on the volatilization of WPCBs pyrolysis slag, 1.000 ± 0.005 g of ground pyrolysis slag samples weighed, and placed in corundum crucibles, then roasted in the furnace. After roasting for 0.5–2 h, the cooled samples were weighed and analyzed for residual tin content by ICP (Thermo Fisher Corporation, U.S.). The volatilization can be calculated using the following equation:

$$(C_{Sn} \times m_0 - C'_{Sn} \times m_1)/C_{Sn} \times m_0 \times 100\% \tag{1}$$

where m_0 is the quality of the sample before the roasting, (g); m_1 is the quality of the sample after the roasting, (g); γ is the volatilization rate of Sn, (wt.%); C_{Sn} is the tin content of the sample before the roasting, (wt.%); C'_{Sn} is the tin content of the sample after the roasting, (wt.%).

Results and Discussion

Thermodynamic Analysis

According to the previous study [2], the oxidation of Sn in the H_2O-H_2 atmosphere was similar to the oxidation in the atmosphere of $CO–CO_2$. The reaction of Sn → SnO → SnO_2 proceeded as a stepwise oxidation reaction in the $H_2O–H_2$ atmosphere. The possible reactions in the WPCBs-H_2O-H_2 system, mainly oriented to Sn, Cu, Ag, and Au, were given according to Table 1, the corresponding $\Delta G_T^\theta-T$ relationships were shown in Table 2, and the corresponding $\Delta G_T^\theta-T$ diagrams were plotted as shown in Fig. 2a.

It was worth noting that Sn and SnO were more easily oxidized under the H_2O-H_2 atmosphere than other phases, while Cu, Ag, and Au required higher temperatures. In addition, the saturated vapor pressures of the main components in WPCBs are shown in Fig. 2b, including Sn, SnO_x, Cu, Ag, and Au. At the same temperature, the saturated vapor pressures of SnO were higher than those of the other phases, and it was more easily converted to the gas phase and volatilized at temperatures higher than 1100 K, whereas Cu, Ag, and Au were enriched in the roasting slag.

Displayed in Fig. 3 were equilibrium diagrams for gas-phase reactions involving prominent elements such as Sn, Cu, Au, and Ag. These reactions occurred between SnO and other phases within the WPCBs-H_2O-H_2 system at a consistent pressure of 1 atm (p^θ). The diagrams specified the partial pressure of $SnO_{(g)}$ within the range of 10^{-7}–10^{-1} atm to provide additional insight into the oxidation equilibrium. The data plotted in Fig. 3 can be obtained from the $\Delta G_T^\theta-T$ relationship for Eqs. (1)−(6), combined with $\Delta G_T = \Delta G_T^\theta + RT\ln Q$, where R is the ideal gas constant (8.314 J/mol·K), T is the Kelvin (K) temperature, and Q is the reaction quotient under the given conditions.

Table 2 $\Delta G_T^\theta-T$ relationship of corresponding reactions

Number	Reaction equations	ΔG_T^θ-T (kJ/mol)
Equation (1)	$Sn + H_2O(g) = SnO(g) + H_2(g)$	$\Delta G_T^\theta = 258.1–0.109\ T$
Equation (2)	$SnO(g) + H_2O(g) = SnO_2 + H_2(g)$	$\Delta G_T^\theta = -347.9 + 0.205\ T$
Equation (3)	$Sn + 2H_2O(g) = SnO_2 + 2H_2(g)$	$\Delta G_T^\theta = -89.9 + 0.097\ T$
Equation (4)	$Cu + 1/2H_2O(g) = 1/2\ Cu_2O + 1/2H_2(g)$	$\Delta G_T^\theta = 38.1 + 0.009\ T$
Equation (5)	$Ag + 1/2H_2O(g) = 1/2\ Ag_2O + 1/2H_2(g)$	$\Delta G_T^\theta = 106.8 + 0.001\ T$
Equation (6)	$Au + 3/2H_2O(g) = 1/2\ Au_2O_3 + 3/2H_2(g)$	$\Delta G_T^\theta = 370.2 + 0.046\ T$
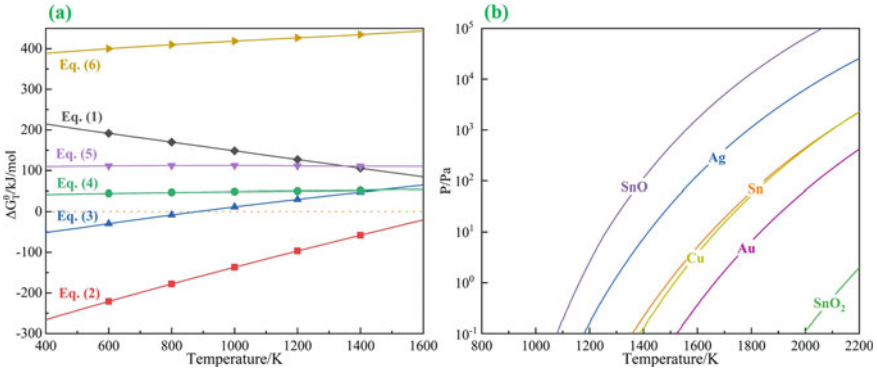
Fig. 2 ΔG_T^θ–T diagram and saturated vapor pressure diagram of WPCBs during the oxidation process
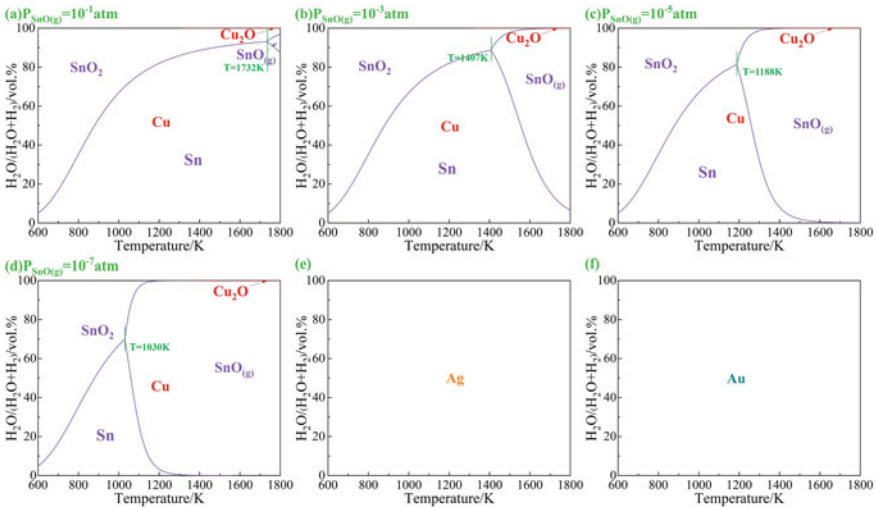
Fig. 3 Gas-phase equilibrium diagram of the Sn-H_2O-H_2, Cu-H_2O-H_2, Ag-H_2O-H_2, and Au-H_2O-H_2 system

The figures displayed in Fig. 3a−d indicated that an increase in H_2O content resulted in higher conversion rates of Sn to $SnO_{(g)}$. At higher temperatures, $SnO_{(g)}$ formation was more favored. The progression of reactions Eqs. (1) and (2) was demonstrated in Table 2. As the partial pressure of $SnO_{(g)}$ decreased, the reaction Eq. (2) was inhibited, and the reaction Eq. (1) was promoted. This led to an expansion of the stabilization region of $SnO_{(g)}$. During this process, Cu remained a monomer, while the generation of Cu_2O was only possible at higher H_2O content and temperature. Additionally, the temperature point at which Sn, SnO, and SnO_2 coexist decreased significantly as the partial pressure of $SnO_{(g)}$ reduced. In Fig. 3d,

the oxidizing system maintains a high gas flow rate, and Sn can be converted to $SnO_{(g)}$ at a temperature of 1030 K when $SnO_{(g)}$ is 10^{-7} atm. However, under the H_2O-H_2 system, Ag and Au remain in their monomer form and do not oxidize. By regulating the H_2O-H_2 atmosphere and reaction temperature, thermodynamic analysis can be utilized to achieve efficient separation of Sn from pyrolysis slag.

Effect of Parameters on the Volatilization of Tin

Thermodynamic analysis has revealed that the roasting atmosphere and temperature have the most significant impact on the separation of Sn oxidation. To explore this further, we studied the effects of different roasting atmospheres and temperatures on the rate of volatilization of Sn oxidation, while keeping the oxidizing roasting time fixed at 2 h and gas flow rate at 4 L/min.

As seen in Fig. 4, the rate of Sn volatilization increased with a rise in $H_2O_{(g)}$ content, given a fixed roasting time of 2 h, a gas flow rate of 4 L/min, and a roasting temperature of 1200 °C. However, if the $H_2O_{(g)}$ content was too high, the H_2 content in the system decreased, which led to a significant trend of SnO_2 generation. Conversely, if the H_2O content was low, the reduction potential in the system was high, making it difficult for Sn to efficiently oxidize to $SnO_{(g)}$ and volatilize. Therefore, the optimal $H_2O_{(g)}$ content for achieving the peak rate of Sn volatilization was 90–95%.

Figure 5 shows that at a fixed roasting time of 2 h, a gas flow rate of 4 L/min, an $H_2O_{(g)}$ content of 92.5%, and a roasting temperature of 800 °C, the rate of Sn volatilization was only 15.2%. The gasification temperature of Sn was not reached. However, at 1100 and 1200 °C, the rate of Sn volatilization reached 88.7% and 95.2%, respectively. Further increasing the temperature to 1300 °C did not significantly

Fig. 4 Effect of H_2O content on tin volatilization
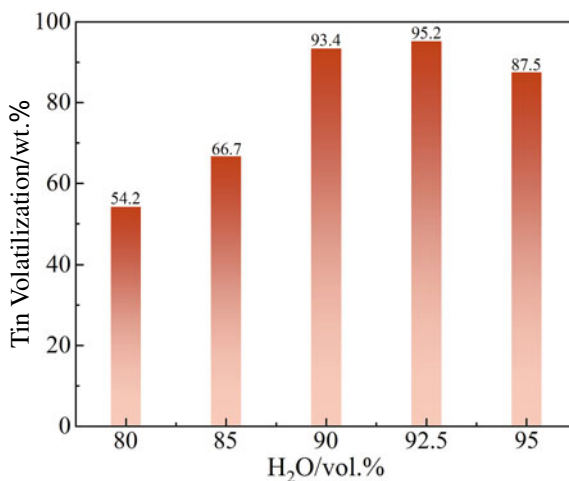
increase the rate of tin volatilization, making 1200 °C the optimal temperature for Sn volatilization.

In Fig. 6, it was evident that the volatilization of Sn begins slowly at the start of the oxidation roasting reaction. However, when the roasting time was extended to 1 h, the rate of Sn volatilization increased significantly. After roasting for 2 h, the rate of tin volatilization leveled off. Hence, the optimal oxidation roasting time was 2 h.

Fig. 5 Effect of oxidation roasting temperature on tin volatilization
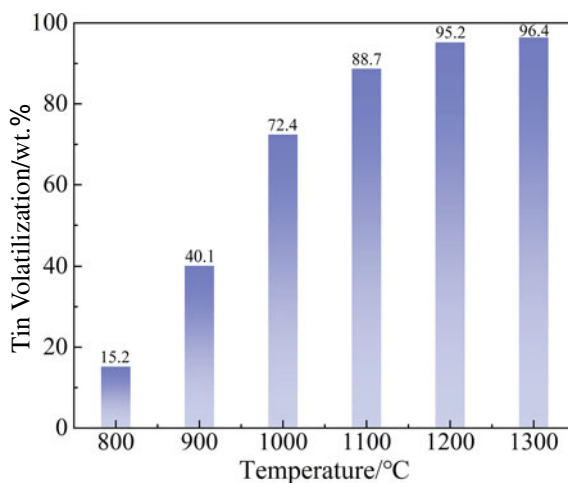
Fig. 6 Effect of oxidation roasting time on tin volatilization
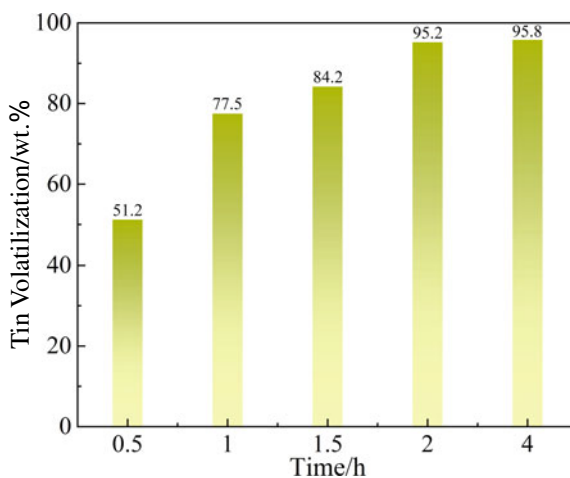
Analysis of Roasting Results and Products

The samples analyzed using XRD were volatiles obtained at a roasting temperature of 1200 °C with an H_2O content of 92.5%. The analysis, as shown in Fig. 7, revealed that the primary phase component was SnO_x with weak tin diffraction peaks. The absence of any copper-containing phase was consistent with thermodynamic calculations. These results indicate that oxidative volatilization is an effective method for separating tin from WPCBs. However, it's worth noting that the volatilized $SnO_{(g)}$ might undergo disproportionation reactions, leading to the formation of complex volatile phases such as tin oxide (SnO_x).

Based on the above results, the optimal roasting parameters were as follows: roasting temperature of 1200 °C for 120 min under 92.5% $H_2O_{(g)}$ atmosphere, gas flow rate of 4 L/min. As shown in Table 3, the Sn recovery of volatile products was 95.2%, with a Sn grade of 74.32%. Cu, Ag, and Au remained in the roasted residues totally.
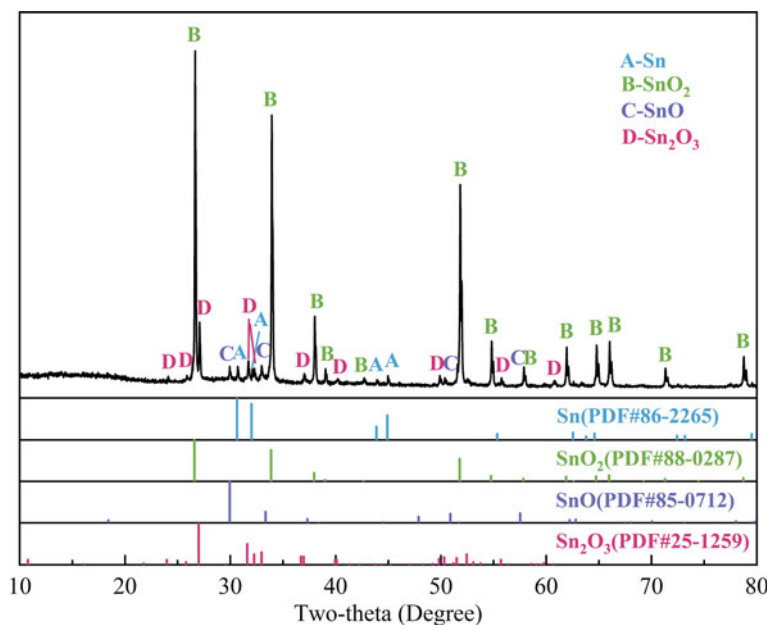
Fig. 7 XRD patterns of volatiles

Table 3 The results obtained under optimal conditions

	Grade				Recovery/wt.%			
	Sn/wt.%	Cu/wt.%	Ag/g·t^{-1}	Au/g·t^{-1}	Sn	Cu	Ag	Au
Raw materials	15.46	38.37	714.2	22.2	–	–	–	–
Roasted residues	0.88	45.60	848.7	26.38	4.8	100	100	100
Volatile products	74.32	–	–	–	95.2	0	0	0

Conclusions

This study proposed a new strategy for separating and recovering tin from WPCBs by selective oxidation under an H_2O atmosphere. According to the thermodynamic analysis results, tin can be selectively volatilized to achieve the separation of tin by adjusting the $H_2O_{(g)}$ content and temperature; tin can be separated and collected as disproportionation products (Sn, SnO$_x$). Under the selected parameters, tin's optimum oxidation volatilization rate reached 95.2% for calcination temperature 1200 °C, $H_2O/(H_2O + H_2)$ content 92.5%, and roasting time 120 min.

References

1. Li H, Qin W, Lin J, Tian Z, Jiao F, Yang C (2021) Tracing the global tin flow network: highly concentrated production and consumption. Resour Conserv Recycl 169:105495
2. Su Z, Hou W, Wang J, Zhang Y, Jiang T (2023) One-step separation of tin from e-waste by a chemical vapor transport process (CVT): preparation of nano-SnO$_2$. Waste Manage 157:330–338
3. Zhou W, Liang H, Xu H (2021) Recovery of gold from waste mobile phone circuit boards and synthesis of nanomaterials using emulsion liquid membrane. J Hazard Mater 411:125011
4. Guo S, He J, Zhu L, Chen H, Zhou K, Xu J, Chen Z (2022) Recovery of metallic copper from waste printed circuit boards via H_3NO_3S-NaCl-H_2O_2 leaching system. J Clean Prod 357:131732
5. Li H, Oraby E, Eksteen J (2021) Recovery of copper and the deportment of other base metals from alkaline glycine leachates derived from waste printed circuit boards (WPCBs). Hydrometallurgy 199:105540
6. Rao M, Singh K, Morrison C, Love J (2021) Recycling copper and gold from e-waste by a two-stage leaching and solvent extraction process. Sep Purif Technol 263:118400
7. Hao J, Wang Y, Wu Y, Guo F (2020) Metal recovery from waste printed circuit boards: a review for current status and perspectives. Resour Conserv Recycl 157:104787

8. Faraji F, Golmohammadzadeh R, Pickles C (2022) Potential and current practices of recycling waste printed circuit boards: a review of the recent progress in pyrometallurgy. J Environ Manage 316:115242

9. Zhan L, Xu Z (2014) State-of-the-art of recycling E-wastes by vacuum metallurgy separation. Environ Sci Technol 48(24):14092–14102

10. Zhan L, Xiang X, Xie B, Sun J (2016) A novel method of preparing highly dispersed spherical lead nanoparticles from solders of waste printed circuit boards. Chem Eng J 303:261–267

11. Su Z, Zhang Y, Liu B, Zhou Y, Jiang T, Li G (2016) Reduction behavior of SnO_2 in the tin-bearing iron concentrates under $CO–CO_2$ atmosphere. Part I: effect of magnetite. Powder Technol 292:251–259

12. Su Z, Zhang Y, Han B, Liu B, Lu M (2017) Synthesis, characterization, and catalytic properties of nano-SnO by chemical vapor transport (CVT) process under $CO-CO_2$ atmosphere. Mater Des 121:280–287

13. Liu J, Wang H, Zhang W, Wang T, Mei M, Chen S, Li J (2022) Mechanistic insights into catalysis of in-situ iron on pyrolysis of waste printed circuit boards: comparative study of kinetics, products, and reaction mechanism. J Hazard Mater 431:128612

Recovery of Indium from Waste Liquid Crystal Display Screen by Reduction Roasting Under H_2-H_2O Atmosphere

Zijian Su, Xiaoning Hu, Qijie Guo, and Yuanbo Zhang

Abstract Indium is a strategic critical metal in manufacturing indium-tin oxide (ITO) thin films for LCD/LED screens. Nevertheless, indium in Earth's crust is a rare dispersion with an average abundance of 0.02 ppm, which is difficult to recover from primary ore. Hence, scholars focused on Indium recovery from waste LCD screens using hydrometallurgy technologies, which were always with long process. In this paper, a novel process for the separation and recovery of indium from waste LCD by roasting under an H_2-H_2O atmosphere is proposed. Under optimal conditions, In_2O_3 can be reduced selectively to gaseous In_2O, and then In_2O can be recovered efficiently. The effects of roasting parameters on indium recovery were studied utilizing thermodynamic analysis, XRD, and ICP. The results showed that the indium in waste LCD can be reduced to $In_2O_{(g)}$ under the H_2-H_2O atmosphere at 1100–1200 °C, the recovery of indium was up to 96.53% with an enrichment ratio of 3700.

Keywords Waste LCD screen · Indium recovery · Reduction roasting

Introduction

Indium has excellent electrical and optical properties at the same time, so it is widely used in computer, semiconductor, and photoelectric devices, and plays an important role in modern society. However, as a rare metal, indium has no independent mineral deposits in the earth's crust, and its average abundance is only 0.02 ppm. It is mainly obtained by the side reaction of lead and zinc smelting, which is difficult to extract and has high mining cost. It has been listed as a strategic resource by many countries. Recovering indium from electronic waste can not only realize the sustainable utilization of indium but also protect the environment, so it is of great significance.

The production of ITO is the main use of indium, accounting for more than 90% of the total indium production. ITO is a mixture of In_2O_3 and SnO_2 (the mass

Z. Su · X. Hu · Q. Guo · Y. Zhang (✉)
School of Minerals Processing and Bioengineering, Central South University, Changsha 410083, China
e-mail: sintering@csu.edu.cn

ratio is usually 90:10 or 95:5), which ensures high light transmittance and high conductivity, so it is very suitable to be used as a glass electrode of liquid crystal display (LCD). The content of indium in LCD is about 200 ppm, which is far greater than that of natural minerals, and it has a high recycling value [1]. At the same time, the consumption of LCD is very large and is widely used in notebook computers, smartphones, televisions, and other electronic devices. These electronic devices are updated very quickly, and the number of discarded LCDs is quite large every year. Therefore, recovering indium from waste LCD is an important source of indium regeneration.

At present, scholar's research on indium recovery in LCD focuses on the hydrometallurgy process. The most studied is to leach indium from LCD with strong acids such as hydrochloric acid, sulfuric acid, and nitric acid, and then realize the separation and recovery of indium by electrolysis and extraction [2–4]. Because strong acid has a great impact on the environment, some scholars try to replace it with weak acid such as organic acid or bioleaching, but the recovery rate of indium will decrease [5, 6]. In addition, hydrometallurgy generally has the problems of long leaching time and low production efficiency, so some scholars have developed a process combining rapid grinding with acid leaching, which can shorten the leaching time while ensuring a high leaching rate [7].

However, the shortcomings of hydrometallurgy, such as a large amount of waste liquid and high requirements for raw material pretreatment, have not been overcome, which greatly limits the practical application of hydrometallurgy in indium recovery of LCD. However, pyrometallurgy, which has been studied relatively little, does not have these problems. Typical processes for recovering indium by pyrometallurgy include chlorination roasting and vacuum metallurgy. In_2O_3 in LCD is converted into indium chloride, and then indium chloride can be separated and recovered at high temperature or under vacuum by using the low boiling point [8–10]. Our previous research also proposed a pyrometallurgical recovery process of indium, which used different saturated vapor pressures to separate indium and tin from ITO waste targets by roasting in a $CO\text{-}CO_2$ atmosphere [11]. However, these traditional pyrometallurgical processes are not environmentally friendly, and today, with the increasingly serious environmental problems, a cleaner recovery method is called for.

In this paper, a new process of roasting, separating, and recovering indium from waste LCD in an $H_2\text{-}H_2O$ atmosphere is studied. Indium can be separated and recovered by selectively reducing In_2O_3 to $In_2O(g)$. In addition, the effects of roasting parameters on indium recovery were studied using thermodynamic analysis, XRD, SEM, and ICP. The results show that indium in waste LCD can be recovered efficiently at 1150°C in the atmosphere of 37.5% $H_2/(H_2 + H_2O)$, and the best recovery rate is as high as 96.53%, which provides an efficient and environmentally friendly recycling idea for waste LCD.

Materials and Methods

Materials

The LCDs used in this study are all purchased from the same waste recycling company. Manually disassemble and crush the LCD to obtain ITO glass. Then the ITO glass was put into a muffle furnace and baked at 600 °C for 1 h to remove the filter film and other organic substances on the surface, and then put into a sample-making machine to prepare ITO glass powder.

The ITO glass powder was analyzed by X-ray fluoroscopy (XRF, Axios mAX, PANalytical Co., Ltd., in Holland), assaying (wt.%) O 53.92, Si 26.27, Al 9.740, Ca 3.96, Sr 3.32, Mg 1.97, Ba 0.44, Fe 0.03 as well as S 0.03. In was not detected by XRF detection because the content of In in LCD did not reach the lower limit of XRF detection. Further quantitative analysis of ITO glass powder by ICP shows that the indium content of the LCD sample used in this study is 266.8 ppm and the tin content is 53.4 ppm.

Methods

The experiment was carried out in a horizontal tube furnace. To study the influence of baking parameters on indium volatilization in waste LCD, 1.0000 ± 0.0005 g of ITO glass powder was weighed, placed in a corundum crucible, and baked in a furnace. After roasting for a period of time, the cooled samples were weighed and the residual indium content was analyzed by ICP (Thermo Fisher Corporation, U.S.). The volatilization amount can be calculated by the following equation:

$$\gamma = \frac{C_{\text{In}} \times m_0 - C_{\text{In}'} \times m_1}{C_{In}} \times m_0 \times 100\% \tag{1}$$

where m_0 is the quality of the sample before the roasting, (g); m_1 is the quality of the sample after the roasting, (g); γ is the volatilization rate of In, (wt.%); C_{In} is the indium content of the sample before the roasting, (wt.%); C'_{In} is the indium content of the sample after the roasting, (wt.%).

Results and Discussion

Thermodynamic Analysis

The fluorescence results showed that the main impurity elements in ITO glass powder were Mg, Al, Si, Ca, Fe, Sr, and Ba. The saturated vapor pressures of the corresponding components of these elements were significantly lower than that of In_2O at the same temperature. Therefore, indium in waste LCD can be converted into gaseous In_2O by reduction conditions, and selective separation from other impurity elements can be realized.

The reduction order of In_2O_3 in the H_2-H_2O atmosphere was $In_2O_3 \rightarrow In_2O \rightarrow$ In [12]. All the possible reactions and their corresponding ΔG_T^θ−T relationships are shown in Table 1.

It can be found that if only thermodynamic conditions are considered, the existence conditions of In_2O were harsh, and the trend of direct reduction of $In_2O_3 \rightarrow$ In obviously exceeded that of reduction to In_2O. However, the reactants and products of these reactions were all involved in the gas phase, and the partial pressures of various gas phases had a great influence on the reactions. Reaction (1) only involved H_2 and H_2O, which was relatively simple, and the corresponding ΔG_T^θ−T−H_2/(H_2 + H_2O) diagram is shown in Fig. 1.

In_2O was involved in reactions (2) and (3), but as a reaction product, the specific partial pressure of In_2O changed with the progress of the reaction, so it cannot be determined. Assuming that the reaction was conducted at a constant pressure of 1 atmosphere, the partial pressures of In_2O are 10^{-2}, 10^{-3}, and 10^{-4}, respectively. The ΔG_T^θ−T−H_2/(H_2 + H_2O) diagram corresponding to reaction (2) is shown in Fig. 2a–c, and the ΔG_T^θ-T-H_2/(H_2 + H_2O) diagram corresponding to reaction (3) is shown in Fig. 2d–f. Figure 2g–i are the projections of the ΔG_T^θ-T-H_2/(H_2 + H_2O) diagram of the reaction (1), (2), and (3) on the ΔG_T^θ = 0 plane, and the zone marked ② is the temperature interval and gas phase range where only the reaction (2) occurs, which is our expected target reaction zone.

Table 1 ΔG_T^θ−T relationship of corresponding reactions

Number	Reaction equations	ΔG_T^θ-T (kJ/mol)
Equation (1)	$3H_2(g) + In_2O_3 = 3H_2O(g) + 2In$	$\Delta G_T^\theta = 188.16–0.1664\ T$
Equation (2)	$2H_2(g) + In_2O_3 = In_2O(g) + 2H_2O(g)$	$\Delta G_T^\theta = 386.93–0.2733\ T$
Equation (3)	$H_2(g) + In_2O(g) = 2In + H_2O(g)$	$\Delta G_T^\theta = -198.77 + 0.1069\ T$
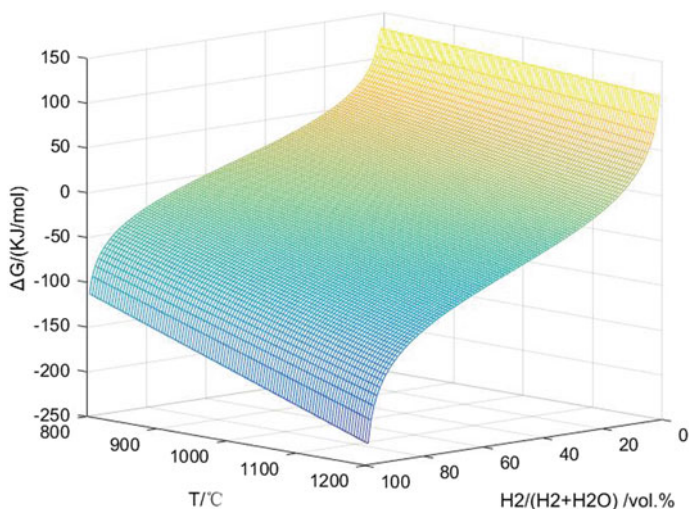
Fig. 1 $\Delta G_T^\theta - T - H_2/(H_2 + H_2O)$ diagram of reaction (1)
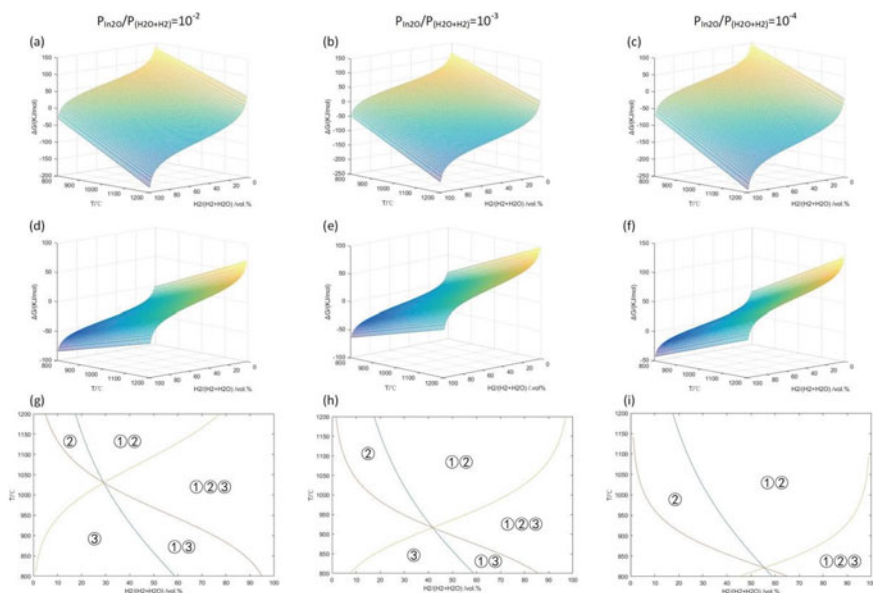
Fig. 2 $\Delta G_T^\theta - T - H_2/(H_2 + H_2O)$ diagrams of reaction (2) and (3) at different In_2O partial pressures and the projections of the $\Delta G_T^\theta - T - H_2/(H_2 + H_2O)$ diagram of the reaction (1), (2), and (3) on the $\Delta G_T^\theta = 0$ plane reaction temperature

Effect of Parameters on the Volatilization of Indium

Thermodynamic analysis has revealed that the roasting atmosphere and temperature have the most significant impact on the separation of indium reduction. To further study the influence of roasting temperature and atmosphere composition on indium volatilization, experiments were carried out at different temperatures and atmosphere compositions, with fixed roasting time of 1 h and total gas flow of 2 L/min.

As shown in Fig. 3, under the conditions of the roasting time of 1 h, total gas flow of 2 L/min, and roasting temperature of 1150 °C, the indium volatilization rate increased at first and then decreased with the increase of H_2 content. This is because when the H_2 content is low, increasing the H_2 content can promote the reduction of In_2O_3 to $In_2O_{(g)}$, so the volatilization rate increases. When the content of H_2 is excessive, $In_2O_{(g)}$ will be over-reduced to indium, which will reduce the volatilization rate.

In Fig. 4, it is obvious that the volatilization rate of indium increased with the increase in temperature, exceeding 90% in the temperature range of 1100–1200 °C, and the optimal volatilization rate can reach 96.53%. This is consistent with the results of thermodynamic analysis. With the increase in temperature, the reaction to form In_2O increased in the forward direction, which is stronger than the reaction to reduce to metal In.

It can be concluded from Fig. 5 that the volatilization rate of indium is very fast, and the reaction is complete at 45 min minutes. And the volatilization rate first increased and then decreased, because the initial partial pressure of $In_2O_{(g)}$ is small,
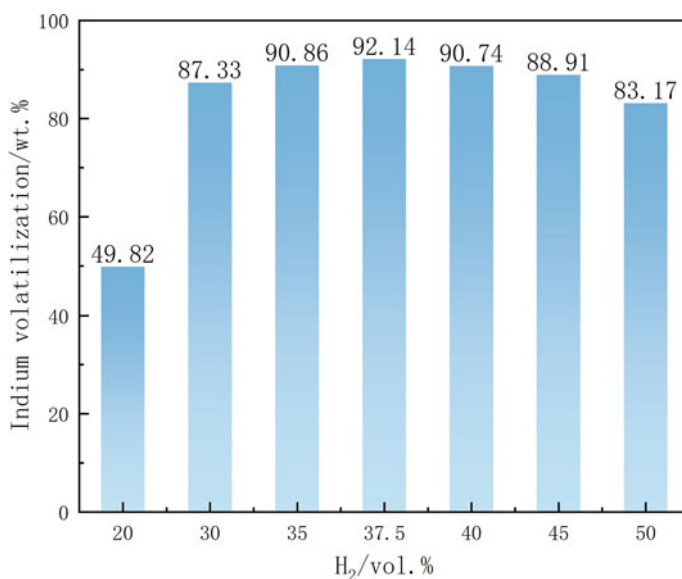
Fig. 3 Effect of H_2 content on indium volatilization
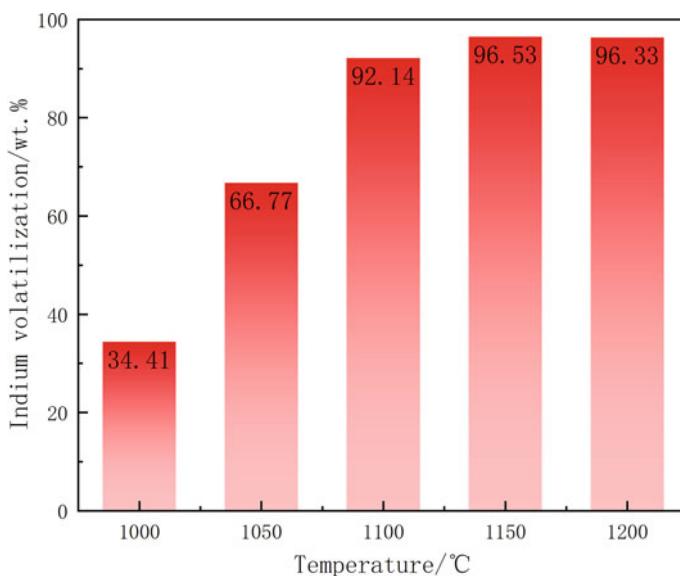
Fig. 4 Effect of temperature on indium volatilization

which is beneficial to the forward progress of the reaction. As the reaction progressed, the partial pressure of In_2O increased, which hindered the reaction and reduced the reaction rate.
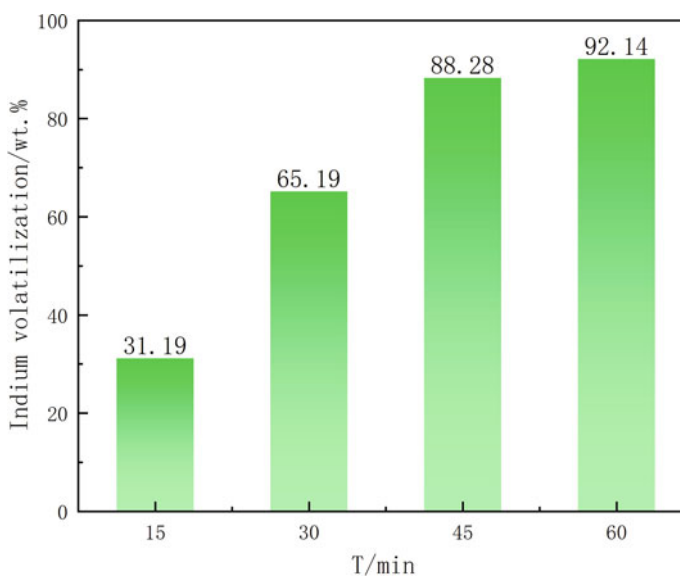
Fig. 5 Effect of roasting time on indium volatilization
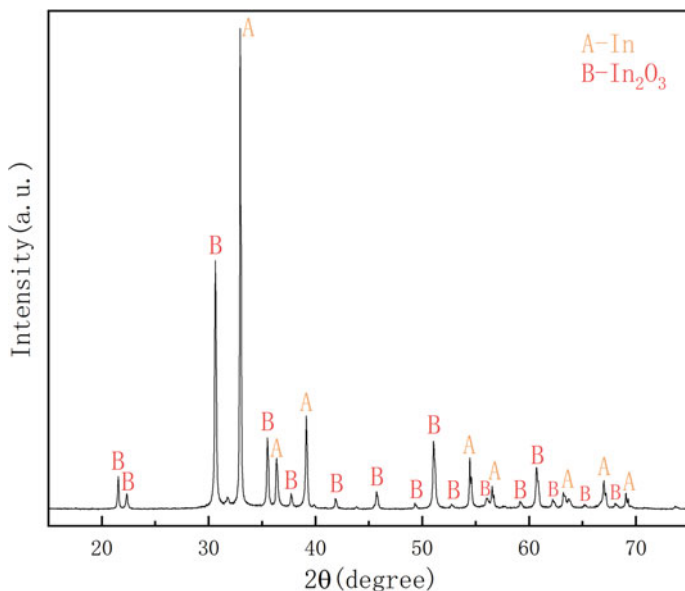
Fig. 6 XRD patterns of volatiles

Analysis of Roasting Results and Products

Because the content of indium in waste LCD was very low, the volatile products obtained from it were too small to be characterized, so we experimented with reagents with the same chemical composition under the best conditions to characterize the products instead. Figure 6 shows the XRD pattern of volatiles collected at the roasting condition 1150 °C with 37.5% H_2 content. It can be seen that the volatiles are mainly composed of In_2O_3 and In, which accords with the disproportionation reaction of $In_2O(In_2O \rightarrow In + In_2O_3)$. The product was very pure, and there were no diffraction peaks of other impurities, which showed that this method can indeed selectively recover In from waste LCD.

Conclusions

This study proposed a new strategy for separating and recovering indium from waste LCD under an H_2-H_2O atmosphere. According to the thermodynamic analysis results, indium can be selectively volatilized to achieve the separation of indium and other impurity metals by adjusting the H_2 content and temperature; indium can be separated and collected as disproportionation products. Under the selected parameters, the optimum reduction volatilization rate of indium reached 96.53% for a

roasting temperature of 1150 °C, $H_2/(H_2 + H_2O)$ content of 37.5%, and roasting time of 60 min.

References

1. Anić Vučinić A, Šimunić S, Radetić L, Presečki I (2023) Indium recycling from waste liquid crystal displays: is it possible ? Processes 11(6):1662
2. Illés IB, Nagy S, Kékesi T (2022) The recycling of pure metallic indium from waste LCD screens by a combined hydro-electrometallurgical method. Hydrometallurgy 213:105945
3. Fortin-Lecomte C, Tran LH, Rioux G, Coudert L, Blais J (2022) Recovery of indium from acidic leach solutions of spent LCD panels using ion exchange. Hydrometallurgy 210:105845
4. Song Q, Liu Y, Zhang L, Zhenming X (2021) Facile indium recovery from waste liquid crystal displays: chloride-facilitated indium electroreduction and stepwise Cu/MoO$_2$ and indium electrodeposition. J Hazard Mater 415:125599
5. Schuster J, Ebin B (2021) Investigation of indium and other valuable metals leaching from unground waste LCD screens by organic and inorganic acid leaching. Sep Purif Technol 279:119659
6. Cui J, Zhu N, Mao F, Pingxiao W, Dang Z (2021) Bioleaching of indium from waste LCD panels by Aspergillus niger: method optimization and mechanism analysis. Sci Total Environ 790:148151
7. Qin J, Ning S, Fujita T, Wei Y, Zhang S, Lu S (2021) Leaching of indium and tin from waste LCD by a time-efficient method assisted planetary high energy ball milling. Waste Manage 120:193–201
8. Zhang L, Xu Z (2017) C, H, Cl, and in element cycle in wastes: vacuum pyrolysis of PVC plastic to recover indium in LCD panels and prepare carbon coating. Acs Sustain Chem Eng 5(10):8918–8929
9. Ma E, Xu Z (2013) Technological process and optimum design of organic materials vacuum pyrolysis and indium chlorinated separation from waste liquid crystal display panels. J Hazard Mater 263:610–617
10. Takahashi K, Sasaki A, Dodbiba G, Sadaki J, Sato N, Fujita T (2009) Recovering indium from the liquid crystal display of discarded cellular phones by means of chloride-induced vaporization at relatively low temperature. Metall Mater Trans A 40:891–900
11. Su Z, Wang Y, Zhang Y, Tao J (2023) A novel method for synchronous separation of In/Sn from waste indium tin oxide (ITO) target: In-situ regeneration of nano-ITO powder. Sep Purif Technol 310:123104
12. Su Z, Zhang Y, Liu B, Zhou Y, Jiang T, Li G (2016) Reduction behavior of SnO$_2$ in the tin-bearing iron concentrates under CO–CO$_2$ atmosphere. Part I: effect of magnetite. Powder Technol 292:251–259

Development and Assessment of Different Hydrometallurgical Processes for Sustainable Recovery of Rare Earths from Spent NdFeB Magnets

Aarti Kumari and Sushanta Kumar Sahu

Abstract The utilization of NdFeB magnets is extensive in cutting-edge technologies such as hybrid electric vehicles and wind turbines. These magnets possess a substantial REE (Rare Earth Elements) content, approximately 30%, which significantly surpasses the concentration found in natural REE ores. Due to their pronounced economic significance and the associated supply risks stemming from limited primary resources, REEs are classified as critical metals. With the NdFeB permanent magnet sector experiencing an annual growth rate of 20%, the recycling of end-of-life magnets emerges as a highly effective strategy for mitigating challenges related to the supply of essential raw materials. In the current investigation, three distinct processes have been developed to recover REEs from spent wind turbine magnets. These processes encompass (1) oxidation roasting-acid leaching, (2) chlorination roasting-water leaching, and (3) electrochemical dissolution. Optimization of process parameters has been meticulously undertaken for each of these methods to achieve the production of high-purity rare earth oxide (>99%). Furthermore, a comparative evaluation has been conducted, taking into account energy efficiency and environmental sustainability, to determine the most viable approach for the sustainable recovery of REEs from spent NdFeB magnets.

Keywords Rare earths · NdFeB magnet · Windmill · Roasting-leaching

A. Kumari (✉)
Department of Fuel, Minerals and Metallurgical Engineering, Indian Institute of Technology (Indian School of Mines), Dhanbad 826004, India
e-mail: aarti@iitism.ac.in

S. K. Sahu
Metal Extraction and Recycling Division, CSIR-National Metallurgical Laboratory, Jamshedpur 831007, India

Introduction

Rare earth elements (REEs) constitute a fundamental component of contemporary technologies. Owing to their escalating demand and constrained availability, these elements have been designated as "critical raw materials" [1]. Primary sources of rare earths are both limited and widely dispersed. Extracting rare earths from primary deposits results in substantial overburden accumulation during excavation and mining operations. Moreover, these natural deposits frequently contain rare earths alongside radioactive elements, complicating their extraction and necessitating energy-intensive processes. Conversely, secondary resources offer a concentrated form of rare earths devoid of any radioactive associations when compared to natural minerals.

Notably, 23% of rare earths find exclusive application in Neodymium Iron Boron (NdFeB) permanent magnets [2]. NdFeB magnets play a pivotal role in clean energy technologies such as wind turbines and electric vehicles, and with the rapid expansion of clean energy, these sectors have emerged as significant consumers of NdFeB magnets [3]. This portends a substantial increase in the generation of spent NdFeB magnets in the near future. Spent NdFeB magnets contain approximately 30 wt. % of rare earths. Recycling these spent magnets to recover rare earths not only utilizes waste but also alleviates the burden on primary resources. Consequently, this present investigation endeavors to establish a sustainable hydrometallurgical process for the recovery of rare earths from spent NdFeB magnets. Three distinct processes, namely, (a) oxidation roasting—acid leaching, (b) chlorination roasting—water leaching, and (c) electrochemical dissolution have been developed for this purpose.

Materials and Methods

The research investigations focused on spent NdFeB magnets, sourced from wind turbines. Preceding the experimentation, the magnets underwent demagnetization and were subsequently ground to produce particles of 100 mesh size. Within the oxidation roasting-acid leaching process, the demagnetized NdFeB powder underwent controlled heating in the presence of air, adhering to predetermined temperature and time parameters. Subsequently, leaching procedures were conducted on the roasted magnet powder within a three-necked glass reactor, employing a magnetic hotplate. Figure 1a provides a comprehensive breakdown of the diverse factors examined to optimize the leaching process, including acid concentration, pulp density, and temperature. The resulting rare earth solution, ensuing from the leaching process, underwent precipitation through the introduction of oxalic acid, culminating in the attainment of rare earth oxide upon calcination.

Alternatively, the chlorination roasting-water leaching process entailed roasting the demagnetized NdFeB powder in conjunction with ammonium chloride and in the presence of air. The impact of various roasting parameters, encompassing temperature, the ratio of ammonium chloride to magnet powder, and roasting duration, was
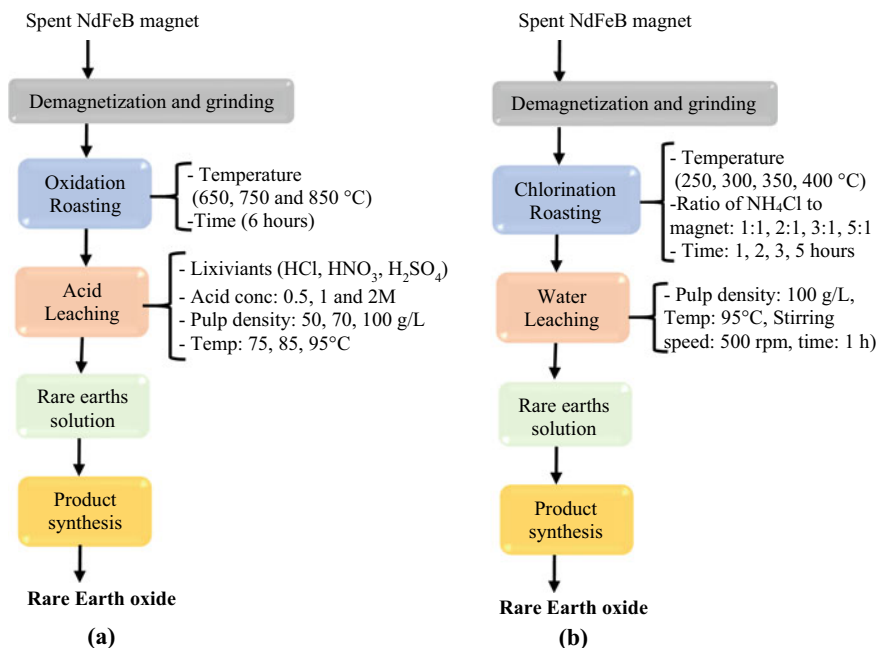
Fig. 1 Developed methodology and studied parameters in **a** oxidation roasting—acid leaching process and **b** chlorination roasting—water leaching process

systematically explored, as elucidated in Fig. 1b. The roasted powder, derived from chlorination roasting, was subsequently subjected to leaching in water under specific conditions. The ensuing rare earth oxide was synthesized utilizing the identical precipitation and calcination technique.

In the case of electrochemical dissolution, the demagnetized magnet block was employed for metal recovery. Electro-dissolution experiments were conducted with the demagnetized magnet block serving as the anode and stainless steel as the cathode, utilizing citric acid as the electrolyte and maintaining a constant temperature. ICP-OES was employed to analyze the chemical composition of the magnet and the metals present in the solution across all experiments. The phases of the initial raw material and the resultant products were characterized through XRD analysis. The magnet was found to contain approximately 29.2% rare earths (Nd, Pr, and Dy), 67% Fe, and minor impurities (B, Al, Co) (Fig. 2).

Fig. 2 Developed
methodology and studied
parameters in
electrochemical dissolution
process

Spent NdFeB magnet

↓

Demagnetization

↓

Electrochemical
Dissolution — - Citric acid concentration (0.25, 0.5, 1 M)
- Current density (50, 200, 300, 500 A/m^2)
- Stirring speed (0, 100, 300, 400 rpm)
- Temperature (25, 40, 50, 70 °C)

↓

Solvent
Extraction — - D2EHPA as extractant

↓

Precipitation
stripping

↓

Calcination

↓
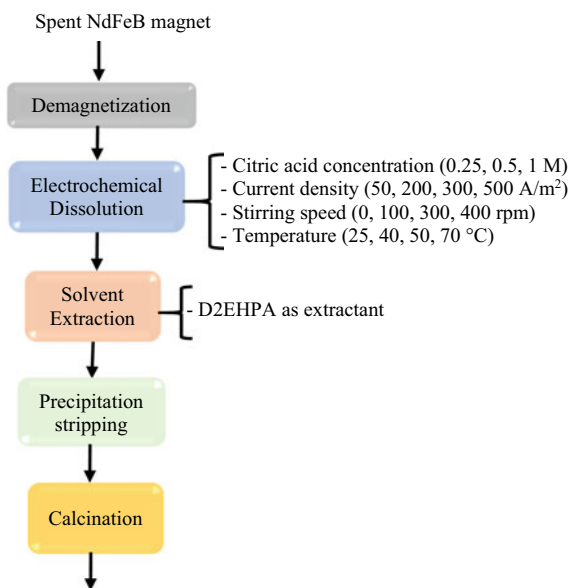
Results and Discussion

In the oxidation roasting—acid leaching process, complete roasting was achieved at 850 °C for a duration of 6 h to facilitate the formation of rare earth oxide and iron oxide. Leaching studies demonstrated the selective and full recovery of rare earths (98%) through the use of 0.5 M HCl at 95 °C, with a pulp density of 100 g/L, over a 5h period [4]. The resulting leach solution yielded a rare earth oxide of 98% purity, while the leach residue was primarily identified as hematite.

On the other hand, the chlorination roasting-water leaching process identified the optimal roasting condition at 300 °C, employing three times the stoichiometric amount of NH4Cl for a duration of 3 h [5]. Under these conditions, rare earths were selectively converted into rare earth chloride, while iron was transformed into iron oxide. Leaching of the roasted powder resulted in the quantitative recovery of rare earths (99%) in the leach solution, ultimately producing rare earth oxide with a purity of 99%, alongside iron oxide as a by-product.

Regarding the electrochemical dissolution studies, it was determined that the dissolution of rare earths in citric acid increased in the presence of electrochemical effects. Furthermore, it was observed that rare earths and iron dissolved together in the electrolyte during electrochemical dissolution, lacking selectivity. As a result, solvent extraction was employed to selectively separate rare earths into the organic phase, utilizing D2EHPA as the extractant. Subsequent precipitation stripping and calcination processes were executed to synthesize rare earth oxide with a purity of 99.9% [6]. The key chemical reactions and the foundation of the study for all three processes are detailed in Table 1.

Table 1 Major reactions and basis of study involved in three processes developed

Process	Major reactions	Basis of study
Oxidation roasting and acid leaching	(*Oxidation process*) $2RE + 1.5O_2 \rightarrow RE_2O_3$ $2Fe + 1.5O_2 \rightarrow Fe_2O_3$ (*Acid leaching*) $RE_2O_3 + 6HCl \rightarrow 2NdCl_3 + 3H_2O$ ($\Delta G^o{}_{298} = -351.8$ kJ/mol) $Fe_2O_3 + 6HCl \rightarrow 2FeCl_3 + 3H_2O$ ($\Delta G^o{}_{298} = -65.2$ kJ/mol) (*in-situ precipitation of Fe*) $2FeCl_3 + 6H_2O \rightarrow 2Fe(OH)_3 + 6HCl$	The solubility difference between RE_2O_3 and Fe_2O_3 in hydrochloric acid is responsible for selective recovery of rare earths
Chlorination roasting and water leaching	(*Selective chlorination of RE*) $RE + 3NH_4Cl + 0.75O_2 \rightarrow RECl_3 + 3NH_3 + 1.5H_2O$ $Fe + 0.75O_2 \rightarrow 0.5Fe_2O_3$ ($RECl_3$ is soluble in water, while Fe_2O_3 is stable phase and insoluble in water)	Selective chlorination of RE and oxidation of iron to iron oxide in the presence of NH_4Cl is liable for selective rare earths recovery
Electrochemical dissolution in organic acid	*Chemical dissolution* $Nd + C_6H_8O_7 \rightarrow NdC_6H_5O_7 + 1.5H_2$ *Electrochemical dissolution* At anode: $Nd \rightarrow Nd^{3+} + 3e^-$ In electrolyte: $Nd^{3+} + C_6H_8O_7 \rightarrow NdC_6H_5O_7 + 3H^+$ At cathode: $2H^+ + 2e^- \rightarrow H_2$	Increase in metal dissolution under electrochemical effect without any selectivity

A qualitative comparison of the three developed processes, encompassing various steps and process parameters, is presented in Table 2. It was established that demagnetization is an essential pre-processing step in all three processes. For the oxidation roasting—acid leaching and chlorination roasting—water leaching methods, finely ground particles are prerequisites to facilitate gas–solid reactions during roasting and enhance solid–liquid interactions during leaching. However, crushing and grinding are unnecessary in the electrochemical dissolution process. When comparing the roasting temperature and time between the first two processes, it was evident that chlorination roasting (300 °C, 3 h) conserves energy compared to oxidation roasting (850 °C, 6 h). Furthermore, rare earths are selectively recovered in the chlorination roasting process using water as the leaching agent. In the electrochemical dissolution process, despite the utilization of biodegradable citric acid as an electrolyte, the dissolution was non-selective for rare earth recovery. Consequently, an additional solvent extraction process is essential for impurity removal and purification purposes. Thus, the chlorination roasting-water leaching process emerged as a sustainable approach, characterized by minimal energy and chemical consumption.

Table 2 Comparison of three processes: (1) oxidation roasting—acid leaching, (2) chlorination roasting—water leaching, (3) electrochemical dissolution processes

Process	Process 1	Process 2	Process 3
Demagnetization	Yes	Yes	Yes
Size reduction	Yes	Yes	No
Roasting step	Yes	Yes	No
Optimum temperature	800 °C	300 °C	No
Optimum time	6 h	3 h	No
Leaching reagent	Hydrochloric acid	Water	Citric acid
Selectivity for rare earths	Yes	Yes	No
Recovery of RE (%)	98%	99%	> 95%
Purification step	No	No	Yes
Final products	Rare earth oxide Iron oxide	Rare earth oxide Iron oxide	Rare earth oxide Iron oxide
Co metal recovery	No	Yes	Yes

Conclusions

The present work gives insight into three processes investigated for the recovery of recovery of REEs from spent NdFeB magnet. From all the three processes, RE oxide and iron oxide are successfully recovered, which can be utilized for various applications. The oxidation roasting—acid leaching process was found energy extensive due to higher roasting temperature and time. In the electrochemical process, REEs are not recovered selectively and further purification steps are required for the removal of impurities. The chlorination roasting-water leaching approach emerged as a sustainable process, characterized by minimal energy and chemical consumption. For quantitative assessment and comparison of all the three processes, the life cycle analysis can be performed in future.

References

1. Kumari A, Sahu SK (2023) A comprehensive review on recycling of critical raw materials from spent neodymium iron boron (NdFeB) magnet. Sep Purif Technol 317:123527
2. Goodenough KM, Wall F, Merriman D (2018) The rare earth elements: demand, global resources, and challenges for resourcing future generations. Nat Resour Res 27(2):201–216
3. Shaw S, Constantinides S (2012) Permanent magnets: the demand for rare earths. In: Presentation in: 8th international rare earths conference. 13–15 November 2012, Hong Kong.

Retrieved from http://roskill.com/wp/wp-content/uploads/2014/11/download-roskillspaper-on-permanent-magnets-the-demand-for-rare-earths.attachment1.pdf

4. Kumari A, Sinha MK, Pramanik S, Sahu SK (2018) Recovery of rare earths from spent NdFeB magnets of wind turbine: leaching and kinetic aspects. Waste Manage 75:486–498

5. Kumari A, Raj R, Randhawa NS, Sahu SK (2021) Energy efficient process for recovery of rare earths from spent NdFeB magnet by chlorination roasting and water leaching. Hydrometallurgy 201:105581

6. Kumari A, Dipali, Randhawa NS, Sahu SK (2021) Electrochemical treatment of spent NdFeB magnet in organic acid for recovery of rare earths and other metal values. J Cleaner Prod 309:127393

High-Performance Solid Phase Extraction Chromatography as Part of a Process for Recycling NdFeB Magnet Waste

Tiaan Punt, Kerstin Forsberg, and Michael Svärd

Abstract The increasing demand for rare earth elements (REEs) in renewable energy technologies and advanced materials has driven a rapid rise in both their economic importance and supply risk. Complementing the supply of REEs through recycling of waste streams is therefore becoming increasingly significant. This study investigated the recycling of NdFeB magnets by separating the REEs (Pr, Nd, Sm, Dy) from impurities (Fe, Co, B) using solvent extraction. The subsequent purification of REEs into individual fractions was investigated using high-performance solid phase extraction chromatography. With solvent extraction, more than 99.5% REEs could be separated in three counter-current stages using D2EHPA. The REEs were stripped using a 1.25 M H_2SO_4 solution, and finally separated into Nd and Pr, Sm, and Dy fractions from the loaded stripping solution in a single chromatographic stage using a D2EHPA-impregnated column and elution with H_2SO_4-gradients. This study found that the column performs well in separating any residual Fe, Co, and B impurities present in the loaded strip liquor fed to the column. The performance of the chromatographic separation is however limited by the column loading capacity at higher metal feed concentrations, where HREEs such as Dy can significantly reduce the separation efficiency of impurities and LREEs which are eluted earlier.

Keywords Rare earth elements · Magnet recycling · Solvent extraction · Extraction chromatography

T. Punt (✉) · K. Forsberg · M. Svärd
Department of Chemical Engineering, KTH Royal Institute of Technology, Stockholm, Sweden
e-mail: tiaan@kth.se

K. Forsberg
e-mail: kerstino@kth.se

M. Svärd
e-mail: micsva@kth.se

Introduction

The use of rare earth elements (REEs) in green technologies, specifically high-performance magnets like NdFeB magnets that are used in electric vehicles, wind turbines, and electronics, has led to their growing economic importance [1, 2]. The European Union (EU) remains dependent for both light REEs (LREEs) and heavy REEs (HREEs) from China, who continue to dominate both the extraction and processing from raw materials, with the current scale of recycled material not yet supplementing a significant portion the required raw materials [3].

The pre-processing and leaching of NdFeB magnets with different acids have been well documented throughout literature [4, 5], but hydrometallurgical processes have been plagued by high impurities in the pregnant leach solution (PLS), such as iron, and other metals that are added to improve the properties of magnets [6, 7]. Another challenge commonly faced when treating magnet waste is the notoriously difficult separation of REEs [8, 9]. Solvent extraction is commonly used for the processing of REEs due to the strong affinity of REEs for organic extractants like D2EHPA and PC-88A (EHEHPA), which are capable of separating adjacent REEs but require large number of equilibrium stages to realize effective separation [10]. This leads to extensive equipment designs, which require large areas, large solvent volumes, and include significant environmental risks.

Chromatography has been proposed as an attractive alternative to solvent extraction for the separation of REEs in recent years due to the reduced organic solvent volumes, recycling potential of chemicals, and the large number of stages possible to achieve in a single column, which reduces the requirements for large equipment designs [11]. High-performance solid phase extraction chromatography is a technique developed for the separation of metals. Based on high-performance liquid chromatography (HPLC), it uses reverse phase (RP) HPLC-type columns impregnated with organic extractants similar to those used in solvent extraction [12–14]. Column impregnation is achieved by elution with the organic extractant dissolved in an aqueous solution containing also an organic solvent such as ethanol or acetone. When the impregnation solution is contacted with the packing material, the hydrophobic ligands of the organic extractant [15] physically adsorb to the hydrophobic functionalized packing material (i.e., octadecyl functionalized porous silica particles). The impregnation solution is then flushed from the column with water, in which the organic extractants are virtually insoluble, leaving the packing material impregnated and active, and capable of complexing with metals through the hydrophilic ligands of the organic extractant. The column can readily be regenerated when performance starts to deteriorate, and overall the method offers excellent flexibility for process design.

Kifle et al. [16], Knutson et al. [17], Ramzan et al. [18, 19], and Sanku et al. [20] have investigated the impregnation of RP-HPLC columns for metal separations, focusing on the effects the impregnation solution, stationary phase, column characteristics, and impregnation procedures have on the column loading capacity and stability. The aforementioned studies have further demonstrated the quantitative REE

separation performance of impregnated RP-HPLC columns for a variety of LREEs and HREEs from diverse synthetic feed solutions using nitric acid as eluant. These studies have not considered the impact of potential impurities from streams such as waste leach liquors, however, and therefore the investigation of this is of key importance for the adoption of this technology in larger scale applications. Furthermore, it is unclear how different aqueous media such as sulfate-based liquors will perform when combined with sulfuric acid as eluant.

This study aims to evaluate the potential of extraction chromatography as part of a process for recycling NdFeB magnet waste, with a specific focus on the integration of chromatographic separation for REEs such as Pr, Nd, Sm, Gd, and Dy. The process targets the bulk separation of the REEs from a SO_4-based NdFeB leach liquor through solvent extraction. The subsequent chromatographic separation of the strip liquor aims to produce separate REE streams, for further processing of a Nd alloy and REE oxides. The chromatographic separation in this study evaluates the performance of a sulfate-based liquor as feed, sulfuric acid elution, the impact of potential impurities that may reach the chromatography process, and the scaling of the metal composition in the feed. It could be of particular importance that the Nd product stream contains no Fe or HREEs such as Dy to ensure the production of a reusable alloy downstream by molten salt electrolysis.

Materials and Methods

Materials and Reagents

Waste NdFeB material was kindly supplied Magneti Ljubljana d.d. (Slovenia) and processed by TU Freiburg (Germany) to ensure that all material is coarsely ground to < 2 mm. The composition of the NdFeB waste was determined by aqua regia digestion[1] using 68 wt.% HNO_3 and 32 wt.% HCl supplied by VWR and Merck, respectively. The digestions were filtered by vacuum filtration, with no residue observed, and analyzed by inductively coupled plasma optical emission spectrometry (ICP-OES). The lixiviant was prepared with 95% $CuSO_4 \cdot 5H_2O$ supplied by VWR and acidified with > 95% H_2SO_4 supplied by Sigma Aldrich.

Solvent extraction tests were performed with an organic phase prepared with 97% D2EHPA and low odor kerosene, supplied by Sigma Aldrich and VWR, respectively. The use of 2 M NH_3OH for pH control was prepared from > 30%, supplied by Honeywell Fluka. Stripping tests were performed with H_2SO_4 (>95%, Sigma Aldrich). The HPLC column was impregnated with D2EHPA and absolute ethanol supplied by Sigma Aldrich. Chromatographic separations were performed with 2.5 M H_2SO_4 (>95%, Sigma Aldrich). All solutions were prepared with MilliQ grade water

---

[1] Molar ratio of 3 HCl to 1 HNO_3 at 50 °C for 24 h.

(18.2 MΩ.cm, Merck). The post-column reaction (PCR) solution was prepared using Arsenazo III supplied by Honeywell Fluka, > 99% acetic acid, and > 99% urea supplied by Sigma Aldrich.

Equipment

Solvent extraction, stripping, and scrubbing tests were performed in 250 mL glass beakers on a magnetically stirred Fischer Scientific Isotemp hotplate. The temperature and pH were continuously measured during extraction tests with a Thermo Scientific 8302BNUMD Ross Ultra triode probe and Orion Star 210 pH meter. After each extraction and stripping test, the mixed phase was transferred to a separatory funnel and the two immiscible phases were allowed to separate completely before a sample of the aqueous phase was drawn.

A Thermo Scientific Dionex ICS-5000+SP Ion Chromatography system connected to a Dionex variable wavelength detector (VWD), and Dionex Ultimate 3000 automated fraction collector was used for chromatographic separations. The chromatographic system used a Kromasil C_{18}-functionalised column (I.D. = 4.6 mm, L = 150 mm) packed with mesoporous spherical particles (particle size = 10 μm, pore size = 100 Å, density = 0.66 g/mL). The column was maintained at 25 °C for all experiments using a BioTek Instruments HPLC 582 thermostat, with eluants placed in a water bath set to 25 °C. A T-junction was used at the column outlet to introduce a PCR reagent with a BioTek Instruments System 522 pump. The column outlet and reagent were pumped through a 750 μL knitted coil to ensure sufficient reaction time before the VWD.

Experimental Procedure

The leaching was performed in a 1 L jacketed vessel placed on a hot plate and overhead stirrer according to a patented leaching process developed by MEAB Chemie Technik GmbH (Aachen, Germany) [21]. The lixiviant was prepared by adding 356 g $CuSO_4 \cdot 5H_2O$ to 1 L of water. The NdFeB waste material was then added to the lixiviant with a 1:9 weight ratio of dry NdFeB waste to lixiviant. After 25 min of leaching the slurry was filtered with a vacuum filter and 0.1 vol% H_2SO_4 added to the PLS to ensure all metals remain soluble during storage. The composition of the NdFeB magnet waste was determined by aqua regia digestions followed by ICP-OES analysis and is summarized in Table 1 with the composition of the PLS after leaching. It was also determined that < 15 mg/L Cu remained in the PLS and therefore Cu was excluded from the results.

Solvent extraction experiments were performed by mixing the two immiscible phases with a magnetic stirrer until well dispersed. The pH was continuously measured and adjusted to the target value at 22 °C. Once the equilibrium pH was

Table 1 Metal composition of the NdFeB magnet waste, PLS, and loaded strip liquor

	NdFeB magnets (wt. %)		PLS (mg/L)		Loaded strip liquor (mg/L)	
	$\bar{x}$ (%)	$\pm \sigma$ (%)	$\bar{x}$	$\pm \sigma$	$\bar{x}$	$\pm \sigma$
B	0.97	$\pm$ 0.02	787.7	$\pm$ 23.4	13.18	$\pm$ 0.41
Fe	65.0	$\pm$ 0.7	62,860	$\pm$ 649	485.2	$\pm$ 2.6
Co	3.2	$\pm$ 0.0	2723	$\pm$ 47	23.64	$\pm$ 0.14
Pr	0.97	$\pm$ 0.00	1522	$\pm$ 166	674.0	$\pm$ 3.7
Nd	22.9	$\pm$ 0.1	20,493	$\pm$ 276	11 050	$\pm$ 51
Sm	0.91	$\pm$ 0.00	594.9	$\pm$ 136.3	200.2	$\pm$ 1.0
Gd	0.14	$\pm$ 0.01	51.49	$\pm$ 8.92	117.8	$\pm$ 0.8
Dy	6.6	$\pm$ 0.0	6 368	$\pm$ 275	703.4	$\pm$ 2.7
Total	100.7	$\pm$ 0.9	95,401	$\pm$ 1582	13 267	$\pm$ 62

reached, the dispersion was further agitated for 10 min without pH control to ensure that the equilibrium point was achieved. Stripping of the organic phase was conducted by adding the organic phase to a beaker with the stripping solution and mixing the two phases well with a magnetic stirrer for 10 min.

The Kromasil C_{18}-functionalized column was impregnated with a 0.75 MD2EHPA solution containing 65 vol.% ethanol according to the procedure described by Sanku et al. [20]. The column was firstl cleaned with 14 column volumes (CVs) of absolute ethanol, and then a 65 vol.% ethanol conditioner was run for 20 CVs. 15 CVs of impregnation solution were added, and the system was then flushed with 20 CVs of MilliQ water. To ensure that only the column was loaded, the column was removed from the system and 10 CVs of absolute ethanol were pumped through the system followed by 10 CVs of MilliQ water before reattaching the column. Titration of the impregnation feed solution, impregnation solution eluate, and the system flushing with 0.5 M NaOH (>99%, Merck) enabled the determination of the column loading.[2] Repeating the impregnation procedure 4 times produced an average loading of 1.044 ± 0.074 mmolD2EHPA on the column. Different elution gradients were tested for 50 µL feed injections by varying the feed flow rate of 2.5 M H_2SO_4 and MilliQ water to achieve the desired H_2SO_4 concentration. Chromatograms were evaluated for organophosphorus compounds at 288 nm and REE complexes at 658 nm, with selected experiments being further quantified ex situ using ICP-OES at 30-s intervals.

---

[2] $D2EHPA_{column} = D2EHPA_{Impreg.\ Feed}$
$-\left[D2EHPA_{Impreg.\ Eluate} + D2EHPA_{H_2O\ flush} + D2EHPA_{Et\ flush}\right]$

Analytical Method

Samples taken from vacuum filtration solutions (aqua regia and leaching samples) were all filtered with 0.22 µm PTFE syringe filters. Aqueous samples were diluted with 0.1 vol.% H_2SO_4 to ensure all metals fall within calibration range and were analyzed with a Thermo Scientific iCAP 7400 ICP-OES utilizing both axial and radial configurations. Each sample was analyzed with three repeats and only spectral lines with a coefficient of determination (R^2) > 0.999 for their calibration and relative standard deviation (RSD) of < 3% for each sample were used. The spectral lines used for the various metals included B (208.959), Co (231.160), Fe (238.204, 239.562), Pr (390.844, 414.311), Nd (401.225, 406.109), Sm (330,639), Gd (335.047), and Dy (353.170, 400.045). The use of initial calibration blanks (ICBs), continuing calibration verifications (CCVs), and quality control standards (QCSs) were utilized for quality control with a warning limit of ± 20% and failure limit of ± 25%.

Results and Discussion

REE Solvent Extraction

Preliminary screening tests for the extraction performance of D2EHPA were conducted to determine the optimal pH for separation of all the REEs from iron, the major impurity in the PLS. These tests were performed within a pH range from 0.9 to 2 at intervals of about 0.1 with 35 vol.% D2EHPA at an O/A ratio of 1 and 22 °C. It was determined that the extraction of Fe, Co, and B is not significantly affected within this pH range, with all three impurities having a co-extraction < 10%. The extraction of the heavier REEs such as Dy and Gd were also unaffected within this range and were extracted > 90% for all conditions. The extraction of Pr, Nd, and Sm gradually increased from roughly 40% at a pH of 1.4 or less to > 75% at a pH of 1.8. It was therefore decided to further investigate the REE separation at a pH of 1.8.

REE Separation and Optimization

The separation of the REEs from the impurities was evaluated by varying the D2EHPA concentration and O/A ratio, both of which affect the metal to extractant ratio and therefore the loading capacity of the organic phase. Figure 1a illustrates the extraction performance for all the REEs in the PLS at D2EHPA concentrations from 15 vol.% to 35 vol.% and O/A ratios of 0.5 to 5. The extraction of Gd was not included due to the low contents in the PLS (see Table 1), which was under the limit of quantification (LOQ) for the ICP-OES analysis. The extraction of Dy was high for all tests and is favored over the other REEs due to being the heaviest REE
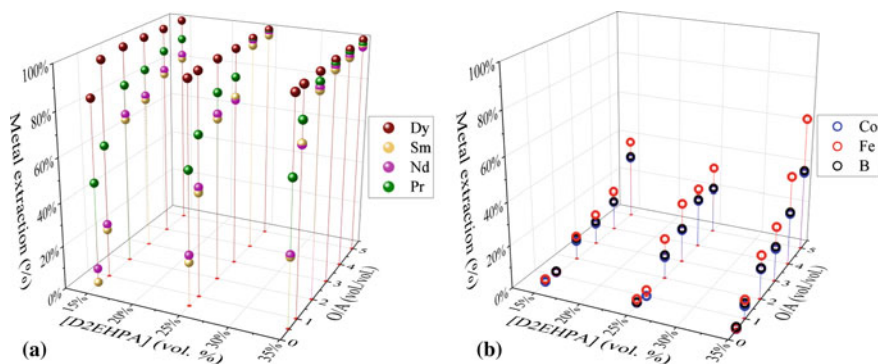
Fig. 1 **a** REE extraction and **b** impurity co-extraction as a function of [D2EHPA] and the O/A ratio at a pH of 1.8 and 22 °C

in the PLS, and consequently having the smallest ionic radius due to the lanthanide contraction [22, 23].

By far the most abundant REE in the PLS is Nd, as summarized in Table 1, and therefore the maximum extraction of Nd was prioritized. It was observed in Fig. 1a that near complete Nd extraction can be achieved with 25 vol.% D2EHPA but this would require an O/A ratio > 3, which also notably increases the co-extraction of Fe (see Fig. 1b). Other major disadvantages of high O/A ratios include large solvent volumes and the dilution of the metals to downstream processes. The extraction of both Pr and Sm increased gradually as the D2EHPA concentration and O/A ratio increased. Figure 1a further illustrates that similar to Nd, a high O/A ratio of 4 or 5 is required for near complete extraction of Sm and Pr with 25 vol.% D2EHPA.

Therefore, 35 vol.% D2EHPA was selected as the optimum concentration for REE separation as this allows for a low O/A ratio between 1 and 2 to be used for > 90% extraction of all REEs in the PLS in a single stage while limiting the co-extraction of Fe, Co, and B. It was further observed during experiments that the lowest O/A ratio that could be used was 1.3 as lower O/A ratios led to organic overloading and subsequent gel formation. A McCabe–Thiele plot was used to determine that more than 99.9% Nd, 99.7% Dy, 92% Pr, and 91.2% Sm can be extracted with 35 vol.% D2EHPA and an O/A ratio of 1.5 at 22 °C when using three counter current stages. The co-extraction of Fe, Co, and B was limited to 7%, 4%, and 2%, respectively.

Organic Stripping

The 35 vol.% D2EHPA organic phase was loaded at an O/A ratio of 2 and pH 1.8 to ensure > 85% REE extraction as no lab-scale equipment was available for bulk multi-stage experiments. The stripping performance of sulfuric acid was investigated to determine the recovery of the REEs from the loaded organic. Figure 2 illustrates the metal stripping performance from the loaded organic at H_2SO_4 concentrations

Fig. 2 Metal stripping as a function of H$_2$SO$_4$ concentration at an A/O ratio of 1 and 22 °C
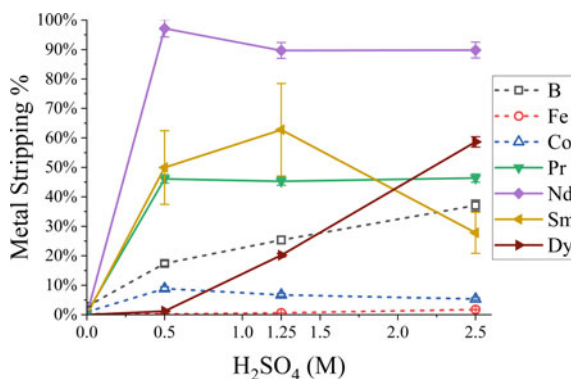
ranging from 0 to 2.5 M at an A/O ratio of 1. The near complete stripping of Nd was achieved in a single stage with 0.5 M H$_2$SO$_4$ in Fig. 2, with roughly 50% of the Pr and Sm also being stripped. Further increasing the H$_2$SO$_4$ concentration does not significantly increase the stripping performance of the LREEs; namely, Nd, Sm, or Pr. A higher A/O ratio and multiple counter current stripping stages are required to further enhance the Pr and Sm stripping performance, with near complete stripping of the LREEs achieved within three counter current stages when using 0.5 M or 1.25 M H$_2$SO$_4$ at an A/O ratio of 2. The Sm stripping was observed to have a high error in Fig. 2, and this was attributed to the low Sm loading on the loaded organic resulting in concentrations closer to the LOQ of the ICP-OES.

The low stripping of Fe, Co, and B with sulfuric acid further enhances the REE separation as the REEs are selectively stripped from the organic phase. The low stripping of Fe is of particular concern due to Fe having the highest co-extraction of the impurities (Fig. 1) and being the most concentrated metal in the PLS (Table 1). The removal of Fe was therefore addressed by a subsequent scrubbing stage. The stripping of Dy was < 5% for 0.5 M H$_2$SO$_4$ or less in Fig. 2, with near complete Dy stripping only achieved with 3 or more counter current stages at 2.5 M H$_2$SO$_4$. This unique characteristic of stripping with H$_2$SO$_4$ provides a great advantage for downstream REE separations, as Dy strongly competes with the other REEs when using organophosphorus extractants such as D2EHPA, as observed in Fig. 1. Dysprosium can, therefore, be separated from the other REEs at the solvent extraction process using separate stripping circuits, in an attempt to enhance the downstream REE separation capacity and performance.

Chromatographic Separation

Screening of Metal Separation by Chromatography

To evaluate both the targeted separation of the REEs as well as the effect of any impurities that might be introduced to the chromatography system, the PLS was used as feed to the chromatographic separation for screening tests. The PLS was diluted 21 times to prevent overloading the column, resulting in a feed composition: 1250 mg/L Fe, 58 mg/L Co, 15 mg/L B, 462 mg/L Nd, 133 mg/L Dy, 38 mg/L Pr, and 5 mg/L Sm.

Figure 3 illustrates the metal recovery of the diluted PLS as quantified by ICP-OES for the first 25 min of a selected multi-gradient elution. It is observed in Fig. 3 that B is eluted almost instantaneously and that nearly 90% can be recovered in the first 4 min, after which the Co and Fe are eluted together in a second fraction between the 7- and 12-min marks. This corresponds well with the solvent extraction data in Fig. 1, which showed B to have the lowest affinity for D2EHPA, followed by Co and Fe.

The first REE to be eluted was Pr, with nearly 60% recovered in a 3rd fraction between the 12- and 16-min marks. A combined fraction of the remaining Pr and > 90% Nd was recovered thereafter in a 4th fraction between the 16- and 25-min marks. The elution of > 80% Sm was found later in a 5th fraction with roughly 0.5 M H_2SO_4, while > 85% Dy was recovered in a 5th fraction with up to 1.2 M H_2SO_4. Given that the impurities are eluted first and therefore do not limit the loading capacity of the column or interfere with the separation of the target REEs, the elution performance of the loaded strip solution was evaluated next.
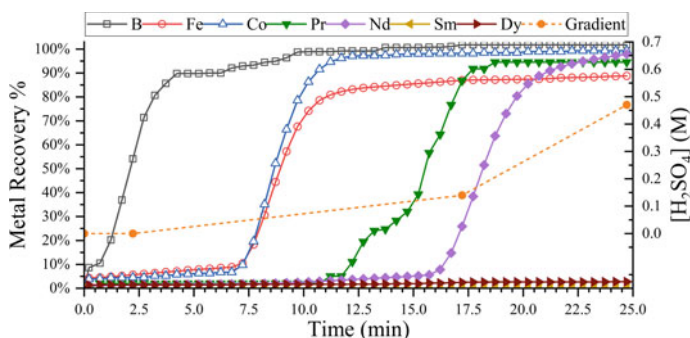
Fig. 3 Elution of diluted PLS as feed to chromatographic separation
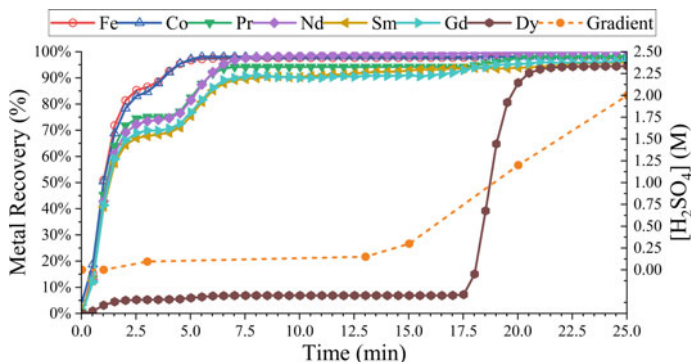
Fig. 4 Elution of 1.25M H_2SO_4 loaded stripping solution

Loaded Strip Liquor Feed

The loaded strip solution with a composition as summarized in Table 1 was tested as feed to the chromatographic separation at various dilution ratios from 20 to 1 to evaluate the loading capacity of the column. Using the loaded strip solution as feed without dilution introduces limited impurities but much more concentrated REEs that may significantly affect the columns' ability to separate the metals.

Figure 4 illustrates the chromatographic separation of the undiluted 1.25 M H_2SO_4 loaded strip solution, with B omitted due to its low content being below the LOQ. The undiluted loaded strip solution in Fig. 4 illustrates that the Dy loads the column preferentially, as was observed during the solvent extraction in Fig. 1, leading to the immediate elution of > 60% of Pr, Nd, Sm, and Gd with > 80% of the impurities in the first 2.5 min. More than 5% of the Dy is also immediately eluted in Fig. 4, illustrating that the column also does not have the capacity for all the Dy in the loaded strip solution.

The remaining 15% of Fe and Co are eluted between the 2.5- and 4-min marks, followed by the remaining 25% Pr and Nd between the 4- and 7-min marks. It was also observed that approximately 20% of the remaining Sm and Gd is eluted with the Pr and Nd between the 4- and 7-min mark, which was attributed to the overloading of the column. A final 5% Sm was recovered between the 12- and 17-min mark, where the Sm elution is expected based on the eluate gradient. Similarly, a final 5% Gd was recovered between the 16- and 17.5-min mark where the elution of Gd was expected based on the eluate gradient. The recovery of 85% Dy occurred between the targeted 17.5- and 21.5-min mark in Fig. 4.

It is thus clear from Fig. 4 that Dy greatly limits the separation capacity of the column for Nd, the main target metal of the chromatographic separation for this study. The separate elution of Dy from the other REEs during the solvent extraction process could therefore enhance the performance of the chromatographic process by increasing the loading capacity of the column for Nd and reducing the elution time required.
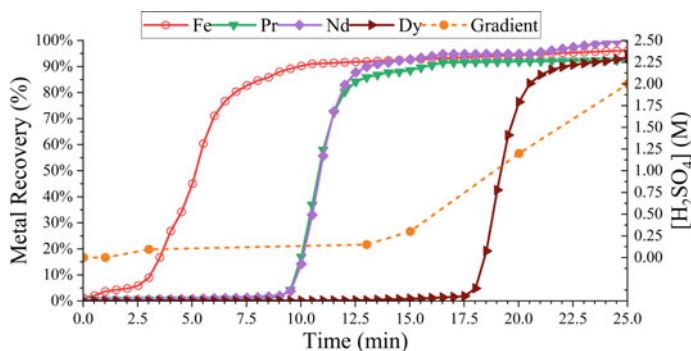
Fig. 5 Elution of 10 times diluted 1.25M H_2SO_4 loaded stripping solution

The loaded stripping solution was therefore diluted 10 times to reduce the Dy content and prevent the overloading of the column. The feed of the 10 times diluted loaded strip solution contained 1107 mg/L Nd, 70 mg/L Dy, 68 mg/L Pr, and 49 mg/L Fe with only 20 mg/L Sm, 12 mg/L Gd, 2 mg/L Co, and 2 mg/L B. Figure 5 illustrates the elution of the major elements from the 10 times diluted loaded strip solution, with the elution of > 85% Fe within the first 9 min. The traces of Co and B are expected to also occur within this fraction based on previous results in Fig. 3. Both Pr and Nd were recovered in the second fraction, where > 90% Pr and > 95% Nd were recovered between the 9- and 16-min mark.

The elution of nearly 95% Dy was observed between the 16- and 25-min mark. The elution of Dy can be accelerated by using higher eluate concentrations as it is the last metal to be eluted. However, due to the higher affinity of Dy for the impregnated extractant and the focus of this study on targeting Nd, it would be beneficial for the purpose of a scaled-up process to strip the Nd at a lower H_2SO_4 concentration in the solvent extraction process to reduce the Dy fed to the chromatographic process. This would enable maximizing the Nd in the chromatographic feed and enable better scaling of the process.

Conclusions

The use of solvent extraction for the processing of REEs is well known and offers high selectivity for the separation of REEs from other impurities present in NdFeB magnets like Fe, Co, and B. It was determined that more than 99% of all the REEs can be separated from the PLS with 3 counter current stages using 35 vol.% D2EHPA at an O/A ratio of 1.5, pH 1.8, and 22 °C. The REEs can further be selectively stripped from the loaded organic, with near complete Nd, Pr, and Sm stripping achieved with three counter current stages using 1.25 M H_2SO_4 at an A/O ratio of 2.

High-performance solid phase extraction chromatography is sensitive to the feed composition and any impurities that may affect the impregnated organophosphorus extractant. Solvent extraction as a precursor is beneficial as it provides a stream with greatly reduced impurities and enables the selective stripping of LREEs and Dy at 0.5 M H_2SO_4 and 1.25 M H_2SO_4, respectively. The stripping of the LREEs without Dy could improve the Nd separation performance as it does not have to compete with Dy, which has a higher affinity for D2EHPA.

Chromatographic separation of the metals in this study allows for an initial fraction containing Fe, Co, and B to be recovered before the REEs to ensure that any impurities in the loaded strip liquor are separated from the REEs. The elution of Pr and Nd occurs after the impurities and cannot be quantitatively separated from each other using the loaded stripping solution as feed. It was observed for select cases that nearly 60% Pr could be separated from Nd in the PLS, however, it is unclear whether this is due to different elution gradients, feed loading, feed acidity, or variance in feed composition. The elution of Sm to a separate fraction occurred thereafter at 0.5 M H_2SO_4 eluate concentration. The elution of Dy was achieved when increasing the H_2SO_4 eluate concentration above 0.8 M but could be avoided if stripped separately after the LREEs with 1.25 M H_2SO_4 or higher.

It is recommended that a future study investigates the chromatographic separation performance for 0.5 M H_2SO_4 loaded strip solution as feed. This will greatly reduce the Dy content and lower the acidity in the feed, allowing for a higher Nd column loading capacity and potentially improving the separation of Pr and Nd to separate fractions.

References

1. Petranikova M, Herdzik-Koniecko I, Steenari B-M, Ekberg C (2017) Hydrometallurgical processes for recovery of valuable and critical metals from spent car NiMH batteries optimized in a pilot plant scale. Hydrometallurgy 171:128–141. https://doi.org/10.1016/j.hydromet.2017.05.006
2. Erust C, Karacahan MK, Uysal T (2022) Hydrometallurgical roadmaps and future strategies for recovery of rare earth elements. Mineral Process Extract Metallurgy Revi 1–15. https://doi.org/10.1080/08827508.2022.2073591
3. European Commission (2023) Study on the critical raw materials for the EU 2023—final report
4. Papagianni S, Moschovi AM, Sakkas KM, Chalaris M, Yakoumis I (2022) Preprocessing and leaching methods for extraction of ree from permanent magnets: a scoping review. AppliedChem 2:199–212. https://doi.org/10.3390/appliedchem2040014

5. Klemettinen A, Żak A, Chojnacka I, Matuska S, Leśniewicz A, Wełna M, Adamski Z, Klemettinen L, Rycerz L (2021) Leaching of rare earth elements from NdFeB magnets without mechanical pretreatment by sulfuric (H_2SO_4) and hydrochloric (HCl) acids. Minerals 11:1374. https://doi.org/10.3390/min11121374

6. Peiró LT, Méndez GV, Ayres RU (2013) Material flow analysis of scarce metals: sources, functions, end-uses and aspects for future supply. Environ Sci Technol 47:2939–2947. https://doi.org/10.1021/es301519c

7. Shaaban A, Senin HB, Idris NH (2007) Effects of Zr substitution in NdFeB permanent magnets. pp 63–67

8. Dewulf B, Riaño S, Binnemans K (2022) Separation of heavy rare-earth elements by non-aqueous solvent extraction: flowsheet development and mixer-settler tests. Sep Purif Technol 290:120882. https://doi.org/10.1016/j.seppur.2022.120882

9. Zhang R, Azimi G (2023) Separation of praseodymium and neodymium from heavy rare earth elements using extractant-impregnated surfaces loaded with 2-Ethylhexyl Phosphonic Acid-Mono-2-Ethylhexyl Ester (PC88A). Ind Eng Chem Res. https://doi.org/10.1021/acs.iecr.3c01547

10. Takahashi H, Miwa K, Kikuchi K (1993) Separation of light rare-earth elements from rare-earth mixture solution by use of electrodialysis with complexing agents. Int J Soc Mater Eng Resour 1:132–139. https://doi.org/10.5188/ijsmer.1.132

11. Sanku M, Forsberg K, Svärd M (2021) Extraction chromatography for separation of rare earth elements. In: Rare metal technology, Springer, Cham, pp 155–161

12. Tsuyoshi A, Akiba K (2000) High-performance liquid chromatography using reversed-phase stationary phases dynamically modified with organophosphorus compound for the separation and determination of lanthanoid elements. Anal Sci 16:843–846. https://doi.org/10.2116/analsci.16.843

13. Sivaraman N, Kumar R, Subramaniam S, Vasudeva Rao PR (2002) Separation of lanthanides using ion-interaction chromatography with HDEHP coated columns. J Radioanal Nucl Chem 252:491–495. https://doi.org/10.1023/A:1015894418606

14. Max-Hansen M, Ojala F, Kifle D, Borg N, Nilsson B (2011) Optimization of preparative chromatographic separation of multiple rare earth elements. J Chromatogr A 1218:9155–9161. https://doi.org/10.1016/j.chroma.2011.10.062

15. Punt T, Luckay RC, Akdogan G, Bradshaw SM, Van Wyk AP (2023) Comparison of phosphorus-based extractants on manganese separation from citrate leach solutions for recycling of lithium-ion batteries. S Afr J Sci 119. https://doi.org/10.17159/sajs.2023/11399

16. Kifle D, Wibetoe G, Frøseth M, Bigelius J (2013) Impregnation and characterization of high performance extraction columns for separation of metal ions. Solvent Extr Ion Exch 31:668–682. https://doi.org/10.1080/07366299.2013.806737

17. Knutson H-K, Max-Hansen M, Jönsson C, Borg N, Nilsson B (2014) Experimental productivity rate optimization of rare earth element separation through preparative solid phase extraction chromatography. J Chromatogr A 1348:47–51. https://doi.org/10.1016/j.chroma.2014.04.085

18. Ramzan M, Kifle D, Wibetoe G (2016) Comparative study of stationary phases impregnated with acidic organophosphorus extractants for HPLC separation of rare earth elements. Sep Sci Technol 51:494–501. https://doi.org/10.1080/01496395.2015.1112400

19. Ramzan M, Kifle D, Wibetoe G (2017) A rapid impregnation method for loading desired amounts of extractant on prepacked reversed-phase columns for high performance liquid chromatographic separation of metal ions. J Chromatogr A 1500:76–83. https://doi.org/10.1016/j.chroma.2017.04.005

20. Sanku MG, Forsberg K, Svärd M (2022) Impregnation of preparative high-performance solid phase extraction chromatography columns by organophosphorus acid compounds. J Chromatogr A 1676:463278. https://doi.org/10.1016/j.chroma.2022.463278

21. Dittrich C, Dittrich L, Dunn GM (2020) Method of dissolution and separation of critical raw materials (CRM)

22. Mohammadi M, Forsberg K, Kloo L, Martinez De La Cruz J, Rasmuson Å (2015) Separation of ND(III), DY(III) and Y(III) by solvent extraction using D2EHPA and EHEHPA. Hydrometallurgy 156:215–224. https://doi.org/10.1016/j.hydromet.2015.05.004
23. Gupta CK (2005) In: Extractive metallurgy of rare earths, CRC Press, Boca Raton, Fla. ISBN 0-415-33340-7alk

Recovery of Rare Earth Sulfate Hydrates Using Antisolvent Crystallization

Nitin Pawar, Michael Svärd, and Kerstin Forsberg

Abstract Rare earth elements (REE) are recognized as critical raw materials because of their crucial role in vital components of numerous green and high-tech applications. In the present study, antisolvent crystallization of REE sulfate hydrates of industrial interest (Nd (III), Pr (III), and Dy (III)) from sulfuric acid solutions by the addition of ethanol has been studied. Crystallization of REEs in the presence of Fe (II) and Fe (III) as major impurities along with Al (III), Cu (II), Co (II), and B (III) as trace elements is investigated. The incorporation of impurities and its effect on the growing REE phase is examined. The effect of controlled supersaturation generation rate on the product quality (e.g. purity) and crystal phase is investigated. The solid phases are characterized using optical microscopy, SEM–EDX, powder-XRD, and ICP-OES. The findings can offer significant insights to understand and optimize the recovery of REEs from leach liquor in the recycling of magnet waste.

Keywords Rare earth elements · Magnet recycling · Antisolvent · Supersaturation · Recovery · Purity

Introduction

Rare earth elements (REEs) are an essential component of modern-day technologies including automotive, renewable energy systems, and various end-user electronics [1, 2]. The global economy is heavily dependent on the need for these elements. The importance of these minerals has grown significantly due to rapid technological development and the increasing demand for renewable energy [3]. However, the limited resources and environmental concerns associated with the extraction of these elements have drawn significant attention to the need to develop effective strategies for their recovery and recycling [4].

The strongest permanent magnets of the type NdFeB contain significant amounts of valuable rare earth elements (i.e. Nd, Pr, and Dy) [5]. These magnets after use

N. Pawar · M. Svärd · K. Forsberg (✉)

Department of Chemical Engineering, KTH Royal Institute of Technology, Stockholm, Sweden
e-mail: kerstino@kth.se

could serve as a reservoir for an additional supply of rare earth elements [6]. The recovery and recycling of spent magnets are also important for balancing the supply of REEs [7]. However, to date, there is no proven commercial technology available for the recovery of REEs from magnet waste. This leads to the need for innovative and sustainable methods for their recovery from various sources. In addition to serving as a secondary source of REEs, recycling spent magnets could also reduce the environmental impact by reducing the amount of waste generated. Typical methods for the recovery of REE from magnets using various techniques such as ion exchange, solvent extraction, and precipitation, in extraction from primary and secondary sources have recently been reviewed [8]. These often involve complex and environmentally harmful processes, leading to the need for sustainable and efficient alternatives.

Antisolvent crystallization provides a novel approach to the recovery of rare earth elements. The addition of another solvent can significantly alter the solubility of a solute in the mixed solvent system, leading to the generation of supersaturation, and eventually resulting in crystal nucleation and growth [9]. Antisolvent crystallization can thus often afford a high yield, while also providing the ability to tune the product quality [10]. Antisolvent crystallization is widely used in the pharmaceutical and fine chemicals industries [11]. The antisolvent selected should have good miscibility with the solvent, and a low dielectric constant indicating the poor ability to solubilize ions. The antisolvent can be recovered and reused in the process.

In this study, antisolvent crystallization of REE from a simulated sulfuric acid leach liquor was examined. The liquor contains Nd, Pr, and Dy as the major REE composition along with La and Y in minor quantities. Either Fe (II) or Fe (III) was added as major impurities and Al (III), Cu (II), Co (II), and B (III) were present as trace impurities. The work aims to recover REE sulfate hydrates as crystals with the desired size, phase, and purity. The ethanol was added all at once, and in semi-batch mode with a controlled rate, to investigate the impact on REE crystallization and impurity incorporation. Optical microscopy, powder-X-ray diffraction (PXRD), scanning electron microscopy coupled with energy-dispersive X-ray spectroscopy (SEM–EDX), and inductively coupled plasma–optical emission spectroscopy (ICP-OES) were used to determine morphology, crystal phase and elemental composition of recovered crystals. The work can give significant insights to better understand the recycling of REEs from waste streams by antisolvent crystallization.

Experimental Setup and Procedure

The experimental setup is shown in Fig. 1. It consists of a jacketed crystallizer of 150 mL capacity. The temperature of the crystallizer jacket was maintained at 25 °C using a cryostatic water bath (Julabo). The solution in the crystallizer was mixed homogeneously using a magnetic stirrer (stirring rate 400 rpm). For the semi-batch experiments, the antisolvent was dosed to the crystallizer from above at a controlled rate using a syringe pump (Kd Scientific, model number 200). The concentrations of

REEs and impurities in the simulated leach liquor along with operating conditions are shown in Table 1. These concentrations are chosen to align with the composition of the metals in NdFeB permanent magnets. In order to investigate the influence of the oxidation state of iron, a set of experiments adding Fe (II) as an impurity was compared to another set adding Fe (III).

For each experiment, 100 g of leach liquor solution was used. Ethanol was added either all at once (one-pot addition) or at a controlled addition rate of 1 mL/min until the final composition corresponding to the targeted organic-to-aqueous (O/A) mass ratios was reached, as presented in Table 1. After the complete addition of ethanol, the solution mixture was left to age for 24 h to allow the system to reach equilibrium. At the end of each experiment, the mother liquor was filtered using a vacuum pump and the recovered crystals were washed with washing solution (2 M sulfuric acid and ethanol (O/A 0,5)) to remove impurities adhering to the surface of the crystals. The crystals were then dried in a ventilated fume hood to avoid phase changes that could
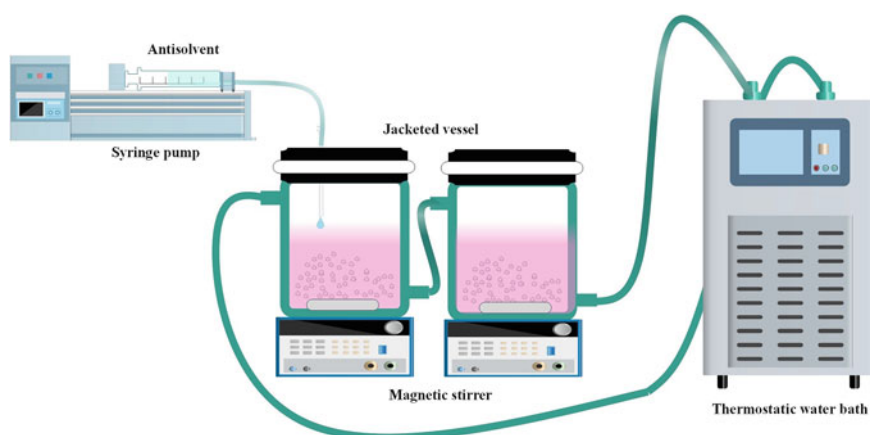
Fig. 1 Schematic of the experimental set-up

Table 1 Operating conditions and composition of the simulated leach liquor

Element	Nd (III)	Pr (III)	Dy (III)	Fe (II)	Fe (III)	La (III)	Y (III)	Cu (II)	Co (II)	Al (III)	B (III)
Concentration (mg/g)	7.91	0.76	0.87	24.3	24.3	0.58	0.27	0.04	0.03	0.03	0.005

Operating conditions	
H_2SO_4 concentration	2.2 m (2 M)
Antisolvent mass	41 g (52 mL)
Final O/A ratio	0.5 (w/w)
Antisolvent addition rate	One-pot and 1 mL/min
Ageing time	24 h

occur at elevated temperatures. The dried crystals were then subjected to further analysis.

To measure the solution concentration, the liquid samples were filtered with a 0.2 µm syringe filter, and the resulting clear solution free of solids was used for analysis. The recovery percentage was calculated using Eq. 1.

$$R = \frac{C_i m_i - C_s m_s}{C_i m_i} \times 100 \tag{1}$$

where C_i and C_s denote the initial and saturation concentration (mg/g) and m_i and m_s the initial and final mass (g) of the solution obtained after 24 h. The solid samples obtained after drying were digested in water to determine the metal content and purity. Liquid and solid sample metal content was determined using ICP-OES (Thermo Scientific iCAP 7000 Plus.) Only Nd, Pr, Dy, and Fe were measured with ICP due to the low concentrations of the trace impurity elements. The powder samples were also analyzed with SEM–EDX and powder-XRD for morphology, elemental composition, and crystal phase.

Results

For crystallization of REE sulfates in the presence of Fe (II), crystals show somewhat different morphologies in the one-pot and controlled addition experiments. Thin plate-like crystals were observed for one-pot addition whereas more elongated crystals were observed for controlled addition of antisolvent (Fig. 2a, b). This could be due to different rates of supersaturation generation leading to differences in growth rates of different crystal faces. Alison et al. (2022) reported hexagonal morphology for Nd for simultaneous addition of solution and antisolvent under different conditions and in the absence of impurities [12]. The presence of Fe (II) in solution might have suppressed the growth of certain crystal faces, leading to an elongated morphology.

In the presence of Fe (III), the recovered crystals are smaller and more agglomerated. This could be due to the Fe (III) impurity acting as a growth inhibitor [13] leading to smaller crystals (Fig. 2c, d). The agglomeration is less for controlled antisolvent addition, showing that the supersaturation generation rate impacts the agglomeration of the crystals to some extent. The agglomeration is not eliminated in the controlled antisolvent addition experiment. However, Fe (III) also leads to delayed nucleation as observed visually, and smaller crystals observed in SEM micrographs (Fig. 2c, d).

For both oxidation states of Fe, the desupersaturation profiles (Fig. 3) show a small decrease in the Fe concentration over time for both antisolvent addition profiles. However, all experiments show significant drops in Nd, Pr, and Dy concentrations. For one-pot addition, the REE concentrations dropped rapidly, due to the rapid attainment of high supersaturation. The Nd recovery was 88% and 85% for trials containing Fe (II) and Fe (III) as impurities, respectively. The recoveries for one-pot and controlled addition showed insignificant differences. With XRD the formation
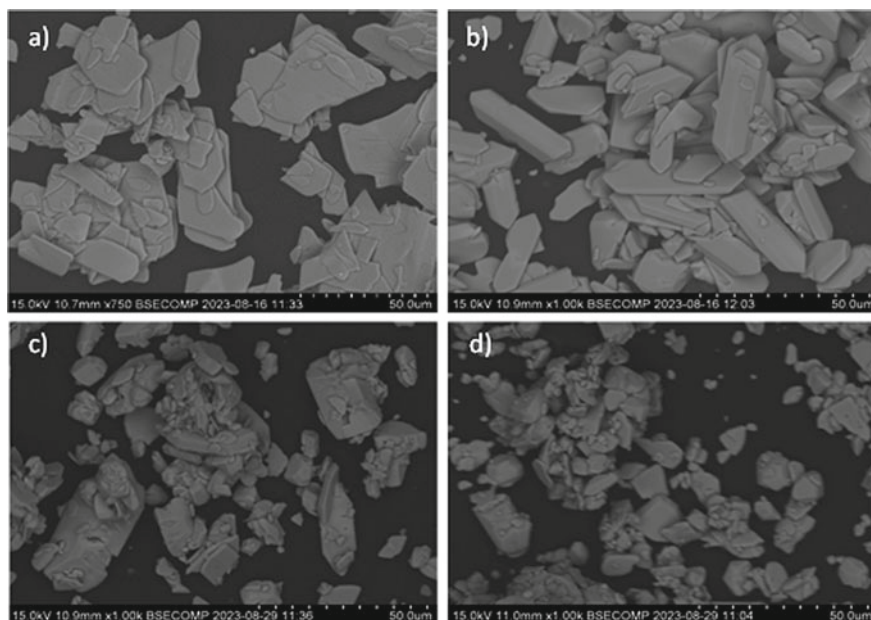
Fig. 2 SEM images of crystals obtained from solutions containing Fe (II) as an impurity for **a** one-pot, and **b** controlled addition rate, and containing Fe (III) as an impurity for **c** one-pot, and **d** controlled addition rate

of a Nd sulphate octahydrate phase (Fig. 4) is confirmed, with a pattern closely matching a standard reference pattern (PDF-card 01–083-0078).

Analysis of the washed solid crystals showed the presence of less than 6% by mass of Fe for one-pot and 1% by mass of Fe for controlled addition experiments (Table 2). Conversely, Pr and Dy were present at the same ratios as in the leach solution. The higher purities with respect to Fe were obtained for controlled addition experiments as shown in Table 2. The EDX mapping also shows signals for Nd, Pr, Dy, and S and low signals for Fe confirming negligible impurity present in samples. The metals are evenly distributed in the Nd phase and no separate crystals were observed. (Fig. 5).

Conclusions

Antisolvent crystallization of REEs was studied for simulated leach solutions containing Fe (II) and Fe (III) as major impurities and other inorganic trace impurities. The Nd recovery obtained was around 85%. The results showed that Fe has a noticeable effect on the morphology of Nd sulfate hydrate crystals. For Fe (II), crystals showed different morphologies for one-pot and controlled antisolvent addition, where elongated crystals were observed in controlled addition experiments and thin
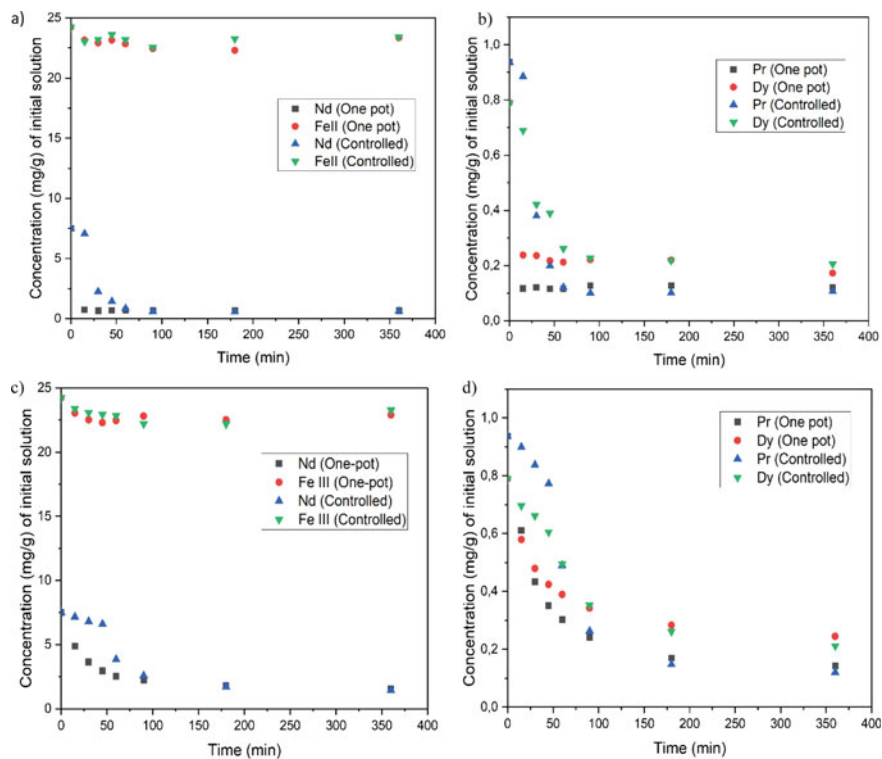
Fig. 3 Desupersaturation profile for Nd, Pr, Dy, and Fe for one-pot and controlled addition of antisolvent

Fig. 4 The XRD pattern of crystals recovered for one-pot and controlled addition from leach liquor containing Fe (II)
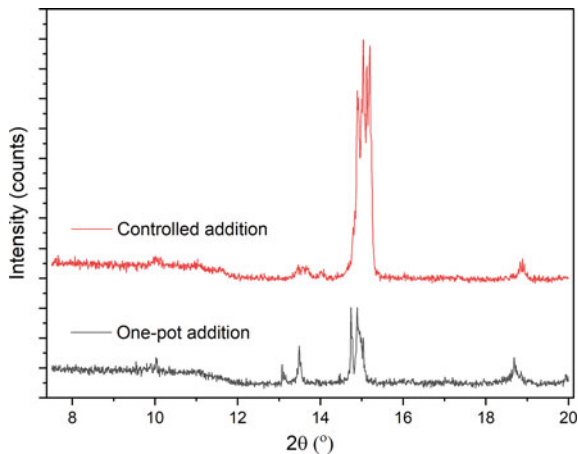
Table 2 The composition of REEs and Fe determined in the recovered solid sample

Experiment	Condition	Nd	Fe	Pr	Dy	Nd (wt%)	Fe (wt%)
REE + Fe (II) (mg/g)	One-pot	226.51	16.91	26.43	23.22	76	5.7
	Controlled addition	310.36	2.75	37.44	32.13	80	0.71
REE + Fe (III) (mg/g)	One-pot	288.02	7.34	36.86	25.18	78	2.0
	Controlled addition	295.84	2.09	38.17	26.91	80	0.56
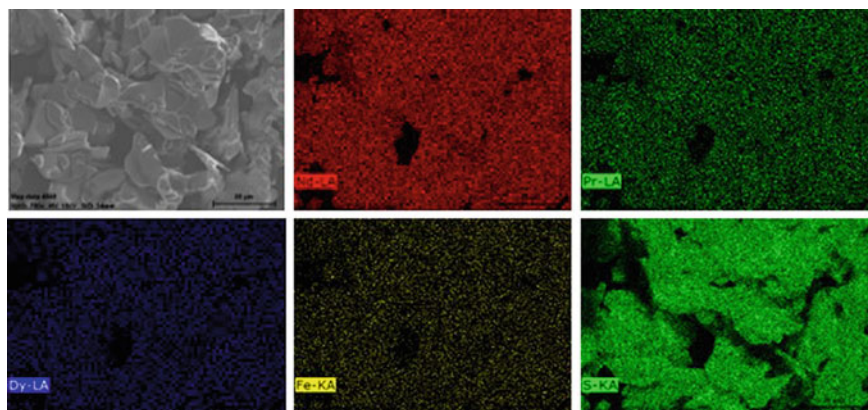
Fig. 5 SEM–EDX mapping of a solid sample obtained using one-pot addition of antisolvent to a REE solution containing Fe (II)

plates in one-pot addition experiments. For Fe (III), crystals were smaller and showed a clear tendency for agglomeration for both one-pot and controlled addition trials. However, no change in the phase of the Nd sulfate hydrate crystals obtained was observed, which was confirmed with powder-XRD to be an octahydrate phase. In all cases, less than 6 and 2% of the Fe (II) and Fe (III) respectively was precipitated. The results give important insights to better understand the process for recycling REEs from waste streams using antisolvent crystallization.

References

1. Communication from the European Commission on the 2017 list of critical raw materials for the EU, COM. Brussels, pp 490 (2017)

2. Ni'am AC, Wang YF, Chen SW, Chang GM, You SJ (2020) Simultaneous recovery of rare earth elements from waste permanent magnets (WPMs) leach liquor by solvent extraction and hollow fiber supported liquid membrane. Chem Eng Process 148:107831

3. Peelman S, Kooijman D, Sietsma Yang JY (2018) Hydrometallurgical recovery of rare earth elements from mine tailings and WEEE. J Sustain Metall 4:367–377

4. Zhang Y, Gu F, Su Z, Liu S, Anderson C, Jiang T (2020) Hydrometallurgical recovery of rare earth elements from NdFeB permanent magnet scrap: a review. Metals 10:841

5. Gergoric M, Ekberg C, Foreman M, Steenari B, Retegan B (2017) Characterization and leaching of neodymium magnet waste and solvent extraction of the rare-earth elements using TODGA. J Sustain Metall 3:638–645

6. Walton A, Han Y, Rowson NA, Speight JD, Mann VSJ, Sheridan RS, Bradshaw A, Harris IR, Williams AJ (2015) The use of hydrogen to separate and recycle neodymium-iron-boron-type magnets from electronic waste. J Clean Prod 104:236–241

7. Dang DH, Thompson KA, Ma L, Nguyen HQ, Luu ST, Duong MTN, Kernaghan A (2021) Toward the circular economy of rare earth elements: a review of abundance, extraction, applications, and environmental impacts. Arch Environ Contam Toxicol 81:521–530

8. Binnemans K, Jones PT, Blanpain B, Gerven TV, Walton YA, Buchert M (2013) Recycling of rare earths: a critical review. J Clean Prod 51:1–22

9. Pawar NP, Agrawal SG, Methekar R (2018) Modeling, simulation, and influence of operational parameters on crystal size and morphology in semibatch antisolvent crystallization of α-lactose monohydrate. Cryst Growth Des 18:4511–4521

10. Pawar NP, Agrawal SG, Methekar R (2019) Continuous antisolvent crystallization of α-lactose monohydrate: impact of process parameters, kinetic estimation, and dynamic analysis. Org Proces Res Dev. 23:2394–2404

11. Jia S, Yang P, Gao Z, Li Z, Fanga C, Gong J (2022) Recent progress in antisolvent crystallization. CrystEngComm 24:3122

12. Sibanda J, Chivavava J, Lewis A (2022) Crystal engineering in antisolvent crystallization of rare earth elements (REEs). Minerals 12:1554

13. Lewis A (2017) In: Precipitation of heavy metals, sustainable heavy metal remediation. Springer International Publishing AG 2017 pp 101–120

Rare Earth Magnet Recycling Via Liquid Magnesium Leaching and Distillation

Emmanuel Offei Opoku, Hiba Khan, Chinenye Chinwego, and Adam Powell

Abstract The need for rare earth metals in clean energy technologies such as wind turbines and electric vehicles has raised a threat to the supply and has spurred researchers to look for sourcing alternatives, with recycling being one of the approaches. Many research investigations have demonstrated the magnet-to-metal approach, in which rare earth metals such as neodymium, praseodymium, dysprosium, and terbium, are leached from magnets by molten metals. These recycled metals can then be involved in the production of new rare earth magnets, providing an environmentally friendly source. This study provides an overview of this method of rare earth magnet recycling, which begins with demagnetization and coating removal. Leaching uses liquid magnesium and bismuth, where distillation is done by a continuous gravity-driven multiple effect thermal system (G-METS). G-METS distillation can potentially improve the efficiency of rare earth metal extraction to help establish a sustainable supply chain for rare earth magnets.

Keywords Recycling and secondary recovery · Magnetic materials · Distillation

Introduction

The recycling of rare earth magnets is gaining ground because of their importance to clean energy applications and the supply risk they pose, as mining and refining these metals is concentrated in very few countries. For rare earth magnet scraps, a number of studies have investigated extraction techniques such as solvent extraction [1, 2], hydrogen decrepitation [3], and bioleaching [4]. The rare earth is recovered in oxide form by solvent extraction. Hydrogen decrepitation, a magnet-to-magnet process, still needs the addition of pure earth metals to prevent degrading the finished product. Liquid metal leaching and advanced distillation is a potential method to obtain pure rare earth metal that can serve as a precursor for magnet production [5, 6].

E. O. Opoku · H. Khan · C. Chinwego · A. Powell (✉)
Worcester Polytechnic Institute, Worcester, MA 01609, USA
e-mail: acpowell@wpi.edu

Background

Due to the rising demand for high-tech consumer goods and the development of clean energy sources over the past few decades, the demand for many specialty metals has increased more rapidly than for significant metals like steel, aluminum, and nickel. Rare earth metals have excellent potential for wide application in modern and energy-efficient machinery due to their distinctively high melting points and strong thermal conductivities. Since Molycorp Minerals, LLC shut down its huge Mt. Pass mine in the middle of the 1990s, production of rare earth metals has shifted from Europe and America to China. They were unable to compete with China's low production costs, which resulted in a prevailing output (97% of production was produced in China as of 2010). Due to export restrictions and price constraints in China by 2011, the Mountain Pass mine reopened, though the processing plant only produced separated rare earth oxides, not metals or magnets. Other nations like Australia and Vietnam have experienced an increase in the development of rare earth mining. Figure 1 displays how the magnet industry's supply chain is heavily focused in China, mainly as it descends from metal refining and mining to magnet production [7].

According to the United States Department of Energy (DOE), the five most critical rare earth elements identified in the medium-term criticality matrix (2015–2025) were Yttrium (Y), Neodymium (Nd), Europium (Eu), Terbium (Tb), and Dysprosium (Dy). Magnets made of neodymium (Nd), praseodymium (Pr), and dysprosium (Dy) are utilized in renewable energy technologies for the manufacture of wind turbines
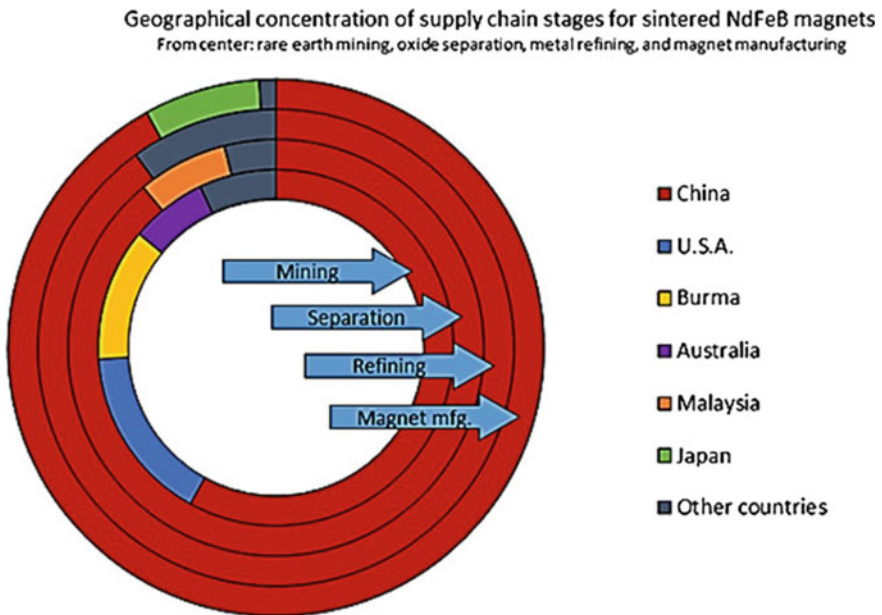
Fig. 1 Geographical concentration of supply chain stages for sintered NdFeB magnets in 2019 [8]

(a) (b)
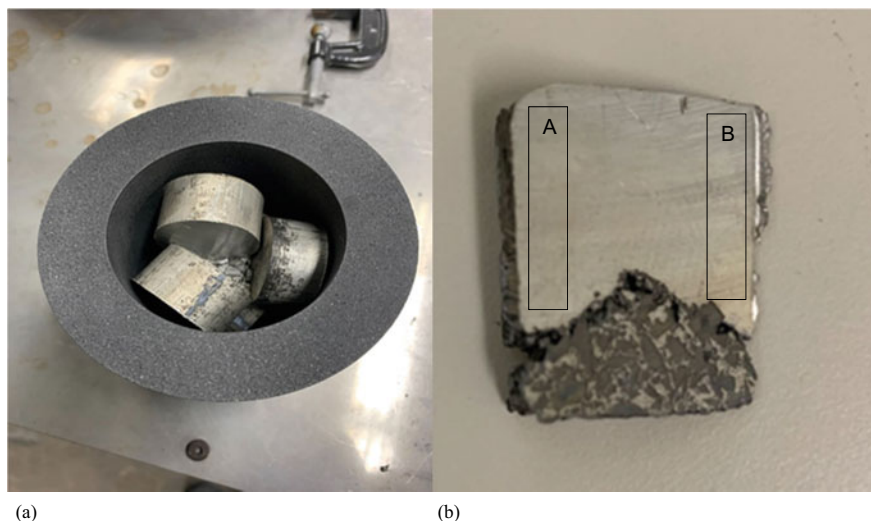
Fig. 2 **a** Mg and Nd before leaching, **b** cross-section of Mg-Nd alloy after leaching

and hybrid/electric cars. Electric vehicle traction motors nearly all use rare earth permanent magnets. Additionally, the development of sustainable energy technologies like fuel cells, gas turbines, and magnetic refrigeration could have a substantial impact on the need for essential materials [9].

Research Methodology

The leaching was carried out in a controlled atmosphere chamber creating an argon environment in a Mellen furnace at 900C for 3 h. Mg rods purchased from Strem were cut into smaller pieces. The rare earth magnets obtained were demagnetized at 350C and then crushed to small particle sizes. The magnesium metal and magnet particles were placed in the graphite crucible at a 3:1 Mg:magnet mass ratio as shown in Fig. 2.

Results

The resulting Mg-Nd alloy samples were characterized using Inductively-Coupled Plasma-Optical Emission Spectroscopy (ICP-OES) and Scanning Electron Microscopy/Energy-Dispersive X-Ray Spectroscopy (SEM/EDX). Elemental analysis of Mg, rare earth elements and nickel as well as Mg to Nd ratios for the top

section, midsection, and bottom section of the leached sample were determined by ICP-OES at two areas of the samples (A and B), as shown in Table 1.

Portions A and B in Fig. 2b were taken for ICP-OES analysis. The Mg to Nd ratio is lowest at the bottom of the sample for both A and B, closest to the magnet material, followed by the middle samples and the top samples, indicating that mass transfer in the sample was relatively slow, as shown in Table 1. In an attempt to identify the traces of nickel, we carried out ICP-OES and observed a relatively small amount of nickel, and somewhat more praseodymium, in the sample. These observations were supported with SEM analysis of the sample as shown in Figs. 3 and 5 (Tables 2 and 3).

The SEM images shown in Figs. 3 and 5 were taken at the bottom and middle of the sample respectively. The light-colored material indicates the presence of high-atomic number rare earth metal, while the darker color shows the magnesium matrix. A much higher prevalence of brighter material at the bottom of the sample corresponds well with the higher measured rare earth concentration there.

EDX results from the bottom and middle of the sample are shown in Figs. 4 and 6 respectively. The spectra and composition tables correspond to the analysis of the whole sample. Again, the much higher Nd concentration in the bottom of the sample, above 25 wt%, corresponds to the ICP-OES analysis described above.

Preliminary data seem to show more Nd in the Mg than was in the magnet and increasing Nd concentration followed by decreasing concentration. Maybe because it's near the interface, so Nd concentration there initially is very high, then as Nd diffuses into the Mg alloy liquid, its concentration near the interface falls. It is challenging to measure the average Nd concentration in the alloy as shown in Fig. 7.

There was an attempt to stir the Mg-Nd alloy during a leaching experiment in order to improve mass transfer. This should both improve rare earth removal from the magnet alloy and also homogenize the Mg-Nd alloy, enabling more accurate

Table 1 Elemental analysis of elements present using ICP-OES

	Composition (wt%)	Composition (wt%)	Composition (wt%)	Composition (wt%)	Composition (wt%)
	Fe	Mg	Nd	Ni	Pr
Sample A top	0.00	99.32	0.08	0.02	0.02
Sample A mid	0.02	98.10	1.19	0.05	0.28
Sample A bottom	36.20	51.57	5.51	0.14	1.19
Sample B top	0.00	98.51	0.06	0.02	0.02
Sample B mid	0.01	95.81	0.50	0.03	0.12
Sample B bottom	11.59	81.15	2.65	0.05	0.60
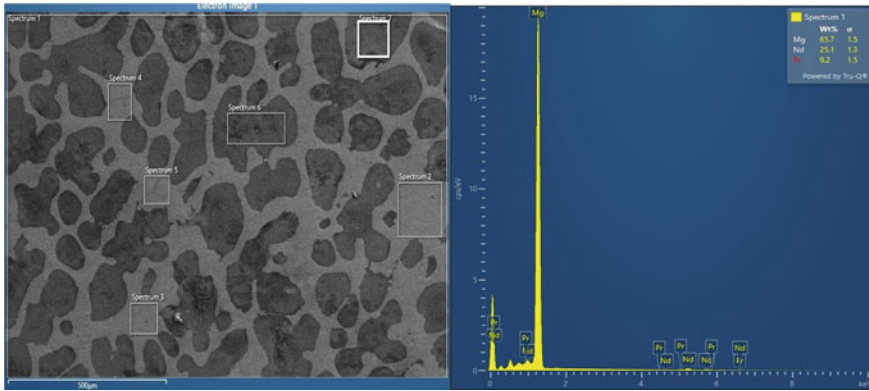
Fig. 3 SEM/EDS results of bottom section interface taken at 100 micron and 10 keV

Table 2 Magnesium to neodymium mass ratio of sample section based on ICP-OES analysis

Mg/Nd ratio	Top	Middle	Bottom
Sample A	1215.57	82.11	9.36
Sample B	1542.34	192.20	30.62

Table 3 Rare earth to nickel mass ratio of sample section based on ICP-OES Analysis

RE/Ni ratio	Top	Middle	Bottom
Sample A	6	32.2	48.6
Sample B	4.9	42.92	61.82
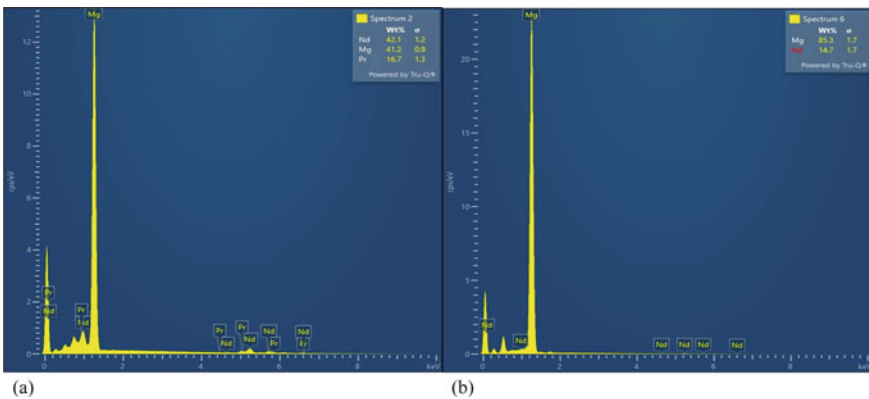
Fig. 4 Sample middle EDS results: (**a**) EDS spectrum and results for Nd-rich section; (**b**) EDS spectrum and results for Mg-rich section
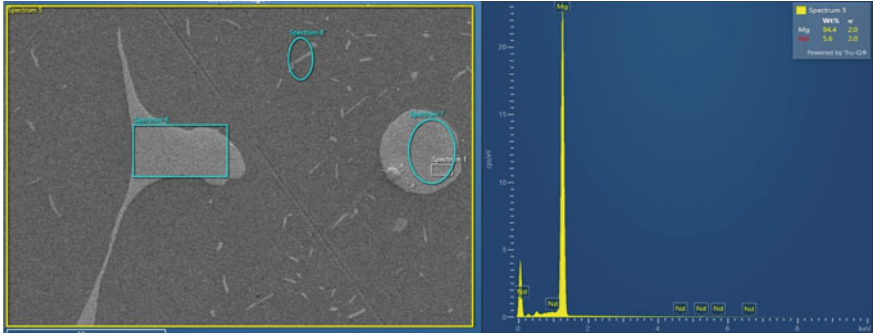
Fig. 5 SEM/EDX results of midsection interface taken at 10 microns and 10 keV
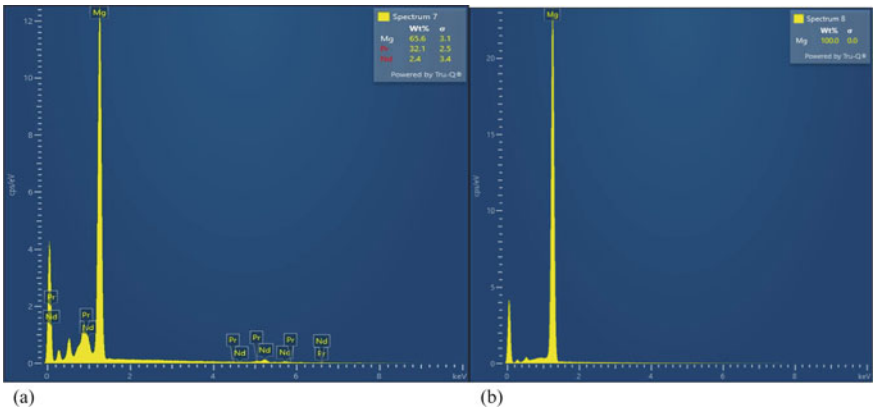
Fig. 6 Sample bottom EDS results: (**a**) EDS spectrum and results for Nd-rich section; (**b**) EDS spectrum and results for Mg-rich section

measurement of rare earth leaching yield. This work used a tungsten rod to try to stir the material during leaching at 900 °C. The tungsten rod bent and twisted easily, leading to poor stirring and little change in composition variation relative to prior experiments.

Discussion

Low nickel concentration in the Mg-Nd alloy is an unexpected and beneficial result. Both Ni and Cu are highly soluble in Mg, and are expected to dissolve, and contaminate the process. If this low-Ni result is confirmed, it might enable a recycling operation to skip coating removal, which is a labor-intensive and expensive step.
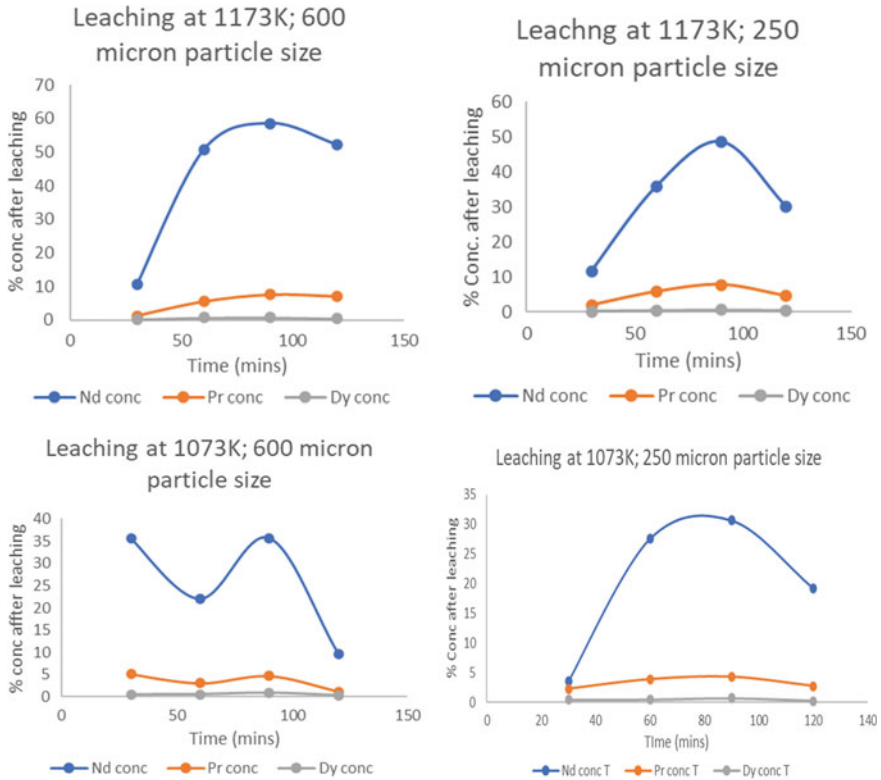
Fig. 7 %wt concentration after leaching at 900C and 800C

That said, it will be essential to determine conformance to magnet alloy producer specifications before making such a decision.

The hypothesis is that surface oxidation during demagnetization in air leads to passivation of the nickel-copper coating material, preventing leaching of the coating into liquid Mg. Subsequent crushing exposes fresh magnet material, but with little Ni-Cu coating exposure to Mg.

References

1. Deshmane VG, Islam SZ, Bhave RR (2020) Selective recovery of rare earth elements from a wide range of E-waste and process scalability of membrane solvent extraction. Environ Sci Technol 54(1):550–558. https://doi.org/10.1021/acs.est.9b05695
2. Xie F, Zhang TA, Dreisinger D, Doyle F (2014) A critical review on solvent extraction of rare earths from aqueous solutions. Miner Eng 56:10–28. https://doi.org/10.1016/j.mineng.2013.10.021
3. Zakotnik M, Afiuny P, Dunn S, Tudor CO (2020) Magnet recycling to create Nd–Fe–B magnets with improved or restored magnetic performance, 9,044,834, 02 June 2015. [Online] Available https://patents.google.com/patent/US9044834B2/en. Accessed 19 Mar 2020
4. Thompson VS et al (2018) Techno-economic and life cycle analysis for bioleaching rare-earth elements from waste materials. ACS Sustain Chem Eng 6(2):1602–1609. https://doi.org/10.1021/acssuschemeng.7b02771
5. Ott RT, McCallum RW (2021) Recovering rare earth metals from magnet scrap. U.S. Patent 10,323,299, 18 June 18 2019 [Online]. Available https://patents.google.com/patent/US10323299B2/en. Accessed 17 May 2021
6. Chinwego C, Wagner H, Giancola E, Jironvil J, Powell A (2022) Technoeconomic analysis of rare-earth metal recycling using efficient metal distillation. JOM 74(4):1296–1305. https://doi.org/10.1007/s11837-021-05045-7
7. Baba K, Nemoto T, Maruyama H, Taketani N, Itayagoshi K, Hirose Y (2010) Hitachi's involvement in material resource recycling
8. U.S. Department of Energy (2022) Rare earth permanent magnets—Supply chain deep dive assessment
9. Bauer D, Diamond D, Li J, Sandalow D, Telleen P, Wanner B (2010) Critical materials strategy. US Department of Energy Office of Policy and International Affairs

Part II
Processing of Rare Earth Elements, Vanadium and Lithium

Extraction of Less Common Metals (REEs and Sc) from Greek Bauxite Residue

Dimitrios Panias and Efthymios Balomenos

Abstract Less common metals including rare earth elements (REEs), as well as Scandium (Sc), play a central role in the development of twenty-first-century economies. Common REE applications are in electronics, renewable energy, the automotive industry, defense and aerospace, medical and health care, glass and ceramics, catalysts, magnets, and metallurgy. Scandium's main applications are in aluminum alloys, solid oxide fuel cells, and in laser technology. REEs and Sc are relatively scarce in nature, and there are a lot of efforts to extract and refine them from several primary and secondary resources such as bauxite residue (BR). This paper describes the mineralogy of REEs and Sc in Greek BR. Then, it summarizes the efforts done by NTUA to extract and refine REEs and Sc either by direct leaching through H_2SO_4 and ion exchange or by direct leaching with task-specific ionic liquids such as the betainium bistriflimide ($HbetTf_2N$) and subsequent stripping with acidic HCl solutions.

Keywords Scandium extraction · Bauxite residue · Ionic liquids

Introduction

The rapid evolution of the 4th Industrial Revolution and the massive use of digital technologies by our society has created a boom in some uncommon metals demand making their supply critical worldwide. A family of such critical metals is the lanthanides, including the 4f transition elements of the periodic table, together with the scandium (Sc) and Yttrium (Y) named collectively as rare earths. Although their name is illusive due to their not scarce abundance in the Earth's crust, they are often

D. Panias (✉)
Laboratory of Metallurgy, National Technical University of Athens (NTUA), Zografos Campus 15780, Athens, Greece
e-mail: panias@metal.ntua.gr

E. Balomenos
Research and Sustainable Development, SA, Metallurgy BU, Ag. Nikolaos Plant, 32003 Viotia, Mytilineos, Greece

found dispersed in low concentrations in several ores and industrial residues, making their extraction and separation labor-intensive and environmentally challenging. Due to their unique physical and chemical properties, they are indispensable in a wide range of modern technologies such as electronics, renewable energy systems, defense technologies, medical devices, and more while at the same time are very valuable in producing vibrant displays, efficient magnets, and catalysts for chemical processes.

It is well known that rare earths are dispersed in the bauxite ore and are concentrated after the metallurgical treatment of bauxites through the Bayer Process into the bauxite residue, which is considered nowadays as a potential intermediate byproduct to produce several critical metals. Greece is the only European country with a vertically integrated aluminum industry including Bauxite Mines, Bauxite Refining to metallurgical grade alumina through the Bayer Process, and alumina smelting for Al metal production through the Hall-Heroult Process. Almost 800,000 tons of filter-pressed BR are produced annually in Greece, out of which only about 100,000 tons are recycled in the cement industry. BR utilization has attracted a lot of scientific interest in Greece with the core of the research performed to be centered on the extraction of rare earths and especially of Scandium. This paper summarizes the efforts done by the research group Technologies for Sustainable Metallurgy (TeSMet) of NTUA to extract and refine REEs and Sc from Greek bauxite residues.

Characterization of Greek Bauxite Residue

The main chemical components of bauxite residue are shown in Table 1 while the trace elements are given in Table 2. Except for the elements shown in Tables 1 and 2, traces of Nb (100 mg/kg), Th (105 mg/kg), V (1029 mg/kg), and Cr (1429 mg/kg) have been detected. The quantitative mineralogical composition is shown in Table 3.

Hematite, goethite, diaspore, boehmite, gibbsite, hydrogarnet, cancrinite, perovskite, and titanium dioxides are the most abundant mineralogical phases. The REE occurrences in bauxite residue, as were experimentally determined by electron probe microanalysis with energy dispersive as well as wavelength dispersive spectroscopy, microscale in-situ Raman spectroscopy, and transmission electron microscopy, are summarized in Table 4 also indicating the typical particle size of REE containing phases.

In bauxite residue, the most abundant REE-bearing phases are light REE (LREE) ferrotitanates that form a solid solution between the phases with major compositions $(REE,Ca,Na)(Ti,Fe)O_3$ and $(Ca,Na)(Ti,Fe)O_3$. These occurrences are further subdivided into cerium-predominant and neodymium-lanthanum-predominant types. The

Table 1 Major oxide composition of Greek bauxite residue [1]

Oxide	Fe_2O_3	Al_2O_3	CaO	TiO_2	SiO_2	Na_2O	MnO	LOI
wt%	44.6	20.2	9.1	5.7	5.3	2.3	0.04	9.2

Table 2 Trace elements composition of Greek bauxite residue [1, 2]

Element	La	Ce	Pr	Nd	Sm	Eu	Gd	Tb	Dy	Ho	Er	Tm	Yb	Lu	Y	Sc	ΣLn	ΣREE
mg/kg	130	480	29	107	19.4	4.6	22	3.3	20.1	4.1	13.3	<2	13.8	2.2	108	97.6	854.4	1060

Table 3 Quantitative mineralogical composition of bauxite residue [2]

Mineral	Boeh	Dia	Gib	Hem	Goe	An	Ru	Cal	Qu	Cha	Hyd	Can	Per	Por	other
wt%	2	13	2.5	31	7.5	0.6	0.7	5	0.3	3.7	14.5	11	4	0.8	3.4

Boeh Boehmite, *Dia* Diaspore, *Gib* Gibbsite, *Hem* Hematite, *Goe* Goethite, *An* Anatase, *Ru* Rutile, *Cal* Calcite, *Qu* Quartz, *Cha* Chamosite, *Hyd* Hydrogarnet, *Can* Cancrinite, *Per* Perovskite, *Por* Portlandite

Table 4 REE phases present in bauxite residue [1]

Phase	Typical size (μm)
LREE carbonate	20–30
Yttrium phosphate (xenotime/churchite)	2–3
Cerium phosphate	5–10
Partly reacted LREE ferrotitanate	10
High LREE content (>5 wt%) ferrotitanate	5–10
Low LREE content (<5 wt%) ferrotitanate	<1
Cerium oxide/oxyhydroxide	5
Cerium oxide/oxyhydroxide associated with manganese	Irregular
Mixed	20–40

cerium predominant form also contains up to 2.7 wt% thorium. LREE ferrotitanates are secondary phases formed during the Bayer process by an in-situ transformation of the precursor bauxite LREE phases. Compared to natural systems, the indicated solid solution resembles the loparite-perovskite series. LREE particles often have a calcium ferrotitanate shell surrounding them, as is seen in Fig. 1, which probably hinders their solubility. A minor amount of LREE carbonate and phosphate minerals as well as manganese-associated LREE phases are also present in bauxite residue. Heavy REEs (HREE) occur in the same form as in bauxites, namely as yttrium phosphates. Minor yttrium amount is incorporated into mixed REE phases that contain cerium as the prevailing REE and neodymium, lanthanum, calcium as well as thorium as other constituents. These results show that the Bayer process has an impact on the initial REE mineralogy contained in bauxite. LREE occurs in bauxite residue as secondary phases mainly in ferrotitanates while HREE remains unaffected mainly as yttrium phosphates during the Bayer process.

Sc is mainly hosted in hematite, where Sc^{3+} isomorphous substitutes Fe^{3+}. The average concentration of Sc in the hematite matrix of bauxite residue is about 170 mg/kg. Goethite was also identified to host Sc with a concentration of about two times more than in hematite 330 mg/kg. Goethite assumes to host adsorbed Sc^{3+} cations on the surface of its particles. Minor hosts of Sc are titanium dioxides and aluminum oxyhydroxides, the latter represented by diaspore and boehmite. Since diaspore and boehmite are digested in the Bayer process, about 10% of Sc contained in them could be released from their lattice and transferred through surface adsorption to goethite of bauxite residue. In bauxite residue, hematite, goethite, and zircon host
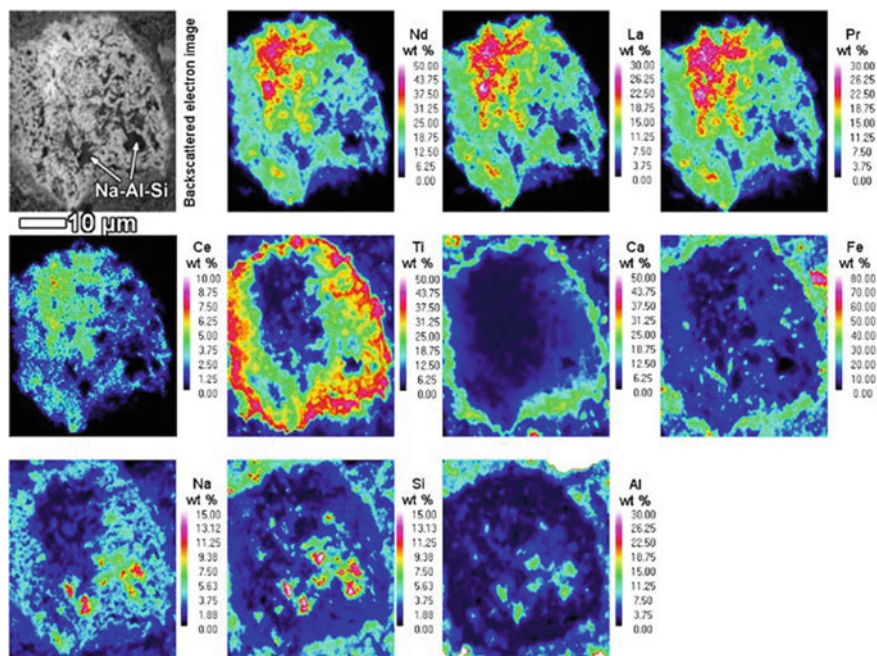
Fig. 1 EPMA-WDS quantitative elemental mapping of light REE (LREE) ferrotitanates [1]

55%, 25%, and 10% of the total Sc while 2% is hosted in diaspore/boehmite and 1% in titanium phases (Table 5). The remaining 7% of Sc is unaccounted. The effect of the Bayer process to the modes of occurrences of Sc in bauxites is minor. The secondary bauxite residue minerals formed during bauxite processing do not capture any or capture very low amounts of Sc.

Table 5 Sc distribution between host minerals in bauxite residue [2]

Host mineral	wt% of total Sc
Hematite	55 ± 20
Goethite	25 ± 20
Zircon	10 ± 5
Diaspore/boehmite	2 ± 2
Titanium phases	1 ± 1
Other/unaccounted	7

REEs and Sc Extraction

Two are the most important systems for extracting REEs and Sc from bauxite residues: (1) leaching with H_2SO_4 solutions and (2) leaching with the task-specific ionic liquid (IL) HbetTf$_2$N.

BR–H$_2$SO$_4$ System

The hydrometallurgical treatment of Greek bauxite residue with H_2SO_4 has a serious drawback concerning the extraction of REEs. It is well-known that light REEs (LREEs) form double sulfate salts with sodium which are sparingly soluble in water and because the BR contains 2–3%wt Na_2O and almost 80% of total REEs are LREEs, the extraction of REEs is negligible and includes only the heavy REEs, which are only 197.1 mg/L (Table 2). Therefore, the sulfuric acid treatment of BR is concentrated on Scandium extraction. The metal recoveries at 20% pulp density, 95 °C as a function of H_2SO_4 concentration and retention time are given in Fig. 2 [3]. The H_2SO_4 concentration substantially affects metal recoveries. Sc extraction increases from 50% to almost 90% with the increase of H_2SO_4 concentration in the range 1–5 M. The effect on Fe extraction is more pronounced. At 1 M, Fe is sparingly dissolved while at high concentrations 4–5 M is totally dissolved. Si is dissolved sparingly in the region 3–5 M while is appreciably dissolved initially at low concentrations 1–2 M forming a gel that hampers the filtration process. Silica gel formation is suppressed either by increasing the retention time at 1–2 M or by increasing the acidity of the leaching solution.

The effect of temperature is shown in Fig. 3a. The results indicate that in order to achieve 90% Sc recovery, the temperature must increase up to 95 °C, at high acid concentration where almost all of Fe co-dissolves while Al and Ti recoveries are about 70% with no Si dissolution. The lower the temperature, the lower the metal recoveries with the most pronounced effect on Fe. The results [4] indicate two leaching approaches: a) leaching at low acidity (1 M) but high retention time and temperature (Fig. 3b) leaching at high acidity (>3 M) and high temperature (Fig. 3c).
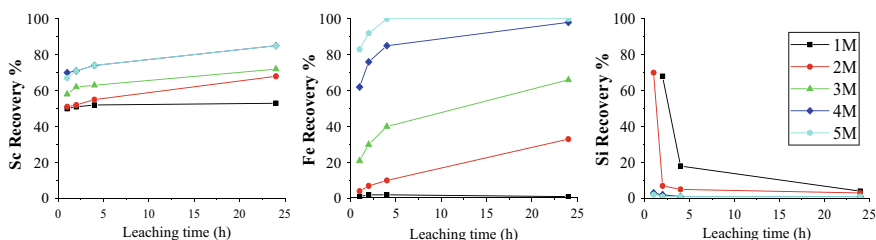
Fig. 2 Metal recoveries at 20% pulp density, 95 °C as a function of H_2SO_4 concentration and retention time [3]
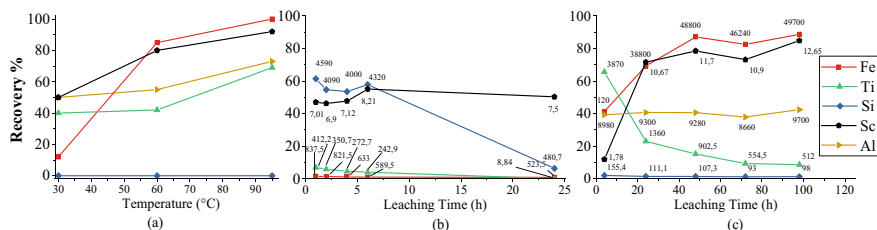
Fig. 3 **a** Effect of temperature at 4 M H_2SO_4, 10% pulp density, 24 h, **b** leaching at low acidity 1 M H_2SO_4, 20% pulp density, 95 °C **c** leaching at high acidity 3 M H_2SO_4, 20% pulp density, 85 °C [3, 4]

The first approach leads to intermediate Sc dissolution (50%) followed by very low Fe, Ti, and Si co-dissolution (Fig. 3b). The second leads to high Sc (70–85%) and Fe (70–90%) dissolution followed by intermediate Al (40%) and negligible Si dissolution. Ti is dissolved massively initially but with time is removed from the solution, as it undergoes hydrolysis at the elevated temperature. The pregnant leaching solution (PLS) due to very low Sc content in BR has low Sc concentration. The composition of the solution at low acidity test is 7.5 mg/L Sc, 524 mg/L Fe, 481 mg/L Si, and 9 mg/L Ti. At high acidity test, the solution contains 10.6–12.6 mg/L Sc, 38.8–49.7 g/L Fe, 98–111 mg/L Si, and 512–1360 mg/L Ti. The extraction of Sc(3+) from such solutions was studied at ambient temperature using several resins [5], the most important of them was the Coherent Selective-Ion Recovery (SIR) resin, the Seplite LSC 730 resin, and the Seplite LSC 790 resin. The metal loading on SIR resin from high acidity tests at 1 h retention time is shown in Fig. 4a. Fe(3+) and Ti(+4) are adsorbed at high capacities due to their very high concentrations in the PLS (18 and 4.5 g/L) with Ti achieving substantially higher capacities although it has 4 times lower concentration in the PLS. Sc(3+) adsorption capacity is extremely low (60 mg/L of resin) due to a significantly higher concentration of impurities relative to Sc. The metal loading on SIR resin from low acidity tests at 16 h retention time is shown in Fig. 4b. Due to substantially lower metal concentrations in the PLS, more bed volumes of PLS can be treated by the same volume of resin. Again, Fe(3+) and Ti(+4) are adsorbed at high capacities but after passing 20BVs of PLS Fe(3+) starts being desorbed in favor of Ti(+4). The Sc adsorption capacity has been improved reaching the value of 500 mg/L of resin due to the lower concentration of impurities in the PLS but it is still very low due to its low initial concentration in the PLS. In case of a spike with Sc(3+) initial PLS to a concentration of 60 mg/L Sc, the Sc adsorption capacity reaches the value of 2640 mg/L of resin, indicating that increased Sc concentrations in the PLS favored the Sc loading on SIR resin over the other cations even in the presence of high level of impurities. Therefore, it is clear that the Fe(3+) and Ti(+4) adsorption on the resins must be suppressed in order to improve their efficiency against Sc(3+). This can be achieved by doing modifications in PLS such as acidification and Fe(3+) reduction by elemental Fe (Fig. 5).

a) High acidity test at 1h: Sc 10mg/L, Fe 18g/L, Ti 4.5g/L

b) Low acidity test at 16h: Sc 8.2mg/L, Fe 560mg/L, Ti 43mg/L
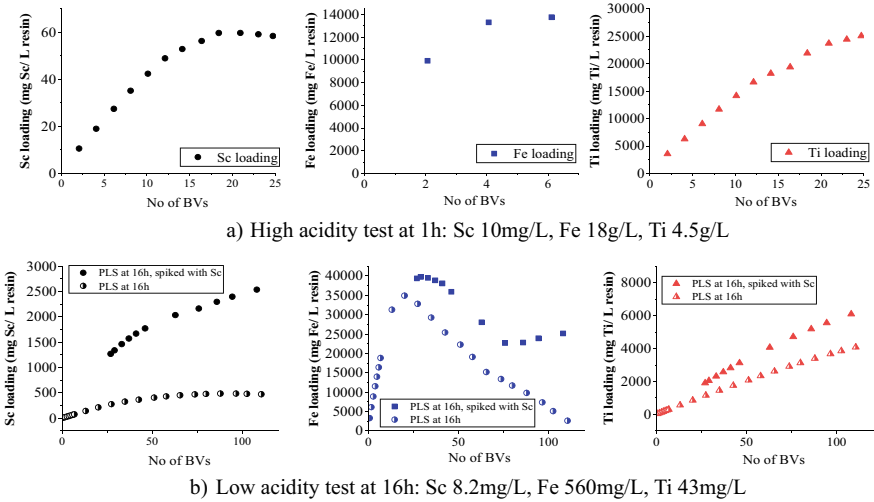
Fig. 4 Sc, Fe, and Ti loading onto the SIR resin **a** from high acidity tests and **b** from low acidity tests [4]
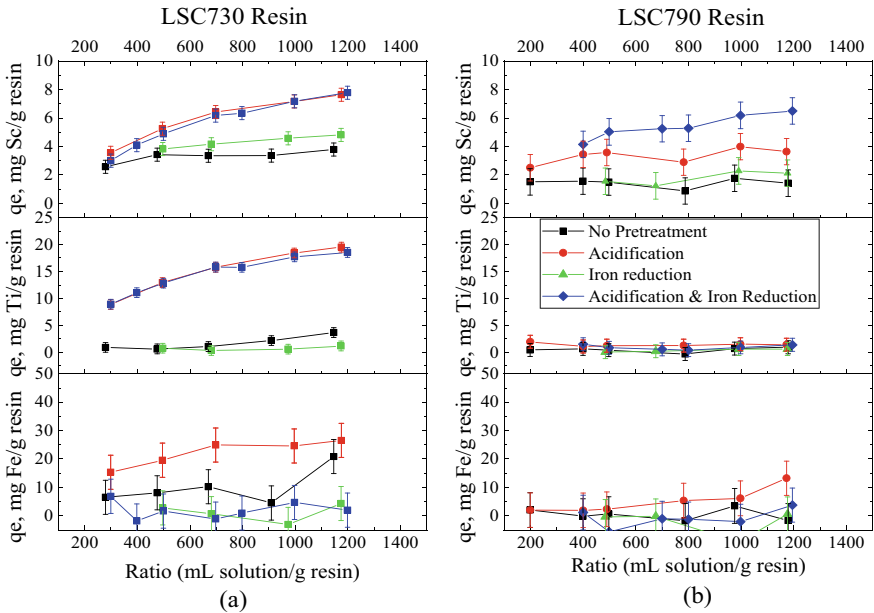
Fig. 5 Suppression of Fe and Ti adsorption by modifications in PLS: (i) no pretreatment, (ii) acidification, (iii) iron reduction by elemental Fe, and (iv) iron reduction and acidification for LSC 730 (**a**) and LSC 790 resins (**b**) [5]

In the case of the LSC 730 resin with monophosphonic functional groups (Fig. 5a), acidification of the solution resulted in a significant increase in the adsorption of scandium, as well as titanium and iron. However, when acidification was accompanied by iron reduction, a high level of scandium and titanium adsorption was achieved without any iron adsorption in the resin. It is observed in Fig. 5a that the results of Sc(3+) adsorption from an acidified solution with and without Fe(3+) reduction are identical, suggesting that in the LSC 730 resin, there was no competitive interaction between the Fe(3+) and Sc ions. Regarding the LSC 790 resin with impregnated D2EHPA functional groups (Fig. 5b), it was observed that neither iron nor titanium adsorption occurred under any condition tested. However, the combination of acidification and iron reduction led to the highest efficiency in terms of scandium adsorption. In summary, the incorporation of elemental iron was found to be a crucial factor in the overall effectiveness of the adsorption process. As depicted in Fig. 5b, the adsorption of scandium was reduced in the acidified solution containing Fe(3+) ions in comparison to the acidified solution containing Fe(2+) ions. Furthermore, there was an increase in iron adsorption from the acidified solution containing Fe(3+) ions, indicating the presence of a competitive interaction between the Fe(3+) and Sc(3+) ions. In conclusion, LSC 790 was found to be more selective for Sc towards Ti and Fe, while LSC 730 had a higher extraction capacity for Sc but in both cases, the solution must be acidified and the Fe(3+) be reduced with elemental iron in order for the resins to exhibit their best performance.

BR-HbetTf$_2$N System

The functionalized ionic liquid betainium bis(trifluoromethylsulfonyl)imide (HbetTf$_2$N) is shown in Fig. 6a. It has a switching thermomorphic behavior as upon addition of water is hydrophobic at temperatures below 55.5 °C whereas above 55.5 °C forms an aqueous solution (Fig. 6b). In addition, the mixtures of the HbetTf$_2$N with water also show a pH-dependent phase behavior: two phases occur at low pH, whereas one phase is present under neutral or alkaline conditions [6]. The thermomorphic behavior will be used in the BR leaching process while the pH-dependent phase behavior will be useful during the pregnant leaching solution striping process development.

The BR leaching will be performed with a 40% v/v mixture of H$_2$O and HbetTf$_2$N to achieve the dissociation of protons from the carboxylic functional group of betaine necessary for the dissolution of metals exist in BR according to the following reaction:

$$6HbetTf_2N + REE_2O_3 = 2REE(bet)_3(Tf_2N)_3 + 3H_2O$$

In addition, the leaching temperature will be higher than the upper critical solution temperature of 55.5 °C to achieve full miscibility in-between H$_2$O and HbetTf$_2$N (Fig. 6b). The leaching behavior is given in Fig. 7 [7]. Temperature is a crucial factor for REE dissolution as its rising to 180 °C increases the extraction of LREEs and
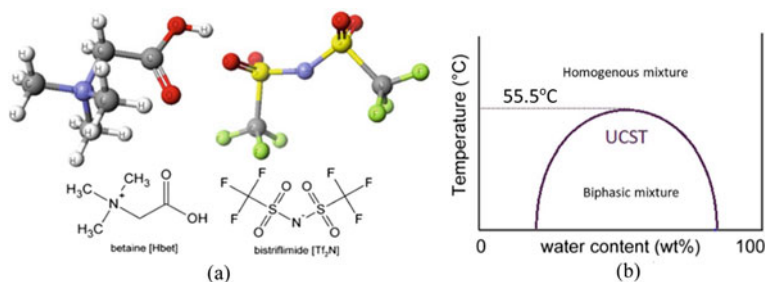
Fig. 6 **a** HbetTf$_2$N molecular structure and **b** schematic phase diagram [Hbet][Tf$_2$N]–H$_2$O [7, 8]

HREEs from 20 and 35% to 80% and 70%, respectively. The Sc extraction is not affected seriously by temperature and remains in the region of 30–40%. Fe dissolution doesn't exceed 3% and as the hematite and goethite are the main hosts of Sc this explains the low Sc extraction. 20–30% of Al is dissolved with almost all Ca and Na of BR. Si and Ti have negligible dissolution. The retention time is crucial again for REE extraction with a substantial increase in extraction from 4 to 24 h and a moderate one at 48 h. Sc, Al, and Fe extractions are more or less constant at 40%, 20%, and 3% with a slight increase with time. Pulp density is crucial for REE extraction as the REE extraction decreases as the S/L ratio increases. The effect on Sc, Al, and Fe is almost insignificant, which makes sense for Sc as high concentrations can be achieved with the use of a small volume of leaching agent. The residues are concentrated in Fe, Ti, and Si and depleted from sodium and calcium as katoite, cancrinite, and calcite dissolve almost completely. The optimum leaching conditions are given in Table 6.
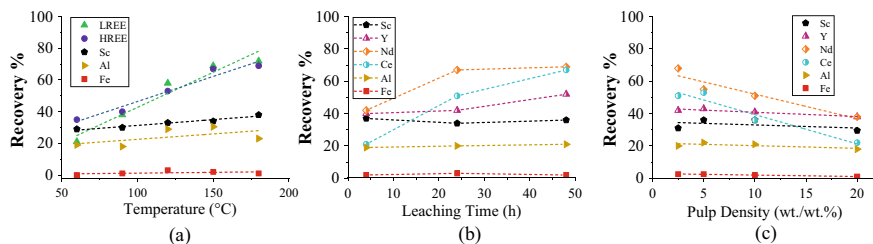
Fig. 7 **a** Temperature effect (4 h, S/L = 5%w/v), **b** Kinetics (90 °C, S/L = 5%w/v), **c** S/L effect (24 h, 90 °C) [7]

Table 6 Composition of IL-PLS after leaching at 90 °C, S/L = 10%w/v, 24 h, water to IL ratio = 40%v/v

Fe (mg/l)	Al (mg/l)	La (mg/l)	Y (mg/l)	Sc (mg/l)	Ca (mg/l)	Na (mg/l)
660.79	4450.85	2.06	4.07	4.73	7575.00	1157.50
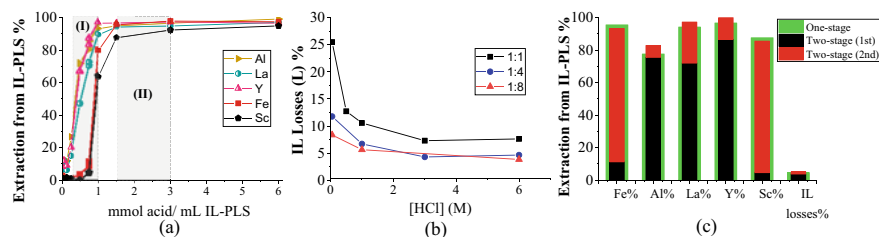
Fig. 8 **a** Extraction vs addition of HCl, **b** IL losses vs HCl concentration, **c** metal extraction versus stripping mode [8]

The PLS stripping will be performed with HCl solutions at 25 °C to make use of the thermomorphic and pH-dependent phase behaviors of the HbetTf2N [8]. The results are shown in Fig. 8.

Two distinct areas of interest, shaded as (I) and (II), are observed in the metal extraction behavior (Fig. 8a). In the area (II), it is observed that with the addition of more than 1.5 mmol of acid/mL IL-PLS, complete extraction of all metals can be achieved. At lower addition of acid 0.5–0.75 mmol HCl/mL IL-PLS (area (I)), selective extraction of metals is observed with high recoveries of Al, La, and Y and very low recoveries of Fe and Sc. The latter two can be extracted from the IL-PLS at higher HCl addition, following a similar trend in their extraction, confirming their high chemical affinity and stronger complexation with the HbetTf2N. In Fig. 8b, it is seen that the losses of the IL are increased when the volume ratio acid:IL-PLS (R) is increased. Moreover, under the same acid:IL-PLS volume ratio, the IL losses decrease by increasing the acidic concentration of the strip solution. This is attributed to a pH-dependent behavior that HbetTf2N exhibits. Based on the metal extraction behavior, as well as the IL losses in the aqueous phase, two possible stripping procedures were examined: a non-selective, one-stage extraction process and a selective two-stage process.

For the one-stage extraction, 1.5 mmol HCl/mL-IL PLS was added at the minimum possible acid:IL-PLS volume ratio to achieve maximum extraction with minimum losses. The results are given in Fig. 8c. The extraction of almost all metals was of the order of 90% with 4.64% HbetTf$_2$N losses. The Sc concentration in the resulting stripping solution was 8 mg/L due to a significant amount of water that was entrapped in IL PLS and removed to the aqueous extract, due to the pH change, increasing the volume of the extract solution (Table 7). For the two-stage stripping process, IL-PLS was subjected to a first stripping step using 6 M HCl solution at a volume ratio of 1:8 so that 0.75 mmols of HCl/mL IL-PLS to be added. As is seen in Fig. 8c and Table 7, all metals with the exception of Fe and Sc were transferred almost massively from the IL-PLS to the aqueous extract. After the first step, the obtained IL phase was subjected to a second stripping step testing different concentrations of HCl by keeping constant the acid:IL volume ratio at 1:8. The optimum Sc extraction with the highest Sc concentration in the extract was achieved with 3 M HCl in the stripping solution (Fig. 9a) due to the increased IL losses into the extract solution at higher

Table 7 Concentration of metals in the aqueous extract streams from the stripping process

	Conditions	mmol/ml IL-PLS	Fe (mg/l)	Al (mg/l)	La (mg/l)	Y (mg/l)	Sc (mg/l)	IL losses (% wt)
One-stage stripping	6 M HCl R = 1:4	1.5	1220	6675	3.75	7.6	8	4.64
Two-stage stripping	1st 6 M HCl R = 1:8	0.75	202	7600	4	9.5	0.594	3.83
	2nd 3 M HCl R = 1:8	0.75	5700	3300	5.3	5.9	39	1.24
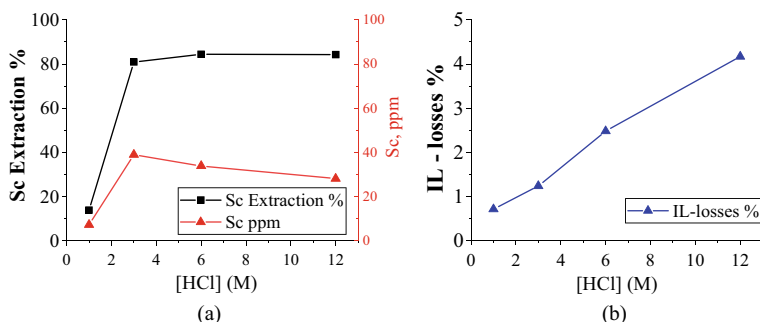
Fig. 9 a Sc extraction and concentration and **b** IL losses in second stage extract versus HCl concentration [8]

HCl concentration (Fig. 9b). The extraction of other metals during the second stage is shown in Fig. 8c. The cumulative IL losses in the two stages process (5.07%) are slightly higher than the ones of the one stage process (Fig. 8c and Table 7) but the Sc concentration in the extract solution is 39 mg/L almost 5 times higher than the one of the one stage process (Table 7).

Conclusions

In bauxite residue, the most abundant REE-bearing phases are the light REE (LREE) ferrotitanates that form a solid solution between the phases with major compositions $(REE,Ca,Na)(Ti,Fe)O_3$ and $(Ca,Na)(Ti,Fe)O_3$. A minor amount of LREE carbonate and phosphate minerals as well as manganese-associated LREE phases are also present. HREEs occur in the same form as in bauxites, namely as yttrium phosphates. Sc is mainly hosted in hematite, goethite, and zircon while minor amounts are hosted in titanium and aluminum oxyhydroxide phases.

Sc can be extracted from Greek BR with H_2SO_4 leaching followed by an ion exchange adsorption process. A PLS concentrated in Fe and Ti is problematic for the IX performance as those metals consume the adsorption sites minimizing the Sc

adsorption. Therefore, the PLS must have the lowest possible Fe and Ti content and the highest Sc one. Moreover, to make more efficient the IX operation, the PLS must be acidified and the aqueous Fe^{3+} species be reduced to Fe^{2+} species. In general, the Sc recovery is at intermediate levels (40–50%). LREEs that constitute 80% of the total REEs in Greek Bauxite cannot be recovered because are precipitated as mixed sodium sulfates.

Sc and REEs can be extracted with the functionalized ionic liquid $HbetTf_2N$ followed by stripping with HCl solution. The Sc recovery does not exceed 40% while REEs are recovered up to 70–80%. Two stages stripping process must be applied to recover efficiently the REEs at the first stage and the Sc at the second one. Fe follows the Sc behavior during stripping but is differentiated from Sc during leaching as the IL $HbetTf_2N$ is not selective for iron.

References

1. Vind J, Malfliet A, Blanpain B, Tsakiridis P, Tkaczyk A, Vassiliadou V, Panias D (2018) Rare earth element phases in bauxite residue. Minerals 8(77). https://doi.org/10.3390/min8020077
2. Vind J, Malfliet A, Bonomi C, Paisted P, Sajóe I, Blanpain B, Tkaczyk A, Vassiliadou V, Panias D (2018) Modes of occurrences of scandium in Greek bauxite and bauxite residue. Min Eng 123:35–48
3. Davris P et al (2018) Hydrometallurgical extraction of scandium from bauxite residue based on sulfuric acid process. In: Paper presented at the 2nd international bauxite residue valorisation and best practices conference, Athens, 7–10 May 2018, pp 449–454
4. Balomenos E et al (2021) Scandium extraction from bauxite residue using sulfuric acid and a composite extractant-enhanced ion-exchange polymer resin. In: Azimi G et al (eds) Rare metal technology 2021. The minerals, metals & materials series. Springer. https://doi.org/10.1007/978-3-030-65489-4_22
5. Toli A, Mikeli E, Marinos D, Balomenos E, Panias D (2023) Assessing the efficiency of ion exchange resins for the recovery of scandium from sulfuric acid leaching solutions. Separations 10(366). https://doi.org/10.3390/separations10070366
6. Nockemann P, Thijs B, Stijn P, Jan T, Glorieux C, Hecke K, Meervelt L, Kirchner B, Binnemans K (2006) Task-specific ionic liquid for solubilizing metal oxides. J Phys Chem B 110:20978–20992
7. Davris P, Balomenos E, Panias D, Paspaliaris I (2016) Selective leaching of rare earth elements from bauxite residue (red mud), using a functionalized hydrophobic ionic liquid. Hydrometallurgy 164:125–135
8. Mikeli E, Balomenos E, Panias D (2021) Utilizing recyclable task-specific ionic liquid for selective leaching and refining of scandium from bauxite residue. Molecules 26(818). https://doi.org/10.3390/molecules26040818

Recovery of High Purity Vanadium Salts from Bayer Liquor

C. Mangunda, M. Svärd, and K. Forsberg

Abstract Bauxite ores used in aluminium oxide production via the Bayer process contain trace elements (REEs, V, Li, Sc, Ga) currently not valorised. Vanadium and Gallium dissolve during the Bayer process forming impurities in the Bayer liquor (sodium aluminate solution). Vanadium application ranges from steel to aircraft industries, and extraction involves ammonium treatment of strip liquor for vanadium salt (AMV, V_2O_5) precipitation. Current crystallization techniques have drawbacks of generating voluminous, highly saline wastewater. This study investigated the use of antisolvent (acetone) crystallization with synthetic solutions as an alternative to the crystallization and calcination step in the conventional production of high purity vanadium salts. The yield, purity, and product characteristics of the crystals for different final organic to aqueous (O/A) ratio at constant addition rate of antisolvent at room temperature have been investigated. A batch time-dependent effect was observed with the best product quality, in terms of size and crystal habit (dominated by hexagonal laths), being attained when $t_b \leq 2$ h at an O/A ratio of 0.5. The early onset of acicular crystal formation and higher yields ($\geq 97\%$), along with higher impurity incorporation into the solid phase, was observed at an O/A ratio of 0.75, and this was attributed to higher levels of supersaturation.

Keywords Vanadium · Crystallization · Bauxite ore · Bayer liquor · Valorisation · Purity · Yield

Introduction

Vanadium is a metal of particular interest with approximately 39% being supplied by China hence the increase in economic importance and supply risk in Europe and beyond [1]. This increase has necessitated the exploration of multiple primary (bauxite ore) and secondary (spent catalysts, fuel oil, steelmaking slag, oil and coal

C. Mangunda (✉) · M. Svärd · K. Forsberg
Department of Chemical Engineering, KTH Royal Institute of Technology, 100-44, Stockholm, Sweden
e-mail: cledwyn@kth.se

residues) sources for its extraction [2] with the Bayer liquor as one of the candidates. The extraction of valuable metals, such as aluminium from bauxite ore via the Bayer process, produces a Bayer liquor laden with inorganic species that have potential value if recovered. The Bayer liquor contains, alongside Al, valuable trace elements like rare earth elements (REEs), V, Li, Sc, Ga that are currently not fully valorised [3–5]. Vanadium and Gallium both dissolve during the Bayer process forming a constant impurity in the Bayer liquor, the sodium aluminate solution which is the heart of the process. If the vanadium is not extracted from the liquor it ends up reporting to the bauxite residue (red mud) as waste. Vanadium, although a minor Bayer liquor constituent, has high tensile strength, resistance to corrosion and improves hardness in alloys rendering it useful in multiple industrial applications covering steel manufacturing, energy storage, green chemistry, aircraft, and defence industries [6, 7]. Novel vanadium applications, such as thermochromic fenestration coatings, catalyst for water-splitting to support the future hydrogen-based economy, intercalation, and solid-state batteries [8], have also added to vanadium demand.

Conventional vanadium extraction from ores or slags involves pyrometallurgy, leaching, SX, and ammonium treatment of strip liquor to precipitate the vanadium salts (ammonium metavanadate (AMV) and vanadium pentoxide). This route has the advantages of easy operation and high product quality but comes with the concomitant challenges of generating significant amounts (20–40 tons of wastewater per ton of V_2O_5—the most stable phase of the vanadium oxides) of highly saline wastewater [9, 10]. The use of high temperature unit operations also increases the energy consumption and the carbon footprint of this process. Other researchers have investigated alternative routes of crystallizing vanadium salts without the aforementioned drawbacks using membrane technology and electrolysis [9, 11]. Another field of study for vanadium crystallization has focused on V_2O_5 nanostructures using techniques such as sol-gel, hydrothermal, chemical vapor deposition, magnetron sputtering, and atomic layer deposition [12]. These nanostructures have been found to coagulate into V_2O_5 nanofibers when subjected to long-term ageing [12]. A common aspect of the previous studies has been the need to better understand the role of process parameters in influencing the product characteristics whilst reducing the negative impacts of the conventional vanadium extraction route. These investigations, however, have not focused on the use of antisolvent crystallization to recover vanadium salts from Bayer liquor.

The present study seeks to investigate how antisolvent crystallization can be used to crystallize high purity vanadium salts from a Bayer liquor, and if this can become an alternative, environmentally friendly route. The anticipated benefit of this approach is that Vanadium will be recovered from the Bayer liquor resulting in little or none of it reporting to the bauxite residue hence further reducing the generation of the red mud.

Materials and Methods

Reagent grade sodium vanadate (Merck), aluminium sulphate (Alfa Aesar), potassium sulphate (VWR), and calcium sulphate (VWR) of 99.9% purity were individually mixed with Millipore water to make synthetic feed solutions for the supply of V, Al, K, and Ca in all the experiments. Reagent grade acetone (VWR) was used as the antisolvent. The selected stock solution concentrations of V and that of the impurities (Al (III), K (I), and Ca (II)) were like those found in industrial loaded strip liquor—LSL [13] and are presented in Table 1. The LSL with V only was the pure system and the one with impurities was the impure system.

Batch experiments were conducted in a 100 mL jacketed glass crystallizer covered by a lid with ports for pH and temperature probes, fitted with an Ika overhead stirrer (operating at 300 rpm to achieve homogeneity) and whose temperature was controlled at 25 ± 0.5 °C using a thermostatic chiller (Julabo FP 50) as shown in Fig. 1. Since the antisolvent is volatile, evaporation effects were minimized by sealing off the crystallizer. The crystallizer was initially fed with 50 mL of synthetic LSL and allowed to attain a steady temperature (25 ± 0.5 °C) before controlled acetone addition using a syringe pump (SyringeSix:1600 New Era Pump Systems). Acetone, which exhibits good miscibility with water and significantly reduces the solubility of vanadium salts in a mixed solvent system, was added at a constant rate of 5 ml/ min to the LSL in proportions corresponding to different final organic-to-aqueous (O/A) volumetric ratios as shown in Table 1. The batch was initially run for 96 h to evaluate the kinetics and approximation of equilibrium. During this period, weighed samples (circa. 1 g) were taken at batch time (t_b) intervals of 1, 2, 4, 6, 24, 48, 72, and 96 h to determine the aqueous metal concentrations and hence understand the variation of yield and purity with time.

In order to be within industrially reasonable batch times, the run was limited to 6 h. Slurry samples, taken at $t_b = 1–6$ h, were quickly analyzed for crystal habit

Table 1 Feed composition and operating conditions used for vanadium salt crystallization

Element	Concentration (mg/L)
V (V)	30,000
Al (III)	25
K (I)	260
Ca (II)	430
Operating conditions	
Antisolvent volume	25; 37.5 mL
Final O/A ratio	0.5; 0.75; 1 (vol/vol)
Stirring speed (overhead)	300 rpm
Antisolvent addition rate	5 mL/min
Maximum batch time	6 h
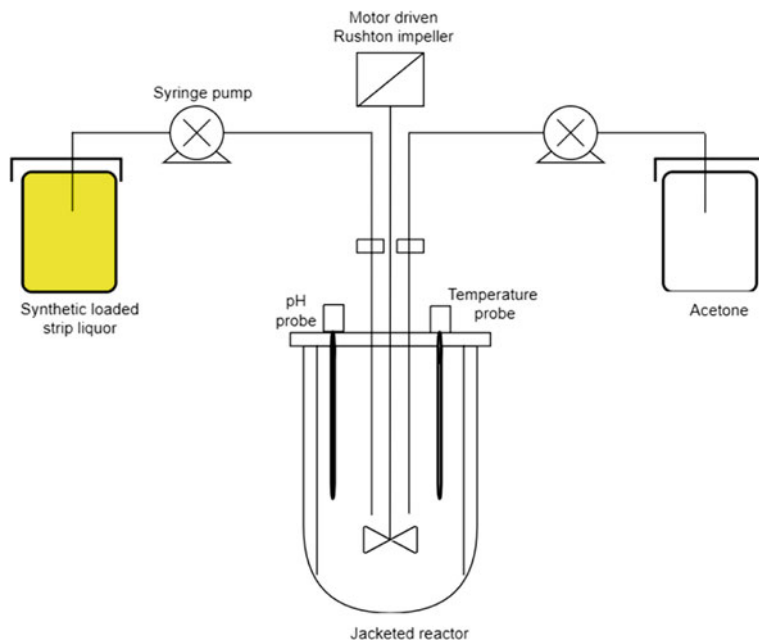
Fig. 1 Reactor setup

using a light microscope (Olympus BH2 at $20\times$ magnification) to identify any time-related changes. The aqueous component, taken at these sampling intervals, was filtered with a 0.22 μm syringe filter, and the solid free solution was diluted to the desired factor using 2% HNO_3 and then used for ICP-OES (Thermo Scientific iCAP 7000 Plus coupled to an autosampler Cetac ASX-520) analysis for concentration determination. The recovery (%) was calculated using Eq. 1.

$$\%\text{Recovery} = \frac{C_i V_i - C_t V_t}{C_i V_i} \tag{1}$$

where C_i and V_i are the initial concentration (mg/L) and volume (L) of the solution and C_t and V_t are the concentrations (mg/L) and volume of solution obtained at time t_b. At the end of the batch, the experiment was stopped, the mother liquor filtered off and the recovered crystals were washed with washing solution to remove any adsorbed impurities. The washing solution was made from an acetone and Millipore water mixture with the same final O/A ratio as for the experiment (similar composition to the metal-free mother liquor). Crystals were air dried in the fume hood to ensure minimal artefacts arose during drying, and then used for further analysis. The powder samples were analysed with SEM–EDS (Hitachi 3700 N with Bruker X-Sense operating at 5 keV) for morphology, elemental composition, and PXRD (Panalytical XPert Pro) for crystal phase identification.

Results and Discussion

The effects of O/A ratio have been shown to be complex and system dependent. Preliminary system behaviour insights were acquired through thermodynamic modelling using OLI Studio 11.5 (OLI Systems, Inc. Cedar Knolls, USA), which predicted a pH of ~5.3 with a vanadium oxide salt containing some calcium $(Ca(VO_3)_2)$ as the dominant salt and small quantities of $Al(OH)_3$ as shown in Fig. 2.

The experimental results (Fig. 3) from varying the O/A ratio for the impure system showed that, at O/A ratio $= 0.5$, the aqueous V concentration gradually decreased in the first 2 h (Fig. 3a) before almost levelling off with increase in t_b. The vanadium salt crystallization yield (Fig. 3b), at an O/A ratio of 0.5, was lower during the period where the Al concentration was high ($t_b \leq 2$ h) but increased subsequently to approximately 70% (2 h $\leq t_b \leq 6$ h).

Increasing the O/A ratio to 0.75 resulted in an opposite behaviour with the aqueous V concentration decreasing significantly in the first 2 h to a point of almost levelling off (Fig. 4a). The impurities in the solid phase generally increased with time within
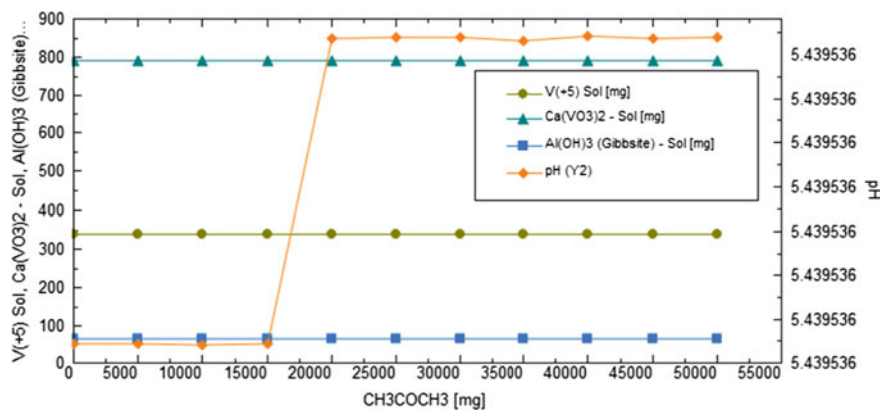
Fig. 2 OLI modelled crystallization of vanadium salts
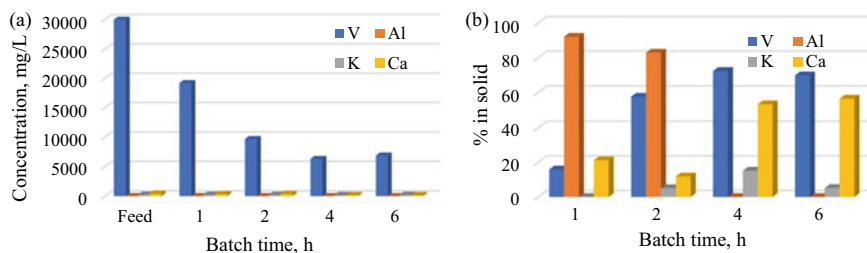
Fig. 3 Vanadium salt crystallization for impure system O/A ratio of 0.5. **a** Aqueous concentration, **b** yield
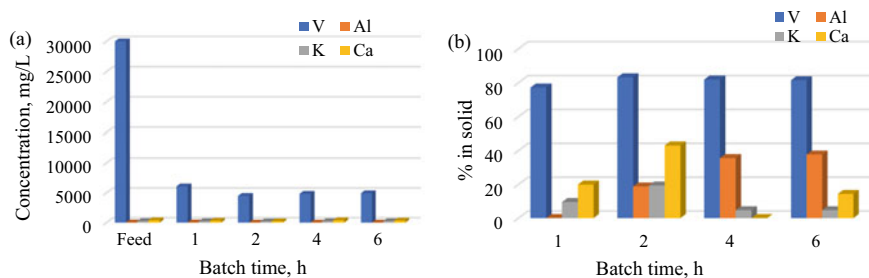
Fig. 4 Vanadium salt crystallization for impure system O/A ratio of 0.75. **a** Aqueous concentration, **b** yield

this period (Fig. 4b) before decreasing in K and Ca were observed with subsequent increase in t_b (2 h $\leq t_b \leq$ 6 h). The vanadium salt crystallization yield (Fig. 4b), at an O/A ratio of 0.75, quickly attains a maximum of approximately 83% within $t_b \leq$ 2 and remains fairly constant beyond this period.

The purity of the vanadium salts, as presented in Fig. 5a, remained almost constant at a set O/A ratio although the values were higher for the O/A ratio of 0.75. The increase in purity at $t_b = 2$, for an O/A ratio of 0.5, is attributed to the decrease in Al and the lower K and Ca concentrations in the solid. This is because the supersaturation increase, with increase in batch time, is slower with respect to other impurities (K, Ca) but is high enough to effect a change in pH. This pH change, from an initial value of 5, allows the impure system to pass through the range where $Al(OH)_3$ is stable but the end pH of 8.4 supports its dissolution [14] hence the decrease in the solid phase is shown in Fig. 3b.

To better understand the vanadium salt crystallization phenomena, a comparison of the pure and impure system, under these two O/A ratios, was investigated and the yield results are shown in Fig. 5b. A comparison of the vanadium salt yields, at the same O/A ratio and specific t_b, indicates that the pure system has lower yields than the impure system. As anticipated, an increase in O/A ratio led to an increase in yield but the extent of differences, with increase in batch time, were not as expected.
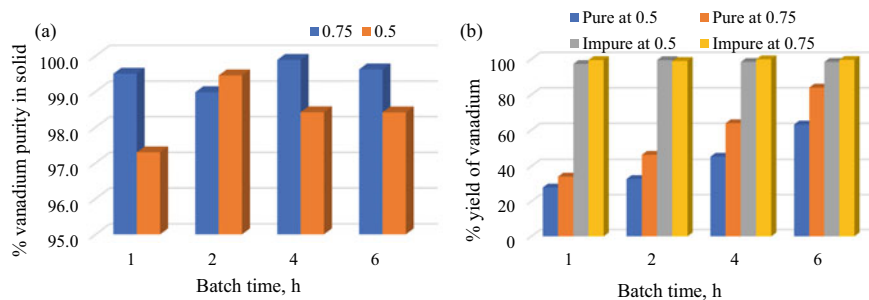
Fig. 5 Vanadium salt **a** purity under varying O/A ratios **b** yield under varying O/A ratios

	1 h	2 h	4 h	6 h
Pure				
With impurities				
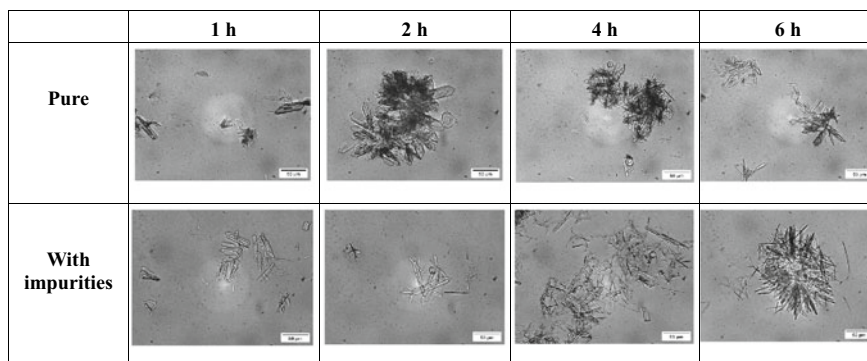
Fig. 6 Changes in crystal habit at $[V^{5+}] = 30$ g/L and O/A $= 0.5$ for pure and impure system

Overall, the results point to initial stages of running the batch ($t_b \leq 2$) at the lower O/A ratio having similar reduced local supersaturation effects as might be obtained through using a dilute antisolvent or significantly reducing the addition rate. The practical advantages of this would be realizing vanadium yields within industrially viable batch times.

The real-time effects of changes in the aqueous chemistry on crystal habit were explored using light microscopy (Fig. 6).

At $t_b \leq 2$ and O/A ratio $= 0.5$, the pure system exhibited elongated, hexagonal laths that grew larger with time (synonymous with low supersaturation) and corroborated the lower yield (Fig. 5b). In the same period, the impure system had smaller hexagonal laths that also grew larger with time, and this points to a relatively higher supersaturation. At higher batch times (2 h $\leq t_b \leq 6$ h), both systems saw the hexagonal laths disappear whilst the acicular (needle-like) particles became dominant but much more in the impure system. The light microscopy results agree with the trend of the vanadium yield (Fig. 5b) and confirm the increase in supersaturation during this period.

The effect of increasing the O/A ratio to 0.75 on crystal habit is shown in Fig. 7. At $t_b \leq 2$, the pure and impure system followed the same trend as at the lower O/A ratio (0.5) but the crystals were smaller with acicular crystals forming earlier in the impure system. This behaviour is typical of higher supersaturation levels prevailing in the system. As batch time increased (2 h $\leq t_b \leq 6$ h), the pure system's dominant crystal habit transitioned from hexagonal laths to ellipsoidal and then acicular particles.

This transition was not observed in the impure system suggesting that the higher supersaturation in the impure systems accelerates the formation of needles. The acicular crystal habit results from the light microscopy were further corroborated by the SEM results (Fig. 8) for the filtered solids taken at the end of the batch.

Further analysis of the filtered solids was carried out using XRD, and the indexed results (Fig. 9) identified the solid phase. The results confirmed the dominance of munirite ($NaVO_3$) for the pure system and a mixture of calcium vanadium oxide

(similar to that predicted by OLI modelling—Fig. 2) and metamunirite ($NaVO_3$) for the impure system.

The distinct, narrow peaks in Fig. 9a are indicative of a more crystalline product with a narrow particle size distribution in comparison to the impure product. The potential to use these crystalline products for commercial vanadium extraction from
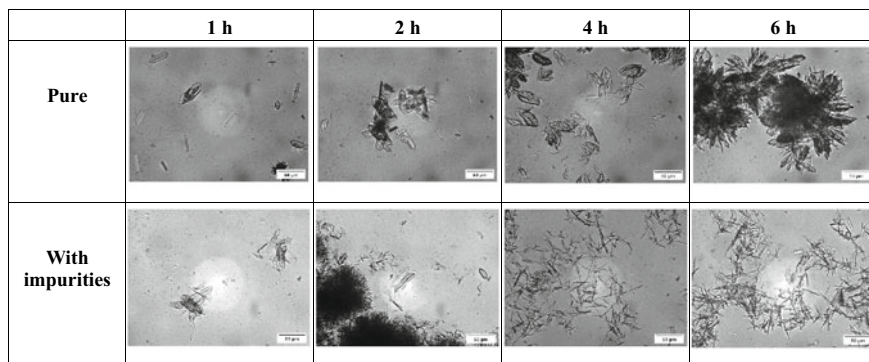
Fig. 7 Changes in crystal habit at $[V^{5+}] = 30$ g/L and O/A $= 0.75$ for pure and impure system
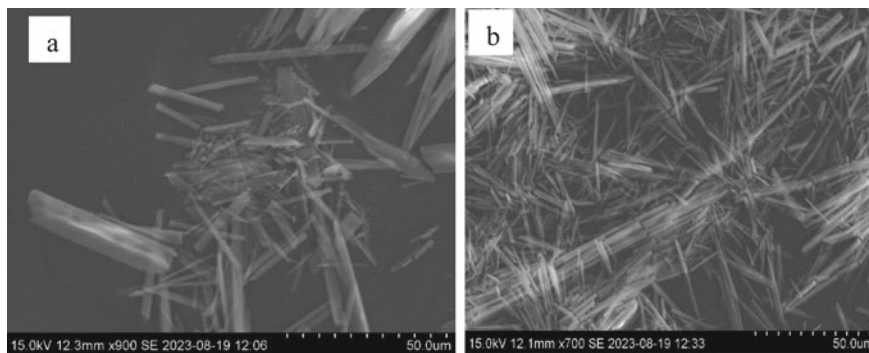
Fig. 8 SEM images for impure system at $[V^{5+}] = 30$ g/L a) O/A $= 0.5$ b) O/A $= 0.75$
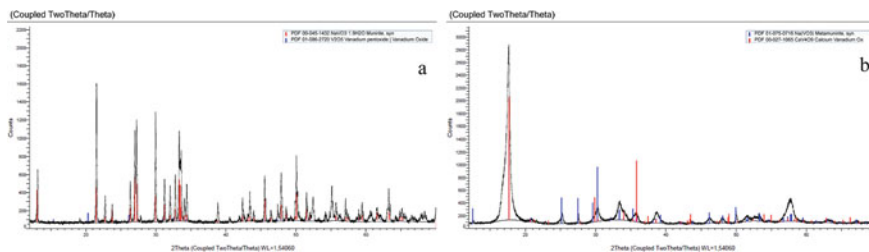
Fig. 9 XRD micrograph **a** pure system and **b** impure system

Bayer liquor, which is high in sodium concentration albeit with trace quantities of vanadium—similar to the impure system investigated, exists through the formation of a $NaVO_3$ intermediate product. This intermediate product is similar to the sodium vanadate formed during calcining in the conventional extraction of vanadium [15].

Conclusion

Antisolvent crystallization has been explored as an alternative candidate to produce a crucial vanadium intermediate product from Bayer liquor without using excessive temperature. The preliminary results for an impure system indicate that a crystalline product with good product characteristics, necessary for easy solid–liquid separation, is attained during the early period ($t_b \leq 2$) of crystallization under a low O/A ratio (0.5). Increasing the O/A ratio not only accelerates the attainment of desirable yields ($\geq 97\%$) but also brings an early onset of acicular crystal formation along with more impurity incorporation into the solid phase. It is anticipated that closer supersaturation control of the impure system, which mimics the Bayer liquor, to attain the desired purity and yield can be achieved through seeding and use of a dilute antisolvent. Further investigations of these effects will be conducted to establish the potential addition of antisolvent crystallization into the flowsheet of the Bayer process.

References

1. Blengini G, Latunussa C, Eynard U, Matos C, Georgitzikis K, Pavel C et al (2020) Study on the EU's list of critical raw materials final report 2020.
2. Tavakolikhaledi M (2014) Vanadium: leaching and solvent extraction. The University of British Columbia, Vancouver
3. Zhao Z, Yang Y, Xiao Y, Fan Y (2012) Recovery of gallium from Bayer liquor: a review. Hydrometallurgy 125–126:115–124
4. Liu Y, Naidu R (2014) Hidden values in bauxite residue (red mud): recovery of metals. Waste Manage 34(12):2662–2673
5. Pan X, Wu H, Lv Z, Yu H, Tu G (2023) Recovery of valuable metals from red mud: a comprehensive review. Sci Total Environ 904:166686
6. Gao F, Olayiwola AU, Liu B, Wang S, Du H, Li J et al (2022) Review of vanadium production Part I: primary resources. Miner Process Extr Metall Rev 43(4):466–488
7. Hu B, Zhang C, Dai Y, Wang X, Wang M (2022) Separation of vanadium and chromium in solution after vanadium precipitation by co-extraction with N263 and selective stripping with NaOH solution. Hydrometallurgy 208:105798

8. Perles T (2020) Vanadium: a green metal critical to aerospace and clean energy. Available from https://www.mobilityengineeringtech.com/component/content/article/adt/pub/features/articles/37376

9. Pan B, Liu B, Wang S, Wenzel M, Weigand JJ, Feng M et al (2020) Ammonium vanadate/ammonia precipitation for vanadium production from a high vanadate to sodium ratio solution obtained via membrane electrolysis method. J Clean Prod 263:121357

10. Du G, Sun Z, Xian Y, Jing H, Chen H, Yin D (2016) The nucleation kinetics of ammonium metavanadate precipitated by ammonium chloride. J Cryst Growth 441:117–123

11. Chen B, Bao S, Zhang Y, Ren L (2022) A novel and sustainable technique to precipitate vanadium from vanadium-rich solutions via efficient ultrasound irradiation. J Clean Prod 339:130755

12. Hu P, Hu P, Vu TD, Li M, Wang S, Ke Y et al (2023) Vanadium oxide: phase diagrams, structures, synthesis, and applications. Chem Rev 123(8):4353–4415

13. Sole KC, Field K, Malulek R, Schulze-Messing J, Viljoen K, Dutton D (2008) Production of high-purity ammonium metavanadate by solvent extraction: pilot plant evaluation. In: International solvent extraction conference (ISEC), Tucson, Arizona, USA. The Canadian Institute of Mining, Metallurgy and Petroleum, Montreal, Canada

14. Davoodi A (2007) Mechanistic studies of localized corrosion of Al alloys by high resolution in-situ and ex-situ probing techniques [Doctor of Philosophy]. KTH—Royal Institute of Technology, Stockholm

15. Habashi F (1998) Handbook of extractive metallurgy. Wiley, Toronto

Molecular Mechanisms in Specific Separation of Late Transition Metals from Rare Earth Elements

Gulaim A. Seisenbaeva

Abstract In recycling, the separation of rare earth elements (REE) from late transition metals (LTM) represents a principal challenge. While iron can easily be separated by controlled increase in pH, separation of Co, Ni, and Cu requires application of advanced approaches including fractional crystallization, solvent extraction, or use of solid adsorbents. The latter can be made selective by grafting of specific ligands reacting in a different manner with targeted classes of metal cations. Applying molecular model approach combined with advanced spectroscopic measurements, we were able to visualize principally different reaction pathways between REE and LTM in uptake by poly-amino ligands. The observed differences permit to tailor adsorbents with pronounced selectivity on both adsorption and desorption of cations of interest.

Keywords Rare earth elements · Late transition metal · Hybrid silica adsorbent · Surface functionalization · Molecular models

Introduction

Recycling of rare earth elements (REE) is rapidly becoming an urgent problem in the view of upcoming transfer to electric cars as major means of transportation. The target materials for recycling are electrodes for nickel metal hydride batteries powering some models of the vehicles and nickel-neodymium and cobalt-samarium magnets involved in the construction of essentially all electric motors. The problem needs to be principally solved within the next decade to secure the future progress of automotive and energy production industries [1]. Principal challenge in developing this technology lies in the need of efficient separation of REE from the late transition metals (LTM), represented in the first hand by nickel, cobalt, and copper. An attractive approach to pursue in this case is application of solid adsorbents bearing new types of specific types of ligands. The latter would possibly form surface complexes,

G. A. Seisenbaeva (✉)

Department of Molecular Sciences, BioCenter, Swedish University of Agricultural Sciences, Almas Allé 5, Box 7015, 75007 Uppsala, Sweden
e-mail: Gulaim.Seisenbaeva@slu.se

targeting distinct metal cations and providing thus well-expressed selectivity towards target metal species. This approach has the potential to result in principally new, and potentially competitive and environmentally friendly technologies. Several research groups worldwide have chosen this track in developing separation methodology [2–4]. An important aspect in pursuing this approach is the quest for understanding the molecular mechanisms of adsorption processes in order to select both the ligands and the adsorption and desorption conditions for its efficient implementation. Most addressed matrices for solid phase extraction in hydrometallurgy are either organic polymers or silica-based materials.

Synthesis and Characterization of Nanoadsorbents

Production of Silica Matrices

In the present studies, we have used custom-tailored spherical silica particles synthesized using modified Stöber technique [5]. Basic catalyst, ammonia solution, was used to carry out uniform polycondensation of tetra-ethoxy-silane resulting in particles of approximately 100 nm in size (see Fig. 1).

An interesting alternative to dense spherical silica particles are industrially produced mesoporous ones, obtained by spray-pyrolysis of silica colloids. These products are available from the Swedish company Nouryon AB both as pure silica of different sizes and as the material functionalized with amino propyl groups (for further functionalization) [7].
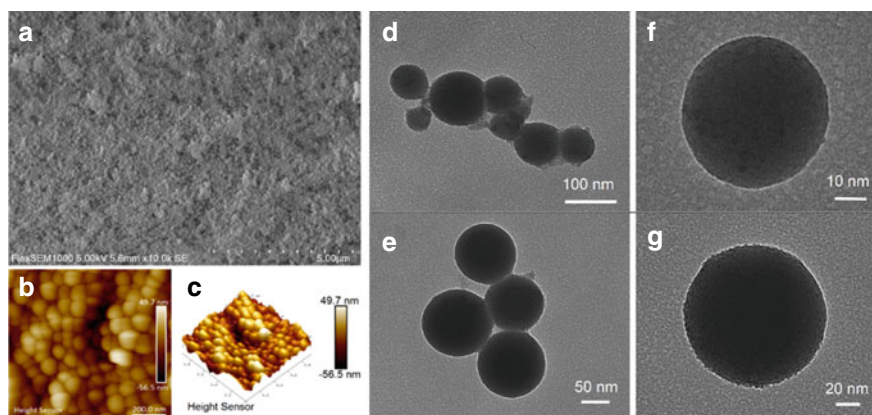
Fig. 1 SEM (**a**) and AFM (**b**, **c**) images of prepared pristine dense silica nanoparticles, and TEM images of **d**, **e**: ligand-grafted silica; **f**, **g**: the adsorbent after uptake of Ni^{2+}-cations. Reprinted with permission from [6]

Table 1 Content of diamino ligands grafted on nitric acid pre-treated 100 nm dense silica nanoparticles (calculated based on TGA and EDS data for each sample)

Sample	Grafted ligand content (mmol/g)
SiO$_2$-L1	1.61
SiO$_2$-L3	1.02
SiO$_2$-L4	0.54
SiO$_2$-L4	1.07
SiO$_2$-L7	1.47

Surface Functionalization

Easiest approach to ligand grafting is surface condensation of a single-source siloxane precursor in inert media, such as, for example, toluene, with or without addition of an alcohol. To complete the condensation, it can be advantageous to apply acidic or basic catalysts. We found that washing the synthesized nanoparticles with 1 M nitric acid for 1 h before the functionalization step with subsequent rinsing in distilled water and drying can be very advantageous for increasing the amount of grafted ligands [8] (see Table 1). The acid washing step leads to protonation of Si–OH groups, which results in catalysis of subsequent condensation with ligand-bearing alkoxy-silane.

Aiming at targeting the adsorbents for selectivity against LTM, the applied ligands were bearing either thio- or poly amino functions (see Fig. 2). The amount of grafted ligand and its stability on the surface was best for the diamino ligands, except for L4, which might have been more prone for auto-condensation.
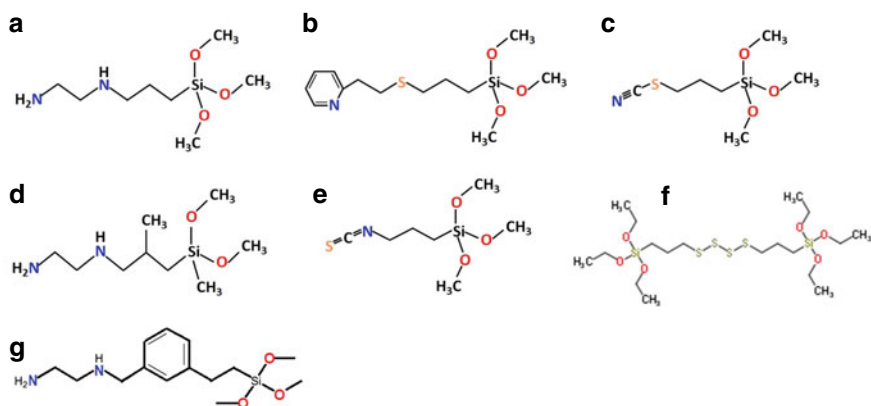
Fig. 2 Chemical structure of selected ligands: A-L1, B-L2, C-L3, D-L4, E-L5, F-L6, G-L7

Functional Properties of Nanoadsorbents

For adsorption experiments, 20 mg of nanoadsorbent was added to a 50 mL falcon tube, followed by the addition of 20 mL of an appropriate metal stock solution with concentrations of 0.5, 1, 2, 3, 4, and 10 mM. After adding $NaNO_3$ solution to retain a constant ionic strength, the samples were left to equilibrate for 48 h before collecting the particles via centrifugation. The pH of initial solution was 7.5 apparently due to protonation of the ligand amino functions. All experiments were carried out at room temperature. The amount of metal uptake was determined by complexometric titration of the supernatant with 5 mM EDTA. Xylenol orange indicator and 1 M acetate buffer were used for REE (Sm, Nd) determination, and murexide and 1 M ammonia buffer were used for LTM (Co, Ni) determination. The titrations were repeated in triplicates for each sample, and the average value was calculated.

The insight into functional characteristics of the produced adsorbents was gained via investigation of adsorption kinetics for selected metal cations, namely Nd^{3+}, Sm^{3+}, Ni^{2+}, and Co^{2+}. The kinetics in all cases was quite quick with achieving about 70% of the total adsorption capacity within the first 30 min of the experiment and approaching the full capacity after 2 h (see Fig. 3) Best fitting of the concentration changes in time was achieved with the pseudo second-order model.

The thermodynamics of adsorption was investigated through studies of adsorption isotherms in broad concentration range. Comparison of different adsorption models demonstrated that the best fit could be obtained for the Langmuir one, assuming uniform active adsorption sites situated in a monolayer on the surface and not interacting with each other (see Fig. 3).

The desorption was investigated for two different desorption media, HNO_3 with three different concentrations and pH values (pH0, pH1, and pH3) and 10 mM EDTA with pH 4.9 at room temperature. Desorption efficiencies were studied in an equimolar mixture of two (Co/Sm, Ni/Nd, Ni/Co, and Sm/Nd) or with all four tested metals. Reusability studies were carried out by three successive adsorption and desorption steps, using one metal solution (20 mM) in the adsorption step and 1 M HNO_3 as the desorption media. Desorption was carried out for 24 h, mixing the samples on the shaker. Afterwards, the samples were centrifuged (10,000 rpm, 10 min), the supernatant collected, neutralized with ammonia to a pH value of 6.5, and titrated with 5 mM EDTA to calculate the amount of desorbed metal.

The adsorbents incorporating diamino ligands displayed pronounced selectivity towards LTM in comparison with REE (see Table 2 based on data of [6, 8]). The selectivity could potentially be enhanced additionally exploiting selective desorption under optimized conditions.

Fig. 3 Adsorption isotherms on the SiO$_2$-L7 material fitted with Langmuir model (**a**) and adsorption kinetics fitted with the pseudo-second-order model (**b**). Reprinted with permission from [6]
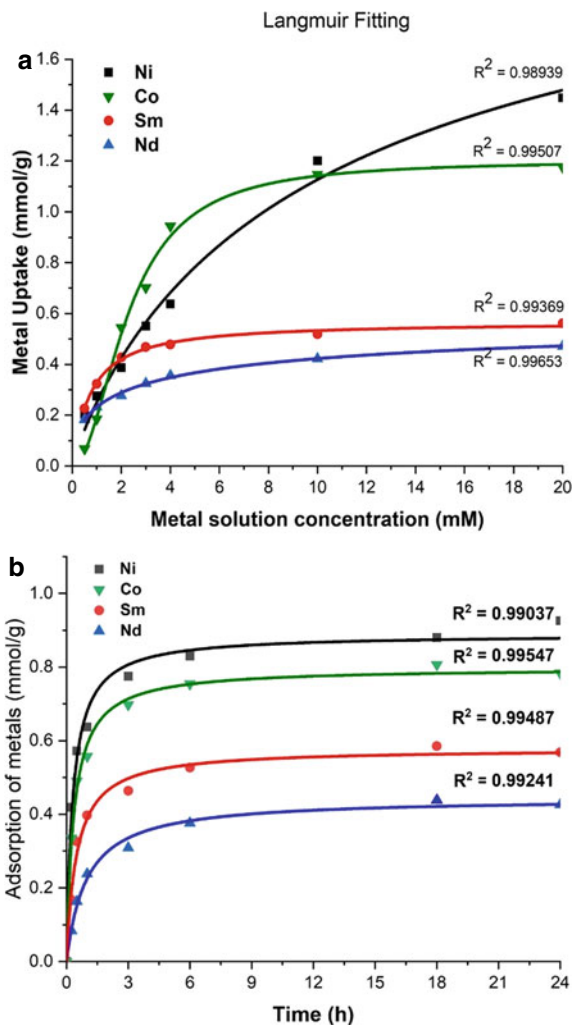
Table 2 Selectivity towards LTM versus REE on primary uptake from solution by EDS analysis

Sample	Ni/Nd ratio	Co/Sm ratio	Ni/Co ratio
SiO$_2$_L1	5.1:1	1:1.65	3.5:1
SiO$_2$_L2	1:1.78	1:12	1.6:1
SiO$_2$_L3	1:1	1:18	1:1
SiO$_2$_L4	1.33:1	1:18	1.85:1
SiO$_2$_L5	1:3	1:1	1.85:1
SiO$_2$_L3_acid	1:2.5	6:1	1.3:1
SiO$_2$_L5_acid	15:1	6:1	2.75:1
SiO$_2$_L7_acid	8.6:1	3.2:1	1:1

Revealing Molecular Mechanisms Using Insights from Crystallographic Models

The interaction between metal cations and ligands could efficiently be revealed using complexation in solution between the cations and the free molecules bearing the same function as the one incorporated in the ligand on the surface. As such function, we have selected first a chelating poly amino molecule tris(amino-ethyl)amine (TAEA), containing three ethylene diamine groups fused together. In nitrate solutions for both Ni^{2+} and Co^{2+}, the complex formation in metal:ligand = 1:1 ratio could be observed. The structures of the produced complexes turned to be analogous, but while the nickel complex maintained the violet color and was containing Ni^{2+} cations, the complex with cobalt underwent an easily noticeable color change from pink to dark green to dark red and in the pure isolated red complex contained exclusively Co(III) species (see Fig. 4).

Same behavior was observed for complexation of LTM with amino-ethyl-amino-methyl-benzene ligand (AEAMB), bearing the same function as the ligand L7. Complexation with Ni^{2+} resulted in a complex with pinkish violet color, while the interaction with Co resulted in color change analogous to the one observed earlier in case of TAEA ligand. The XPS study demonstrated that while Ni remained in the complexes in the +II oxidation state, the Co(II) complex was oxidized into Co(III) compound. The structure of the Ni-derivative (see Fig. 5) featured two ethylene diamine fragments attached to the cation, forming a "propeller-like" cation, bearing two additional nitrate anions connected via hydrogen bonds.

It could thus be concluded that interaction of poly amino ligands with LTM occurred via inner-sphere complexation mechanism with stronger binding of Co(III) cations, compared to Ni(II), which could further be exploited for selective separation of cobalt from nickel.

Unexpectedly, the mechanism of interaction between REE and poly amino cations turned to be strikingly different. In case of the AEAMB ligand, only the gelation
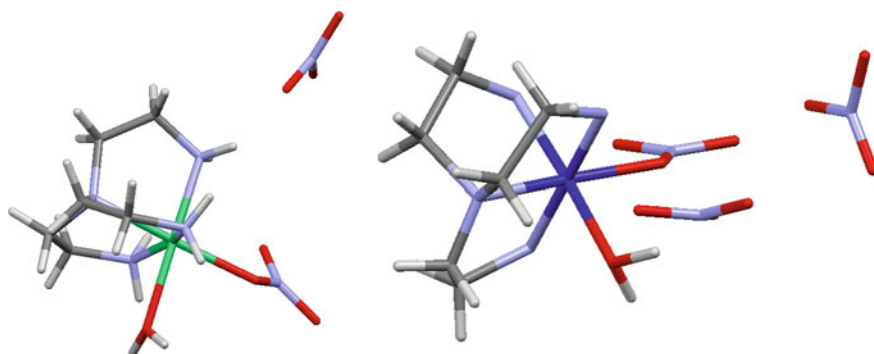
Fig. 4 Line art presentation of the molecular structures of [Ni(TAEA)(H$_2$O)(NO$_3$)](NO$_3$) (left) [9] and [Co(TAEA)(H$_2$O)(NO$_3$)](NO$_3$)$_2$ (right) [6]
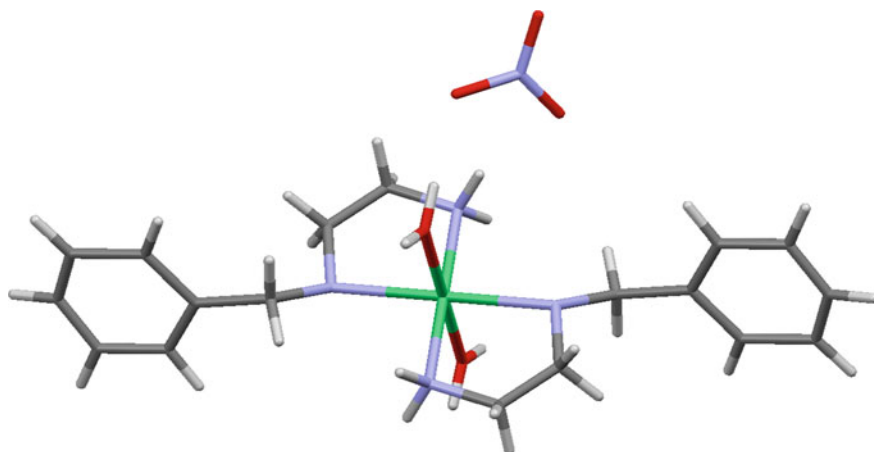
Fig. 5 Line art presentation of the molecular structure of [Ni(AEAMB)$_2$(H$_2$O)$_2$](NO$_3$)$_2$

occurred on drying in air. For the TAEA ligand with both Nd^{3+} and Sm^{3+} cations, we were able to isolate only one and the same colorless crystalline product that turned out to be the nitrate salt of the protonated ligand itself, H$_3$TAEA(NO$_3$)$_3$ (see Fig. 6).

These results implied that interaction of REE with polyamino ligands occurs not as complexation but rather as hydrolysis caused by the local basicity conditions merging due to protonation of the ligand functions. This opens for strongly increased selectivity on repeated adsorption and desorption of REE and LTM using solid adsorbent-bearing polyamino ligands.
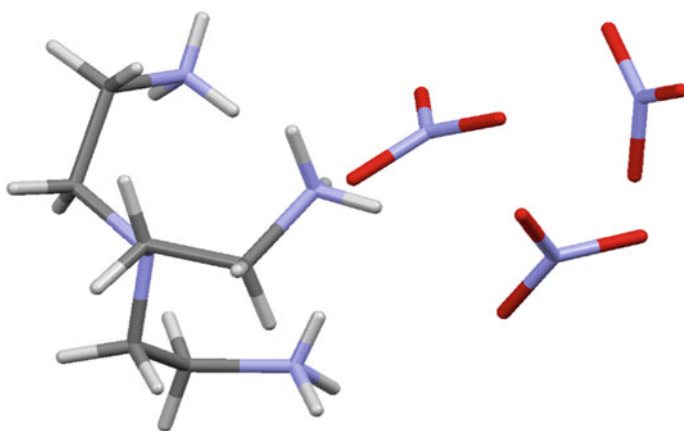
Fig. 6 Line art presentation of the molecular structure of H$_3$TAEA(NO$_3$)$_3$

Conclusions

The selected strategy in using polyamino ligand functions turned out to be successful. Already the initial uptake indicates higher affinity of such adsorbents to LTM compared to REE. The molecular model structures indicated that the interaction mechanisms between LTM and REE are strikingly different with inner sphere complexation in the former case and simply precipitation of hydrolyzed species on the materials in the latter. This opens for development of highly efficient protocols for separation of LTM from REE and brings even perspective for selective release of first nickel and then cobalt on controlled desorption.

References

1. Zero emission vehicles: first 'Fit for 55' deal will end the sale of new CO_2 emitting cars in Europe by 2035. European Commission—Press release, Brussels, 28 Oct 2022
2. Dupont D, Brullot W, Bloemen M, Verbiest T, Binnemans K (2014) ACS Appl Mater Interfaces 6:4980–4988
3. Dupont D, Luyten J, Bloemen M, Verbiest T, Binnemans K (2014) Ind Eng Chem Res 53:15222–15229
4. Callura JC, Perkins KM, Noack CW, Washburn NR, Dzombak DA, Karamalidis AK (2018) Green Chem 20:1515–1526
5. Tadanaga K, Morita K, Mori K, Tatsumisago M (2013) J Sol-Gel Sci Tech 68:341–345
6. Lakic M, Breijaert TC, Daniel G, Svensson FG, Kessler VG, Seisenbaeva GA (2023) Sep Purif Technol 323:124487
7. Seisenbaeva GA, Ali LMA, Vardanyan A, Gary-Bobo M, Budnyak TM, Kessler VG, Durand J-O (2021) J Haz Mat 406:124698
8. Vardanyan A, Guillon A, Budnyak T, Seisenbaeva GA (2022) Nanomater 12:974
9. Breijaert TC, Budnyak TM, Kessler VG, Seisenbaeva GA (2022) Dalton Trans 51:17978–17986

Investigation of the Solvometallurgical Leaching Performance of Light Rare Earth Elements in Beylikova, Eskisehir Ores

Cisem Celik Kurtulan, Sevki Samet Kaplan, Gulsah Turker, Belma Soydas Sozer, Sebahattin Gurmen, Gokhan Orhan, and M. Seref Sonmez

Abstract Rare earth elements (REE) have emerged as a hot topic of discussion in the literature. The reason for increasing interest is the usage of these elements playing a key role in especially green technology. With the increasing REE demand, the search for an alternative, and environmentally friendly extraction method is increasing day by day. At this point, it is seen that the concept of solvometallurgy has attracted a considerable attention as an alternative method to traditional extraction methods. In this research, REE in Eskisehir-Beylikova Bastnasite ore is investigated using solvometallurgical methods. In the first step of the study, the ore is characterized. After the characterization, calcination was applied at different times, temperatures, and grain size configurations. The calcination experiments were designed, and conducted based on response surface experimental design. REE extraction efficiency was determined as a response, and temperature, time, particle size were identified as experimental parameters. According to results obtained from this design, temperature was found to be the most critical parameter, and calcination at 500, 600, and 700 °C was conducted to find the highest efficient experimental parameters. The experiment conducted at 500 °C yielded the highest extraction efficiency value with light REE solvoleach efficiency as 73.773 wt% while Ce leaching value was found to be 86.648 wt%. It is well understood that the ore can be leached successfully with a newly developed extraction method, solvometallurgy.

C. C. Kurtulan · S. S. Kaplan · S. Gurmen · M. Seref Sonmez (✉)
Metallurgical and Materials Engineering Department, Faculty of Chemical and Metallurgical Engineering, Istanbul Technical University, 34469, Maslak Istanbul, Turkey
e-mail: ssonmez@itu.edu.tr

C. C. Kurtulan · G. Turker · B. S. Sozer
Rare Earth Elements Research Institute, Turkish Energy, Nuclear and Mineral Research Agency, 06980 Ankara, Turkey

G. Orhan
Metallurgical and Materials Engineering Department, Engineering Faculty, Istanbul University-Cerrahpasa, 34320 Istanbul, Turkey

Keywords Solvometallurgy · Deep eutectic solvents (DES) · Green solvents · Green chemistry · Rare earth elements · Extractive metallurgy

Introduction

Rare earth elements (REE), which are on the "Critical Raw Materials" list collected by the European Union Commission, are known to provide significant improvements in material properties even with the addition of small amounts [1, 2]. Compared to commercial elements, REE is found in smaller quantities in nature; however, their usage is steadily growing over time in technological devices [3–5]. All these reasons serve as a driving force to study REE further. The most widely found REE minerals in nature are bastnasite, monazite, and xenotime minerals, and these minerals are generally found together [6].

There are mainly four rare earth deposits in Turkey, which are located at Kızılcaoren (Sivrihisar-Eskisehir), Canaklı (Isparta), Mortas-Dogankuzu (Seydisehir-Konya), and Sofular (Malatya). The Kızılcaoren deposit is defined as the only commercial source in Turkey that is also known as thorium ore with 380,000 tons of the reserve according to results of the study conducted at 1971 [7, 8]. With the increasing demand to REE, more detailed reserve studies on the area are still conducted. The structure of the ore has large veins and cements of tectonic breccias. REE grade of the Kızılcaoren ore deposit is almost 30,000 ppm. Kızılcaoren ore deposit contains mostly bastnasite mineral as REE source [9]. Kizilcaoren has four separate mineralized areas. From north to south, these areas are named as the Kocayayla, Yaylabasi, Hoyuklu, and Devebagirtan areas. The most commercially important REE minerals are in the Devebagirtan area and the minerals have vein form. The mineralogical studies have revealed the presence of REE minerals accompanied by fluorite and barite [10, 11].

Hydrometallurgy is an efficient and well-known method that is frequently used in metal extraction [12]. Because of the high amount of water consumption in these systems and the formation of considerable amounts of acidic waste, there is a growing new trend in scientific world toward exploring alternative methods. In light of this, many innovative studies have been carried out in the field of solvometallurgy within recent years [13–23]. It is a new and alternative method that eliminates or significantly reduces the use of water, acids, and bases involved in the conventional leaching process. Instead, it utilizes environmentally friendly solvents that are non-toxic, highly bio-soluble, non-volatile under application conditions, and recyclable [24–27]. The focus of this study is the characterization of samples obtained from the Beylikova bastnaesite ore in Eskisehir and the determination of the optimal calcination conditions with respect to solvoleach efficiency for light rare earth elements (LREE), which are La, Ce, Nd, Pr, and Sm.

Table 1 Box-Behnken experimental design boundary conditions

Box-Behnken	−1	0	1
Particle size (μm)	−25	+25 −40	+40 −180
Temperature (°C)	400	650	900
Time (min.)	60	270	480

Materials and Experimental

The fluorite-barite-bastnasite complex ore used in the studies was procured from Eskisehir-Kızılcaoren by the Rare Earth Elements Research Institute (NATEN). Ethylene glycol (100949) was purchased from Merck, Germany and $FeCl_3$ (157740) was purchased from Sigma Aldrich, Germany.

In characterization stage of the study, sieve analysis was conducted to determine the particle size distribution in which the concentration of bastnaesite ore increases. The liberation particle size of bastnaesite ore is known to be 16 μm in the literature [28, 29]. Consistent with the information in the literature, it was expected in the sieve analysis results that the concentration of REEs increases with decreasing particle size. After characterization study of the ore, calcination process was conducted in order to increase dissolution of rare earth minerals. Calcination experiments were designed with using response surface method. Boundary parameters in the experimental design are given in Table 1.

After the calcination process, each sample calcined at different conditions was leached under the same conditions. Identical leaching parameters applied to all calcined samples are type-IV DES solution (1 M EG-$FeCl_3$), temperature (80 °C), duration (6 h), solid/liquid ratio (1/20). Following to leaching process, LREE extraction percentages were calculated, and calcination parameters influence on LREE extraction were elaborated. Leaching efficiencies were evaluated as a response in Box-Behnken modelling design. With the information obtained from this modelling, new calcination experiments at different temperatures as 500, 600, and 700 °C were also conducted to find the highest efficient temperature.

Results and Discussion

Experimental results are examined with two different sections, which are characterization results of Eskisehir Beylikova complex bastnasite ore; and experimental design results.

Characterization Results of Eskisehir Beylikova Complex Bastnasite Ore

In the characterization of particle size distribution, 10 different sieve openings were used from 5 mm to 25 μm. It has been found that REEs were highly concentrated at final three sieves, namely, $-25, +25 -40, +40, -180\,\mu$m. The LREE concentration at these sieve openings is given in Table 2. Their concentration above 25 μm in the ore was found to be as 2.925 wt%. This value increased to 12.228 wt% below 25 μm.

Investigation of XRD analysis for all particle size ranges and literature reviews show that fluoride, barite, calcite, bastnasite, monazite, fluor phlogopite exist in the Beylikova ore. The main phases were found as fluoride, and barite as given in Fig. 1. From XRD patterns, Rietveld analysis was conducted to understand the phase composition of the ore. Phase composition of the ore at different particle sizes is given in Fig. 2. When the figure is examined, it is seen that REE quantity is increased exponentially, which is also supported by ICP-MS analysis in Table 2. Bastnasite increased from 3.8 wt% to 9 wt%, and monazite increased from 0.1 wt% to 3.3 wt%.

Table 2 ICP-MS analysis of LREE in final three sieve openings

Elements (wt%) (μm)	La	Ce	Nd	Pr	Sm	Total LREE
-25	5.684	5.073	0.895	0.516	0.060	12.228
$+25 -40$	2.375	2.122	0.353	0.270	0.027	5.147
$+40 -180$	1.238	1.224	0.187	0.145	0.015	2.809
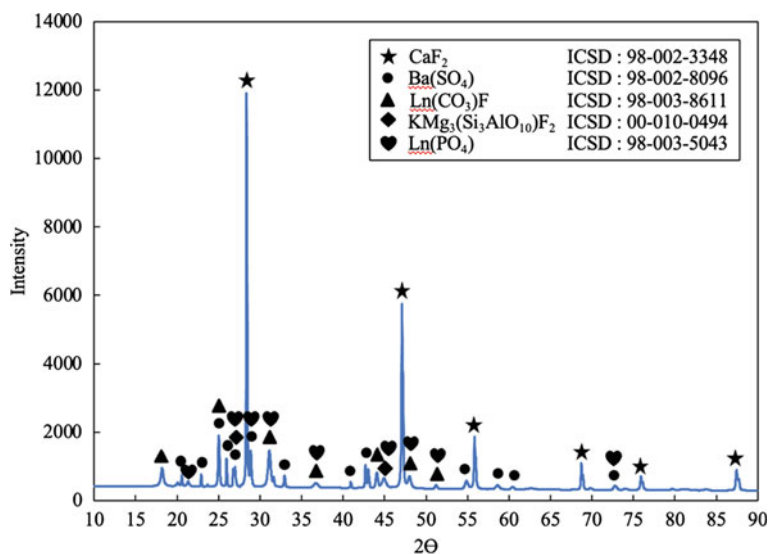
Fig. 1 XRD pattern of particles below 25 μm size
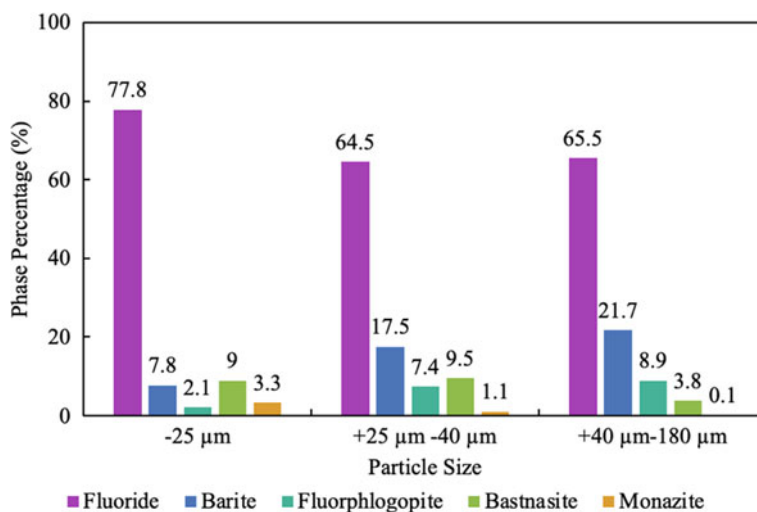
Fig. 2 Phase compositions of final three sieve openings calculated from rietveld analysis

Experimental Design Results

The experimental design parameters given in Table 1 were investigated in order to determine the optimal calcination parameters for achieving the highest extraction efficiency, and relevant graphs showing mean extraction efficiencies at the relevant parameters (at x-axis) are given in Fig. 3. As seen in Fig. 3b, except from Ce all LREE extraction mean value increases with increasing temperature. That is because of the Ce phase transformation from soluble Ce_2O_3 to insoluble CeO_2. Also, because Ce constitutes the largest portion of the ore, total LREE extraction also decreases with increasing temperature. It is seen that in Fig. 3b, the highest Ce extraction is somewhere between 400, and 700 °C. That is why control experiments were conducted at 500, 600, and 700 °C temperatures to find the highest extraction point. During these control experiments, other parameters, time and particle size ranges were kept constant at 180 min and below 25 μm, respectively.

Control experiments results conducted at three different temperatures, and also non-calcined sample leaching efficiency results are given in Table 3. The calcination carried out at 500 °C exhibited the highest LREE extraction efficiency as 73.773 wt%. As for the remaining temperatures, the efficiency of LREE extraction efficiencies showed a declining trend. Ce extraction efficiency has dropped around 17 wt% from 500 to 700 °C. Non-calcined sample extraction efficiency was found to be 10.977 wt%. This result exhibits that calcination operation drastically increases the leaching efficiency, and so it is a required step in REE extraction from Eskisehir-Beylikova bastnasite ore.
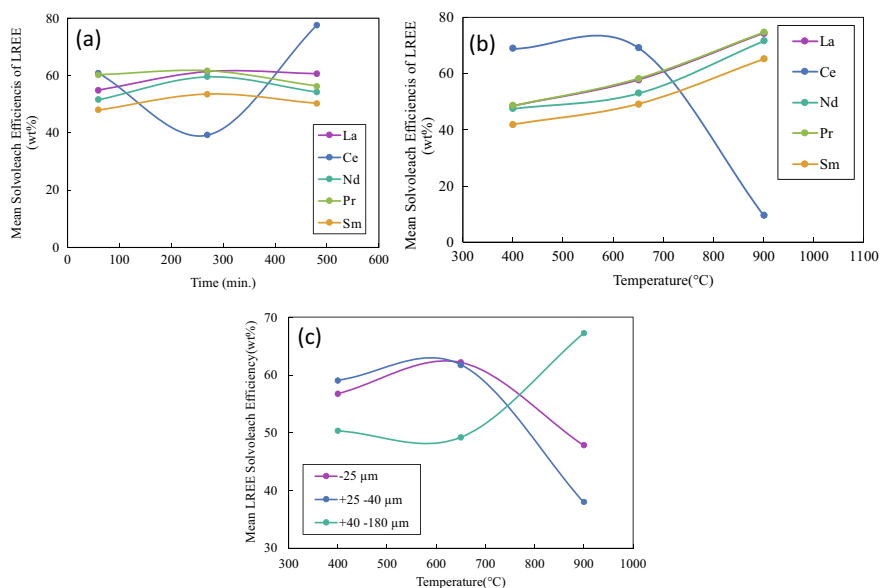
Fig. 3 Experimental design results. **a** LREE solvoleach efficiency with respect to time for the particle size below 25 µm samples; **b** LREE solvoleach efficiency with respect to temperature for the particle size below 25 µm samples; **c** LREE solvoleach efficiency with respect to temperature for all particle size ranges used in experimental modelling

Table 3 Solvoleach efficiencies with respect to calcination temperatures

Elements (%)	Non-calcined	500 °C	600 °C	700 °C
La	3.392	64.149	63.538	59.393
Ce	21.480	86.648	70.086	69.703
Pr	1.273	71.943	62.485	59.722
Nd	11.232	65.996	59.738	59.164
Sm	3.523	50.615	46.061	40.040
LREE	10.977	73.773	65.951	63.496

Conclusion

In the current study, bastnasite ore from Eskisehir-Beylikova region was character-ized, and total LEE concentration in the ore was measured as 3.959 wt%. This value increased to 12.228 wt% below 25 µm particle size. Based on the XRD analysis, the phases present in the ore were found as fluorite, barite, fluor-phlogopite, calcite, bastnasite, and monazite. Following to chemical, and phase analysis, calcination studies were conducted and found that temperature is the most efficient parameter on extraction efficiencies. The highest LREE extraction efficiency was obtained at

the experiment conducted at 500 °C during 180 min using the ore below 25 µm. Total LREE extraction efficiency was found to be 73.773 wt% Very low extraction efficiency obtained at non-calcined sample explained that calcination is a required step before leaching. With the result of the study, it is clear that REE in Eskisehir-Beylikova region can be extracted with a newly developed environmentally friendly solvometallurgical method with high yield.

References

1. Yan D, Ro S, Sunam O, Kim S (2020) On the global rare earth elements utilization and its supply-demand in the future, IOP Conf Ser Earth Environ Sci. 508. https://doi.org/10.1088/1755-1315/508/1/012084
2. European Commission (2020) Critical raw materials factsheets. https://doi.org/10.2873/92480.
3. Atanassova M (2021) Solvent extraction chemistry in ionic liquids: an overview of f-ions. J Mol Liq 343:117530. https://doi.org/10.1016/j.molliq.2021.117530
4. Gupta CK, (Nagaiyar) Krishnamurthy N (2005) Extractive metallurgy of rare earths, CRC Press. https://doi.org/10.1179/imr.1992.37.1.197.
5. Charalampides G, Vatalis KI, Apostoplos B, Ploutarch-Nikolas B (2015) Rare earth elements: industrial applications and economic dependency of Europe. Procedia Econ Finance 24:126–135. https://doi.org/10.1016/s2212-5671(15)00630-9
6. Gupta CK (2003) Chemical metallurgy : principles and practice. Wiley
7. Kaplan H (1977) Eskişehir – Sivrihisar • Kızılcaören Köyü Yakın Güneyi «Nadir Toprak Elementleri ve Toryum Kompleks Cevher Yatağı. Jeoloji Mühendisliği Dergisi 1:29–34. http://dergipark.gov.tr/jmd/issue/28146/296114. Accessed 4 Mar 2019
8. Pirajno F, Ünlü T, Dönmez C, Bahadır Şahin M (2019) Modern approaches in solid earth sciences, Mineral resources of Turkey
9. Öztürk H, Altuncu S, Hanilçi N, Kasapçı C, Goodenough KM (2019) Rare earth element-bearing fluorite deposits of Turkey: an overview. Ore Geol Rev 105:423–444. https://doi.org/10.1016/j.oregeorev.2018.12.021
10. Gültekin AH, Örgün Y, Suner F (2003) Geology, mineralogy and fluid inclusion data of the Kizilcaören fluorite–barite–REE deposit, Eskisehir, Turkey. J Asian Earth Sci 21:365–376. https://doi.org/10.1016/S1367-9120(02)00019-6
11. Gültekin AH, Örgün Y, Kızılcaören (Sivrihisar - Eskişehir) Yöresi Tersiyer Alkali Volkanitlerle İlişkili Nadir Toprak Elementli Fluorit-Barit Yatakları. Anadolu Üniversitesi Bilim ve Teknoloji Dergisi A - Uygulamalı Bilimler ve Mühendislik. https://earsiv.anadolu.edu.tr/xmlui/handle/11421/1562. Accessed 11 Mar 2019
12. Fathi H (1997) Handbook of extractive metallurgy. Wiley
13. Van Loy S, Binnemans K, Van Gerven T (2018) Mechanochemical-assisted leaching of lamp phosphors: a green engineering approach for rare-earth recovery. Engineering 4:398–405. https://doi.org/10.1016/j.eng.2018.05.015
14. Li X, Monnens W, Li Z, Fransaer J, Binnemans K (2020) Solvometallurgical process for extraction of copper from chalcopyrite and other sulfidic ore minerals. Green Chem 22:417–426. https://doi.org/10.1039/c9gc02983d
15. Hanada T, Goto M (2022) Cathode recycling of lithium-ion batteries based on reusable hydrophobic eutectic solvents. Green Chem. https://doi.org/10.1039/d1gc04846e

16. Peeters N, Binnemans K, Riaño S (2020) Solvometallurgical recovery of cobalt from lithium-ion battery cathode materials using deep-eutectic solvents. Green Chem 22:4210–4221. https://doi.org/10.1039/d0gc00940g

17. Riaño S, Binnemans K (2015) Extraction and separation of neodymium and dysprosium from used NdFeB magnets: an application of ionic liquids in solvent extraction towards the recycling of magnets. Green Chem 17:2931–2942. https://doi.org/10.1039/C5GC00230C

18. Peeters N, Binnemans K, Riaño S (2022) Recovery of cobalt from lithium-ion battery cathode material by combining solvoleaching and solvent extraction. Green Chem. https://doi.org/10.1039/D1GC03776E

19. Önal MAR, Riaño S, Binnemans K (2020) Alkali baking and solvometallurgical leaching of NdFeB magnets. Hydrometallurgy 191. https://doi.org/10.1016/j.hydromet.2019.105213

20. Orefice M, Binnemans K (2021) Solvometallurgical process for the recovery of rare-earth elements from Nd–Fe–B magnets. Sep Purif Technol 258. https://doi.org/10.1016/j.seppur.2020.117800

21. Dewulf B (2018) Development of a solvometallurgical process for the separation of trivalent yttrium and europium. KU Leuven

22. Palden T, Regadío M, Binnemans K (2018) Selective solvometallurgical leaching of lead and zinc from jarosite residues from the zinc industry. In: 4th International symposium on enhanced landfill mining, pp 133–136

23. Chekmarev AM, Chizhevskaya SV, Buchikhin EP, Cox M (2001) Solvometallurgical methods in the treatment of rare and non-ferrous metal raw materials. In: VI SHMMT/XVII ENTMME, pp 441–444

24. Binnemans K, Jones PT (2017) Solvometallurgy: an emerging branch of extractive metallurgy. J Sustain Metal 3:570–600. https://doi.org/10.1007/s40831-017-0128-2

25. Horváth IT, Anastas PT (2007) Innovations and green chemistry. Chem Rev 107:2169–2173. https://doi.org/10.1021/cr078380v

26. Binnemans K (n.d) Solvometallurgy for rare earths

27. Chekmarev AM, Chizhevskaya SV, Buchikhin EP (2000) Solvometallurgy as a novel trend in XXI century metallurgy. Khim Tekhnol 2–7

28. Carrillo Garcia A (2019) Thermal decomposition of a rare earth ore [Ph.D. thesis, Polytechnique Montréal]. PolyPublie. https://publications.polymtl.ca/4147/

29. Carrillo García A, Latifi M, Chaouki J (2021) Kinetic study of calcination of a rare earth ore. Hydrometallurgy 200:105557. https://doi.org/10.1016/J.HYDROMET.2021.105557

Leaching Kinetics of Vanadium from Calcification Roasted Vanadium Slag in $(NH_4)_2CO_3$

Jie Cheng, Hong-Yi Li, Cheng-Chao Wei, Xin-Mian Chen, Jiang Diao, and Bing Xie

Abstract $(NH_4)_2CO_3$ leaching method is an efficient and green selective vanadium extraction method. Studying its leaching kinetic mechanism can improve the adaptability and industrial production of this method and further promote the development of green extraction of vanadium resources. This work used different leaching temperatures to study the variation of vanadium leaching efficiency with leaching time to elucidate the leaching kinetics of vanadium. Results showed that the leaching process consists of two stages and both of which complied with shrinking core model (SCM). The apparent activation energies (E_a) of leaching process were 8.80 kJ/mol (0–15 min) and 9.68 kJ/mol (15–70 min), respectively. The leaching rate in 0–15 min was controlled by solid product layer diffusion, and the leaching rate in 15–70 min was controlled by solid product layer diffusion and chemical reactions, and diffusion control played a significant role.

Keywords Leaching kinetics · $(NH_4)_2CO_3$ · Vanadium extraction · Calcification roasted vanadium slag

Introduction

Vanadium is a high-value, strategic metal widely used in national defense, chemical, and metallurgical fields [1, 2]. The vanadium slag obtained from V–Ti magnetite ores has always been the most important raw material for vanadium extraction [3, 4]. At present, the most commonly used method for extracting vanadium is alkaline roasting-water/acid leaching [5, 6].

However, these methods currently have some drawbacks. Toxic gases (Cl_2, HC1, SO_2, and SO_3) are generated during the sodium roasting process, which can corrode

J. Cheng · H.-Y. Li (✉) · C.-C. Wei · X.-M. Chen · J. Diao · B. Xie
College of Materials Science and Engineering, Chongqing University, Chongqing 400044, China
e-mail: hongyi.li@cqu.edu.cn

H.-Y. Li · J. Diao
National Engineering Research Center for Magnesium Alloys, Chongqing University, Chongqing 400044, China

equipment and harm the environment [7, 8]. For calcification roasting-acid leaching, due to the reaction between $Ca_2V_2O_7$ and H_2SO_4 during the leaching process, $CaSO_4$ precipitation is generated and enters the vanadium extraction tailings. Its high S content makes it impossible to recover the vanadium extraction tailings into previous vanadium extraction steps such as blast furnaces and converters to recover iron and manganese resources [9]. For P containing vanadium slag undergoing calcification roasting-acid leaching, the impurity phosphorus element will be leached out with vanadium at the same time during the leaching process to form heteropolyacids, resulting in the low vanadium leaching efficiency. Based on this, a novel leaching method of $(NH_4)_2CO_3$ leaching method has been proposed by our group to selectively leach vanadium, which can efficiently inhibit the leaching of phosphorus and the generation of S [10]. To further improve the vanadium leaching efficiency of this novel vanadium extraction method, it is necessary to study the vanadium leaching in the $(NH_4)_2CO_3$ leaching process. More importantly, the lack of research on the vanadium leaching kinetics from calcification roasted vanadium slag by ammonium carbonate will hinder the industrialization and application of ammonium carbonate leaching.

Some researchers have studied the acid leaching kinetics model of vanadium through SCM [11–13]. However, impurities in the acid leach liquid required further treatment such as solvent extraction [14]. Compared with acid leaching, the composition of $(NH_4)_2CO_3$ leach liquid had changed greatly. Therefore, further studies on the $(NH_4)_2CO_3$ leaching kinetics of vanadium were required.

Thus, the effect of leaching time on vanadium leaching efficiency was investigated in this study with different leaching temperatures to clarify the vanadium leaching kinetics. The leaching kinetics model was studied using SCM.

Materials and Methods

Materials and Characterizations

The vanadium slag (from Pan Steel, China) was sieved into a particle size of less than 45 um and then dried at 373 K for 3 h. The CaO powder was calcined at 1323 K prior to use to eliminate CO_2 molecules to ensure purity.

XRF (Shimadzu XRF-1800, Japan) was used to analyze the chemical composition of the vanadium slag (Table 1). The vanadium slag was mainly composed of spinel phase and silicate phase, among which vanadium existed as vanadium spinel. The concentration of vanadium in the leach liquid was analyzed using ICP-OES (Optima 8000, USA).

Table 1 The chemical compositions of the vanadium slag, wt%

FeO	SiO$_2$	TiO$_2$	V$_2$O$_5$	MnO	CaO	MgO	P$_2$O$_5$
36.09	18.86	11.45	15.44	6.67	2.87	3.53	0.55

Calcification Roasting

The vanadium slag and CaO were mixed in mass ratio of 100:7.2 and then placed in muffle furnace at 1173 K for 2 h. After roasting, the roasted vanadium slag was cooled to room temperature and ground into powder.

(NH$_4$)$_2$CO$_3$ Leaching

The roasted vanadium slag was leached for 0–70 min using 600 g/L (NH$_4$)$_2$CO$_3$ solution with a S/L ratio of 1:20 g/mL in a magnetically stirred water bath at temperature 60–90 °C and stirring speed of 250 r/min. Then the leach liquid was separated from the leach residue through filtration.

Results and Discussion

Effects of Leaching Temperature on Vanadium Leaching Kinetics

The leaching temperature was an important parameter that affected the leaching kinetics of vanadium. As shown in Fig. 1, the leaching efficiency of vanadium and the slope of the leaching efficiency curve increased with the increase of the leaching temperature. It can be clearly seen that the extraction of vanadium involves two leaching stages. In the initial 15 min, the extraction amount of vanadium increased sharply, and over a longer leaching time, the extraction efficiency of vanadium slightly improved.

Leaching Kinetic Model

SCM was used to describe the vanadium leaching kinetics model. In SCM, the solid–fluid reaction can be expressed by the following reaction:

$$A(\text{fluid}) + b B(\text{solid}) \rightarrow \text{Products} \tag{1}$$

Fig. 1 Effects of leaching temperature on the vanadium leaching kinetics
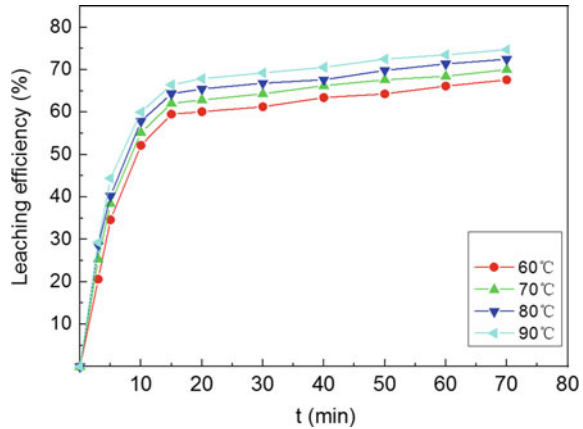
where A represents $(NH_4)_2CO_3$, B represents roasted vanadium slag, and b represents stoichiometric coefficient, respectively. The $(NH_4)_2CO_3$ leaching process can be controlled by the following steps: (1) by diffusion through the fluid film or through the product layer; (2) by the chemical reaction. The relative integral rate equations are shown in Eqs. (2)–(4) [15].

Solid product layer diffusion control:

$$1 - 3(1 - x)^{2/3} + 2(1 - x) = k_d t \tag{2}$$

Chemical reaction control:

$$1 - 3(1 - x)^{1/3} = k_r t \tag{3}$$

Liquid film diffusion control

$$1 - (1 - x)^{2/3} = k_l t \tag{4}$$

where x is the vanadium leaching efficiency; k_d is the apparent rate constant for pore diffusion; k_r is the apparent rate constant for chemical reaction; k_l is the apparent rate constant for liquid film diffusion, and t is the leaching time.

As shown in Fig. 1, there were two stages in the kinetics of leaching. The first stage occurred at 0–15 min and the second stage occurred after 15 min. Thus, kinetics was analyzed in two stages separately.

Short Time Stage

For the short time stage of $(NH_4)_2CO_3$ leaching (0–15 min), kinetic data have been fitted with Eqs. (2)–(4) in different leaching conditions. Table 2 lists the resulting regression rate constants and correlation coefficients. The regression coefficient corresponding to solid layer diffusion control was the largest, suggesting that the $(NH_4)_2CO_3$ leaching rate in the initial stage was controlled by the diffusion through solid product layer. Linear plots according to Eq. (2) are shown in Fig. 2a. Rate constants k_d obtained from slopes were used to show the relevance between $\ln k_d$ and $1/T$ to calculate the activation energy. According to Arrhenius equation, the E_a of $(NH_4)_2CO_3$ leaching in the short time stage was 8.80 kJ/mol ($R^2 = 0.9999$) (Fig. 2b). It is known that the E_a of the diffusion control process is usually below 12 kJ/mol [16]. The calculated E_a (8.80 kJ/mol) is below than 12 kJ/mol, indicating that the $(NH_4)_2CO_3$ leaching rate in the initial stage was controlled by the diffusion through solid product layer, which agrees with the result of kinetic model fitting.

Table 2 Apparent rate constants for kinetics models and correlation coefficients (0–15 min)

Parameter (°C)	Diffusion through the liquid film		Surface chemical reaction		Diffusion through the solid product layer	
	$1 - (1 - x)^{2/3}$		$1 - (1 - x)^{1/3}$		$1 - 3(1 - x)^{2/3} + 2(1 - x)$	
	k_l	R^2	k_r	R^2	k_d	R^2
60	0.0299	0.9170	0.0173	0.9398	0.0120	0.9777
70	0.0306	0.8880	0.0180	0.9183	0.0131	0.9824
80	0.0317	0.8743	0.0188	0.9090	0.0144	0.9820
90	0.0328	0.8532	0.0197	0.8919	0.0156	0.9777
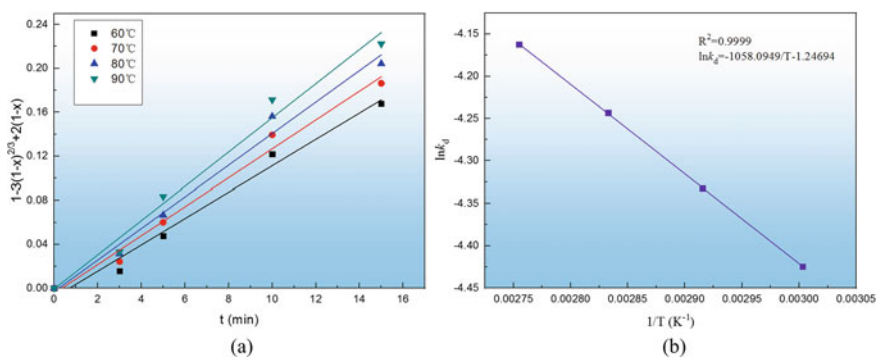
Fig. 2 **a** Plot of $1 - 3(1 - x)^{2/3} + 2(1 - x)$ *vs.* time in different leaching temperatures; **b** Arrhenius plot for the leaching system (0–15 min)

Long-Time Stage

For the long-time stage of $(NH_4)_2CO_3$ leaching (15–70 min), Eqs. (2)–(4) cannot be directly applied because the boundary condition of the long-term stage was different from that of initial stage. Under the new boundary conditions, new integral equations were obtained.

Solid product layer diffusion control:

$$1 - 3((1 - x)/(1 - x_1))^{2/3} + 2\big(1 - (1 - x_1)^{1/3}(x - x_1)\big) = k_d(t - t_1) \quad (5)$$

Chemical reaction control:

$$1 - ((1 - x)/(1 - x_1))^{1/3} = k_r(t - t_1) \quad (6)$$

Liquid film diffusion control:

$$1 - ((1 - x)/(1 - x_1))^{2/3} = k_l(t - t_1) \quad (7)$$

where t_1 was 15 min. Experimental data have been fitted with Eqs. (5)–(7) in various conditions. Regressed rate constants and corresponding correlation coefficients are listed in Table 3. As can be seen in this table, the correlation coefficients of regression with Eqs. (5) and (6) were relatively high in all conditions, suggesting that the leaching rate may be controlled by both chemical reactions and solid product layer diffusion in the long-time stage. Data fitting with Eq. (5) in different conditions are plotted in Fig. 3a. The E_a of long-time stage was calculated by plotting $\ln k_d$ agnsit $1/T$. The E_a was 9.68 kJ/mol ($R^2 = 0.9849$) (Fig. 3b), which was still below 12 kJ/mol. The value of E_a illustrated that leaching process was controlled by diffusion. Based on the above analysis, it can be concluded that the leaching rate in the long-time stage is controlled by diffusion and chemical reactions, with diffusion control playing a dominant role.

Table 3 Apparent rate constants for kinetics models and correlation coefficients (15–70 min)

Parameter (°C)		Diffusion through the liquid film		Surface chemical reaction		Diffusion through the product layer	
		$1 - ((1 - x)/(1 - x_1))^{2/3}$		$1 - ((1 - x)/(1 - x_1))^{1/3}$		$1 - 3((1 - x)/(1 - x_1))^{2/3} + 2(1 - (1 - x_1)^{1/3}(x - x_1))$	
		k_l	R^2	k_r	R^2	k_d	R^2
60	0.0025		0.9923	0.0013	0.9916	0.0054	0.9921
70	0.0034		0.7670	0.0014	0.9929	0.0058	0.9922
80	0.0037		0.7894	0.0015	0.9888	0.0065	0.9891
90	0.0039		0.7666	0.0016	0.9917	0.0072	0.9905
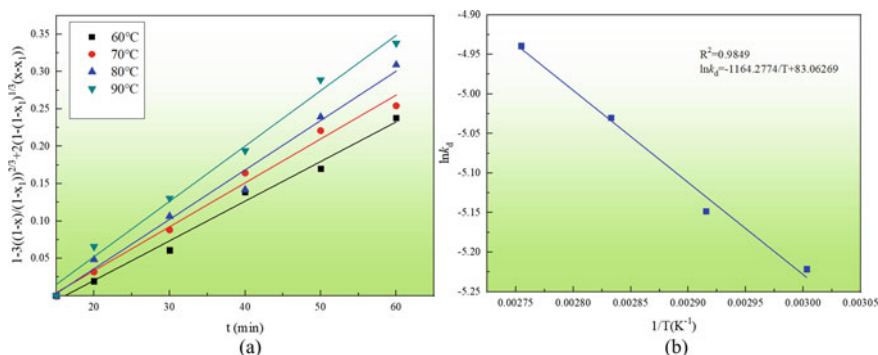
Fig. 3 **a** Plot of $1 - 3((1 - x)/(1 - x_1))^{2/3} + 2(1 - (1 - x_1)^{1/3}(x - x_1))$ versus time in different leaching temperatures; **b** Arrhenius plot for the leaching system (15–70 min)

Conclusions

1. The effects of leaching conditions on vanadium leaching kinetics have been systematically investigated. The $(NH_4)_2CO_3$ leaching proceeds as two stages: the initial stage of 0–15 min and the long-time stage of 15–75 min. In the initial stage, the leaching efficiency increased sharply, while at the long-time stage, the leaching efficiency increased gradually.

2. Kinetic studies showed that the $(NH_4)_2CO_3$ leaching process followed the SCM. The leaching rate in the initial stage was controlled by the diffusion through the solid product layer. In the long-time stage of $(NH_4)_2CO_3$ leaching, both solid layer diffusion (main) and surface chemical reaction contributed to the control of leaching rate.

Conflict of Interest The authors declare no competing interests.

References

1. Li H-Y, Wang C, Lin M, Guo Y, Xie B (2020) Green one-step roasting method for efficient extraction of vanadium and chromium from vanadium-chromium slag. Powder Technol 360:503–508
2. Li M, Liu B, Zheng S, Wang S, Du H, Dreisinger DB, Zhang Y (2017) A cleaner vanadium extraction method featuring non-salt roasting and ammonium bicarbonate leaching. J Clean Prod 149:206–217
3. Li H-Y, Wang C-J, Yuan Y-H, Guo Y, Diao J, Xie B (2020) Magnesiation roasting-acid leaching: a zero-discharge method for vanadium extraction from vanadium slag. J Clean Prod 260

4. Jiang T, Wen J, Zhou M, Xue X (2018) Phase evolutions, microstructure and reaction mechanism during calcification roasting of high chromium vanadium slag. J Alloys Compd 742:402–412

5. Wen J, Jiang T, Zhou W, Gao H, Xue X (2019) A cleaner and efficient process for extraction of vanadium from high chromium vanadium slag: Leaching in $(NH_4)(2)SO_4$–H_2SO_4 synergistic system and NH^{4+} recycle. Sep Purif Technol 216:126–135

6. Zhang J, Zhang W, Xue Z (2019) An environment-friendly process featuring calcified roasting and precipitation purification to prepare vanadium pentoxide from the converter vanadium slag. Metals 9

7. Li H-Y, Cheng J, Wang C-J, Shen S, Diao J, Xie B (2022) Ecofriendly selective extraction of vanadium from vanadium slag with high chromium content via magnesiation roasting-acid leaching, metallurgical and materials transactions b-process metallurgy and materials processing. Science 53:604–616

8. Li H-Y, Chen X-M, Li D-Q, Guo Y, Diao J, Xie B (2021) Quick valence analysis method of vanadium toward accurate toxicity assessment of vanadium-containing hazardous wastes. Trans Nonferrous Metals Soc China 31:3602–3612

9. Wen J, Jiang T, Wang J, Lu L, Sun H (2020) Cleaner extraction of vanadium from vanadium-chromium slag based on $MnO2$ roasting and manganese recycle. J Clean Prod 261

10. Li H-Y, Wang K, Hua W-H, Yang Z, Zhou W, Xie B (2016) Selective leaching of vanadium in calcification-roasted vanadium slag by ammonium carbonate. Hydrometallurgy 160:18–25

11. Yang Z, Li H-Y, Yin X-C, Yan Z-M, Yan X-M, Xie B (2014) Leaching kinetics of calcification roasted vanadium slag with high CaO content by sulfuric acid. Int J Miner Process 133:105–111

12. Gao H, Jiang T, Xu Y, Wen J, Xue X (2020) Leaching kinetics of vanadium and chromium during sulfuric acid leaching with microwave and conventional calcification-roasted high chromium vanadium slag. Miner Process Extr Metall Rev 41:22–31

13. Aarabi-Karasgani M, Rashchi F, Mostoufi N, Vahidi E (2010) Leaching of vanadium from LD converter slag using sulfuric acid. Hydrometallurgy 102:14–21

14. Lu G, Zhang T, Zhang G, Zhang W, Zhang Y, Dou Z, Wang L, Wang Y, Xie G (2019) Process and kinetic assessment of vanadium extraction from vanadium slag using calcification roasting and sodium carbonate leaching. JOM 71:4600–4607

15. Abdel-Aal EA, Rashad MM (2004) Kinetic study on the leaching of spent nickel oxide catalyst with sulfuric acid. Hydrometallurgy 74:189–194

16. Ashraf M, Zafar ZI, Ansari TM (2005) Selective leaching kinetics and upgrading of low-grade calcareous phosphate rock in succinic acid. Hydrometallurgy 80:286–292

Direct Recycling of Lithium-Ion Batteries Using Hydrothermal Relithiation

Ka Ho Chan and Gisele Azimi

Abstract This study aims to develop a direct recycling process of spent lithium-ion batteries (LIBs) from an electric vehicle. In this direct recycling process, the electric vehicle battery pack is first discharged and disassembled to obtain the spent cathode material, which is then hydrothermally relithiated at 220 °C for 2 h followed by sintering at 850 °C for 4 h in air. The product after these steps is the regenerated cathode material, which is used to fabricate new LIBs to evaluate the electrochemical performance. The regenerated cathode material delivers an initial discharge capacity of 151 mAh g^{-1} at 0.33C (50 mA g^{-1}) with a capacity retention of 91% after 50 cycles. By combining hydrothermal relithiation with sintering, lithium deficiency, structural defects, and electrochemical activity of the spent cathode material are successfully restored.

Keywords Lithium-ion batteries (LIBs) · Electric vehicles · Degradation · Hydrothermal relithiation · Sintering

Introduction

With the widespread applications of lithium-ion batteries (LIBs) in electric transportation and energy storage system, countless spent LIBs will inevitably be generated after they reach their end of life. It is estimated that 11 million metric tons of waste LIBs will be produced by 2030 [1]. From the perspectives of environmental protection and resource sustainability, recycling is an effective solution to handle the end-of-life LIBs.

K. H. Chan · G. Azimi (✉)
Laboratory for Strategic Materials, Department of Chemical Engineering and Applied Chemistry, 200 College Street, Toronto, ON M5S 3E5, Canada
e-mail: g.azimi@utoronto.ca

G. Azimi
Department of Materials Science and Engineering, University of Toronto, 184 College Street, Toronto, ON M5S 3E4, Canada

Currently, the state-of-the-art approach to recycle spent LIBs is mainly focused on a closed-loop hydrometallurgical process [2]. In this process, a leachate containing multiple metal ions undergoes a co-precipitation reaction to produce a precursor, and then the precursor is mixed with a lithium source to fabricate a new cathode material through solid-state reaction. However, this recycling process consumes lots of caustic chemicals, which generates additional waste. In this respect, an emerging direct recycling technology has been developed. Direct recycling supplements the lithium loss and restores the crystal structure of spent cathodes, which can be directly used to fabricate new LIBs. Unlike the traditional recycling processes, direct recycling is a relatively green approach, which does not require intensive chemical usage and does not generate significant waste [3].

Most previous studies have mainly focused on recycling spent LIBs from electric vehicles through hydrometallurgy; however, only few studies have reported recycling of spent LIBs from electric vehicles using direct recycling. A review paper by Wei et al. discussed the challenges and opportunities toward practical application for direct recycling of spent LIBs [4]. The difficulties in direct recycling encompass manual disassembly, precise sorting, and technological constraints. Although both researchers and industry stakeholders are actively investigating automated disassembly technologies to enhance the efficiency and scalability of the recycling process, the variability in battery designs, sizes, electrical connections, and packaging formats continues to pose persistent challenges in the development and adoption of automated disassembly solutions.

Additionally, precise sorting constitutes a crucial aspect of spent LIBs recycling, particularly concerning direct regeneration, where only a single cathode type can be processed to recover high-quality materials. However, achieving accurate sorting without damaging batteries remains a significant challenge, primarily due to the absence of readily available chemical information labeled on the exterior of the batteries. The process of disassembling a large quantity of spent LIBs for chemical characterization is both costly and inefficient, especially within an industrial context. Researchers are actively exploring advancements in battery characterization techniques to devise non-destructive methods for identifying cathode materials.

Furthermore, beyond considering the various degradation mechanisms inherent to cathode materials, it is crucial to account for the structural integrity of these materials during the regeneration process. Different cathode materials demonstrate varying degrees of stability in diverse environments, necessitating tailored approaches to the regeneration process. Following a series of pretreatment steps, the cathode powder acquired from spent LIBs can be regenerated through various relithiation techniques, typically involving a subsequent annealing phase. One particular challenge arises from the presence of impurities in the collected cathode powder post-pretreatment, including the binder, conductive carbon, metal fragments, and graphite particles, which complicate the direct regeneration procedure.

The intricate landscape of materials in the market and the continuous evolution of battery materials pose significant obstacles for direct recycling technologies. The pursuit of higher energy density and longer life cycles has prompted modifications to cathode materials, such as coating and doping, which further intricate the direct

recycling process. Throughout the relithiation process, there exists a risk of doped elements leaching out or the destruction of coating layers, potentially impacting the quality of the regenerated cathode materials. Additionally, cathodes with elevated nickel content exhibit intricate degradation mechanisms and heightened sensitivity to their surrounding environment, necessitating precise control and meticulous design to ensure the successful direct recycling of such materials.

As mentioned above, direct recycling of LIBs holds significant promise in terms of mitigating environmental repercussions and fostering a circular economy within the LIB industry but it is still at the initial stages of research and development and more work is needed to make this process suitable for scaleup from the laboratory scale to the industrial scale. This study is a novel attempt to directly recycle spent LIBs from an electric vehicle. In this study, the spent cathode material from an electric vehicle was hydrothermally relithiated followed by sintering. The product after these steps is the regenerated cathode material, which was used to fabricate new LIBs. The composition, structure, and electrochemical performance of the regenerated cathode materials were investigated.

Materials and Methods

Chemicals and Materials

Lithium hydroxide monohydrate (98%, Alfa Aesar) was used for direct regeneration experiment. Carbon black (>99%, Alfa Aesar), polyvinylidene fluoride (Sigma-Aldrich), *N*-methyl-2-pyrrolidone (>99%, Alfa Aesar), and lithium hexafluorophosphate (1.0 M LiPF$_6$ in ethylene carbonate (EC) and diethyl carbonate (DEC), EC:DEC = 1:1, Sigma-Aldrich) were used for battery fabrication.

Pretreatment of Spent Lithium-Ion Batteries

The electric vehicle battery pack (Honda Civic Hybrid 2012) was collected from Carcone's Auto Recycling. After discharging and dismantling the battery pack, the cathode material was removed from the aluminum foil using ultrasonic treatment (VWR 97043-964 ultrasonic bath). The spent cathode material was filtered and dried at 50 °C for 24 h. The dried cathode material was ground into fine powder for the following direct regeneration experiment.

Direct Regeneration Experiment

For the hydrothermal relithiation, the spent cathode material was added to an auto-clave (Parr 4560 Mini) filled with 100 mL of 4.0 M lithium hydroxide (LiOH) solution. The autoclave was maintained at 220 °C for 2 h with continuous stirring at 300 rpm. The relithiated cathode material was washed thoroughly with deionized water, dried at 80 °C for 24 h, and then sintered at 850 °C for 4 h in air to obtain the final regenerated product.

Material Characterization

The spent and regenerated cathode materials were dissolved in 1.0 M H_2SO_4 with 1.0 wt% H_2O_2 at 50 °C and then the lithium composition in the materials was measured by inductively coupled plasma optical emission spectrometry (ICP-OES, PerkinElmer Optima 8000). The crystal structure of the samples was characterized using X-ray diffraction (XRD, Rigaku MiniFlex 600). The surface morphology of the samples was investigated using scanning electron microscopy (SEM, Hitachi SU7000). The microstructures of the samples were observed using high-resolution transmission electron microscopy (HR-TEM, Hitachi HF-3300).

Electrochemical Measurements

To evaluate the electrochemical performance, the spent and regenerated materials were separately mixed with carbon black and polyvinylidene fluoride (PVDF) in a mass ratio of 8:1:1 with N-methyl-2-pyrrolidone (NMP) solvent. The slurries were cast uniformly on the aluminum foils using a doctor blade and then dried in a vacuum oven at 80 °C for 10 h. The active mass loading of the cathodes was controlled at ~3 mg cm^{-2}. Coin cells were assembled with a lithium metal as the anode, 1.0 M LiPF$_6$ as the electrolyte, and a glass fiber as the separator inside an argon-filled glovebox. The cells were charged and discharged using a multi-channel battery tester (Neware CT-4008) in the voltage range of 2.8–4.4 V.

Results and Discussion

Degradation of Spent Lithium-Ion Batteries

The composition of the spent cathode material was determined by dissolving the sample in 1.0 M H_2SO_4 with 1.0 wt% H_2O_2 at 50 °C followed by measuring the metal ion concentration using ICP-OES. In this process, all the solids were dissolved and no residue remained in the system. Based on the ICP-OES analysis, the composition of the spent cathode material was determined as $Li_{0.76}Ni_{0.15}Mn_{0.15}Co_{0.70}O_2$, which has ~25% lithium deficiency after long-term cycling, likely due to the solid electrolyte interface (SEI) formed on the anode surface. Figure 1a, b shows the SEM images of a spent cathode particle. It was observed that some microcracks appeared on the surface of primary particles due to the anisotropic volume change during the charging/discharging process [5]. Moreover, phase transformation was also observed using HR-TEM. As shown in Fig. 1c, the spent cathode particle has a layered phase in the bulk region whereas a spinel phase near the particle surface is observed.
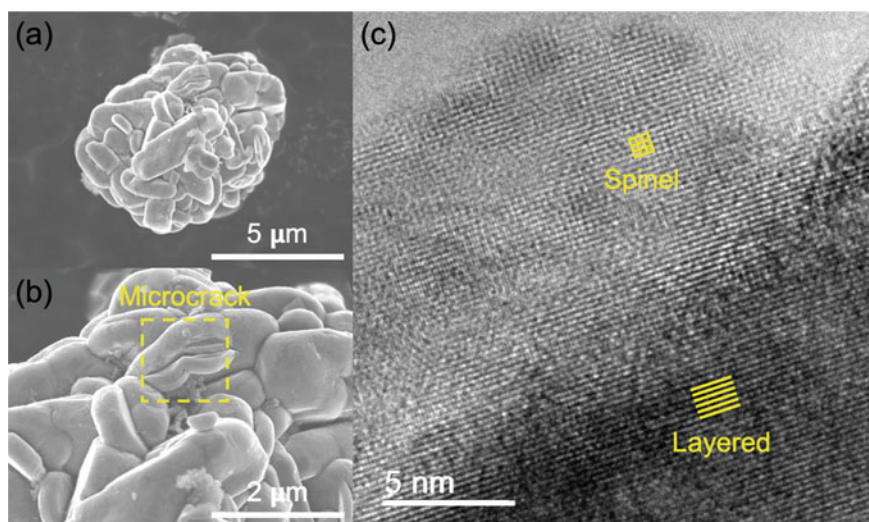
Fig. 1 Characterization of the spent cathode materials. **a**, **b** SEM. **c** HR-TEM

Direct Regeneration Through Hydrothermal Relithiation Followed by Sintering

To resolve the lithium deficiency and structural defects, the spent cathode material was first hydrothermally relithiated in the autoclave with 4.0 M LiOH solution at 220 °C for 2 h followed by sintering at 850 °C for 4 h in air. After these steps, the regenerated cathode material reached the ideal stoichiometry ($Li_{1.00}Ni_{0.15}Mn_{0.15}Co_{0.70}O_2$).

Figure 2a shows the XRD spectrum of the spent and regenerated cathode materials. The diffraction peaks of all samples can be indexed as the α-NaFeO$_2$ structure with a space group of R$\overline{3}$m. . After long-term cycling, the (003) peak of the spent cathode material shifted to a lower angle (Fig. 2b), corresponding to an expansion of the unit cell along the c-axis due to the electrostatic repulsion between the oxygen layers [6]. Meanwhile, the separation between the peaks in the (108)/(110) doublets increased (Fig. 2b), corresponding to a shrinkage of the unit cell along the a-axis due to the oxidation of transition metals to compensate the lithium deficiency [7]. After the regeneration process, the (003) peak shifted to a higher angle and the separation between the doublets decreased. Moreover, the intensity ratio of I_{003}/I_{104} is directly related to cation mixing, and a value smaller than 1.2 indicates a high degree of cation mixing [8]. The intensity ratio of I_{003}/I_{104} of the spent cathode material was determined to be 1.09, indicating undesired cation mixing due to the migration of some transition metals to the Li$^+$ deficient sites. It was found that the regenerated cathode material has a higher intensity ratio of I_{003}/I_{104} (1.69) than the spent cathode material, indicating that the sample treated with hydrothermal relithiation and sintering steps has lower cation mixing.

The surface morphology and microstructures of the regenerated cathode material were carefully examined by SEM and HR-TEM. After the regeneration process, the microcracks on the primary particle surface disappeared (Fig. 3a, b). In addition, the undesired spinel phase on the particle surface was converted back to the layered phase
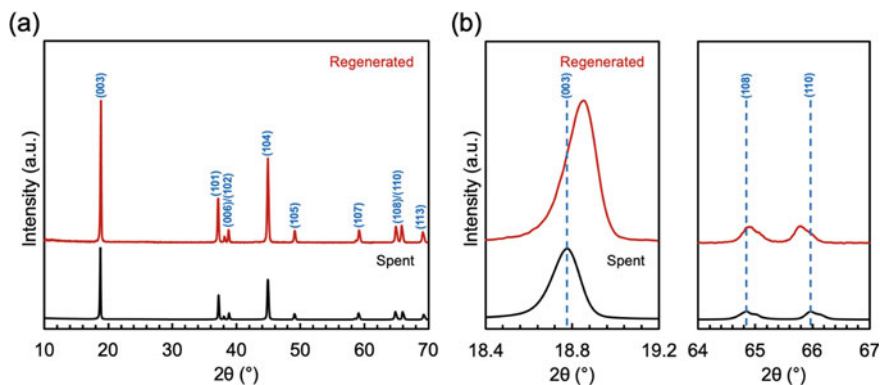
Fig. 2 XRD spectrum of the spent and regenerated cathode materials
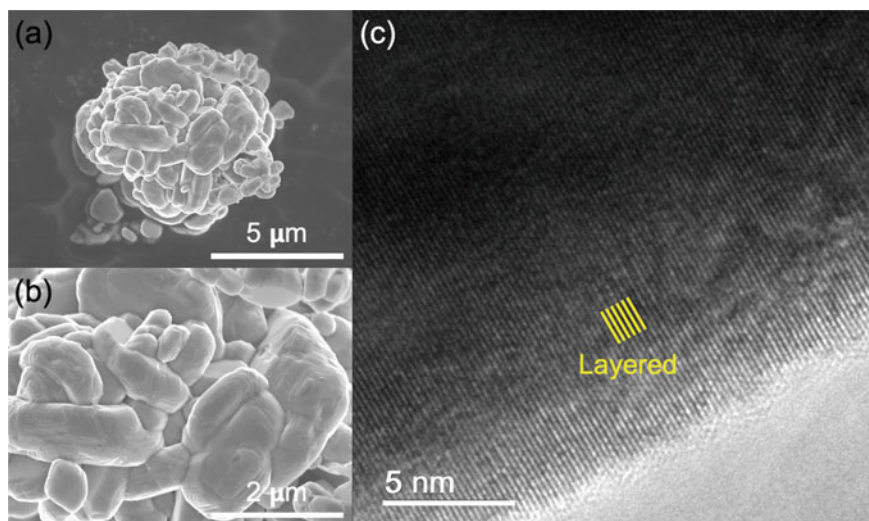
Fig. 3 Characterization of the regenerated cathode materials. **a**, **b** SEM. **c** HR-TEM

(Fig. 3c). The removal of microcracks and spinel phase indicates that the structural defects of the spent cathode material were resolved.

Electrochemical Performance

To evaluate the cycling performance, all samples were used to fabricate coin cells and tested in the voltage range of 2.8–4.4 V at 0.33C (50 mA g^{-1}) for 50 cycles (Fig. 4a). For the spent cathode material, the initial discharge capacity was 97 mAh g^{-1} with a capacity retention of 78% after 50 cycles. The poor cycling performance of the spent cathode material is due to the presence of spinel phase on the particle surface (Fig. 1c). With direct regeneration, the cycling performance of the spent cathode material was fully recovered. The regenerated cathode material delivered an initial discharge capacity of 151 mAh g^{-1} with a capacity retention of 91% after 50 cycles, which is comparable to the commercial cathode material $LiNi_{0.33}Mn_{0.33}Co_{0.33}O_2$ (an initial discharge capacity of 151 mAh g^{-1} with a capacity retention of 93% after 50 cycles) tested under the same condition in the previous study [9]. It should be mentioned that the slight difference in capacity retentions between the commercial and regenerated cathode materials is due to the difference in the cathode composition.

The rate performance and voltage profiles of the spent and regenerated cathode materials at different C-rates are shown in Fig. 4b–d. The spent sample showed the worst rate capability such that the discharge capacity failed to recover when the current density changed from 5C (750 mA g^{-1}) to 0.1C (15 mA g^{-1}). In contrast, the discharge capacity of the regenerated sample could be quickly recovered when
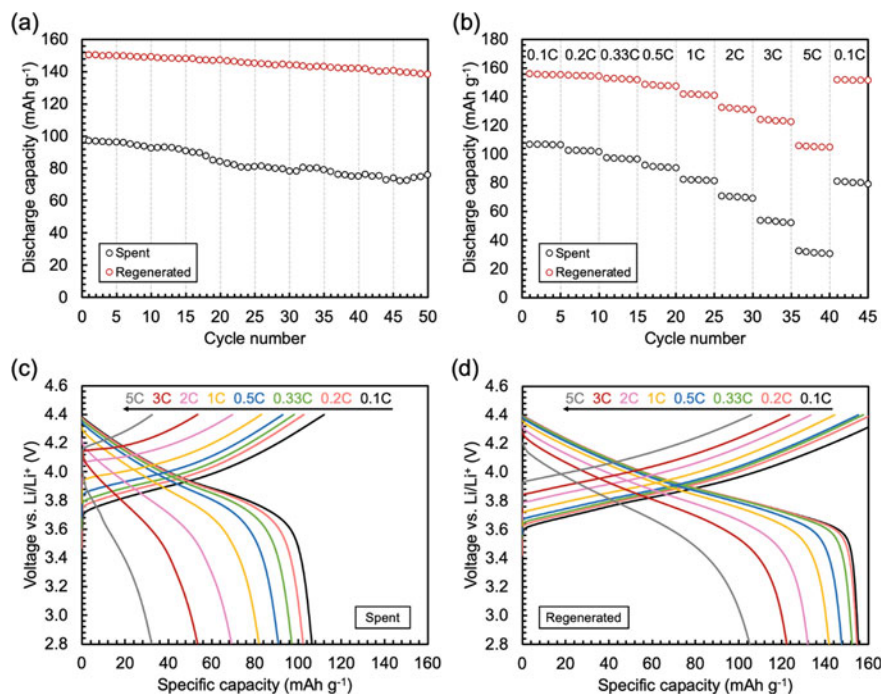
Fig. 4 Electrochemical performance of the spent and regenerated cathode materials. **a** Cycling performance. **b** rate performance. **c, d** voltage profiles

the current density changed from 5C to 0.1C. The superior rate capability of the regenerated sample is related to its lower cation mixing.

Conclusions

A direct recycling process of spent LIBs from an electric vehicle is developed. After the electric vehicle battery pack is discharged and disassembled, the obtained spent cathode material is hydrothermally relithiated at 220 °C for 2 h and then sintered at 850 °C for 4 h in air. The regenerated cathode material delivers an initial discharge capacity of 151 mAh g^{-1} at 0.33C (50 mA g^{-1}) with a capacity retention of 91% after 50 cycles. By combining hydrothermal relithiation with sintering, lithium deficiency, structural defects, and electrochemical activity of the spent cathode material are fully restored. Direct recycling is still at the early stages of research and further development is needed prior to its commercialization. It is believed that this study opens the door for future studies by confirming the feasibility of this direct recycling process in the LIB recycling industry.

References

1. Lu Y, Peng K, Zhang L (2022) Sustainable recycling of electrode materials in spent Li–ion batteries through direct regeneration processes. ACS ES&T Eng 2:586–605. https://doi.org/10.1021/acsestengg.1c00425
2. Chan KH, Anawati J, Malik M, Azimi G (2021) Closed-loop recycling of lithium, cobalt, nickel, and manganese from waste lithium–ion batteries of electric vehicles. ACS Sustain Chem Eng 9:4398–4410. https://doi.org/10.1021/acssuschemeng.0c06869
3. Xu P, Tan DHS, Jiao B et al (2023) A materials perspective on direct recycling of lithium-ion batteries: principles, challenges and opportunities. Adv Funct Mater 33:2213168. https://doi.org/10.1002/adfm.202213168
4. Wei G, Liu Y, Jiao B et al (2023) Direct recycling of spent Li-ion batteries: challenges and opportunities toward practical applications. iScience 26:107676. https://doi.org/10.1016/j.isci.2023.107676
5. Yin S, Deng W, Chen J et al (2021) Fundamental and solutions of microcrack in Ni-rich layered oxide cathode materials of lithium-ion batteries. Nano Energy 83:105854. https://doi.org/10.1016/j.nanoen.2021.105854
6. Mohanty D, Kalnaus S, Meisner RA et al (2013) Structural transformation of a lithium-rich $Li_{1.2}Co_{0.1}Mn_{0.55}Ni_{0.15}O_2$ cathode during high voltage cycling resolved by in situ X-ray diffraction. J Power Sources 229:239–248. https://doi.org/10.1016/j.jpowsour.2012.11.144
7. Mohanty D, Gabrisch H (2012) Microstructural investigation of $Li_xNi_{1/3}Mn_{1/3}Co_{1/3}O_2$ ($x \leq 1$) and its aged products via magnetic and diffraction study. J Power Sources 220:405–412. https://doi.org/10.1016/j.jpowsour.2012.08.005
8. Malik M, Chan KH, Azimi G (2022) Review on the synthesis of $LiNi_xMn_yCo_{1-x-y}O_2$ (NMC) cathodes for lithium-ion batteries. Mater Today Energy 28:101066. https://doi.org/10.1016/j.mtener.2022.101066
9. Xu P, Yang Z, Yu X et al (2021) Design and optimization of the direct recycling of spent Li-ion battery cathode materials. ACS Sustain Chem Eng 9:4543–4553. https://doi.org/10.1021/acssuschemeng.0c09017

Leaching of Critical Metals from Spent Lithium-Ion Battery Using Acidic Organophosphorus Extractant

Kurniawan Kurniawan, Sookyung Kim, Hyunju Lee, Mooki Bae, Hongin Kim, and Jae-chun Lee

Abstract Recycling of cathode material of spent lithium-ion batteries (LIBs) is important for recovering critical metals and protecting the environment. This study thus proposes a sustainable recycling process for cathode material (nickel-cobalt-manganese/NCM chemistry) via leaching with an acidic organophosphorus extractant, di-(2-ethylhexyl)phosphoric acid/D2EHPA and copper (current collector) as the reducing agent. The effects of leaching parameters, including stirring speed, Cu amount, D2EHPA concentration, temperature, and time were investigated. The leached metals on the loaded D2EHPA were recovered via stripping using pH-controlled aqueous solutions. Using D2EHPA for leaching allows process intensification because it integrates leaching and solvent extraction (SX) in one-stage operation. It also reduces the consumption of aqueous solutions, thereby minimizing wastewater generation.

Keywords NCM chemistry · Recycling · D2EHPA · Sustainable

Introduction

The continuous demand and consumption of lithium-ion batteries (LIBs) have grown concern about (i) supply security of battery materials and (ii) generation of huge amount of spent LIBs. Examples of battery materials include metals like lithium, cobalt, nickel, and manganese (these metals are labeled as critical metals), which are used in the manufacture of cathode of LIBs in the forms of $LiCoO_2$ (LCO), $LiFePO_4$ (LFP), $LiNi_xCo_yMn_{1-x-y}O_2$ (NCM), etc. [2]. Currently, these metals are produced from mining/primary ores, but it will not be sufficient for securing future supply due to depletion of high-grade and economic recoverable ores. Moreover, LIBs are

K. Kurniawan (✉) · S. Kim · J.-c. Lee
Resource Recycling, University of Science and Technology, Daejeon 34113, Republic of Korea
e-mail: k.kurniawan@kigam.re.kr

K. Kurniawan · S. Kim · H. Lee · M. Bae · H. Kim · J.-c. Lee
Mineral Resources Research Division, Korea Institute of Geoscience and Mineral Resources (KIGAM), Daejeon 34132, Republic of Korea

subject to ageing, LIBs in small electronic products have lifetimes of 3 years and those used in electric transportation are about 5–10 years. Therefore, spent LIBs are generated in an alarming rate; spent LIBs generation will exceed 11 million tons by 2030, which however, only 5% of spent LIBs generated is being treated properly [4]. In fact, spent LIBs are hazardous materials as they contain heavy metals and toxic/carcinogenic compounds which are harmful for human health and the environment. Therefore, establishing a system for proper management of spent LIBs is critical for now and in future. In particular, recycling of spent LIBs, particularly cathode materials (the most important part of spent LIBs), appears to be an economically and environmentally viable solution.

Cathode materials of spent LIBs can be directly recycled (regenerated) [11]. However, it (direct recycling) depends on the quality of spent cathode materials and suits only for same types of cathode materials. Therefore, metal recovery from cathode materials is favored. There are three basic processes for metal recovery from cathode materials: (i) thermal processes via smelting, (ii) aqueous processes via leaching, and (iii) their combinations [4]. Leaching is often favored due to advantages of easier control, scope of small-scale production, and more importantly, possibility of total recycling [3]. Considering the nature of metals in cathode materials, the leaching is usually carried out using acids (either using mineral acids or organic acids), while using hydrogen peroxide (H_2O_2) as the reducing agent [3]. Another type of reductant, such as current collectors in LIBs (copper/aluminum) or even nickel matte) has also been introduced [6].

Acid leaching is capable of quantitatively recovering almost all the critical metals in cathode materials. However, it faces challenges during the downstream processing of leach solutions for metal separation. Most common methods used for metal separation involve selective precipitation or solvent extraction (SX) [1, 8, 10, 12], both processes, however, require significant pH adjustment which then leads to high reagent consumption due to the very acidic leach solutions and generation of high volume of wastewater [9]. Alternative of total precipitation to obtain similar cathode materials is viable, but it requires careful control of the metal concentrations in leach solutions [7].

There is a need to develop more sustainable leaching process of cathode materials. Therefore, the present study proposes the leaching of cathode materials (NCM-type) using an acidic organophosphorus extractant, di-(2-ethylhexyl)phosphoric acid/D2EHPA, as the lixiviant. The use of D2EHPA as the lixiviant allows for process intensification as leaching and SX are carried out in a single-stage operation. The leaching integrates the use of copper (current collector) as the reducing agent, thereby reducing the need for additional reagents in the overall recycling process. The leach solution obtained (loaded D2EHPA) can be directly stripped for metal recovery, and the stripped D2EHPA can be directly reused to lower reagent consumption. Limited aqueous solution (mostly for stripping) is consumed, which will substantially reduce wastewater generation.

Materials and Methods

Materials

Sample of NCM (+0.45 μm) was obtained from a local recycler and used as-received. The metal compositions of the samples analyzed by an inductively coupled plasma-atomic emission spectroscopy (ICP-AES, Model: iCAP6000 series, Thermo Scientific, USA) comprised of 11.52% Ni, 7.71% Co, 7.48% Mn, 2.94% Li, 0.70% Al, 0.45% Cu, and the remaining is graphite. X-ray diffraction (XRD, D8 Advance, Bruker, USA) analysis (Fig. 1) depicts the presence of $LiNi_xCo_yMn_{1-x-y}O_2$ (NCM-433) and graphite phases. D2EHPA (Sigma Aldrich, USA), diluted in kerosene (Junsei, Japan), was used as the lixiviant. Copper powder (Sigma Aldrich, USA) was used as the reducing agent.

Methods

The leaching experiments were performed in a glass vial of 50 mL placed in a water bath to control the temperature and equipped with a magnetic stirring bar. In all experiments, 20 mL of D2EHPA at desired concentrations were used. The leaching parameters were optimized by varying one factor at a time in the range: 300–800 rpm stirring speed, 0–0.25:1 (g/g) Cu/NCM mass ratio, 0.5–2.3 M D2EHPA concentration, 25–90 °C temperature and 1–6 h time. The metal concentrations in loaded D2EHPA were determined by ICP-AES after stripping with 4.0 M H_2SO_4 solution at an organic/aqueous (O/A) phase ratio of 3/5. The leaching percentage
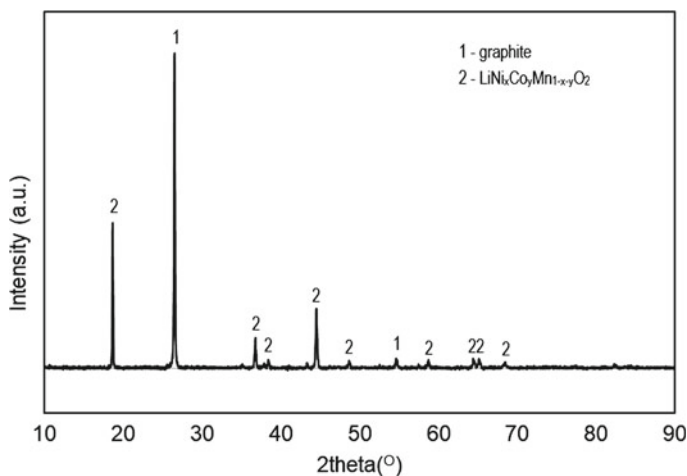
Fig. 1 XRD pattern of NCM cathode material

was calculated via Eq. (1). All the leaching experiments were carried out three times while reporting the mean values.

$$\text{Leaching } (\%) = \frac{\left[M_{\text{org}}\right] \times V_{\text{org}}}{m_{\text{NMC}} \times \text{wt\%}_{\text{metal}}} \times 100\% \tag{1}$$

where $\left[M_{\text{org}}\right]$ is metal concentration in loaded D2EHPA, V_{org} is volume of D2EHPA, m_{NMC} is mass of NCM sample and $\text{wt\%}_{\text{metal}}$ is the weight percent of metal in NCM samples.

For the stripping experiments, loaded D2EHPA was contacted with aqueous solutions with different pH (O/A = 1/1) for 5 min. The equilibrium pH was then measured after finishing. And the metal concentrations were measured by ICP-AES to calculate the stripping efficiency via Eq. (2):

$$\text{Stripping } (\%) = \frac{M_{\text{aq}} \times V_{\text{aq}}}{\left[M_{\text{org}}\right] \times V_{\text{org}}} \times 100\% \tag{2}$$

where M_{aq} is metal concentration in stripping solution.

Results and Discussion

Effect of Leaching Parameters

All the leaching results are presented in Fig. 2 and discussed as follows.

Effect of Stirring Speed

Results on the effect of stirring speed (Fig. 2a) demonstrate that the metal leaching

increased as stirring speed increased. Co, Ni, and Mn (from NCM) and Cu leaching was 16.0%, 15%, 12.7%, and 25.4%, respectively, at 300 rpm, and attained to be 54.6%, 49.9%, 24.5%, and 59.2% at 700 rpm. The change was negligible at the higher stirring speed (800 rpm). In all situations, the leaching of Al was always below 5%. In the leaching reactions, sufficient contact between solid (NCM) and lixiviants (D2EHPA) must be provided; clearly, higher stirring speed aided in contact between the two phases. Therefore, a stirring speed of 700 rpm was chosen for further experiments.
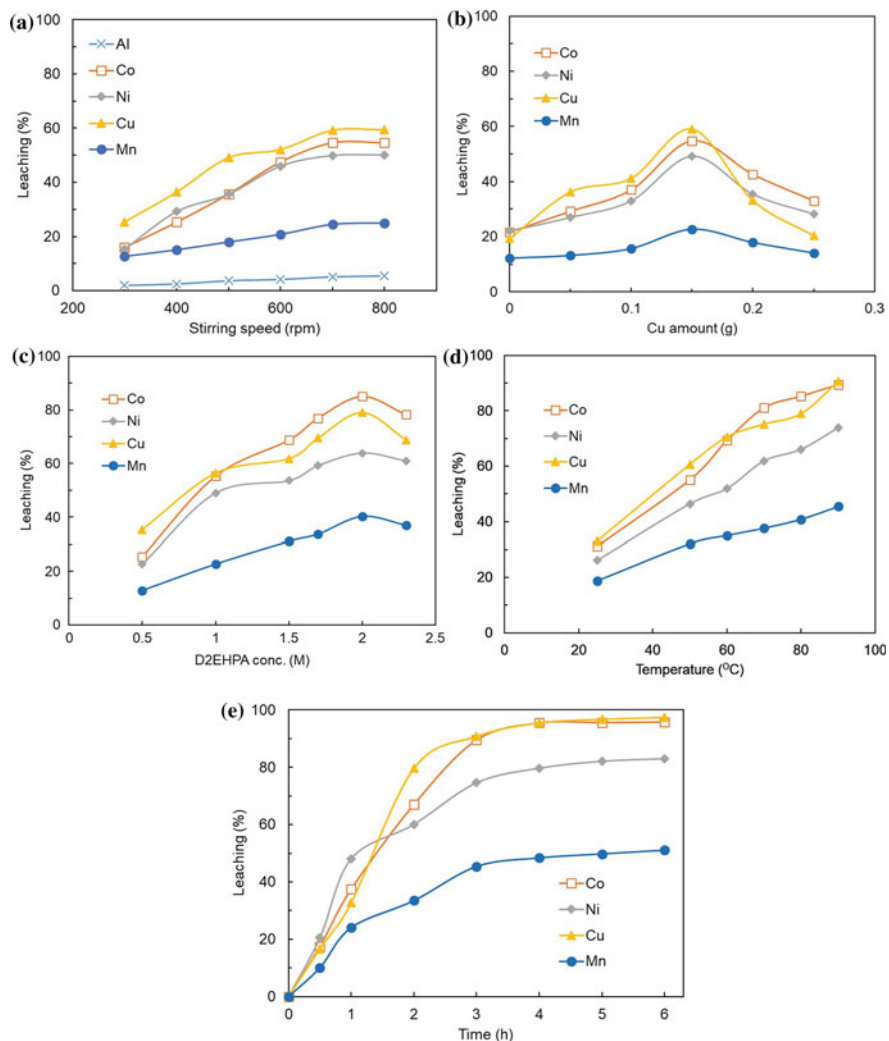
Fig. 2 Leaching results at different **a** stirring speeds, **b** Cu amount, **c** D2EHPA concentration, **d** temperature and **e** time

Effect of Cu Amount

Cu has a positive potential ($E^0 = 0.337$ V) and, therefore, can be used as a reducing agent for metal oxides. The leaching reactions can be given as Eqs. (3–5); no reaction between NiO and Cu as Ni is already present as Ni^{2+}. As presented in Fig. 2b, low metal leaching (below 20% for all metals) was obtained without reducing agent, and it increased as the amount of Cu increased. Adding 0.15 g Cu, for instance, the leaching of Co, Ni, and Mn was found to be 54.8, 49.2, and 22.7%, with Cu leaching

of 59.0%. Further addition of Cu, however, decreased the metal leaching due to it (Cu) also consumed D2EHPA, thereby reducing its (D2EHPA) availability to react with metals from NCM. Thus, a 0.15 (g/g) of Cu/NCM ratio was chosen for further experiments.

$$Co_3O_4 + Cu + 8H^+ = 3Co^{2+} + Cu^{2+} + H_2O, \Delta G^0 = -252.07 \, kJ/mol \quad (3)$$

$$NiO + 2H^+ \rightarrow Ni^{2+} + H_2O, \Delta G^0 = -71.2 \, kJ/mol \quad (4)$$

$$MnO_2 + Cu + 4H^+ = Mn^{2+} + Cu^{2+} + H_2O, \Delta G^0 = -170 \, kJ/mol \quad (5)$$
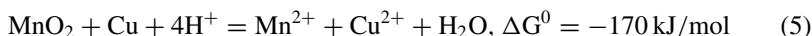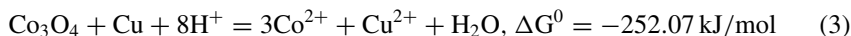
Effect of D2EHPA Concentration

As shown in Fig. 2c, metal leaching increased proportionally with increasing D2EHPA concentrations, until a point (D2EHPA conc. > 2.0 M) at which it began to decrease. Leaching of Co, Ni, Mn, and Cu at 2.0 M was 85.0%, 63.9%, 40.3%, and 79.0%, respectively, and decreased to 78.2%, 61.0%, 37.0%, and 68.8% at the above D2EHPA concentration. The higher D2EHPA concentration implies the more available of D2EHPA molecules to react with the metals; however, at the very high concentration, the solution has a very high viscosity. A 2.0 M D2EHPA concentration was chosen.

Effect of Temperature

Results (Fig. 2d) show that the temperature significantly affected the metal leaching. As the temperature increased from 25 to 70 °C, the leaching efficiency of respective metals, Co, Ni, Mn, and Cu, increased from 31.1% to 81.1%, 26.2% to 61.9%, 18.8% to 37.6%, and 33.1% to 75.2%. And leaching efficiency further increased to 89.5% (Co), 73.9% (Ni), 45.4% (Mn), and 90.6% (Cu) at 90 °C. Higher temperatures can reduce the viscosity of D2EHPA, increase dissociation of D2EHPA (more H^+ available), and provide more energy for the molecules' movement and chemical reactions. Further experiments were then carried out at 90 °C.

Effect of Time

Figure 2e shows that the leaching efficiency continued to increase as the leaching time increased. Clearly, this was accomplished by extending the leaching time from 30 min to 4 h. After 4 h, the leaching efficiency was found to be 95% Co, 79.7%
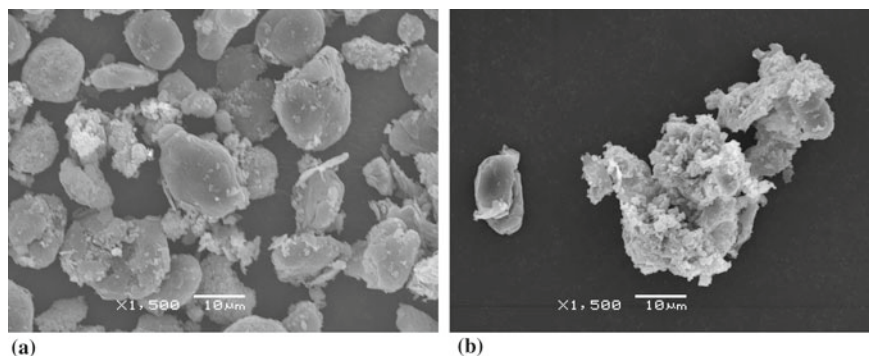
Fig. 3 SEM of **a** initial NCM and **b** leaching residue

Ni, 48.4% Mn, and 95.5% Cu. And it was negligibly changed at the longer time. A prolonged time provides more scope for the leaching reactions, which involved the dissociation of D2EHPA, cation exchange between metal cations and H atom from D2EHPA and complexation.

Analysis of Leaching Residue

The leaching residue after 4 h leaching was analyzed by SEM (Fig. 3) and XRD (Fig. 4). Apparently, a significant difference in the surface morphology of NCM particle before and after the leaching can be seen. The NCM surface became porous and rough after leaching, as compared to that of the initial particles which had smooth surface. The XRD spectra showed the decrease in intensities of $LiNi_xCo_yMn_{1-x-y}O_2$ phases after the leaching while the intensity of Al phase increased. This is consistent with the leaching results that Al was not leached. No new phases formed during the leaching as the leaching of metals in NCM only produced metal cations and H_2O (Eqs. 3–5).

Stripping

The stripping of Co, Ni, Mn, and Cu from loaded D2EHPA was carried out by controlling the equilibrium pH values. As shown in Fig. 5, Co and Ni behave similarly as a function of equilibrium pH, as do Cu and Mn. These results are nearly consistent with the respective pKa values of the metal cations; pKa, $Ni^{2+} = 9.9$, $Co^{2+} = 9.7$, $Mn^{2+} = 10.6$ and $Cu^{2+} = 7.5$ [5]. These results imply that such separation is possible. For example, Co and Ni can be stripped first at pH between 1.7 and 2.0, and Cu and Mn at the lower pH.

Fig. 4 XRD pattern of leaching residue
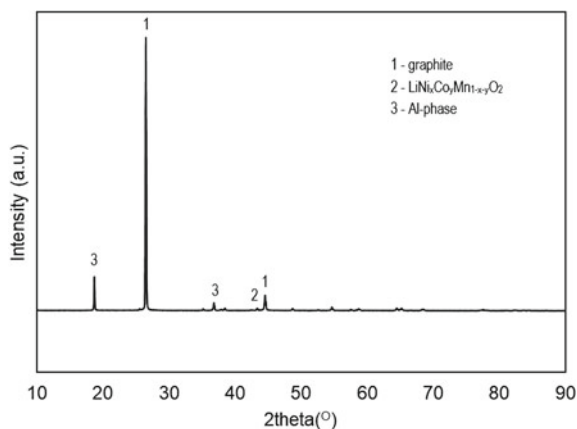
Fig. 5 Stripping behavior of metals (Co, Ni, Cu, Mn) as a function of equilibrium pH
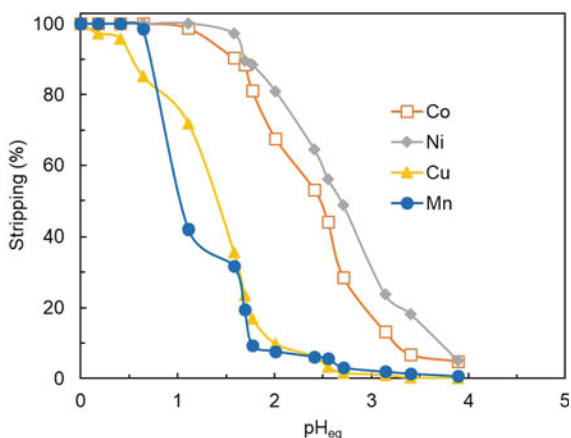
Conclusions

The leaching of critical metals (Co, Ni, Mn) from NCM chemistry of spent LIBs was carried out using D2EHPA as the lixiviant and Cu metal as the reducing agent. The effects of leaching parameters, including stirring speed, Cu amount, D2EHPA concentration, temperature, and time were investigated, showing their critical influences on the metal leaching. Under the conditions of 700 rpm stirring speed, 0.15 (g/g) Cu/NCM, 2.0 M D2EHPA, 4 h, 90 °C and 1.0 g NCM/20 mL D2EHPA, the metal leaching achieved was 94.6% Co, 79.2% Ni, 47.3% Mn and 96.4% Cu. The loaded D2EHPA can be stripped using pH-controlled aqueous solutions for metal recovery and further metal separation.

Development of 539 critical metal recovery technologies (capacity of 200 kg/day) from low-grade solid wastes for the 540 foundation of open access recycling platform).

References

1. Chen X, Chen Y, Zhou T, Liu D, Hu H, Fan S (2015) Hydrometallurgical recovery of metal values from sulfuric acid leaching liquor of spent lithium-ion batteries. Waste Manage 38:349–356
2. Chen Z, Zhang W, Yang Z (2019) A review on cathode materials for advanced lithium ion batteries: microstructure designs and performance regulations. Nanotechnology 31(1):012001
3. Dalini EA, Karimi G, Zandevakili S, Goodarzi M (2021) A review on environmental, economic and hydrometallurgical processes of recycling spent lithium-ion batteries. Miner Process Extr Metall Rev 42(7):451–472
4. Garole DJ, Hossain R, Garole VJ, Sahajwalla V, Nerkar J, Dubal DP (2020) Recycle, recover and repurpose strategy of spent Li-ion batteries and catalysts: current status and future opportunities. Chemsuschem 13(12):3079–3100
5. Hawkes SJ (1996) All positive ions give acid solutions in water. J Chem Educ 73(6):516
6. Joulié M, Billy E, Laucournet R, Meyer D (2017) Current collectors as reducing agent to dissolve active materials of positive electrodes from Li-ion battery wastes. Hydrometallurgy 169:426–432
7. Kang J, Sohn J, Chang H, Senanayake G, Shin SM (2010) Preparation of cobalt oxide from concentrated cathode material of spent lithium ion batteries by hydrometallurgical method. Adv Powder Technol 21(2):175–179
8. Lei S, Sun W, Yang Y (2022) Solvent extraction for recycling of spent lithium-ion batteries. J Hazard Mater 424:127654
9. Nguyen VT, Lee J-C, Jeong J, Kim BS, Pandey BD (2014) Selective recovery of cobalt, nickel and lithium from sulfate leachate of cathode scrap of Li-ion batteries using liquid-liquid extraction. Met Mater Int 20:357–365
10. Shuya L, Yang C, Xuefeng C, Wei S, Yaqing W, Yue Y (2020) Separation of lithium and transition metals from leachate of spent lithium-ion batteries by solvent extraction method with Versatic 10. Sep Purif Technol 250:117258
11. Wu J, Zheng M, Liu T, Wang Y, Liu Y, Nai J, Zhang L, Zhang S, Tao X (2022) Direct recovery: a sustainable recycling technology for spent lithium-ion battery. Energy Storage Mater 54:120–134
12. Yang H, Deng B, Jing X, Li W, Wang D (2021) Direct recovery of degraded $LiCoO_2$ cathode material from spent lithium-ion batteries: efficient impurity removal toward practical applications. Waste Manage 129:85–94

Mechanochemical Extraction of Lithium from α-Spodumene at Low Temperatures

Tyler Del Rose, Yuting Li, Long Qi, and Ihor Z. Hlova

Abstract The growing commitment to green energy technologies coupled with the rising usage of portable electronic devices has caused a rapid increase in lithium market demand. Currently, in the USA brines are the primary source for lithium due to their utilization of cheap and inexpensive processes; however, long lead times and low extraction yields raise concerns for potential supply chain disruptions. In this work, we examine a novel mechanochemical process for rapid lithium extraction from lithium-rich spodumene ore. We demonstrate multiple mechanochemically assisted ion-exchange reactions between α-spodumene and various solid leaching agents resulting in lithium extraction yields of up to 40 or 77% without or with a secondary dilute hydrochloric acid leach, respectively. Furthermore, we propose mechanisms for this enhanced lithium extraction from α-spodumene both with and without a secondary acid leach.

Keywords Lithium extraction · α-spodumene · Mechanochemical extraction

Introduction

Driven by the increase in portable devices, electric vehicles, and grid storage markets, the demand for lithium–ion batteries (LiBs), and consequently lithium, has accelerated significantly over recent years [1, 2]. It is estimated that 80% of the global end-use for lithium goes toward battery technologies [3]—an increase from 39%

T. Del Rose (✉) · L. Qi · I. Z. Hlova
Critical Materials Innovation Hub, Ames National Laboratory, Iowa State University, Ames, IA 50010, USA
e-mail: tdelrose@ameslab.gov

T. Del Rose
Division of Materials Science and Engineering, Ames National Laboratory, Iowa State University, Ames, IA 50010, USA

Y. Li · L. Qi
Division of Chemical and Biological Sciences, Ames National Laboratory, Iowa State University, Ames, IA 50010, USA

in 2017 [4]. In the USA, brines consisting of diluted quantities of lithium are the primary source for lithium extraction due to the application of an inexpensive but slow solar evaporation process [5, 6]. However, the increasing market demands coupled with the potential supply chain risks from relying on the sluggish solar evaporation process necessitate the use of richer lithium supplies and expedited extraction protocols. Consequently, hard-rock sources, containing a magnitude more lithium than brines, and extracted through expedient thermal/acidic methodology, have garnered increased attention and research [7–9].

One of the most promising hard-rock sources for lithium extraction, containing up to ~ 8.0 wt.% Li_2O, is spodumene ($LiAlSi_2O_6$). Spodumene consists of two main polymorphs (illustrated in Fig. 1): the naturally occurring α polymorph—closed structure that is highly resistant to ion-exchange reactions and acid attacks, and the β polymorph—open structure with ~ 33% increased volume making it more susceptible to lithium extraction methodologies [10, 11]. Thus, it is common for lithium extraction processes to employ an α to β polymorph thermal decrepitation at 1100 °C [12, 13]. However, a decrepitation process requires large energy inputs, indirectly resulting in considerable greenhouse emission. To overcome this issue, a significant effort is being devoted to developing alternative extraction processes [14–18].

Mechanochemical approaches are one of the most promising alternative lithium extraction processes. Milling α-spodumene in a planetary-style mill for only 30 min drastically reduces the particle size, increases surface area, destroys crystallinity, and cleaves O-M (M = Li, Al, and Si) bonds [19, 20]. Further, employing a conventional sulfuric-acid roasting after mechanochemical activation achieves complete lithium extraction from α-spodumene [19]. Other studies proposed taking this a step further—heat treating amorphous spodumene at 600–800 °C to form a new γ polymorph; however, this methodology is currently in its infancy with unproven application [20].
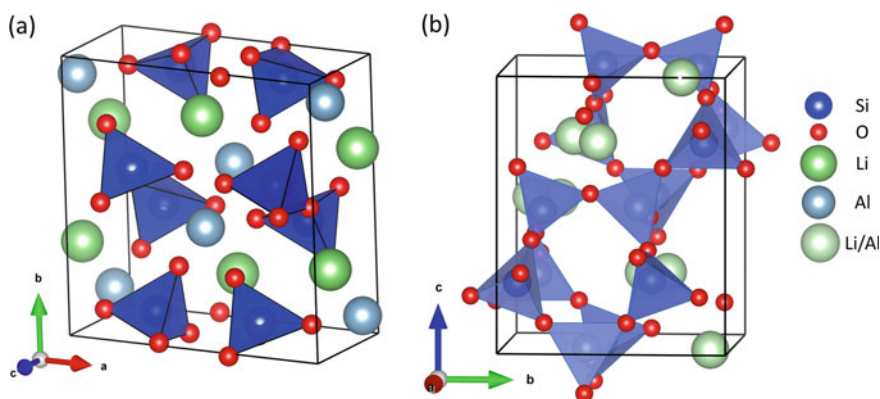
Fig. 1 Crystal structures of **a** α- and **b** β-spodumene polymorphs

The work presented herein examines a novel mechanochemical approach to lithium extraction, leveraging mechanochemistry to facilitate an ion-exchange reaction between α-spodumene and various solid leaching agents. Due to the similarities in Na- and Li-spodumene crystal structures, a variety of Na-based solid leaching agents are examined. Considering the necessity for lithium extraction from spodumene to become both more affordable and energy efficient, this research adopts low-temperature techniques ($\leq 100\,°C$ where neither β- nor γ-spodumene form) and dilute acids to reduce waste streams, greenhouse gas emissions, and overall reagent expenses.

Methods

Lithium extraction was performed through a mechanochemical reaction between α-spodumene and various solid leaching agents (with 50% excess of stoichiometry) in a steel vial using a SPEX 8000D Mixer/Mill with a steel grinding media to sample mass ratio of 20:1. After grinding, samples were stirred in 90 °C deionized water (or, when specified, diluted HCl) for 3 h followed by a room temperature 16-h stir. The final products were centrifuged and decanted to remove solid particles, and the resulting solution was characterized for lithium content using an Agilent 5800 inductively coupled plasma-optical emission spectroscopy (ICP-OES). Lithium extraction yields were calculated using Eq. 1. The spodumene concentrate, obtained from the Carolina Tin belt (provided by Piedmont Lithium), contains ~ 6.1 wt% Li_2O and is 80.1 wt% pure Li-spodumene with major impurities of Na-spodumene and SiO_2. To ensure homogeneity between samples, the batch of spodumene (as-received size of ~ 5–10 mm) was pre-milled in a low-energy magnetic rotary mill for 10 min and sieved to < 700 μm prior to the mechanochemical reaction step. A full chemical analysis of the as-received α-spodumene can be found in Table 1. All other leaching agents, of research-grade quality, were obtained from Alfa Aesar.

$$\text{Li extraction yield} = \frac{x_{\text{ICP}}}{v} * \frac{1}{m_{\text{spodumene}} * \eta} * \frac{\text{MM}_{\text{Product}}}{\text{MM}_{\text{Li}}} \qquad (1)$$

where x_{ICP} is the ICP-OES determined Li concentration (g/L), v (typically $= 0.3$) is the ICP dilution ratio, η ($= 0.8$) is the spodumene purity, m is the mass of spodumene (g) used in the reaction, and MM is the molar mass (g/mol).

Powder X-ray diffraction (PXRD) samples were prepared in a glove box under an inert Ar atmosphere, sealed with Kapton film to reduce water contamination, and performed on a PANalytical X'Pert Pro powder diffractometer with Cu Kα radiation. Phase determination employed the JADE software. Samples prepared for scanning electron microscopy (SEM) imaging and electron dispersion spectroscopy (EDS) mapping utilized an epoxy resin to hold powder particles for polishing and imaging. All SEM/EDS samples were polished with 1 μm colloidal diamond solutions. To avoid dissolving the Na and Li water-soluble compounds, the samples milled with

Table 1   Chemical assay of the as-received α-spodumene

Element	Abundance (wt%)
O	46.9
Si	29.4
Al	13.4
Li_2O	6.1
Ca	0.84
Fe	0.57
K	0.57
Na	0.50

Impurities under 0.5 wt% are excluded from the table

Na_2CO_3 were polished using an oil-based solution. SEM samples were then sputtered with gold to mitigate electron beam charging effects. SEM and EDS measurements utilized an FEI Teneo SEM equipped with an oxford instruments Aztec EDS system.

Results and Discussion

Several initial control assessments were performed to evaluate the effectiveness of mechanochemical processing. First, as-received spodumene was soaked at room temperature in DI water for 72 h. In a second experiment, concentrated HCl was used instead of DI water to soak the spodumene. In a third control experiment, spodumene was boiled in a concentrated HCl solution for 1 h. After filtering and evaporation, all three experiments did not result in any noticeable lithium extraction. Finally, to verify the reported Li content, a Li leaching using the well-established sulfuric-acid roast approach was conducted. For this purpose, α-spodumene was converted into β via thermal decrepitation at ~ 1050 °C, and then boiled in concentrated sulfuric acid at 250 °C for 2 h. The obtained lithium concentration corresponds to roughly 6 wt% LiO_2 content in the virgin α-spodumene, confirming the analysis depicted in Table 1.

The lithium extraction yields for Li-spodumene mechanochemically reacted with various Na-based solid leaching agents are shown in Table 2. Each mechanochemical reaction underwent the same procedure: ball milling a total of 1 g of material (with Li to Na stoichiometric ratio of 1:1.5) for 12 h followed by dissolution of obtained product in an aqueous medium (H_2O or HCl). Noting the lack of lithium extracted in the reference experiments, it becomes clear that the mechanochemical process facilitates an ion-exchange reaction between the Na-leaching agents and Li-spodumene:

$$xLiAlSi_2O_6 + Na_xA \rightarrow Li_xA + xNaAlSi_2O_6 \qquad (2)$$
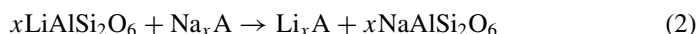
where A is the anion group.

Table 2 Lithium extraction yields of spodumene milled with various solid leaching agents

Leaching Agent	Lithium Yield (H_2O) (%)	Lithium Yield (HCl) (%)
Na_2CO_3	23	77
NaOH	13	73
$NaHCO_3$	40	54
NaCl	20	42
Na_2SO_4	31	55
Pristine	2	6

The "Pristine" entry indicates no solid leaching agent was used but the spodumene was still milled

Interestingly, $NaHCO_3$ has the highest lithium extraction yield when dissolved in water. This likely results from the preferable formation of $HAlSi_2O_6$ over its Na-equivalent—both isostructural to spodumene with H/Na occupying the Li atomic sites—and the increased mobility of H over Na. However, it is necessary to understand how Na and H substitution likely results in different degrees of replacement depending on depth within a particulate. Lithium vacancies near the surface are expected to be unbiasedly filled with Na and H, but as distance from the surface increases, it becomes harder for lithium to diffuse out and for Na and H to diffuse into the spodumene structure. Considering that H is much smaller than Na and readily diffuses into many materials to form hydrides, it is reasonable to assume that H may reach Li vacancies at a greater depth in the particle than Na, and thus H content may increase with particle depth. It is worth noting that lithium extraction yields are not 100%, implying that even H has a limit to the depth which it can extract Li.

The substitution of water for diluted HCl (~ 0.04 M) increases lithium extraction yields dramatically (see Table 2). Surprisingly, the pristine sample milled without any solid leaching agents had a lithium extraction yield increase of just 4% while other samples milled with solid leaching agents saw lithium extraction yields increase up to 60%. Considering this increase in lithium extraction yields between secondary H_2O and HCl leaches (with respect to the leaching agent's nature) implies that the leaching agents are acting as process control agents modifying the milling process and, hence, the spodumene structure in such a way as to allow for increased extraction yields. Furthermore, building on the mechanism proposed above for $NaHCO_3$, a solid leaching agent with only Na, and not H, may create Na-spodumene near the particle surface, increasing spodumene unit cell volumes. These increased unit cell volumes may aid in the diffusion of Li and H (from dilute acid) allowing H to diffuse further into the spodumene particles and extract more lithium. However, due to the decreased atomic radii of H when compared to both Na and Li, H-spodumene has a decreased unit cell volume hindering Li, H, and Na diffusion. Thus, a reasonably large particle undergoing the proposed lithium extraction process may have a core–shell structure with Li-spodumene surrounded by H-spodumene further encapsulated with Na-spodumene.

Figure 2 depicts the PXRD patterns of Li-spodumene at various processing stages in the mechanochemical lithium extraction protocol using Na_2CO_3 as a solid leaching

agent. The large Fe peak in the milled spodumene PXRD pattern (Fig. 2, red pattern) stems from wear of the steel SPEX vial and grinding media, while the lack of Fe peaks in the Na_2CO_3 containing patterns (Fig. 2, blue and magenta patterns) is directly related to the soft nature of Na_2CO_3 decreasing the vial and grinding media wear. The increased background noise (Fig. 2, red pattern) is a direct result of the background subtraction used for ease of comparison. The absence of spodumene PXRD peaks in all mechanochemically processed samples (Fig. 2, red, blue, and magenta patterns) indicates a significant decrease in long-range crystallographic order. This is typically attributed to a considerable reduction in the size of crystalline domains and the onset of amorphization. Previous studies on the milling process of spodumene suggest that amorphization is accompanied by cleavage of Li–O, Al-O, and Si–O-Si bonds [19], a possible explanation for the enhanced chemical activity of spodumene after the application of mechanochemistry.

The addition of HCl converts the Li and Na products into chlorides, which recrystallize upon evaporation, creating very sharp LiCl and NaCl PXRD peaks. The lattice parameters for the spodumene milled with Na_2CO_3 forgoing and undergoing secondary HCl treatment are, respectively, 5.6405(4) and 5.6408(3) for the NaCl phase and 5.1523(8) and 5.1534(5) for the LiCl phase. These lattice parameters are consistent with literature values indicating that there is no substitution of Li in the NaCl structure and vice-versa.

SEM micrographs of the pre-treated (10 min low-energy milling) and shaker milled (12 h high-energy milling) spodumene are presented in Fig. 3. A particle size comparison between the pre-treated and shaker milled spodumene reveals that an
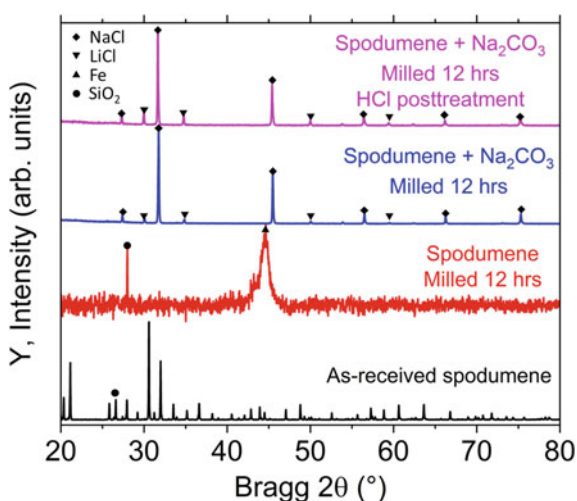
Fig. 2 X-ray diffraction of as-received spodumene (black), spodumene following a 12-h milling (red), spodumene and Na_2CO_3 milled together for 12 h (blue), and spodumene and Na_2CO_3 milled together for 12 with a subsequent HCl secondary leaching (magenta). All patterns are background subtracted to aid in visual comparison
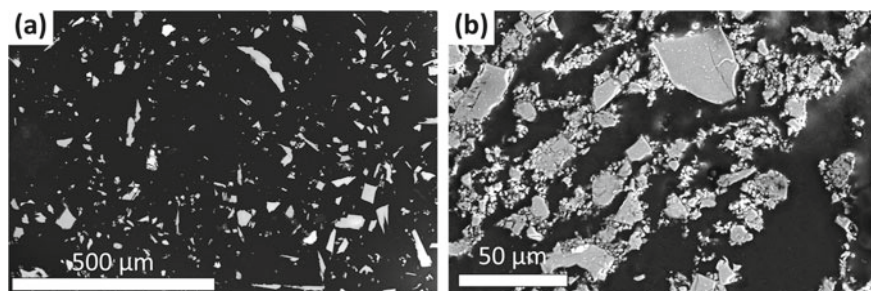
Fig. 3 SEM micrographs of spodumene after undergoing **a** magnetic milling pre-treatment for 10 min and **b** high-energy shaker milling for 12 h

overwhelming majority of the particles underwent considerable size reduction with high-energy milling. Most of the observed particles underwent comminution from roughly 100–200 µm to < 50 µm with a majority of particles < 10 µm. This large reduction in particle size consequently results in a drastic increase in surface area aiding in surface- and diffusion-based reactions.

Elemental mapping of spodumene milled with sodium carbonate with and forgoing a secondary HCl treatment is presented in Fig. 4. Due to the polymer window used on the Axtec EDS detector Li is undetectable and O/C ratio can only be qualitatively determined. The elemental mapping reveals high homogeneity between Na, Al, Si, and Fe. A comparison between the particle sizes in pre-treated spodumene (Fig. 3a) and spodumene milled with Na_2CO_3 in a high-energy shaker mill (Fig. 4a) indicates that some particles have counterintuitively increased in size. Given the chemical homogeneity within these large particles and the absence of Na-rich regions within the remainder of the micrograph, expected to appear as red regions, despite the addition of a substantial amount of Na_2CO_3, it can be inferred that these large particles are agglomerates of Li-spodumene, Na_2CO_3, and likely their reaction products—Li_2CO_3 and Na-spodumene as well as Fe contaminants.

Upon post-processing with hydrochloric acid (Fig. 4b), these large Na_2CO_3-spodumene agglomerates are disintegrated implying that the soft Na_2CO_3 and Li_2CO_3 compounds are serving as binding agents holding these large particulates together. The increase in lithium extraction yields—beyond the 4% noted when no solid leaching agent was used (see pristine sample in Table 2)—implies that Na_2CO_3 is acting as a process control agent preventing spodumene particulates from mechanochemically welding to each other. This, in turn, preserves small particle sizes with large surface areas. Assuming the reaction with HCl happens at the surface, the decreased particle size and higher surface area aids in diffusion-based lithium extraction methods and further supports our proposed mechanism for lithium extraction.
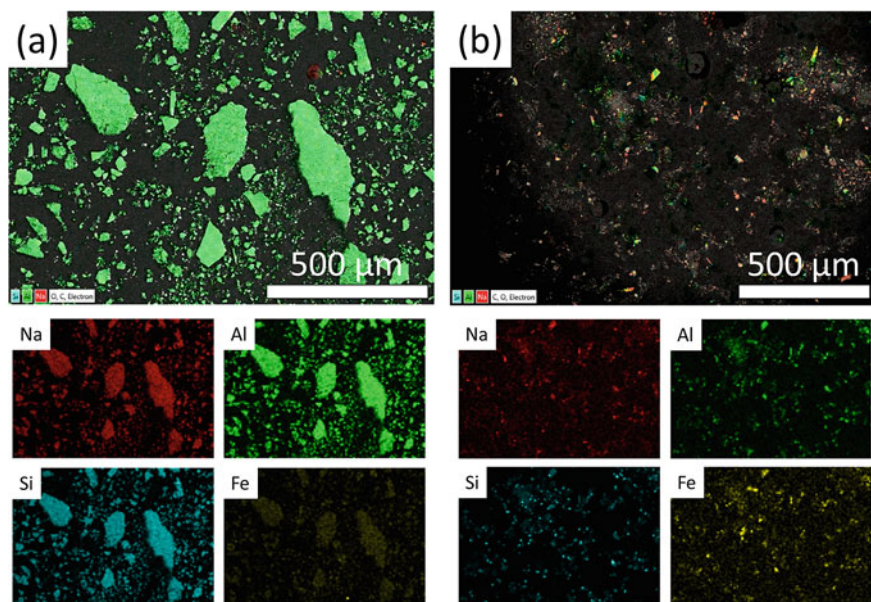
Fig. 4 Elemental mapping of spodumene milled with sodium carbonate **a** forgoing and **b** with a secondary HCl leach treatment. The top images are composites of the individual elemental mappings presented below excluding Fe

Conclusion

Li-spodumene was milled with various solid leaching agents to initiate Na-Li ion-exchange reactions, and the resulting Li-based products were recovered and examined for lithium extraction yields. The applied methodology improved lithium extraction yields from 0% (without a mechanochemical process) to 2% (milled without a solid leaching agent) to 40% (milled with $NaHCO_3$) when dissolved in water to 77% (milled with Na_2CO_3) when dissolved in dilute hydrochloric acid. Further, it was found that the Na_2CO_3 acts as a process control agent maintaining small spodumene particles with large surface area which aid in the ion-exchange diffusion-based reaction.

References

1. Dessemond C, Lajoie-Leroux F, Soucy G, Laroche N, Magnan JF (2019) Spodumene: the lithium market, resources and processes. Minerals 9(6):334
2. Seddon D (2016) Economics: lithium production. Chem Aust, 34–35
3. USGS (2023) Minerals commodity summaries 2023. https://doi.org/10.3133/mcs2023
4. USGS (2017) Minerals commodity summaries 2017. https://doi.org/10.3133/70180197
5. Liu G, Zhao Z, Ghahreman A (2019) Novel approaches for lithium extraction from salt-lake brines: a review. Hydrometallurgy 187:81–100
6. Chagnes A, Swiatowska J (eds) (2015) Lithium process chemistry: Resources, extraction, batteries, and recycling. Elsevier
7. Rioyo J, Tuset S, Grau R (2022) Lithium extraction from spodumene by the traditional sulfuric acid process: a review. Miner Process Extr Metall Rev 43(1):97–106
8. Gao TM, Fan N, Chen W, Dai T (2023) Lithium extraction from hard rock lithium ores (spodumene, lepidolite, zinnwaldite, petalite): technology, resources, environment and cost. China Geology 6(1):137–153
9. Yelatontsev D, Mukhachev A (2021) Processing of lithium ores: industrial technologies and case studies–a review. Hydrometallurgy 201:105578
10. Clarke PT, Spink JM (1969) The crystal structure of β spodumene, $LiAlSi_2O_6$-II. Zeitschrift für Kristallographie-Cryst Mater 130(1–6):420–426
11. Clark J, Appleman D, Papike J (1969) Crystal-chemical characterization of clinopyroxenes based on eight new structure refinements. Mineral Soc Amer Spec Paper 2:31–50
12. Rezaee M, Han S, Sagzhanov D, Hassas BV, Slawecki TM, Agrawal D, Akbari H, Mensah-Biney R (2022) Microwave-assisted calcination of spodumene for efficient, low-cost and environmentally friendly extraction of lithium. Powder Technol 397:116992
13. Talens Peiró L, Villalba Méndez G, Ayres RU (2013) Lithium: sources, production, uses, and recovery outlook. Jom 65:986–996
14. Han S, Sagzhanov D, Pan J, Vaziri Hassas B, Rezaee M, Akbari H, Mensah-Biney R (2022) Direct extraction of lithium from α-spodumene by salt roasting-leaching process. ACS Sustain Chem Eng 10(40):13495–13504
15. Dessemond C, Soucy G, Harvey JP, Ouzilleau P (2020) Phase transitions in the α–γ–β spodumene thermodynamic system and impact of γ-spodumene on the efficiency of lithium extraction by acid leaching. Minerals 10(6):519
16. Qiu S, Sun T, Zhu Y, Liu C, Yu J (2022) Direct preparation of water-soluble lithium salts from α-spodumene by roasting with different sulfates. Ind Eng Chem Res 62(1):685–697
17. Qiu S, Liu C, Yu J (2022) Conversion from α-spodumene to intermediate product Li_2SiO_3 by hydrothermal alkaline treatment in the lithium extraction process. Miner Eng 183:107599
18. Necke T, Stein J, Kleebe HJ, Balke-Grünewald B (2023) Lithium extraction and zeolite synthesis via mechanochemical treatment of the silicate minerals lepidolite, spodumene, and petalite. Minerals 13(8):1030
19. Kotsupalo NP, Menzheres LT, Ryabtsev AD, Boldyrev VV (2010) Mechanical activation of α-spodumene for further processing into lithium compounds. Theor Found Chem Eng 44:503–507
20. Rosales GD, Resentera AC, Wuilloud RG, Rodriguez MH, Esquivel MR (2022) Optimization of combined mechanical activation-leaching parameters of low-grade α-spodumene/NaF mixture using response surface methodology. Miner Eng 184:107633

Synthetic Alkali Aluminosilicate-Hydroxide Systems as an Analogue to Optimize Lithium Recovery from LCT Pegmatites

Nail R. Zagrtdenov, Yves Thibault, Joanne Gamage McEvoy, and Dominique Duguay

Abstract In a study focusing on alternate energy-efficient approaches to recover lithium from LCT pegmatites, we demonstrated that single-stage decomposition of α-spodumene in caustic media can be achieved below 450 °C without the conventional pretreatment at temperatures exceeding 1000 °C, typically required to induce a phase transition to the more reactive β-form (Gamage McEvoy et al. in Energy technology 2023, TMS Springer, pp 81–87, 2023). Considering the challenges in characterizing and monitoring the evolution of lithium, an experimental phase stability study using synthetic sodium aluminosilicates analogues along the $NaAlO_2$-SiO_2 join (e.g. carnegieite: $NaAlSiO_4$) exposed to melted KOH was undertaken. The findings will be discussed in the context of optimizing the extent of alkali exchange and effective partitioning of silica and alumina in the solid residue that has implications for achieving selective lithium recovery in the pregnant leach solution.

Keywords Lithium · Alkali aluminosilicates · Ion exchange

N. R. Zagrtdenov (✉) · Y. Thibault · J. Gamage McEvoy · D. Duguay
CanmetMINING, Natural Resources Canada, 555 Booth Street, Ottawa, ON K1A 0G1, Canada
e-mail: nail.zagrtdenov@nrcan-rncan.gc.ca

Y. Thibault
e-mail: yves.thibault@nrcan-rncan.gc.ca

J. Gamage McEvoy
e-mail: joanne.gamagemcevoy@nrcan-rncan.gc.ca

D. Duguay
e-mail: dominique.duguay@nrcan-rncan.gc.ca

151

Introduction

Lithium recovery from Li-Cs-Ta (LCT) pegmatites is highly energy intensive, with conventional processes requiring an initial heat treatment at temperatures exceeding 1000 °C to induce a phase transition of the refractory aluminosilicate carrier minerals (α-spodumene, petalite) to the more reactive β-spodumene$_{ss}$ form having higher ion mobility, where lithium can then be accessed in a subsequent extraction stage such as acid baking in concentrated H_2SO_4 at temperatures around 250–300 °C [1, 2]. However, based on extrapolation of results from high-pressure studies, the stability field for the inversion to β-spodumene$_{ss}$ at atmospheric conditions extends to significantly lower temperatures, down to ~ 680 °C for $LiAlSi_4O_{10}$ (petalite) and $\leq$ 500 °C for $LiAlSi_2O_6$ (α-spodumene) compositions, respectively [3–5], implying that the required high-temperature pretreatment stage used in practice is not dictated by thermodynamics but rather sluggish kinetics.

Recent evidence suggests that the transition to β-spodumene$_{ss}$ can be induced by alkali-rich fluids, providing access to the low-temperature regions of the stability field, and opening opportunities for the development of more energy-efficient strategies to recover lithium directly from the primary aluminosilicates [6]. Our previous work demonstrated that specific temperature–time pathways within a narrow window between 400 and 500 °C allow for the direct decomposition of mm-sized α-spodumene crystals in less than 30 min in the presence of mixed (Na, K) alkali hydroxides, with excellent Li fractionation from Na and K. However, decomposition in the presence of hydroxide seemingly results in a complex phase mixture, which is highly dependent on the temperature–time pathway selected [7]. As the nature of the residual water-insoluble phases produced during caustic treatment will dictate the purity of the pregnant leach solution, and considering the challenges associated with monitoring lithium non-destructively at the crystal scale, a complementary study was initiated with the objective of clarifying some phase stability relationships, and ion-exchange characteristics using synthetic sodium aluminosilicate in the presence of KOH as an analogue system. This paper summarizes initial results focusing on $NaAlSiO_4$ having a Si:Al ratio of unity, a stoichiometry comparable to eucryptite ($LiAlSiO_4$).

Materials and Methods

Materials

The starting aluminosilicate material was synthesized from a mixture of silica glass (SiO_2), aluminum hydroxide (Al[OH]$_3$), and anhydrous sodium carbonate (Na_2CO_3), in proportions consistent with $NaAlSiO_4$ stoichiometry. Two cycles of grinding, pelletization, and 48-h sintering at 1350 °C led to the formation of a single-phase
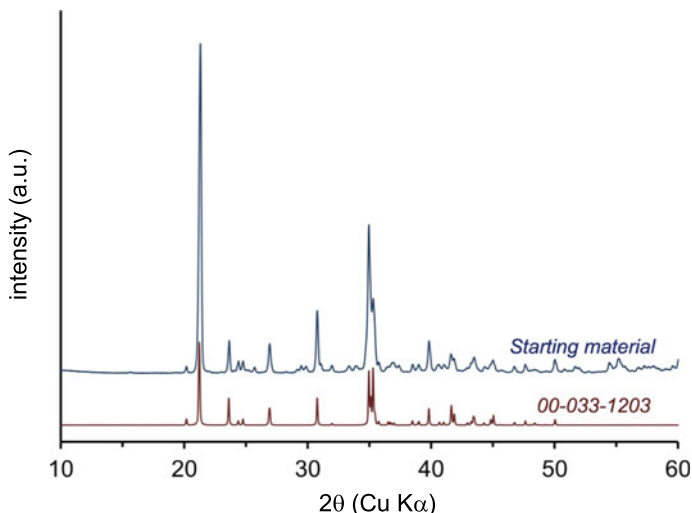
Fig. 1 Powder-XRD pattern of the synthetic carnegieite (NaAlSiO$_4$) used in this study. A simulated ICDD reference pattern for low carnegieite (00-033-1203; [8]) is shown for comparison

feed with a low carnegieite crystalline structure (Fig. 1) that was ground and sieved to a − 300/+ 45 µm size fraction.

Alkali Exchange Experiments Between Synthetic Carnegieite (NaAlSiO$_4$) and Potassium Hydroxide (KOH)

Caustic treatment experiments on the carnegieite − 300/+ 45 µm feed were performed in the presence of potassium hydroxide (KOH), keeping a molar proportion of 3 KOH: 1 NaAlSiO$_4$ (K/[Na + K] = 0.75). About 1 g of the mixture was pelletized, loaded in a covered Ni dish, dried at 200 °C for 5 min, and then immediately transferred to a muffle furnace which was heated at a rate of 250 °C/hour up to a peak temperature either above (450 °C: CK-450) or below (350 °C: CK-350) the KOH melting point at ≈ 404 °C (Fig. 2). For the lower temperature experiment (CK-350), the dynamic heating step was followed by an isothermal dwell of 100 min. In each case, the load was removed from the furnace at peak temperature and rapidly cooled in air. The product was then leached overnight in 450 mL of deionized water. After vacuum-filtration, the insoluble residue was recovered for characterization.
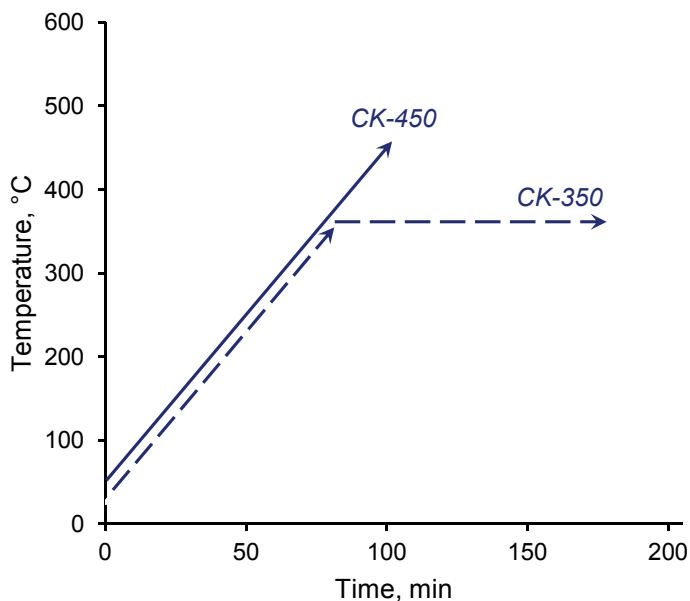
Fig. 2 Temperature–time path for the experiments discussed in this study, performed in the 3 KOH: 1 NaAlSiO$_4$ system at peak temperatures of 450 °C (CK-450) and 350 °C (CK-350), respectively

Analytical Methods

Powder X-ray diffraction (XRD) analyses were performed using a Rigaku D/MAX 2500 rotating anode system with monochromatic Cu Kα radiation. The diffractograms were collected in the 5°–70° two theta angular range, using a step size of 0.020, at 40 kV and 200 mA.

Quantitative analyses of the phases within the solid residues were obtained by wavelength-dispersive spectrometry (WDS) using a JEOL JXA 8230 electron probe X-ray microanalyzer (EPMA) operated with an accelerating voltage of 20 kV and a probe current of 15 nA. Counting times for analyses ranged from 10 to 15 s on peak and background.

Modal abundances and phase distributions were determined by energy-dispersive spectrometry and backscattered electron (BSE) imaging using a Tescan Integrated Mineralogical Analyser (TIMA), with an accelerating voltage of 25 kV, beam current of 5 nA, and step size of 3 μm.

Results and Discussion

Irrespective of whether the peak temperature was above (CK-450) or below (CK-350) the melting point of KOH, powder-XRD analyses of the water-leached residues indicate that the caustic treatment led to the full decomposition of carnegieite (Fig. 3). At each condition, the residue is dominated by an amorphous component associated with a minor crystalline phase, which can be indexed as a cubic Si-poor potassium aluminosilicate [9], which appeared more abundant at the highest peak temperature (450 °C).

Characterization by EPMA and TIMA reveals the coexistence of four distinct phases. Two of these likely represent the amorphous component, having comparable yet significant variation in their relative abundances of Si, Al, and alkalis (Figs. 4c, d and 5c, d) while displaying distinct BSE contrast (Figs. 4a, 5a) that can be attributed to variation in the extent of porosity. The two other identified phases show more crystalline habits with a significantly narrower compositional range, where the significant decrease in their modal contribution at lower temperature (Figs. 4 and 5) is consistent with the XRD data (Fig. 3).

For both experimental conditions, the bulk residue composition, calculated by mass balance knowing the composition of each phase as measured by WDS-EPMA and their modal distribution as determined by TIMA, maintains the Al:Si and Al:alkali ratios of unity from carnegieite, strongly suggesting that its decomposition
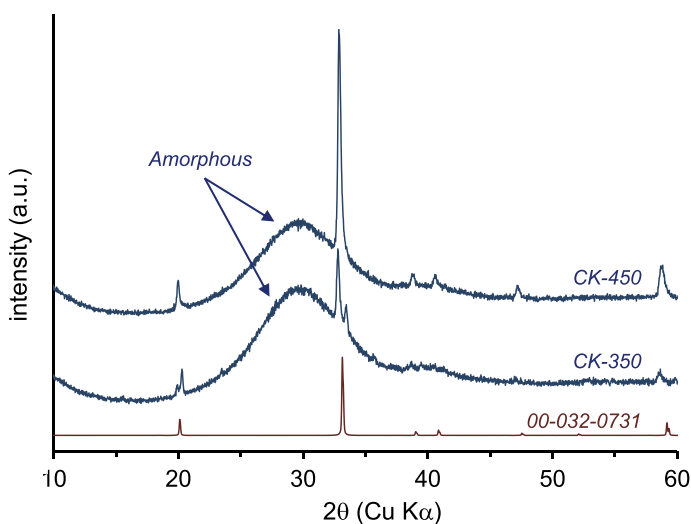
Fig. 3 Powder-XRD patterns collected on the solid residues recovered from the water leach after the CK-450 and CK-350 experiments. A simulated ICDD reference pattern for cubic $K_{1.25}Al_{1.25}Si_{0.75}O_4$ (00-032-0731; [9]) is shown for comparison
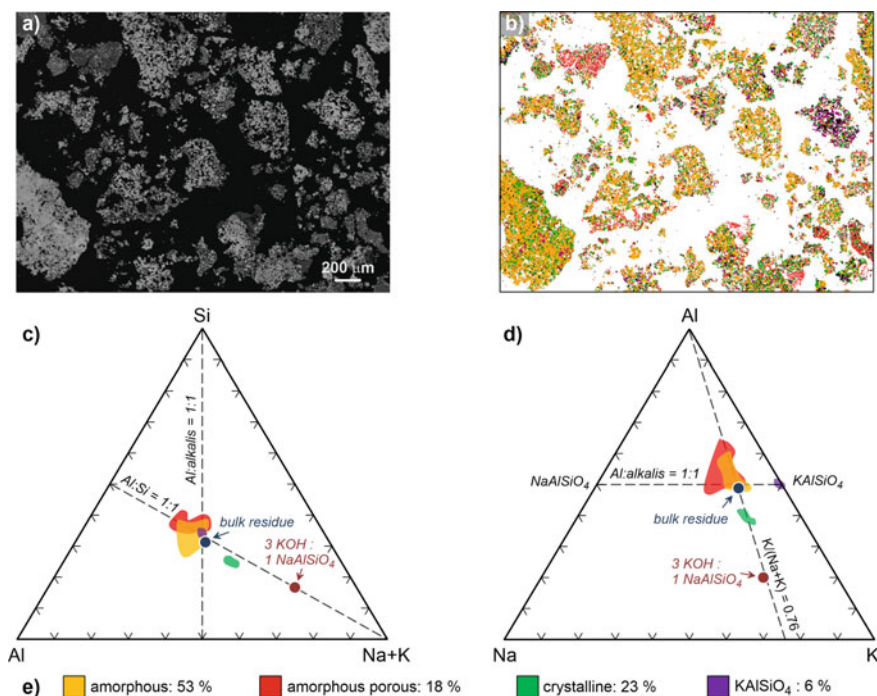
Fig. 4 Textural and compositional characteristics of the water-leached solid residue from the CK-450 caustic experiment: **a** BSE image; **b** phase map collected by quantitative mineralogy; **c**, **d** ternary diagrams displaying the relative molar concentrations of Si, Al, Na, and K in the identified phases, as determined by WDS-EPMA; and **e** phase legend with modal proportions as measured by TIMA. The range of composition for each phase is represented as colored fields. The starting material (3 KOH: 1 NaAlSiO$_4$) and the calculated bulk residue are shown as filled circles on each ternary plot (**c**, **d**)

is achieved without releasing alumina and silica into the leach solution. Additionally, when comparing the extent of alkali exchange (K/[K + Na]) in the residues, not only are the values very close to each other, estimated at 0.76 and 0.74 for CK-450 and CK-350, respectively, (Figs. 4d and 5d), but they essentially reflect the relative molar proportion of potassium in the hydroxide and sodium in carnegieite within the starting material (3 KOH: 1 NaAlSiO$_4$), indicating that sodium and potassium have similar aluminosilicate/hydroxide partition coefficients. Considering the number of phases of variable compositions and crystallinities produced (Figs. 3, 4, and 5), such temperature-independent control on the Na–K-Al-Si stoichiometry of the final bulk residue is very interesting and, in the context of an equivalent lithium aluminosilicate-(Na,K)OH system [7], should provide opportunities to optimize the recovery and purity of the leach solution.
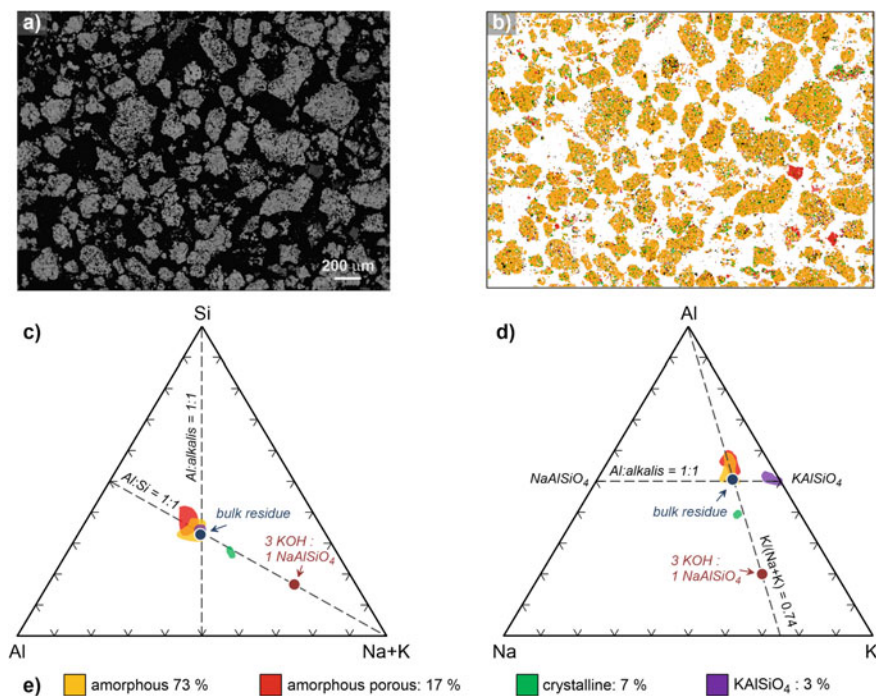
Fig. 5 Textural and compositional characteristics of the water-leached solid residue from the CK-350 caustic experiment: **a** BSE image; **b** phase map collected by quantitative mineralogy; **c, d** ternary diagrams displaying the relative molar concentrations of Si, Al, Na, and K in the identified phases, as determined by WDS-EPMA; and **e** phase legend with modal proportions as measured by TIMA. The range of composition for each phase is represented as colored fields. The starting material (3 KOH: 1 NaAlSiO$_4$) and the calculated bulk residue are shown as filled circles on each ternary plot (**c, d**)

Conclusions

These results suggest that, at least for NaAlSiO$_4$, decomposition in the presence of KOH leads to a water-insoluble residue that, despite the complexity of its phase assemblage, maintains the Si:Al and Al:alkali ratio of unity, indicating minimal release of alumina and silica in the leach solution with efficient alkali exchange. Similar experiments are currently being performed on analogues with NaAlSi$_2$O$_6$ and NaAlSi$_3$O$_8$ stoichiometries to investigate the implication of higher Si:Al ratio on the purity of the leach solution due to the potential formation of soluble alkali silicates, as this is relevant to strategies directly accessing lithium from major Li-bearing minerals such as α-spodumene (LiAlSi$_2$O$_6$) and petalite (LiAlSi$_4$O$_{10}$).

Derek Smith and Talia Beckwith (CanmetMINING) for support with the XRD characterization and polished section preparation, respectively.

References

1. Yelantontsev D, Mukhachev A (2021) Processing of lithium ores: industrial technologies and case studies—a review. Hydrometallurgy 201:105578
2. Salakjani NK, Singh P, Nikoloski N (2021) Production of lithium—a literature review part 2: extraction from spodumene. Min Proc Ext Met Rev 42:268–283
3. Roy R, Roy DM, Osborn EF (1950) Compositional and stability relationships among the lithium aluminosilicates: eucryptite, spodumene, and petalite. J Am Ceram Soc 33:152–159
4. Munoz JL (1969) Stability relations of $LiAlSi_2O_6$ at high pressure. In: Papike JJ (ed) Mineralogical Society of America Special Paper 2, pyroxenes and amphiboles: crystal chemistry and phase petrology. Mineralogical Society of America: Menasha, WI, pp 203–209
5. Edgar AD (1966) The α-β-$LiAlSi_2O_6$ (spodumene) transition from 5000 to 45000 lb/in^2 P_{H2O}. In: Proceedings of the papers and proceedings of the international mineralogical association, 5th General meeting, Cambridge, England, 30 Aug–3 Sept 1966; Mineralogical Society of London, London, UK, 1968, pp 222–231
6. Thibault Y, Gamage McEvoy J (2023) Alkali-induced phase transition to β-Spodumene along the $LiAlSi_2O_6$-$LiAlSi_4O_{10}$ join. Crystals 13(8):1182. https://doi.org/10.3390/cryst13081182
7. Gamage McEvoy J, Thibault Y, Zagrtdenov NR, Duguay D (2023) Rethinking the decomposition of refractory lithium aluminosilicates: opportunities for energy-efficient Li recovery from LCT pegmatites. In: Energy technology 2023. TMS Springer, pp 81–87
8. Kligenberg R, Felsche J, Miehe G (1981) Crystal data for the low-temperature form of carnegieite $NaAlSiO_4$. J Appl Crystallogr 14(1):66–68
9. Cook LP, Roth RS, Parker HS, Negas T (1977) The system K_2O-Al_2O_3-SiO_2; part 1, phases on the $KAlSiO_4$-$KAlO_2$ join. Am Miner 62(11–12):1180–1190

Part III
Biometallurgy and Flotation

Bacteriophage-Based Sorption of Rare Earth Elements from Dilute Aqueous Solutions

Inseok Chae, Fiona M. Doyle, and Seung-Wuk Lee

Abstract To address an ongoing need for environmentally benign approaches for extracting rare earth elements (REEs) from ores and secondary sources, we present a novel biosorption method for separating REEs from dilute aqueous solutions using bacteriophage. Our approach involves the genetic engineering of the major coat protein pVIII of the M13 bacteriophage (phage) with the lanmodulin mimetic peptide, which binds REEs. We present results demonstrating the ability of the modified bacteriophage to extract REEs from dilute aqueous chloride solutions (on the order of μM concentrations) buffered by sodium acetate at pH 5, the structural changes of the pVIII protein, and the aggregation of the engineered phage induced by the REE uptake. We also report on the ability to desorb REE from the phage by pH modulation and demonstrate the recyclability of phage. Finally, we discuss how phage-based biosorption might be scaled up for commercial application.

Keywords Rare earth elements · Bacteriophage · Lanmodulin mimetic peptide · Biosorption

Introduction

Rare earth elements (REEs) hold a pivotal role in modern technology, contributing significantly to the advancement of electronics, clean energy technologies, and a diverse array of cutting-edge applications [1, 2]. These elements are indispensable in the manufacture of strong permanent magnets; phosphors for displays and lighting;

I. Chae · S.-W. Lee (✉)
Department of Bioengineering, University of California, Berkeley, CA 94720, USA
e-mail: leesw@berkeley.edu

Biological Systems and Engineering, Lawrence Berkeley National Laboratory, Berkeley, CA 94720, USA

F. M. Doyle
Department of Materials Science and Engineering, University of California, Berkeley, CA 94720, USA

catalysts in green energy production; and vital components in electric vehicles, wind turbines, and smartphones [3]. Because their immense utility is creating unprecedented demand, the global supply of REEs faces an array of formidable challenges. Traditional mining and processing methods have potential environmental impacts, including radioactive waste and habitat destruction [4, 5]. Furthermore, the geopolitical complexity of REE mining and processing, with most orebodies and processing plants concentrated in a handful of countries, introduces supply chain vulnerabilities and price fluctuations. There is significant interest in better techniques for recycling rare earths. Yet because of the chemical similarity of the rare earths, their separation is particularly challenging, typically requiring multiple stages of solvent extraction [5]. Given these issues, it would be highly advantageous to develop more efficient, environmentally benign techniques for separating and purifying REEs extracted and recovered from complex sources.

Recent advances in bacteriophage (phage)-based bionanotechnology offer novel opportunities to tackle these pressing challenges. Phage is a bacterial virus that infects bacterial host cells. It presents a naturally occurring nanoscaled structure amenable to modification. The M13 phage has a single-stranded DNA encapsulated in 2700 copies of the pVIII major coat protein. It is 880 nm in length and 6.6 nm in diameter, offering ample surface area for functionalization [6]. The ease of mass production through bacterial host infection makes phage attractive for potential engineering applications [7]. Through genetic engineering, the physical and chemical properties, along with the size of the phage, can be tailored for various needs. Previous applications of engineered phage have demonstrated their potential as a versatile nanomaterial; they have served as templates for the controlled growth of inorganic and semiconductor materials, enabling precise nanoscale fabrication. Additionally, the self-assembly properties of phage have been harnessed in fields such as biomedical regenerative tissue engineering, biosensor development, and bioenergy production matrices [8–10]. The adaptability and programmability of phage open doors to innovative applications, making them a promising tool for REE separation and purification. By leveraging the unique properties of genetically engineered phage, we are working to develop a sustainable and efficient REE recovery system that could be helpful in addressing the environmental and geopolitical challenges associated with the global REE supply chain.

Here, we report results that could be leveraged in a novel bioseparation process for rare earth elements (REEs) using genetically engineered phage. First, we employed genetic engineering of the major coat protein (pVIII) of the M13 phage to express a REE-binding peptide on this major coat protein. Specifically, we inserted the EF1 segment of the lanmodulin peptide sequence (DPDKDGTID) [11, 12] into the N-terminal region of all pVIII proteins on the phage through gene VIII (gVIII) modification, as depicted in Fig. 1a. The resulting phage, which we have termed "lanmodulin-like phage" (LMPh), is 1,080 nm long and possesses 3300 copies of REE-binding peptides on the outer major coat protein (pVIII). The engineered LMPh demonstrated superior binding affinity over unmodified phage for five light and heavy REEs (Nd^{3+}, Sm^{3+}, Eu^{3+}, Gd^{3+}, Tb^{3+}) in aqueous solution. Upon interaction with REEs, LMPh undergoes changes of its secondary structure within the pVIII major coat proteins
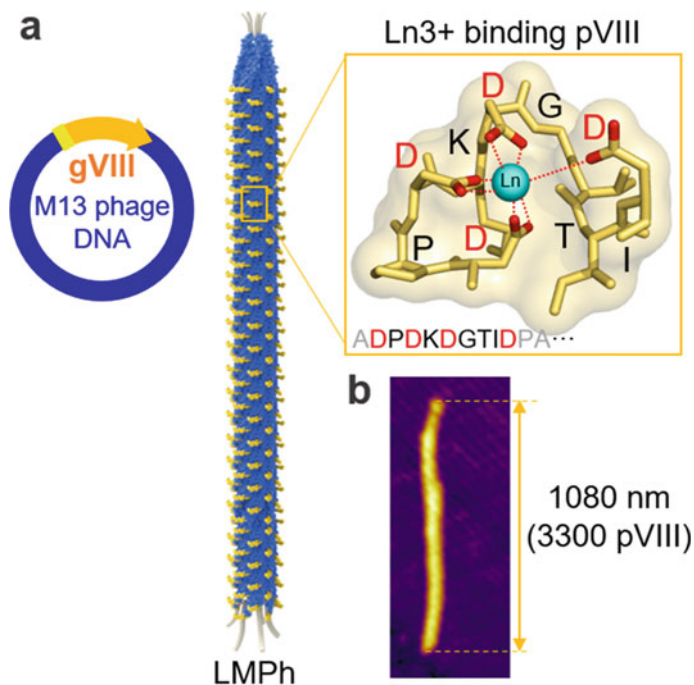
Fig. 1 Genetic engineering of LMPh. a Modification of genome VIII (gVIII) in M13 phage DNA to express 3300 copies of the Ln3 + binding major coat protein (pVIII). The lanmodulin mimicking peptide (DPDKDGTID, PDB: 6MI5) was inserted at the N-terminal of pVIII. **b** AFM topography image of LMPh. The length of the engineered LMPh is 1080 nm

and forms large aggregates amenable to physical separation from the REE-depleted solution. By controlling the pH, we were able to release the adsorbed REEs from the pVIII binding sites of LMPh, and assess the relative affinity of the pVIII protein for different REEs. Our novel engineered phage-based bioseparation approach shows potential for the selective recovery and purification of REEs at a commercial scale.

Experimental Procedures

Materials and Instruments

Phusion high-fidelity DNA polymerase, Pst1 restriction enzyme, T4 DNA ligase, and dNTP were purchased from New England Biolabs (Ipswich, MA). Primers were obtained from Integrated DNA Technologies, IDT (Newark, NJ). DNA purification was performed using the QIAprep Spin Miniprep Kit from QIAGEN (Valencia, CA).

REEs (LnCl$_3$, Ln = Nd, Sm, Eu, Gd, Tb) were purchased from Sigma Aldrich (St. Louis, MO).

Images were taken using an MFP-3D Asylum Research (Santa Barbara, CA) atomic force microscope (AFM). The circular dichroism (CD) spectrum was collected using a Jasco J-815 CD spectrometer (Oklahoma City, OK). Particle sizes were analyzed by dynamic light scattering (DLS) using a Zetasizer Nano ZS from Malvern Panalytical (Malvern, United Kingdom). Phage-REE mixtures were centrifuged using an LE-80 centrifuge with a SW60 Ti rotor from Beckman (Brea, CA). The REE concentrations were measured using inductively coupled plasma optical emission spectroscopy (ICP-OES), Optima 7000 DV from Perkin Elmer (Waltham, MA).

Genetic Engineering and Amplification of Phage

The lanmodulin mimicking peptide was inserted at the N-terminal of pVIII after the end Ala (ADPDKDGTIDPA; 8 inserted amino acids underlined) through gVIII manipulation following the protocol reported by Merzlyak et al. [13]. The gVIII engineering was performed with M13 phage DNA through polymerase chain reaction (PCR) followed by Pst1 restriction and T4 DNA ligase, then the engineered DNA was inserted into XL1-Blue competent cells at 42 °C. Using an IPTG/XGAL Agar plate, infected cells were selected and amplified, then their DNA was sequenced at the DNA sequencing facility at the University of California, Berkeley.

Replication and purification of phages were performed following the protocol by Lee et al. [14]. Wild-type (WT) and newly engineered LMPh were replicated using ultracompetent XL10-Gold *E. coli* in Luria Broth (LB) media for 16 h with shaking at 200 rpm at 37 C°. After the replication, DNA sequencing was performed to confirm that the amplified phages are stable and had no mutation. Polyethylene glycol (PEG)-NaCl-induced precipitation [14] and centrifugation were performed to separate phages from *E. coli* and LB media. The purified phages were stored in sodium acetate buffer at pH 5.

Characterization of LMPh-Tb Complexes

First, WT and LMPh 0.1 mg/ml (17 μM pVIII; concentration calculated with the molar mass of whole phage 16.4 MDa/2700 copies of pVIII) were mixed with TbCl$_3$ in solution at pH 5 with various molar ratios. After mixing, variations of the secondary structure of pVIII and particle size of the LMPh-REE complex were measured using CD and DLS, respectively, at room temperature.

Phage-REE Adsorption and Desorption

Phages (WT or LMPh 0.6 mg/ml, 100 µM pVIII) were added to an aqueous solution containing 4 REEs (a mixture of Nd, Sm, Eu, and Gd, all at the same concentration) with a molar ratio of pVIII: total REE = 1: 1 at pH 5. The mixed solutions were incubated overnight at room temperature, then centrifuged at 300 k-rcf for 2 h to separate the phage-REE complexes from the solution. After centrifugation, the REE concentrations in the supernatants were measured to quantify the adsorption of REEs onto the phages. The phage-REE pellets were redispersed in sodium acetate adjusted to pH 2, 3, and 4 using HCl, to allow desorption of REEs from the phage. The same centrifugation procedure was repeated at these different pHs to separate the phage, and then the REE concentrations in the supernatants were measured to quantify the desorption of REEs from the phage. All REE concentration measurements were performed using ICP-OES after digestion in 35% nitric acid at 90 °C for 2 h followed by dilution ($\times 1/8$) with deionized water.

Results and Discussion

Genetic Engineering of LMPh

We genetically engineered REE-binding peptide on the pVIII major coat proteins of M13 phage. We inserted the lanmodulin mimicking peptide into the N-terminal (outer surface) of all pVIII on the phage body through the recombinant DNA engineering as shown in Fig. 1a. The inserted REE-binding peptide, DPDKDGTID, originates from EF1, one of four REE-binding sites of lanmodulin, which is the highest lanthanide-binding protein reported to date (lowest dissociation constant, $K_d = 4 \times 10^{-13}$ M) [1, 2]. The inserted peptide possesses four negatively charged aspartic acids (D) and a single proline (P) at the second position. The electrostatic interactions between the negative charges distributed at specific distances in the REE-binding peptide and the positive charge on Ln^{3+} dominate the strong binding. The length of LMPh was measured as 1080 ± 100 nm as shown in Fig. 1b, and the REE-binding motifs were added to all ~ 3300 pVIII on the body of LMPh. Due to the large number of REE-binding motifs on LMPh, it is expected to exhibit a high binding capacity for REEs.

Molecular Interaction Between Phage and Tb^{3+}

Spectroscopic characterization shows that the engineered phage can specifically bind to REE ions and then aggregate. The engineered LMPh shows a secondary structural change induced by interaction with Tb^{3+} in aqueous solution at pH 5, as shown in
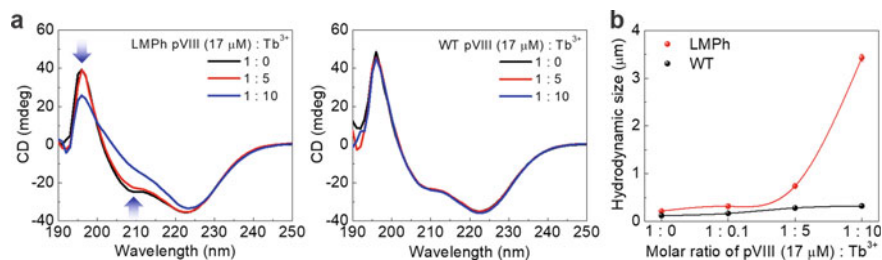
Fig. 2 Secondary structure of pVIII and particle size analysis. a CD spectrum of LMPh and WT phages (0.1 mg/ml phage, 17 μM pVIII) with different molar ratios of Tb^{3+} in pH 5 buffer solution. **b** Particle sizes of LMPh and WT with the different molar ratios of Tb^{3+}

Fig. 2a. The pVIII of the M13 phage has a mostly α-helix structure, with major CD peaks at 196, 209, and 223 nm. After binding with Tb^{3+} ions in solution, the magnitude of the 196 and 209 nm peaks decreased significantly, particularly at the highest Tb^{3+} to LMPh-pVIII molar ratio (10:1). A slight shift and decrease in the magnitude of the 223 nm peak was also observed. These changes in CD spectrum represent the transition from the α-helix to the β-form or a random structure induced by the adsorption of Tb^{3+} onto pVIII. The inserted DPDKDGTID peptide is responsible for the secondary structure change of pVIII with Tb^{3+} whereas WT does not show such variations under the same condition.

Figure 2b shows that large LMPh aggregates are formed in solution after interaction with Tb^{3+}. Without Tb^{3+}, the LMPh shows a hydrodynamic diameter of 200 nm, but the particle sizes increased significantly upon mixing with Tb^{3+} in solution. Adsorption of Tb^{3+} onto the pVIII protein reduces the electrostatic repulsive forces between LMPh, thereby allowing large aggregates to form. In contrast, much smaller increases in particle size were observed for WT after mixing with the same amount of Tb^{3+} in solution, probably due to double layer compression at higher ionic strengths. This means that the inserted DPDKDGTID peptide enhances the electrostatic interactions between phages and Tb^{3+} ions in solution. It is likely that the formation of these large aggregates would induce settling, which could facilitate separation of phage from solution.

Adsorption and Desorption of REEs

The engineered phage can bind and precipitate Nd, Sm, Eu, and Gd ions from the pH 5 solution containing these four REEs. To quantitatively measure the binding capacity of LMPh for REEs, the adsorption and desorption of REE ions on LMPh were investigated. Adsorption was induced by contacting the LMPh and REEs (Nd, Sm, Eu, Gd) in aqueous solution at pH 5, then the mixtures were separated by centrifugation. Aspartic acid (D) has an isoelectric point (pI) of 2.8, thus at pH above 2.8, the negatively charged aspartic acids in pVIII attract positively charged REE

ions and form the LMPh-REE complex. Deblonde et al. reported that the repeating aspartic acids with intervals and single proline at the second place form a selective binding loop that holds REEs in the peptide [12, 15]. After adsorption, the LMPh-REE complexes were separated by centrifugation and collected. We confirmed that almost all LMPh was removed by centrifugation, as no UV–Vis signal of phage was detected in the supernatant. The REE concentrations remaining in the supernatant were measured to quantify the adsorption of REE onto LMPh. The results show that at a pVIII to REE molar ratio of 1:1, over 70% of REEs on average were adsorbed to LMPh and removed from solution (Fig. 3). The pVIII to REE molar ratio was 1 to 1; thus, 3300 copies of pVIII on LMPh captured around 2300 REE ions from the solution. In contrast, only ~ 10% of the REEs were bound to WT phage—2700 copies of pVIII on WT captured only 270 REE ions in solution. This significant difference between LMPh and WT shows the enhancement in binding capacity induced in the phage through the genetic insertion of the lanmodulin mimicking peptide.

Upon exposing LMPh loaded with REEs at pH 5 to acetate solutions of lower pH, some of the REEs were desorbed, with greater desorption at lower pH values, as shown in Fig. 4. The REE ions were released from LMPh by lowering pH, and then LMPh was separated from the released REEs by centrifugation. The result in Fig. 4b shows that > 70% of REEs were desorbed from LMPh at pH 2. At pH 3 and 4, less REEs were released—30–50% REEs and 20% REEs, respectively. Lowering the pH increases protonation of the carboxylate groups in peptides, specifically aspartic acid in this case, weakening the Coulombic interactions with REE ions. The pI of aspartic acid (D) is 2.8, and the inserted DPDKDGTID peptide is neutralized below the pI. The significant increase of REE desorption between pH 3 and 2 was also observed from lanmodulin [12]. More work will be done to determine whether the apparent differences in affinity of different REEs for LMPh seen in Figs. 3 and 4 are statistically significant. However, due to the controlled adsorption and desorption capacity, LMPh shows promise as a recyclable REE extraction reagent.
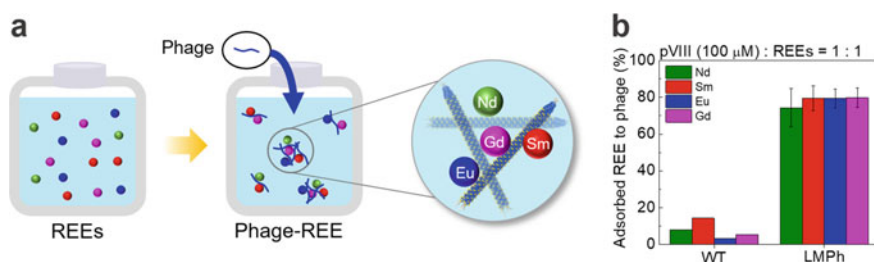
Fig. 3 Quantitative analysis of adsorbed REE to phage. a Schematics of phage-REE complex formation in aqueous solution at pH 5. **b** Quantification of adsorbed REEs to WT and LMPh using ICP-OES. The mean and standard deviation for LMPh were obtained from three independent measurements
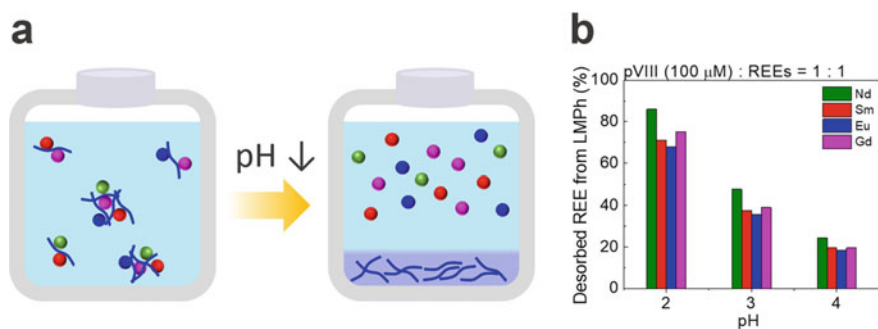
Fig. 4 Quantitative analysis of desorbed REEs from phage. a Schematics of released REEs from LMPh in aqueous solution at pH ≤ 4. **b** Quantification of desorbed REEs from LMPh at pH 2, 3, and 4 using ICP-OES

Stability, Scalability, and Recyclability of LMPh for REE Processing

The engineered phage designed to adsorb and separate REEs appears to be stable over the pH ranges tested in this work, which correspond well to the pH ranges likely in processing systems that use organic acids as environmentally benign lixiviants. Although much work clearly remains to be done, we believe that a phage-based approach has the potential for commercial application for REE processing. Through the infection of *E. coli* host cells, the phage replicates millions of times in 4.5 h [7]. This makes a larger scale REE purification system realistic to contemplate. We have confirmed that LMPh, after incubation in an aqueous solution at pH 2 with REEs, does not lose its infectivity (Fig. 5). After incubating LMPh at pH 2 with REEs, we observed blue plaques that represent the infected XL-10G *E. coli* cells on an IPTG/XGAL agar plate. DNA sequencing results showed that no mutations were observed after the adsorption and desorption processes of REEs. We further confirmed that, after rigorous solution processing, the engineered phage could infect *E. coli* cells and replicate LMPh as normal at pH 2, 3, 4, and 5. This result indicates that LMPh is not functionally altered by adsorption/desorption, which suggests that it could be repeatedly used for REE adsorption and desorption under the given pH conditions, with the potential for use in the development of a larger scale REE recovery system. In the future, we will investigate the efficiency of REE recovery using LMPh on a larger scale with multiple cycles.
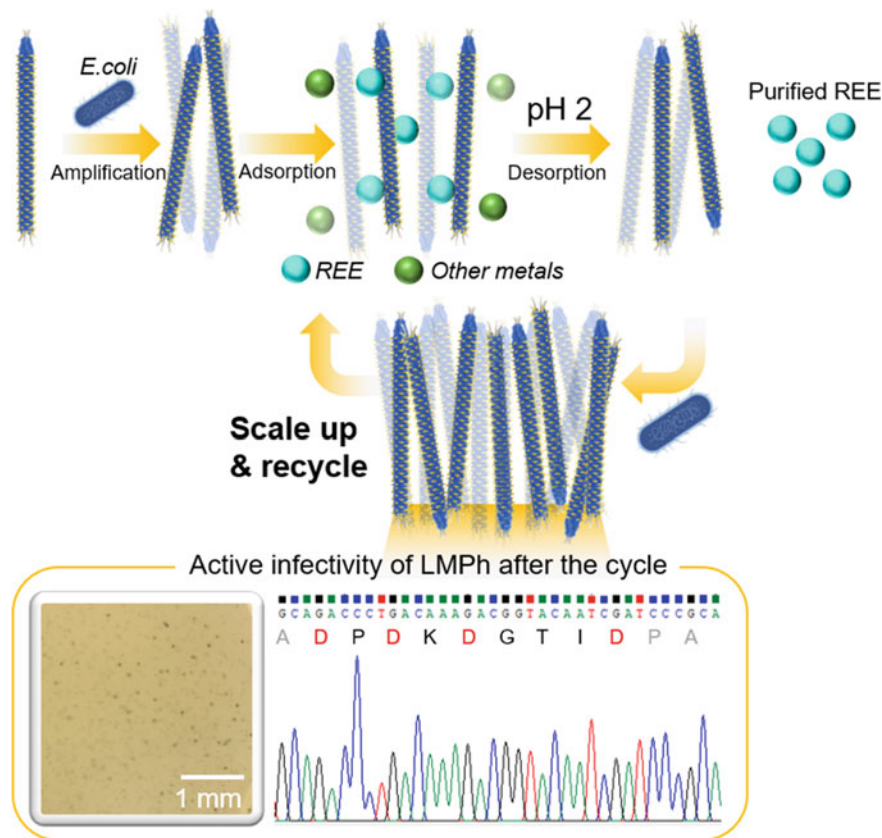
Fig. 5 Conceptual design of a phage-based REE separation system. Schematic depiction of the scalable generation of genetically engineered LMPh on *E. coli*, and recycling through adsorption and desorption stages. Active infectivity and no mutation of LMPh confirmed after the incubation with REEs at pH 2. Photo image of the IPTG/XGAl agar plate shows XL-10G *E. coli* cells infected by LMPh which had been incubated with REEs at pH 2 overnight. The DNA sequencing result shows no mutation of LMPh after treatment

Conclusions

We present here the concept of a novel bioseparation process using genetically engineered phage. We successfully created a REE-binding phage by inserting a lanmodulin mimicking peptide into the N-terminal of the pVIII major coat protein. Due to the large amount of pVIII (~3300 copies) on the phage surface, LMPh showed a superior binding capacity for REEs—almost one LMPh to ~ 2300 Ln^{3+} ions in aqueous solution, which is around 8 times larger than that of WT. The CD and DLS analyses showed that the secondary structure of pVIII on LMPh changes after uptake of Tb^{3+} and large aggregates were formed. LMPh shows promise as a recyclable REE extraction agent as the adsorption and desorption capacity can be controlled by adjusting

pH. Using LMPh, we will further explore developing a REE separation system that could practically be used for commercial REE processing.

References

1. Cheisson T, Schelter EJ (2019) Rare earth elements: Mendeleev's bane, modern marvels. Science 363(6426):489–493
2. Sholl DS, Lively RP (2016) Seven chemical separations to change the world. Nature 532(7600):435–437
3. Balaram V (2019) Rare earth elements: a review of applications, occurrence, exploration, analysis, recycling, and environmental impact. Geosci Front 10(4):1285–1303
4. Ali SH (2014) Social and environmental impact of the rare earth industries. Resources 3(1):123–134
5. Xie F, Zhang TA, Dreisinger D, Doyle F (2014) A critical review on solvent extraction of rare earths from aqueous solutions. Miner Eng 56:10–28
6. Lee S-W, Lee SK, Belcher AM (2003) Virus-based alignment of inorganic, organic, and biological nanosized materials. Adv Mater 15(9):689–692
7. Warner CM, Barker N, Lee S-W, Perkins EJ (2014) M13 bacteriophage production for large-scale applications. Bioprocess Biosyst Eng 37(10):2067–2072
8. Chung W-J, Oh J-W, Kwak K, Lee BY, Meyer J, Wang E, Hexemer A, Lee S-W (2011) Biomimetic self-templating supramolecular structures. Nature 478(7369):364–368
9. Jin H-E, Lee S-W (2018) Engineering of M13 bacteriophage for development of tissue engineering materials. In: Wege C, Lomonossoff GP (eds) Virus-derived nanoparticles for advanced technologies: methods and protocols. Springer, New York, New York, NY, pp 487–502
10. Lee BY, Zhang J, Zueger C, Chung W-J, Yoo SY, Wang E, Meyer J, Ramesh R, Lee S-W (2012) Virus-based piezoelectric energy generation. Nat Nanotechnol 7(6):351–356
11. Cotruvo JA Jr, Featherston ER, Mattocks JA, Ho JV, Laremore TN (2018) Lanmodulin: a highly selective lanthanide-binding protein from a lanthanide-utilizing bacterium. J Am Chem Soc 140(44):15056–15061
12. Deblonde GJP, Mattocks JA, Park DM, Reed DW, Cotruvo JA Jr, Jiao Y (2020) Selective and efficient biomacromolecular extraction of rare-earth elements using lanmodulin. Inorg Chem 59(17):11855–11867
13. Merzlyak A, Lee S-W (2009) Engineering phage materials with desired peptide display: rational design sustained through natural selection. Bioconjug Chem 20(12):2300–2310
14. Lee JH, Warner CM, Jin H-E, Barnes E, Poda AR, Perkins EJ, Lee S-W (2017) Production of tunable nanomaterials using hierarchically assembled bacteriophages. Nat Protoc 12(9):1999–2013
15. Liu S, Featherston ER, Cotruvo JA, Baiz CR (2021) Lanthanide-dependent coordination interactions in lanmodulin: a 2D IR and molecular dynamics simulations study. Phys Chem Chem Phys 23(38):21690–21700

Bioleaching of Post-consumer LiCoO$_2$ Batteries Using *Aspergillus Niger*

Sadia Ilyas, Rajiv Ranjan Srivastava, and Hyunjung Kim

Abstract Soaring demands for rechargeable Li-ion batteries in portable electronics and electric vehicles drive the unprecedented increase in post-consumer waste generation. Additionally, to fill the gaps between supply and demand for the critical elements in electrode materials, the recycling of waste batteries has become essential. Traditional recycling using high-energy smelting and high-reagent leaching processes generates harmful waste, hence, a new biotechnological process is being searched as a green alternative. Therefore, this study discloses a bioleaching option of LiCoO$_2$ cathode powder using fungi, *Aspergillus niger* as the source of metabolic excreted organic acids lixiviant. The results of one-step bioleaching yielded 96% (w/w) lithium, whereas this efficiency was ~ 94% (w/w) with two-step bioleaching of cathode powder fed at a pulp density of 5% (w/v). The efficiency of cobalt in both types of fungal bioleaching was below 1% (w/w). Thus, the study demonstrates the potential of *Aspergillus niger* in lithium extraction from cathode powder of the battery waste, and the results will further be utilized to improve the design of bioleaching protocols for environmentally friendly recovery of both metals from LiCoO$_2$ powder.

Keywords Spent Li-ion battery · Resource circulation · Metabolic acid · Fungi leaching · One- and two-step bioleaching

S. Ilyas (✉) · H. Kim
Department of Earth Resources & Environmental Engineering, Hanyang University, Seongdong-gu, Seoul 04763, Republic of Korea
e-mail: sadiailyas1@yahoo.com

R. R. Srivastava
Center for Advanced Chemistry, Institute of Research and Development, Duy Tan University, Da Nang 550000, Vietnam

Resource Management, Faculty of Natural Sciences, Duy Tan University, Da Nang 550000, Vietnam

Introduction

In addition to the severe environmental and health risks created by spent lithium-ion batteries (LIBs) [1, 2], they contain a significant quantity of critical metals in the waste volume. For example, spent LIBs may contain 10–30% copper, 5–20% manganese, 5–30% cobalt, 5–20% nickel, and 2–7% lithium, which vary with different types of batteries and manufacturers as well [3, 4]. Hence, spent batteries are regarded as a rich source of the metals present in waste discard, thereby following a circular economy route for the re-use of energy-critical elements [5, 6]. It makes recycling vital to developing sustainable solutions to waste management and resource recovery of critical metals as well [7].

The recovery of metal values from the black mass has been investigated using both the pyrometallurgical and hydrometallurgical processes [8]. The pyrometallurgical process smelts cathode active materials into metal alloys using reducing agents at a temperature of 800–1000 °C while leaving both lithium and other metals in slags [9]. Unfortunately, the pyrometallurgical process recovers transition metals only, and many other battery components and elements, such as graphite and lithium, are wasted. Alternatively, hydrometallurgical extraction has also been extensively investigated [10–12]. Metals in cathode materials are leached using inorganic acids (e.g., H_2SO_4 or HCl), organic acids, and ammonia, which undergo separation and purification steps to recover the metals in their value-added forms [13]. These processes also generate a significant quantity of effluent discharge containing heavy metals.

In the recent past, biohydrometallurgy has been considered an environmentally friendly technique suitable for low-grade sources that need a mild reaction condition [14]. In this method, interactions between microorganisms and the surfaces of metal-bearing bodies cause metal solubilization in ionic form [15]. In most cases, bacteria are used to perform the bioleaching of metals from spent LIBs [16]; however, it has been found that fungi have a higher tolerance to metal toxicity. Moreover, the organic acids excreted by fungi are mild in nature, along with their ability to form both soluble and insoluble metal complexes [17, 18]. Accordingly, heavy metal toxicity is reduced for biomass by forming metal complexes or precipitation by excreted metabolites [19]. Such advantages of bioleaching motivated this study to examine the ability of *A. niger* for metal extraction from the cathode powder of spent LIBs while performing one-step and two-step bioleaching methods. It is a preliminary study performed on $LiCoO_2$ cathode material, and the results will be further utilized to improve the design of bioleaching protocols for environmentally friendly recycling of all types of spent LIBs.

Experimental

The fungal isolation and growth process using the culture media composed of 100 g/L sucrose, 1.5 g/L NaNO$_3$, 0.5 g/L KH$_2$PO$_4$, 0.025 g/L MgSO$_4$·7H$_2$O, 0.025 g/L KCl, and 1.6 g/L yeast extract can be found in our previously published article [20]. The spent LIBs used in this were LiCoO$_2$ types cylindrical cells collected from a local vendor that contained 6.3% Li and 54.4% Co, while 0.2% of Mn was also observed in the analysis of the cathode mass. All the experiments were performed in 250-mL autoclaved Erlenmeyer flasks containing 100 mL of bioleaching medium at a pH of 5.5 and 1% (w/v) cathode mass using an orbital shaker incubator at 150 rpm and 30 °C. In the one-step bioleaching process, 1 mL of spore suspension was inoculated into the bioleaching medium with the cathode mass and incubated for 21 days. Whereas, in a two-step approach, the fungi were first pre-cultured in a media solution; no cathode mass was added until the fungi entered the logarithmic phase. The logarithmic phase commences with a rapid pH decrease caused by the metabolic acids' excretion, which usually takes 3 days. Then, the cathode mass was introduced to the culture medium and bioleached in a shaker incubator for the next 18 days. A control was set using a fresh bioleaching medium without inoculation, while water evaporation was compensated by adding sterilized distilled water in comparison to the initial weight. All experiments were run in triplicate.

Results and Discussion

Metabolic Excretion by the Fungal Activity

The high-performance liquid chromatography (HPLC) tests were conducted to analyze the organic acids secreted by *A. niger*, which showed the presence of mainly four types of acids: oxalic, citric, tartaric, and gluconic acids. The results summarized in Table 1 indicate the occurrence of metabolic activity via glucose oxidation that increases with time; consequently, their dissociation causes a decrease in pH values [21, 22]. As can be seen, up to the initial 3 days of incubation, the acid excretion was not much, and then only a rapid change in pH was observed. It can be explained by the enzymatic action of invertase, which hydrolyzes sucrose to glucose and fructose [15]. It can also be seen that among the metabolic products, oxalic acid and gluconic acid were the most prominent species, revealing the induction of the enzyme oxaloacetate hydrolase by de novo synthesis [23]. In line with the reduction in pH, the excretion of citric acid increased when pH decreased below 3.5 on the 14th day [24]. However, no further decrease and later on a slight increase in pH might be due to the secretion of intracellular metabolites with an alkaline buffering nature. The dissociation of major organic acids and their participation in metal complexolysis reactions can be described as follows:

Table 1 The organic acid production with prolonged activity of *A. niger* and respective change in pH of the system

Duration (days)	Metabolic acid excretion by the activity of fungi, *A. niger* (mmol/L)				
	Oxalic acid	Citric acid	Tartaric acid	Gluconic acid	pH
1	Not found	Not found	Not found	Not found	5.5
2	0.2	0.1	Not found	3.2	5.5
3	0.8	0.4	0.2	7.4	4.2
6	1.2	0.6	2.1	11.6	4.0
10	7.2	5.3	3.8	15.8	3.8
14	12.8	8.5	4.3	18.6	3.4
18	17.6	8.5	4.6	18.8	3.4
21	16.1	6.1	4.6	14.6	3.6

Citric acid:

$$C_6H_8O_7 \leftrightarrow (C_6H_7O_7)^- + H^+ \qquad (pKa1 = 3.09) \tag{1}$$

$$M^{n+} + n(C_6H_7O_7)^- \rightarrow M(C_6H_7O_7)_n \tag{2}$$

$$(C_6H_7O_7)^- \leftrightarrow (C_6H_6O_7)^{2-} + H^+ \qquad (pKa2 = 4.75) \tag{3}$$

$$2M^{n+} + n(C_6H_6O_7)^{2-} \rightarrow M_2(C_6H_6O_7)_n \tag{4}$$

$$(C_6H_6O_7)^{2-} \leftrightarrow (C_6H_5O_7)^{3-} + H^+ \qquad (pKa_3 = 6.40) \tag{5}$$

$$3M^{n+} + n(C_6H_5O_7)^{3-} \rightarrow M_3(C_6H_5O_7)_n \tag{6}$$

Gluconic acid:

$$C_6H_{12}O_7 \leftrightarrow (C_6H_{11}O_7)^- + H^+ \qquad (pKa = 3.86) \tag{7}$$

$$M^{n+} + n(C_6H_{11}O_7)^- \rightarrow M(C_6H_{11}O_7)_n \tag{8}$$

Oxalic acid:

$$C_2H_2O_4 \leftrightarrow (C_2HO_4)^- + H^+ \qquad (pKa1 = 1.25) \tag{9}$$

$$M^{n+} + n(C_2HO_4)^- \rightarrow M(C_2HO_4)_n \tag{10}$$

$$(C_2HO_4)^- \leftrightarrow (C_2O_4)^{2-} + H^+ \qquad (pKa2 = 4.14) \qquad (11)$$

$$2M^{n+} + n(C_2O_4)^{2-} \rightarrow M_2(C_2O_4)_n \qquad (12)$$
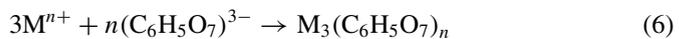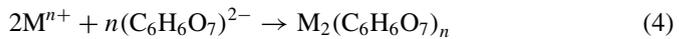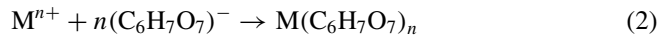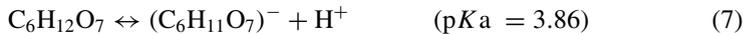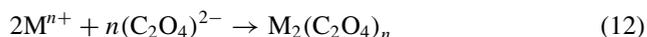
One-Step Bioleaching Process

In a one-step bioleaching process, 1 mL of spore suspension was inoculated into a bioleaching medium together with the cathode mass at a pulp density of 5% (w/v) and a pH of 5.5 to be incubated for 21 days. Results shown in Fig. 1 clearly depict that the bioleaching process was selective for lithium dissolution, leaving cobalt unleached in the residue. This selectivity can be attributed to the lithium solubility via hydrolysis in the neutral pH range, while cobalt in the same pH range remained insoluble. In particular, the dominance of oxalic acid in the metabolically excreted acid species also inhibits cobalt solubility in the solution [20]. On the other hand, a rapid increase in pH by adding the cathode mass was due to the alkaline nature of the electrode material [19], which reached again around a pH near the starting pH value on the 6th day, which could be corroborated with the lagged phase of fungi growth. Then, because of organic acid secretion, the pH was reduced continuously, reaching about 5.0 after the 18th day.

Two-Step Bioleaching Process

As it was observed during the fungal incubation and metabolic excretion study in Sect. 3.1, a significant change in the pH of the system on day 3 indicated that the microbial system was leading to a transfer from the lag-phase to the log-phase (refer to Table 1). Henceforth, in a two-step bioleaching system, the cathode mass was added after 3 days of microbial incubation. The experimental findings are shown in Fig. 2. A sudden change in system pH was observed, rising from 4.2 to 6.2, which can be defined as the alkaline nature of the electrode material. The pH slowly decreased up to the 6th day, then a rapid decrease was observed on the 8th day, reaching a pH value of 5.6. It shows that during this period, the acid produced was consumed to neutralize the alkalinity released from the cathode mass. It was also evident from a lower change in the bioleaching efficiency of lithium up to the 6th day, albeit this efficiency was higher than that obtained by performing one-step bioleaching in Sect. 3.2. The relative increase in bioleaching of lithium can be linked to the increased activity of fungi due to their possible increased growth in the absence of cathode mass. In addition, it also indicates the adverse effect of metal toxicity on fungi growth during
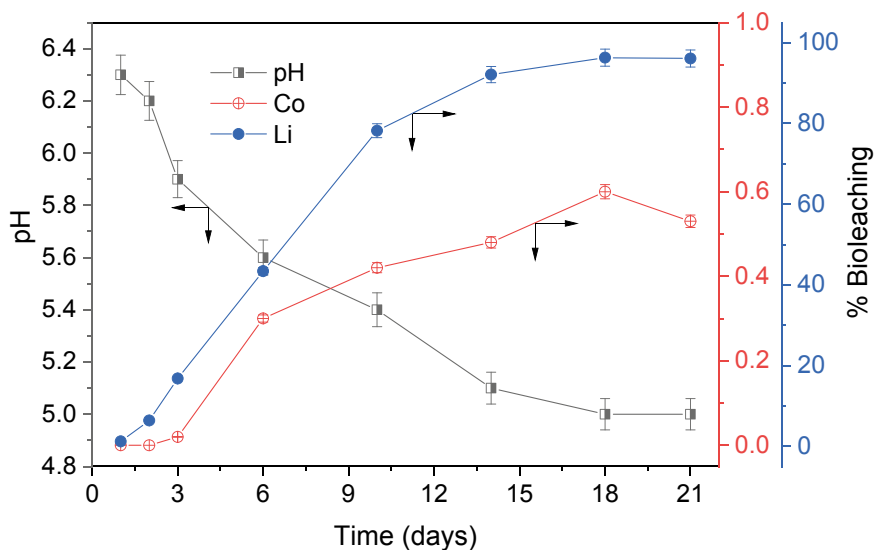
Fig. 1 One-step bioleaching behavior of LCO cathode mass from spent LIBs as a function of time while the experimental condition was maintained to be pulp density = 5% (w/v), initial pH = 5.5, temperature = 30 °C, shaking speed = 150 rpm

one-step bioleaching. Interestingly, although the initial dissolution of lithium in two-step bioleaching was greater than in one-step bioleaching, the final efficiency was a little lower at 94% in comparison to 96% with two-step bioleaching. This might be corroborated by the difference in the final pH of the solution as well, which was noted to be 5.4 at the end of 21 days of two-step bioleaching in comparison to a pH value of 5.0 in one-step bioleaching. This behavior was in line with the reported study by Horeh et al. [19]. Therefore, it can be understood that the two-step bioleaching system is better in terms of an improved rate of lithium dissolution and not for the overall yield. It needs to be mentioned here that, similar to one-step bioleaching, the two-step bioleaching system was also selective for lithium dissolution, and only < 1% of cobalt was observed in the leached solution.
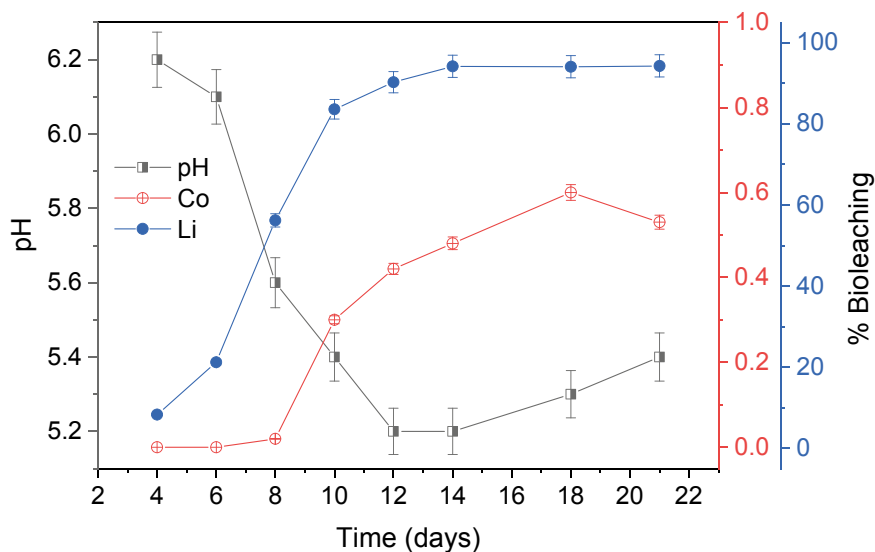
Fig. 2 Two-step bioleaching behavior of LCO cathode mass from spent LIBs as a function of time while the experimental condition was maintained to be pulp density = 5% (w/v), initial pH = 5.5 at starting day 1 of the inoculation, temperature = 30 °C, shaking speed = 150 rpm, and cathode addition to the system was done after day 3

Conclusions

In this research, we examined the shake-flask bioleaching behaviors of LCO cathode mass from the spent Li-ion batteries while using the fungus *A. niger* as the microorganism source for metabolic excretion of organic acids to dissolve the metals therein. Two different approaches were applied, i.e., one-step and two-step bioleaching, to determine the effect of contact on the microbial system, which indicated the metal toxicity on fungi growth. One-step bioleaching was found to give a higher yield of 96% lithium, while two-step bioleaching could improve the rate of dissolution, albeit with a lower yield at the end (94%). Both types of bioleaching showed selectivity for lithium dissolution and left > 99.3% cobalt in the bioleached residue.

References

1. Zhao S, You F (2019) Comparative life-cycle assessment of Li-ion batteries through process-based and integrated hybrid approaches. ACS Sustain Chem Eng 7:5082–5094
2. Rajak DK, Guria C, Gope L, Jibran JA (2023) Hydrometallurgical recovery of critical metals from spent Li-ion batteries using simple leaching-precipitation techniques. Geosystem Eng (in press) https://doi.org/10.1080/12269328.2023.2208124
3. Munir H, Srivastava RR, Kim H, Ilyas S, Khosa MK, Yameen B (2020) Leaching of exhausted LNCM cathode batteries in ascorbic acid lixiviant: a green recycling approach, reaction kinetics and process mechanism. J Chem Technol Biotechnol 95:2286–2294
4. Shaw-Stewart J, Alvarez-Reguera A, Greszta A, Marco J, Masood M, Sommerville R, Kendrick E (2019) Aqueous solution discharge of cylindrical lithium-ion cells. Sustain Mater Techno 22:e00110
5. Chen Q, Lai X, Gu H, Tang X, Gao F, Han X, Zheng Y (2022) Investigating carbon footprint and carbon reduction potential using a cradle-to-cradle LCA approach on lithium-ion batteries for electric vehicles in China. J Clean Prod 369:133342
6. Fahimi A, Ducoli S, Federici S, Ye G, Mousa E, Frontera P, Bontempi E (2022) Evaluation of the sustainability of technologies to recycle spent lithium-ion batteries, based on embodied energy and carbon footprint. J Clean Prod 338:130493
7. Zhao R, Yang Z, Bloom I, Pan L (2021) Significance of a solid electrolyte interphase on separation of anode and cathode materials from spent Li-ion batteries by froth flotation. ACS Sustain Chem Eng 9:531–540
8. Chabhadiya K, Srivastava RR, Pathak P (2021) Two-step leaching process and kinetics for an eco-friendly recycling of critical metals from spent Li-ion batteries. J Environ Chem Eng 9(3):105232
9. Agrawal A, Pathak P, Mishra D, Sahu KK (2012) Solvent mediated interactions for the selective recovery of cadmium from Ni-Cd battery waste. J Mol Liq 173:77–84
10. Ilyas S, Srivastava RR, Singh VK, Chi R, Kim H (2022) Recovery of critical metals from spent Li-ion batteries: sequential leaching, precipitation, and cobalt–nickel separation using Cyphos IL104. Waste Manag 154:175–186
11. Ilyas S, Srivastava RR, Kim H (2023) Cradle-to-cradle recycling of spent NMC batteries with emphasis on novel Co^{2+}/Ni^{2+} separation from HCl leached solution and synthesis of new ternary precursor. Process Saf Environ Prot 170:584–595
12. Pathak P, Chabhadiya K, Singh VK (2021) Sequential leaching of strategic metals from exhausted LNCM-cathode batteries using oxalic and sulfuric acid lixiviants. JOM 73:1386–1394
13. Ilyas S, Srivastava RR, Kim H (2023) Green separation of Co^{2+} over Ni^{2+} by split-phosphinate complexation using phosphonium-based ionic liquid as extraction carrier. Environ Chem Lett 21:673–680
14. Deng X, Chai L, Yang Z, Tang C, Wang Y, Shi Y (2013) Bioleaching mechanism of heavy metals in the mixture of contaminated soil and slag by using indigenous *Penicillium chrysogenum* strain F1. J Hazard Mater 248–249:107–114
15. Amiri F, Mousavi SM, Yaghmaei S (2011) Enhancement of bioleaching of a spent Ni/Mo hydroprocessing catalyst by *Penicillium simplicissimum*. Sep Purif Technol 80:566–576
16. Ijadi Bajestani M, Mousavi SM, Shojaosadati SA (2014) Bioleaching of heavy metals from spent household batteries using *Acidithiobacillus ferrooxidans*: statistical evaluation and optimization. Sep Purif Technol 132:309–316
17. Srivastava RR, Ilyas S, Kim H, Choi S, Trinh HB, Ghauri MA, Ilyas N (2020) Biotechnological recycling of critical metals from waste printed circuit boards. J Chem Technol Biotechnol 95:2796–2810
18. Ilyas S, Kim M, Lee J (2018) Integration of microbial and chemical processing for a sustainable metallurgy. J Chem Technol Biotechnol 93(2):320–332
19. Horeh NB, Mousavi SM, Shojaosadati (2016) Bioleaching of valuable metals from spent lithium-ion mobile phone batteries using *Aspergillus niger*. J Power Sources 320:257–266

20. Ilyas S, Chi R, Lee JC, Bhatti HN (2012) One step bioleaching of sulphide ore with low concentration of arsenic by *Aspergillus niger* and Taguchi orthogonal array optimization. Chin J Chem Eng 20(5):923–929
21. Santhiya D, Ting Y-P (2006) Use of adapted *Aspergillus niger* in the bioleaching of spent refinery processing catalyst. J Biotechnol 121:62–74
22. Deng X, Chai L, Yang Z, Tang C, Tong H, Yuan P (2012) Bioleaching of heavy metals from a contaminated soil using indigenous *Penicillium chrysogenum* strain F1. J Hazard Mater 233–234:25–32
23. Kubicek CP, Schreferl-Kunar G, Wohrer W, Rohr M (1988) Evidence for a cytoplasmic pathway of oxalate biosynthesis in *Aspergillus niger*. Appl Environ Microbiol 54:633–637
24. Ruijter GJG, van de Vondervoort PJI, Visser J (1999) Oxalic acid production by *Aspergillus niger*: an oxalate-non-producing mutant produces citric acid at pH 5 and in the presence of manganese. Microbiology 145:2569–2576

Extraction of Platinum Group Metals from Metallurgical Plant Effluent Using Bioadsorbents

Yen Ning Lee and Shafiq Alam

Abstract Platinum Group Metals (PGMs) comprising platinum, palladium, and rhodium are rare and they are naturally occurring precious metals. They are often used in electronic components and cell phones as capacitors, and catalytic converters found in fuel-consuming vehicles typically contain platinum additives to help treat exhaust fumes. In this research, platinum and palladium were extracted from gold plant effluent solution by adsorption using biobased materials. Data analysis revealed that 97.4% platinum and 99.8% palladium were extracted with modified bioadsorbents and the adsorption rate of PGMs progressed via the pseudo-second-order rate model. Adsorption isotherm model studies indicated that the adsorption of platinum and palladium followed the Freundlich and Langmuir adsorption isotherm, respectively.

Keywords Mineral processing · PGM · Platinum · Palladium · Adsorption · Biomaterials · Effluent

Introduction

In the modern age, PGMs are used extensively in electronics and industrial components for their ductility, corrosion resistance, and general chemical stability [1]. As the naturally occurring PGM resources are declining, efforts are being made by the scientific community to study various methods of recycling, primarily from electronic wastes and industrial effluent/residue in a sustainable manner. The content of PGMs in secondary sources is significantly higher than those found in natural ores [1]. Therefore, electronic wastes and industrial effluents are indispensable resources in the production of marketable PGMs. A flow chart proposing the procedures for recycling gold and silver from used cell phones is shown in Fig. 1 leaving behind platinum (Pt) and palladium (Pd) in the leach residue.

Y. N. Lee · S. Alam (✉)

Department of Chemical and Biological Engineering, University of Saskatchewan, 57 Campus Drive, Saskatoon, SK S7N 5A9, Canada

e-mail: shafiq.alam@usask.ca
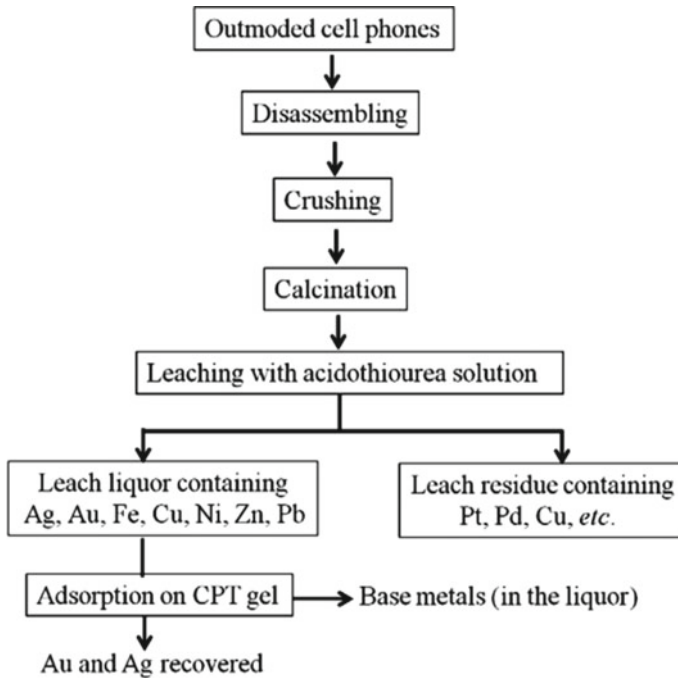
Fig. 1 A flow sheet detailing the recommended procedures for recycling gold and silver from printed circuit boards [2]

Urban mining to recover precious metals from secondary sources can be done via conventional hydrometallurgical recovery methods such as adsorption via activated carbon and ion exchange resins, precipitation, and solvent extraction [3]. However, these processes create large amounts of waste, have high capital costs, and generally exhibit poor selectivity [4, 5]. Also, adsorbents/ion-exchange resins produced from petroleum-derived materials, which aside from high costs, are non-biodegradable and can negatively impact the environment [6]. The use of biosorbents for the recovery of metals is advantageous when compared to conventional adsorbents for their lower operating costs, reusability, and non-toxic nature [5]. Additionally, biomass in its natural state that may perform poorly as adsorbents can be immobilized with novel functional groups to enhance adsorption and selectivity.

This research is related to the recovery of PGMs from plant effluent by adsorption using biobased materials. A Canadian mineral processing company produces gold and silver from different feedstocks coming from mining and recycling industries including electronic wastes (e-waste). In their hydrometallurgical process, precious metals (such as gold, silver, and platinum group metals (PGM) including platinum and palladium) are leached in chloride media. However, the company only recovers gold and silver from the pregnant leach solution (PLS) as they do not have a suitable process to recover other expensive PGMs such as platinum (Pt) and palladium

(Pd) from the PLS. This research focused on developing an efficient, cost-effective, environmentally friendly process to recover Pt and Pd from the effluent stream of the gold processing plant.

Experimental Procedure

In this study, different biomass wastes such as wheat straw (WS), canola meal (CM), and wood bark (WB) were prepared into biosorbents and were immobilized with different functional groups, such as dithiooxamide (DTO), ethylenediamine (EN) and primary amine (PA) to create 12 novel biosorbents. All biomasses used in this research were obtained from local sources and all chemicals used in the experiment were of reagent grade purchased from either Sigma Aldrich or Fischer Scientific. ICP analysis of each test sample was performed by the Geoanalytical Laboratory of the Saskatchewan Research Council. FT-IR characterization was carried out at the Saskatchewan Structural Sciences Center. Particle size analysis was conducted using Malvern Mastersizer 3000 while BET pore size analysis and CHNS elemental analysis were performed by a technician within the University of Saskatchewan's Department of Chemical Engineering.

Adsorption experiments were carried out according to the conventional batch method to evaluate the adsorption behavior of the prepared 12 bioadsorbents. To find out the most effective biosorbent for recovering Pt and Pd, each of the 12 biosorbents was introduced into effluent solution collected from the waste stream of the gold processing plant under the same experimental conditions in a one-point adsorption test. In this experiment, 1 g of adsorbent was added to 20 mL of diluted effluent solution containing 76 ppm Pt and 204 ppm Pd, which was shaken at 200 rpm at room temperature (around 25 °C) for 24 h. After shaking, the mixture was left to settle undisturbed for an additional 48 h for observational purposes and then filtered using Whatman no. 40 filter paper, and the concentration of Pt and Pd was measured by ICP-OES. Concentration measurements were then used to evaluate the amount of adsorption capacity (q) and adsorption percentage for both Pt and Pd, which were determined using Eqs. 1 and 2, respectively.

$$q = \frac{(C_i - C_e)V}{W} \tag{1}$$

$$\%\text{Adsorption} = \frac{(C_i - C_e)}{C_i} \times 100 \tag{2}$$

For these equations, C_i and C_e are the concentrations of metal ions in the aqueous solution at the initial point and the equilibrium point, respectively. V represents the volume of the test solution in mL and W is the weight of adsorbent in mg.

Results and Discussion

Figure 2 shows the results of the percent adsorption of Pt and Pd with prepared bioadsorbents with or without functional groups. It is noted that DTO-CM did not show signs of adsorption towards Pt, which could be due to the experimental error, thus its data was omitted from the graph. It was found that DTO-WB was the most effective adsorbent, achieving 97.4% and 99.8% adsorption for Pt and Pd, respectively.

Table 1 shows the rate constants of pseudo-first-order and pseudo-second-order as K_1 and K_2, respectively. The higher R^2 correlation values indicate that the rate of adsorption for DTO-WB for Pt and Pd follows the pseudo-second-order kinetic model.

The maximum adsorption capacities of Pt and Pd by DTO-WB adsorbent were observed to be 51 ppm/mg and 100 ppm/mg, respectively. The R^2 values obtained from trendlines of Langmuir and Freundlich isotherm plots are shown in Table 2, where it was found that the R^2 of the Langmuir model for Pt adsorption is 0.847 and 0.878 for temperatures at 25 °C and 30 °C, respectively. However, for the Freundlich model, Pt adsorption R^2 is from 0.850 and 0.956 for these temperatures. This suggests that the recovery of Pt on DTO-WB follows a heterogeneous multilayer adsorption behavior. For the adsorption of Pd, the Langmuir isotherm's R^2 values are high at about 0.997 for both temperatures whereas R^2 for the Freundlich model is 0.789 at
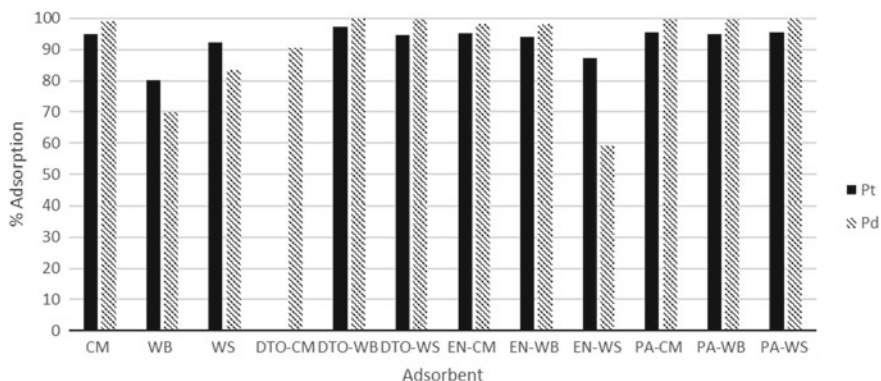
Fig. 2 Results of the one-point adsorption experiment to compare all 12 biosorbents and their efficiency in recovery of Pt (black bar) and Pd (grey bar) from effluent solution

Table 1 Summary of pseudo-first-order and pseudo-second-order kinetic parameters

	Pseudo-first-order model		Pseudo-second-order model	
Temp. (°C)	K_1 (h^{-1})	R^2	K_2 (mg ppm^{-1} h^{-1}) $\times 10^4$	R^2
Pt: 25	0.021	0.875	0.064	0.922
Pd: 25	0.034	0.940	5.660	0.999

Table 2 Summary of obtained R^2 correlation coefficients for the Langmuir and Freundlich isotherm plots

Temperatures (°C)	R^2 coefficients values	
	Langmuir	Freundlich
Pt		
25	0.847	0.850
30	0.878	0959
Pd		
25	0.998	0.789
30	0.996	0.984

25 °C and 0.984 at 30 °C. This information signifies that the adsorption of Pd on DTO-WB is most likely homogenous and monolayer in nature.

Conclusion

Platinum group metals (PGM) were separated from gold processing plant effluent using biomaterials with novel functional groups. Different biomass wastes, such as wheat straw, canola meal, and wood bark nuggets were used and immobilized with dithiooxamide (DTO), ethylenediamine (EN), and primary amine (PA) to create 12 novel biosorbents. These biosorbents were examined for their effectiveness in recovering platinum (Pt) and palladium (Pd) from effluent collected from a gold refining plant. From these 12 biosorbents, it was determined that dithiooxamide-immobilized wood bark (DTO-WB) was the most effective. The rate of adsorption of Pt and Pd on DTO-WB progressed via the pseudo-second-order rate model. Adsorption isotherm model studies indicated that the adsorption of Pt and Pd by DTO-WB followed the Freundlich and Langmuir adsorption isotherm, respectively.

References

1. Won SW, Kotte P, Wei W, Lim A, Yun Y-S (2014) Biosorbents for recovery of precious metals. Bioresour Technol 160:203–212. https://doi.org/10.1016/j.biortech.2014.01.121
2. Gurung M, Adhikari BB, Kawakita H, Ohto K, Inoue K, Alam S (2013) Recovery of gold and silver from spent mobile phones by means of acidothiourea leaching followed by adsorption using biosorbent prepared from persimmon tannin. Hydrometallurgy 133:84–93. https://doi.org/10.1016/j.hydromet.2012.12.003
3. Rubcumintara T (2015) Adsorptive recovery of Au(III) from aqueous solution using modified bagasse biosorbent. Int J Chem Eng Appl 6:95–100. https://doi.org/10.7763/IJCEA.2015.V6.459
4. Khunathai K, Matsueda M, Biswas BK, Kawakita H, Ohto K, Harada H, Inoue K, Funaoka M, Alam S (2011) Adsorption behavior of lignophenol compounds and their dimethylamine derivatives prepared from rice and wheat straws for precious metal ion. J Chem Eng Jpn 44:781–787. https://doi.org/10.1252/jcej.10we246

5. Sari A, Mendil D, Tuzen M, Soylak M (2009) Biosorption of palladium(II) from aqueous solution by moss (*Racomitrium lanuginosum*) biomass: equilibrium, kinetic and thermodynamic studies. J Hazard Mater 162:874–879. https://doi.org/10.1016/j.jhazmat.2008.05.112
6. Inoue M, Nakano T, Yamasaki A (2015) Fabrication of precious metals recovery materials using grape seed-waste. https://doi.org/10.1016/j.susmat.2014.11.005

Concentrated-Solar-Thermal-Driven Recycling of Li-Ion Battery Waste Through Carbothermic Reduction: Thermodynamic Assessment and Experimental Verification

Bintang A. Nuraeni, Deddy C. Nababan, A. D. P. Putera, and M. Akbar Rhamdhani

Abstract Following the global trend towards electric transportation, automakers are transitioning from internal combustion engines to electric vehicles. To overcome the expected increase in spent batteries, recycling li-ion batteries is vital in securing the raw materials. While the pyrometallurgical route offers an effective metallurgical separation, its drawback lies in the high energy consumption from the high-temperature requirement. A high-temperature process by a cleaner energy source like concentrated solar energy is an alternative to address this issue. Solar energy proves promising due to its renewable nature. In this study, the battery waste containing various cathode metals was extracted through carbothermic reduction using anode carbon in a solar simulator furnace. A thermodynamic assessment was conducted using the FactSage™ thermochemical package in conjunction with selected experimental data within the temperature range of 400–800 °C. The development of a concentrated-solar-thermal-driven recycling route is a necessary step towards a sustainable process for recycling spent li-ion batteries.

Keywords Recycling · Material recovery · Secondary resource · Concentrated solar power · Li-ion battery · Thermodynamic assessment

B. A. Nuraeni (✉) · D. C. Nababan · A. D. P. Putera · M. A. Rhamdhani
Fluid and Process Dynamics (FPD) Group, Department of Mechanical and Product Design Engineering, Swinburne University of Technology, Melbourne, VIC 3122, Australia
e-mail: bnuraeni@anl.gov

M. A. Rhamdhani
e-mail: arhamdhani@swin.edu.au

B. A. Nuraeni
Argonne National Laboratory, Lemont, IL, USA

D. C. Nababan
CSIRO Mineral Resources, Clayton, VIC 3169, Australia

Introduction

In the past decade, the surge in demand for Li-ion batteries, driven primarily by the rising popularity of electric vehicles, has created a substantial need for essential raw materials like cobalt, lithium, and nickel. To meet this growing demand and address the environmental concerns associated with spent batteries, recycling has become essential. Pyrometallurgical recycling, a widely adopted industrial method, has emerged as the dominant approach due to its straightforward process, high efficiency, and versatility in handling diverse types of spent batteries as source materials. However, the limitation of pyrometallurgical recycling lies in the utilization of high temperatures which leads to high energy consumption as well as environmental impact from the heat produced by electricity generated from coal-fired power plants.

Utilizing a cleaner energy source such as concentrated solar power (CSP) to provide high-temperature process heat is a crucial strategy for mitigating these challenges. Solar energy stands out as a promising option due to its renewable nature and environmentally friendly attributes. CSP represents an electricity generation technology that harnesses sunlight as its primary heat source, utilizing mirrors or reflective lenses to concentrate sunlight onto a fluid, thus raising its temperature significantly. This heated fluid is directed towards a heat engine, where it is converted into electricity [1]. In essence, CSP operates much like conventional thermal power plants, with the distinction of replacing the boiler with optical devices that serve as solar flux concentrators [2].

Previously, the authors have conducted a series of fundamental research on reductions of cathode materials (Lithium Cobalt Oxide-LCO) using carbon, hydrogen, and aluminium as reductants [3–7]. In these studies, a resistance heating furnace was utilized. To actively contribute to the advancement of sustainable recycling processes for spent Li-ion batteries, a thorough assessment and the development of a solar-powered recycling method are conducted. In this study, an extensive examination of metal extraction, focusing on lithium, cobalt, and nickel separation, was conducted through reduction processes using carbon facilitated by a concentrated solar simulator to aim for the most efficient approach for recycling spent Li-ion batteries.

Materials and Methodology

Black Mass Characterization

The raw material of black mass, which encompasses cathode, anode, and other elements from waste Li-ion batteries was provided by an industry partner, Envirostream Australia Pty Ltd. Table 1 outlines the elemental composition of the black mass, while Table 2 categorizes its components. The black mass primarily consists of cathode materials, including Lithium Cobalt Oxide (LCO) and Lithium Nickel

Table 1 Element analysis of as-received black mass μ

Element	Wt%
C	37–40
Co	8–9
Mn	1–5
Ni	14–16
Al	3–4
Cu	2–4
Fe	< 5
Li	2–4
P	2–4
F	< 2
O	Bal.

Table 2 Component classification of as-received black mass

	Material	Wt%
Anode	Graphite	~ 35 to 50
Cathode	Lithium nickel manganese COBALT oxide (NMC)	~ 5 to 30
	Lithium cobalt oxide (LCO)	~ 10 to 30
	Lithium manganese oxide	~ 0 to 5
	Lithium ferro phosphate (LFP)	~ 0 to 5
Other	Electrolyte (LiPF$_6$)	~ 0 to 5
	Binder (PVDF)	
	Substrate (Al, Cu foil)	

Manganese Cobalt Oxide (NMC), as the predominant types of Li-ion batteries. The typical morphology and cross-section image of the black mass powder of the particles are shown in Fig. 1a, b, respectively.

Thermodynamic Assessment

A thermodynamic analysis was conducted using FactSage™ 8.2 (Thermfact/CRCT-Ecole Polytechnique de Montreal, QC, Canada), specifically utilizing the Equilib module. This module computes the equilibrium state of a system while considering specified constraints, drawing upon data from the selected database(s). In this study, two built-in databases, FactPS (database for pure substances) and FToxid (database for oxides), were employed [9–11]. However, as the thermodynamic data for the mentioned cathode chemistries were not readily available in the built-in
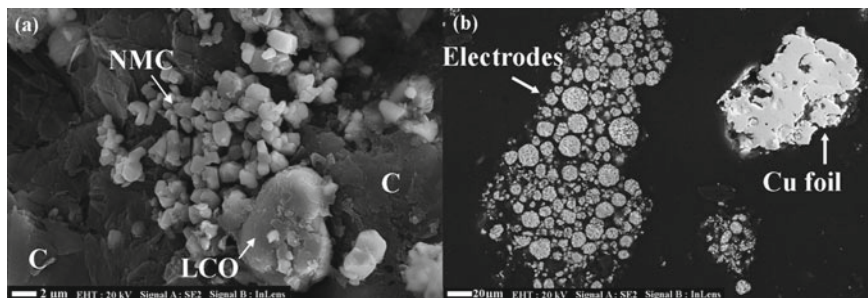
Fig. 1 **a** Morphology of black mass powder [8], **b** cross-section image of black mass powder from Li-ion battery waste, left: electrodes powder containing cathode (various oxides) and anode (graphite), right: dense Cu foil from the other substrate

databases, a custom database was created by referencing pertinent thermodynamic data documented in the literature [11–23].

Reduction Experiment and Characterization

As the material pre-treatment, the black mass was weighed and blended in a ball mill measuring 146 mm × 203 mm, using 100 alumina balls each with an 8 mm diameter. The powders and balls were introduced into the milling jar and subjected to a 3-h rotation at a speed of 100 rpm. Subsequently, the blended powders were compacted into pellets using a cold press, applying a force of 10 tons for 5 min at room temperature. The resulting pellets had dimensions of 13 mm-diameter and 12 mm-thickness.

The experiments were performed using a solar simulator, custom-designed and constructed by Swinburne University of Technology, comprising a circular arrangement of seven metal halide lamps, each rated at 6 kW (OSRAM HMI 6000 W/SE, Hydrargyrum medium-arc Iodide metal halide lamp). The spectral distribution of the metal halide lamps closely resembles natural sunlight, making them a preferable choice for the simulator design when compared to Xenon lamps. In this setup, all seven lamps are intricately connected to an ellipsoidal reflector. The peak flux from each lamp ranged from 117 to 148 kW/m^2. When all the lamps were in operation simultaneously, the solar reactor's cavity could concentrate a maximum peak flux of 1 MW. An image of the solar simulator setup is depicted in Fig. 2. For the purpose of this experiment, only two lamps were used.

A pellet sample was placed inside a 34 mm diameter quartz tube and heated isothermally at 400, 600, and 800 °C for 30 min and 3 h at each temperature. The tube was constantly purged with Ar (0.5 L/min) to create an inert atmosphere in the system. The N-type thermocouple was used for temperature calibration and measurement.

Fig. 2 Solar simulator at Swinburne University of Technology [24]

The temperature and mass were recorded using data acquisition before and during the experiments.

X-ray Powder Diffraction (XRD) analysis was carried out to identify the existing phases, conducted using a Bruker XRD instrument (Bruker AXS GmbH) equipped with Co K α radiation, operating at 40 kV and 40 mA. The scans were performed over a 2θ angle range of 5°–90° with a scanning step size of 0.02° and a dwell time of 1 s. To identify the XRD peaks corresponding to the individual phases present in the samples, the diffraction patterns were indexed and matched with known spectra from the Crystallography Open Database.

Scanning Electron Microscope (SEM) analyses (Zeiss SUPRA-40) were carried out using an emission current of 276 mA applied under a pressure of 2.8×10^{-6} Torr. The accelerating voltage ranged from 10 to 20 kV, and the working distance was set between 10 and 18 mm. Secondary Electron (SE) signal was used to show the microstructure of the phases, In addition to SEM imaging, Energy Dispersive X-ray spectroscopy (EDX) analyses were conducted to generate semi-quantitative elemental composition.

Results and Discussion

Thermodynamic Assessment of Black Mass Reduction by C and H$_2$

A thermodynamic evaluation was conducted to study how the phases resulting from carbothermic reduction evolve with temperature under a total pressure of 1 atm. The calculations predicted equilibrium phases across the temperature range of 400–800 °C. The reaction was originated using the following expression: $LiCoO_2 + LiNi_{0.333}Mn_{0.333}Co_{0.333}O_2 + LiMn_2O_4 + LiFePO_4 + 3C$. The molar ratio applied for all the cathode's compositions relative to the carbon content was determined based on typical battery construction.

Metallic Co and Ni recovery were feasible to be reduced across the entire temperature range (Fig. 3a). However, it is important to note that minor phases of CoO and NiO might still be present (Fig. 3c). In contrast, Mn and Fe could only be reduced to MnO and FeO (Fig. 3c), with traces of spinel phases like Fe_3O_4 and $CoNi_2O_4$ (Fig. 3d). Pure metallic Li recovery was not achievable; instead, it was recovered as various compounds including Li_3PO_4, Li_2CO_3, and $LiFeO_2$ (Fig. 3b). The gas by-products produced included CO and CO_2 (Fig. 4), where elevated temperatures favoured the generation of CO over CO_2. The increase in CO was linked to the complete consumption of C, which occurred around 750 °C (Fig. 3a).

Experimental Verification

To verify the thermodynamic assessment, XRD and SEM–EDX analyses were conducted. In Fig. 5, the XRD analysis reveals the phases in the reduced pellets at 400, 600, and 800 °C. Across all temperatures, metallic Ni and Co were successfully recovered, as indicated by peaks no. 4 and 7, respectively. A closer look at the corresponding peaks, shown on the right-hand side of Fig. 5 (represented by sample reduced at 600 °C), reveals that the two peaks were observed adjoin and identified as two distinct phases: Co and Ni. Meanwhile, Li was present in various phases of Li_2CO_3, Li_2O, and Li_2O_2. Li_2CO_3 was consistently obtained at all temperatures, while Li_2O and Li_2O_2 were only observed at 400 and 600 °C.

The appearance of Co grains was observed by the high magnification SEM-SE and EDX, found at the samples reduced at 600 and 800 °C after 3 h of reduction, as shown in Fig. 6 and Table 3. From Fig. 6a, the Co grains are light-grey in colour, shown as a separated structure with clear boundaries from its surrounding and nearly forming a cubical shape, which is the common crystal structure of Co above 422 °C [25–27]. The higher magnification of the green-squared area (Fig. 6b) shows a dark-coloured mass surrounding the Co grains. The surface of the dark-coloured mass was measured by EDX to contain a balanced amount of C and O, which was then deduced as a mix of Li_2O and C as a most probable assumption, since the observed
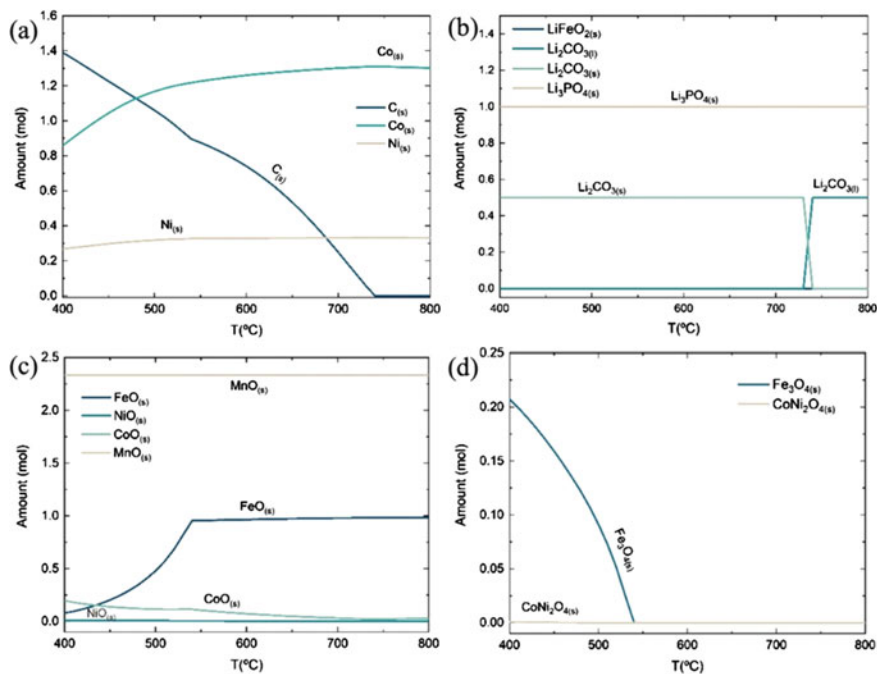
Fig. 3 Predicted equilibrium molar amounts **a** C, Co, Ni, **b** Li compounds: Li_3PO_4, Li_2CO_3, $LiFeO_2$, **c** monoxides: MnO, FeO, CoO, NiO, **d** spinel: Fe_3O_4, $CoNi_2O_4$

Fig. 4 Predicted equilibrium molar amount of the gas phases: CO, CO_2
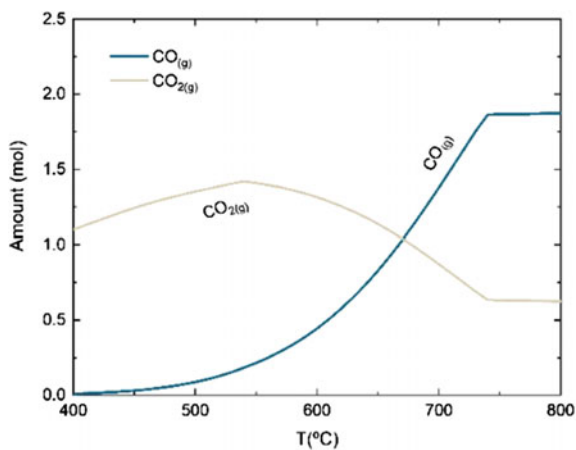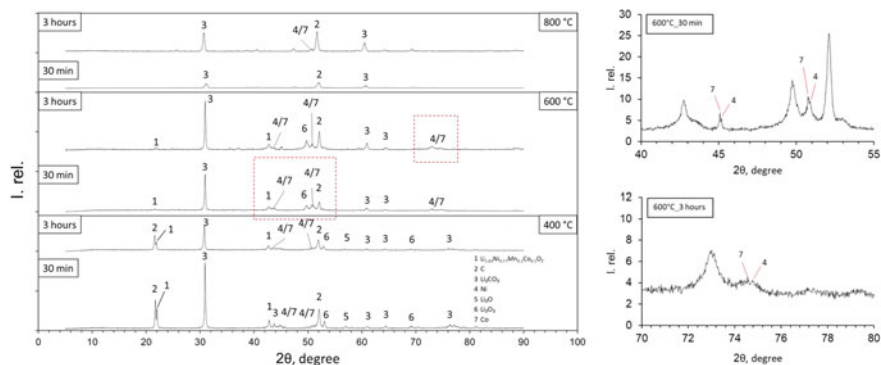
Fig. 5 XRD analysis of reduced samples at 400, 600, and 800 °C

weight ratio of C and O was far from Li_2CO_3 (refer to Table 3). The Co formation was found to be more progressive at higher temperature, as shown in Fig. 6c, taken from the sample reduced at 800 °C after 3 h. The formation of reduced Co was shown in Fig. 6, taken from the sample reduced at 1000 °C.

Figure 7a, b depict the presence of Ni, which appeared as a large surface in contrast to the micro-grains of Co. EDX analysis of this surface revealed the presence of solely Ni, and some points have a small amount of oxygen O, however still confirmed
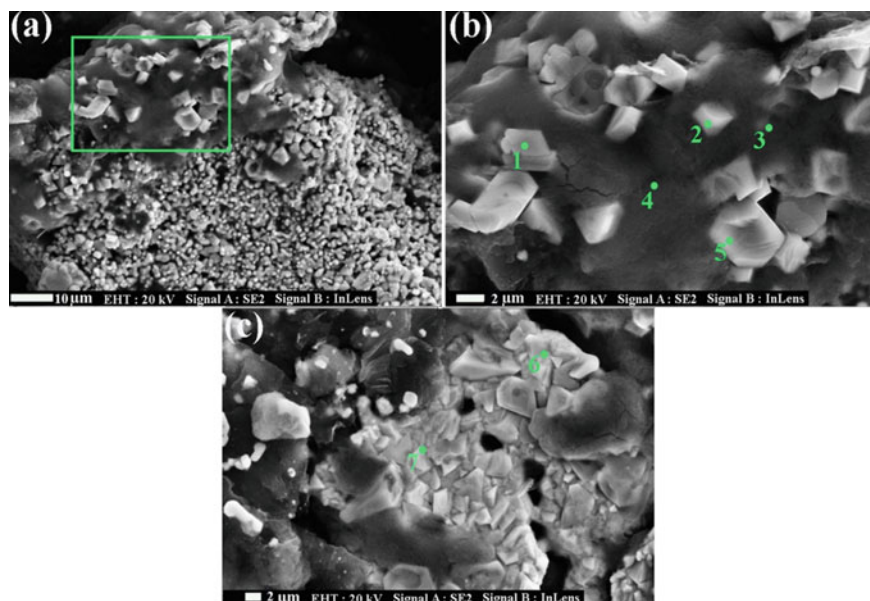
Fig. 6 SEM-SE image of Co grains found at reduced samples **a** 600 °C after 3 h, **b** magnification of green-squared area from figure a, **c** 800 °C after 3 h

Table 3 Semi-quantitative elemental composition from EDX analysis

	Point	Ni	Co	Mn	O	C	Deduced phase
Figure 6	1	–	95.06	–	4.94	–	Co
	2	–	97.23	–	2.77	–	Co
	3	–	–	–	44.02	55.98	Mix of Li_2O and C
	4	–	–	–	42.78	57.22	Mix of Li_2O and C
	5	–	95.54	–	4.46	–	Co
	6	–	99.04	–	0.96	–	Co
	7	–	98.12	–	1.88	–	Co
Figure 7	1	98.81	–	–	1.19	–	Ni
	2	96.25	–	–	3.75	–	Ni
	3	97.74	–	–	2.26	–	Ni
	4	100	–	–	–	–	Ni
	5	100	–	–	–	–	Ni
Figure 8	1	–	–	–	–	100	C
	2	59.49	6.02	4.38	30.11	–	$Li_{1.03}Ni_{0.77}Mn_{0.1}Co_{0.1}O_2$
	3	55.23	5.91	3.41	35.45	–	$Li_{1.03}Ni_{0.77}Mn_{0.1}Co_{0.1}O_2$
	4	–	–	–	0.14	99.86	C
	5	55.51	4.98	7.39	32.12	–	$Li_{1.03}Ni_{0.77}Mn_{0.1}Co_{0.1}O_2$
	6	51.32	5.14	4.33	39.21	–	$Li_{1.03}Ni_{0.77}Mn_{0.1}Co_{0.1}O_2$
Figure 9	1	–	–	–	84.46	15.54	Li_2CO_3
	2	–	–	–	70.82	29.18	Li_2CO_3
	3	–	–	–	88.15	11.85	Li_2CO_3
Theoretical value		51.02	6.65	6.20	36.12	–	$Li_{1.03}Ni_{0.77}Mn_{0.1}Co_{0.1}O_2$
		–	–	–	79.98	20.02	Li_2CO_3

the presence of metallic Ni, as indicated in Table 3. This outcome aligns with the thermodynamic calculations presented in Fig. 2a, affirming the feasibility of Ni recovery.

The dark-coloured area surrounding the metallic nickel in Fig. 7a, was then observed by SEM–EDX and shown in Fig. 8a. This particular structure was identified as the remnants of the initial reactants, consisting of C and NMC-type cathode materials ($Li_{1.03}Ni_{0.77}Mn_{0.1}Co_{0.1}O_2$). The C component exhibited a flaky morphology, while the remaining $Li_{1.03}Ni_{0.77}Mn_{0.1}Co_{0.1}O_2$ displayed a structure in between spherical and cubical structure, reminiscent of its original form (see Fig. 1a). Further examination through EDX point analysis of this phase is detailed in Table 3. XRD analysis and SEM-SE image (Fig. 8b) indicated the persistence of the $Li_{1.03}Ni_{0.77}Mn_{0.1}Co_{0.1}O_2$ phase even at temperatures as high as 600 °C. This suggests that, despite the presence of a substantial amount of C, the kinetics of the reduction process limited its effectiveness.
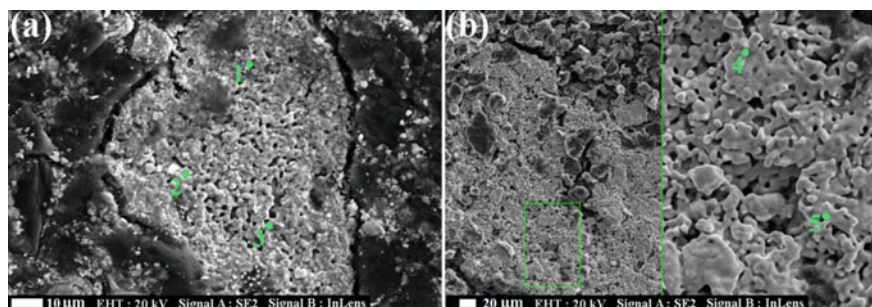
Fig. 7 SEM-SE image of Ni layer found at reduced samples **a** 400 °C after 3 h, **b** 600 °C after 3 h
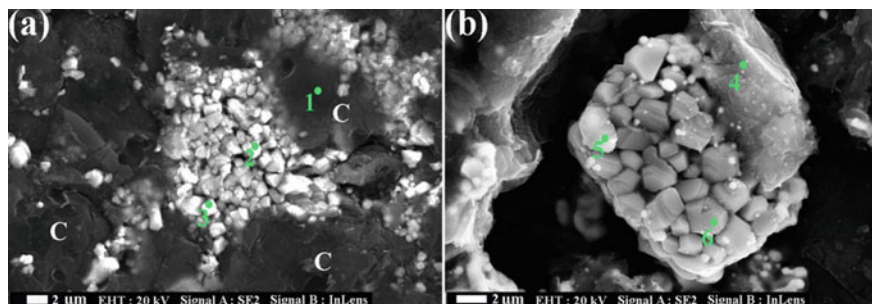
Fig. 8 SEM-SE image of remaining cathode materials ($Li_{1.03}Ni_{0.77}Mn_{0.1}Co_{0.1}O_2$) found at reduced samples **a** 400 °C after 3 h, **b** 600 °C after 3 h

Figure 9 presents SEM-SE images capturing the visual characteristics of Li_2CO_3 on the top surface of samples after 3 h reduction at 400 and 600 °C. Notably, a distinct separation of the phase was evident, detached from the surface. Upon closer inspection in Fig. 9b, the structure exhibited a whisker-shaped morphology. To confirm its composition, an. EDX point analysis conclusively identified the phase as Li_2CO_3, as detailed in Table 3. The formation of Li_2CO_3 whiskers was observed to exhibit a more advanced progression at elevated temperatures (600 °C), as depicted in Fig. 9c, which was taken with a low magnification imaging. In comparison to the thermodynamic predictions shown in Fig. 2b, the obtained results did not yield another Li-containing compound of Li_3PO_4, which was supposed to result from the decomposition of the other cathode material, $LiFePO_4$. This could be possibly due to the minor amount of the material that XRD and SEM could not capture.
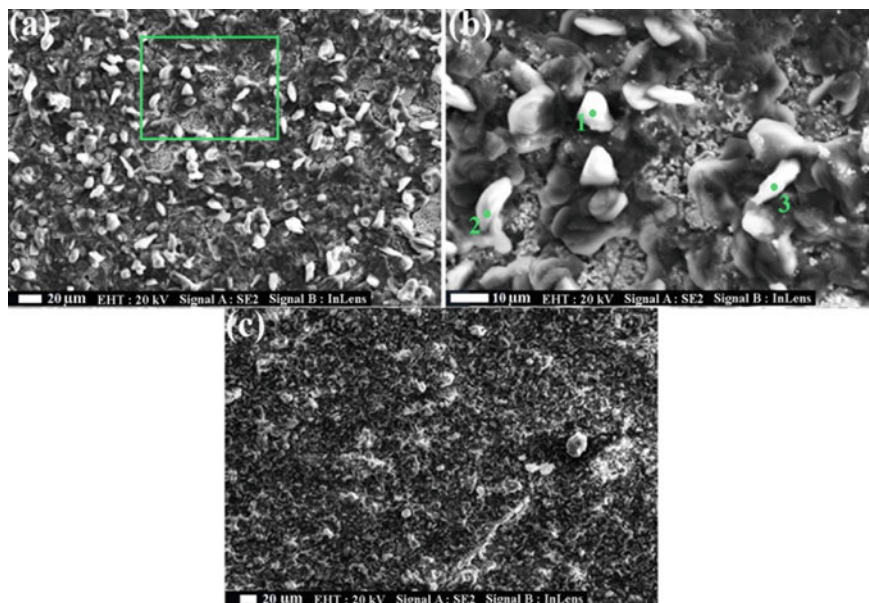
Fig. 9 SEM-SE image of Li$_2$CO$_3$ whiskers found at reduced samples **a** 400 °C after 3 h, **b** 600 °C after 3 h

Conclusion

Systematic study of C and H$_2$ reduction of Li-ion battery waste has been carried out at 400–1000 °C that included thermodynamic assessment supported by experimental verifications. Below conclusions were drawn from the study:

- Thermodynamic assessment: The formation of metallic Co and Ni phases was thermodynamically viable across the entire temperature range of 400–800 °C. On the other hand, Mn and Fe were predicted to exist in oxide forms, specifically MnO and FeO, rather than as metallic elements. As for Li, it was expected to manifest in various Li compounds such as Li$_3$PO$_4$, Li$_2$CO$_3$, and LiFeO$_2$, with LiFeO$_2$ becoming more prevalent at higher temperatures, starting at approximately 900 °C. Complete gasification of C into CO occurred above 750 °C, while a minor amount of CH$_4$ formation took place below 800 °C. Lower temperatures favoured the utilization of CO and H$_2$, whereas higher temperatures resulted in an increased CO/CO$_2$ and H$_2$/H$_2$O ratio, creating a more favourable reducing environment.
- Experimental results: Metallic Co could be reclaimed from temperatures as low as 400 °C, and higher temperatures facilitated a more extensive reduction into metallic Co. Throughout the entire temperature range, Li was obtained in the form of Li$_2$CO$_3$.

References

1. Jacobson MZ, Delucchi MA (2011) Providing all global energy with wind, water, and solar power, part i: technologies, energy resources, quantities and areas of infrastructure, and materials. Energy Policy 39(3):1154–1169
2. Py X, Azoumah Y, Olives R (2013) Concentrated solar power: current technologies, major innovative issues and applicability to West African countries. Renew Sustain Energy Rev 18:306–315
3. Nuraeni BA et al (2022) Carbothermic reduction of $LiCoO_2$ cathode material: thermodynamic analysis, microstructure and mechanisms. Sustain Mater Technol 34:e00526
4. Nuraeni BA et al (2023) Hydrogen reduction of $LiCoO_2$ cathode material: thermodynamic analysis, microstructure, and mechanisms. Metall Mater Trans B, 2023: p 1–26
5. Nuraeni BA et al (2023) Recovery of cobalt and lithium by carbothermic reduction of $LiCoO_2$ cathode material: a kinetic study. Metall and Mater Trans B 54(2):602–620
6. Nuraeni BA et al (2023) Recovery of valuable metals from Li-ion battery waste through carbon and hydrogen reduction: thermodynamic analysis and experimental verification. In: TMS annual meeting & exhibition, 2023. Springer
7. Nababan D et al (2023) Separation of Li and Co from $LiCoO_2$ cathode material through aluminothermic reduction using different aluminum sources: chemical grade, swarf, and dross. In: TMS annual meeting & exhibition, 2023. Springer
8. Nuraeni B et al (2023) Recovery of valuable metals from Li-ion battery waste through carbon and hydrogen reduction: thermodynamic analysis and experimental verification, 2023, pp 437–448
9. Chase MW (1986) JANAF thermochemical tables, 3rd edn. American Chemical Society, Washington
10. Dinsdale AT (1991) SGTE data for pure elements. Calphad 15(4):317–425
11. Jung I-H et al (2004) Thermodynamic evaluation and modeling of the Fe–Co–O system. Acta Mater 52:507–519
12. Chernova NA et al (2007) Layered LixNiyMnyCo1-2yO2 cathodes for lithium ion batteries: understanding local structure via magnetic properties. Chem Mater 19(19):4682–4693
13. Cupid D et al (2017) Interlaboratory study of the heat capacity of LiNi1/3Mn1/3Co1/3O2 (NMC111) with layered structure. Int J Mater Res
14. Cupid DM et al (2016) Enthalpy of formation and heat capacity of Li_2MnO_3. J Ceram Soc Jpn 124(10):1072–1082
15. Gotcu P, Seifert HJ (2016) Thermophysical properties of $LiCoO_2$–$LiMn_2O_4$ blended electrode materials for Li-ion batteries. Phys Chem Chem Phys 18(15):10550–10562
16. Idemoto Y, Matsui T (2008) Thermodynamic stability, crystal structure, and cathodic performance of Li x (Mn 1/3Co 1/3Ni 1/3)O 2 depend on the synthetic process and Li content. Solid State Ionics 179:625–635
17. Jankovský O et al (2016) Thermodynamic properties of stoichiometric lithium cobaltite $LiCoO_2$. Thermochim Acta 634:26–30
18. Kawaji H et al (2002) Low-temperature heat capacity of layer structure lithium nickel oxide. Solid State Ionics 152–153:195–198
19. Knyazev AV et al (2014) Study of the phase transition and thermodynamic functions of $LiMn_2O_4$. Thermochim Acta 593:58–64

20. Lee WK, Choy CL (1975) Heat capacity of fluoropolymers. J Polym Sci Polym Phys Ed 13(3):619–635
21. Masoumi M (2019) Thermochemical and electrochemical investigations of Li(Ni, Mn, Co)O$_2$ (NMC) as positive electrode material for lithium-ion batteries
22. Masoumi M et al (2017) Enthalpies of formation of layered LiNixMnxCo1–2xO2 (0 ≤ x ≤ 0.5) compounds as lithium ion battery cathode materials. Int J Mater Res 108(11):869–878
23. Wang S et al (2018) First-principles Study on LiFePO4 Materials for lithium-ion battery. In: International workshop on materials, chemistry and engineering—IWMCE, 2018. Xiamen, China
24. Ekman BM (2016) The design, construction and performance of a novel solar simulator and hybrid reactor
25. Kazantseva NV, Stepanova NN, Rigmant MB (2018) Superalloys: analysis and control of failure process, 1st edn. CRC Press, Boca Raton, FL
26. Knapek M et al (2020) The effect of different thermal treatment on the allotropic fcc↔hcp transformation and compression behavior of polycrystalline cobalt. Materials 13(24):5775
27. Schuett FM et al (2020) Controlled-atmosphere flame fusion single-crystal growth of non-noble fcc, hcp, and bcc metals using copper, cobalt, and iron. Angew Chem Int Ed 59(32):13246–13252

Beneficiation of Low-Grade Lithium Ores from Eastern Kazakhstan by Dense Media Separation (DMS) and Froth Flotation

Daulet Sagzhanov, Junichiro Ito, Batnasan Altansukh, Labone L. Godirilwe, Sanghee Jeon, Kazutoshi Haga, and Atsushi Shibayama

Abstract Lithium is one of the critical elements required for clean energy technology to achieve a carbon-neutral target. In this study, the beneficiation of a low-grade spodumene ore (0.3–0.6% Li_2O) from Eastern Kazakhstan is investigated by dense medium separation (DMS) and froth flotation to obtain lithium concentrate. The main gangue minerals in the spodumene ore are feldspar, quartz and mica. The highest lithium grade in concentrate from DMS of 1000/+ 850 μm size fractions of the low-grade spodumene ore is achieved at approximately 5.7% from 0.6% (Li_2O), with a recovery of about 90%. Furthermore, the spodumene ore is beneficiated by reverse flotation using NaOL and DAA as mixed collectors. The maximum lithium recovery of approximately 30% with the highest lithium grade of 1.0% was obtained from a low-grade spodumene ore under flotation condition of 1000 g/t NaOL/DAA, ratio of 1:5, pH 10. Conditioning the pulp with starch has little effect on the flotation recovery of lithium from low-grade spodumene ore improving lithium grade from 1.0 to 1.45%.

Keywords Low-grade spodumene ore · Lithium · DMS · Flotation · Mixed collector

Introduction

Lithium is one of the critical elements due to the rapid widespread applications in next-generation clean technologies, including grid storage, electric vehicles (EV), and cordless devices influencing the sustainable development of the world economy and the push for strict CO_2 emission limits [1]. The electric vehicle market is expanding, leading to projections of increased demand for lithium. Recent studies

D. Sagzhanov (✉) · J. Ito · B. Altansukh · L. L. Godirilwe · S. Jeon · K. Haga · A. Shibayama
Department of Earth Resource Engineering and Environmental Science, Faculty of International Resource Sciences, Mineral Processing & Extractive Metallurgy, Akita University, 1-1 Tegata-Gakuen Machi, Akita 010-8502, Japan
e-mail: d6522103@s.akita-u.ac.jp

[2, 3] estimate that the demand for lithium carbonate equivalent (LCE) will rise from 0.5 Mt in 2021 to between 3 and 4 Mt in 2030. By 2050, the demand is expected to increase by 965% compared to the 2017 level of 0.23 Mt in LCE. These projections are based on various scenarios of vehicle electrification. Therefore, the efficient development and utilization of lithium resources is of great significance [4, 5].

Currently, the brines of some highly saline lakes with the concentration of 200–4000 mg/L constitute the largest (59%) and cheapest primary sources of lithium worldwide, followed by its mineral (25%) with grades of 1–4% that is found in igneous rocks, while ignoring other resources including the low-grade ores and seawater [6–8]. While lithium-bearing pegmatites are abundant, their lithium content must be high enough to allow for economically feasible extraction [9]. Spodumene mineral is the major source of high-purity lithium, which theoretically contains approximately 8% Li_2O, 27.4% Al_2O_3, and 64.6% SiO_2 [8]. For lithium extraction to be economically viable, spodumene concentrates normally target a lithia content of over 6.0%. However, the beneficiation of spodumene is a complex process, complicated by the similarities in physicochemical properties of the associated pegmatite minerals (e.g., quartz, feldspar, mica) [10].

In recent years, there has been significant exploration and development of lithium-bearing deposits in Kazakhstan. According to preliminary estimates, some mineral deposits in Eastern Kazakhstan found in six locations: Yubileynoye, Akhmetkino, Bakkennoye, Verkhne-Baymurzinskoye, Akhmirov, and Maralushenskoye have promising reserves of lithium and other critical elements [11]. The ability to access reserves has a major impact on technological advancement [12].

Depending on the mineralogy of the deposit, the primary choice of the spodumene beneficiation involves standard mineral processing steps such as sizing and classification, dense media separation (DMS) and magnetic separation, de-sliming, flotation, and washing steps to produce spodumene concentrate containing 5–7% of lithia [13–15]. Gravity separation methods, such as jigging, spiral beneficiation, and shaking table, are not highly effective in separating spodumene from the gangue minerals due to the relatively small density difference between them [16]. Heavy liquid beneficiation or dense medium separation has proven to be successful and serves as the primary concentration process in spodumene beneficiation. Spodumene has a reported specific gravity (S.G.) of 3.15, while quartz and feldspar have S.G. between 2.5 and 2.6, and mica has an SG between 2.8 and 3.0. The spodumene, therefore, sinks while lighter silicate minerals float in the dense medium of appropriate S.G., and thus separated from each other. The sink product is expected to have a lithium assay approximately of 7.0% (Li_2O). However, like all mineral separation techniques, DMS efficiency is influenced by the degree of mineral liberation and association at the coarsest grain size. Although DMS is a viable beneficiation method for spodumene concentration, flotation separation may still be required to process the DMS middlings and/or the undersize fraction which is outside the particle size range having a very nominal difference in specific gravity between the valuables and the rejects [15, 17]. Especially, it has permitted the processing of complex or low-grade ores which have otherwise been regarded as uneconomic or secondary resources

[18–20]. Recovering low-grade spodumene through positive flotation remains challenging, even with the introduction of novel collectors [21]. Therefore, improving the flotation effect of low-grade spodumene is of major economic and scientific significance. In the present study, the potential role of DMS and froth flotation in the lithium ore beneficiation from low-grade spodumene ore from Eastern Kazakhstan were investigated. The beneficiation processing was carried out with three size fractions using DMS and froth flotation with a mixed collector composed of dodecylamine acetate (DAA) and sodium oleate (NaOL) to recover lithium from low-grade spodumene demonstrating the role of mixed anionic/cationic collectors systems in lithium flotation.

Materials and Methods

Materials and Chemicals

The spodumene sample utilized in this study was obtained from the Akhmetkino deposit in Eastern Kazakhstan. The ore sample was first crushed to 100% passing 5.00 mm, ground into a size of 1.00 mm, and classified on $-$ 1000/+ 850 µm, $-$ 850/+ 500 µm, and $-$ 500 µm screen. The two coarse fractions were fed to DMS, and the fines were reground and screened to $-$ 74/+ 38 µm for the flotations test followed by de-sliming at 20 µm. The composition of sample and separation products was determined by whole-rock analysis using XRF (Rigaku ZSX Primus II) and XRD (Rigaku Miniflex) for major elements, except for lithium. Lithium concentration in the raw sample analyzed by MP-AES (Agilent). The chemical composition and XRD analysis of the three composite samples were shown in Table 1 and Fig. 1, respectively. As can be seen from Table 1 the grade of Li_2O in the sample indicates the characteristics of the ore sample with a high content of gangue and a low content of lithium. The XRD analysis in Fig. 1 illustrates that the main phases of the ore sample were quartz (SiO_2), feldspar ([K,Na]$AlSiO_3$), muscovite ($KAl_2(AlSi_3O_{10})(OH)_2$), and spodumene ($LiAl(SiO_2)_3$).

Sodium polytungstate ($3Na_2WO_4 \cdot 9WO_3 \cdot H_2O$, solid density: 2.82 g/cm³) used for DMS was purchased from *TC-Tungsten Compounds*, Germany. This nontoxic solid can be mixed with water to form a liquid with a fluid density that can be adjusted from pure water with a density of 1 g/cm³ to a saturated solution with a density of 3.10 g/

Table 1 Chemical composition of the ore sample (wt%)

Size fraction	Li_2O	Al_2O_3	SiO_2	Fe_2O_3	Na_2O	CaO	K_2O	Total
$-$ 1000/+ 850 µm	0.67	20.78	64.98	0.63	5.98	0.28	3.30	96.62
$-$ 850/+ 500 µm	0.49	20.25	63.41	0.43	4.69	0.20	3.01	92.48
$-$ 74/+ 38 µm	0.26	21.36	61.95	0.42	6.24	0.30	3.28	93.81
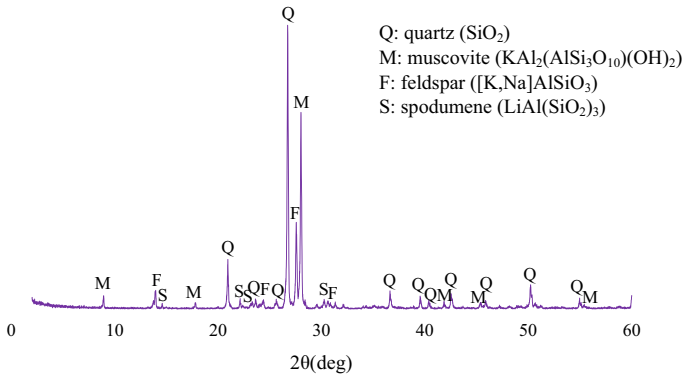
Fig. 1 XRD pattern of the spodumene sample

cm³ [22]. Sodium oleate (NaOL, 97.0%) and dodecylamine acetate (DAA, 98.0%) were purchased from the Tokyo Chemical Industry Co, Ltd as a collector in the batch flotation experiment. Sodium hydroxide (NaOH, > 98%), hydrochloric acid, and starch were used as pH regulators and dispersant, respectively. The deionized water (DI water) with a resistivity of 18.25 MΩ cm was used for the experiments.

Procedure

Dense Media Separation (DMS)

In this study, DMS testing was conducted using sodium polytungstate (density of 3.10 g/cm³) dissolved with distilled water. The test was conducted with heavy media densities ranging from 2.70 to 3.00 g/cm³ in increments of 0.10 g/cm³, according to the flowsheet shown in Fig. 2. The DMS test was initiated with 300 g of 1000/+ 850 µm, and − 850/+ 500 µm feed materials at the highest liquid density (3.00 g/cm³), using a separatory funnel to facilitate separation of heavy material (spodumene) from light material (quartz, feldspars, muscovite). The float fraction from the first DMS stage formed to feed to the second DMS stage, conducted at a specific gravity cut point of 2.90. This procedure continued for all densities in the series, beginning at the highest density (3.00 g/cm³) and ending at the lowest density (2.60 g/cm³). The sink product from the DMS stages formed the spodumene concentrate at each specific gravity (4 total), and the float product formed the final silicate tailings product (1 total). The density of the media was measured before and after each test to ensure the target was maintained. The sink and float products were washed, filtered, dried, and weighed and subsamples were obtained for analysis by XRD and MP-AES.
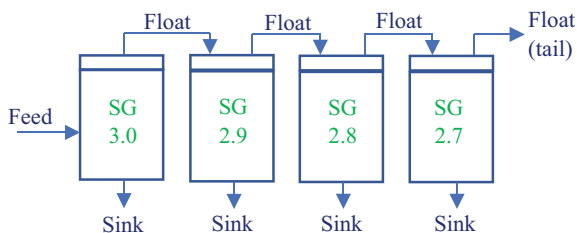
Fig. 2 Dense media separation experiments procedure

Spodumene Flotation

Laboratory flotation experiments were carried out by adding 17.50 g of ore sample to 350 mL of deionized water in the hitch groove flotation cell under constant stirring (800 rpm), and this was followed by the addition of pH regulators (HCl or NaOH) to adjust slurry pH to target pH ranging from 2 to 12 and conditioned for 10 min. After adding the desired amount of NaOL, DAA, or mixture of NaOL/DAA (collectors), the suspension was agitated for 5 min before adding MIBC at 200 g/t into the slurry. The flotation was conducted for 3 min. The froth products and tails were weighed separately after filtration and drying, and the recovery was calculated based on the dry weight of the product.

Results and Discussion

DMS Testwork

The dense media separation test was done with specific gravities of the media ranging from 2.7 to 3.00 with two size fractions ranging between 1000/+ 850 µm and 850/+ 500 µm, respectively. Figure 3 shows the grade-recovery relationship as a function of the specific gravity of the media at the two size fractions. The best DMS performance was achieved with a size fraction of 850/+ 500 µm at 30.78% lithium recovery and the highest lithia grade content (7.05%). However, in both size fractions, the spodumene concentrate grade dropped when the specific gravity of the media dropped. A significant change in mass recovery was observed within a specific gravity range of 2.60–2.70. The observed change can be ascribed to the fact that quartz and feldspar were included in the sink fraction when the specific gravity of the media dropped below that of these minerals. As the highest SG stage of the DMS directly controls the mass and lithium reporting to the final tailing, a lower SG results in less mass (and subsequently, less lithium) being reported to the tailings [23].

The products from dense media separation were analyzed using XRD. Figure 4 shows the mineral distribution in the sink fraction at each specific gravity. It can
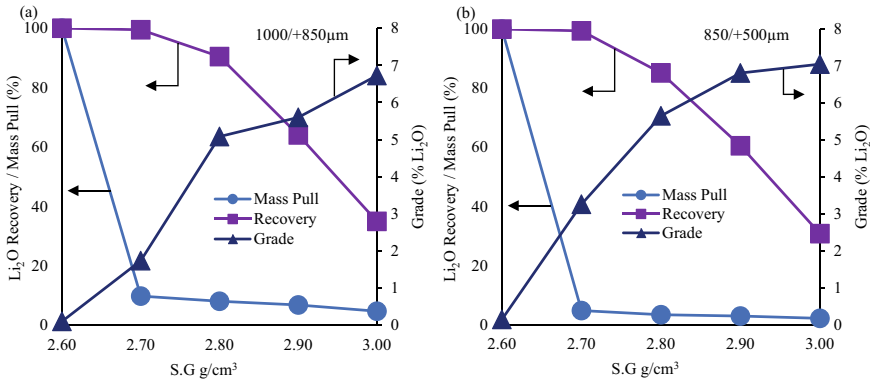
Fig. 3 Dense media separation cumulative sink results. **a** Li$_2$O recovery and mass pull at a size fraction of 1000/+ 850 µm; **b** Li$_2$O recovery and mass pull at a size fraction of 850/+ 500 µm

be seen that the increase in mass to the sink product and decrease in sink grade (% Li$_2$O) at S.G. 2.60 resulted from more silicate gangue minerals reporting to the sink fraction, specifically feldspar and quartz. An increase in spodumene concentrate at the highest specific gravity (3.00) had the highest lithium grade (7.05% Li$_2$O or ~ 91% spodumene) for the size fraction of 850/+ 500 µm, while the separation on the size fraction of 1000/+ 850 µm demonstrated a slightly lower concentration (6.72% Li$_2$O or ~ 87% spodumene). The lower recovery is likely due to non-liberated particles in the float products. The liberation and association data play a crucial role in comprehending flotation behavior and interpreting flotation studies conducted on finer size fractions.
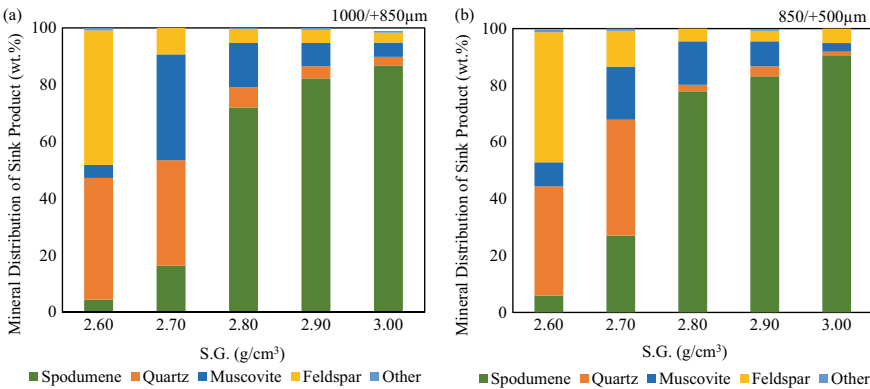
Fig. 4 Mineral Distribution (wt.%) of sink products for different S.G. **a** Size fraction of 1000/+ 850 µm; **b** size fraction of 850/+ 500 µm

Studies have shown that when lithium recovery surpasses 85%, the recovery of gangue minerals with higher specific gravity also increases (i.e., muscovite). Furthermore, given the heterogeneous nature of ores, any alterations to the modal mineralogy of feed to the DMS can impact the mass distribution. These findings indicate that DMS has potential as a pre-concentration of spodumene ore (pegmatite deposit) [23]. The remaining portion of the low-grade spodumene ore (undersize fraction) was subjected to the flotation study for additional recovery.

Flotation

Effects of Collectors

Flotation experiments were performed for the lithium recovery from the low-grade spodumene ore (0.26% Li_2O) using NaOL, DAA, and mixed NaOL/DAA, as collectors. To obtain a relatively high Li_2O recovery and guarantee a certain grade at the same time, a collector dosage of 1000 g/t and pulp pH of 10 are chosen in the following study and the results are shown in Fig. 5. The highest lithium recovery (29.40% Li_2O) was achieved with mixed NaOL/DAA while the recoveries with single collectors were lower than 10%. Using either the anionic collector NaOL or the cationic collector DAA alone is not enough to successfully separate spodumene from silicate gangue minerals due to the surface chemistry complexity of aluminosilicates [18]. Since spodumene is negatively charged in solution over a broad pH range, electrostatic repulsion occurs between spodumene and the anionic collector reducing the floatability of spodumene while cationic collectors adsorb onto mineral surfaces through weak electrostatic interactive forces, leading to poor performance in reverse flotation [21]. Compared with single collectors, mixed collectors are attractive for applications because they demonstrate a strong synergetic interaction. In the mixed NaOL/DAA system, the anionic collector NaOL first reacts with aluminum sites on the mineral surface, then, the cationic collector DAA forms an electroneutral complex with the anionic collector NaOL and co-adsorbs on the Stern layer because of the chemisorption of NaOL [24].

Effects of pH on the Recovery of Lithium

Figure 6 shows the flotation response of spodumene as a function of pH in the single collector NaOL and DAA and mixed collectors NaOL/DAA with 1000 g/t collector dosage. It can be seen that the maximum lithium recovery (approximately 40%) using only NaOL was achieved at an initial pH (6.75) with the highest grade of 0.52% Li_2O since NaOL has a limited ability to flotation-separate spodumene from other gangue minerals, such as feldspar, quartz, and muscovite. Under the condition that only DAA was added, lithium grade was improved to a maximum of 0.92% Li_2O at pH 8, recovery of lithium was only 5%, however. It can be noted that the pH of the
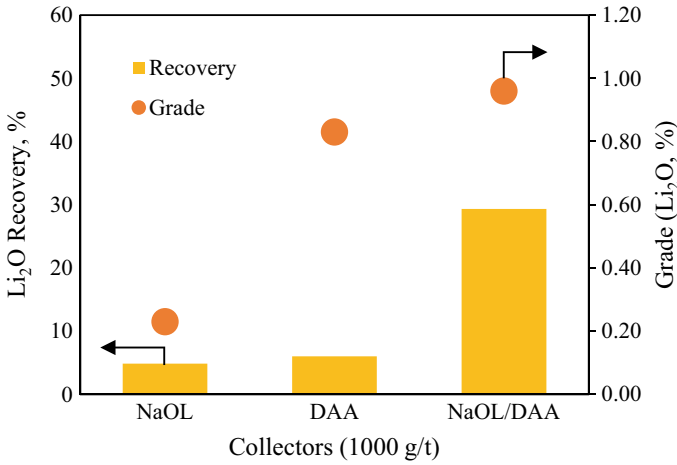
Fig. 5 Lithium recovery and grade in the presence of 1000 g/t NaOL, DAA, and mixed NaOL/DAA (pH = 10)

pulp is crucial for the reverse flotation recovery of lithium in low-grade spodumene ore. In the pH range from 4 to 8, the recovery of lithium first decreased slightly with increasing lithium grade and then sharply increased at pH 8. It is attributed to the role of electrical double-layer forces and the solution chemistry of flotation agents, both of which are dependent on pH [25]. At pH 10, the reverse flotation recovery of lithium reached approximately 30% and a grade value of 1%, indicating that the formation of acid-soap species in an alkaline environment is responsible for this maximum adsorption and flotation [26]. Obviously, the mixed collector NaOL/DAA shows better flotation separation performance than the single collector NaOL and DAA.
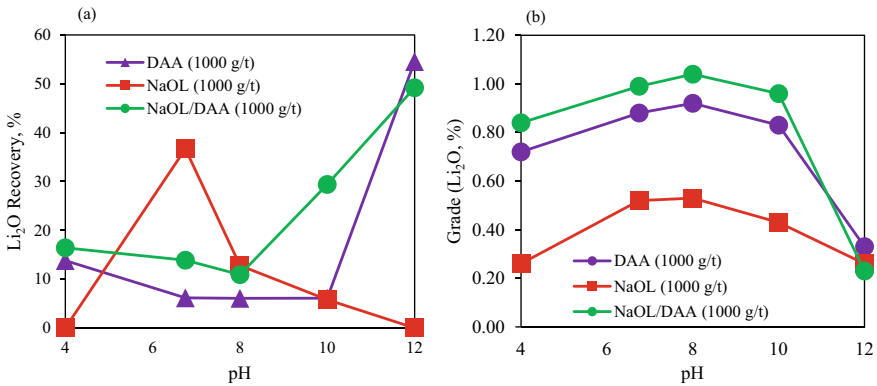
Fig. 6 (**a**) lithium recovery and (**b**) grade as a function of pH in the presence of NaOL, DAA, and NaOL/DAA (ratio of 1:5)

Effects of NaOL/DAA Ratio on the Recovery of Lithium

It is well known that in reverse flotation, cationic collectors with a mixture of anionic effectively float gangue minerals, leaving spodumene as the tailing due to high absorption capacity on the surface of the ore. The ratio of the mixed collectors has been found to be a crucial criterion in the flotation test, thus the flotation performances of the mixed 1000 g/t NaOL/DAA with various ratios have been investigated at pH 10 and 25 °C to determine the optimum mixture dosage in the low-grade spodumene ore. Figure 7 presents the effect of the ratio of NaOL to DAA on the flotation recovery of lithium. As can be observed from Fig. 6, with the increase of DAA dosage, the recovery of lithium demonstrated a trend of first increase and decrease slightly. When the ratio of NaOL to DAA is 1:3, the flotation recovery of lithium reaches the maximum of 35.94%, and lithium grade keeps slightly increasing to approximately 1.0% Li_2O at a mixture ratio of 1:5. No significant difference in lithium grade was observed between mixture ratios of 1:5 and 1:9. Considering the above factors, a separation window seems to exist using the mixed collectors with 1:3 and 1:5 NaOL/DAA ratios, therefore, the ratio of 1:5 is selected for our following flotation study.
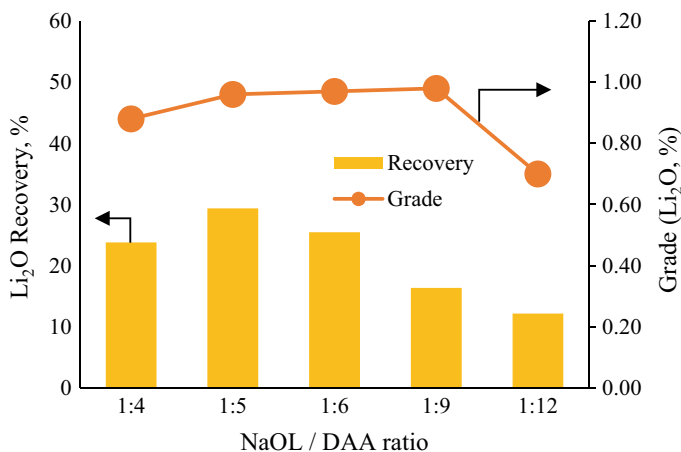
Fig. 7 The effect of the ratio of NaOL to DAA on flotation recovery of lithium (pH 10, NaOL/DAA mixed: 1000 g/t)

Effect of Collector Dosage

To determine the optimum dosage of mixed collector at the ratio of 1:5 in the lithium flotation, condition flotation tests are carried out and the changes in the recovery and grade of concentrate with NaOL/DAA dosage are shown in Fig. 8. An increase of
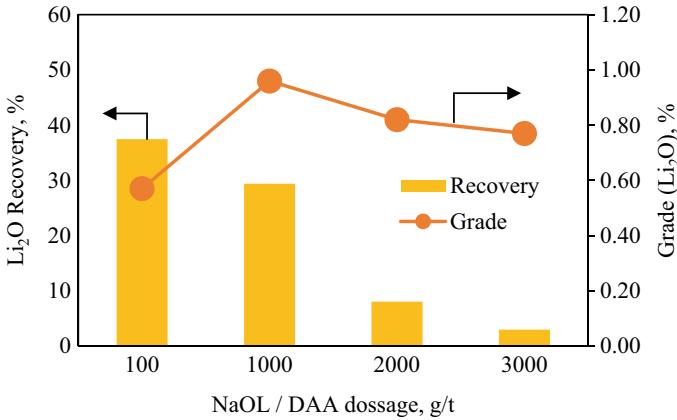
Fig. 8 The effect of NaOL/DAA dosage on flotation recovery of lithium (pH = 10, ratio of 1:5)

the NaOL/DAA dosage from 100 to 3000 g/t decreases the lithium recovery from 37.5 to 3.0%. The trend shows that lithium grade first increases with the increased collector of 1000 g/t dosage reaching a maximum of 1% Li_2O, then decreases with the further increase in collector dosage. Hence, the mixed collector dosage of 1000 g/t was maintained as it gives the best flotation performance.

Effect of Depressant

As is well known, silicate minerals cannot be efficiently separated using traditional anionic/cationic collectors due to their similar physicochemical properties, unless a suitable depressant is used [24]. To investigate the effects of starch dosage on lithium flotation, experiments were conducted at pH 10 using 1000 g/t NaOL/DAA. The results, which are shown in Fig. 9, indicate that increasing the starch dosage from 100 to 4000 g/t leads to an increase in lithium concentrate from 1.0 to 1.45%. However, the recovery rate initially increases from 15.1% to 20.5% as the starch dosage is increased from 100 to 1000 g/t, but then declines as the starch dosage is further increased. A maximum recovery rate of 25.0% is achieved with an increase in starch dosage from 2000 g/t to 4000 g/t.
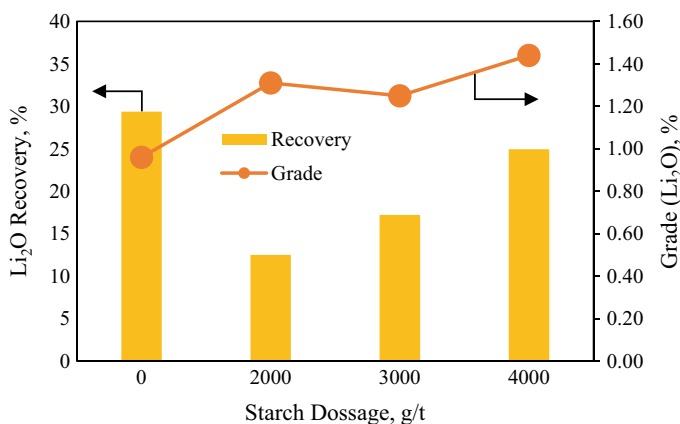
Fig. 9 The effect of starch dosage on flotation recovery of lithium (pH = 10, NaOL/DAA mixed: 1000 g/t)

Conclusion

In this study, the DMS and flotation behavior of mixed collector composed of NaOL and DAA to recover lithium from low-grade spodumene ore have been investigated. Pre-concentration using DMS processed the 1000/+ 850 μm and 850/+ 500 μm size fractions of low-grade lithium ore (0.6% Li_2O) and 85–90% of the lithium oxide can be recovered in 5–10% of the mass with lithium grades ranging from 5.1% to 5.7% Li_2O at a separation specific gravity of 2.80. The main requirement in DMS is to have well-liberated spodumene at a relatively grain size. The reverse flotation of spodumene has also been considered. The maximum lithium recovery of approximately 30% with the highest lithium grade of 1.0% was obtained under flotation condition of 1000 g/t NaOL/DAA, ratio of 1:5, pH 10. Conditioning the pulp with starch has little effect on the flotation recovery of lithium from low-grade spodumene ore.

References

1. Liu Y, Ma B, Lü Y, Wang C, Chen Y (2023) A review of lithium extraction from natural resources. Int J Miner Metall Mater 30(2):209–224
2. Jaskula B (2020) Lithium, mineral commodity summaries USGS

3. Kundu T, Rath SS, Das SK, Parhi PK, Angadi SI (2022) Recovery of lithium from spodumene-bearing pegmatites: a comprehensive review on geological reserves, beneficiation, and extraction. Powder Technol, p 118142

4. Rezaee M, Han S, Sagzhanov D, Vaziri Hassas B, Slawecki TM, Agrawal D, Akbari H, Mensah-Biney R (2021) Microwave-assisted calcination of spodumene for efficient, low-cost and environmentally friendly extraction of lithium. Powder Technol 397:116992

5. Han S, Sagzhanov D, Pan J, Vaziri Hassas B, Rezaee M, Akbari H, Mensah-Biney R (2022) Direct extraction of lithium from α-spodumene by salt roasting–leaching process. ACS Sustain Chem Eng 10(40):13495–13504

6. Garcia LV, Ho Y-C, Myo Thant MM, Han DS, Lim JW (2023) Lithium in a sustainable circular economy: a comprehensive review. Processes 11(2):418

7. Dessemond C, Lajoie-Leroux F, Soucy G, Laroche N, Magnan J-F (2019) Spodumene: the lithium market, resources and processes. Minerals 9(6):334

8. Meng F, McNeice J, Zadeh SS, Ghahreman A (2021) Review of lithium production and recovery from minerals, brines, and lithium-ion batteries. Miner Process Extr Metall Rev 42(2):123–141

9. Cook BK, Aghamirian M, Li H, Nabiri N, Nottingham J, Quinn J, Gunning C, Gibson CE, Brindle P (2022) Production of spodumene concentrate from the North Carolina Piedmont Lithium Project. in conference of metallurgists, 2022. Springer

10. Gibson CE, Aghamirian M, Grammatikopoulos TA (2017) A review: the beneficiation of lithium minerals from hard rock deposits. Min Eng

11. Bishimbayeva G, Zhumabayeva D, Zhanabayeva A, Nalibayeva A, Abdikalykov E, Bakenov ZB (2020) Prospects for creating a full cycle of lithium production in Kazakhstan–from ore processing to lithium batteries

12. Berdikulova FA, Serikbayeva AK, Tabylganov MT, Syrlybekkyzy S, Suleimenova BS (2022) Methods for lithium-bearing raw materials processing. J Chem Technol Metall 57(6)

13. Yelatontsev D, Mukhachev A (2021) Processing of lithium ores: industrial technologies and case studies–a review. Hydrometallurgy 201:105578

14. Legault-Seguin E, Mohns C, Rylatt M, Lakefield O (2016) Dense medium separation–an effective and robust pre-concentration technology. In: 48th Annual Meeting of the Canadian Mineral Processors, 2016, vol 44, pp 1–32

15. Oliazadeh M, Aghamirian M, Ali S, Legault E, Gibson C (2018) Flowsheet development for beneficiation of lithium minerals from hard rock deposits. Extraction 2018. Springer, pp 2293–2307

16. Manser RM (1975) Handbook of silicate flotation. Warren Spring Laboratory

17. Aghamirian M, Mohns C, Grammatikopoulos T, Imeson D, Pearse G (2012) An overview of spodumene beneficiation. In: 44th Annual meeting of the Canadian mineral processors, Ottawa, Ontario, 2012

18. Xie R, Zhu Y, Liu J, Li Y, Wang X, Shumin Z (2021) Research status of spodumene flotation: a review. Miner Process Extr Metall Rev 42(5):321–334

19. Tadesse B, Makuei F, Albijanic B, Dyer L (2019) The beneficiation of lithium minerals from hard rock ores: a review. Miner Eng 131:170–184

20. Wills BA, Finch J (2006) Froth flotation. In: Wills' mineral processing technology (seventh edition): an introduction to the practical aspects of ore treatment and mineral recovery. Elsevier. Butterworth-Heinemann, pp 267–2344

21. Bian Z, Zhang H, Ye J, Ning Z (2023) Flotation behavior of oleate and dodecylamine as mixed collector for recovery of lithium and rubidium from low-grade spodumene tailings: experiment, characterization and DFT calculation. Appl Surf Sci, p 158117

22. Skipp G, Brownfield IK (1993) Improved density gradient separation techniques using sodium polytungstate and a comparison to the use of other heavy liquids. US Department of the Interior, US Geological Survey, Denver, CO

23. Gibson CE, Aghamirian M, Grammatikopoulos T, Smith DL, Bottomer L (2021) The recovery and concentration of spodumene using dense media separation. Minerals 11(6):649

24. Xu L, Wu H, Dong F, Wang L, Wang Z, Xiao J (2013) Flotation and adsorption of mixed cationic/anionic collectors on muscovite mica. Miner Eng 41:41–45

25. Rai B, Sathish P, Tanwar J, Moon K, Fuerstenau D (2011) A molecular dynamics study of the interaction of oleate and dodecylammonium chloride surfactants with complex aluminosilicate minerals. J Colloid Interface Sci 362(2):510–516
26. Kulkarni R, Somasundaran P (1980) Flotation chemistry of hematite/oleate system. Colloids Surf 1(3–4):387–405

Investigating the Selectivity of Xanthates for the Flotation Separation of Base Metal and PGM Ores

T. Z. Sehume, Z. Magaxeni, M. Dlame, T. T. Phadi, and L. F. Mabena

Abstract The current study investigated the effects of thiol collectors on the flotation of base metals (BMs) and platinum group metals (PGMs) ores. The properties of a single-mineral flotation test were conducted using sodium isobutyl xanthate (SIBX), sodium ethyl xanthate (SEX), potassium ethyl xanthate (PEX), and sodium isopropyl xanthate (SIPX) at concentrations of 40, 60, 80, 100, and 120 g/t and pH 9. Rougher flotation recoveries higher than 85% were obtained at typical rougher mass pulls using these xanthates at various dosages, which demonstrated high selectivity properties towards both ores. The dosages of these collectors were monitored by UV-Vis in solution as a function of time at a constant pH. The UV-Vis results showed high mineral-collector interaction between the mineral surface and xanthate at 300 nm. The thiol collectors (SIPX, SEX, SIBX, and PAX) were found to be selective towards PGMs and BMs as similar increased cumulative recoveries were obtained. The structures of xanthates had an impact on the flotation recovery. For instance, iso-alkyl xanthate (SIBX) showed better consistency in terms of maximum cumulative recovery at various dosages when compared to other xanthates.

Keywords Xanthates · Flotation · Adsorption · PGMs & BMs ores · Selectivity · Recovery

T. Z. Sehume (✉) · Z. Magaxeni · T. T. Phadi
Measurements and Control Division, Mintek, Private Bag X3015, Randburg 2125, South Africa
e-mail: ZachS@mintek.co.za

M. Dlame
Minerals Processing Division, Mintek, Private Bag X3015, Randburg 2125, South Africa

L. F. Mabena
Tshwane University of Technology, Pretoria, South Africa

Introduction

Xanthates are widely used as thiol collectors in both sulphide and oxide flotation due to their fundamental role in selectively adsorbing on certain mineral surfaces, by enhancing the hydrophobicity of the mineral surface [1–3]. The hydrophobic mineral particles attach to dispersed air bubbles that float to the froth layer that is readily separated in the flotation cells [4]. These thiol collectors primarily consist of two functional groups in their structure, namely, ionic and hydrocarbon chains, where the first functional group is adsorbed by chemisorption or electrostatic interaction and the second functional group is responsible for the hydrophobic character given to the mineral surface [5, 6]. During the flotation process, the xanthate dosages could range between 30 and 300 grams per ton of ore, and the consumption of xanthates (alkyl types) worldwide within the mineral process has been estimated to be in the vicinity of 60,000 tonnes per year [7]. However, despite the advances in froth flotation, there is limited understanding relating to the optimum dosages, improved selectivity and low-efficiency recovery of minerals of interest due to the complexity of the collector-mineral interactions or the chemistry involved in the adsorption mechanism. The mechanism of mineral-collector bonding depends on the collector type, mineral surface nature, collector charge, and these can result in the collector being physisorbed or chemisorbed [8]. Therefore, the establishment of the fundamentals of froth flotation needs to be investigated using traditional thiol collectors to investigate their selectivity towards different types of ores. Ores response in flotation is specific to different collectors and the structure of these alkyl hydrocarbon collectors can influence flotation performance [9].

According to the literature, PGMs are the leading main sources of mineral revenue in South Africa. The deposits of PGMs can be found along the Merensky Reef, UG2 Reef, and Platreef [10–12]. South Africa accounts for the majority of PGMs world production (58%) and it contains more than two-thirds of the world's PGMs reserves [13]. The current primary PGMs production is derived from sulphide ores, which are the major source of base metals such as copper, nickel and gangue minerals. For instance, UG2 ore is dominated by hydrophilic chromite gangue that comprises 60–90% by volume of silicate minerals, viz., 5–30 pyroxene and 1–10% plagioclase [11]. According to McFadzean et al. [11], the presence of chromite in the flotation concentrate by entrainment could lead to issues for the downstream smelting processes or inefficiency in the selective flotation of chromite. In contrast, the Platreef ore consists of a complex collection of pyroxenites, serpentinites, and calc-silicates. Calc-silicate samples showed the worst flotation response according to the batch flotation test results from the enrichment ratio and recovery relationships for various rock types [14]. Additionally, Platreef ore may require high xanthate dosages due to the low sulphide content of the ore and the need to use high dosages to recover tellurides, alloys, and arsenides [15]. For instance, high dosages of PAX used as a collector were found to increase the overall adsorption of the collector onto other platinum (arsenide) minerals but found only to improve the recovery to a maximum of 45% [16]. The dosage of a thiol collector is one of the critical factors that determine

the efficiency of a froth flotation process in terms of selectivity and recovery [17]. The most common thiol collectors used in flotation include sodium isobutyl (SIPX), sodium ethyl (SEX), potassium amyl (PAX), and sodium isobutyl (SIBX) xanthates [18, 19]. Additionally, the processing of complex mineral ores during flotation can pose some difficulty during the process depending on the interaction with xanthate collectors.

Özün and Ergen [18] investigated the effects of xanthate concentration (150 ppm) on the flotation of galena. They found that branched-chain xanthates (SIPX and SIBX) resulted in higher flotation recovery values compared to straight-chain xanthates (PEX and potassium amyl; PAX). This showed the selection of C-H chain length is generally limited to 25 carbon atoms, as longer chain lengths could result in a decrease in the concentration of xanthate species adsorbed on the mineral surface. These thiol collectors can be less expensive compared to other suitable collectors. However, these have been reported to show a lack of selectivity (i.e., pyrite) and insufficient kinetics in some cases [9]. Ackerman et al. [20] compared the micro-flotation results of different chain lengths of xanthates with pyrite and copper sulphides. Their study showed that ethyl xanthates performed poorly compared to amyl xanthate. Furthermore, branched (iso) propyl (C3) xanthate showed greater recoveries for pyrite than for straight-chained xanthates. Ores containing sulphide minerals tend to have different reactivity due to sulphur's variable oxidation state [21]. In addition, the oxidation of minerals can be detrimental to flotation recovery over an extended period, as this can inhibit collector adsorption by decreasing the hydrophobicity of the sulphide surface. Ralston [6] found that for sulphide minerals, pyrite was more readily oxidized than galena, and galena is ranked as having a higher relative collectorless floatability than pyrite. Overall, collectors' selectivity has been shifted towards finding the most suitable flotation parameters, with limited understanding regarding mineral-collector behaviour that might affect flotation performance using traditional thiol collectors. The selectivity of collectors towards different mineral ores can assist in understanding the ability of the collectors to interact with various mineral surfaces of ores.

The study aims to evaluate the performance and selectivity of four different types of thiol collectors (SIBX, PAX, SIPX, and SEX) towards PGM and BM ores. The effect of collector concentrations or dosages was also investigated for flotation recovery during flotation tests. The Ultraviolet-visible (UV-Vis) spectrophotometer and Fourier Transform infrared spectroscopy (FTIR) techniques were used to establish the mechanism behind the adsorption of thiol collectors on the mineral surface of the different ores used in this study.

Materials and Methods

Materials

Sample Collection and Preparation

PGM and BM ores were collected from mines in the northern limb of the Bushveld Igneous Complex and Botswana's Kalahari Copper Belt, respectively. The PGM ore was received as a coarse ROM sample with a top size of about 150 mm. The sample was further stage crushed to -6 mm using a pilot comminution plant, which included an open jaw and closed circuit cone crusher. For the purpose of bench-scale flotation testing, a 50 kg sub-sample was removed from the -6 mm remainder after the pilot campaign and crushed down further to 100% ($-$ 1.7 mm) and subsequently apportioned to representative 1.7 kg batches using a rotary splitter. For the preparation of flotation feed, a milling curve was generated by grinding three 1.7 kg at different time intervals. The mill contents after each time interval were fully sized, and the PSDs were used to generate the milling curve from which the grinding time to attain 80% passing 75 µm was estimated. The PGM ore contained 4.02 ppm 2E + Au and other elements, as shown in Table 1.

The base metal or copper ore sample was already at $-$ 1.7 mm crush size upon receipt. The initial preparation step involved homogenization and splitting into representative 1.7 kg batches. The mill contents after each time interval were fully sized, and the PSDs were used to generate the milling curve from which the grinding time to attain 80% passing 106 µm was estimated. The BM feed sample contained 1.91% Cu and other elements, as shown in Table 2.

Table 1 Chemical composition of the PGM ore sample (ppm)

Pt	Pd	Au	2E + Au
1.91	2.07	0.40	4.02

[a]Pt—platinum, Pd—palladium, Au—gold
[b]2E: Pt and Pd

Table 2 Elemental assay of the BMs ore sample (%)

Al	Ca	Fe	Cu	Mg	Mn	Si	Ti	Ni	Co	Cr
4.96	11.10	2.15	1.91	1.83	0.19	22.30	0.28	< 0.05	< 0.05	< 0.05

[a]Al—aluminium, Cu—copper, Fe—iron, Mg—magnesium, Si—silicon, Ti—titanium, Ni—nickel, Co—cobalt, Cr—chromium

The Reagents

The reagents used were xanthate (SIPX, SIBX, SEX, and PEX) collectors in pellet form at a purity close to 95%, a polyglycol ether frother (Senfroth XP 200, received in liquid form), and a high-purity depressant (Finnfix 300), supplied by AECI Mining Company.

Analysis Method

The adsorption tests were carried out using a UV-Vis spectrometer (Molecular Devices SpectraMAX ABS Plus) and the experiments consisted of measuring the UV-Vis absorption spectrum of the xanthate collectors in the wavelength range of 200 to 350 nm. The measurements were carried out in triplicate and as a result, the average value is reported. The error experienced in the measurements was less than 5% (95% confidence interval of a Student's t-distribution). The samples were taken using a 0.5 μm filter at flotation times of 3, 7, and 20 minutes (before scraping of the concentrates). The samples were then analyzed on the same day to prevent sample degradation.

The FTIR measurements were measured using the PerkinElmer Spectrum 100 FTIR Spectrometer. The transmittance spectra were obtained by performing 40 scans between 420 and 1700 cm^{-1}, with a resolution of 4 cm^{-1}. The PGM and BM ores were characterized by their chemical properties, and bulk chemical analysis was performed using ICP-OES (Agilent 5800 ICP-OES).

Methods

Batch rougher froth flotation test work was conducted by transferring a milled slurry to a mechanical batch flotation cell (Denver D12), where the slurry volume was made up using distilled water to produce 34% (wt.%/wt.%) solids. The impeller speed was set and kept at 1200 rpm. The conditioning time was set at 2 minutes while the air was maintained at a flow rate of 10.5 L/min (i.e., 50% of 21 L/min) in all tests. All reagents were prepared at a 0.01 g/mL concentration immediately before flotation experiments. The frother and depressant dosages were kept constant throughout the test work. However, the depressant was not used for the base metal ore sample. Each flotation test was conducted with xanthate at dosages of 40, 60, 80, 100, and 120 g/ton and a starting pH value of 9. Three concentrates (RC-1:RC-3) were collected at 3, 7, and 20 minutes of flotation time (as shown in Fig. 1) by scraping the froth every 15 seconds into a collecting pan. The slurry level was adjusted and kept constant by adding distilled water to the flotation cell. Concentrates and rougher tailings (RT)
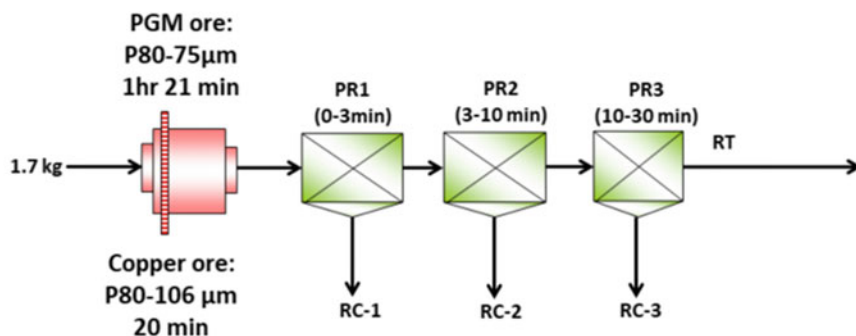
Fig. 1 Flotation test flowsheet for both PGM and base metal ores

were filtered, dried, and weighed before the ICP-OES analysis of these solid products. The same procedure was followed for all the experiments.

Results and Discussion

Figures 2 and 3 show the milling curves obtained for the PGM and BM (copper) ores, respectively. The results obtained showed that the time required to obtain a grind time of 80% passing 75 and 106 µm was 80 and 20 mins for PGMs and BMs, respectively. The particle size of minerals is considered another factor that has been reported to affect flotation efficiency. These results are in line with literature reporting that high performance for flotation with a particle size range of approximately 10–100 µm for minerals is expected [22]. In contrast, other studies showed that the recoveries of copper were found to be maximum at a particle size between 30 and 150 µm with a distinct drop in recovery outside this range [23]. Furthermore, this may result in the loss of ultrafine (< 10 µm) and coarse particles into tailings, which necessitate recovery from tailings. The observed results indicate that the particle size of the ores used in this study may be sufficient to enhance particle collision efficiency, which could result in high flotation recovery. However, PGM ore may require longer grinding times (120 mins) for passing of 95% when compared with copper ore (30 mins).

Figure 4 illustrates that increasing the collector dosages leads to an increase in the recovery of the combined platinum group elements (PGE) using xanthates at a pH of 9. The cumulative recovery increased substantially using SIBX, PAX, SIPX, and SEX at different dosages (40–120 g/t). It was observed that the xanthates used in this study had a positive influence on the PGM ore. This observation is based on high recoveries (> 90%) at a flotation time of 30 mins from lowest dosage to highest (40–120 g/t). At a flotation time of 30 mins, all four xanthates behaved similarly to each other at 60 g/t dosages attaining the highest cumulative recovery of approximately 95%. All four thiol xanthates were effective at selectively altering the hydrophobicity of the PGM

Fig. 2 Milling curve for PGM ore
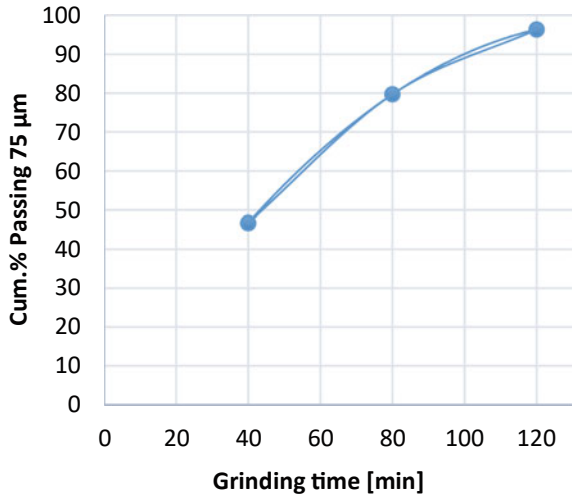
Fig. 3 Milling curve for base metal (copper) ore
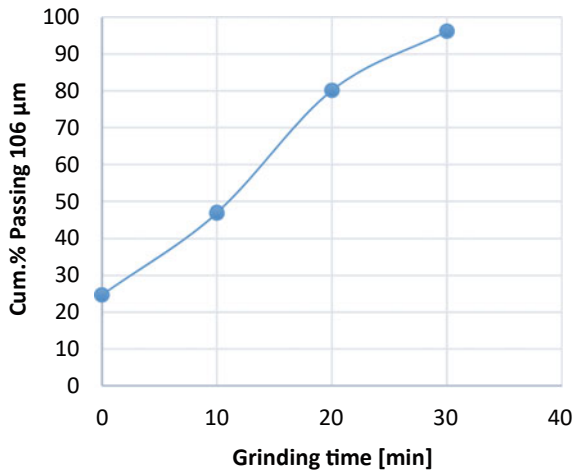
mineral surface in order to achieve high recoveries over extended flotation times. However, at lower flotation times, the observed small variation could be attributed to the complexity of the pulp solution. The trend of cumulative recovery was consistent at longer flotation times indicating that increasing dosages were sufficient to achieve high flotation recovery.

Figure 5 illustrates the relationship between BM ore and the xanthate collector concentrations at a pH of 9. From Fig. 5, the overall cumulative Cu recovery using xanthates increased with increasing flotation time [24]. The cumulative recovery was observed to be the lowest at a dosage of 40 g/t for SEX and PAX, reaching a maximum recovery of 85% at a flotation time of 30 mins. The cumulative recovery from using
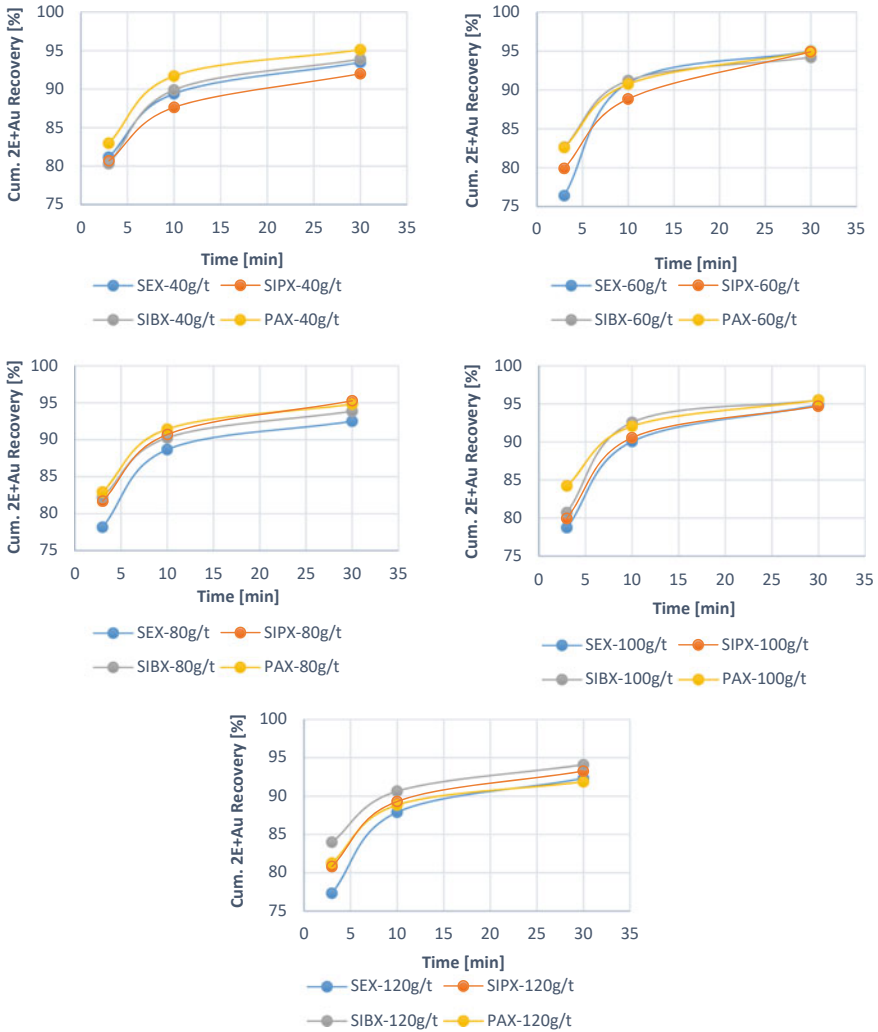
Fig. 4 Cumulative 2E + Au recoveries obtained with thiol collectors

SEX and PAX improved with an increase in dosage from 60 g/t to 80 g/t, where there were no significant changes to the recovery above 80 g/t as the cumulative recovery was nearly close to 90% for both xanthates. However, SIPX and SIBX performed well from 40 g/t to 120 g/t, reaching a maximum cumulative recovery of more than 90%. The cumulative recovery declined from 95% to 90% at 120 g/t for PAX, as this might suggest that a higher dosage may lead to a negative effect on the recovery of BM ore, but not significantly. The use of high concentrations for better flotation recovery may not be the case, especially for PAX at more than 100 g/t. However, all thiol collectors behaved similarly in terms of maximum cumulative recovery of

close to 95% at dosages of 100 g/t. At 100 g/t dosage, ethyl, iso-alkyl, and amyl xanthates displayed similar characteristics, such as reactivity and selectivity [25]. However, iso-alkyl xanthate (SIBX) was more selective towards BMs, as cumulative Cu recoveries of close to 95% were observed throughout flotation tests at various dosages when compared to other xanthates. This could be due to some findings that branched iso-alkyl xanthates tend to achieve higher flotation recoveries than their corresponding straight-chain analogues due to their greater contact angles [20, 26].
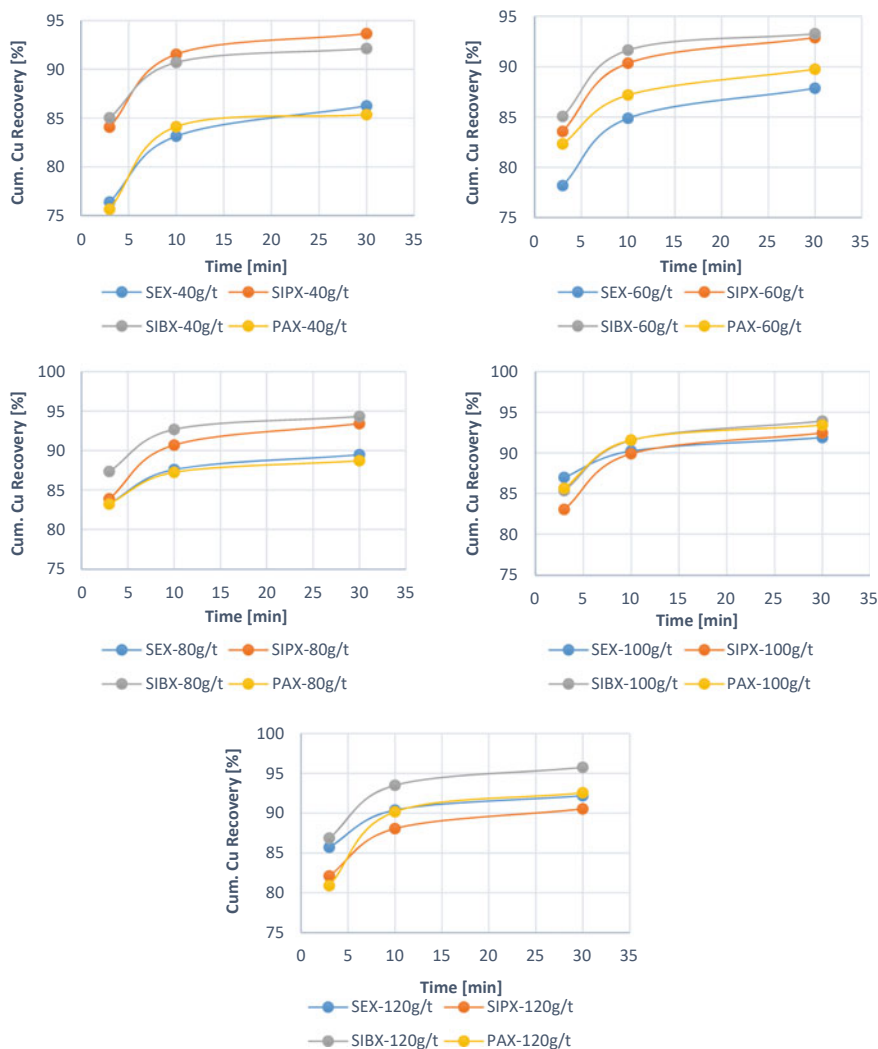
Fig. 5 Cumulative BMS recoveries obtained with thiol collectors

The performance of the flotation reagents is mostly based on the recovery and grade of minerals in the concentrates. Figure 6 shows the cumulative 2E + Au grade versus cumulative 2E + Au recovery from the use of PGM ore with SIBX, SEX, PAX, and SIPX at various dosages. These curves show a shift upward and to the right, indicating a performance improvement. Grade-recovery curves represent a clear way of showing the trade-off between achieving a high-grade concentrate while sacrificing as little recovery as possible [27]. PAX showed higher overall concentrate grades and cumulative recovery at a dosage of 40 g/t, which was higher than other xanthates. This is corroborated by the high cumulative recoveries obtained as a function of time in Fig. 4. However, the overall concentrate grades of nearly 20 g/t were achieved with a cumulative recovery of more than 90% with the use of four thiol xanthates' when the grind size was at a P80: 75 µm. These results show that using SIPX, PAX, SIBX, and SIPX, may be indicative of high selectivity for PGM ore based on high cumulative recoveries achieved at various dosages.

Figure 7 shows cumulative copper grade versus cumulative copper recovery from SEX, PAX, SIBX, and SIPX. The curves show a general trend where the decrease in cumulative copper grade increases cumulative recovery with increasing xanthate dosages [17, 24]. The iso-alkyl xanthates (SIPX and SIBX) collectors showed high cumulative concentrate grades of 10 g/t from dosages of 40 g/t to 60 g/t when compared to ethyl and amyl xanthates. However, SEX at a dosage of 80 g/t improved in cumulative concentrate grade with a cumulative recovery of close to 95%, while PAX remained stagnant at a grade of 13% for a recovery of 89%. The thiol xanthates showed consistent overall concentrate grades of 10% at a dosage higher than 100 g/t (the most efficient dosage for xanthates) in BM ore when the grind size was at P80:106 µm. The cumulative copper grades in the following order with the collector need at the highest dosage (120 g/t) was SIBX > PAX: SEX > SIPX whilst at the lowest dosage of 40 g/t was SIPX > SIBX > SEX > PAX (Harris, 1984). This clearly shows that the concentrations and dosages of these thiol xanthates play a critical role in the recovery, as they have a significant effect on the selectivity of BM ore.

Xanthates play an important role in the recovery of minerals of interest since these collectors are organic compounds that selectively adsorb on certain mineral surfaces. This effect could be monitored by sudden changes in the absorbance values at 300 nm. The UV-spectrophotometer was used to monitor changes in absorbance that could be related to surface adsorption at a pH value of 9. UV-visible absorption spectra were recorded at various dosages for each thiol collector (SEX, SIBX, SIPX, and PAX) and flotation times of 3, 7, and 20 min (Fig. 8). The maximum absorption peak for xanthate was observed around 300 nm. The highest intensity peak located at 300 nm corresponds to the xanthate anion ($ROCS_2$) [28]. The peak at 300 nm indicates a trace of normalized chemisorbed xanthate remaining on the surface of the mineral. The differences in absorption intensity at various times show how each xanthate was adsorbed in the mineral, PGM ore. Lower absorption peaks (with no distinct separation) were observed for four xanthates at dosages of 40 g/t. This may indicate xanthates were quickly adsorbed to the surface of the mineral within flotation times. However, at higher dosages of 60–120 g/t, the absorption peaks of xanthates showed distinct peaks that could indicate the residual xanthate in the pulp solution.
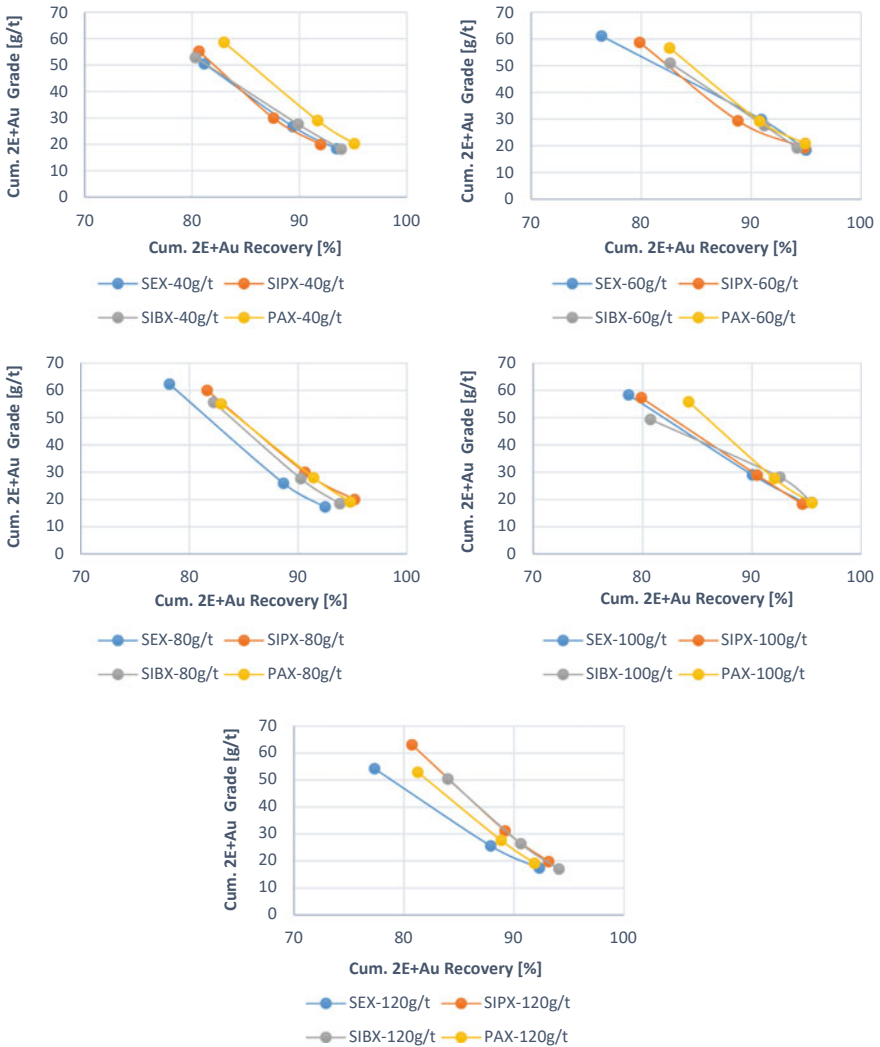
Fig. 6 Cumulative 2E + Au grade versus cumulative 2E + Au recoveries obtained with thiol collectors

The key issue for the current study is to see how these thiol collectors are adsorbed in order to understand which mechanism is at play under the conditions used in this study. The main issue in developing a mechanism for these thiol collectors lies in the absorption process, viz., an ion-exchange mechanism or chemical adsorption [29]. Furthermore, the UV spectra show changing absorbance with lower intensities around 210, which may indicate the formation of the undesirable species carbon disulphide (CS_2), a product of hydrolysis [1]. In addition, the generation of carbon disulphide has been reported to be lower in alkaline aqueous solutions. Oxidation
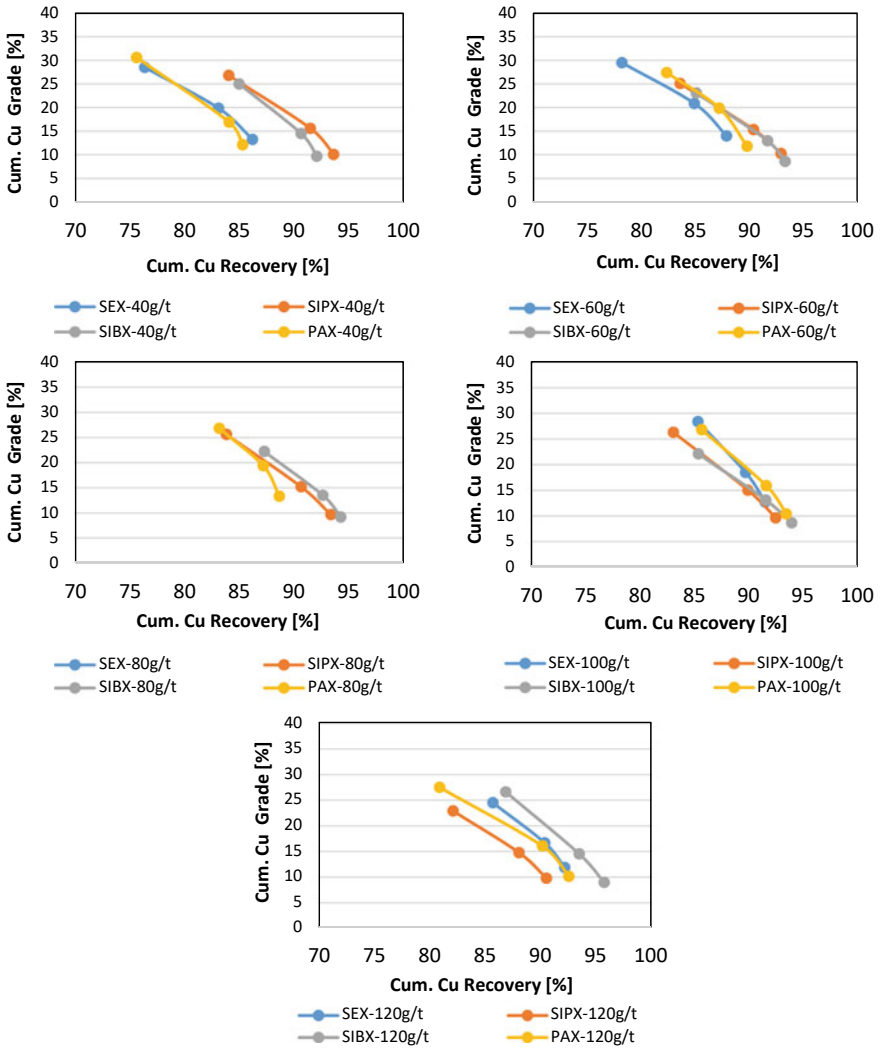
Fig. 7 Cumulative copper grade versus cumulative copper recoveries obtained with thiol collectors

is less likely to occur under neutral conditions, and the collector is more easily adsorbed on the mineral surface at a pH of around 8, as high flotation recoveries (> 90%) at higher dosages were achieved in this study (see Fig. 4) [5, 30]. Similar to UV-Vis results obtained using PGM ore, the UV-Vis results of BMs using thiol xanthates show shoulder peaks associated with the absorbance of xanthate species around 300 nm (Fig. 9). This shoulder peak was consistent with thiol dosages of 40 g/t to 120 g/t. No overall distinct peaks were observed for BMs, as this might indicate that they are quickly adsorbed onto the mineral surface. The absorptivity was more

pronounced towards BM than PGM ores based on low-intensity peaks around 300 nm. It appears BM ore may have more active sites on the mineral surface that suggest thiol collectors were more selectively adsorbed. However, based on the flotation recovery results (see Fig. 5), iso-alkyl xanthate was more quickly adsorbed to the surface than other collectors at dosages of 40 g/t to 80 g/t, based on recoveries close to 95%. The mechanism of mineral-collector bonding depends on the collector type, mineral surface nature, and charge and can result in the collector being chemisorbed [8]. The decrease of peaks at 300 nm for PGM ore may suggest slow adsorption rates. However, these rates did not negatively affect flotation performance, as high recoveries were observed for both ores.

The FTIR spectra of the various flotation concentrate and tailings samples obtained using the lowest and highest dosages of thiol xanthates are shown in Figs. 10 and 11. Little et al. [31] studied the adsorption of xanthates on metals and their sulphide minerals by assigning spectral frequencies to the vibrational modes of the xanthate group. The $C = S$ stretching mode associated with xanthates has been reported in the range of 1020–1070 cm^{-1} while the stretching vibrations of the C–O–C linkage are in the range of 1110–1140 cm^{-1}. Thiol collectors primarily consist of two functional groups in their structure, namely, ionic and hydrocarbon chains, where the first functional group is adsorbed by chemisorption or electrostatic interaction and the second functional group is responsible for the hydrophobic character given to the mineral surface [5, 6]. The presence of $C = S$ stretching mode and stretching vibrations of the C–O–C linkage may indicate an ionic portion of the xanthate that adsorbed to the minerals that were collected as concentrates. The presence of these bands close to 1000 cm^{-1} may be indicative of the interaction between the xanthate and mineral surface where chemical adsorption of the collector may have occurred on ore sites. Silicate (Si–O) vibration features associated with silica (quartz) were characterized by vibrational bands in the region from 670 to 820 cm^{-1} [32]. The FTIR spectra of the various samples show the consistency of functional groups and minerals at the lowest and highest dosages of xanthate in the flotation process. However, the functional groups observed in the samples in the tails at 40 g/t and 120 g/t show decreased intensity after flotation, especially for PGMs, which may indicate less presence of xanthates in the tailings between 800 and 1200 cm^{-1}. These changes should be expected since high recoveries (close to 95%) were obtained from using thiol xanthates for PGM ore. Similar trends were also observed for the FTIR spectra of flotation concentrate samples obtained at the lowest and highest dosages for the base metal ore shown in Figs. 12 and 13. However, the FTIR spectra show relative peaks in the regions close to 1000 cm^{-1} in the tailings, and there is a presence of a changing peak observed around 1400 cm^{-1}, observed in the concentrate samples as well. The observed band around 1400 cm^{-1} is characterized by asymmetric stretching of carbon–oxygen (C–O) bonds [32]. These results show the effect of the thiol collector on ores, especially for the base metals, as seen from the UV-Vis
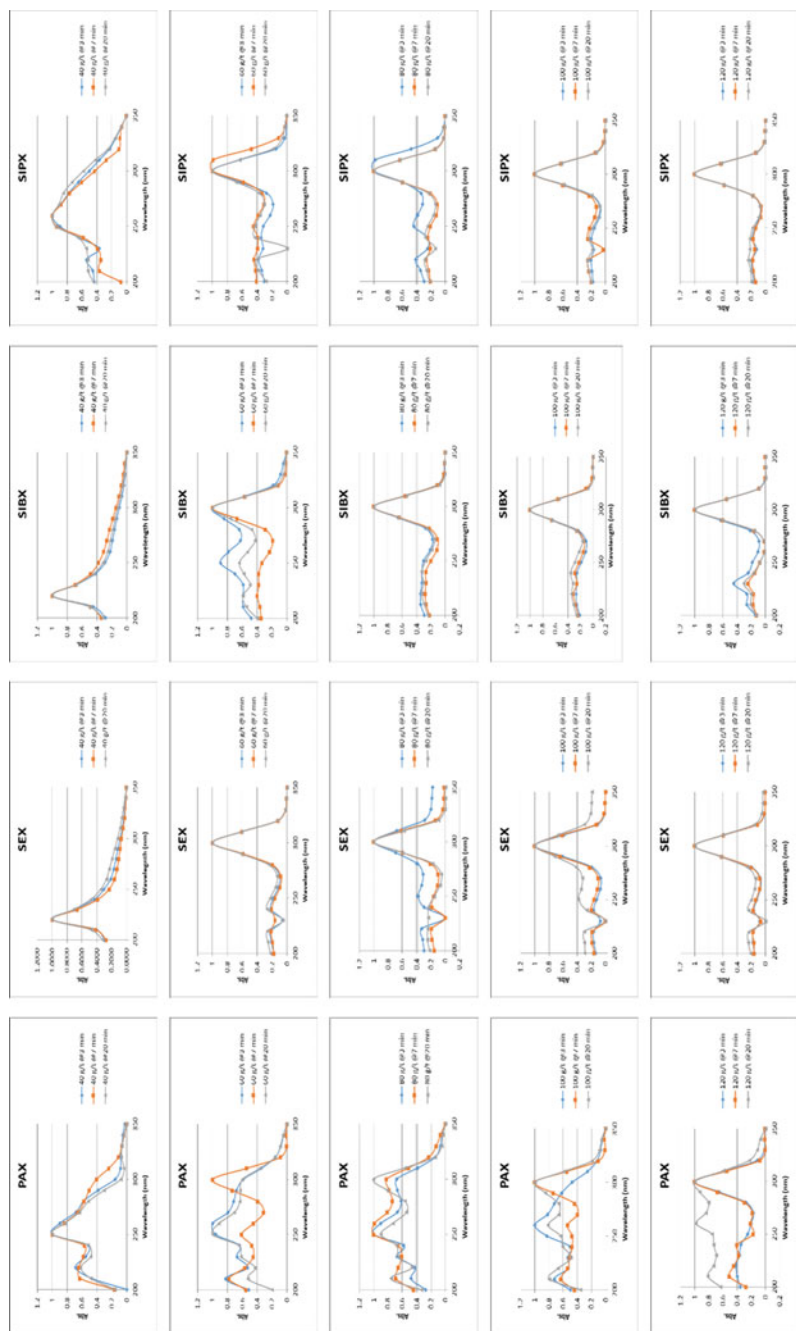
Fig. 8 UV absorbance curves of thiol xanthate-PGM system at various times
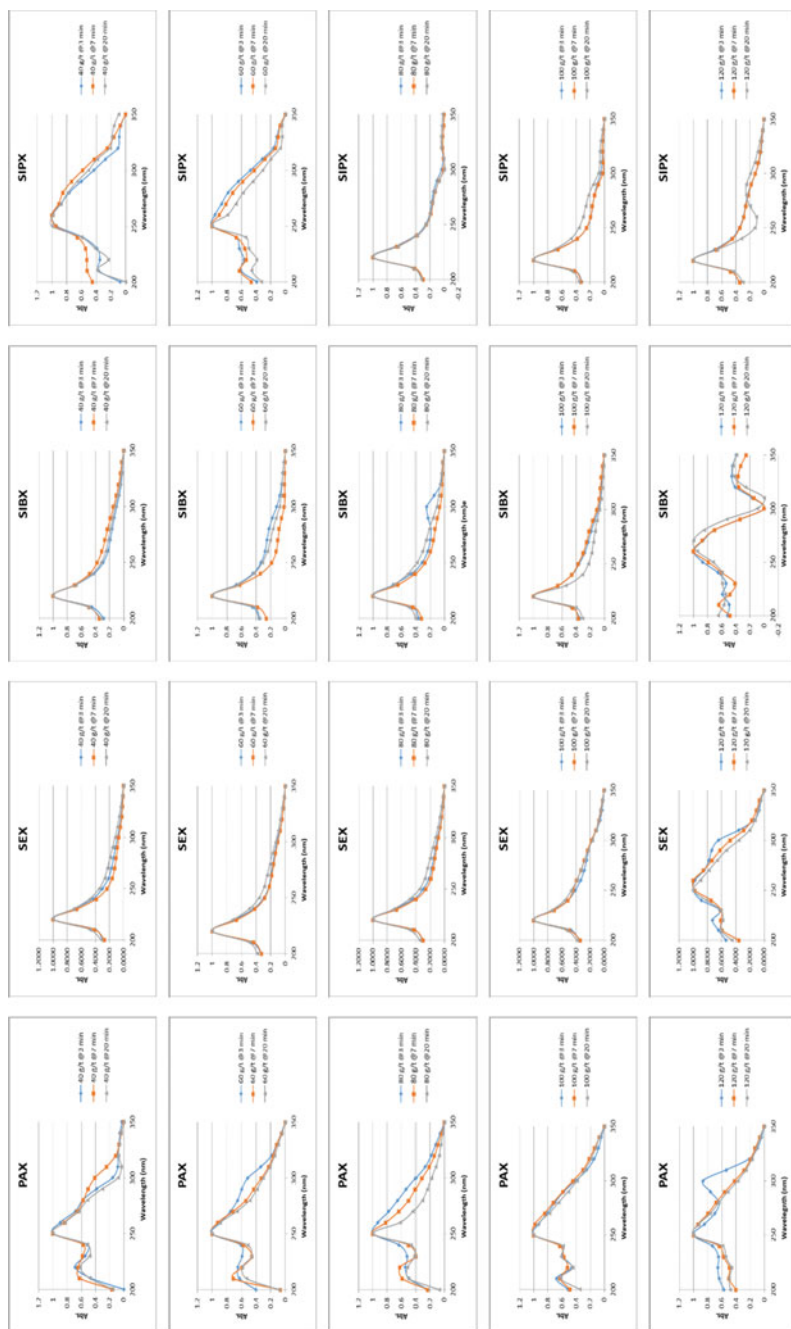
Fig. 9 UV absorbance curves of thiol xanthate-BMS system at various times
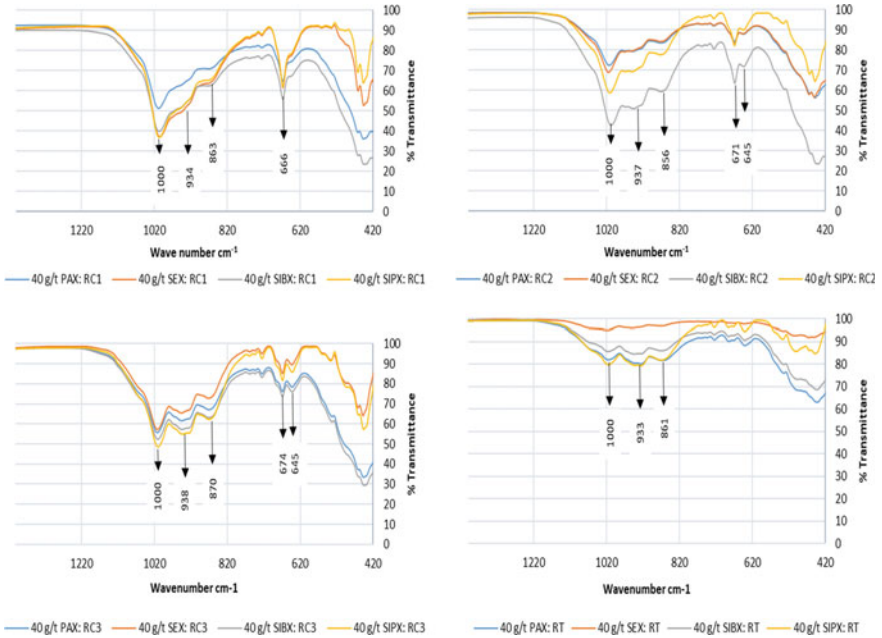
Fig. 10 FTIR spectra of PGM flotation concentrate samples obtained at 40 g/t dosage

results that xanthates in the pulp were quickly adsorbed when compared to the flotation of PGMs. The thiol collector is highly selective towards the base metal ores, as they quickly react with them when compared with PGM ore.
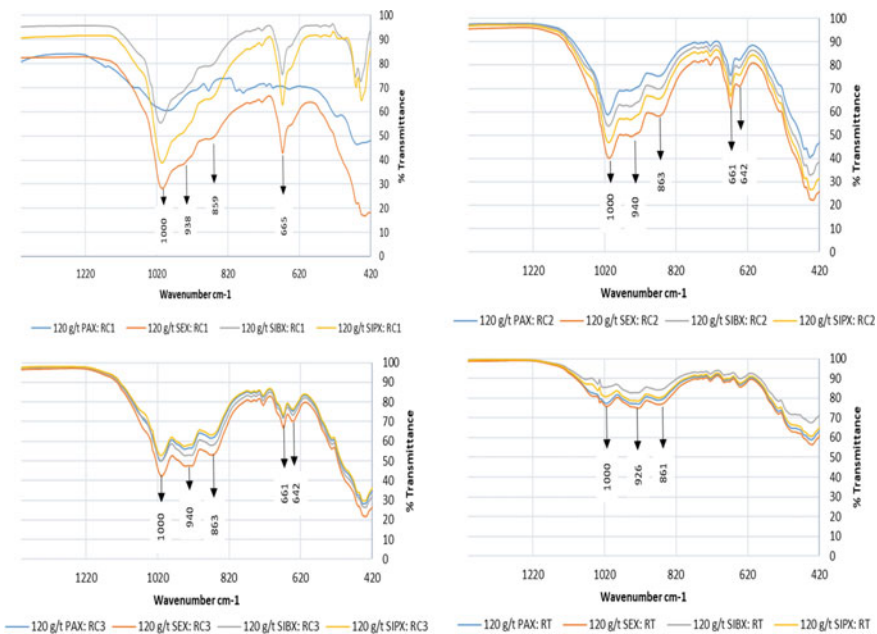
Fig. 11 FTIR spectra of PGM flotation concentrate samples obtained at 120 g/t dosage
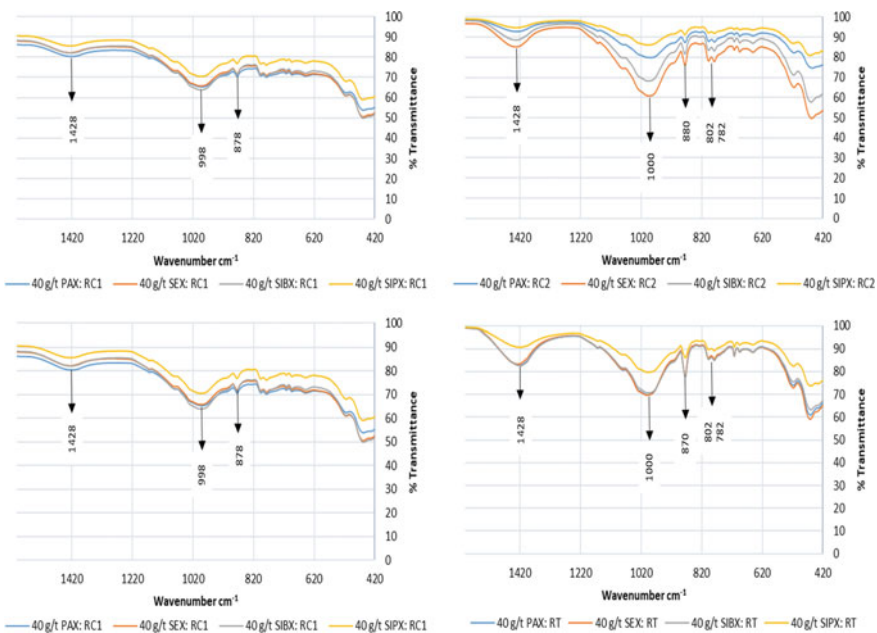
Fig. 12 FTIR spectra of base metal flotation concentrate samples obtained at 40 g/t dosage
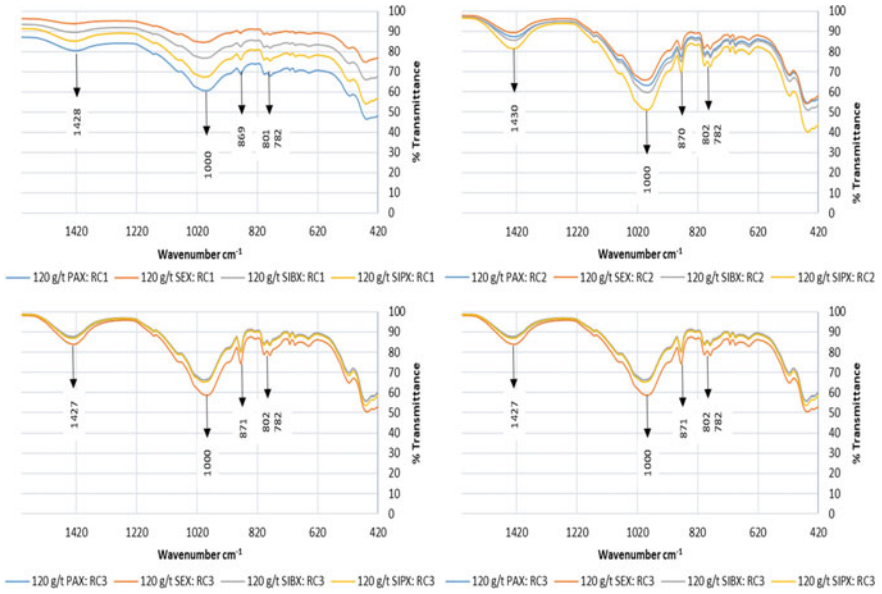
Fig. 13 FTIR spectra of base metal flotation concentrate samples obtained at 120 g/t dosage

Conclusions

The current study investigated the effects of thiol collectors on the flotation recovery of PGM and BM ores at pH 9. The flotation results show thiol xanthates were effective for both BM and PGM ores, as high cumulative recoveries were achieved with increasing dosages. From the results obtained, it can be concluded that thiol collectors (SIPX, SEX, SIBX, and PAX) were selective towards PGMs and BMs as similar recoveries were obtained. However, SIBX was found to be the best-performing xanthate based on consistency when compared to other xanthates tested for both PGM and BM ores. This shows that the chemical structure of xanthates can influence cumulative recoveries to a greater degree due to steric effects. However, further studies are required to link laboratory-scale investigations with industrial-scale results for better optimization of the froth flotation process. In addition, the measurements of xanthate absorbance could assist with future studies in terms of monitoring concentration levels in the pulp solution for better flotation performance, such as efficient dosing of xanthate.

Conflict of Interest The authors declared no conflict of interest.

References

1. Elizondo-Álvarez MA, Uribe-Salas A, Bello-Teodoro S (2021) Chemical stability of xanthates, dithiophosphinates and hydroxamic acids in aqueous solutions and their environmental implications. Ecotoxicol Environ Saf 207. https://doi.org/10.1016/j.ecoenv.2020.111509
2. Hanson JS, Fuerstenau DW (1991) The electrochemical and flotation behavior of chalcocite and mixed oxide/sulfide ores
3. Huang X, Huang K, Jia Y, Wang S, Cao Z, Zhong H (2019) Investigating the selectivity of a xanthate derivative for the flotation separation of chalcopyrite from pyrite. Chem Eng Sci 205:220–229. https://doi.org/10.1016/j.ces.2019.04.051
4. Silvester E, Truccolo D, Hao FP (2002) Kinetics and mechanism of the oxidation of ethyl xanthate and ethyl thiocarbonate by hydrogen peroxide. J Chem Soc Perkin Trans 2(9):1562–1571. https://doi.org/10.1039/b204222c
5. Chander S, Fuerstenau DW (1975) Effect of potential on the flotation and wetting behavior of chalcocite and copper. Trans Soc Min Eng AIME 258(4):284–285
6. Ralston J (1994) The chemistry of galena flotation: principles & practice
7. Harris GH (1998) Xanthates. In: Kirk-Othmer encyclopedia of chemical technology, vol 25. Wiley, New York, pp 713–734
8. Bradshaw DJ (1997) Synergistic effects between thiol collectors used in the flotation of pyrite. University of Cape Town
9. Adkins SJ, Pearse MJ (1992) The influences of collector chemistry on kinetics and selectivity in base-metal sulphide flotation
10. Cawthorn RG (1999) The platinum and palladium resources of the bushveld complex. S Afr J Sci 95:481–489

11. McFadzean B, Pani S, Wiese J, O'Connor CT (2015) The interactive effects of chemical and process parameters on the flotation performance of a UG2 ore. Miner Eng 70:92–98. https://doi.org/10.1016/j.mineng.2014.08.016

12. Moja MG, Otunniyi IO, Mendonidis P (2020) Thiol collector blends for improved PGM recovery: a case study of a UG2 ore. J South Afr Inst Mining Metall 120. https://doi.org/10.17159/2411

13. Sinisalo P, Lundström M (2018) Refining approaches in the platinum group metal processing value chain—a review. Metals 8(4). https://doi.org/10.3390/met8040203

14. Schouwstra RP, De Vaux DV, Snyman Q (2017) Further development of a chemistry proxy for geometallurgical modelling at the Mogalakwena mine. J South Afr Inst Min Metall 117(7):719–726. https://doi.org/10.17159/2411-9717/2017/v117n7a13

15. O'Connor C, Alexandrova T (2021) The geological occurrence, mineralogy, and processing by flotation of platinum group minerals (PGMs) in South Africa and Russia. Minerals 11(1):1–15. https://doi.org/10.3390/min11010054

16. Wali A, O'Connor CT, McFadzean B (2023) An investigation into the use of xanthate, trithiocarbonate and thiourea collectors on the flotation of sperrylite (PtAs2). Miner Eng 199. https://doi.org/10.1016/j.mineng.2023.108103

17. Langa NTN, Adeleke AA, Mendonidis P, Thubakgale CK (2014) Evaluation of sodium isobutyl xanthate as a collector in the froth flotation of a carbonatitic copper ore. Int J Indl Chem 5(3–4):107–110. https://doi.org/10.1007/s40090-014-0025-5

18. Özün S, Ergen G (2019) Determination of optimum parameters for flotation of galena: effect of chain length and chain structure of xanthates on flotation recovery. ACS Omega 4(1):1516–1524. https://doi.org/10.1021/acsomega.8b02841

19. Wiese J, Harris P, Bradshaw D (2005) Investigation of the role and interactions of a dithiophosphate collector in the flotation of sulphides from the Merensky reef. Miner Eng 791–800. https://doi.org/10.1016/j.mineng.2005.01.032

20. Ackerman PK, Harris GH, Klimpel RR, Aplan FF (1987) Evaluation of flotation collectors for copper sulfides and pyrite, III. Effect of xanthate chain length and branching

21. Ramachandra S, Leja J (2004) Surface chemistry of froth flotation. Reagents and mechanisms, 2nd ed, vol 2. Academic/Plenum Publishers, New York

22. Bilal M et al (2022) The challenges and prospects of recovering fine copper sulfides from tailings using different flotation techniques: a review. Minerals 12(5). https://doi.org/10.3390/min12050586

23. Mankosa MJ, Kohmuench JN, Christodoulou L, Luttrell GH (2016) Recovery of values from a porphory copper tailings stream

24. Mpongo MK, Siame E (2006) Effect of collector, frother and depressant addition on the copper recovery and concentrate grade of the Nchanga underground scavenger circuit of Konkola copper mine-Zamnbia

25. Wills BA, Napier-Munn T, Julius Kruttschnitt Mineral Research Centre (2006) Wills' mineral processing technology : an introduction to the practical aspects of ore treatment and mineral recovery. Elsevier/BH

26. Wark IW, Cox AB (1934) Principles of flotation, I. An experimental study of the effect of xanthates on contact at mineral surfaces. Trans. AIME 112:189–244

27. Neethling SJ, Cilliers JJ (2012) Grade-recovery curves: a new approach for analysis of and predicting from plant data. Miner Eng 36–38:105–110. https://doi.org/10.1016/j.mineng.2012.02.018

28. Rao SR (2004) Reagents and mechanisms. In: Surface chemistry of froth flotation. Springer, New York

29. Montalti M, Fornasiero D, Ralston J (1991) Ultraviolet-visible spectroscopic study of the kinetics of adsorption of ethyl xanthate on pyrite

30. Fairthorne G, Fornasiero D, Ralston J (1997) Interaction of thionocarbamate and thiourea collectors with sulphide minerals: a flotation and adsorption study. Int J Miner Process 50:227–242

31. Little LH, Poling GW, Leja J (1961) Infrared spectra of xanthate compounds. Can J Chem 39:745–754
32. Nyembwe KJ, Fosso-Kankeu E, Waanders F, Nyembwe KD (2019) Structural, compositional and mineralogical characterization of carbonatitic copper sulfide: run of mine, concentrate and tailings. Int J Miner Metall Mater 26(2):143–151. https://doi.org/10.1007/s12613-019-1718-8

Part IV
Separation and Purification

Hydrometallurgical Recovery of Zinc from Municipal Solid Waste Incineration Fly Ash

Rajiv Ranjan Srivastava, Sadia Ilyas, Hyunjung Kim, Dilip Kumar Rajak, Pankaj Pathak, Yuti Desai, and Vinay Kumar Singh

Abstract The recovery of heavy metals from municipal solid waste incinerated fly ash (MSW-IFA) before its final disposal is highly desirable for sustainable waste management and resource recovery. Recycling of zinc via leaching-solvent extraction techniques has been studied, therefore yielding > 90% efficiency of zinc dissolution at a H_2SO_4 concentration of 1.5 mol/L, a temperature of 90 °C, a S/L ratio of 150 g/L, a time of 2 h, and a stirring speed of 300 rpm. Further, zinc was efficiently extracted using 0.6 mol/L D2EHPA at an equilibrium pH of 2.0 and an organic-to-aqueous phase ratio of 1. Finally, the highly pure zinc solution could be quantitatively stripped in a solution containing 1.5 mol/L H_2SO_4. This could lead to a circular economy of zinc with MSW-IFA as a possible secondary source.

R. R. Srivastava (✉)
Center for Advanced Chemistry, Institute of Research and Development, Duy Tan University, Da Nang 550000, Vietnam
e-mail: r2.srivastava@gmail.com

Resource Management, Faculty of Natural Sciences, Duy Tan University, Da Nang 550000, Vietnam

S. Ilyas · H. Kim
Department of Earth Resources and Environmental Engineering, Hanyang University, Seongdong-Gu, Seoul 04763, Republic of Korea

D. K. Rajak
Department of Chemical Science and Engineering, Kathmandu University, Dhulikhel 45200, Nepal

P. Pathak
Resource Management Lab, Department of Environmental Science and Engineering, SRM University-AP, Amaravati, Andhra Pradesh 522502, India

Y. Desai · V. K. Singh
Department of Environmental Studies, Faculty of Science, The Maharaja Sayajirao University of Baroda, Vadodara, Gujarat 390002, India

V. K. Singh
Department of Chemistry, Faculty of Science, The Maharaja Sayajirao University of Baroda, Vadodara, Gujarat 390002, India

Introduction

Rapidly increasing urbanization is causing a large generation of solid waste, which is expected to reach 10 billion by 2050. This has been foreseen as a major issue in their sustainable management [1, 2]. As per the increasing global volume, municipal solid waste (MSW) is also a great matter of concern in India, which generates 119.1 g/day/capita of solid waste with the world's largest population of 1.4 billion people [3]. More than 56 million metric tons/annum of MSW generation in India with a yearly growth rate of 5% has been predicted [4]. With growing environmental concerns, landfilling MSW is no longer a sustainable waste management process [5], and incineration has become more attractive in recent years. The possible waste volume reduction up to 90% and mass reduction up to 75% [6] along with the parallel waste-to-energy generation have been advantageous to the incineration process [7, 8]. However, the inevitable generation of about 20% incinerated fly ash (IFA) is worrisome [9] due to the heavy metals therein, which include Pb, Zn, Cu, Cd, Ni, As, etc., along with Cl^- and SO_4^{2-}, and organic toxicants, viz., furans, dioxins, etc. [10, 11].

The presence of heavy metals makes landfill disposal difficult and is also seen as their loss in value, which should be taken back into the system by the resource circulation. Due to the significant contents of Zn and Cu types of valuable metals, IFA has been considered a potential resource to be processed for metals' recovery [12], despite their toxicity in the waste material [13, 14]. Although they have been used for H_2S removal, thermochemical energy storage material, wastewater treatment, and zeolite-based catalysts [5, 8, 15], the potential release of heavy metals must be minimized before IFA disposal [5, 16]. The environmental guidelines in several countries clearly state that the IFA cannot be used for direct construction purpose [17], and the heavy metals should be mandatorily recovered before disposal [18].

Since hydrometallurgical tools have gained traction for heavy metal recovery from primary minerals [19] and waste materials [20, 21], they are also actively employed to treat IFA. The processes, namely, FLUWA and FLUWA-FLUREC, are feasible to recover heavy metals at a higher scale [15], wherein the acid generated by a wet flue-gas cleaning system is used as the lixiviant medium. In the FLUWA process, the acid or alkaline scrub water is slurried with IFA to react in several cascade reactors, then the slurry is filtered and the leach liquor undergoes the desired metal separation and recovery process. It is noteworthy to mention that the recovery of heavy metals from IFA does vary depending upon the type of metal and the mineral composition of that metal, as well as factors like waste input for incineration [1, 22]. Moreover, the elemental contents of IFA differ not only on a seasonal basis but also vary from one facility to another [22]. Hence, a particular process is not always suitable for all types of MSW-IFA, and different routes should be explored for heavy metals' recovery.

In this study, we performed sulfuric acid leaching to leach Zn while keeping Pb undissolved in the sulfate medium. Subsequently, Zn was extracted using di-2-ethyl-hexyl phosphoric acid (D2EHPA) to make it a concentrated and high-purity end product.

Experimental

One of the incineration facilities located in western India supplied the MSW-IFA sample. The sample was dried and ball milled to collect the homogenized particles of size -100 mesh. The wet chemical digestion performed for analysis purposes revealed the metal contents in the sample to be 3.1% Zn, 1.2% Pb, 0.006% Co, and 0.01% Cd using atomic absorption spectroscopy (3500 AAS, Thermo Scientific), along with 4.1% S (analyzed by a CHNS analyzer, 2400 series II, PerkinElmer). The mineral composition of the sample was analyzed using an X-ray diffractogram (XRD, D/MAX 2200, Rigaku) using Cu-kappa at a scan speed of 5 degrees per minute. XRD analysis (refer to Fig. 1) revealed that the presence of zinc was both $ZnSO_4$ (JCPDS file no. 72-1249) and ZnO (JCPDS file no. 79-0206), while the mineral phase of lead was identified to be anglesite ($PbSO_4$, JCPDS file no. 36-1461). The low intensity and amorphous-type peaks, along with a few metallic weight fractions obtained in chemical analysis, reveal the major composition of ashes and dust particles in the IFA sample.

All the leaching tests were performed at a 100-mL scale in a 250 mL glass beaker covered with watch glass under a constant magnetic stirring of 300 rpm. For acid leaching, H_2SO_4 (98%, s d fine-chem limited, India) was used to prepare the desired concentration of acid and pre-heated at a desired temperature using a hot-plate cum magnetic stirrer (Remi-2MLH). After the completion of leaching, the

Fig. 1 XRD pattern of the MSW-IFA sample used in this study
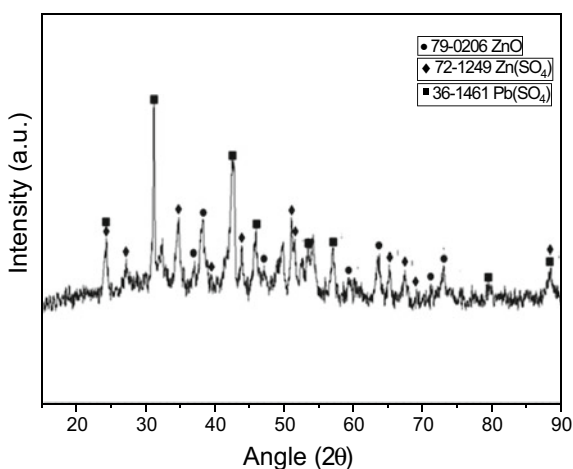
slurry was filtered using a vacuum filter, and the filtrate was collected after washing with 10 mL of hot water. The thus collected filtrate was analyzed after a proper dilution in 4.0 N HCl solution (SRL, India) using AAS to determine the metal contents therein and then the leaching efficiency was calculated as follows:

$$\text{Leaching, \%} = \left\{ \left(1 - \frac{C_{LL}}{C_0} \right) \times 100 \right\} \tag{1}$$

where C_{LL} = metal concentration in leach liquor and C_0 = initial concentration in IFA, whose ratio can directly express as the leaching efficiency of heavy metals.

Further, the solvent extraction of Zn was studied using D2EHPA (Sigma-Aldrich, 97% pure) of the desired concentration prepared in distilled kerosene of 30 mL volume into a 100-mL separatory funnel and contacted for 5 min with the same volume of leach liquor at an organic-to-aqueous (O/A) ratio = 1. After settling of both phases (in 10 min), the raffinate was analyzed using AAS to determine the metal contents, and the metal in the organic phase was determined by knowing the distribution coefficient (D) as follows:

$$D = \frac{CE_{org}}{CE_{aq}} \tag{2}$$

$$\text{Extraction, \%} = \left\{ \frac{\left(D \times \frac{V_{org}}{V_{aq}} \right)}{\left(D \times \frac{V_{org}}{V_{aq}} + 1 \right)} \right\} \times 100 \tag{3}$$

where CE_{org} and CE_{aq} are post-extraction metal concentrations, and V_{org} and V_{aq} are volumes of the organic and aqueous phases, respectively. Further, the zinc extracted organic phase was contacted with different concentrations of H_2SO_4 solution at an O/A phase ratio of 1, whereas for the recovery of the final product, back-extraction was performed at a higher O/A ratio of 5, yielding pure $ZnSO_4$ solution.

Results and Discussion

Effect of Water and H_2SO_4 Concentrations

As per the XRD analysis of MSW-IFA, the major mineral phase of $ZnSO_4$ and ZnO seems either to be water soluble or dissolved in an acid solution. Whereas, $PbSO_4$ is neither water soluble nor it can be solubilized in sulfuric acid due to the insolubility of lead in sulfate media [23, 24]. Hence, the selectivity in leaching was hypothesized with water and sulfuric acid and tested. For this, the leaching behaviour of zinc and lead was investigated in 0–2.0 mol/L H_2SO_4 solutions at a fixed S/L ratio of 100 g/L for 1 h in room temperature of 30(± 2) °C. Results shown in Fig. 2
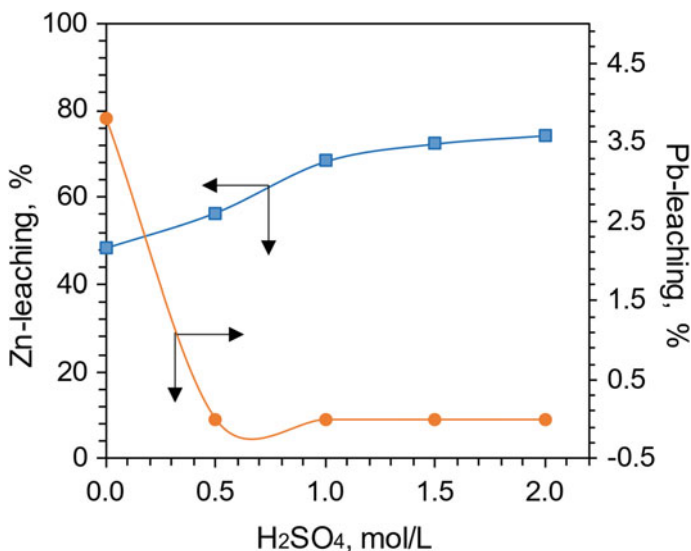
Fig. 2 Effect of sulfuric acid concentration on zinc and lead leaching, while the experimental condition was maintained to be S/L ratio = 100 g/L, Temperature = 30(±2) °C, time = 1 h, and stirring speed = 300 rpm

depict that about a-half of the zinc from its total content of 3.1% was water soluble which can be referred to ZnSO$_4$. Whereas, only a 3.8% lead could be dissolved in water confirmed its major presence as insoluble anglesite (PbSO$_4$). The addition of sulfuric acid could mobilize more zinc from the MSA-IFA and reached the maximum above 74% using 2.0 mol/L H$_2$SO$_4$ which was ~ 56% in 0.5 mol/L H$_2$SO$_4$ solution. This behaviour showed that the mineral phase of ZnO dissolved in sulfuric acid along with the simultaneous conversion of a little soluble lead (2.8% in water alone) into insoluble PbSO$_4$ (K$_{sp}$ = 1.6 × 10^{-8}). Because of a little progress in leaching efficiency (which was only 2.6% of zinc) between the acid concentrations used of 1.5 mol/L and 2.0 mol/L H$_2$SO$_4$, we optimized 1.5 mol/L H$_2$SO$_4$ to be used in the next sets of leaching experiments.

Effect of Temperature

The leaching behavior of heavy metals from MSW-IFA in 1.5 mol/L H$_2$SO$_4$ was examined at different temperatures between 30 and 90 °C for 1 h duration. The results shown in Fig. 3 revealed significant progress in the leaching efficiency of zinc. Zinc dissolution increased from ~ 74% to 88% when the temperature was raised from 30 to 90 °C. This increase in zinc leaching at a higher
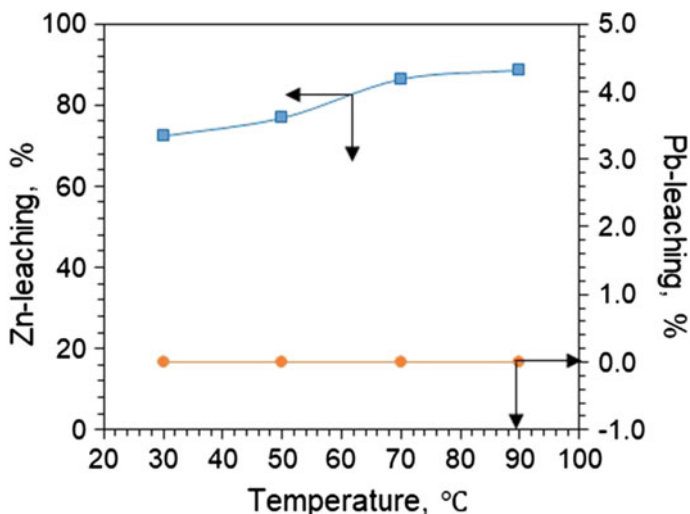
Fig. 3 Effect of leaching temperature on metals leaching from MSW-IFA, while the experimental condition was maintained to be H_2SO_4 concentration = 1.5 mol/L, S/L ratio = 100 g/L, time = 1 h, and stirring speed = 300 rpm

temperature can be ascribed to the increase in dissolution kinetics at a higher temperature [25]. This can also be understood as the leaching process shifts from the diffusion-controlled to the chemically controlled region with a variance in temperature [11, 16]. No lead could be leached at any temperature indicating the formation of insoluble $PbSO_4$ that remained with the leached residue. Due to the maximum leaching efficiency obtained at 90 °C, this temperature was optimized.

Effect of Time

To increase zinc leaching efficiency from MSW-IFA, the effect of time was investigated with prolonged leaching up to 2 h in a 1.5 mol/L H_2SO_4 solution. The results shown in Fig. 4 depicted that time has a greater influence on zinc dissolution in the acidic solution. It can be seen that initially zinc leaching was only ~ 37% in the starting 10 min of duration along with 1.6% lead analyzed in the leach liquor. In the next 20 min of leaching, zinc dissolution increased to reach 66% but the lead was totally suppressed to nil. Further, 120 min of leaching yielded ~ 94% of zinc in the leach liquor without dissolving lead in H_2SO_4. The behavior of zinc dissolution clearly indicated that prolonged leaching was favorable might be due to the breaking of the passivated layer at the reaction interface between the MSW-IFA particle and acid solution of the bulk [16]. On the other hand, the leaching of water-soluble $ZnSO_4$ can be understood faster in comparison to the leaching of ZnO. Not achieving a 100%
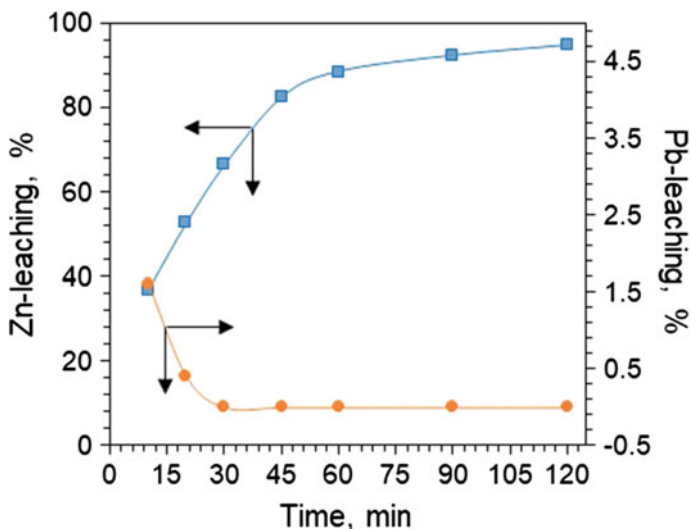
Fig. 4 Effect of time on metals leaching from MSW-IFA, while maintaining the experimental condition H_2SO_4 concentration $= 1.5$ mol/L, Temperature $= 30(\pm2)$ °C, S/L ratio $= 100$ g/L, and stirring speed $= 300$ rpm

leaching of zinc can be corroborated by the possible presence of some ferrite albeit it was not confirmed by XRD (as the iron content was very less in the sample).

Effect of S/L Ratio

Leaching behaviour of heavy metals from MSW-IFA in 1.5 mol/L H_2SO_4 was examined at different S/L ratios in a range from 50 to 250 g/L. The results in Fig. 5 show that a maximum zinc leaching ~ 96% was achieved when the MSW-IFA was charged at a S/L ratio of 50 g/L. Zinc dissolution then slightly decreased for an increase in pulp density, reaching about 94% at the S/L $= 100$ g/L. The leaching efficiency was observed to further decrease for a higher S/L ratio (~84% at S/L $= 200$ g/L and reaching up to 76% at S/L $= 250$ g/L). This behaviour can be ascribed to the decrease in surface area available per unit volume for the leaching process at increasing pulp densities [16, 23]. Hence, S/L ratio of 150 g/L was optimized here, yielding 4.2 g/L zinc in the leach liquor.
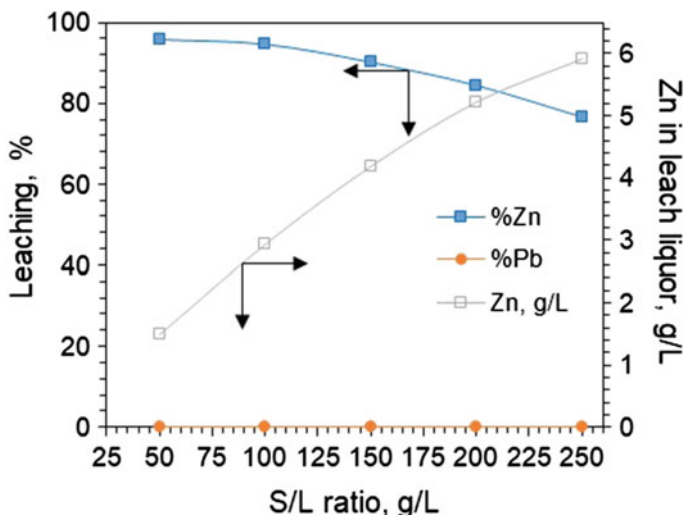
Fig. 5 Effect of S/L ratio on metals leaching from MSW-IFA, while the experimental condition was maintained to be H_2SO_4 concentration = 1.5 mol/L, Temperature = 30($\pm$2) °C, time = 2 h, and stirring speed = 300 rpm

Solvent Extraction of Zinc

The solvent extraction of zinc from leach liquor was conducted using 0.7 mol/L D2EHPA at different equilibrium pH in the range of 0.2–5.2, while keeping an O/A ratio = 1. Results in Fig. 6a showed zinc extraction increased from 7 to 95% by increasing the equilibrium pH from 0.2 to 2.3. Based on the extraction data, a graph was plotted for log[D] versus equilibrium pH which showed that zinc distribution greatly changes between −1.16 and 1.26, while the slope value obtained from the straight line of the plot (Fig. 6b) indicated that about 2 mol of proton exchanged with one mole of zinc ion in the extraction process. Hence, zinc extraction with D2EHPA, $\overline{(HA)_2}$ can be written as

$$Zn^{2+} + \overline{2(HA)_2} = \overline{Zn(H.HA)_2} + 2H^+ \tag{4}$$
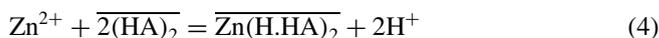
The equilibrium constant (K_{ex}) for Eq. (4) in terms of distribution coefficient (D) can be written in simplified form, as follows:

$$K_{ex} = [D]_{Zn} * \left(\frac{[H^+]^2}{[\overline{(HA)_2}]^2} \right) \tag{5}$$

Rearranging and taking the logarithm of Eq. (5) comes as

$$\log[D]_{Zn} = \log K_{ex} - 2\log[H^+] + 2\log[\overline{(HA)_2}] \tag{6}$$
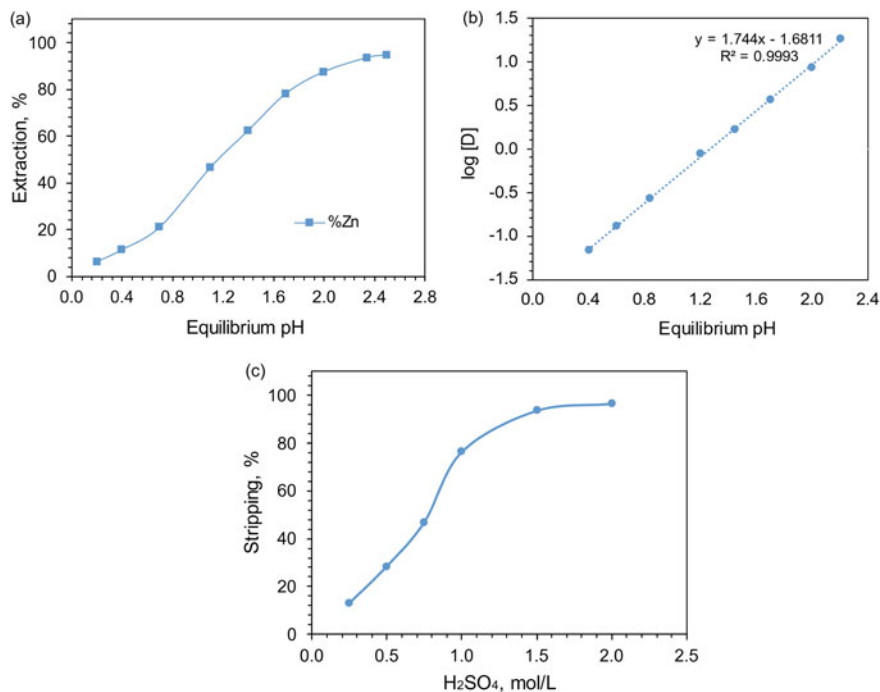
Fig. 6 Effect of equilibrium pH on (**a**) zinc extraction efficiency with D2EHPA while contacted at an O/A ratio of 1 (**b**) and plot against the logarithmic distribution of zinc. (**c**) The stripping efficiency of zinc with respect to acid concentration contacted at an O/A ratio of 1

Further, the recovery of high pure zinc solution from the loaded organic was carried out by contacting with the acid solution of different concentrations (ranging $0.25-2.0$ mol/L H_2SO_4) at an $O/A = 1$. As can be seen from Fig. 6c, the stripping efficiency of zinc increased from 12.8% to 97% with increasing acid concentrations from 0.25 mol/L to 2.0 mol/L. The stripping reaction can be written as

$$\overline{Zn(A.HA)_2} + H_2SO_4 = ZnSO_4 + \overline{2(HA)_2} \tag{7}$$
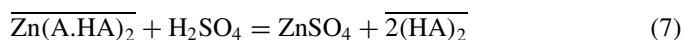
Conclusions

This study demonstrated the removal and recovery of zinc from MSW-IFA as a sustainable waste management technique for not only the recirculation of zinc but also for environmental beneficiation. The sulfuric acid leaching process selectively leached out zinc, leaving lead in residue that yielded > 90% efficiency using an H_2SO_4 solution of 1.5 mol/L at a temperature = 90 °C, S/L ratio = 150 g/L, time

$= 2$ h, and stirring speed $= 300$ rpm. Further, zinc was efficiently extracted using 0.7 mol/L D2EHPA at an equilibrium pH of 2.0 and an O/A ratio of 1. Finally, the high-purity zinc solution was efficiently stripped using a 1.5 mol/L H_2SO_4 solution.

References

1. Ilyas S, Singh VK, Kim H, Srivastava RR (2022) Recovery of metal values by treating the municipal solid waste incineration ashes. In: Pathak P, Palani SG (eds) Circular economy in municipal solid waste landfilling: biomining & leachate treatment: sustainable solid waste management: waste to wealth. Springer International Publishing, pp 253–267
2. Ajorloo M, Ghodrat M, Scott, Strezov JV (2022) Heavy metals removal/stabilization from municipal solid waste incineration fly ash: a review and recent trends. J Mater Cycles Waste Manag 24:1693–1717
3. PARIVESH-CPCB (2012). In: Municipal solid wastes. http://www.cpcbenvis.nic.in/cpcb_newsletter/SOLID%20WASTE.pdf. Accessed 16 Aug 2023
4. CPCB (2022). In: Annual report 2022–21 on implementation of solid waste management rules, 2016. https://cpcb.nic.in/uploads/MSW/MSW_AnnualReport_2020-21.pdf. Accessed 18 Feb 2023
5. Pujara Y, Pathak P, Sharma A, Govani J (2019) Review on Indian municipal solid waste management practices for reduction of environmental impacts to achieve sustainable development goals. J Environ Manage 248:109238
6. Li R, Zhang B, Wang Y, Zhao Y, Li F (2019) Leaching potential of stabilized fly ash from the incineration of municipal solid waste with a new polymer. J Environ Manage 232:286–294
7. Jahromy SS, Jordan S, Azam M, Werner A, Harasek M, Winter F (2019) Fly ash from municipal solid waste incineration as a potential thermochemical energy storage material. Energy Fuels 33(7):5810–5819
8. Tejaswini MSSR, Pathak P, Gupta DK (2022) Sustainable approach for valorization of solid wastes as a secondary resource through urban mining. J Environ Manage 319:115727
9. Dontriros S, Likitlersuang S, Janjaroen D (2020) Mechanisms of chloride and sulfate removal from municipal-solid-waste-incineration fly ash (MSWI FA): effect of acid-base solutions. Waste Manag 101:44–53
10. Chen W, Kirkelund GM, Jensen PE, Ottosen LM (2017) Comparison of different MSWI fly ash treatment processes on the thermal behavior of As, Cr, Pb and Zn in the ash. Waste Manag 68:240–251
11. Ilyas S, Srivastava RR, Kim H (2022) Mobilization of platinum and palladium from exhausted catalytic converters using bio-cyanide and an ionic-liquid as mass transport carriers. Green Chem 24(13):5204–5218
12. Ayres RU, Peiro, LT(2013) Material efficiency: rare and critical metals. Philos Trans Math Phys Eng Sci 371(1986):20110563
13. Ilyas N, Ilyas S, Yousaf S, Zia A, Sattar S (2018) Removal of copper from an electroplating industrial effluent using the native and modified spirogyra. Water Sci Technol 78(1):147–155
14. Ilyas S, Srivastava RR, Singh VK, Chi R, Kim H (2022) Recovery of critical metals from spent Li-ion batteries: Sequential leaching, precipitation, and cobalt–nickel separation using Cyphos IL104. Waste Manag 154:175–186

15. Quina MJ, Bontempi E, Bogush A, Schlumberger S, Weibel G, Braga R, Funari V, Hyks J, Rasmussen E, Lederer J (2018) Technologies for the management of MSW incineration ashes from gas cleaning: new perspectives on recovery of secondary raw materials and circular economy. Sci Total Environ 635:526–542
16. Ilyas S, Srivastava RR, Kim H, Ilyas N (2022) Biotechnological recycling of hazardous waste PCBs using Sulfobacillus thermosulfidooxidans through pretreatment of toxicant metals: Process optimization and kinetic studies. Chemosphere 286:131978
17. CPHEEO (2016). In: Municipal solid waste management manual, part II: the manual. Central Public health and environmental engineering organisation (CPHEEO), Ministry of Urban Development, Government of India. http://cpheeo.gov.in/upload/uploadfiles/files/Part2.pdf. Accessed 6 Aug 2023
18. Swiss Confederation (2015). In: Ordinance on the avoidance and the disposal of waste (Waste Ordinance, ADWO); Swiss Conferderation: Bern, Switzerland, pp 1–46
19. Ilyas S, Srivastava RR, Kim H (2023) Cradle-to-cradle recycling of spent NMC batteries with emphasis on novel Co^{2+}/Ni^{2+} separation from HCl leached solution and synthesis of new ternary precursor. Process Saf Environ Prot 170:584–595
20. Ilyas S, Srivastava RR, Kim H (2023) Green separation of Co^{2+} over Ni^{2+} by split-phosphinate complexation using phosphonium-based ionic liquid as extraction carrier. Environ Chem Lett 21:673–680
21. Ilyas S, Srivastava RR. Jin S, Kim H (2023) Liquid-liquid separation of copper and nickel ammine complexes using phenolic oxime mixture with tributyl phosphate. Geosystem Eng 26(2):58–66
22. Zucha W, Weibel G, Wolffers M, Eggenberger U (2020) Inventory of MSWI fly ash in Switzerland: heavy metal recovery potential and their properties for acid leaching. Processes 8(12):1668
23. Cheema HA, Bhatti IA, Srivastava RR, Jahan N, Zia MA (2022) Dissolution of molybdenite roasting flue dust in sulfuric acid: kinetics and mechanism for molybdenum and rhenium leaching. Chem Pap 76(7):4049–4058
24. Guler E, Seyrankaya A, Cocen I (2011) Hydrometallurgical evaluation of zinc leach plant residue. Asian J Chem 23(7):2879–2888
25. Sattar R, Ilyas S, Kousar S, Khalid A, Sajid M, Bukhari SI (2020) Recycling of end-of-life $LiNi_xCo_yMn_zO_2$ batteries for rare metals recovery. Environ Eng Res 25(1):88–95

Innovative Solvent Extraction Processes for the Separation of Indium, Germanium, and Gallium from Iron

Toni Helbig, Norman Kelly, and Ajay B. Patil

Abstract Germanium, gallium, and indium are valuable elements due to their great economic importance and growing utilization in high-tech and green-tech applications. The exploitation of secondary resources, for example, tailings, slags, or end-of-life products, as well as the application of sustainable biotechnological methods, results in the challenge of separating Fe(III) from In(III), Ge(IV), or Ga(III). With common methods, such as precipitation, the selectivity for In, Ga, and Ge is often insufficient. The application of innovative solvent extraction processes is a promising approach to separate valuable metals from iron in order to make them available for an efficient recovery. In this study, we present the development of extraction methods using amine extractants for the selective separation of Fe(III) from In(III), Ga(III), and Ge(IV) in sulphate solutions. The influence of different parameters, e.g. the pH value and the composition of the organic phase, as well as possibilities to re-extract iron from the loaded organic phase, will be discussed.

Keywords Indium · Germanium · Gallium · Iron removal · Solvent extraction · Amine extractants

T. Helbig (✉) · N. Kelly (✉) · A. B. Patil
Helmholtz Centre Dresden-Rossendorf, Helmholtz Institute Freiberg for Resources Technology, Chemnitzer Straße 40, 09599 Freiberg, Germany
e-mail: tonihelbig@yahoo.de

N. Kelly
e-mail: n.kelly@hzdr.de

A. B. Patil
e-mail: a.patil@hzdr.de

A. B. Patil
Department of Chemistry, Faculty of Science and Mathematics, The University of Jyväskylä, P.O. Box 35, 40014 Jyvaskyla, Finland

Introduction

Many modern technologies, such as touch screens (indium-tin oxide), semiconductors (gallium arsenide), or optical fibers (germanium dioxide), are based on the special properties of indium (In), gallium (Ga), and germanium (Ge). Due to the economic importance and the additional supply risk, the European Union lists Ge and Ga as critical raw materials [1].

To encounter the increasing demand for In, Ga, and Ge, an optimization of the metal recovery from primary production streams and residues as well as the utilization of tailings from former mining activities must be considered. The majority of processes are based on a hydrometallurgical route to recover In, Ga, and Ge from low-concentrated aqueous solutions. A prominent issue during these processes is the separation of the target element from iron (Fe). As a very abundant element, Fe is found in many resources and appears in hydrometallurgical solutions. Hydrometallurgical approaches to recover the target elements are precipitation [2, 3] or extraction processes, such as solvent extraction [4, 5]. However, the selectivity for In, Ge, and Ga is often insufficient in the presence of Fe, especially Fe(III). Also, new biotechnological approaches, which apply siderophores [6] or peptides [7], show only a low selectivity over Fe.

The focus of this study was on the solvent extraction of Fe by amines. Previous investigations found that amines are promising extractants for efficient Fe removal and thus, different processes for the extraction of Fe from sulphate [8–10] or chloride solutions [11] have been suggested. The aim of this study was to compare primary, secondary, and tertiary amines in terms of their selectivity for Fe over In, Ge, and Ga as well as to characterize the most suitable extraction system in more detail. The model solutions were based on the composition of sulphate bio-leaching solutions produced within the project "ReMining".

Materials and Methods

The aqueous solutions were prepared using the following chemicals: $Fe_2(SO_4)_3$ (VWR Chemicals, > 99%), $FeSO_4 \cdot 7H_2O$ (Carl Roth GmbH, > 99.5%), GeO_2 (Sigma Aldrich > 99.99%), $Ga_2(SO_4)_3 \cdot xH_2O$ (Alfa Aesar, 99.999%), $In_2(SO_4)_3$ (Merck, synth.), $Al_2(SO_4)_3 \cdot 18H_2O$ (Carl Roth GmbH, 98%), $CuSO_4 \cdot 5H_2O$ (Merck, > 99.5%), $ZnSO_4 \cdot 7H_2O$ (Merck, > 99%), H_2SO_4 (Carl Roth GmbH, 98%), HCl (Carl Roth GmbH, 37%), HNO_3 (Merck, 65%), NaOH (pellets, Carl Roth GmbH, ≥ 99%). The following organic extraction reagents have been used: Primene 81R (Primary amine mixture of isomers (RNH_2, R = $C_{12–14}$), Dow), DTDA (Ditridecylamine mixture of isomers (R_2NH, R = C_{13}), BASF, 93.9%) and Alamine 336 (Tertiary amine (R_3N, R = $C_{8–10}$), BASF). Kerosene J.T. Baker 8387 (light distillate with a low-aromatic content, always referred to as "kerosene" in the text), Escaid 100 (Exxon Mobil, high-aromatic content 20–22%), trichloromethane (Carl Roth, ≥ 99.8%) and toluene

(VWR chemicals, technical) have been applied as organic diluents. *n*-octanol (Alfa Aesar, 99%) was used as a modifier. All chemicals were applied as supplied by the manufacturer.

The experiments have been conducted at room temperature (20 ± 2 °C) in 5 mL or 15 mL polypropylene tubes. Defined volumes of the aqueous stock solutions, acid (2–5 mol/L H_2SO_4), water, and the organic phase were pipetted into the tube. Mixing of both phases was conducted in an overhead shaker (Heidolph Reax 2). After a defined mixing time, a centrifuge (Eppendorf 5804) was used to ensure a complete phase separation. Samples of the aqueous and/or organic phase were taken for analysis. A pH electrode (Mettler Toledo InLab Micro, Ag/AgCl, 3 mol/L KCl) was used to measure the pH of the aqueous solution. Loading of the organic phase for stripping experiments was performed in beakers using an overhead stirrer (IKA RW 20) for mixing and a separating funnel for phase separation. The element concentrations in aqueous phases were analyzed by ICP-OES (Analytik Jena, PlasmaQuant PQ9000). The XRD analysis of the iron precipitate was conducted with an Empyrean diffractometer (PANalytical, Almelo, Netherlands) equipped with a PIXcel3D-Medipix area detector (in combination with a Fe-filter) and a proportional counter (with monochromator) as well as a Co X-ray tube ($K\alpha_1 = 1.789010$ Å) anode. A voltage of 35 kV and a current of 35 mA were applied. The scan range was 5–80° with a step size of 0.0131° and an overall measurement time of 10 h. The irradiated area was kept constant (15 mm $\times$ 12 mm) by means of an automated divergence slit.

Results

Comparison of Extractants

The extraction efficiency for Fe(III), In(III), Ga(III), and Ge(IV) from single-element solutions has been compared using a primary (Primene 81R), secondary (DTDA), and tertiary (Alamine 336) amine extractant. The results for Fe(III) and In(III) are shown in Fig. 1. The chosen contact time of 30 min was sufficient since preliminary experiments showed that the Fe(III) extraction already reached the equilibrium after 15 min.

The results in Fig. 1a indicate that at pH < 0.7 the extraction of Fe(III) is more pronounced with the primary amine compared to the secondary or tertiary amine. In the range of 0.7 < pH < 1.6 the extraction of Fe(III) is more efficient with the secondary amine. The tertiary amine extracts Fe(III) only at pH > 1.2 and the extraction is limited to a pH of 2.1 due to the precipitation of Fe(III) at higher pH values. Additional investigations (not shown in Fig. 1) also reveal that Fe(II) is not extracted by the secondary amine. The extraction of iron by amines is often associated with the interaction between the amine and anionic iron-sulphate complexes [8, 12, 13]. Since
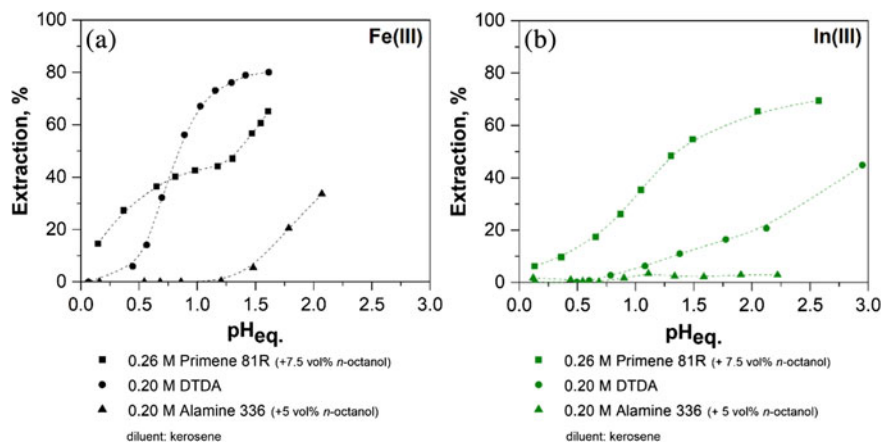
Fig. 1 Comparison of reagents for the extraction of **a** Fe(III) and **b** In(III). Initial aqueous sulphate solutions with 7.0 g/L Fe(III) or 0.5 g/L In(III), A:O = 1:1, $t_{contact}$ = 30 min

Fe(II) does not form sulphate complexes [14], it is very likely that this explains why Fe(II) is not extracted by secondary amine (DTDA).

Figure 1b shows that the extraction efficiency for In(III) follows the order: primary > secondary > tertiary amine. There is almost no In(III) extraction with the tertiary amine. The extraction of In(III) with the secondary amine increases continuously for pH > 0.6. Similar behavior is observed for the primary amine. However, in the entire range of 0.1 < pH < 2.6 the highest In(III) extraction is obtained with the primary amine. Further experiments were conducted with single-element solutions containing 0.5 g/L Ge(IV) or 0.5 g/L Ga(III). With all amines the extraction efficiency for both Ge(IV) and Ga(III) is very low or even negligible. In the range of 0.1 < pH < 2.4 the extraction of both Ge(IV) and Ga(III) with the secondary and the tertiary amine is < 5%. In the same pH range, the primary amine shows a maximum Ge(IV) extraction of 9% and a maximum Ga(III) extraction of 13% with a tendency to increase with increasing pH value.

It is also observed that the formation of a third phase is much more pronounced with Primene 81R and Alamine 336 compared to DTDA. For both, Primene 81R and Alamine 336 the addition of *n*-octanol is necessary to avoid the formation of a third phase. No modifier had to be used together with DTDA. In these experiments, third phases occurred with DTDA only at pH < 0.4 and it was ascertained that there is a tendency to form a marginal third phase (slight fog) at pH < 0.8.

Based on these results, DTDA was selected as the most promising reagent for the selective separation of In(III), Ge(IV), and Ga(III) from Fe(III).

Fig. 2 Extraction from two-element sulphate model solutions. Initial aqueous solutions with 7.2 g/L Fe(III) + 0.5 g/L In(III), 7.3 g/L Fe(III) + 0.5 g/L Ga(III) or 7.2 g/L Fe(III) + 0.5 g/L Ge(IV), organic phase: 0.2 mol/L DTDA in kerosene, A:O = 1:1, $t_{contact}$ = 30 min
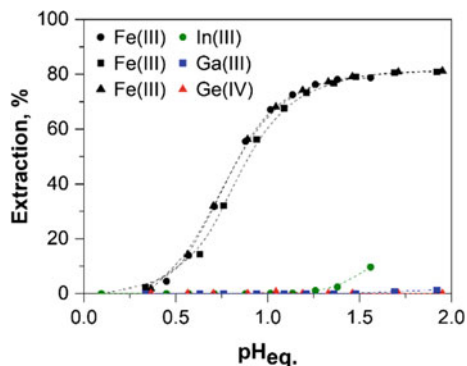
Extraction from Two-Element Model Solutions

Figure 2 summarizes the results of the Fe(III), In(III), Ge(IV), and Ga(III) extraction from two-element model solutions (Fe(III) + In(III), Fe(III) + Ga(III), Fe(III) + Ge(IV)) using 0.2 mol/L DTDA in kerosene.

The extraction of Fe(III) shows the expected pH-dependent behavior for all model solutions. The Fe(III) extraction reaches a plateau at 81%, which is equivalent to 0.1 mol/L. This indicates that a complex with a DTDA:Fe(III) stoichiometry of 2:1 could be formed in the organic phase. With efficiencies of < 1%, the extraction of Ge(IV) and Ga(III) is neglectable in the range of 0.4 < pH < 1.9. The extraction of In(III) is < 1% in the range of 0.2 < pH < 1.3 and increases slightly at higher pH values as it was already observed in a comparable manner in the experiments with the single-element solutions (Fig. 1). However, in the two-element solution with Fe(III), the extraction efficiency of In(III) is much lower. It is assumed that Fe(III) is preferably extracted by DTDA and thus, suppresses the In(III) extraction.

Extraction from a Multi-element Model Solution

In the next step, a multi-element model solution with a composition that simulates a pregnant leach solution from a (bio)-hydrometallurgical process was prepared. Besides 20.4 g/L Zn(II), 2.1 g/L Cu(II) and 2.0 g/L Al(III), the solution contained only low amounts of the target elements: 26 mg/L In(III), 20 mg/L Ge(IV) and 26 mg/L Ga(III). In contrast to that, the initial concentration of Fe(III) (7.3 g/L) leads to a high ratio of Fe(III)/Me > 300:1 with Me = In(III), Ga(III), and Ge(IV). The extraction results at different pH values are shown in Fig. 3.

The pH dependence of the extraction of Fe(III) follows again the same trend as with the single- and two-element model solutions. As indicated with the unfilled symbols, no extraction of trivalent Al(III) and the divalent metal ions of Cu(II) and Zn(II) is observed in the range of 0.4 < pH < 1.9. The same applies to the extraction

Fig. 3 Extraction from
multi-element sulphate
model solution. Initial
aqueous solution with 7.3 g/
L Fe(III) + 20.4 g/L Zn(II)
+ 2.1 g/L Cu(II) + 2.0 g/L
Al(III) + 26 mg/L In(III) +
20 mg/L Ge(IV) + 26 mg/L
Ga(III), organic phase:
0.2 mol/L DTDA in
kerosene, A:O = 1:1, $t_{contact}$
= 30 min
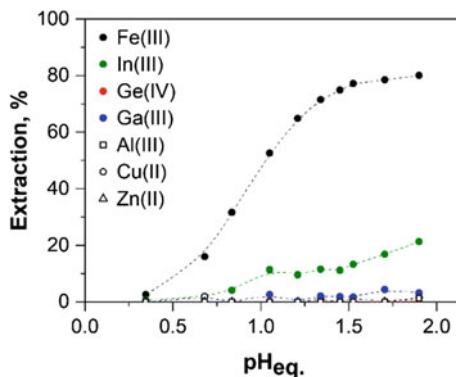
of Ge(IV). The extraction of Ga(III) increases slightly at pH > 1 but remains <
5%. The coextraction of In(III) from this multi-element model solution increases
at pH > 0.8 and reaches 21% at pH 1.9. At lower pH, the coextraction of In(III) is
more pronounced compared to the coextraction from the two-element model solution
(Fig. 2).

Influence of the Organic Phase Composition

The influence of the type of organic diluent and the addition of *n*-octanol has been
investigated using the multi-element model solution. The concentration of DTDA
was kept constant at 0.2 mol/L.

The results in Fig. 4 reveal that the extraction efficiency of Fe(III) decreases
in the following order: low-aromatic kerosene > high-aromatic kerosene > toluene
> chloroform. This order shows that with increasing polarity of the diluent, the
extraction of Fe(III) is decreased. It is presumed that this effect can be attributed
to the larger influence of secondary bonding in the outer coordination sphere which
is favored in diluents with low polarity but needs to be investigated in more detail
in future studies [15]. The influence of the addition of different concentrations of
n-octanol was investigated using low-aromatic kerosene as diluent. It was found that
with increasing concentration of *n*-octanol, the extraction of Fe(III) is decreased.
The effects are less pronounced for the extraction of In(III). Chloroform slightly
increases the extraction of In(III), whereas a slight decrease of the In(III) extraction
was observed when 6.9 vol.-% *n*-octanol was added. However, neither a more polar
diluent nor the addition of *n*-octanol improves the separation of Fe(III) and In(III).
The extraction of the other elements from the multi-element model solution was
too low (< 5%) to identify significant changes caused by the different diluents or
n-octanol.
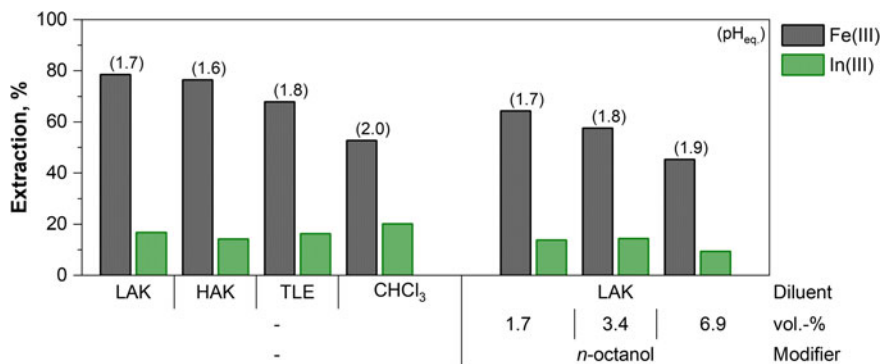
Fig. 4 Influence of the organic diluent (LAK = low-aromatic kerosene, HAK = high-aromatic kerosene, TLE = toluene) and the addition of n-octanol. Initial aqueous solution with 7.3 g/L Fe(III) + 20.4 g/L Zn(II) + 2.1 g/L Cu(II) + 2.0 g/L Al(III) + 26 mg/L In(III) + 20 mg/L Ge(IV) + 26 mg/L Ga(III), extractant concentration: 0.2 mol/L DTDA, A:O = 1:1, $t_{contact}$ = 30 min

Stripping of the Loaded Organic Phase

Stripping of the Fe(III)-loaded organic phase (0.2 mol/L DTDA with 5.1 g/L Fe(III) in kerosene) was investigated using HCl, HNO_3, and H_2SO_4 with initial concentrations of 1 mol/L and 3 mol/L, respectively. The results are shown in Fig. 5.

A 1 mol/L HCl solution re-extracts 99% of the Fe(III) from the organic phase. With an increase of the HCl concentration (3 mol/L), the stripping efficiency of Fe(III) decreases. It is very likely that at higher HCl concentrations Fe(III)-chloro complexes, such as $[FeCl_4]^-$, are formed, which interact with the protonated DTDA and remain in the organic phase. The stripping of Fe(III) is quantitative for both HNO_3 and H_2SO_4 with 1 and 3 mol/L, respectively. However, when the H_2SO_4 solutions were used, poor phase separation and the formation of a third phase were observed.

Another approach uses precipitation stripping to re-extract Fe(III) from the organic phase by forming a barely soluble compound. A 0.5 mol/L NaOH solution was used to precipitate Fe(III) directly from the organic phase. The equilibrium pH in the aqueous

Fig. 5 Comparison of the iron stripping efficiency using different mineral acids with initial concentrations of 1 or 3 mol/L. Loaded organic: 0.2 mol/L DTDA with 5.1 g/L Fe(III) in kerosene, A:O = 1:1, $t_{contact}$ = 60 min
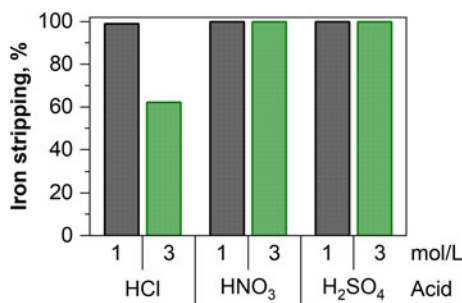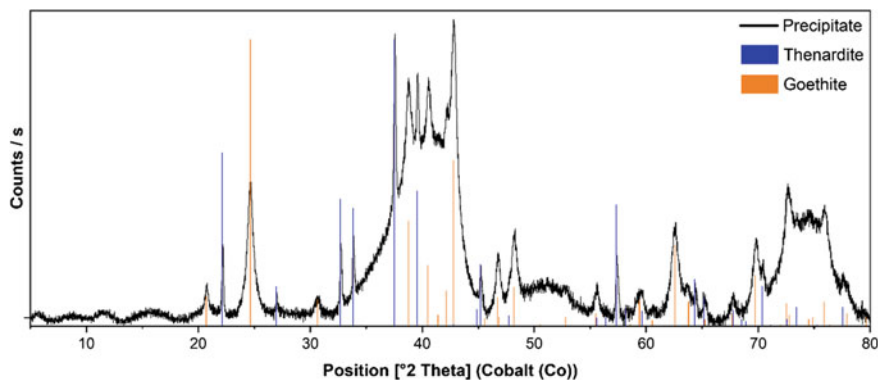
Fig. 6 XRD diffractogram of the iron precipitate after stripping with 0.5 mol/L NaOH. Loaded organic: 0.2 mol/L DTDA with 5.1 g/L Fe(III) in kerosene, A:O = 1:1, $t_{contact}$ = 60 min

solution was 12.8 after a contact time of 60 min. A good settling of the precipitate and a clear organic phase was observed. The Fe(III) precipitate was separated, dried, and characterized by XRD. The diffractogram in Fig. 6 indicates that under these conditions mainly thenardite (Na_2SO_4) and goethite (FeOOH) are formed during the precipitation from the organic phase.

Conclusions

It was found that in the range of 0.7 < pH < 2.0 the secondary amine DTDA is more suitable for the selective extraction of Fe(III) from aqueous sulphate solutions than the primary amine (Primene 81R) or the tertiary amine (Alamine 336). The characteristics of the iron extraction by DTDA can be summarised as follows:

- Fe(II) is not extracted under the chosen experimental conditions.
- Very high selectivity for Fe(III) over Ge(IV), Ga(III), Al(III), Zn(II) and Cu(II).
- Good selectivity for Fe(III) over In(III), which decreases with increasing pH value.
- Diluents with high polarity and the presence of *n*-octanol decrease the Fe(III) extraction.
- Quantitative re-extraction of Fe(III) can be achieved by the use of mineral acids or precipitation stripping with sodium hydroxide.

The separation of In(III), Ga(III), and Ge(IV) from Fe(III) by selective solvent extraction with the extractant DTDA is an innovative approach to improve the recovery of In(III), Ga(III), and Ge(IV) in (bio-)hydrometallurgical processes. In addition to this, other processes that struggle with high iron concentrations might benefit from the combination with selective iron solvent extraction.

References

1. Grohol M, Veeh C (2023) Study on the critical raw materials for the EU 2023—final report. Publications Office of the European Union. https://doi.org/10.2873/725585
2. Jibo J et al (2011) Precipitation of indium using sodium tripolyphosphate. Hydrometallurgy 106:165–169. https://doi.org/10.1016/j.hydromet.2010.12.009
3. Bayat S et al (2016) Germanium separation and purification by leaching and precipitation. J Cent South Univ 23:2214–2222. https://doi.org/10.1007/s11771-016-3279-6
4. Fortes MCB et al (1998) Separation of Indium and Iron by Solvent Extraction. Miner Eng 11:447–451
5. Harbuck DD (1992) Gallium and germanium recovery from domestic sources. In: Report 9419. US Bureau of Mines
6. Rohan J et al (2019) Recovery of gallium from wafer fabrication industry wastewaters by Desferrioxamine B and E using reversed-phase chromatography approach. Water Res 158:203–212. https://doi.org/10.1016/j.watres.2019.04.005
7. Schöneberger N (2020) Identification and characterization of gallium-binding peptides. Ph.D. thesis, TU Bergakademie Freiberg
8. Li M (2011) Removal of iron from industrial grade aluminum sulfate by primary amine extraction system. Hydrometallurgy 106(3–4):170–174. https://doi.org/10.1016/j.hydromet.2010.12.018
9. Feller HF (1967) Method of removing iron from aluminum sulfate solutions. US Patent 3331662
10. Qifeng W et al (2016) Recovery and separation of sulfuric acid and iron from dilute acidic sulfate effluent and waste sulfuric acid by solvent extraction and stripping. J Hazard Mater 304:1–9. https://doi.org/10.1016/j.jhazmat.2015.10.049
11. Preuss AF (1963) Removal of ferric chloride from iron-aluminum chloride solutions. US Patent 3082062A
12. Cattrall RW, West BO (1966) The extraction of iron (III) from aqueous sulphate solutions by di(3,5,5-trimethylhexyl)amine—I: the nature of the extracted species. J Inorg Nucl Chem 28(12):3035–3042. https://doi.org/10.1016/0022-1902(66)80031-3
13. Alguacil FJ, Amer S (1986) Extraction equilibrium between primary amine primene 81R and iron(III) sulphate. Polyhedron 5(11):1747–1753. https://doi.org/10.1016/S0277-5387(00)848 52-4
14. Gil AF et al (1995) Predominance-zone diagrams of Fe(III) and Fe(II) sulfate complexes in acidic media Voltammetric and spectrophotometric studies. Talanta 42(3):407–414
15. Wilson AM et al (2014) Solvent extraction: the coordination chemistry behind extractive metallurgy. Chem Soc Rev 43:123–134. https://doi.org/10.1039/C3CS60275C

Antagonistic Separation of Nickel Over Copper from Ammoniacal Binary Solution Using LIX 84-IC Mixture with TBP

Sadia Ilyas, Hyunjung Kim, and Rajiv Ranjan Srivastava

Abstract In recent times, ammoniacal leaching has received widespread attention in extractive metallurgy, mainly to process the lateritic ores of nickel. Copper has always been found as the companion metal ion in ammoniacal solutions, whose effective separation is highly desirable to achieve product purity. Usually, LIX series extractants are applied to co-extract and their selective stripping is a function of acid concentration, resulting in large hold-up volumes of the solvent. Henceforth, to achieve high selectivity in the extraction step, we studied the antagonistic effect of tributyl phosphate (TBP) mixing with LIX 84-IC, which inhibited nickel extraction with copper from the ammoniacal solution. The determined distribution coefficient values as $D_{(mix)} < < D_{(LIX\ 84\text{-}IC)} + D_{(TBP)}$ and negative ΔD values clearly demonstrate the antagonistic effect caused by the extractant mixture. The highest separation factor, i.e., $\beta_{(Cu/Ni)} = 1330$, was obtained at a molar mixture of LIX 84-IC:TBP = 0.4:0.6 and an organic-to-aqueous (O:A) phase ratio of 1. The extraction thermodynamics indicate an endothermic process ($\Delta H° = 5.4$ kJ/mol) that forms the *inner*-sphere organometallic complexation. The copper-loaded organic phase was quantitatively stripped by contacting it with a 1.0 mol/L H_2SO_4 solution at an O:A ratio of 1.

Keywords Ammoniacal leach liquor · Antagonistic extraction · LIX 84-IC · TBP

S. Ilyas (✉) · H. Kim · R. R. Srivastava
Department of Earth Resources and Environmental Engineering, Hanyang University, Seongdong-gu, Seoul 04763, Republic of Korea
e-mail: sadiailyas1@yahoo.com

R. R. Srivastava
Center for Advanced Chemistry, Institute of Research and Development, Duy Tan University, Da Nang 550000, Vietnam

S. Ilyas
Resource Management, Faculty of Natural Sciences, Duy Tan University, Da Nang 550000, Vietnam

Introduction

Ammoniacal leaching of roast-reduced nickel laterites has remained in traction due to its higher selectivity over iron as a major element [1–3]. The dissolution of copper (Cu) and nickel (Ni) in an ammoniacal solution can be given by the Eqs. (1–2) [4].

$$m + 1/2O_2 + (x - 2)NH_3 + 2NH_4^+ \rightarrow m(NH_3)_x^{2+} + H_2O \tag{1}$$

and,

$$mO + (x - 2)NH_3 + 2NH_4^+ \rightarrow m(NH_3)_x^{2+} + H_2O \tag{2}$$
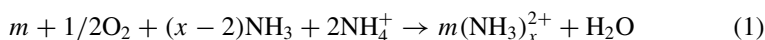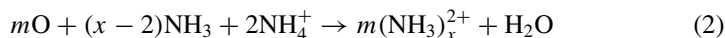
where m stands for nickel and cobalt within the value of x ranges from 1 to 6 and 5, respectively; while for iron x ranges from 1 to 4.

Thus formed metal ammine complexes are required to separate from each other for their high purity in the end-products. A number of techniques like solvent extraction, hydrothermal reduction, metal hydroxide precipitation, resin ion exchange, membrane separation, and carbon adsorption have been largely employed to efficiently recover copper and nickel as individual products [5–7]. Due to the high mass transfer rate, high volume handling capacity, and greater loading capacity of organic solvents, the isolation of target metal ions from the leach liquor is widely carried out using the solvent extraction technique [8–11].

The organic extractants having functional groups of oximes/ketones are preferentially employed in this direction [3]. The liquid ion exchange (LIX) extractants, namely, LIX 54 [11], LIX 63 [12], LIX 64N [13], LIX 84, LIX 84-I [14], LIX 84-IC, LIX 87QN [15], LIX 973N [16], and LIX 984N [17] have been reported in literature for the separation of Ni and Cu from ammoniacal solution. The aldoxime extractant, Acorga M5640, and its mixture with ketoxime are also applied which show a greater affinity for Cu extraction [16]. Despite of a good extractability of metal ions from ammine solution, the poor selectivity between Ni and Cu has been identified as a major issue, which often needs of scrubbing and selective stripping as a function of acid concentrations, ableit it is still problematic to achieve the cathode metal purity of three-9.

In the recent past, the application of extractant mixtures inhibiting the co-extraction of metals has been applied by several researchers [18–20]. In this context, the separation factor of Cu over Ni has been obtained to be > 35,000 while adding (2 v/v%) TRPO with (10 v/v%) Acorga M5640 [19]. By mixing LIX 84-I and Aliquat 336, Cu-separation significantly improved from the ammoniacal solution [18], but Aliquat 336 is a costly extractant. Hence, this study employed a cheaper additive extractant (namely tri-n-butyl phosphate (TBP) that having good compatibility with most of the organic extractants) with the main extractant 2-hydroxy-5-nonylacetophenone oxime (LIX 84-IC) to get the higher separation between Cu and Ni from the ammoniacal medium.

Experimental

The stock solution containing 3.0 g/L each of Cu and Ni was prepared in ammoniacal solution to simulate the ammoniacal leach liquor of nickel laterite as described elsewhere by Sridhar et al. [16]. For this, $CuSO_4 \cdot 5H_2O$ (Sigma Aldrich) and $NiSO_4 \cdot 6H_2O$ (Sigma Aldrich) were dissolved in an ammoniacal solution containing total ammonia 3.0 mol/L with 60 g/L $(NH_4)_2CO_3$ in the solution. The aqueous solution was prepared using NH_4OH (Junsei Chemical Co., sp. gr. 0.896 g/cm^3), $(NH_4)_2CO_3$ (Merck, assay > 98%), and H_2SO_4 (Junsei Chemical Co., sp. gr. 1.836 g/cm^3), while the organic solution was prepared by mixing LIX 84-IC (BASF Global Mining Sol., sp. gr. 0.94 g/cm^3), TBP (Sigma Aldrich, sp. gr. 0.979 g/cm^3), and kerosene (Junsei Chemical Co., sp. gr. 0.80 g/cm^3) without any purification.

All the extraction studies were performed by equilibrating 30 mL of both the organic and aqueous phases in 100 mL separating funnel for 5 min, and then, allowed to be settled for 10 min before separating both phases. The thus separated raffinate was properly diluted using 10 wt.% HCl solution and analyzed using the inductively coupled plasma optical emission spectrometer (ICP-OES, iCAP6000 series, Thermo Scientific). After knowing the metal concentration in the aqueous phase, the concentration of corresponding metal extracted into the organic phase was determined by the mass balance (i.e., initial metal concentration in feed solution–metal concentration in the raffinate). The distribution (D) of metal ions and the extraction efficiency were further calculated as

$$D = \frac{CE_{org}}{CE_{aq}} \tag{3}$$

where CE_{org} and CE_{aq} are post-extraction metal concentration in the organic and aqueous phases, respectively. Using D value, the extraction efficiency (in %) was determined as follows:

$$\text{Extraction } (\%) = \left[\frac{D \times \left(\frac{V_{org}}{V_{aq}} \right)}{D \times \left(\frac{V_{org}}{V_{aq}} \right) + 1} \right] \times 100 \tag{4}$$

where V_{org} and V_{aq} are volumes of the organic and aqueous phases, respectively.

Further, the loaded organic was scrubbed by contacting with a scrub solution of pH2.5 at an O/A ratio of 2. The thus obtained scrubbed organic was taken for metal stripping by contacting the pre-determined concentration of sulfuric acid solutions at an O/A of 1. After phase separation, the stripped solution was analyzed using ICP-OES to further calculate the stripping efficiency as follows:

$$\text{Stripping } (\%) = \left[\frac{CS_{aq} \times V_{aq}}{CS_{org} \times V_{org}} \times 100 \right] \tag{5}$$

where CS_{org} and CS_{aq} are post-stripping metal concentration in the organic and aqueous phases, respectively.

Further, ΔD values for each metal were calculated as below:

$$\Delta D = D_{mix} - (D_{LIX\ 84-IC} + D_{TBP}) \tag{6}$$

where D_{mix} is the distribution ratio by the mixture of LIX 84-IC and TBP, $D_{LIX\ 84-IC}$, and D_{TBP} are distribution ratios by respective organic extractant alone.

Results and Discussion

Studies on Copper and Nickel Extraction Using Solvent Mixture of LIX 84-IC and TBP

The influence of mixing two different extractants (i.e., LIX 84IC and TBP) was examined at different molar ratios (see Table 1). The other parameters like the O/A ratio of 1, temperature at 22 °C, and total ammonia-ammonium carbonate buffer solution of pH 9.5 that contains 3.0 g/L copper and nickel each into the aqueous feed solution were kept constant. Results in Table 1 showed the effect of individual organic extractant concentrations on the distribution coefficients of copper and nickel, and with the mixed system as well. As can be seen from Table 1 that the organic mixture driven extraction yielded a lower distribution (D_{mix}) value than the added individual distribution values ($D_{LIX\ 84-IC} + D_{TBP}$), i.e., $D_{mix} < < D_{LIX\ 84-IC} + D_{TBP}$. Moreover, the negative values of ΔD_{Cu} and ΔD_{Ni} revealed the antagonistic effect exhibited by the organic mixture of LIX 84-IC and TBP.

Table 1 The distribution coefficients of copper and nickel using individual organic extractants and their mixture prepared of different ratios

LIX 84-IC, mol/L	TBP, mol/L	Copper extraction			Nickel extraction		
		$D_{LIX84-IC} + D_{TBP}$	D_{mix}	ΔD_{Cu}	$D_{LIX84-IC} + D_{TBP}$	D_{mix}	ΔD_{Ni}
1.0	0.0	374	374	0	21.05	21.05	0
0.8	0.2	14.96	8.933	− 6.03	3.87	0.093	− 3.78
0.6	0.4	7.11	3.58	− 3.53	2.36	0.033	− 2.33
0.4	0.6	4.98	2.60	− 2.38	1.14	0.002	− 1.138
0.2	0.8	0.96	0.48	− 0.48	0.48	0.002	− 0.48
0.0	1.0	0.005	0.005	0	0.002	0.002	0

Effect of Extractant Concentration on Separation Factor of Copper Over Nickel

Further, the effect of extractant concentrations and their mixing ratio was investigated by varying the LIX 84-IC/TBP molar ratio between 0:1 and 1:0 while keeping the other parameters constant at an O/A ratio of 1, temperature at 22 °C, total ammonia-ammonium carbonate buffer solution of pH 9.5 that containing 3.0 g/L copper and nickel each into the aqueous feed solution. Results in Fig. 1 showed that the extraction of copper significantly improved with increasing concentration of LIX 84-IC and reached 99.7% while using only LIX 84-IC of concentration 1.0 mol/L without any TBP addition contrary to 0.53% copper extraction using 1.0 mol/L TBP and no addition of LIX 84-IC into the organic phase. On the other side, nickel extraction was almost nil until adding a higher proportion of TBP into the organic phase (i.e., $\geq$ 0.4 mol/L TBP mixture with $\leq$ 0.6 mol/L LIX 84-IC). Whereas, going above 0.6 mol/L LIX 84 I in an organic mixture with TBP below 0.4 mol/L significantly improved nickel co-extraction that reaches > 88% along with 99.7% copper into the organic phase. It clearly depicted the antagonistic extraction of nickel caused by the addition of TBP at a higher proportion with LIX 84-IC. The extraction reaction of metal ammine complex with an organic mixture of LIX 84-IC and TBP differs from the commonly written extraction reaction using LIX 84-IC alone. The change in extraction reaction can be written as follows:

Using LIX 84-IC alone [3]:
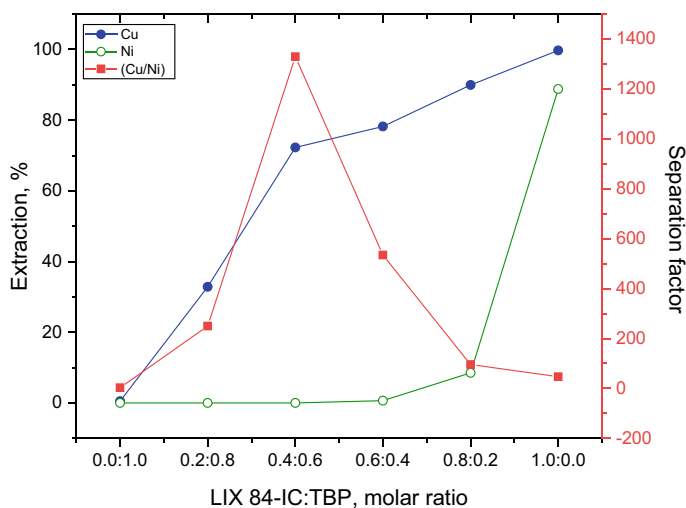
Fig. 1 Effect of molar ratio concentrations on extraction efficiency of copper and nickel from ammoniacal solution and their separation factor obtained at an O/A ratio = 1, temperature = 22 °C, total ammonia concentration = 3.0 mol/L with 60 g/L carbonate, and 3.0 g/L concentration of copper and nickel each into the solution

$$m(\text{NH}_3)_q^{p+} + p\overline{(RH)_2} \leftrightarrow \overline{m(R_2)_p} + 2(\text{NH}_4)^+ + (q - p)\text{NH}_3 \qquad (7)$$
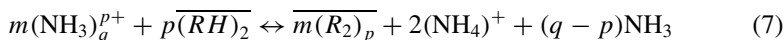
Using LIX 84-IC mixture with TBP in this study [1]:

$$m(\text{NH}_3)_q^{p+} + p\overline{(RH)_2} + n\overline{\text{TBP}} \leftrightarrow \overline{m(R_2)_p \cdot (\text{TBP})_n} + 2(\text{NH}_4)^+ + (q - p)\text{NH}_3$$
$$\tag{8}$$
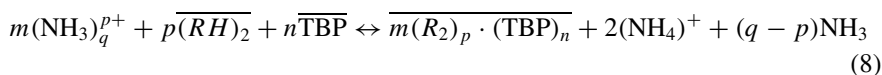
Moreover, in order to determine the optimal condition for the selective extraction of copper over nickel from the ammoniacal solution, the separation factor ($\infty_{\text{Cu/Ni}}$) was also calculated at each varied ratio of the organic mixture. Figure 1 shows that the highest separation factor within the varied ratio of extractant molecules was found to be 1329.3 at a LIX 84-IC:TBP molar ratio of 0.4:0.6 into the organic phase. Interestingly, it can be seen that using only LIX 84-IC of 1.0 mol/L, the separation factor was very low about 47.2 which decreased further as low as 2.7 with 1.0 mol/ L TBP (in the absence of LIX 84-IC molecules). These results also confirmed that in the organic mixture only LIX 84-IC drives the extraction with metal ammine complexes while the role of TBP is to hinder the nickel extraction. It is supposed that the presence of oxygen-atom of P = O molecules occupying the enolic proton that potentially prevents the nickel ammine to be complexed with the free molecules of LIX 84-IC.

Effect of Total Ammonia Concentration on Metal Extraction

In an ammoniacal system, the total ammonia concentration is an important factor as it significantly affects the buffer pH of the solution, and thus, alters the equilibrium pH of the system. Hence, the effect of total ammonia concentration was varied in the range of (1.0–4.0 mol/L) using the organic mixture at LIX 84-IC:TBP molar ratio of 0.4:0.6 and contacted at an O/A ratio of 1. Results in Fig. 2 showed the quantitative extraction of copper (i.e., ~ 72%) regardless of the equilibrium pH which changes between 9.22 and 9.68. However, copper extraction slightly declined at a total ammonia concentration of > 3.5 mol/L along with the co-extraction of 5.2% nickel. This phenomenon can be corroborated by the extraction of NH_4^+ ions along with the metal ions that occupying the extraction sites of the LIX 84-IC molecules. Also, the high ammonia concentration leads to form the stable metal ammine species of copper like $\text{Cu}(\text{NH}_3)_4^{2+}$ and $\text{Cu}(\text{NH}_3)_3\text{OH}^+$ with greater stability constant values, causing hindrance to Cu extraction into the organic phase. In contrast, Ni-extraction was found to increase at ≥ 3.5 mol/L of total ammonia concentration in the aqueous feed which can be related to the change in nickel ammine species towards forming a stable $\text{Ni}(\text{NH}_3)_6^{2+}$ complex at a higher ammonia concentration and increased pH as well. Here, 3.0 mol/L total ammonia concentration was optimized.
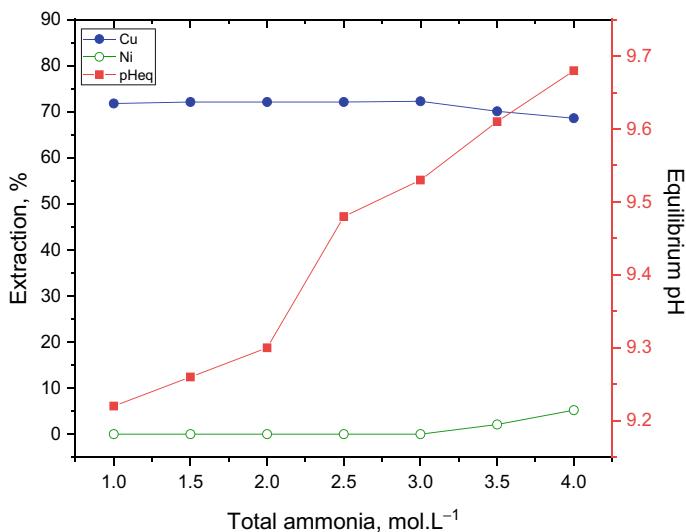
Fig. 2 Effect of total ammonia concentration on extraction efficiency of metals while keeping 60 g/L carbonate fixed in the aqueous solution contacted with LIX 84-IC:TBP molar ratio = 0.4:0.6, O/A ratio = 1, temperature = 22 °C, and 3.0 g/L concentration of copper and nickel each into the solution

Effect of Extraction Temperature

The effect of extraction temperature on the selectivity of copper metal ammine complexation with the organic mixture was investigated at different temperatures between 22 and 50 °C while contacting two phases at an O/A ratio of 1. Figure 3a shows an increased extraction of copper from 72.3% to 76% with increasing temperature from 22 °C to 50 °C, respectively. This behaviour, indicative of the endothermic process, reveals that the ability of metal-binding sites of the organic mixture improves with increasing temperature. In contrast, nickel extraction was zero regardless of any temperature change. Furthermore, the thermodynamic properties for extraction equilibria were determined using the Van't Hoff equation:

$$\log [D]_{\text{Cu}} = -\frac{\Delta H^{\circ}}{2.303 \text{R} T} + \frac{\Delta S^{\circ}}{2.303 \text{R}} \tag{9}$$

Figure 3b shows the plots of log [D] *versus* 1/T that yield the straight lines with regression coefficient values > 0.99. Utilizing the slope and intercept values of the straight lines, the apparent enthalpy change (ΔH°) and entropy change (ΔS°) values for copper extraction were determined to be 5.4 kJ/mol and 26.3 J/K/mol, respectively. It confirmed the endothermic nature of copper complexation into organic phase, possibly through an *inner*-sphere coordination [21]. Whereas, the positive ΔS° value indicated a decreased order of extracted metal species into the organic phase.
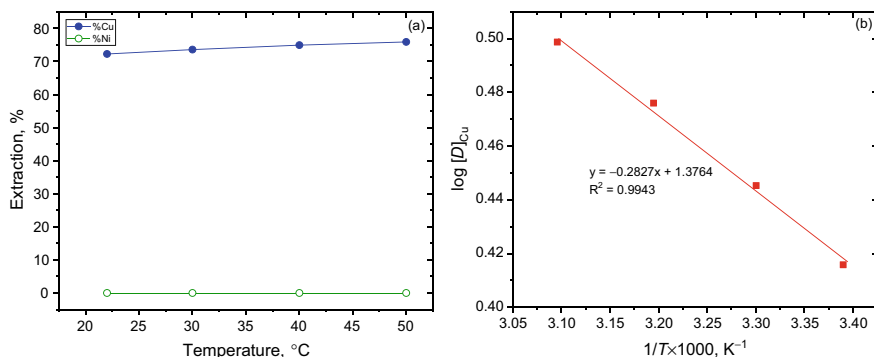
Fig. 3 Effect of temperature on extraction efficiency of metals from ammoniacal solution of total ammonia concentration = 3.0 mol/L with 60 g/L carbonate, and 3.0 g/L concentration of copper and nickel each into the solution contacted with LIX 84-IC:TBP molar ratio = 0.4:0.6 at an O/A ratio = 1 (**a**); Van't Hoff plot for log $[D]_{Cu}$ vs. $1/T$ (**b**)

Thus, determining enthalpy and entropy values were put in Eq. (10) to evaluate the standard Gibbs free energy change ($\Delta G°$). The negative value of $\Delta G°_{298 K}$ − 2.4 kJ/mol revealed the spontaneity of the extraction process.

$$\Delta G° = \Delta H° - T \Delta S° \tag{10}$$

Effect of O/A Volume Phase Ratio

The effect of volume phase ratios on selective extraction of copper over nickel from ammoniacal solution of concentrations 3.0 g/L each was examined using the organic mixture at LIX 84-IC:TBP molar ratio of 0.4:0.6 at room temperature (22 °C). As can be seen from the results summarized in Table 2, the O/A phase ratio exhibits a significant role in the complete separation of copper over nickel. The extraction of copper increased from 99.9 to 24.6% with a change in O/A ratio from 4/1 to 1/4. In contrast, the co-extraction of nickel was observed to decrease from 38.2% to zero with the change in O/A ratio from 4/1 to 1/4. It can be attributed to the lacking extractant molecules at a higher phase ratio [19], suggesting a complete copper and nickel separation by adjusting the O/A ratio.

Stripping of Copper from the Loaded Organic Phase

During the proton exchange of LIX 84-IC with the metal ions, the extraction of ammonium ions (NH_4^+) is always possible. Hence, the co-extracted ammonium

Table 2 The effect of volume phase ratio on extraction efficiency of copper and nickel from ammoniacal solutions

O/A ratio	% Copper	% Nickel
4/1	99.9	38.2
3/1	98.6	18.3
2/1	89.2	10.6
1/1	72.3	0
1/2	61.6	0
1/3	39.4	0
1/4	24.6	0

ions were first scrubbed with a solution of pH 2.5 (prepared by diluting H_2SO_4 in distilled water) and at O/A = 2. It also helps to reduce the viscosity of the system by preventing the formation of double salt in the presence of ammonium ions. About 480 mg/L of NH_3 concentration was analyzed in the thus obtained scrubbed raffinate with a < 5 mg/L of copper therein the solution. Then after, the scrubbed organic was used for stripping study at different concentrations of sulfuric acid solutions at the unit phase ratio (i.e., O/A = 1). Results presented in Fig. 4 showed that the stripping efficiency significantly increased with increasing the acid concentration in strip feed. Approximately 99.8% copper could be recovered back into the aqueous phase by contacting the loaded organic with 1.0 mol/L H_2SO_4 solution, while the stripping efficiency was only 12.7% using 0.1 mol/L H_2SO_4 solution which could surpass the 50% mark with 0.4 mol/L H_2SO_4 solution. The stripping reaction from the loaded organic mixture can be given as

$$\overline{m(R_2)_p \cdot (\text{TBP})_n} + 2(\text{H}^+)_p \leftrightarrow p\overline{(RH)_2 \cdot (\text{TBP})_n} + p(m^{2+}) \tag{11}$$
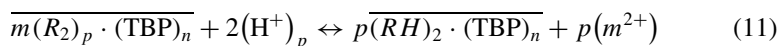
Fig. 4 Effect of sulfuric acid concentration on stripping efficiency from the loaded organic mixture containing 2.3 g/L copper contacted at an O/A ratio = 1 and temperature = 22 °C
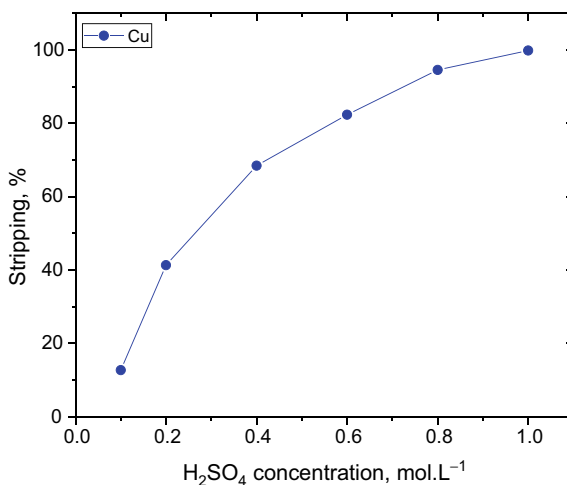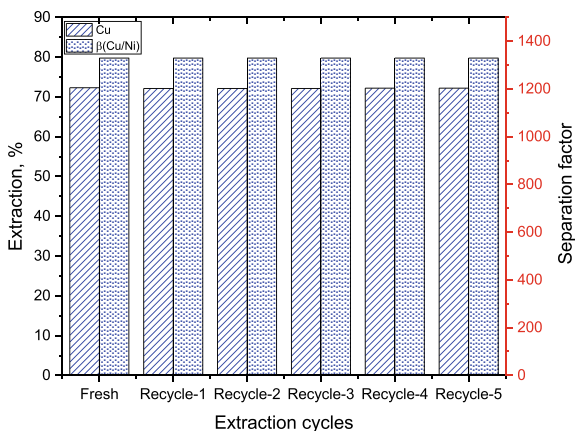
Fig. 5 The recyclability of the organic mixture used in this study for the selective extraction of copper over nickel from an ammoniacal solution of total ammonia concentration $= 3.0$ mol/L with 60 g/L carbonate, 3.0 g/L of each copper and nickel therein, organic feed of LIX 84-IC:TBP molar ratio $= 0.4{:}0.6$, O/A ratio $= 1$, and temperature $= 22\,°C$; whereas, the scrubbing with a solution of pH 2.5 and at O/A ratio $= 2$ and stripping solution $= 1.0$ mol/L H_2SO_4 and O/A ratio $= 1$

Recyclability of the Organic Mixture

The reuse behaviour of the organic mixture (prepared at a molar ratio of LIX 84-IC:TBP $= 0.4{:}0.6$) was re-used for extraction after regenerating the organic phase via scrubbing and stripping with H_2SO_4 solutions at an O/A ratios of 2 and 1, respectively. To explore the reusability of the organic mixture, the extraction-scrubbing-stripping cycles were repeatedly performed to separate both the valuable transition metals from each other. As can be seen from Fig. 5, a total of five sequential cycles were performed and at each stage of the extraction, the efficiency of copper did not affect regardless of the recycle stage with a higher selectivity over nickel. This result indicated the stability of the organic mixture along with its excellent reusability performance, which is highly desirable in terms of the practical applicability of the demonstrated process.

Conclusions

The organic mixture of LIX 84-IC and TBP was successfully employed to selectively extract copper from the ammoniacal solution, leaving all nickel in the raffinate. The antagonistic behavior of TBP added with the hydroxyoxime was confirmed by the exhibited extraction to be $D_{\text{mix}} < \ < D_{\text{LIX 84-IC}} + D_{\text{TBP}}$. Under the optimized condition of LIX 84-IC:TBP molar ratio at 0.4:0.6, the separation factor ($\infty_{\text{Cu/Ni}}$) was determined to be more than 1329 while feeding a 3.0 g/L solution of each

metal. The XPS spectral analysis of (Cu-Ni)-loaded LIX 84-IC in comparison to the Cu-loaded organic mixture of LIX 84-IC and TBP clearly depicted the role of TBP that exhibits the antagonistic effect on Ni-extraction. The thermodynamic data revealed that the antagonistic extraction of copper was spontaneous that exhibited the endothermic nature at extraction equilibria with ΔH°, 5.4 kJ/mol and $\Delta G^\circ_{298\ K}$, -2.4 kJ/mol. Further, the copper extracted into the organic phase was quantitatively stripped using a 1.0 mol/L H_2SO_4 solution. The demonstrated separation process via the antagonistic effect of TBP can be very important for the liquid–liquid separation of copper and nickel from ammoniacal medium, in particular for the processing of laterite ore.

References

1. Ilyas S, Srivastava RR, Jin S, Kim H (2023) Liquid–liquid separation of copper and nickel ammine complexes using phenolic oxime mixture with tributyl phosphate. Geosystem Eng 26(2):58–66
2. Caron MH (1950) Fundamentals and practical factors in ammonia leaching of nickel and cobalt ores. JOM 2:67–90
3. Ilyas S, Srivastava RR, Kim H, Ilyas N, Sattar R (2020) Extraction of nickel and cobalt from a laterite ore using the carbothermic reduction roasting-ammoniacal leaching process. Sep Purif Technol 232: Article 115971
4. Ilyas S, Kim H, Srivastava RR (2021) Carbothermic reduction roasting of a low-grade nickel laterite ore in the modified Caron process. In: C Anderson et al (eds) Ni-Co 2021: the 5th international symposium on nickel and cobalt, the minerals, metals and materials series. Springer, Cham, pp 317–328
5. Agrawal A, Sahu KK (2010) Problems, prospects and current trends of copper recycling in India: an overview. Resour Conserv Recycl 54(7):401–416
6. Srivastava RR, Mishra AN, Singh VK (2013) Co-precipitation study of nickel and cobalt from ammoniacal leach liquor of laterite ore. J Metall Mater Sci 55(1):67–72
7. Vargas C, Navarro P (2016) Adsorption of copper from an ammonia-thiosulfate media using DOWEX 550A ion exchange resin. Int J Nonferrous Met 5(4):33–44
8. Liu Y, Lee MS (2016) Separation of cobalt and nickel from chloride leach solution of nickel laterite ore by solvent extraction. Geosystem Eng 19(5):214–221
9. Truong HT, Lee MS (2017) Separation of rhenium(VII), molybdenum(VI), and vanadium(V) from hydrochloric acid solution by solvent extraction with TBP. Geosystem Eng 20(4):224–230
10. Wang L, Lee MS (2016) Solvent extraction of cobalt and nickel from chloride solution by mixtures of acidic organophosphorus extractants and amines. Geosystem Eng 19(6):261–265
11. Alguacil FJ, Cobo A (1998) Solvent extraction equilibrium of nickel with LIX 54. Hydrometallurgy 48(3):291–299
12. Xing WD, Lee MS, Senanayake G (2018) Recovery of metals from chloride leach solutions of anode slimes by solvent extraction. Part II: Recovery of silver and copper with LIX 63 and Alamine 336. Hydrometallurgy 1(180): 49–57
13. Pandey BD, Kumar V, Bagchi D, Akerkar DD (1989) Extraction of nickel and copper from the ammoniacal leach solution of sea nodules by LIX 64N. Ind Eng Chem Res 28(11):1664–1669

14. Sengupta B, Bhakhar MS, Sengupta R (2007) Extraction of copper from ammoniacal solutions into emulsion liquid membranes using LIX 84 I$^®$. Hydrometallurgy 89(3):311–318

15. Sandhibigraha A, Bhaskara Sarma PVR (1997) Co-extraction and selective stripping of copper and nickel using LIX 87QN. Hydrometallurgy 45: 211–219

16. Sridhar V, Verma JK, Shenoy NS (2010) Separation of nickel from copper in ammoniacal/ammonium carbonate solution using ACORGA M5640 by selective stripping. Miner Eng 23(5):454–456

17. Sridhar V, Verma JK, Kumar SA (2009) Selective separation of copper and nickel by solvent extraction using LIX 984N. Hydrometallurgy 99(1–2):124–126

18. Hu J, Wang S, Hu H, Li H, Peng K, Liu D, Liu D, Chen Q (2013) Improvement of separation efficiency of Cu(II) and Ni(II) in ammoniacal solutions by antagonistic effect of Aliquat336 on LIX84I. Sep Purif Technol 118:828–834

19. Yang R, Wang S, Duan H, Yuan X, Huang Z, Guo H, Yang X (2016) Efficient separation of copper and nickel from ammonium chloride solutions through the antagonistic effect of TRPO on Acorga M5640. Hydrometallurgy 163:18–23

20. Zhu Z, Zhang W, Pranolo Y, Cheng CY (2012) Separation and recovery of copper, nickel, cobalt and zinc in chloride solutions by synergistic solvent extraction. Hydrometallurgy 127–128:1–7

21. Kislik VS (2012) Solvent extraction: classical and novel approaches. Elsevier Science Publishers, Amsterdam

Separation of Critical Metals Using Supported Liquid Membranes PTFE-Cyanex 272

Amilton Barbosa Botelho Junior, Ana Carolina Miyashita, Jorge Alberto Soares Tenório, and Denise Crocce Romano Espinosa

Abstract Most common separation processes in hydrometallurgical processes are ion exchange and precipitation. However, novel technologies have been developed aiming at greener technologies and lower energy consumption and greenhouse gas emissions. Membrane technologies are being studied as a potential separation technique in hydrometallurgical processes including ultrafiltration, nanofiltration, and electrodialysis. Supported liquid membranes have been studied due to their selectivity and easy synthesis supported with organic extractants. This study aimed at the evaluation of Co(II) separation from Ni(II) through a membrane supported with phosphinic acid extractant. Experiments were carried out with two chambers at 25 °C, where the feed chamber contained the metals in sulfuric media and receiving acid solution. The membrane was prepared with PTFE/PVDF and Cyanex 272 10% diluted in kerosene as carrier. The effect of membrane preparation, Cyanex concentration, and pH in receiving chamber were evaluated. Results demonstrated the Ni/Co separation factor reached 4 without the use of concentrated acid for stripping.

Keywords Hydrometallurgy · Nickel · Cobalt · Membrane technology

Introduction

The raw materials classified as critical have the risk of supply interruption in a short and medium term [1]. Among them, the critical metals play an important role in green technologies, mainly batteries for electric vehicles where Ni and Co are the most valuable elements and critical (with Li) [2]. Due to the growing demand for these technologies to attend the goals for a sustainable development, the search for primary sources has been increasing facing several challenges as high contaminant content and low grade of target metals [3]. In addition, the use of residues as secondary

A. B. Botelho Junior (✉) · A. C. Miyashita · J. A. S. Tenório · D. C. R. Espinosa
Department of Chemical Engineering, Polytechnic School, University of São Paulo, São Paulo, Brazil
e-mail: amilton.junior@usp.br

sources is important to promote the circular economy and decrease the CO_2 emissions [3, 4].

Hydrometallurgical processes to obtain critical metals have several advantages against pyrometallurgical, including: (i) obtaining pure products; (ii) extraction/recovery of metals in low concentrations; (iii) less energy consumption; (iv) process temperature usually lower than 100 °C; (v) lower CO_2 emissions; and (vi) flexibility [5, 6]. On the other hand, the treatment of wastewater and high volumes of solutions and low kinetic rate are some drawbacks [7]. Leaching is the first step of the hydrometallurgical process, which is usually done using acid to extract the metals into the solution. Then, several purification and separation techniques are used to obtain the products, solvent extraction being the most common [8]. This technique involves the use of organic extractant diluent (kerosene being the most common) which is related to the presence of volatile and flammable compounds. Despite that, the solvent extraction technique is largely used due to its high selectivity and fast kinetic [9].

In order to overcome the aforementioned drawbacks, alternative technologies have been studied. Among them, the membrane technique has been demonstrated with potential use for hydrometallurgical processes [10]. Ultrafiltration, nanofiltration, and reverse osmosis have been used for wastewater treatment but represent no (or lower) selectivity for metallic ions separation [11]. Electrodialysis represents a potential use for the separation of monovalent ions as Li [12] and cations/anions such as Ni and SO_4^{-2} [13]; on the other hand, there is no selective separation of Co and Ni.

Supported liquid membranes have been shown as a potential technology for the selective separation of metals [11, 14]. In this system, the membrane is supported with the extractant (the same as in solvent extraction) between two chambers, where the feed contains the metallic ions and the receiving a solution to strip the metals from the membrane impregnated with the extractant. In the process, the metallic ion reacts with the organic extractant in the membrane and passes through the membrane, which is further stripped in the receiving chamber [15]. Studies reported in the literature demonstrated potential use for the separation of metals in acid solution, including Sc [16], Co [15], and lanthanides ions including Nd [17, 18].

The present study aimed at the evaluation of supported liquid membranes for the separation of Co over Ni. The type of membrane, extractant concentration impregnated in the membrane, and pH of the chambers were evaluated.

Materials and Methods

Figure 1 presents the experimental set-up used for experiments. The membrane was soaked in a solution with Cyanex 272 diluted in kerosene (10%), which is the extractant reported for the separation of Ni and Co [19] and rare earth elements [20] in solvent extraction experiments. The membrane was prepared before experiments in ultrasound for 10 min. Two chambers were connected, where the feed chamber contained 100mL of synthetic solution (500 ppm) containing critical metals, and
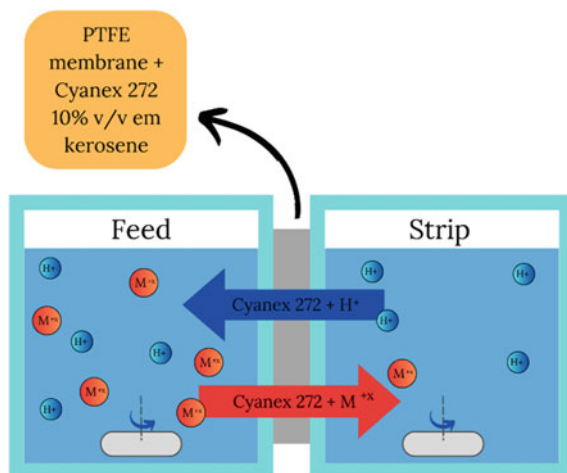
the receive chamber contained water (100 mL) adjusted at different pH values. The solution in the feed and receiving chambers remained under magnetic stirring. The membranes evaluated were polytetrafluoroethylene (PTFE) and poly(vinylidene fluoride) (PVDF).

The experiments were divided into two parts. First, the flux of Ni and Co through the membrane was studied. The type of membrane was evaluated. Further, the effect of pH in feed and receiving chambers were evaluated from pH 3 until pH 5 as these values the extractant is more selective for Co than Ni [21]. The type of membrane and extractant concentration were preliminary experiments. The pH was adjusted using NaOH or H_2SO_4. Samples of the feed and receiving chamber were analysed by energy dispersive X-ray fluorescence spectrometry (EDXRF), and the ultrasound equipment (100 W) was used for membrane preparation. Ni and Co synthetic solutions were prepared with sulfate salts dissolved in ultrapure water.

The flux was calculated according to the amount of metallic ions that migrated from the feed to the receive chamber per area of membrane and time, as depicted in Eq. 1 where J is the flux (mol/m^2 s), M is the amount of metallic ions (mol), A is the area (m$^2 = 7.8 \times 10^{-10}$) and t is the time (s). The selectivity (α) for Co/Ni separation was calculated by the ratio of Ni and Co (Eq. 2).

$$J_{(flux)} = \frac{M}{A.t} \tag{1}$$

$$\alpha_{(selectivity)} = \frac{Ni_{(Co)}}{Co_{(Ni)}} \tag{2}$$
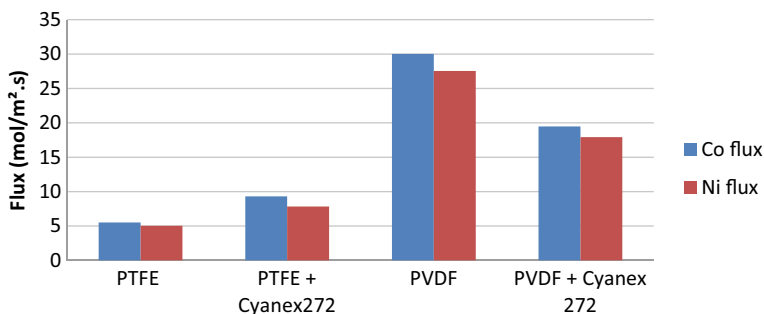
Fig. 2 Co and Ni fluxes according to the membrane type

Results and Discussion

Separation of Ni(II) and Co(II)

First, the effect of the type of membrane was evaluated for Ni and Co flux. PTFE and PVDF membranes were tested with Cyanex 272 as a carrier. The experiments were performed with membranes without treatment and after an ultrasound procedure [22] for 10 min. The results are presented in Fig. 2. In the feed, the pH was 5, while for the receiving chamber H_2SO_4 solution at pH 4.0 was used, and the experiments were carried out for 1 h. The goal of these experiments was to evaluate the effect of carrier in the separation process. As Cyanex 272 in kerosene is commonly used for Co separation over Ni, the selectivity was aimed. To support the liquid membrane technique, it was expected that the extractant in the membrane (as carrier) interacts with the ions being selective for Co, and further stripped in receiving chamber.

As observed, the fluxes of Ni and Co were higher for PVDF than PTFE in both systems (with and without carrier). In PVDF and PTFE experiments (without carrier), the migration of Ni and Co might be occurred due to concentration gradient as a diffusion process (diffusion dialysis). As the solution in receiving chamber has no Ni and Co, the ions would migrate from feed to receiving chamber to equalize the concentration [23]. Diffusion of ions through the membrane by diffusion dialysis was also reported by DuChanois [24].

The PTFE + carrier system was slightly more selective for Co than Ni ($\alpha = 1.02$). Comparing the membranes, the PVDF + carrier system presented higher migration flux for both metallic ions than PTFE + carrier system. According to Yuksekdag et al. (2022), it occurs because PVDF membranes have a thicker structure and can hold a higher organic phase volume although these membranes exhibit a relatively lower contact angle. Consequently, this characteristic leads to higher distribution coefficient values observed with the PVDF membrane [25]. However, the selectivity was low (Co/Ni = 1.02), and other parameters were further evaluated.
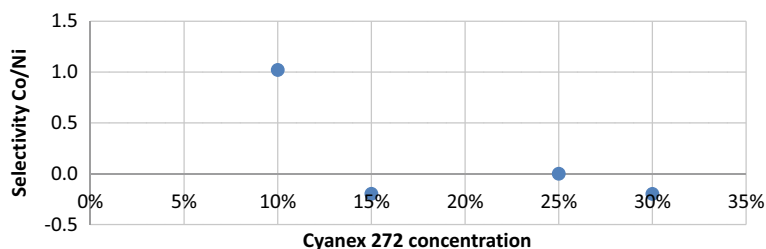
Fig. 3 Co/Ni selectivity (α) varying the concentration of Cyanex 272 in the membrane

The effect of carrier concentration (Cyanex 272) in kerosene was evaluated. The increase in organic extractant concentration is an important factor in a solvent extraction process, as the increase results in high extraction yield; however, a decrease in selectivity may be observed [26]. Figure 3 presents the results for the effect of the concentration of Cyanex 272 in kerosene in the membrane, where a decline in Co/Ni selectivity and metallic ions flux was observed. The increase in Cyanex 272 concentration as carrier decreased the selectivity of Co over Ni as there was an excess of extractant. As reported in solvent extraction experiments, the increase in the extractant concentration also increased the extraction of metals which declines the selectivity. In this study (Fig. 3), the selectivity declines due to the increase of Ni extraction. For this reason, the selectivity was close to zero. As reported by Li et al. (2022), the separation of metals by supported liquid membranes has a high dependence on carrier concentration [27].

The effect of pH in receiving chamber was evaluated. For these experiments, the pH of feed chamber was controlled as 5.0, and the receiving chamber was filled with water and the pH was adjusted. The solutions remained under magnetic stirring. These pH values were chosen according to the selectivity of Cyanex 272 in the sulfate system, where the extraction of Co system would increase from pH 3 until pH 5, and extraction of Ni is achieved over pH 6 [21]. However, in a bielementary solution, there is coextraction of Ni with Co at a pH lower than 6, as reported by Santanilla et al. (2021).

As depicted in Fig. 4, the selectivity of Co over Ni (Co/Ni) increased achieving the maximum at pH 5.0. As reported in the literature, the extraction of Co increases and the separation over Ni reaches the maximum in pH 5.0–5.4 [28, 29] which is the pH used for Co separation in the extractive process from Ni laterite [30, 31]. According to the results obtained in this study, the solution in the receiving chamber at pH 5.0 achieved better results for Co separation over Ni.

In this process, the stripping was not carried out with a concentrated acid as usually [30, 31]. Instead, water at pH 5.0 was used; in addition, it did not require a two-step process (extraction followed by stripping) and the Co separation occurred in a continuous pathway. On the other hand, the use of supported liquid membranes is not mature yet and more investigation is required before experiments at a pilot level.
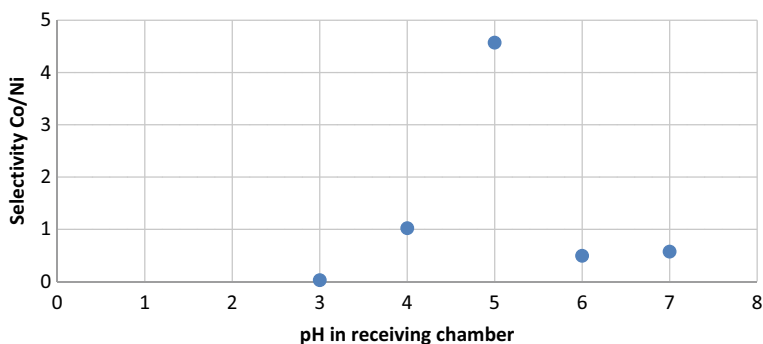
Fig. 4 Co/Ni selectivity (α) varying the pH in the receiving chamber

Table 1 Co/Ni selectivity (α) varying the pH of feed and receiving chambers

pH feed/strip	Separation Co/Ni
4/2	1.489
4/3	2.600
5/5	4.572

Table 1 presents the Co/Ni ratio varying the pH of feed and receiving chambers. As observed, the selectivity of Co over Ni was higher for solutions with the same pH. As aforementioned, this proposed process not require concentrated acid and only water in a determined pH for Co stripping. In addition, the use of supported liquid membrane may be beneficial as the chambers can be connected in series improving the purity of the solution. Despite the Co/Ni separation rate of 4.5, lower than 30% of Co extraction was achieved after 1 h, while all Co can be separated after 15min of reaction by solvent extraction technique. The kinetic may represent a drawback to be overcome in future studies.

Conclusions

This study aimed at the evaluation of supported liquid membranes for the separation of critical metals. The selective separation of Co over Ni was tested using Cyanex 272 in kerosene as a carrier. The type of membrane, extractant concentration, and pH of feed and receiving chambers were evaluated. The results have demonstrated the process can be selective for Co separation from Ni. Although the stripping in solvent extractant plants uses concentrated acids as sulfuric acid, this study proposes the use of water at pH 5.0 for stripping (in the receiving chamber). So, the separation of Co may be carried out as continuous with chambers connected. However, the kinetics is a drawback to the process compared to solvent extraction. The study of supported liquid membranes is important to the development of hydrometallurgical process.

References

1. Bobba S, Carrara S, Huisman J, Mathieux F, Pavel C (2020) Critical raw materials for strategic technologies and sectors in the EU—a foresight study. Eur Union. https://doi.org/10.2873/58081
2. Martins LS, Guimarães LF, Botelho Junior AB, Tenório JAS, Espinosa DCR (2021) Electric car battery: an overview on global demand, recycling and future approaches towards sustainability. J Environ Manage 295:113091. https://doi.org/10.1016/j.jenvman.2021.113091
3. Sovacool BK, Ali SH, Bazilian M, Radley B, Nemery B, Okatz J, Mulvaney D (1979) Sustainable minerals and metals for a low-carbon future. Science 367(2020):30–33. https://doi.org/10.1126/science.aaz6003
4. Soergel B, Kriegler E, Weindl I, Rauner S, Dirnaichner A, Ruhe C, Hofmann M, Bauer N, Bertram C, Bodirsky BL, Leimbach M, Leininger J, Levesque A, Luderer G, Pehl M, Wingens C, Baumstark L, Beier F, Dietrich JP, Humpenöder F, von Jeetze P, Klein D, Koch J, Pietzcker R, Strefler J, Lotze-Campen H, Popp A (2021) A sustainable development pathway for climate action within the UN 2030 Agenda. Nat Clim Chang 11:656–664. https://doi.org/10.1038/s41558-021-01098-3
5. Zhang L, Xu Z (2016) A review of current progress of recycling technologies for metals from waste electrical and electronic equipment. J Clean Prod 127:19–36. https://doi.org/10.1016/j.jclepro.2016.04.004
6. Perez JPH, Folens K, Leus K, Vanhaecke F, Van Der Voort P, Du Laing G (2019) Progress in hydrometallurgical technologies to recover critical raw materials and precious metals from low-concentrated streams. Resour Conserv Recycl 142:177–188. https://doi.org/10.1016/j.resconrec.2018.11.029
7. Tesfaye F, Lindberg D, Hamuyuni J, Taskinen P, Hupa L (2017) Improving urban mining practices for optimal recovery of resources from e-waste. Miner Eng 111:209–221. https://doi.org/10.1016/j.mineng.2017.06.018
8. Free ML (2022) Hydrometallurgy: fundamentals and applications, 2nd ed. Springer Cham. https://doi.org/10.1007/978-3-030-88087-3
9. Kislik VS (2014) Solvent extraction: classical and novel approaches. https://doi.org/10.1007/s13398-014-0173-7.2
10. Mwewa B, Tadie M, Ndlovu S, Simate GS, Matinde E (2022) Recovery of rare earth elements from acid mine drainage: a review of the extraction methods. J Environ Chem Eng 10:107704. https://doi.org/10.1016/j.jece.2022.107704
11. Botelho Junior AB, Tenório JAS, Espinosa DCR (2023) Separation of critical metals by membrane technology under a circular economy framework: a review of the state-of-the-art. Processes 11:1256. https://doi.org/10.3390/pr11041256.
12. Gmar S, Chagnes A, Lutin F, Muhr L (2022) Application of electrodialysis for the selective lithium extraction towards cobalt, nickel and manganese from leach solutions containing high divalent cations/li ratio. Recycling 7. https://doi.org/10.3390/recycling7020014
13. Song Y, Zhao Z (2018) Recovery of lithium from spent lithium-ion batteries using precipitation and electrodialysis techniques. Sep Purif Technol 206:335–342. https://doi.org/10.1016/j.seppur.2018.06.022
14. Parhi PK (2013) Supported liquid membrane principle and its practices: a short review. J Chem 2013:1–11. https://doi.org/10.1155/2013/618236

15. Zante G, Boltoeva M, Masmoudi A, Barillon R, Trébouet D (2020) Selective separation of cobalt and nickel using a stable supported ionic liquid membrane. Sep Purif Technol 252:117477. https://doi.org/10.1016/j.seppur.2020.117477

16. Rout PC, Sarangi K (2022) A systematic study on extraction and separation of scandium using phosphinic acid by both solvent extraction and hollow fibre membrane. Mineral Process Extr Metall Trans Inst Min Metall 131:166–176.https://doi.org/10.1080/25726641.2021.1908079

17. Léniz-Pizarro F, Liu C, Colburn A, Escobar IC, Bhattacharyya D (2021) Positively charged nanofiltration membrane synthesis, transport models, and lanthanides separation, J Memb Sci 620. https://doi.org/10.1016/j.memsci.2020.118973

18. Ni'Am AC, Liu YH, Wang YF, Chen SW, Chang GM, You SJ (2020) Recovery of neodymium from waste permanent magnets by hydrometallurgy using hollow fibre supported liquid membranes. Solvent Extr Res Dev 27:69–80. https://doi.org/10.15261/serdj.27.69

19. Santanilla AJM, Aliprandini P, Benvenuti J, Tenorio JAS, Espinosa DCR (2021) Structure investigation for nickel and cobalt complexes formed during solvent extraction with the extractants Cyanex 272, Versatic 10 and their mixtures. Miner Eng 160:106691. https://doi.org/10.1016/j.mineng.2020.106691

20. Botelho Junior AB, da Silva NOM, Tenório JAS, Espinosa DCR (2023) Structure investigation of La, Y, and Nd complexes in solvent extraction process with liquid phosphine oxide, phosphinic acid, and amine extractants. Metals (Basel) 13:1434. https://doi.org/10.3390/met13081434

21. CYTEC, CYANEX 272 extractant (2008) 16. http://www.cytec.com/sites/default/files/datasheets/CYANEX272Brochure.pdf. Accessed 16 Jan 2018

22. Chen L, Wu Y, Dong H, Meng M, Li C, Yan Y, Chen J (2018) An overview on membrane strategies for rare earths extraction and separation. Sep Purif Technol 197:70–85. https://doi.org/10.1016/j.seppur.2017.12.053

23. Lightfoot EN (1996) Membrane separations technology: Principles and applications. Chem Eng Sci 51:325–326. https://doi.org/10.1016/s0009-2509(96)90039-1

24. DuChanois RM, Mazurowski L, Fan H, Verduzco R, Nir O, Elimelech M (2023) Precise cation separations with composite cation-exchange membranes: role of base layer properties. Environ Sci Technol. https://doi.org/10.1021/acs.est.3c00445

25. Yuksekdag A, Kose-Mutlu B, Wiesner MR, Koyuncu I (2022) Effect of pre-concentration on membrane solvent extraction process for the recovery of rare earth elements from dilute acidic leachate. Process Saf Environ Prot 161:210–220. https://doi.org/10.1016/j.psep.2022.03.035

26. Janiszewska M, Markiewicz A, Regel-Rosocka M (2019) Hydrometallurgical separation of Co(II) from Ni(II) from model and real waste solutions. J Clean Prod 228:746–754. https://doi.org/10.1016/j.jclepro.2019.04.285

27. Li L, Davis K, King A, Dal-Cin M, Nicalek A, Yu B (2022) Efficient separation of Nd(III) and La(III) Via supported liquid membrane using EHEHPA (P507) as a carrier. J Sustain Metall 8:1215–1224. https://doi.org/10.1007/s40831-022-00560-6

28. Takahashi VCI, Botelho Junior AB, Espinosa DCR, Tenório JAS (2020) Enhancing cobalt recovery from Li-ion batteries using grinding treatment prior to the leaching and solvent extraction process. J Environ Chem Eng 8:103801. https://doi.org/10.1016/j.jece.2020.103801

29. Mubarok MZ, Hanif LI (2016) Cobalt and nickel separation in nitric acid solution by solvent extraction using cyanex 272 and versatic 10. Procedia Chem 19:743–750. https://doi.org/10.1016/j.proche.2016.03.079

30. Crundwell FK, Moats MS, Ramachandran V, Robinson TG, Davenport WG (2011) Extractive metallurgy of nickel, cobalt and platinum-group metals, first. Elsevier, Oxford

31. Botelho Junior AB, Espinosa DCR, Dreisinger D, Tenório JAS (2019) Recovery of nickel and cobalt from nickel laterite leach solution using chelating resins and pre-reducing process. Can J Chem Eng 97:1181–1190. https://doi.org/10.1002/cjce.23359

Solvent Extraction of Fe^{3+} with 2-Octanol from Wastewater After Gallium Recovery

Xiaozhou Zhou, Mingyu Wang, Wenjuan Guan, Shengxi Wu, Zuoying Cao, Qinggang Li, and Guiqing Zhang

Abstract The process of gallium extraction from fly ash produces a large amount of acidic wastewater. The presence of Fe^{3+} and heavy metal ions in the wastewater after gallium recovery makes it impossible to return to the fly ash leaching process for recycling. In this study, 2-Octanol diluted with sulphonated kerosene was used to extract Fe^{3+} from the acidic wastewater. In a six-stage counter-current with the conditions of O/A = 2/1, 25 °C, 5 min, 4.5 mol/L of HCl, the extraction of Fe^{3+} can reach more than 99%. Over 99.9% of Fe^{3+} could be stripped in a six-stage counter-current batch simulation test using 0.1 mol/L HCl. The mechanism of Fe^{3+} extraction using 2-Octanol was discussed according to FT-IR spectra results.

Keywords Fe^{3+} · 2-Octanol · Solvent extraction

Introduction

Fly ash is the main by-product of coal-fired power generation, which has a large yield and is difficult to use. However, fly ash contains many active silicon, aluminum components, and useful elements such as iron, carbon, gallium, and germanium, especially gallium content up to 30–200 g/t has great economic recovery value. In the last few years, the extraction of aluminum [1] and gallium [2] from fly ash has received extensive attention.

In China, a technology for the recovery of Al and Ga from fly ash was developed by Shenhua Zhungeer Energy and Resources Comprehensive Development Co., Ltd. The complete process involves leaching fly ash with a hydrochloric acid solution, followed by resin adsorption to recover Ga, removal of Ca, and crystallization of

X. Zhou · M. Wang · W. Guan · S. Wu · Z. Cao · Q. Li · G. Zhang (✉)
School of Metallurgy and Environment, Central South University, Changsha 410083, Hunan, China
e-mail: gq_zhang@163.com

Key Laboratory of Metallurgical Separation Science and Engineering in Nonferrous Industry, Central South University, Changsha 410083, Hunan, China

aluminum chloride. In the process of Ga recovery by resin, nearly all iron and gallium, as well as a significant number of heavy metals, are adsorbed from the leachate, along with a minor quantity of aluminum [3]. The solution obtained after desorption with hydrochloric acid is utilized for gallium extraction. The residual solution post gallium extraction primarily comprises Fe, Al, Ca, and a small number of heavy metals including Zn, Cu, Pb, and Mn. The HCl concentration in this wastewater is 1.5–2.5 mol/L. How to treat this acid wastewater economically and effectively is an urgent problem for enterprises at present.

In this study, a novel process for the treatment of acid wastewater was proposed and the flowsheet is shown in Fig. 1. In this process, iron is first extracted and then heavy metals such as copper and lead are removed, and the remaining solution is returned to the fly ash leaching process for recycling. The iron content in acid wastewater is the highest. How to separate and recover iron economically and effectively is the key step of the new technology.

Precipitation [4], ion exchange [5], and solvent extraction [6] are the conventional separation methods of Fe(III). The treatment of the wastewater by precipitation method will produce a large amount of iron slag as well as introduce a large number of cationic impurities, which makes the wastewater cannot be recycled. The treatment of solution with high iron concentration by ion exchange method will produce many secondary wastewaters. Solvent extraction has the advantages of low cost, high recovery rate, and product of high purity [7, 8]. The neutral extractants, TBP and MIBK, have been extensively investigated for their ability to extract Fe^{3+} from hydrochloric acid systems, particularly in the production of high-purity iron compounds [9–11]. However, MIBK exhibits a low flash point, and high solubility in an aqueous phase [12]. The use of TBP presents two challenges, namely the formation of a third phase and its high cost. Compared to MIBK and TBP, 2-Octanol exhibits lower water solubility (0.08% (v/v)), lower volatility, lower cost, and no third phase. In the present study, 2-Octanol was used for the extraction of iron from a

Fig. 1 Flow sheet for extraction of acid wastewater
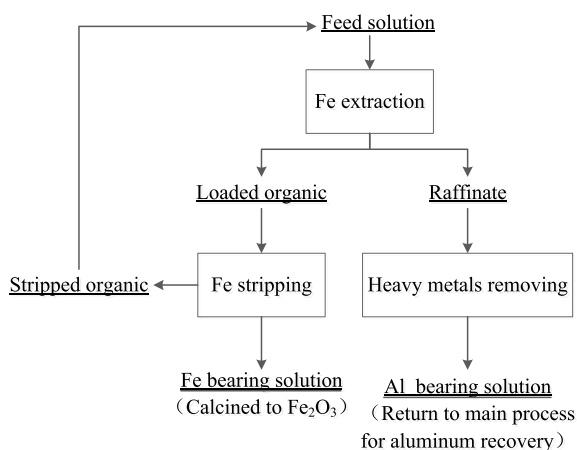
Table 1 Chemical composition of the wastewater (mg/L)

Fe^{3+}	Al^{3+}	Ca^{2+}	Mn^{2+}	Zn^{2+}	Pb^{2+}	Cu^{2+}	Cl^-
91,530	2570	2430	90.6	11.43	10.98	19.79	267,880

solution containing 91.53 g/L Fe^{3+} and 2.04 mol/L HCl. The extraction mechanism of Fe^{3+} was also investigated.

Materials and Methods

Materials

The wastewater after gallium recovery used in this study was obtained from Shenhua Zhungeer Energy and Resources Comprehensive Development Co., Ltd. The chemical composition of the wastewater is shown in Table 1. The HCl concentration in the wastewater was 2.04 mol/L. All the chemical reagents used in this study, such as HCl, $CaCl_2$, and $FeCl_3$, were of analytical grade. The extractant of 2-Octanol (99%) and the diluent of sulfonated kerosene used in this study were obtained from Shanghai Rare-Earth Chemical Co., Ltd., China.

Experimental Procedures

In the extraction experiment, the wastewater and organic phase were first poured into a 125-mL separating funnel according to the required organic/aqueous ratio (O/A). Then, the funnel was placed in a water bath oscillator at the reaction temperature for a specified time. The reaction temperature and time were varied. After phase separation, 1 mL of the raffinate was sampled for analysis. For the stripping experiments, the loaded organic phase and 0.1 mol/L HCl were mixed and added to a separating funnel. The specific testing process was the same as for the extraction tests. After phase separation, 1 mL of stripping liquor was sampled for analysis.

The concentrations of Al^{3+}, Zn^{2+}, Ca^{2+}, Mn^{2+}, Pb^{2+}, and Cu^{2+} in the aqueous phase were determined by ICP-OES (iCAP 7200 Radial, Thermo Fisher Scientific, USA). The concentrations of Fe were determined by the potassium dichromate ($K_2Cr_2O_7$) volumetric method, and the concentrations of ions in the loaded organic phase were obtained by mass balance calculations. The acid content in the aqueous solution was determined by potentiometric titration with aqueous NaOH. The total element analysis of the strip liquor was determined by ICP with mass spectrometric detection (ICP-MS). A Nicolet iS50 instrument was applied to obtain the IR spectrums of the organic phase.

The extraction efficiency (E, %) and stripping efficiency (S, %) of Fe were calculated using Eqs. (1) and (2), respectively.

$$E = 100\% \times (C_0 V_0 - C_1 V_1)/C_0 V_0 \tag{1}$$

$$S = 100\% \times C_2 V_2/C_{\text{org}} V_{\text{org}} \tag{2}$$

where V_0 and V_1 denote the volume of the aqueous phase before and after extraction, respectively; C_0 and C_1 are the concentrations of Fe in the aqueous phase before and after extraction, respectively; V_{org} and V_2 denote the volumes of the loaded organic phase and strip liquor, respectively; and C_{org} and C_2 are the Fe concentration of the loaded organic phase and strip liquor, respectively.

Results and Discussion

Solvent Extraction of Fe^{3+}

Effect of 2-Octanol Concentration

To determine a suitable extractant concentration, the tests were carried out using different 2-Octanol concentrations in the organic phase ranging from 50 to 100 vol%, and the results are shown in Fig. 2. As can be seen, the extraction of Fe^{3+} increased from 59.52% to 72.09% with an increase in 2-octonal concentration from 50 vol % to 80 vol %. A further increase in the concentration of 2-octanol only results in a small increase in the extraction of Fe^{3+}. Therefore, the optimum extraction concentration of 2-octanol is determined to be 80 vol %.

Effect of HCl Concentration

Figure 3 shows the effect of HCl concentration on the extraction of Fe^{3+}. With HCl concentration increasing from 2.5 mol/L to 6.5 mol/L, the extractions of Fe^{3+} increased from 45.55% to 94.70%. It means that the higher the concentration of hydrochloric acid, the higher the extraction of Fe^{3+}. However, a higher concentration of hydrochloric acid is not better. On the one hand, a high concentration of hydrochloric acid increases acid consumption. On the other hand, more HCl would be brought into the organic phase, resulting in a lower iron stripping efficiency. Therefore, the concentration of hydrochloric acid in the aqueous phase must be appropriate.

Fig. 2 Effect of 2-Octanol
concentration (O/A = 2/1,
extraction time = 5 min, HCl
concentration = 4.5 mol/L,
temperature = 25 °C)
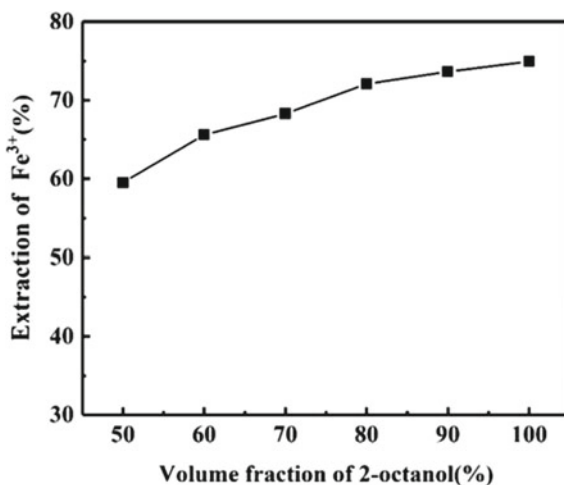
Fig. 3 Effect of HCl
concentration (O/A = 2/1,
extraction time = 5 min,
80%(*v/v*) 2-Octanol in
sulfonated kerosene,
temperature = 25 °C)
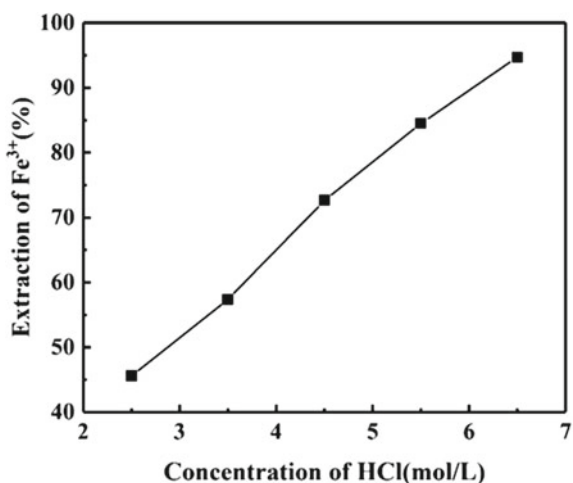
Effect of Temperature

The extraction efficiency of Fe^{3+} at different temperatures is shown in Fig. 4. When
the temperature rose from 10 °C to 50 °C, the extraction efficiency of Fe^{3+} rapidly
increased from 65% to 82.5%. These results may be due to the endothermic nature of
the extraction reaction at experimental temperature, which means that a high temper-
ature is preferable for the extraction. Nonetheless, high temperature brings about a
high loss of the organic phase dissolution and energy consumption. Therefore, room
temperature (25 °C) is considered the optimum one for the following experiments.

Fig. 4 Effect of temperature (O/A = 2/1, HCl concentration = 4.5 mol/L, extraction time = 5 min, 80%(*v/v*) 2-Octanol in sulfonated kerosene)
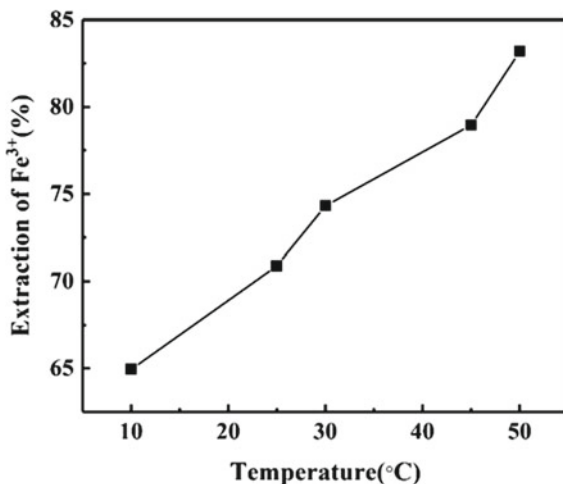
Effect of Time

Figure 5 illustrates the effect of reaction time on the extraction of Fe^{3+}. At the extraction time of 0.5 min, the Fe^{3+} extraction efficiency was about 72%. Upon extending the extraction time from 0.5 to 8.0 min, the Fe^{3+} extraction efficiency remained unchanged. These findings indicated that as the organic phase and feed liquor mixed gradually, the Fe^{3+} extraction balance could be reached within 0.5 min.

Fig. 5 Effect of time (O/A = 2/1, HCl concentration = 4.5 mol/L, temperature = 25°C, 80%(*v/v*) 2-Octanol in sulfonated kerosene)
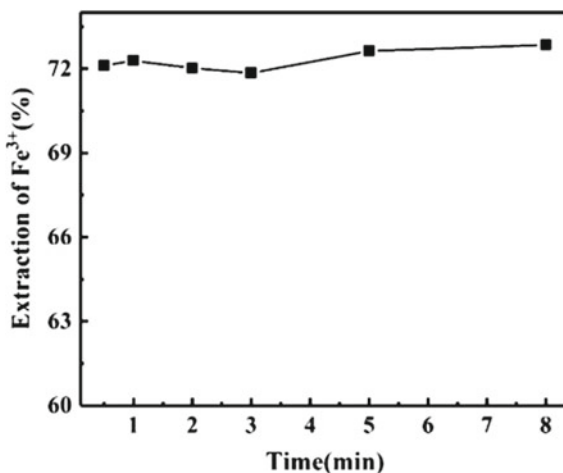
Extraction Equilibrium Isotherm of Fe^{3+}

The Fe^{3+} extraction equilibrium isotherm is obtained in Fig. 6. The saturated capacity of Fe^{3+} extraction reached 54.25 g/L in the presence of 4.5 mol/L hydrochloric acid. McCabe–Thiele analysis predicted that the concentration of Fe^{3+} in the raffinate can be reduced to less than 1 g/L by adopting a five-stage continuous counter current extraction at an O/A ratio of 2/1 in the HCl concentration of 4.5 mol/L. In the actual operation process, due to stage efficiency, one to two more stages were generally added on the basis of the theoretical series. To confirm this, a six-stage counter-current batch simulation test was carried out. The results are shown in Table 2. The extraction of Fe^{3+} was above 99% after equilibrium.
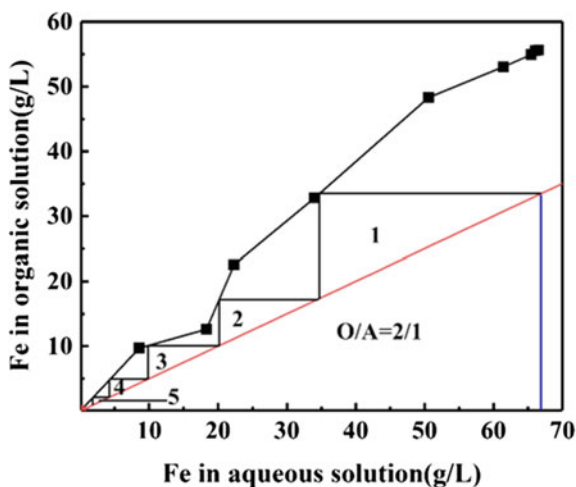
Fig. 6 The extraction equilibrium isotherm of Fe^{3+} (HCl concentration $= 4.5$ mol/L, time $=$ 5 min, temperature $= 25$ °C, 80%(v/v) 2-Octanol in sulfonated kerosene, the extraction equilibrium isotherm was generated from individual tests with different O/A ratios keeping iron feed concentration constant in each test)

Table 2 The result of six-stage counter-current batch simulation test (HCl concentration $= 4.5$ mol/L, O/A $= 2$, time $= 5$ min, temperature $= 25$°C, 80%(v/v) 2-Octanol in sulfonated kerosene)

Number of row	Fe^{3+} in raffinate, mg/L	Extraction of Fe^{3+}, %
11	0.74	98.89
14	0.53	99.21
16	0.54	99.19
18	0.52	99.22
20	0.50	99.25

Fig. 7 The stripping equilibrium isotherm of Fe^{3+} (contact time = 5 min, temperature = 25 °C, stripping agent: 0.1 mol/L HCl)
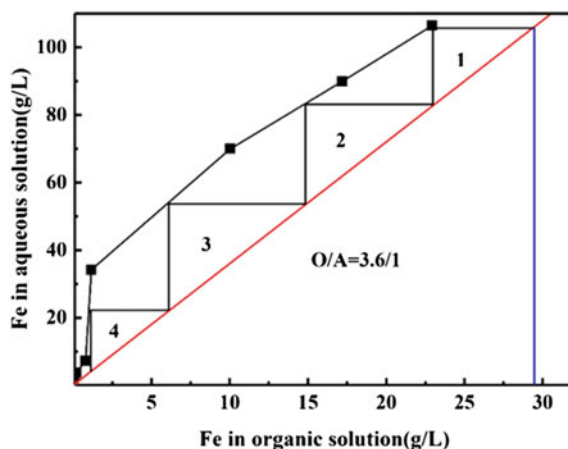
Table 3 The total element analysis of the strip liquor(mg/L)

Fe^{3+}	Zn^{2+}	Ti^{4+}	Pb^{2+}	Ni^{2+}	Co^{2+}	Mn^{2+}	K^+	Cu^{2+}	Cr^{3+}	Ca^{2+}	Al^{3+}
90,410	5.24	0.27	0.08	0.31	4.7	4.23	1.20	0.02	0.8	3.77	0.46

Stripping

Stripping Equilibrium Isotherm of Fe(III)

The McCabe–Thiele diagram for the stripping of Fe^{3+} is shown in Fig. 7. Four stripping stages using an O/A phase ratio of 3.6/1 led to quantitative stripping of Fe^{3+} from the loaded organic. In the actual operation process, considering stage efficiency, one to two more stages were generally added on the basis of the theoretical series. To confirm this, a six-stage counter-current batch simulation test was conducted under present conditions and the typical stripped organic and strip liquor were sampled and analyzed. For the strip liquor and stripped organic contented 90.41 g/L and 0.08 g/L of Fe^{3+}, respectively, the stripping efficiency was over 99.9%. The total element analysis of the strip liquor is listed in Table 3. With low impurity content and high ferric chloride concentration, the strip liquor can be directly applied to synthesize ferric oxide red or polyferric chloride.

Analysis of IR Spectra

To explore the extraction mechanism of Fe^{3+}, the FT-IR spectra of the extractant (Fig. 8) before and after extraction were investigated in detail. It can be seen from Fig. 8 that there is a clear –OH peak at 3421 cm^{-1} before 80%(*v/v*) 2-Octanol in

Fig. 8 FT-IR spectra of extractant before and after extraction. 80%(v/v) 2-Octanol in sulfonated kerosene (**a**), 80%(v/v) 2-Octanol in sulfonated kerosene extraction of Fe^{3+} in HCl (**b**), 80%(v/v) 2-Octanol in sulfonated kerosene extraction of HCl solution (**c**)
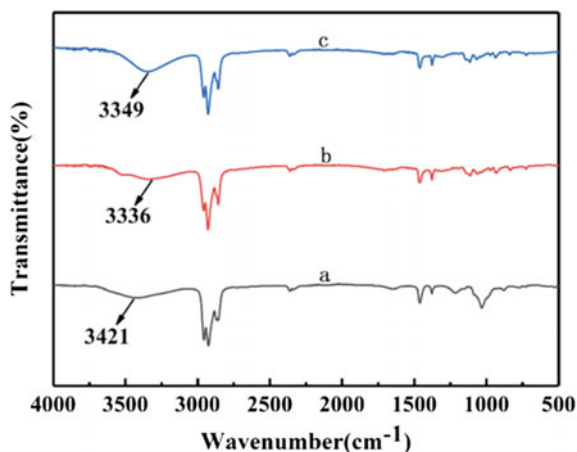
sulfonated kerosene extraction (Fig. 8a). After the HCl solution was extracted by the 80%(v/v) 2-Octanol in sulfonated kerosene extraction, the –OH peak redshifts to 3349 cm^{-1} (Fig. 8c), which means that ROH uses –OH to extract HCl. When Fe^{3+} in HCl solution was extracted by 80%(v/v) 2-Octanol in sulfonated kerosene, the –OH peaks are red-shifted to 3336 cm^{-1} (Fig. 8b), which implies that Fe^{3+} is extracted by ROH because of the role of –OH.

Conclusions

(1) 2-Octanol was an effective extractant for the selective separation of iron from hydrochloric acid leaching solution of fly ash leaching. The result of FT-IR spectra indicated the mechanism of iron extraction using 2-Octanol extractant.

(2) The extraction efficiency of Fe^{3+} was above 99% under the conditions of six-stage counter-current batch simulation test, O/A = 2/1, 25 °C, 5 min, 4.5 mol/L of HCl.

(3) The loaded organic phase can be stripped completely and regenerated in a six-stage counter-current batch simulation test using 0.1 mol/L HCl. With low impurity content and high ferric chloride concentration, the strip liquor could be used to synthesize ferric oxide red or polyferric chloride directly.

References

1. Guo YX, Li YY, Cheng FQ, Wang XM (2013) Role of additives in improved thermal activation of coal fly ash for alumina extraction. Fuel Process Technol 110:114–121

2. Gutiérrez B, Pazos C, Coca J (1997) Recovery of gallium from coal fly ash by a dual reactive extraction process. Waste Manage Res 15:371–382

3. Zhou XZ, Shen YJ, Peng J, Liu Q (2021) Separation of Fe (III) and Al via tributyl phosphate and 2-Octanol in the comprehensive recovery process of metals from hydrochloric acid leaching solution of fly ash. Solvent Extr Res Dev Jpn 28(1):59–68. https://doi.org/10.15261/serdj.28.59

4. Kim JK, Oh HS, Jo CW, Suh YJ, Jang HD, Koo KK (2020) Recovery of iron as a form of ferrous acetate precipitates from low-grade magnetite ore. Chem Eng Res Des 88(11):1467–1473. https://doi.org/10.1016/j.cherd.2009.08.011

5. McKevitt B, Dreisinger D (2009) A comparison of various ion exchange resins for the removal of ferric ions from copper electrowinning electrolyte solutions Part II: electrolytes containing antimony and bismuth. Hydrometallurgy 98(1–2):122–127. https://doi.org/10.1016/j.hydromet.2009.04.007

6. Biswas RK, Begum DA (1998) Solvent extraction of Fe^{3+} from chloride solution by D2EHPA in kerosene. Hydrometallurgy 50(2):153–168. https://doi.org/10.1016/S0304-386X(98)00048-6

7. Kumar JR, Kim JS, Lee JY, Yoon HS (2011) A brief review on solvent extraction of uranium from acidic solutions. Sep Purif Rev 40(2):77–125. https://doi.org/10.1080/15422119.2010.549760

8. Wang WW, Cheng CY (1996) Separation and purification of scandium by solvent extraction and related technologies: a review. J Chem Technol Biotechnol 86(10):1237–1246. https://doi.org/10.1002/jctb.2655

9. Reddy BR, Sarma PVRB (1996) Extraction of iron (III) at macro-level concentrations using TBP MIBK and their mixtures. Hydrometallurgy 43(1–3):299–306. https://doi.org/10.1016/0304-386X(95)00117-Y

10. Saji J, Reddy MLP (2001) Liquid–liquid extraction separation of iron (III) from titania wastes using TBP–MIBK mixed solvent system. Hydrometallurgy 61(2):81–87. https://doi.org/10.1016/S0304-386x(01)00146-3

11. Yi XT, Huo GS, Tang W (2020) Removal of Fe (III) from Ni-Co-Fe chloride solutions using solvent extraction with TBP. Hydrometallurgy 192:105265. https://doi.org/10.1016/j.hydromet.2020.105265

12. Cai XC, Wei B, Han JX, Li YX, Cui Y, Sun GX (2016) Solvent extraction of iron (III) from hydrochloric acid solution by N, N, N′, N′-tetra-2-ethylhexyldiglycolamide in different diluents. Hydrometallurgy 164:1–6. https://doi.org/10.1016/j.hydromet.2016.04.010

Manipulating Iron Precipitation and Gold Deportment During Pressure Oxidation

James Vaughan, Peter Legge, James Gudgeon, and Hong Peng

Abstract Pressure oxidation (POX) is the most utilized method for chemically liberating gold from sulfides. However, in the context of decreasing gold grades and increasingly complex mineralogy as well as variable qualities of process solutions, operations using POX can be challenged by high reagent consumption and in ensuring high gold recoveries. While POX technology is considered mature, a complete understanding of the phase transformations and gold deportment has yet to be described. In this work, by manipulating autoclave conditions, we report on batch pressure oxidation experiments where jarosite-only and hematite-only precipitates are obtained. The pressure oxidation reaction kinetics are monitored in-situ, via oxidation–reduction potential and pH measurements and interpreted with respect to recently calibrated equilibrium chemical thermodynamic data for the $Fe(II)$-$Fe(III)$-SO_4-H_2O system. Using a combination of assays, X-ray diffraction, and high-resolution SEM–EDS spectroscopy of feed and residue samples, insight into the chemical reactions taking place and gold redistribution is obtained. This research approach of combining in-situ measurements, chemical equilibrium and advanced sample characterisation will help in establishing new ways to improve process operations with existing process infrastructure.

Keywords Pressure oxidation · Refractory gold · Jarosite · Hematite · Iron precipitation

Introduction

Australia was the second largest gold producer in 2022 with 330 t produced with an associated $25.8 billion of export revenue (USGS, 2022). Around 2/3 of gold reserves are finely disseminated and hosted in sulfide minerals [1]. These ores are called "refractory", since gold liberation requires the destruction of the crystal structure of the host sulfide. This can be achieved via three main routes: (i) roasting at high

J. Vaughan · P. Legge · J. Gudgeon · H. Peng (✉)
School of Chemical Engineering, The University of Queensland, Brisbane, QLD 4072, Australia
e-mail: h.peng2@uq.edu.au
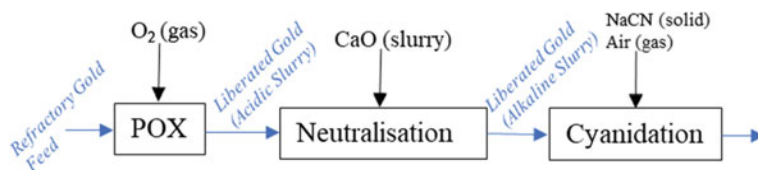
Fig. 1 Simplified process flow diagram for the extraction of gold from refractory sulfide feed

temperature (> 800 °C), an approach that has been phased out in Australia; (ii) BIo-OXidation (BIOX) which relies on sulfur-oxidising microbes at low temperatures in the range of 40–65 °C; and (iii) pressure oxidation (POX), which is a hydrometallurgical process conducted at intermediate temperatures (200–230 °C). The kinetics of pressure oxidation are much faster than BIOX. Compared to the other methods, POX yields higher gold recovery and enables better handling of environmentally sensitive impurities such as arsenic [2, 3].

Key aspects of the POX process remain poorly understood because in-situ observations of the process at elevated pressure and temperature remain challenging. Significant knowledge gaps include the nature and kinetics of the phase transformation of the gold-bearing sulfides and gold re-distribution and recovery of the precipitation of Fe-rich minerals. Most refractory gold ores contain "invisible gold", which occur mostly in the sulfide minerals arsenopyrite and pyrite [4]. "Invisible" gold usually cannot be detected via conventional optical microscopy or scanning electron microscopy (SEM) and comprises mainly ionic gold chemically bonded in the crystal structure of the sulfides [5, 6] or within lattice defects [7] or nano-size inclusions of metallic gold [1, 5, 8, 9]. The gold-bearing acidic slurry exiting the autoclave is then neutralised using lime. Finally, gold is leached using cyanide or alternative strong Au-complexing ligands (see Fig. 1).

Despite the industrial importance of the technology, limited knowledge exists in the public domain on the mineralogical and phase transformation in refractory gold ores at pressure oxidation, neutralisation, and cyanidation leaching stages. This is partly due to a lack of appropriate research infrastructure in university laboratories. In 1991, pyrite pressure oxidation reaction kinetics were studied at the University of Toronto. The leaching kinetics were found to be consistent with the shrinking particle model with reaction order of 0.5 at higher temperatures and pressures, the process is assumed to be kinetically limited by surface reaction control [10]. More recently, the University of Queensland PhD thesis of Ivana Ambrosia calculated a new set of equilibrium chemical thermodynamic data for iron precipitation, which was experimentally determined at 220 °C via rapid solid–liquid separation of autoclave flash sample, providing a reliable model at autoclave conditions including the stabilities of freshly precipitated basic ferric sulfate, potassium jarosite and hematite [11].

In this research, we investigated the effects of changing the pressure oxidation conditions (different initial acid concentration and extra potassium), we present examples where jarosite-only and hematite-only POX residues were generated. Then

using a combination of assays, X-ray diffraction, and high-resolution SEM–EDS spectroscopy of feed and residue samples, insight into the chemical reactions taking place and gold redistribution is obtained. Using this approach, it is expected that a deeper understanding of the reaction mechanisms and gold deportment will reveal more efficient pathways to enhance the gold extraction rate and reduce lime consumption, hence improving the economics of the POX process and the competitivity of the gold industry.

Experimental

Materials and Reagents

The gold ore tested was provided by Newcrest-Lihir (Papua New Guinea). All chemicals were of analytical grade. Dilute acid was prepared by diluting concentrated acids (98 wt% sulfuric acid, 70 wt% nitric acid) with either deionised or MilliQ water in either volumetric flasks or bottles depending on the required accuracy. Sodium hydroxide solutions were prepared by dissolving pellets in deionised water and then diluting using a volumetric flask.

Pressure Oxidation

All POX were performed at approximately 20 wt% (solids/slurry) solid loading, 230 g solids, 1.15 kg feed slurry, in a 2L titanium autoclave as shown in Fig. 2. Slurry was prepared at room temperature, loaded into the autoclave and then heated to the target temperature of 210 °C. Then oxidation was initiated by introducing pressurised oxygen gas into the reactor; and measured by pressure drop in a gas burette of known volume. 60 min after oxidation was initiated, the oxygen injection line was closed and the autoclave was cooled to a temperature below 60°C before opening the reactor. Liquor was recovered, its pH measured, and assayed by ICP and free acid titration. The solids were washed, dried at 105–150 °C, weighed, and submitted for XRD analysis. Select samples were also analysed using Coulter particle size analysis and/or characterised using scanning electron microscopy (SEM).

In situ Oxidation Reduction Potential (ORP) was measured between an external balanced 0.1 M KCl reference probe and the titanium body of the reactor. In Situ pH was measured between a ZrO_2-based probe and the same 0.1 M KCl reference probe. Both probes were sourced from Corr Instruments, LLC and fitted to the 2L Parr vessel, which was manufactured with a non-standard head to accommodate them.
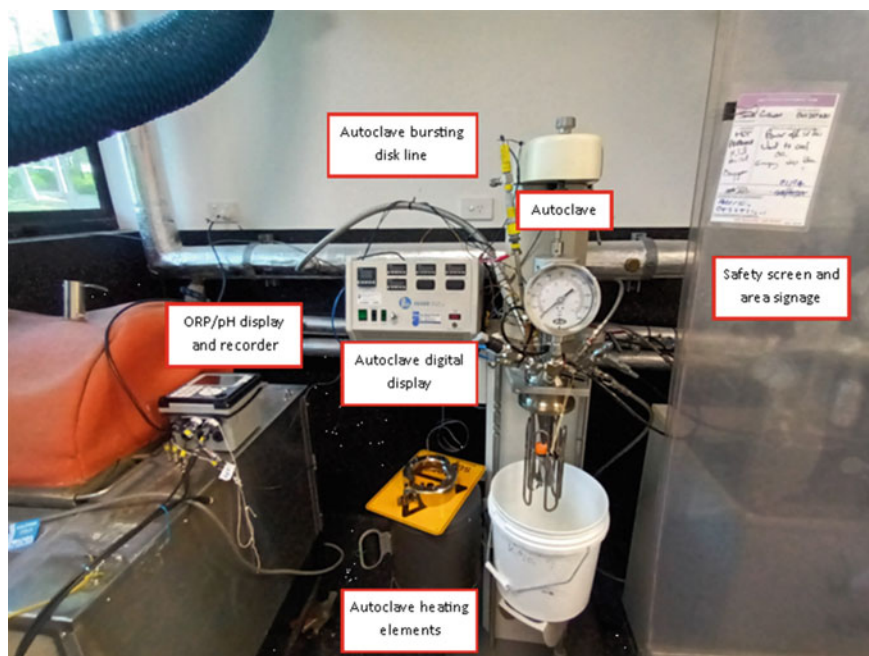
Fig. 2 Autoclave and related instruments. Note, the oxygen burette is behind the safety screen and area signage

Characterisation

The carbon-coated samples were imaged by scanning electron microscopy (SEM, HITACHI SU3500). The SEM operation conditions were at ambient temperature with an accelerating voltage of 5 kV with spot size of 30 nm. The samples were brought into focus at high resolution with working distances of 5–7 mm. The SEM–EDS elemental maps were taken with an accelerating voltage of 15 kV and spot size of 60 nm and working distance of 10 mm.

Dried (105 °C) and ground filter cakes were submitted for XRD analysis using a Bruckner Diffractometer at the Centre for Microscopy and Microanalysis (CMM). The samples were analysed between 5 and 60 (2θ) using a step size of 0.02 (2θ). The intensity peaks were compared to the PDF cards of mineral phases to identify major mineralogical phase samples.

The filtrate's final free acid was measured via potentiometric titration using potassium oxalate as a complexing agent to prevent ferric hydrolysis. Sufficient potassium oxalate was added to a 1–2 mL aliquot of filtrate to prevent hydrolysis of the dissolved ions at elevated pH. The analyte was diluted with de-ionised water and mixed with a magnetic stirrer to dissolve the potassium oxalate. Using a burette, 0.1 M NaOH titrant was added gradually, after each addition the pH was recorded. The largest increase in pH versus volume of titrant added was found to be the reaction endpoint

and the final concentration was calculated according to Eq. 1. The concentration of the 0.1 M NaOH was confirmed via an additional titration using 0.1 M HCl.

$$\text{Free acid } H_2SO_4\left(\frac{g}{L}\right) = \frac{\text{Endpoint(mL)}.C_{\text{Titrant}}(M)}{\text{Aliquot of anlayte (mL)}} . \frac{98.08\left(\frac{g}{mol}\right)}{2} \quad (1)$$

For some samples, an additional 1 mL of 95 g/L H_2SO_4 was added, requiring additional potassium oxalate due to higher levels of dissolved ions. The free acid concentration was adjusted for any additional acid.

Results and Discussion

Feed Sample Characterisation

The elemental composition of the feed sample was determined by a combination of methods (XRF, Dissolution-ICP-MLA, Leco-S, Fire Assay) as shown in Table 1.

Key minerals assumed and quantified by MLA were Orthoclase (44%), Muscovite (28%), Pyrite (15%), Quartz (3.8%), Gypsum (2.2%), Biotite (1.6%), Calcite (1.0%). Phases identified by XRD were K-Feldspar (Orthoclase), Muscovite, Pyrite, Quartz, Calcium Sulfate Hemihydrate, and Bentonite (Fig. 3).

The volume-based D50 of the feed is 15 μm, determined by Coulter laser sizing as shown in Fig. 5 with an apparent bimodal or even trimodal distribution. The particle morphology and elemental maps are shown in Fig. 4. The coarse fraction is mainly K-feldspar, bentonite, and quartz while the fine fraction is mainly pyrite and calcium sulfate hemihydrate. The association of Fe and Ca with S is evident. The gold signal in the elemental mapping is not sufficiently strong to resolve any associations, however, it is understood from that the gold is largely associated with the pyrite, thus the need for pressure oxidation to chemically liberate the gold from this host mineral matrix.

Table 1 Lihir feed sample composition

XRF (wt%)						LECO (wt%)	ICP-MS (g/t)	Fire assay (g/t)
O	Si	Fe	Al	K	Ca	S	Cu	Au
39	23	8.3	8.1	7.1	1.9	8.8	510	3
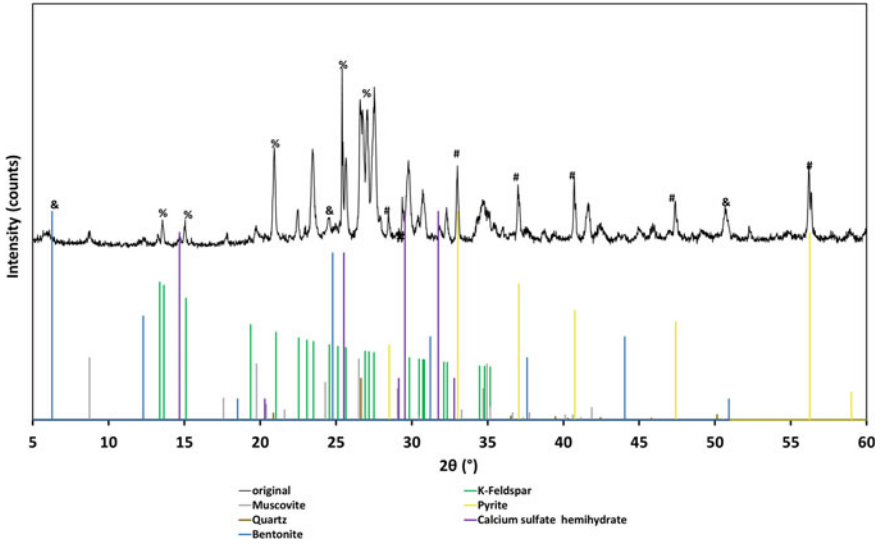
Fig. 3 XRD pattern for ore feed where major crystalline phases are identified (&: bentonite; %: K-feldspar; #: pyrite)
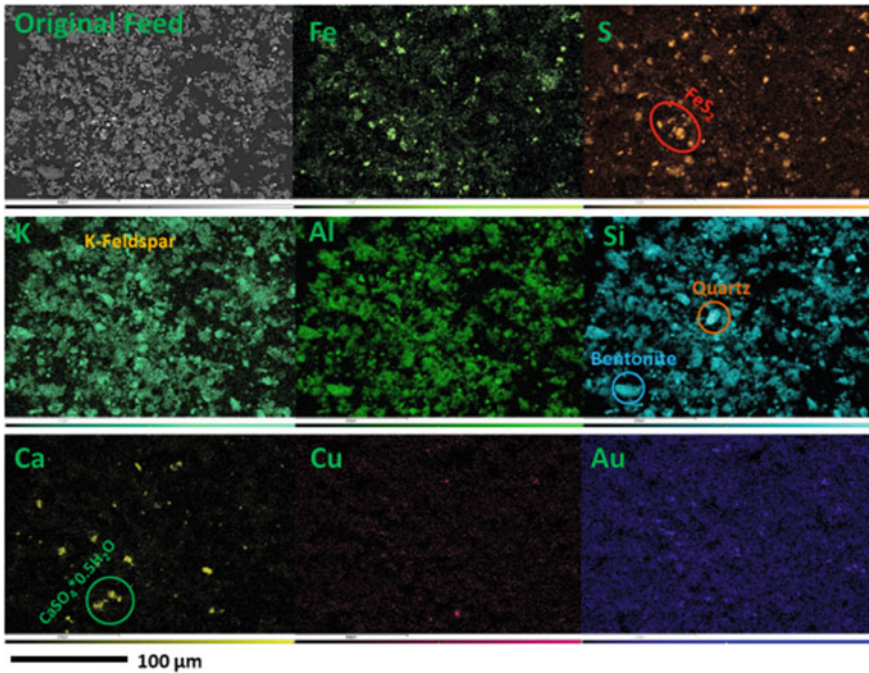
Fig. 4 SEM–EDS elemental maps of the feed
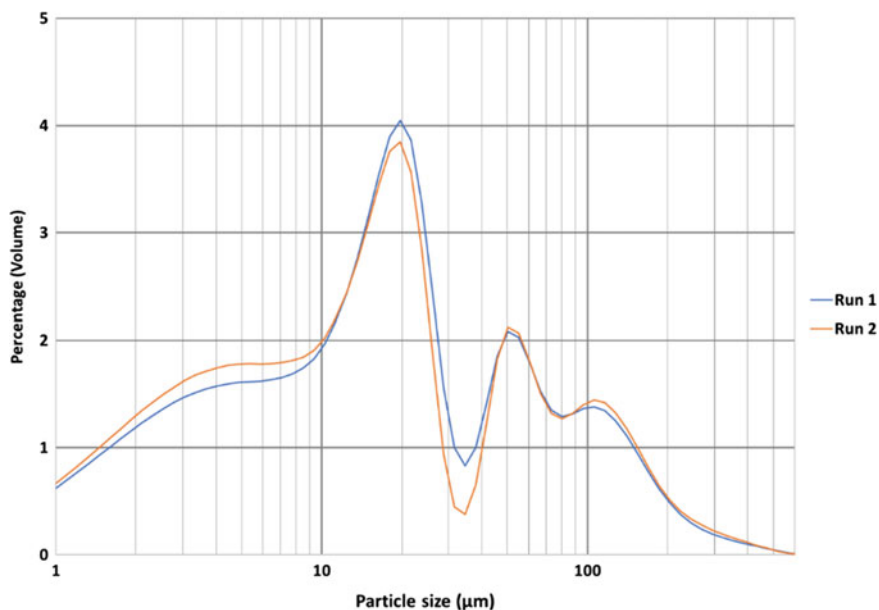
Fig. 5 Particle size distribution of ore samples with two repeat runs

Pressure Oxidation Results and Discussion

We report here on four pressure oxidation experiments, shown in Table 2 where the variables were the initial concentrations of potassium sulfate (0 or 20 g/L K_2SO_4) and sulfuric acid (0 or 20 g/L H_2SO_4). Pressure oxidation reactions resulted in the generation of 20–23 g/L H_2SO_4. A small amount of potassium was leached from the feed material during the experiments and a significant amount of the added potassium was precipitated, as potassium jarosite.

Table 2 Pressure oxidation experiments initial and final conditions

Initial conditions			Final conditions			
Test	K_2SO_4 g/L	H_2SO_4 g/L	K_2SO_4 g/L	H_2SO_4 g/L	ORP mV	Major iron phase
Determination	Mass	Mass	ICP-OES	Titration	In-situ	XRD
POX13 control	0	0	0.2	23	573	Hematite
POX19 acid	0	20	0.2	41	779	Hematite
POX21 potassium	14	0	4.7	25	655	Jarosite
POX20 acid + potassium	14	20	3.8	43	710	Jarosite

The final elemental solution compositions are shown in Table 3. The terminal iron in solution concentration was significantly lower at conditions where potassium jarosite was formed. Aluminium concentration was significantly reduced in the presence of potassium. Calcium and silicon were consistent for all the test conditions.

The oxygen supply was not limited and so it was consumed until the reaction was completed. It was similar for all four conditions, estimated to be 30–35 g-O_2, which is close to the expected requirement for pyrite to ferric oxidation. Increased acid, sulfate, and potassium in the feed solution will favour precipitation of potassium jarosite over hematite, based on reaction stoichiometry. The main expected oxidation and precipitation reactions are shown in Eqs. 2–5.

Pyrite Oxidation

$$FeS_{2(s)} + 3.5O_{2(g)} + H_2O_{(l)} = Fe^{2+}_{(aq)} + 2SO^{2-}_{4(aq)} + 2H^+_{(aq)} \tag{2}$$

Ferrous Oxidation

$$Fe^{2+}_{(aq)} + 0.25O_{2(g)} + H^+_{(aq)} = Fe^{3+}_{(aq)} + 0.5H_2O_{(l)} \tag{3}$$
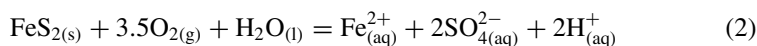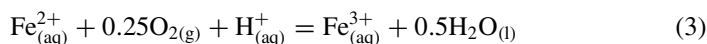
Potassium Jarosite Precipitation

$$K^+_{(aq)} + 3Fe^{3+}_{(aq)} + 2SO^{2-}_{4(aq)} + 6H_2O_{(l)} = KFe_3(SO_4)_2(OH)_{6(s)} + 6H^+_{(aq)} \tag{4}$$

Hematite Precipitation

$$2Fe^{3+}_{(aq)} + 3H_2O_{(aq)} = Fe_2O_{3(s)} + 6H^+_{(aq)} \tag{5}$$
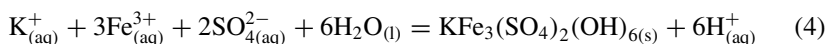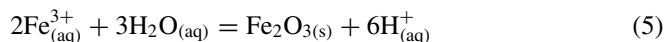
When considering solution speciation at 220 ˚C, the relevant potential pH diagram is similar to that determined by Ivana in 2020 (Fig. 6). At lower pH (below about 1.5), potassium jarosite is favoured over hematite when there is 3 g/L potassium in solution. At potentials above about 500 mV versus SHE, ferrous will be oxidized to ferric, which may be in the form of an aqueous sulfate-bisulfate complex. At the conditions specified, ferrous exceeds the solubility limit and may precipitate in

Table 3 Final solution from in-house ICP-OES for key elements (g/L)

	Al 396.152 nm	Ca 315.887 nm	Fe 238.204 nm	K 766.491 nm	S 181.972 nm	Si 288.158 nm
POX13 control	1.0	0.8	4.9	0.1	16	0.6
POX19 acid	2.3	0.8	2.0	0.1	21	0.6
POX21 potassium	0.2	0.8	0.5	2.1	13	0.7
POX20 acid + potassium	1.0	0.9	0.5	1.7	19	0.6
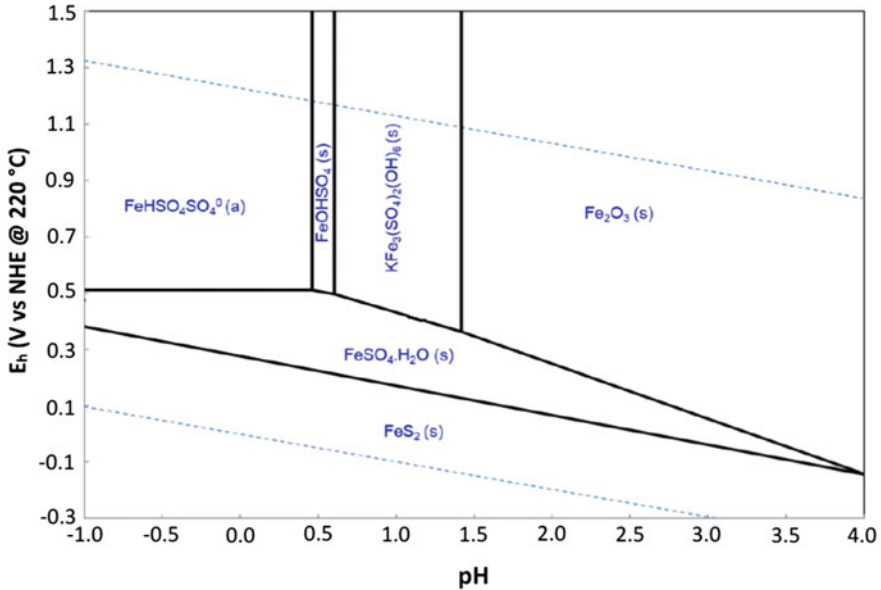
Fig. 6 E_h–pH diagram at 220 °C. Aqueous species concentrations [Fe^{3+}] = 1 g/L, [Fe^{2+}] = 2 g/L, [K^+] = 3 g/L, [$HSO4^-$] = 20 g/L, activity coefficients assumed to be equal to 1. Figure adapted from Ivana (2020)

the autoclave as ferrous sulfate monohydrate. Ferrous sulfate monohydrate and basic ferric sulfate exhibit reverse solubility and tend to dissolve upon exiting the autoclave when the slurry is cooled.

The pressure oxidation reactions were monitored in-situ by ORP and pH. ORP requires a temperature-dependent offset to adjust from 0.1 M KCl to SHE. This has been performed as specified in the document "Conversion of Ag/AgCl Electrode Potential to Standard Hydrogen Electrode Scale" provided by Corr Instruments and shown in Eq. 6.

$$E_{W,SHE,T} = \Delta E'_{meas} + 288 - \left(-3.0 \times 10^{-6}\Delta T^3 + 2.4 \times 10^{-3}\Delta T^2 + 0.7485\Delta T\right)$$
(6)

where $\Delta E'_{meas}$ is the reading if the external junction is maintained at 25 °C, and $E_{W,SHE,T}$ is the ORP at operating temperature (mV Ti vs. SHE). The current installation has insufficient external probe cooling to maintain 25 °C, which is a source of error. The expected error with an 80 °C external junction is around 30 mV, in this case, the external junction reached 57 °C so a ΔT of (210 − 57) has been used.

ZrO_2-based pH measurement does not perform well at low temperatures, so calibration must be performed at high temperature. For this work, calibration was performed at 95 °C and atmospheric pressure using commercially available pH 4 and

7 buffers. This does mean that the calibration is still lower than operating temperature, extrapolated operating pH; however, results were reasonably close to expected values. Most tests had pH drift below 90–110 °C but minimal change between this and + 150 °C.

Prior to oxygen being added into the reactor, the ORP in all tests was quite low, once the oxygen line is opened, the ORP jumps up into the range of 300–550 mV versus SHE where it would likely be pinned by the ferrous/ferric couple. As the reaction proceeds, the ORP gradually increases as ferrous if further oxidised to ferric and the supply of ferrous from the reacting pyrite diminishes. The experiments with acid exhibited a higher ORP, consistent with the sloping E-pH boundary between jarosite or hematite and ferrous sulfate hydrate.

As for the pH, there is a dramatic decrease within the first 10 min of reaction time and then a gradual decrease in pH as ferric is precipitated from solution. As expected, the experiments with higher initial (and final) acid concentrations exhibit a lower pH. It should be noted that due to the extrapolated pH calibration, the values shown may not me directly comparable with the pH values on the E_h–pH diagram as shown in Fig. 7, however, the values between experiments are comparable. Final free acid was determined by titration on the cooled solution.

The colour of the feed and POX residues varies considerably as shown in Fig. 8. The pyrite and clay-rich feed is grey, the hematite-rich residues (control and extra acid) are the characteristic rust-red and the jarosite-rich residues are light and dark beige for the extra K + acid and extra K conditions, respectively.

The XRD patterns of the solids are shown in Fig. 9. The feed exhibits the characteristic pyrite peaks, the potassium added test residues contain the characteristic
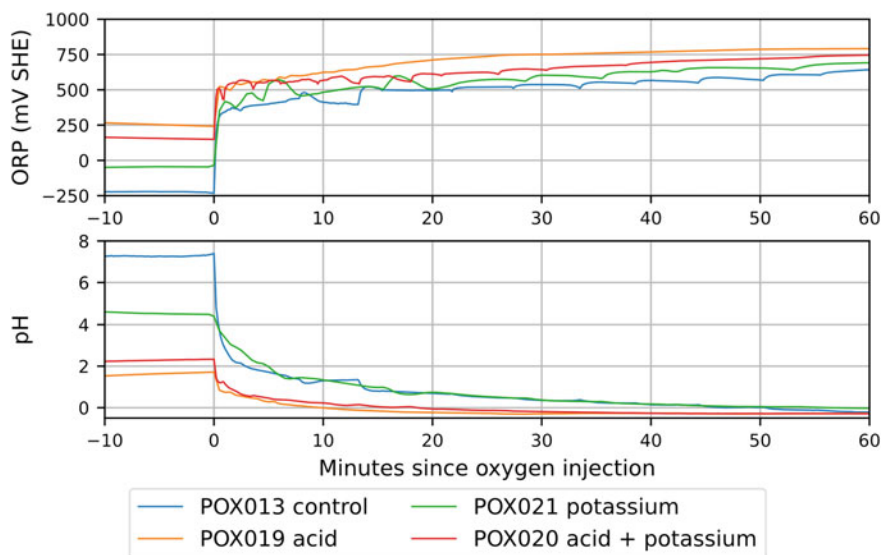
Fig. 7 In-situ oxidation–reduction potential measurement and in-situ pH measurement

Fig. 8 Photographs of feed sample and POX residues, showing the distinct colours

K-Jarosite peaks and the control and acid only tests exhibit the characteristic hematite peaks. The K-feldspar peaks also appear strongly in the residues. Since no jarosite is observed if we did not add potassium to the solution, it seems that the potassium in the feed K-feldspar only has a small or negligible contribution to the formation of K-jarosite.

Figure 10 is the elemental maps of the control test residue (hematite), and Fig. 11 is the elemental maps for the residue from the test with extra acid + K test (jarosite). When inspecting Fig. 10, we can see that with the hematite residue, the gold is diffuse and distributed, presumably associated the hematite. When inspecting Fig. 11, we see stronger localised signals for gold which appears to be associated with Ca and Cu rather than with Fe, S, or Si. This means that with jarosite formation, the gold is released from the iron and selectively redistributes.
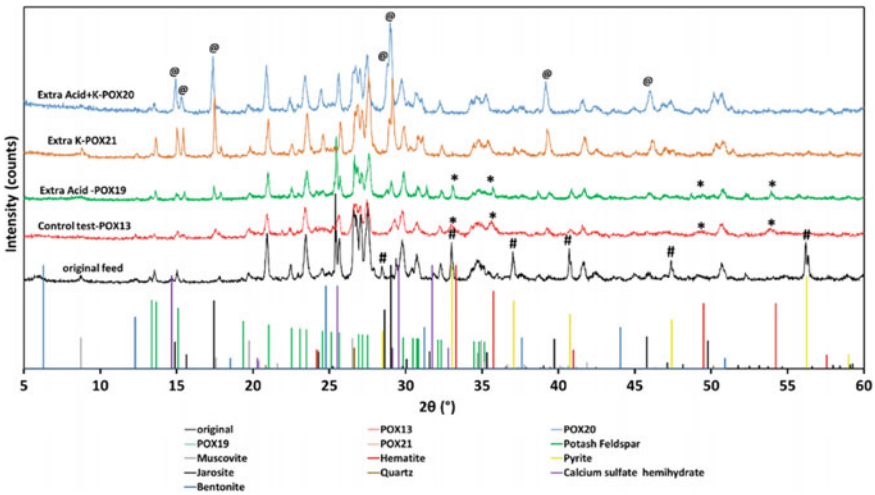
Fig. 9 XRD pattern of leaching residue at different conditions (&: bentonite; *: hematite; #: pyrite)
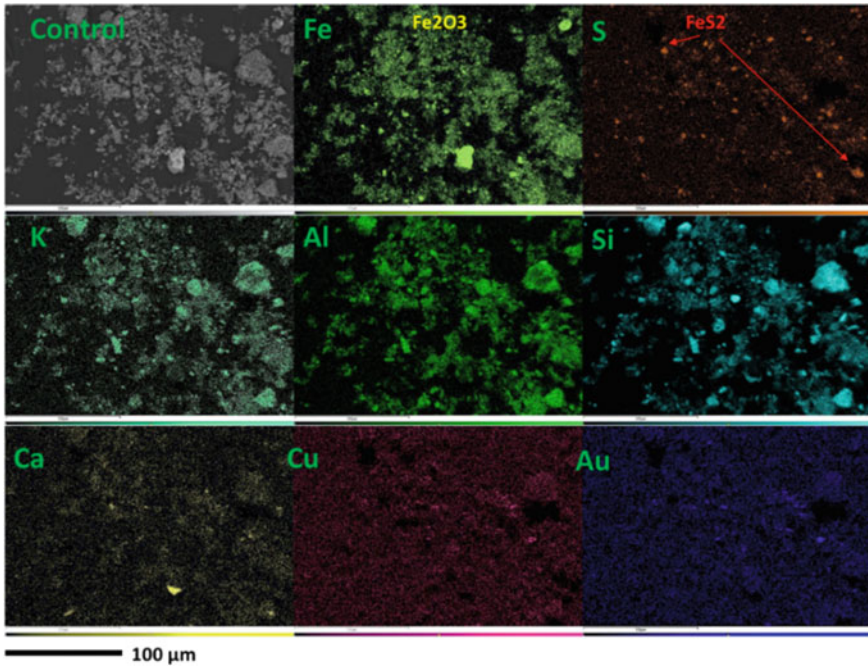
Fig. 10 SEM–EDS elemental maps of the POX13, control condition (no additives)

Conclusions

1. The presence of potassium in feed solution (20 g/L) strongly promotes the formation of jarosite.
2. From inspection of the jarosite-only POX residues, Au is selectively re-distributed during POX and shows a strong affinity for calcium sulphate and copper phase.
3. From inspection of the hematite-only residues, the gold is more evenly distributed and does not exhibit a strong signal, we assume it is associated with the freshly precipitated hematite.
4. Due to clay minerals in the original feed, silica gel is formed during POX leaching.
5. The K-feldspar in the feed is clearly present in the residues indicating that it only partly reacted.
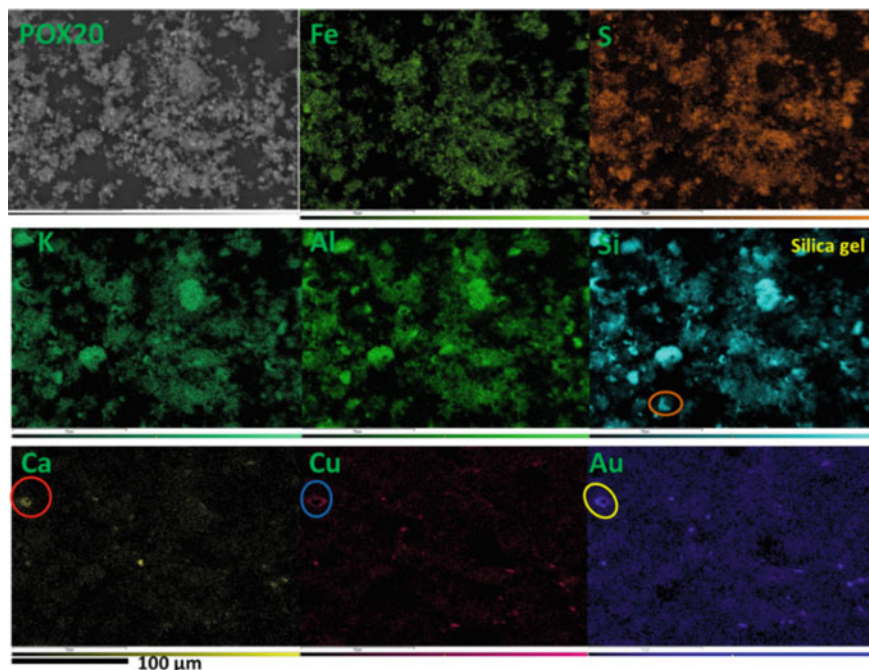
Fig. 11 SEM–EDS map of POX products for POX 20 (extra acid and extra potassium)

References

1. Fraser K, Walton R, Wells J (1991) Processing of refractory gold ores. Miner Eng 4(7–11):1029–1041
2. Evangelou V (2018) Pyrite oxidation and its control. CRC press
3. Rimstidt JD, Vaughan DJ (2003) Pyrite oxidation: a state-of-the-art assessment of the reaction mechanism. Geochim Cosmochim Acta 67(5):873–880
4. Maddox L et al (1998) Invisible gold: comparison of Au deposition on pyrite and arsenopyrite. Am Miner 83(12):1240–1245
5. Zhou JY, Cabri LJ (2004) Gold process mineralogy: objectives, techniques, and applications. Jom 56:49–52
6. Chen T, Cabri L, Dutrizac J (2002) Characterizing gold in refractory sulfide gold ores and residues. Jom 54:20–22
7. Li K et al (2016) Ore petrography using megapixel X-ray imaging: rapid insights into element distribution and mobilization in complex Pt and U-Ge-Cu ores. Econ Geol 111(2):487–501

8. Vaughan J (2004) The process mineralogy of gold: the classification of ore types. Jom 56:46–48
9. Piervandi Z (2022) Pretreatment of refractory gold minerals by ozonation before the cyanidation process: a review. J Environ Chem Eng 109013
10. Papangelakis V, Demopoulos G (1991) Acid pressure oxidation of pyrite: reaction kinetics. Hydrometallurgy 26(3):309–325
11. Ivana A (2020) Fundamentals of partial pressure oxidation of gold bearing sulphide minerals. PhD Thesis, The University of Queensland

Selective Precipitation of Valuable Metals from Steel Slag Leach Liquor: Experimental and Theoretical Approaches

Jihye Kim and Gisele Azimi

Abstract In this study, we develop a selective precipitation process for the recovery of titanium, magnesium, and aluminum from the steel slag leach liquor. To accurately predict the precipitation behavior of the target elements in the complex sulfate system, we conduct thermodynamic modeling and experimental measurement of metal hydroxide precipitation titration curves. The investigation focuses on three key operating parameters: initial solution pH, initial metal ion concentration, and reaction temperature. We examine the ion interaction, precipitation pH, amount of precipitant required, and species equilibrium. Subsequently, hydroxide precipitation testing is performed using sodium hydroxide as a single precipitant to selectively recover the target elements. We evaluate the effects of precipitation pH level, reaction temperature, stabilization time, and precipitant reagent type on metal recovery and product purity. Following process optimization, we achieve an 83% purity of titanium precipitate with 85% recovery, along with > 90% purity of magnesium and aluminum precipitates with 100% recovery.

Keywords Chemical precipitation · Steel slag · Thermodynamic modeling · Titration curve · Metal recovery · Titanium

Introduction

The steel industry produces a substantial amount of steel slag, reaching 190–290 million tons per year (Mt/year) in 2022 [1]. Notably, roughly 25–40 Mt/year of steel slag ends up in landfills without practical applications [2]. To address the adverse environmental impact of industrial waste slags, metal recovery from steel slag has

J. Kim
Colorado School of Mines, 1500 Illinois Street, Golden, CO 80401, USA
e-mail: jihyekim@mines.edu

G. Azimi (✉)
University of Toronto, 200 College Street, Toronto, ON M5S3E5, Canada
e-mail: g.azimi@utoronto.ca

emerged as a promising technology to support the global transition towards a carbon neutral economy.

Current state-of-the-art metal recovery from steel slag primarily involves pyrometallurgical or hydrometallurgical processes, both of which have significant limitations including high energy consumption, significant chemical usage, and substantial waste production. To this end, our group has developed a novel and sustainable process combining both pyrometallurgical and hydrometallurgical technologies to extract titanium, magnesium, and aluminum from steel slag [3]. This process yielded over 85% titanium extraction along with nearly complete magnesium and aluminum extraction in the acidic leachate. However, open questions remained related to the selective separation of each metal dissolved in the leachate and their transformation into value-added solid products.

Of the three elements in the leach liquor, titanium holds the highest value. Its outstanding corrosion resistance, high strength at high temperatures, and lightweight properties make it indispensable across various industries, including aerospace, automobile, medical, and metallurgy [4–6]. Magnesium and aluminum also find wide utility in aerospace, defense, automotive, and manufacturing sectors due to their desired properties, such as lightweight nature, high strength, exceptional corrosion resistance, and high machinability [7].

Despite the recent surge in attention towards secondary resources and the common co-occurrence of titanium, magnesium, and aluminum in these resources, there is a notable scarcity of work on the chemical separation of these elements in a selective manner. We base our work on the premise that judicious material selection and process design can be employed to develop a selective precipitation technology for metal recovery from waste steel slag. This premise is supported by previous investigations [8–12], which demonstrated that titanium, magnesium, and aluminum can be selectively recovered from acidic leach liquors through selective precipitation. However, to the best of our knowledge, no prior research has been dedicated to the selective precipitation of these metals from steel slag leach liquors.

In this study, we developed an efficient and selective precipitation process to separate titanium, magnesium, and aluminum from the steel slag leach liquor. We first conducted thermodynamic modeling and experimental measurements of precipitation titration curves on a simulated synthetic solution to predict the precipitation behavior of each element. We investigated ion interactions, precipitation pH, amount of precipitant required, and species equilibrium as functions of initial solution pH, initial metal ion concentration, and reaction temperature. This was followed by precipitation process development using a single precipitant to produce final solid products with the desired chemistry and properties. We assessed the impact of precipitation pH levels, reaction temperature, stabilization time, and precipitant reagent type and evaluated the relative significance of these key parameters. Comprehensive characterization techniques were employed to ensure the favorable properties of the final products. The outcomes demonstrate the feasibility of the developed selective precipitation process, achieving over 83% purity and recovery of titanium alongside over 90% purity and recovery of magnesium and aluminum.

Experimental

Materials

The steel slag was provided by an undisclosed source and the slag leach liquor was prepared following the process detailed in the authors' previous study [3]. All chemicals were of analytical grade purity and used without further purification. Sulfuric acid and nitric acid were procured from VWR (USA) while sodium hydroxide was sourced from Caledon Laboratories Ltd. (Canada). Magnesium and calcium sulfate hydrates were obtained from Alfa Aesar (USA), and aluminum and manganese sulfate hydrates were supplied by MilliporeSigma (Canada). Iron sulfate hydrate was purchased from American Elements (USA).

Thermodynamic Modeling of Precipitation Titration Curves

We developed the thermodynamic model for precipitation titration curves based on the modified Bromley-Zemaitis activity coefficient model [13]. The Bromley-Zemaitis model is well-suited for calculating activity coefficients in single- and multi-component solutions and assumes complete electrolyte dissociation. As our model needs to account for the non-complete dissociation of sulfuric acid and bisulfate ions at low pH values, we adapted the Bromley-Zemaitis model using Wirth's proposed theoretical calculation approach [14]. Detailed information about thermodynamic modeling can be found in the authors' previous study [15].

Experimental Measurement of Precipitation Titration Curves

We prepared a synthetic solution containing magnesium, aluminum, calcium, manganese, and iron sulfate hydrates based on the elemental composition and pH of the actual steel slag leach liquor. The synthetic solution was stirred and heated to a specified temperature. The solution's pH was continuously monitored throughout the measurement. Once the pH stabilized, 1 mol/L sodium hydroxide solution was introduced to the solution to achieve the desired pH. After adding the precipitant, we allowed at least 20 min for stable pH measurement.

Precipitation of Titanium, Magnesium, and Aluminum from Slag Leach Liquor

The selective precipitation of titanium, magnesium, and aluminum from slag leach liquor was carried out using a single precipitant, namely sodium hydroxide. Initially, the steel slag leach liquor was filtered, followed by stirring and heating to a specified temperature. The solution's pH was continuously monitored. After the initial pH measurement, either 1 mol/L sodium hydroxide solution or solid sodium hydroxide pellets were introduced to the solution to increase the pH and induce precipitation. The solution was sampled at approximately regular pH intervals and immediately filtered and diluted for subsequent sample analysis.

Compositional and Mineralogical Characterization

For compositional analysis, the liquid sample was filtered using a 0.45 μm nylon syringe filter and then diluted with a 5 wt% nitric acid solution. Subsequently, the concentrations of titanium, magnesium, aluminum, and other elements were determined using inductively coupled plasma–optical emission spectroscopy (ICP-OES, PerkinElmer Optima 8000, USA). The mineralogical characteristics of the solid sample were analyzed through X-ray diffraction (XRD, Rigaku MiniFlex 600, Japan).

Results and Discussion

Precipitation Titration Curves Established Using the Thermodynamic Model and Experimental Measurements

We constructed the precipitation titration curve for the five-component sulfate system, comprising Mg, Al, Ca, Mn, and Fe, employing the thermodynamic model developed based on the Bromley-Zemaitis model and Wirth's calculation method (Fig. 1a). This curve visually illustrates the pH changes concerning the amount of added titrant. As can be seen in Fig. 1a, the first buffered phase emerges between the initial pH of 0.7 and the iron precipitation pH. In this phase, sodium hydroxide, introduced as the precipitant, is exclusively utilized to elevate the solution's pH. Since this process is an acid–base titration, the titrant quantity added depends solely on the initial solution pH and the number of hydrogen ions released per acid molecule.

Following the first buffered phase, precipitation plateaus for iron, aluminum, manganese and magnesium, and calcium were observed at pH 2.7, 3.9, 9.3, and 12.6, respectively. During these plateaus, the precipitation reactions of the metal hydroxides occur. At this stage, the pH remains relatively stable, forming plateaus
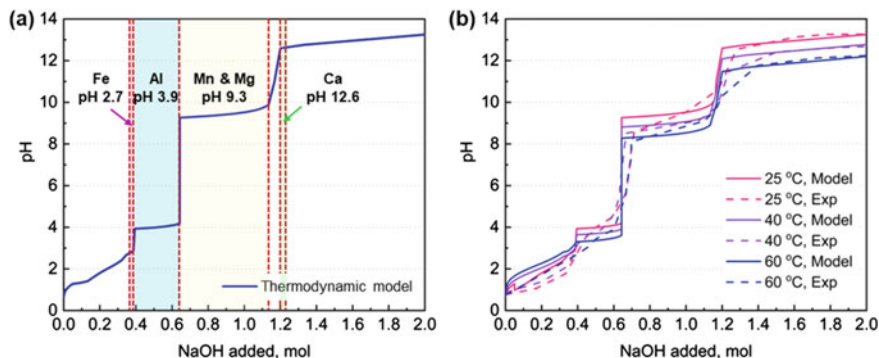
Fig. 1 **a** The precipitation titration curve constructed using the thermodynamic model for the sulfate system comprising Mg, Al, Ca, Mn, and Fe. The initial solution pH was 0.7, the temperature was maintained at 25 °C, and the initial metal ion concentrations are detailed in Fig. 2a. **b** Precipitation titration curves established using the thermodynamic model (Model) and experimental measurements (Exp) at temperatures of 25, 40, and 60 °C

because all the added precipitant is engaged in converting soluble metal ions into insoluble metal hydroxides. In these plateau regions, the metals precipitate as hydroxides, i.e., $Fe(OH)_3$, $Al(OH)_3$, $Mn(OH)_2$, $Mg(OH)_2$, and $Ca(OH)_2$. The quantity of precipitant required for each metal ion's precipitation is determined based on their initial concentration and valence.

In the second buffered phase following precipitation, there is an absence of significant pH fluctuations since the precipitation process has reached completion, and the solution has become alkaline. The introduction of additional precipitant causes only a marginal elevation in the solution's pH.

To compare the precipitation titration curves established using the thermodynamic model and experimental measurements, we conducted analyses on the five-component sulfate system. As displayed in Fig. 1b, the precipitation titration curves obtained through the thermodynamic modeling and experimental measurements generally aligned, although slight discrepancies were noted. One prominent difference was the absence of distinct precipitation plateaus in the experimental measurement, unlike in the thermodynamic model. This can be attributed to pH electrode junction clogging, sample heterogeneity, and the stirring effect during experimental pH measurements. These factors were not considered during thermodynamic modeling, resulting in unclear precipitation plateaus observed exclusively in the experimental measurement.

We conducted a series of thermodynamic modeling and experimental measurements of the titration curve to investigate the influence of initial solution pH, initial metal ion concentration, and reaction temperature on the precipitation titration curve. The findings revealed that the initial solution pH affects not only the initial section of the precipitation titration curve (i.e., the buffered phase before precipitation) but also the pH at which the target metal hydroxide precipitates. This is logical as the initial

solution pH governs the quantity of sodium hydroxide needed to initiate precipitation, alters the concentration of sodium ions present before precipitation commences, and consequently, impacts species equilibrium.

The initial concentration of metal ions was found to be a determinant of the length of the precipitation plateau, i.e., the quantity of sodium hydroxide needed to complete the precipitation process. When initial metal ion concentrations were lower, an experimentally evident local pH maximum point was observed due to the hydroxide ion supersaturation.

Lastly, elevating the reaction temperature led to a decrease in the precipitation pH of the target metal hydroxide, while leaving the quantity of precipitant required unaffected (Fig. 1b). Additionally, the initial section of the titration curve, namely the buffered phase before precipitation, shifted upwards with rising temperature. This shift was attributed to the adverse influence of temperature on the dissociation constants of sulfuric acid.

Characterization of Steel Slag Leach Liquor

The elemental composition of the steel slag leach liquor, prepared in accordance with the methodology outlined in the authors' earlier work [3], was analyzed using ICP-OES to establish an accurate baseline for subsequent precipitation testing. The results are presented in Fig. 2a. Among the major elements found in the slag leach liquor, the current study places particular emphasis on the selective recovery of titanium, magnesium, and aluminum due to their high values and concentrations.
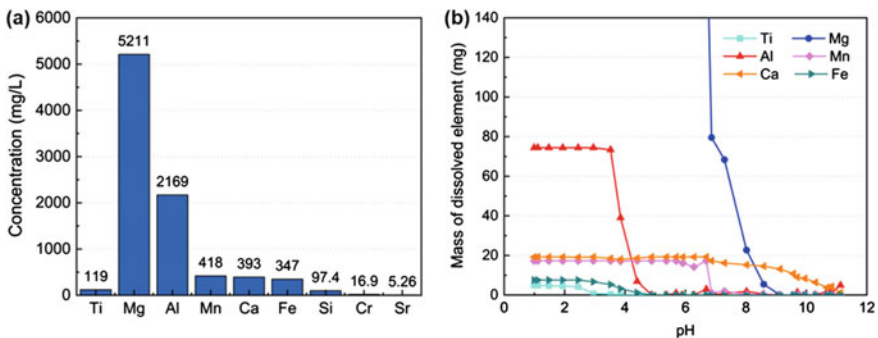
Fig. 2 **a** Elemental composition of the steel slag leach liquor. **b** Mass of dissolved elements in the leach liquor at different pH levels. The solution pH was raised by adding 1 mol/L sodium hydroxide solution

Hydroxide Precipitation Testing

We developed a selective precipitation process employing a sole precipitant, sodium hydroxide, and conducted a series of precipitation tests to investigate the impact of precipitation pH levels, stabilization time, reaction temperature, and precipitant reagent type on metal recovery and precipitate purity.

Changes in stabilization time, ranging from 5 to 20 min, had no substantial effect on the metal recovery and precipitate purity of all elements of interest. This observation suggests that hydroxide precipitation was completed within 5 min. However, to ensure stable pH, a 20-min stabilization time was introduced after each precipitant addition step in subsequent experiments.

The reaction temperature emerged as the primary factor contributing to increased precipitate purity for titanium and aluminum. As the reaction temperature shifted from 25 °C to 80 °C, the precipitate purity for titanium and aluminum surged from 5.2% to 82.9% and 76.5% to 90.0%, respectively. This improvement can be attributed to the heightened kinetic energy of ions at elevated temperatures, reducing the likelihood of impurity ions becoming trapped in the precipitate products [16]. Regarding magnesium, its precipitate purity at 25 °C already exceeded 90% due to its high initial concentration, low levels of co-extracted impurities (i.e., manganese and calcium), and a narrow co-precipitation pH range. Consequently, the magnesium precipitate purity only marginally increased from 91.3% to 95.3% with a temperature increase from 25 °C to 80 °C.

In terms of the precipitant reagent type, the use of solid sodium hydroxide pellets, as opposed to a 1 mol/L sodium hydroxide solution, resulted in lower precipitate purity for titanium and aluminum, while it had negligible effects on magnesium precipitate purity. This divergence is primarily because the selective precipitation of titanium and aluminum necessitates precise pH control, as they tend to co-precipitate with iron over a wide pH range. In terms of magnesium, its precipitate purity remained consistently above 90%, irrespective of the type of precipitant reagent used, owing to its narrow co-precipitation pH range with other elements. These findings collectively indicate that solid sodium hydroxide pellets are unsuitable for small-scale testing with a leach liquor volume of < 500 mL.

Considering the influence of key operating parameters, we determined the optimized conditions for the selective precipitation process utilizing a single precipitant (sodium hydroxide) to be a stabilization time of 20 min, a reaction temperature of 80 °C, and the use of a 1 mol/L sodium hydroxide solution as the precipitating reagent. Under these conditions, experiments were conducted, the results of which are illustrated in Fig. 2b. In the pH range of 2.5–3.0, titanium concentration sharply decreased due to titanium dioxide precipitation. In this range, slight iron co-precipitation was observed, leading to a titanium precipitate purity of 82.9%. In the pH range of 3.5–4.9, nearly complete aluminum precipitation occurred, accompanied by iron co-precipitation. Manganese was primarily precipitated in a narrow pH range of 6.7–7.3, while magnesium precipitated as magnesium hydroxide within the pH range of 6.7–9.6, coinciding with the precipitation of manganese and calcium. Based on these

results, it was concluded that an 83% titanium precipitate purity with 85% recovery, alongside > 90% magnesium and aluminum precipitate purity with approximately 100% recovery could be yielded utilizing only hydroxide precipitation steps, without the need for stabilizing agents or oxidizing/reducing agents.

Characterization of Precipitate Products

We carried out analyses on the purities, elemental compositions, and normalized oxide/ hydroxide-equivalent mass compositions of the primary solid products generated in the precipitation experiments. We also conducted XRD analyses to identify the crystallographic attributes of the final solid samples precipitated at pH 3.0, 4.9, and 9.6.

The product precipitated at pH 3.0 primarily consists of titanium in the form of TiO_2, with a notable co-precipitation of aluminum and magnesium. The substantial presence of co-extracted aluminum and magnesium, namely 29.0 wt% $Al(OH)_3$ and 7.4 wt% $Mg(OH)_2$, leads to a titanium precipitate purity of 72.1%, which falls short of the purity calculated on the basis of the liquor sample composition. The lower-than-expected purity of the titanium precipitate in the solid product can be attributed to the liquid retained within the wet filter cake during the solid/liquid separation process.

The solid product obtained at pH 4.9 exhibits an aluminum precipitate purity of 93.4% and an oxide/hydroxide-equivalent mass of 95.0 wt% $Al(OH)_3$. Based on the XRD results, aluminum precipitated in the form of three primary phases: $Al(OH)_3$, $AlO(OH)$, and Al_2O_3. This product also contains 3.0 wt% $Mg(OH)_2$ and 1.3 wt% $FeO(OH)$. The presence of $Mg(OH)_2$ can be attributed to the residual liquor within the filter cake, as previously discussed. The detection of small quantities of $FeO(OH)$ is linked to the co-precipitation of iron with aluminum under this pH condition.

The product precipitated at pH 9.6 is predominantly composed of magnesium in the form of $Mg(OH)_2$, with a purity of 95.4%. The high purity of the magnesium precipitate underscores that the developed precipitation process can produce industrial-grade $Mg(OH)_2$, suitable for direct market sale without requiring post-treatment or purification steps. The other co-extracted elements identified are manganese and calcium, amounting to 1.6 wt% $Mn(OH)_2$ and 1.7 wt% $Ca(OH)_2$, respectively.

Conclusions

In this comprehensive study, we conducted a systematic investigation integrating both theoretical and experimental approaches to advance selective precipitation technology, thereby enhancing the commercial and economic potential of waste steel slag while simultaneously contributing to the environmental benefits of slag valorization.

We first developed a thermodynamic model capable of predicting metal precipitation behaviors. This model was then rigorously compared with experimental measurements, revealing a strong agreement between the model's predictions and actual experimental results. This alignment substantiates the model's accuracy in describing the precipitation pathway, predicting hydroxide precipitation behaviors, elucidating the impact of key operating parameters, and simulating precipitation titration curves.

Subsequently, we developed a selective precipitation process for the recovery of titanium, magnesium, and aluminum from the acidic steel slag leach liquor. We investigated the influence of precipitation pH levels, reaction temperature, stabilization time, and precipitant reagent type on metal recovery and precipitate purity, and optimized the process. Remarkable results were achieved, with the process yielding an 83% purity of titanium products along with an 85% recovery rate. Furthermore, we obtained precipitates of magnesium and aluminum with purities exceeding 90% and full recovery. Our process produced several value-added solid products, including TiO_2, $Al(OH)_3$, and $Mg(OH)_2$, at pH levels of 3.0, 4.9, and 9.6, respectively.

References

1. U.S. Geological Survey (2023) Mineral commodity summaries 2023: U.S. Geological Survey
2. Branca TA, Colla V, Algermissen D et al (2020) Reuse and recycling of by-products in the steel sector: Recent achievements paving the way to circular economy and industrial symbiosis in Europe. Metals (Basel) 10:1–18
3. Kim J, Azimi G (2021) Valorization of electric arc furnace slag via carbothermic reduction followed by acid baking—water leaching. Resour Conserv Recycl 173:1–12. https://doi.org/10.1016/j.resconrec.2021.105710
4. Wang D, Chu J, Liu Y et al (2013) Novel process for titanium dioxide production from titanium slag: NaOH-KOH binary molten salt roasting and water leaching. Ind Eng Chem Res 52:15756–15762. https://doi.org/10.1021/ie400701g
5. Begum N, Maisyarah A, Bari F et al (2012) Leaching behaviour of langkawi black sand for the recovery of titanium. APCBEE Proc 3:1–5. https://doi.org/10.1016/j.apcbee.2012.06.036
6. Jaffee RI, Promisel NE (2013) The Science. Elsevier, Technology and Application of Titanium
7. Demas A (2018) Interior releases 2018's final list of 35 minerals deemed critical to U.S. national security and the economy. In: U.S. Geological Survey. https://www.usgs.gov/news/national-news-release/interior-releases-2018s-final-list-35-minerals-deemed-critical-us. Accessed 31 Aug 2023
8. Quintero C, Dahlkamp JM, Fierro F et al (2020) Development of a co-precipitation process for the preparation of magnesium hydroxide containing lithium carbonate from Li-enriched brines. Hydrometallurgy 198:1–7. https://doi.org/10.1016/j.hydromet.2020.105515
9. Gao J-M, Zhang M, Cheng F, Guo M (2017) Process development for selective precipitation of valuable metals and simultaneous synthesis of single-phase spinel ferrites from saprolite-limonite laterite leach liquors. Hydrometallurgy 173:98–105. https://doi.org/10.1016/j.hydromet.2017.08.004
10. He L, Xu W, Song Y et al (2017) Selective removal of magnesium from a lithium-concentrated anolyte by magnesium ammonium phosphate precipitation. Sep Purif Technol 187:214–220. https://doi.org/10.1016/j.seppur.2017.04.028
11. Seo EY, Cheong YW, Yim GJ et al (2017) Recovery of Fe, Al and Mn in acid coal mine drainage by sequential selective precipitation with control of pH. Catena (Amst) 148:11–16. https://doi.org/10.1016/j.catena.2016.07.022

12. Berkovich SA (1975) Recovery of titanium dioxide from ores
13. Zamaitis In JF, Newman SA, Barner HE, Klein M (1980) Thermodynamics of aqueous systems with industrial applications. ACS Symposium Series 133. American Chemical Society, Washington, DC, pp 227–246
14. Wirth HE (1971) Activity coefficients in sulphuric acid and sulphuric-acid-sodium-sulphate mixtures. Electrochim Acta 16:1345–1356. https://doi.org/10.1016/0013-4686(71)80007-5
15. Kim J, Liu H, Azimi G (2023) A comparative study of thermodynamic modeling and experimental measurement of precipitation titration curves for single- and multi-component sulfate systems. Hydrometallurgy 219:1–12. https://doi.org/10.1016/j.hydromet.2023.106080
16. Liu H, Azimi G (2021) Process analysis and study of factors affecting the lithium carbonate crystallization from sulfate media during lithium extraction. Hydrometallurgy 199:1–15. https://doi.org/10.1016/j.hydromet.2020.105532

Purification of an Indigenous Molybdenite for Enhanced Steel Production

Alafara A. Baba, Mamata Mohapatra, Christianah O. Adeyemi, Abdul G. F. Alabi, Rasheed A. Agava, Bernard O. Ozigi, and Jimoh M. Abdul

Abstract Due to their high thermal and mechanical stability, increasing demands for high-grade molybdenum compounds for improved steel properties warrant continuous extraction for defined industrial applications. In this study, molybdenum-*cum*-silica compound preparation from indigenous molybdenite was examined via oxidative roasting and chemical leaching. The influence of pertinent parameters such as leachant concentration, reaction temperature, and particle size on the extent of molybdenite ore reacted was thoroughly investigated. The degree of molybdenite dissolution rate increased from 52 to 90% at optimal conditions. The leach liquor obtained at optimal conditions was purified through solvent extraction technique and beneficiated to an Industrial Sodium Aluminosilicate (ISA)/Industrial Sodium Molybdate Dihydrate (ISMD) compound. This prepared compound as characterized is recommended as industrial raw material in some defined steel operations.

A. A. Baba (✉) · C. O. Adeyemi (✉)
Department of Industrial Chemistry, University of Ilorin, P.M.B. 1515, Ilorin 240003, Nigeria
e-mail: alafara@unilorin.edu.ng

C. O. Adeyemi
e-mail: christianah.adeyemi@fedpoffaonline.edu.ng

M. Mohapatra (✉) · C. O. Adeyemi
Department of Hydo- and Electrometallurgy, CSIR-Institute of Minerals and Materials
Technology, Bhubaneswar 751013, India
e-mail: mamata@immt.res.in

C. O. Adeyemi
Department of Biochemical and Chemical Sciences, Federal Polytechnic, P.M.B. 420, Offa,
Nigeria

A. G. F. Alabi
Department of Material Science and Engineering, Kwara State University, P.M.B. 1530, Malete,
Nigeria

R. A. Agava · B. O. Ozigi
National Agency for Science and Engineering Infrastructure, Abuja, Nigeria

J. M. Abdul
Kwara State Polytechnic, Ilorin, Kwara State, Nigeria

Introduction

Molybdenum is a pertinent strategic commodity of this era and finds a wide array of applications, particularly in alloy steel, medicine, aviation, nuclear, industrial motors, filament, pigments, and a necessary element for the human body and plants [1–3]. However, the low-grade molybdenum ores (20–45% Mo) have to be purified differently as compared with the high-grade molybdenum ores (50–60% Mo). As a result of fast tremendous demand for pure molybdenum for the aforementioned applications, different processing methods for processing and recovery have been considered, which include roasting with lime or soda ash followed by sulphuric acid leaching, acid baking followed by water leaching, and selective adsorption of molybdenum with activated charcoal, among others [4, 5]. In addition, the processing and recovery of molybdenum from molybdenite ore by bioleaching have been studied using a thermophilic bacterium *sulfurous metallicus*, though the dissolution rate recorded is quite low [6].

Furthermore, technological advancement is appreciably increasing the demand for pure molybdenum and molybdenum compounds. Molybdenum has thus attracted significant attention in recent years due to its contribution to the hardness of ductile materials most especially in steel making, aircraft parts, and telecommunications, among others [6]. The traditional processing routes have been limited due to increased environmental factors. However, it is feasible to process low-grade molybdenite ores by hydrometallurgical routes that are more eco-friendly than the traditional pyrometallurgical processes [7, 8]. These could involve dissolving molybdenum in chloride, sulfate, or nitrate media and further purifying the obtained leach liquor via different methods such as precipitation and solvent extraction, among others [9].

The influences of parameters including leachant concentration, reaction temperature, particle size, and leaching time on the extent of molybdenite dissolved were examined. After sulphuric acid leaching, the residual product was further leached with sodium hydroxide solution for molybdenum recovery by solvent extraction using bis(2—ethyl hexyl) phosphoric acid (D2EHPA) extractant. The optimal leaching time, reaction temperature, particle size, and sulphuric acid concentration were also determined for the processing of molybdenite ore for economic viability. Thus, this study examines the possibility of leaching-*cum*-selective roasting routes in the purification of indigenous molybdenite as industrial raw materials for enhanced steel properties.

Materials and Method

Material

The molybdenite ore used for this investigation was sourced from Kigom village (9°45′50″ N, 8°37′31″ E), Jos, Plateau State, Nigeria. The molybdenite sample was pulverized and sieved using *Test sieve I.S.S. 460* into three particle sizes: < 50 µm, < 63 µm, and < 75 µm.

Leaching Investigation

The leaching investigations were performed in 100 mL of the prepared H_2SO_4 solution to 10.0 g molybdenite sample in closed glass flasks. The ore slurry was then stirred at the required reaction temperature using a magnetic hotplate for the desired leaching time. At the end of each leaching investigation, the resultant solution was filtered and the leach liquor was analyzed by Inductively Coupled Plasma-Optical Emission Spectrometry (ICP-OES) for leached metal ions [10–14]. Selected leach products at optimal conditions were tested for material purity assessment at a set of optimal conditions. In addition, the pregnant leach solution obtained at optimal leaching conditions (3.0 mol/L H_2SO_4, 75 °C, < 50 µm, 120 min) was further processed, and a quantitative amount of Mo (VI) was extracted and beneficiated to obtain industrial molybdenum compound as raw material in steel operations [5, 14].

Results and Discussion

Ore Characterization

The chemical composition of the untreated molybdenite ore analyzed by EDXRF gave: 60.80 wt% SiO_2, 11.16 wt% MoO_3, 9.59 wt% Al_2O_3, and 1.69 wt% Fe_2O_3. The XRD results confirmed that the ore under study majorly consisted of *quartz* (SiO_2: 01-083-2466) and *molybdenum disulfide* (MoS_2: 01-073-1508).

Leaching Investigation

The leaching examinations in this study affirmed that the molybdenite ore dissolution rate in sulphuric acid solution increases with increasing leachant concentration, reaction temperature, and decreasing particle size as follows:

(i) **Influence of H$_2$SO$_4$ concentration**: H$_2$SO$_4$ concentration varied between 0.1 and 3.0 mol/L at 55 °C within 5–120 min with < 50 μm particle size. For instance, increasing the H$_2$SO$_4$ concentration increases the molybdenite dissolution up to 3.0 mol/L H$_2$SO$_4$ solution where 52.5% recovery was achieved within 120 min.

(ii) **Influence of reaction temperature**: The influence of reaction temperature on the extent of molybdenite reacted was carried out from 27 to 75 °C. Other important experimental conditions considered were 3.0 mol/L H$_2$SO$_4$, 5–120 min, and < 50 μm particle size. Increasing the reaction temperature from 27 to 75 °C increases the extent of molybdenite dissolution from 23.7 to 90.5%. However, the reaction temperature was not considered above 75 °C due to evaporation at higher temperatures.

(iii) **Influence of particle size**: The molybdenite dissolution rate for particle sizes: < 50 μm, < 63 μm, and < 75 μm gave 90.5, 82.1, and 66.4%, respectively, at established conditions (3.0 mol/L H$_2$SO$_4$, 75 °C, 120 min).

Extraction Studies

The associated gangues including iron present in the leach liquor were precipitated from molybdenum in the solution by adjusting the pH of the solution to 3.6 ± 0.2 at 27 ± 2 °C. At established extraction conditions using bis(2—ethyl hexyl) phosphoric acid, ([D2EHPA] = 0.45 mol/L, equilibrium pH = 1.6, contact time = 20 min.), 96.7% Mo (VI) extraction efficiency was achieved. The pure Mo (VI) solution was subsequently beneficiated to obtain industrial molybdenum compound [14].

Purification Test

The un-leached product (9.5%) at established conditions (3.0 mol/L H$_2$SO$_4$, 75 °C, < 50 μm, 120 min) examined by SEM morphology is characterized by bulky irregular structure-*cum*-whitish layer suggesting the presence of molybdenum disulfide (Fig. 1).

However, the leach liquor obtained at optimal conditions was precipitated using sodium hydroxide (NaOH) solution and beneficiated to obtain Industrial Sodium Aluminosilicate Compounds (ISAC), recommended for use in alloy steels as corrosion resistance. This among others is expected to contribute to enhancing indigenous steel production for economic and quality products.
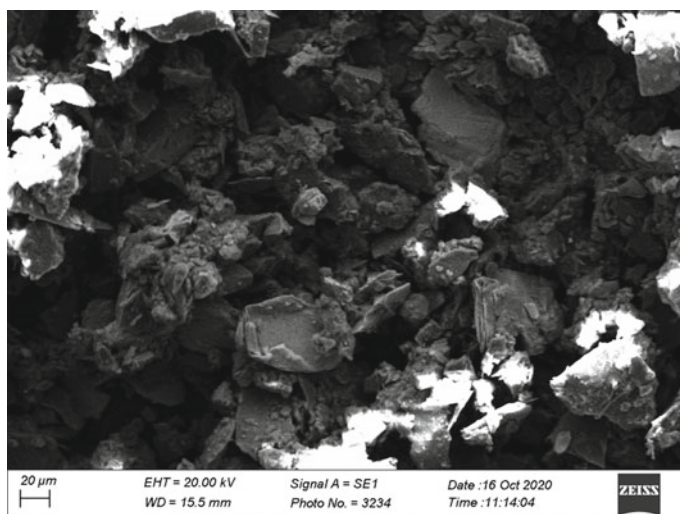
Fig. 1 SEM morphology of the un-leached product

Conclusion

In this investigation, the purification of an indigenous molybdenite ore for improved molybdenum extraction was examined. The experimental results indicate this method to be an effective and feasible technique for indigenous molybdenite ore processing with high percentage recovery. At established conditions (3.0 mol/L H_2SO_4, 75 °C, < 50 μm, 120 min), the degree of molybdenite dissolution increased from 52 to 90.5%. In addition, the leach liquor obtained at the above-stated conditions was purified through solvent by D2EHPA extractant for Mo recovery. The pure Mo solution was beneficiated in obtaining Industrial Sodium Aluminosilicate (ISA)/Industrial Sodium Molybdate Dihydrate (ISMD) compounds useful as raw materials in alloy steels for corrosion resistance [14].

References

1. Mishra D, Chaudhury GR, Kim DJ, Ahn JG (2010) Recovery of metal values from spent petroleum catalyst using leaching-solvent extraction technique. Hydrometallurgy 101:35–40
2. Saberyan K, Ghannadi Maragheh M, Ashtari P, Keshavarz Alamdari S (2003) Liquid–liquid extraction of molybdenum (VI) from acidic media with Cyanex–301. Min Eng 16:391–393
3. Barik SP, Park K, Parhi PK, Park JT (2012) Direct leaching of molybdenum and cobalt from spent hydrodesulfurization catalyst with sulphuric acid. Hydrometallurgy 111–112:46–51
4. Park KH, Mohapatra D, Nam CW (2007) Two-stage leaching of activated spent HDS catalyst and solvent extraction of Al using organo-phosphinic extractant, cyanex-272. J Hazard Mater 148:287–295
5. Van den Berg JAM, Yang Y, Nauta HHK, Van Sandwijk A, Reuter MA (2002) Comprehensive processing of low-grade sulphidic molybdenum ores. Min Eng 15:879–883
6. Chen J, Gao C, Zhang Q, Xiao L (2010) Leaching of nickel−molybdenum sulfide ore in membrane biological reactor. J Trans Non-Ferrous Metals Soc China 21:135–140
7. Ilhan S, Kalpakli AO, Kahruman C, Yusufoglu I (2013) The use of oxalic acid as a chelating agent in the dissolution reaction of calcium molybdate. Metall Mater Trans B 44:495–505 https://doi.org/10.1007/s11663-013-9811-2
8. U.S. Geological Survey (2012) Mineral commodity summaries. Molybdenum 106
9. Lasheen TA, El-Ahmady ME, Hassib HB, Helal AS (2013) Oxidative leaching kinetics of molybdenum-uranium ore in H_2SO_4 using H_2O_2 as an oxidizing agent. Front Chem Sci Eng 7(1):95–102
10. Raji MA, Baba AA, Bale RB, Alabi AGF, Ghosh MK (2020) Removal of iron impurities from a Nigerian biotite-rich kaolinite ore by a sulphuric acid solution. J Chem Technol Metall 55(6):2128–2135
11. Adeyemi CO, Berma SD, Mohapatra M, Baba AA, Suddhasatwa B (2023) Integrated approach for extraction of molybdenum and silica from an unexploited Nigerian molybdenum rich ore. In: Sustainable chemical, minerals and materials processing. https://doi.org/10.1007/978-981-19-7264-2_12
12. Baba AA, Raji MA, Abdulkareem AY, Ghosh MK, Bale RB, Adeyemi CO (2019) Dissolution kinetics potential of a biotite-rich kaolinite ore for industrial applications by oxalic acid solution. J Min Metall Explor 36(6):1091–1099
13. Baba AA, Raji MA (2023) Preparation of industrial ammonium Diuranate from a Boltwoodite ore as a mediator for nuclear fuel and catalytic utilizations. Progr Nucl Ener 165:104916. https://doi.org/10.1016/j.pnucene.2023.104916
14. Adeyemi CO (2023) Preparation and application of high-grade industrial molybdenum and silica compounds from a Nigerian low-grade Molybdenite by hydrometallurgical process. Ph.D. Thesis, Department of Industrial Chemistry, University of Ilorin, Ilorin, Nigeria

Part V
Electrometallurgy and High Temperature Processes

Direct Preparation of Aluminum-Vanadium Intermediate Alloy Through Electrolysis in Na_3AlF_6-K_3AlF_6-AlF_3-$NaVO_3$ Molten Salts

Xianwei Hu, Yifan Zhang, Zhongning Shi, and Zhaowen Wang

Abstract The preparation of aluminum-vanadium (Al-V) intermediate alloys through the electrolysis of $NaVO_3$ in the Na_3AlF_6-K_3AlF_6-AlF_3 molten salt system using liquid aluminum as cathode is a novel process. In the present study, the forms of the Al-V intermetallic compounds and the contents of vanadium in the intermediate alloys were investigated at different current densities. The results showed that the cathode product contained aluminum matrix and $Al_{10}V$ at a current density of 0.6 A/ cm^2. As the current density increased to 0.7 A/cm^2, the Al_3V phase started to form while the vanadium content was still very low in the cathode product. At 0.8 A/cm^2, the vanadium content in the cathode alloy product reached 7.83 wt.% with a current efficiency of 34.54%. However, no significant change in the vanadium content was noticed at current densities of 0.9 and 1.0 A/cm^2.

Keywords Electrometallurgy · Aluminum-vanadium alloy · $NaVO_3$ · Molten salt

Introduction

Aluminum-vanadium alloys have been widely utilized in aerospace, aviation, atomic energy and military industries owing to their high specific strength, strong corrosion resistance, and high-temperature working performance. In particular, aluminum and vanadium are the key elements in the production of aerospace-grade vanadium-bearing titanium alloys, which are added into titanium alloys in the form of aluminum-vanadium intermediate alloys to enhance the comprehensive mechanical properties and corrosion resistance of them.

In industrial production of aluminum-vanadium intermediate alloys, V_2O_5 is generally used as the raw material, which is primarily extracted from vanadium

X. Hu (✉) · Y. Zhang · Z. Shi · Z. Wang
Key Laboratory for Ecological Metallurgy, Multimetallic Mineral (Ministry of Education), School of Metallurgy, Northeastern University, Shenyang 110819, China
e-mail: huxw@smm.neu.edu.cn

slag. In the production process of V_2O_5, sodium metavanadate ($NaVO_3$) is first recovered from vanadium slag through roasting-leaching processes, and then V_2O_5 is further obtained from $NaVO_3$ by ammonium precipitation and thermal decomposition. $NaVO_3$ is an indispensable intermediate product in the vanadium slag treatment process. Moreover, ammonium precipitation and thermal decomposition processes are environmentally harmful and require high energy consumption.

To solve these issues, Weng et al. [1] have proposed a novel short green process for the direct conversion of $NaVO_3$ into metal vanadium or aluminum-vanadium intermediate alloys through the electrolysis of $NaVO_3$ in the molten salts.

In 2016, Weng et al. [2] demonstrated the feasible preparation of metal vanadium through direct electroreduction of $NaVO_3$ in molten $CaCl_2$–$NaCl$ to yield metal vanadium with the purity of 96.8 wt.%. In 2019, Xu et al. [3] prepared aluminum-vanadium intermediate alloys through electrolysis of $NaVO_3$ in NaCl-KCl melts using liquid aluminum as cathode.

In our previous study [4], the electrochemical behavior of $NaVO_3$ on a solid molybdenum and liquid aluminum electrodes was investigated in the NaF-KF-AlF_3 molten salt. Furthermore, Al-V intermetallic compounds were obtained on the liquid aluminum electrode by potentiostatic electrolysis. However, the forms of produced Al-V intermetallic compounds still require investigation.

Herein, in the present study, the electrolysis experiments in NaF–KF–AlF_3–$NaVO_3$ molten salt were conducted with the liquid aluminum cathode, and the forms of produced Al-V intermetallic compounds were acquired through morphological and structural study. The contents of vanadium in the formed intermediate alloy at different current densities were investigated.

Experimental

A schematic diagram of the electrolysis apparatus used in the present study is provided in Fig. 1. In this system, the electrolyte ((30 mol%NaF—30 mol%KF—40 mol% AlF_3)—$NaVO_3$) was held in a corundum crucible, and placed in a furnace. A Φ 30 mm $\times$ 50 mm graphite cylinder was used as the anode and the liquid aluminum was employed as the cathode. The liquid aluminum was put on a graphite sheet with a steel rod for electric conduction. During the electrolysis process, the argon gas was inlet into the crucible through a quartz tube, and $NaVO_3$ was continually added to maintain the concentration of it at a certain level.

The formed cathode products were analyzed by X-ray diffraction (XRD, X Pertpro) equipped with Cu Kα radiation ($\lambda = 1.5406$ Å) for structural determination, as well as scanning electron microscopy (SEM, Ultra Plus, Zeiss) for morphological viewing. The contents of vanadium in the cathode products were analyzed by inductively coupled plasma atomic emission spectroscopy (ICP-AES Optima 8300DV, Perkin Elmer).
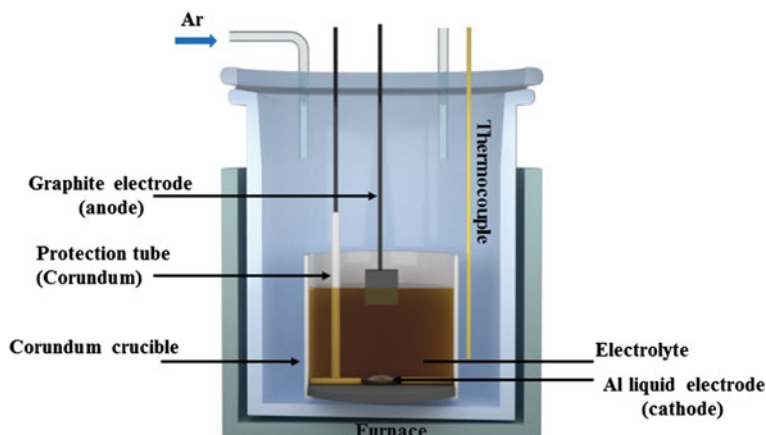
Fig. 1 Schematic diagram of the electrolysis apparatus

Results and Discussion

An optical photograph of a typical cathode product is shown in Fig. 2. It is smooth with metallic luster.

The XRD patterns of the obtained electrolysis products at different current densities are compared in Fig. 3. Obviously, the current density influenced the phase compositions of the cathode products. At low current density(0.6 A/cm^2), the product contained metal aluminum matrix and Al$_{10}$V. As the current density increased to 0.7 A/cm^2, Al$_3$V phase appeared in addition to metal aluminum and Al$_{10}$V. Furthermore, the intensity of each diffraction peak of Al$_{10}$V and Al$_3$V increased with the current density. However, the rise in current density to 0.8 A/cm^2 resulted in little change in the intensity of each diffraction peak for the aluminum-vanadium intermetallic compounds.

The micro-morphologies and elemental compositions/distributions of aluminum and vanadium elements in cathode alloy products at different current densities were analyzed through SEM–EDS technique. As shown in Fig. 4a, the backscattered electron (BSE) image of the cathode alloy obtained at a current density of 0.6 A/cm^2,

Fig. 2 Optical photograph of the cathode product after electrolysis of NaVO$_3$ in NaF-KF-AlF$_3$ molten salt at a current density of 0.9 A/cm^2
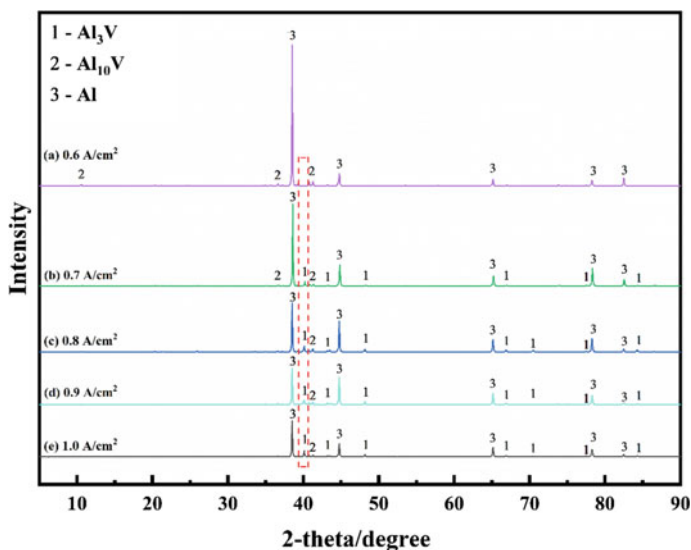
Fig. 3 XRD patterns of the electrolysis products at different current densities

revealed two distinct phase regions. The EDS mapping in Fig. 4b, c identified the grey area in Fig. 4a as the aluminum matrix. However, the light grey regions were primarily composed of aluminum and vanadium elements. These data were corroborated by the EDS technique in Fig. 4d, e. The area A in Fig. 4a consisted of aluminum (91.11 at.%) and vanadium (8.89 at.%) elements, identified as Al-V intermetallic compound phase. The atomic ratio value confirmed that area A as the $Al_{10}V$ phase, consisted with the XRD phase composition (Fig. 4f). By comparison, area B in Fig. 4a primarily consisted of aluminum element, representing the aluminum matrix.

The BSE image of the formed cathode product at a current density of 0.7 A/cm^2 in Fig. 5a showed three distinct phase regions. The EDS mapping shown in Fig. 5b, c confirmed the grey area in Fig. 5a to be the aluminum matrix, while the white and light grey regions mainly consisted of aluminum and vanadium elements. Further examination through EDS analysis (Fig. 5d, e) determined the elemental composition in area A of Fig. 5a as 76.34 at.% for aluminum element and 23.66 at.% for vanadium element, identified as an Al-V intermetallic compound phase. The value of atomic ratio confirmed the dendritic white area in point A as the Al_3V phase. The elemental composition in area B in Fig. 5a consisted of aluminum (91.5 at.%) and vanadium (8.5 at.%) elements, also represented an Al-V intermetallic compound phase. Further atomic ratio calculations confirmed area B as the $Al_{10}V$ phase, consistent with XRD data of the cathode product in Fig. 5f.

The BSE image of the cathode product obtained at a current density of 0.8 A/cm^2, manifested three distinct phase regions (Fig. 6a). The EDS mapping displayed in Fig. 6b, c confirmed the grey area in Fig. 6a to be the aluminum matrix, while the white and light grey regions predominantly consisted of aluminum and vanadium
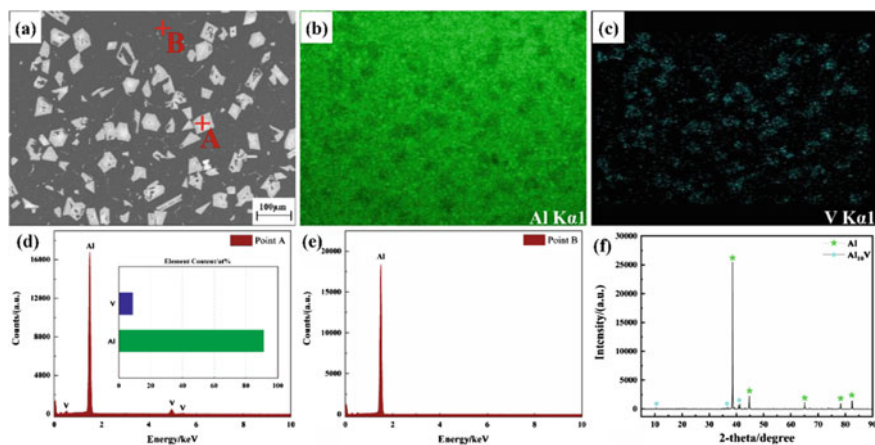
Fig. 4 BSE image of the cross-section of the cathode product obtained at a current density of 0.6 A/cm² (**a**); Element distribution map images (**b–c**) of Al, V in **a**; **d–e** EDS spectra measured over the specified position in **a**; XRD pattern of the cathode product obtained at a current density of 0.6 A/cm² (**f**)
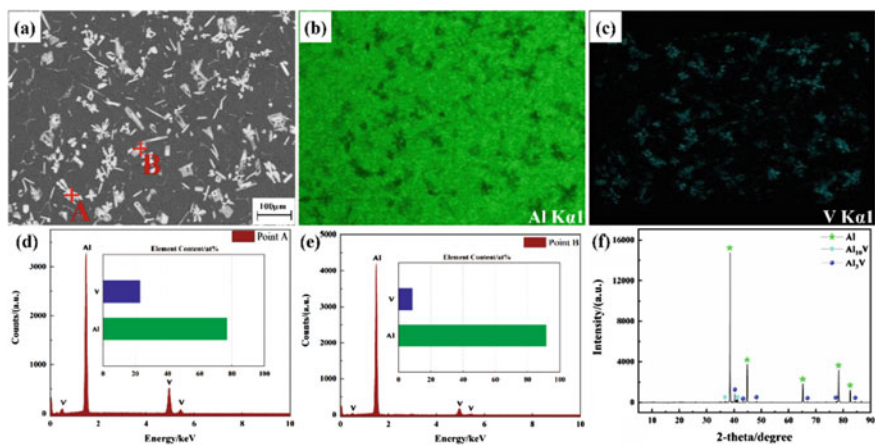
Fig. 5 BSE image of the cross-section of the cathode product obtained at a current density of 0.7 A/cm² (**a**); Element distribution map images (**b, c**) of Al, V in **a**; **d–e** EDS spectra measured over the specified position in **a**; XRD pattern of the cathode product obtained at a current density of 0.7 A/cm² (**f**)

elements. This was further confirmed by EDS analysis (Fig. 6d, e). The element composition in area A in Fig. 6a comprised aluminum (75.14 at.%) and vanadium (24.86 at.%) elements, forming an Al-V intermetallic compound phase. The atomic ratio data revealed the blocky white area at point A as the Al₃V phase.

Likewise, the elemental composition at point B in Fig. 6a consisted of aluminum (90.7 at.%) and vanadium (9.3 at.%), forming an Al-V intermetallic compound phase.
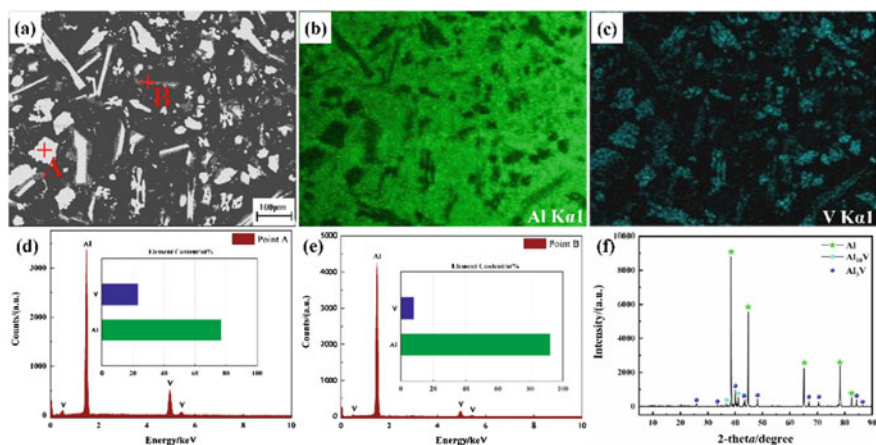
Fig. 6 BSE image of the cross-section of the cathode product obtained at a current density of 0.8 A/cm^2 (**a**); Element distribution map images (**b–c**) of Al, V in **a**; **d–e** EDS spectra measured over the specified position in **a**; XRD pattern of the cathode product obtained at a current density of 0.8 A/cm^2 (**f**)

The atomic ratio value affirmed area B as the $Al_{10}V$ phase, corroborating the XRD phase composition analysis results (Fig. 6f).

The BSE images along with the EDS and XRD of cathode products formed at current densities of 0.9 and 1.0 A/cm^2 are displayed in Figs. 7 and 8, respectively. The micro-morphology and elemental distribution patterns within these products closely resembled acquired at a current density of 0.8 A/cm^2 in Fig. 6. As the current density increased, it can be observed that the distribution area of the Al_3V phase rose accordingly.

The vanadium contents of the cathode products at different current densities are illustrated in Fig. 9. At lower current densities (0.6 and 0.7 A/cm^2), the products manifested relatively limited vanadium content. However, the mass fraction of vanadium sharply rose at a current density of 0.8 A/cm^2 to yield 7.83 wt.%. Afterward, the vanadium content did not significantly change as a function of the current density to yield only around 8 wt.%, consistent with XRD and SEM results.

The current efficiency can be calculated by Eq. (1). Also, considering the occurrence of both electrochemical and aluminothermic reduction processes for vanadium ions, the current efficiency calculated should be more aptly described as "apparent current efficiency".

$$\eta = \frac{m_V}{0.38It} \times 100\% \tag{1}$$

where, η represents the current efficiency, m_V is the mass of vanadium in the cathode product in g, calculated from the total mass of the product and the corresponding vanadium content, I denotes the current in A, and t refers to the electrolysis duration in h.
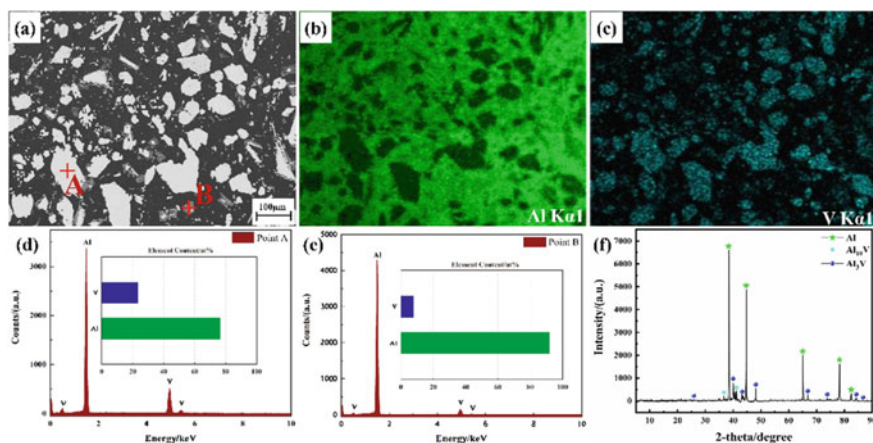
Fig. 7 BSE image of the cross-section of the cathode product obtained at a current density of 0.9 A/cm^2 (**a**); element distribution map images (**b–c**) of Al, V in **a**; **d–e** EDS spectra measured over the specified position in **a**; XRD pattern of the cathode product obtained at a current density of 0.9 A/cm^2 (**f**)
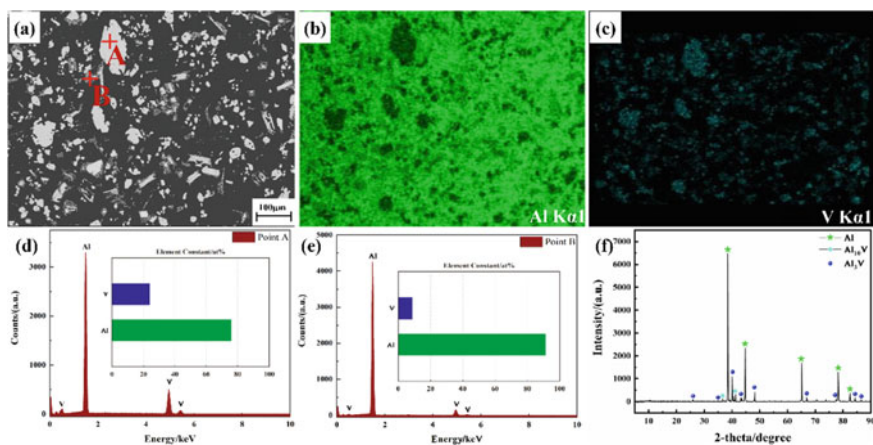
Fig. 8 BSE image of the cross-section of the cathode product obtained at a current density of 1.0 A/cm^2 (**a**); Element distribution map images (**b–c**) of Al, V in **a**; **d–e** EDS spectra measured over the specified position in **a**; XRD pattern of the cathode product obtained at a current density of 1.0 A/cm^2 (**f**)

The calculated apparent current efficiencies at various current densities are also illustrated in Fig. 9.

Obviously, the variations in the apparent cathodic current efficiency aligned well with vanadium contents in the products at different current densities. At the current density of 0.8 A/cm^2, the current efficiency reached its peak value of 34.54%. As
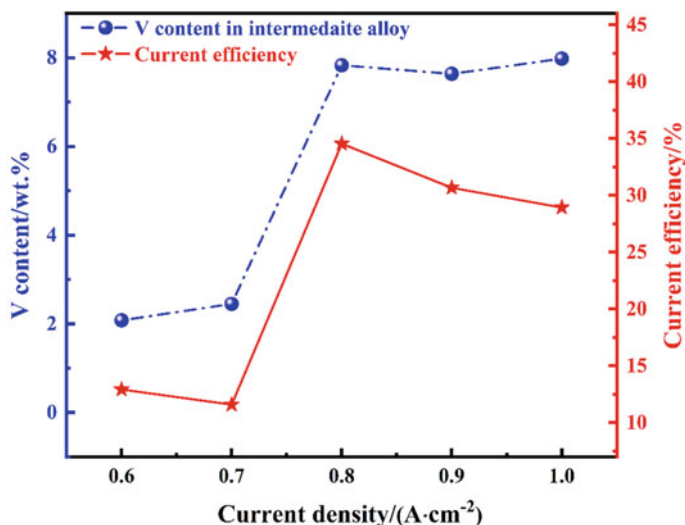
Fig. 9 Vanadium content in cathode product and the current efficiency at different current densities

the current density continued to increase, a subsequent decline in cathodic current efficiency was noticed, intrinsically linked to the vanadium content in the products.

The current efficiency shown in Fig. 9 was relatively low, which can be due to several factors. The first had to do with vanadium, which is a refractory metal with a melting point significantly higher than the temperature of the electrolyte. As a result, only a fraction of vanadium was actively involved in alloying with aluminum during the electrolysis process. The remaining portion flowed toward the graphite anode through convective diffusion, where it is subsequently oxidized by the gases produced at the anode to lead to vanadium losses. The second factor was related to vanadium existing in multiple oxidation states, inevitably participating in disproportionation reaction. The third had to do with the electrolysis process, which may generate an intermediate vanadium product (V_2O_3), with extremely low solubility in the electrolyte. Thus, its precipitation on the cathode surface impeded the transfer of active materials, thereby increasing the resistive barriers to electrochemical reduction.

Conclusion

Aluminum-vanadium intermediate alloys were successfully produced via the direct electrolysis of $NaVO_3$ in NaF-KF-AlF$_3$ molten salt system using liquid aluminum as the cathode at 820 °C. At lower current densities (0.6 A/cm^2), the primary constituents of the cathode products consisted of aluminum matrix and $Al_{10}V$. As the current density rose to 0.7 A/cm^2, the Al_3V phase started to form in the cathode products. At a current density of 0.8 A/cm^2, the current efficiency reached the highest value

of 34.54%, to yield vanadium content reaching 7.83 wt.%. Further increasement in the current density to 0.9 and 1.0 A/cm^2 did not result in significant alterations in the vanadium content present in the cathode products.

References

1. Weng W, Wang M, Gong X et al (2016) One-step electrochemical preparation of metallic vanadium from sodium metavanadate in molten chlorides. Int J Refract Metal Hard Mater 55:47–53
2. Weng W, Wang M, Gong X et al (2016) Thermodynamic analysis on the direct preparation of metallic vanadium from NaVO$_3$ by molten salt electrolysis. Chin J Chem Eng 24(05):671–676
3. Xu Y, Jiao H, Wang M et al (2019) Direct preparation of V-Al alloy by molten salt electrolysis of soluble NaVO$_3$ on a liquid Al cathode. J Alloy Compd 779:22–29
4. Zhang Y, Hu X, Yang J et al (2023) Clean separation of vanadium from NaVO$_3$ in NaF-KF-AlF$_3$ molten salt by electrochemical reduction. Sep Purif Technol 312:123389

Gas Evolution During Nd and DyFe Electrowinning

Ole S. Kjos, Samuel Senanu, Arne Petter Ratvik, Karen Osen, Ana Maria Martinez, Wojciech Gebarowski, Anne Støre, Thomas-Park Simonsen, Henrik Gudbrandsen, Kent-Robert Molvik, and Egil Skybakmoen

Abstract Rare earth electrolysis from fluoride melts has a lot in common with aluminium electrolysis; however, there are significant differences that need to be understood and investigated in order to develop efficient process control. A laboratory setup was developed to efficiently trap gases and obtain a mass balance of the components in the gas phase to understand the anode reactions. Using the described setup with a NdF_3-LiF electrolyte, it was possible to concentrate the off-gas (CO and CO_2) to approximately 10% facilitating increased sensitivity of PFC components. The laboratory cell produced metal, and the metal yield was 83% based on mass balance of $CO + CO_2$. The results are also discussed in context of results obtained in a small pilot cell designed and operated for metal production.

Keywords DyFe electrowinning · Molten salt · CF_4 · Current density · Anode effect

Introduction

To create a complete mass balance of the electrolysis process, the capture of the evolved gas species is useful. During regular electrolysis, the expected anode reaction is formation of CO or CO_2 according to reactions (1) and (2)

$$C + O^{2-}_{(dis)} \rightarrow CO_{(g)} + 2e^-$$
<div align="right">(1)</div>

$$C + 2O^{2-}_{(dis)} \rightarrow CO_{2(g)} + 4e^-$$
<div align="right">(2)</div>
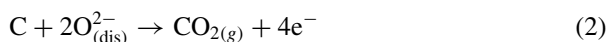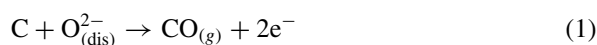
O. S. Kjos (✉) · S. Senanu · A. P. Ratvik · K. Osen · A. M. Martinez · W. Gebarowski · A. Støre · T.-P. Simonsen · H. Gudbrandsen · K.-R. Molvik · E. Skybakmoen
SINTEF Industry, P.O. Box 4760, Torgarden, 7465 Trondheim, Norway
e-mail: ole.kjos@sintef.no

Both reactions convert the same amount of charge per oxygen ion, but the consumption of carbon differs. The preferred reaction will depend on operation temperature and electrode potential/current density.

In addition, CO and CO_2 both can partake in equilibrium reactions for example reaction (3) and (4)

$$CO_{2(g)} + C \rightarrow 2CO_{(g)} \tag{3}$$

$$2CO_{(g)} + O_{2(g)} \rightarrow CO_{2(g)} \tag{4}$$
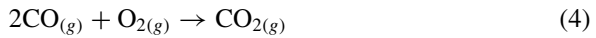
When the oxygen content in the electrolyte decreases the mass transport of oxygen to the anode surface will eventually be lower than the actual requirement of oxygen dictated by the electrolysis current fed through the system. The limiting current (I_{lim}) is defined as the current giving a surface oxide concentration of 0 on the anode, i.e. the consumption of oxide to sustain reactions (1) and (2) is equal to the mass transport rate of oxide to the surface. I_{lim} will depend on the bulk oxide concentration in the electrolyte, and hence it is important to keep oxide concentrations a stable and high levels through the operation of an electrolysis cell.

If a higher current is applied to the cell than I_{lim} the voltage will rise until the potential is sufficient to sustain other unwanted anodic reactions. Many reactions are possible, but literature and previous studies from aluminium industry have identified the following three as the most important reactions giving perfluorocarbons (PFC) [1, 2]. In a closed system, CO_2 formed can undergo reaction according to reaction (3) and convert to CO. The mass balance on an oxygen basis will not change and total oxygen balance can be used to estimate the actual current efficiency on the anode. In an open furnace, it will not be possible to conduct a mass balance since O_2 from the atmosphere will be available to react with $CO_{(g)}$ but also other carbon parts of the system such as anode top, carbon crucible, etc.

$$C + O^{2-}_{(dis)} + 2F^{-}_{(dis)} \rightarrow COF_{2(g)} \tag{5}$$

$$C + 4F^{-}_{(dis)} \rightarrow CF_{4(g)} \tag{6}$$

$$2C + 6F^{-}_{(dis)} \rightarrow C_2F_{6(g)} \tag{7}$$
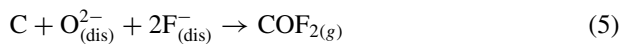
For the best change of studying the gases, it is important to capture the evolved gases efficiently and keep control of dilution effects. PFCs have a global warming potential of $7390 \times$ that of CO_2 for CF_4, and $12,200 \times CO_2$ for C_2F_6 [3]. Even trace amounts of these gases will have significant impact on the environmental footprint of the process.

Methods

To understand primary gas components and how they form during electrolysis of rare earth oxides, a dedicated closed setup with full mass balance of the gases (oxygen basis) was designed. In addition, the results obtained were compared with results from an open furnace for long-term electrolysis experiments.

Closed Setup with Mass Balance

Determination and quantification of gaseous species in the off-gas were done with an FTIR analyser (AtmosFIR from Protea Ltd.). This instrument is well suited to quantify the gas mixtures expected from both industrial operations as well as laboratory scale electrolysis experiments as it has a small internal volume. In these experiments, the applied calibration has a level of quantification (LOQ) for CO_2 of 400 ppm, CF_4 of 0.05 ppm and CO at 100 ppm.

One challenge when working in laboratory-scale setups is that the dead volume of the furnace is significantly larger than in industrial processes. This leads to longer dwell time for the gas before it is extracted and analysed, and hence more time for gas components to undergo secondary reactions.

To mitigate this, a dedicated setup had to be designed to efficiently trap and lead any evolved gases out of the furnace with minimal ingression of air since moisture and oxygen will react with the gases of interest. The design shown in Fig. 1 uses a hollow graphite anode with a closed top. In the top, there was feedthrough for oxide feeding, cathode assembly and thermocouple. These feedthroughs are insulated with boron nitride (BN) bushings to avoid stray currents. The BN bushings also help contain the gas within the inside of the electrode assembly. The cathode rod was created hollow, allowing gas to be extracted through the centre of the cathode rod as shown in Fig. 1. Ar flushing gas was introduced into the furnace void outside the electrode compartment. As gas was extracted from the anode at a higher rate than it was produced in the anodic reactions, additional amounts of Ar would leak in through the openings ensuring that the direction of flow brings inert gases into the anode cavity and extract produced gases efficiently to the analyser.

Gas flow through the FTIR was controlled by a SKC pocket pump from SKC Ltd, while purge gas into the furnace was controlled by digital mass flow controllers.

The gas outlet of the furnace was led through a Al_2O_3 trap for capturing HF, and then directly into the FTIR analyser. Gas was sampled from inside the hollow electrode assembly at a rate of 350 mL/min, while there was a flushing of 400 mL/min Ar in the furnace void outside the anode assembly. The amount of evolved gases from the electrolysis process was always lower than 350 mL/min, in this way, it could be established a flow pattern from the outside of the furnace, into the electrode assembly where the inert gas helped sweep the evolved gases out to the analyser. It

Fig. 1 Drawing of setup. The outer box is the furnace void. Within it is the crucible and electrode assembly. The arrows show the flow of the gas, 1: 400 mL/min controlled flushing, 2: flow of gas from furnace void to inner part of electrode assembly. 3: evolved gases + Ar flushing gas escaping through hollow cathode assembly. 4: controlled flow of 350 mL/min into analyser
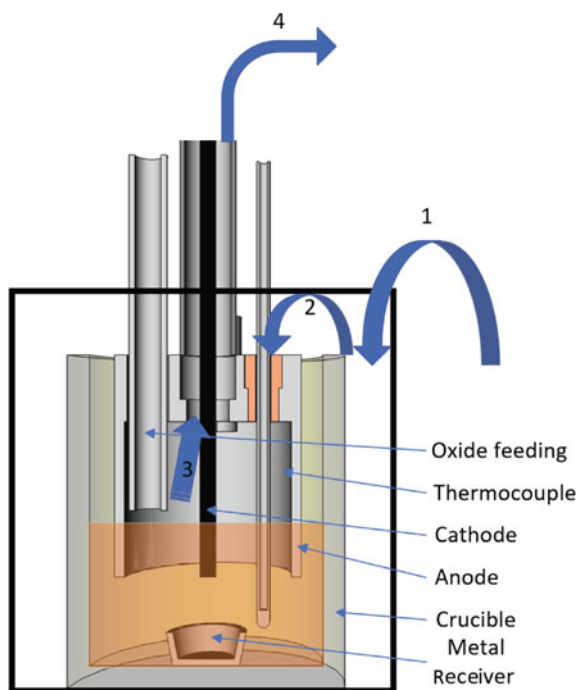
is assumed that due to the flow pattern only neglectable amounts of evolved gases go from the anode cavity to the furnace void.

The experimental procedure was to apply a fixed electrolysis current until the onset of CF_4 was detected by the FTIR. The CF_4 threshold was selected to be when the analyser indicated more than 2 ppm, which is significantly above the detection limit of 0.05 ppm. When the electrolysis current was stopped a sample of the electrolyte was taken for oxide analysis, and a dose of fresh Nd_2O_3 was added and a dissolution time of 20 min was allowed to reset the system for the next electrolysis run. Just prior to the start of the next electrolysis run a new sample of the electrolyte was taken for oxide analysis. In that way, the concentration changes of oxide could be monitored, and the oxide concentration at anode effect could be determined. This procedure was repeated 3–4 times for each current density.

The electrolyte samples were analysed by LECO (TC-436 DR Leco Corp.). Although the LECO methodology itself gives accurate results, there are some challenges in the sample preparation as any oxide contaminant such as grains of dispersed undissolved Nd_2O_3 will give erroneous high results. There are, however, few foreseeable sampling errors that will give to low analytical results. Therefore by doing multiple LECO analysis samples and discarding outliers that are significantly above the average, it is possible to obtain trustworthy data.

Long-Term Electrolysis

An electrolysis experiment was also conducted as part of the same activity. The setup is described with the main finings in a manuscript by Senanu et al. [4]. Although this was a different electrolyte consisting of DyF_3-LiF and a Dy_2O_3 feed the anodic reactions are expected to be similar. Gas evolution was monitored through this experiment by use of a Protea PROTIR FTIR analyser. A total of 30 h of electrolysis was achieved with currents of 450–500 A, yielding around 10 kg of DyFe alloy. FTIR was used continuously during this experiment to monitor dynamics in the off-gas composition and trends in CO, CO_2 as well as CF_4 evolution, and how these trends related to operational changes.

Results

Verification of Setup

Water was not expected to be formed in this experiment, and hence it could be used as an evaluator for leakage of ambient atmosphere. The water in the analytical results was lower than 2.5% of the ambient atmosphere that day. This confirms that the setup has a good recovery of produced gases and that more than 97.5% of the gas reaching the analyser is either flushing gas or gases evolved in the reaction.

The detection limit for CF_4 was about 50 ppb (0.05 ppm), with a typical gas evolution of 5–10% CO, this represents a cut-off when CF_4 content reaches 1/1,000,000th of the electrochemical evolved gas, using the assumption that PFCs has an average GWP of $10,000 \times CO_2$, it will be possible to determine all CF_4 evolution where CF_4 contributes more than 1% of the CO_2 contribution from the process.

Another important point was the ability for the setup to produce metal alloy consistently, as this is a confirmation that the desired cell reactions are occurring rather than unwanted side reactions.

The long-term experiment successfully produced more than 10 kg of DyFe alloy, more details can be found in [4]. The aim of this experiment was primarily to produce metal which was successfully achieved [4]. The results for current efficiency and metal quality were consistent with expectations from commercial rare earth electrolysis. The anode gas from the long-term experiment was collected and analyzed in order to have a better understanding of the reaction kinetics and fundamental reactions. However, as metal production was the main goal for that experiment a completely closed system was not possible, and hence mass balance of the system could not be done in the same way as on the small closed cells.

Long-Term Electrolysis

From the long-term electrolysis experiments, it is not possible to achieve any mass balance based on the evolved gas species. The electrolysis was run in an open furnace, and there was a significant additional contribution to CO and CO_2 evolution from airburn of the crucible and parts of the anode that was above the electrolyte as this setup could not be made airtight. In Fig. 2, we can see the trends. During tapping and other furnace operations, the positioning of the gas sampling probe could be altered slightly. Between 09:00 and 10:30 on August 24, the cell was covered with a lid. We can see that in this timeframe CO is the dominating gas species. It was also discovered that the cell produced significantly less metal in this timeframe, possibly due to a conductive layer of carbon forming at the surface [4].

The primary emitted gas species changed between CO_2 and CO depending on if the top of the furnace was covered or not. It is not possible to conclude on which of these gas species are primary evolved in the electrolysis process. CO will burn in contact with oxygen to form CO_2, but CO_2 will likewise react with carbon to form CO. Within the furnace there is a lot of exposed carbon parts.

The electrolysis run was not stopped at first signs of CF_4 as the trials for oxide dissolution were, as it was desired to operate the electrolysis cell in a manner consistent with existing procedures. Instead stirring of the electrolyte and feeding of additional oxides were initiated. CF_4 is, by far, the dominant carbon-fluor species in the gas, but traces of C_2F_6 were also found. The ratios of CF_4 to C_2F_6 are in the area between 1:50 and 1:200 with C_2F_6 concentrations approaching 1 ppm while CF_4 concentrations are in the range of 50–200 ppm.

In the experiments with the closed setup C_2F_6 concentrations exceeded 0.3 ppm only once, despite CF_4 levels ranging from 200 to 1000 ppm, resulting in the CF_4 to C_2F_6 ratio in the closed setup to exceed 1:1000. Despite differences in concentration and concentration ratios, there are clear signs of C_2F_6 in both of these experimental designs.
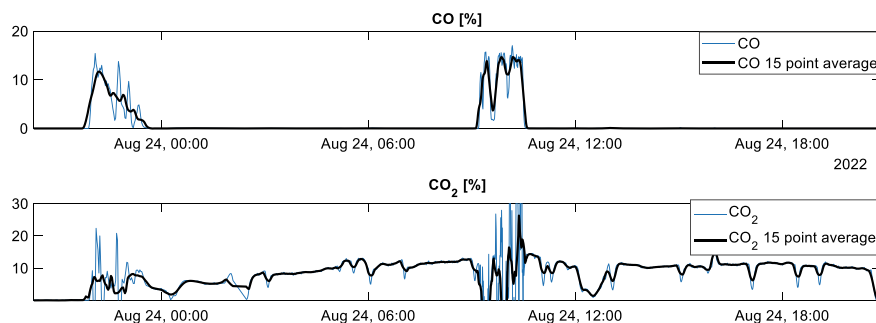
Fig. 2 Trends for CO and CO_2 for the final part of the long-term experiment

Critical Oxide Concentration for Given Current Densities

Using the closed setup for gas the studies, samples of the electrolyte were taken before and after each electrolysis run and used to establish the correlation between I_{lim} and current densities to avoid the formation of any carbon-fluor compounds.

Figure 3 shows the relationship measured by averaging the LECO results for each of the current densities in experiment 2. As expected, there is a clear correlation between the amount of dissolved oxide in the electrolyte and the current density. The results for experiment 1, however, suffered from high inaccuracies in the Leco analysis.
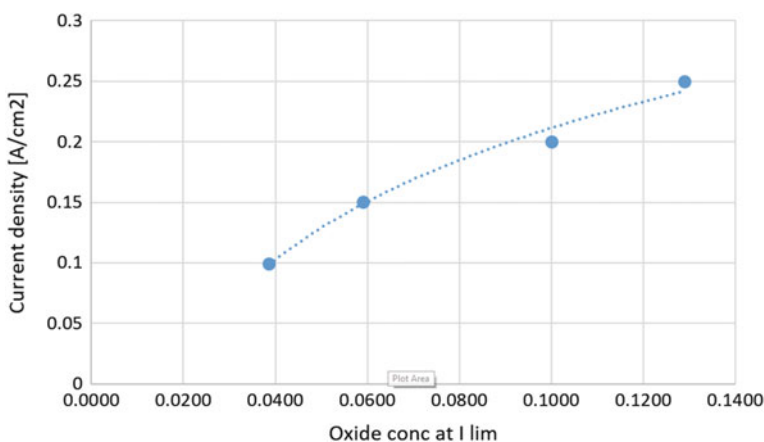
Fig. 3 Measured relationship between I_{lim} and oxide concentration in the electrolyte

Signs Before AE

Voltage Trends

As we can see from Fig. 4, there is a consistent increase in cell voltage when approaching anode effect. In experiment 1, the overall cell voltage was slightly lower, probably due to better external connections, however, the rising trends in cell voltage are still clear. The voltage window from start of electrolysis until onset of AE is between 300 and 500 mV, which should provide for sufficient change in overall voltage to have a potential be used as input for feeding control. A change in cell voltage over time will occur, but a control mechanism using the slope of the voltage trend from last oxide feeding compared to a predicted slope has a potential to be used as a process control input to avoid anode effect. Potentially, it can also be used
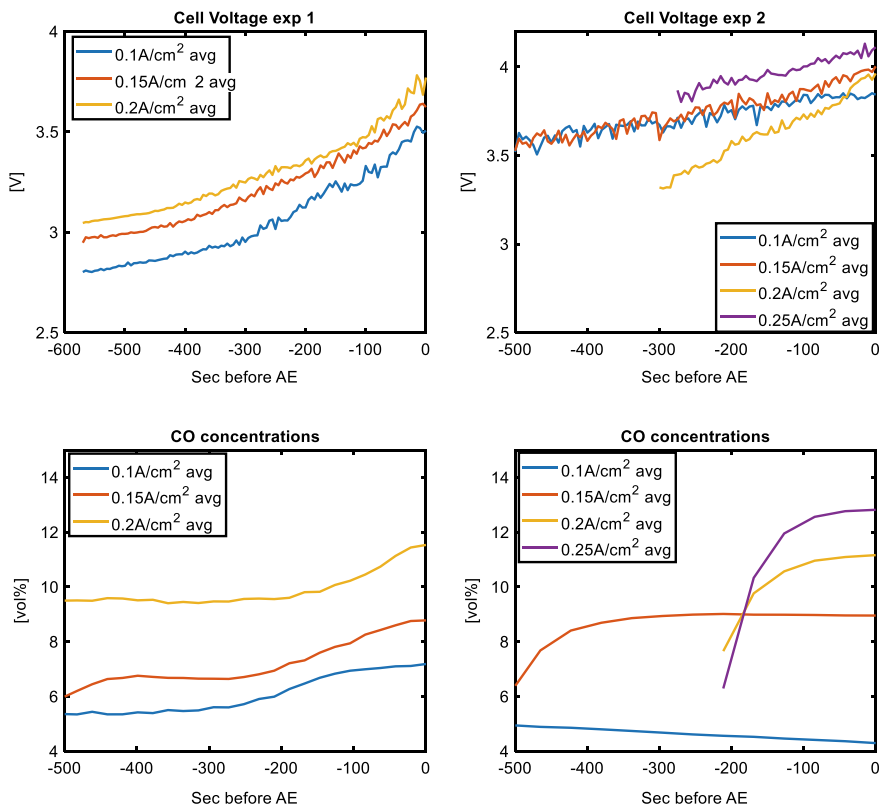
Fig. 4 Plot of voltage trends (upper) and CO concentrations in off-gas (lower) in seconds before AE at different current densities

to turn off or reduce the current until oxide new has been fed, thus avoiding running into CF_4 evolution.

Gas Composition

Interestingly, we can see that in experiment 1 there was a consistent and pronounced change in cell gas composition the final 3 min before onset of AE. We did, however, not see the same trends in experiment 2. We see the same rising trends in the data from the large cell experiments, however, in these cases, it is more reflected in the CO_2 trends.

An effort was specifically put into looking for COF_2 as we expect it to form according to reaction 5, but there are no traces in the off-gas. From research conducted on aluminium/cryolite systems, it is highly likely that COF_2 [1] is produced at the anode, but still very few reports of detection are made due to its fast reactions with other materials as well as self-decomposition into CF_4 and CO [2].

Produced Metal

In both trials, metal was produced, in the first trial, 20.4 g of Nd was formed, while in the second trial, 40.5 g was produced. Current efficiency was not high, but within a confined geometry like this, it can be expected that a lot of the current is lost in back reaction (reduction of Nd metal at the anode surface) due to short anode cathode distance. However, the amount of metal produced fits very well with the overall amount of gas evolved ($CO + CO_2$). In the first experiment, we got 83% of the metal that could be expected based on the integrated gas concentrations, while in experiment 2, we got more than 90% indicating that the mass balance of the system fits well.

Primary Gas Species

It remains an open question if the primary gas species is CO or CO_2 within this process. In small-scale experiments like this, it is not possible to determine since any CO_2 will react with the carbon materials to form CO immediately in the closed atmosphere. Likewise, in an open system, CO will burn in the presence of air to from CO_2. However, for a production cell, CO_2 will be the main emitted gas as the trials showed that the electrolysis process needs to be run in an open atmosphere to achieve acceptable current densities [4].

In the aluminium production, it is determined that CO_2 is the primary gas formed at the anode at the current densities applied (approximately 1 A/cm^2), but that the amount of CO in the off-gas increases with lower current densities. Although these processes operate in different electrolytes, it can be expected that similar current density dependences exist for Nd electrolysis.

It can be seen that CF_4 is produced only at timeframes when we expect oxide depletion of the electrolyte. The short timeframes with CF_4 evolution are not sufficient to produce the amounts of metal recovered. Hence, it can be concluded that the bulk part of Nd metal is produced without any PFC evolution, and that Nd and other rare earth metals can be produced without harmful PFC gases given that sufficient efforts are put into developing process controls in the same way as it has been implemented in aluminium industry during the last 20 years.

Conclusions

- The closed cell design works well, the leakage of air (O_2/H_2O) into the system is less than 2.5% of the evolved gases, and the cell atmosphere responds rapidly to changes in cell voltage

- Metal is produced at a current efficiency between around 20 and 40%, but on a mass balance basis from gas ($CO + CO_2$) evolution, there is 83–95% efficiency in the metal production. Probably explained by a back reaction or a parallel circuit of electronic conductivity.
- Oxide additions give a reproducible extension of CF_4-free electrolysis operations.
- Production rates of Nd metal indicate a setup that is a representable scaled reproduction of a real metal-producing cell.
- It is possible to produce both Nd and DyFe alloy without any PFC gases given that efficient process control routines are developed.

References

1. Doreen M (1998) Sulfur and fluorine containing anode gas produced during normal electrolysis and approaching an anode effect. In: Light metals 1998, pp 311–316
2. Kjos OS, Aarhaug T, Skybakmoen E, Solheim A (2012) Studies of perfluorocarbon formation on anodes in cryolite melts. In: Light metals 2012
3. The Intergovernmental Panel on Climate Change (IPCC). Global Warming Potentials (IPCC Fourth Assessment Report). IPCC
4. Senanu S, Ratvik AP, Kjos O, Osen K, Martinez AM, Gebarowski W, Støre A, Simonsen T-P, Gudbrandsen H, Molvik K-R, Skybakmoen E, Hall C, Pradeep V, Henvey D, Johnson J (2024) Parameter study for the production of DyFe by molten salt electrolysis. In: Light metals 2024

Parameter Study for the Production of DyFe by Molten Salt Electrolysis

Samuel Senanu, Arne Petter Ratvik, Ole Kjos, Karen Osen, Ana Maria Martinez, Wojciech Gebarowski, Anne Støre, Thomas-Park Simonsen, Henrik Gudbrandsen, Kent-Robert Molvik, Egil Skybakmoen, Chris Hall, Vipin Pradeep, Darren Henvey, and Jake Johnson

Abstract A parameter study of DyFe alloy production by molten salt electrolysis in an equimolar DyF_3-LiF electrolyte added Dy_2O_3 at temperatures in excess of 1000 °C using a power supply system that could deliver up to 500 A is reported. A cylindrical carbon anode with a pure iron cathode in the centre was used. Oxide concentration of electrolyte determined by inert gas fusion technique varied from ca. 1.5–3 wt%. The formation of perfluorocarbon (PFC) gases was monitored using an online Fourier Transform Infrared Spectrometer (FTIR). The investigations showed a close relationship between the cathodic current density and the amount of DyFe metal alloy produced with the highest metal production occurring at cathodic current densities above 6 A/cm^2. Inductively coupled plasma (ICP) analysis of the produced DyFe metal ingots showed a composition of 83 wt% Dy and 17 wt% Fe. Carbon content varied between 0.04 and 0.16 wt%.

Keywords DyFe electrowinning · Molten salt electrolysis · Cathodic current density · Permanent magnets

Introduction

The importance of rare earth elements, especially Nd, Pr, and Dy, is mainly connected to their superior magnetic properties [1]. These superior magnetic properties are essential to produce strong permanent magnets necessary for making efficient and compact magnets for wind turbines, electrical vehicles, etc. [2]. The demand for rare

S. Senanu (✉) · A. P. Ratvik · O. Kjos · K. Osen · A. M. Martinez · W. Gebarowski · A. Støre · T.-P. Simonsen · H. Gudbrandsen · K.-R. Molvik · E. Skybakmoen
SINTEF Industry, P.O. Box 4760, Torgarden, NO-7465 Trondheim, Norway
e-mail: samuel.senanu@sintef.no

C. Hall · V. Pradeep · D. Henvey · J. Johnson
Less Common Metals Ltd., Unit 2 Hooton Park, North Road, Ellesmere Port, Cheshire CH65 1BL, UK

earth elements is projected to increase significantly over the next few years because of these green transitions. It is projected that neodymium and dysprosium will increase in demand by 700 and 2600%, respectively, over the next 25 years [3]. Despite the present and future projected demands for these elements, the supply may become very challenging for many countries as China alone stands for more than 36% of the global reserves [4] and, currently, totally dominating the global rare earth value chain [4, 5]. Hence, it is important for Europe and the rest of the western world to establish their own value chain for these crucial elements. The European Union Horizon 2020-funded project SecREEts (www.secreets.eu) has attempted to help in this regard. Production of the rare earth elements from the rare earth oxides from the SecREEts project was accomplished by an electrolysis process in a fluoride-based molten salt. Although other techniques such as calciothermic reduction and chloride electrolysis may be used for the production of rare earth metals for permanent magnets, fluoride-based molten salt electrolysis is the most common industrial method [6]. The electrowinning involves the dissolution of rare earth oxides in a fluoride-based molten salt electrolyte and passing current through the melt to produce liquid rare earth elements at the cathode. The fluoride melt is mostly composed of the rare earth fluoride (ca. 87 wt%) and lithium fluoride to decrease the melting point and increase the electrical conductivity of the melt [3, 5, 6]. Advantages such as high product purity and high current efficiencies are some of the reasons why molten fluoride salt electrolysis is the dominant industrial production [3, 6, 7]. Despite the advantages that come with the molten salt electrolysis in fluoride melts, some issues regarding emissions exist. The use of graphite as anode material leads to the formation of CO and CO_2 gases [6, 8]. Also, the low solubility of rare earth oxides in their fluoride melts leads to a situation where the fluoride melt may decompose to form perfluorocarbon gases, mainly CF_4, during the electrolysis process in an event called anode effect [7, 9, 10].

The rare earth elements are divided into light and heavy rare earth elements based on the atomic weight and the peculiar chemical and magnetic properties. Dysprosium is considered a heavy rare earth element and is in very high demand as stated earlier [3]. This high demand for dysprosium is mostly connected to its application in the production of neodymium-iron-boron (NdFeB) permanent magnets where it plays a crucial role of improving the magnet's resistance to demagnetisation at higher temperatures [11]. However, being a heavy rare earth element, Dy has a high melting point of 1407 °C, making it difficult to obtain in its pure form using molten salt electrolysis [8]. Thus, a technique involving the use of a suitable transition metal as a cathode that forms a low-melting alloy with dysprosium is employed during the electrolysis process. The cathode material of choice in this case is iron, Fe, which is very convenient considering the fact that the dysprosium iron alloy, DyFe, produced can be employed directly in the production of NdFeB permanent magnets [8].

Experimental

A new experimental setup specifically designed to produce DyFe metal alloys while studying important parameters such as temperature, cathodic and anodic current densities, variations in oxide concentrations, and cell voltage during electrolysis experiments in molten fluoride salts was developed. The experimental setup employed is a scaled down cylindrical geometry design based on the industrial furnace design at Less Common Metals (LCM) in England. For the trials, a consumable, high-purity iron cathode rods ($\varnothing = 30$ mm) were provided by LCM. A pure iron cathode was positioned in the centre of a graphite crucible ($\varnothing_i = 275$ mm and $\varnothing_o = 315$ mm) with a cylindrical graphite anode ($\varnothing_i = 195$ mm and $\varnothing_o = 235$ mm) leaving a spacing of about 20 mm to the walls of the outer graphite crucible.

The anode-to-cathode distance (ACD) based on this setup was 82.5 mm. The cylindrical carbon anode was bolted into a steel frame for electrical connection at the top of the anode that was, for this purpose, made 40 mm thicker than the remaining part. The graphite crucible and graphite anode were provided by Schunk Carbon Technology AB. A steel receiver for the produced metal was also fixed into a cavity in the graphite crucible. The whole assembly was then placed into a resistance-heated furnace with a dedicated control system. The tubes for collecting process gases for measurements were placed between the anode and the cathode. In contrast to the anode design in industrial cells, consisting of several individual anodes, the anode for the trials was machined from one solid block of graphite. Gas for FTIR analysis (Protea AtmosFIR) was extracted via steel tubes placed above the electrolyte and close to the anode at a controlled flow of 350 Nm L/min using an SKC Touch sampling pump.

At the start of the experiment, 70 kg of electrolyte composed of 50 mol% LiF and 50 mol% DyF_3 was applied. All the fluoride chemicals and the oxide had a purity
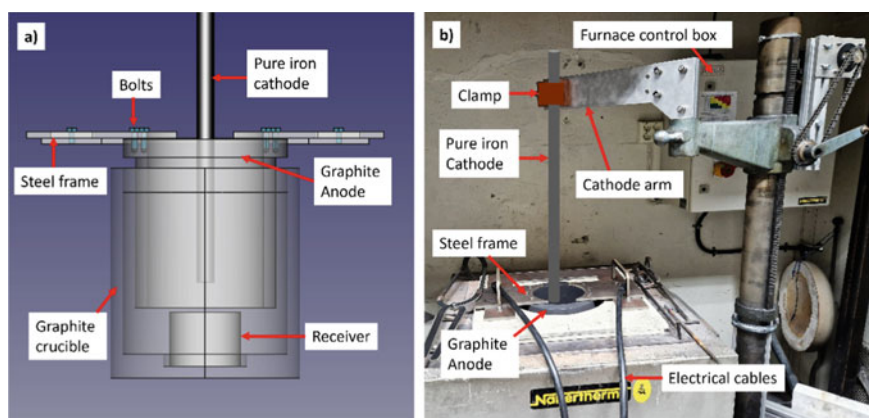
Fig. 1 **a** A sketch of the setup showing the different parts. **b** A picture of the furnace containing the parts illustrated in Fig. 1a

level greater than 99% and were provided by LCM. Due to the voluminous nature of the DyF_3–LiF powder mix, it was pre-melted at a temperature of ca. 1000 °C prior to the tests to have space for the diverse measuring instruments. Before starting the electrolysis process, the electrolyte was added 2.4 wt% Dy_2O_3. This was done to avoid any PFC generation during startup.

The power needed for the electrolysis was supplied by an EA-PSI 9080-510 3U bench top power supply system that could operate with a maximum voltage and current of 80 V and 510 A, respectively, with a total power output of 15 kW. The power supply system was also programmable providing an opportunity to set a maximum voltage that cannot be exceeded for safety reasons, e.g. during anode effects.

The cell voltage, current, and temperature variations were logged during the electrolysis campaign by means of a multichannel Keithley 2000 Multimeter. Electrolyte sampling and oxide additions were done manually every 15 min. Electrolyte samples as well as core drilled DyFe metal alloy samples were analysed for oxide concentration and carbon content by the inert gas fusion technique using a LECO TC-436 DR (Leco Corp.) instrument. Powder X-ray diffractometry using the D8-Davinci 1 and D8-Focus instruments was used to determine the phases present in the electrolyte during the electrolysis process. The core drilled samples from the DyFe metal alloy ingots were also characterised by ICP (Inductively Coupled Plasma) analysis using the Agilent 8900 Triple Quadrupole ICP-MS (ICP-QQQ) with SPS 4 Autosampler to determine the elemental composition.

Metal tapping was one of the most critical operations and was done in the following sequence:

1. Shutting down the power supply to pause the electrolysis.
2. Moving the cathode arm to create space for lifting the metal receiver.
3. Retrieving the receiver from the crucible.
4. Pouring the receiver content into a mould to cast the produced metal alloy.
5. Placing the receiver back into the crucible.
6. Adjusting and repositioning the iron cathode to the centre of the cell (centre of the anode).
7. Restarting the electrolysis process.

Results

Approximately 10 kg of pure DyFe alloy ingots were produced after two trials using ca. 11 kg of dysprosium oxide and 2 kg of pure iron cathodes. The first trial had to be aborted just after 5 and half hours due to extensive air burn of the crucible and the anode caused by an air leak to the furnace. Close to 1 kg (855 and 158 g) of DyFe was produced during the first trial. The electrolyte from the first trial was used for the second trial, which started in the evening the next day. The operation data, consisting of the cell voltage (Vcell), current, metal tapping operations labelled T1, T2, T3, etc. and other events from the trials are shown in Figs. 2 and 3.
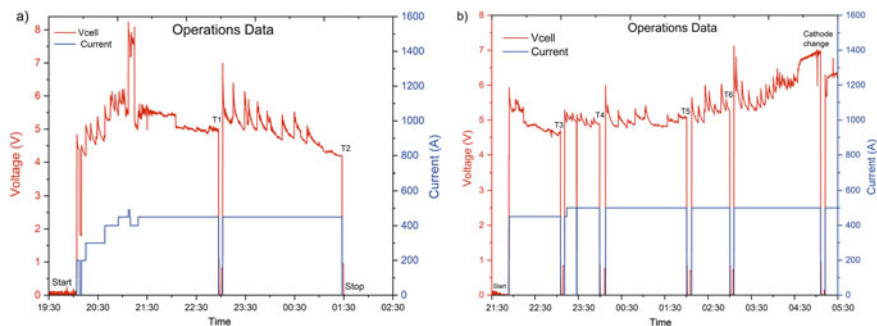
Fig. 2 **a** Operations data from first trial on 22nd August, T1 and T2 indicate the metal tapping operation for tapping 1 and 2. **b** Operations data from first shift of second trial on 23rd August, T3, T4, etc. indicate the metal tapping operations for tapping 3, 4 etc. The stop after 05:00, as shown on plot, was for cathode rod change
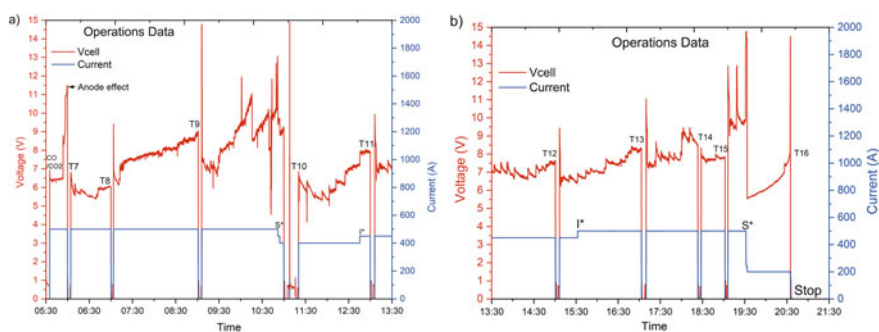
Fig. 3 **a** Operation data from second shift of second trial on 24th August, the stop at 05:30, shown by CO/CO_2 in the plot, was to investigate if CO/CO_2 formation was electrochemical. T7, T8, etc. indicate the metal tapping operations for tapping 7, 8, etc. S* indicates a drop in current and a consequent stop of electrolysis due to high voltage. I* indicates an increase in current, **b** operations data from the last shift of the second trial on 24th August from the afternoon to the evening when operations ended (stop). T12, T13, etc. indicate the metal tapping operations for tapping 12, 13, etc. I* indicates an increase in current, S* indicate current drop due to high voltage

The metal alloy production reaction is given by Eq. 1.

$$Dy_2O_3(\text{diss}) + 3C(s) + Fe_{2x}(s) = 2DyFe_x(\text{liq}) + 3CO(g) \tag{1}$$
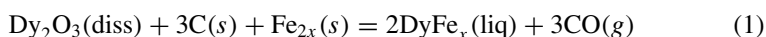
Due to the extensive evaluation of operational parameters, there were also periods of anode effect where the cell voltage rapidly increased due to depletion of oxide resulting in the decomposition of the electrolyte during the trials. Equation 2 describes the reaction leading to anode effect. The gas measurement instruments confirmed the anode effect by detecting perfluorocarbons. Some of the results from the gas measurement activities are summarised in the section below.

Fig. 4 DyFe metal alloy ingots from the trials showing some frozen electrolytes on them

$$DyF_3(diss) + 3C(s) + Fe_{4x}(s) = 4DyFe_x(liq) + 3CF_x(g) \qquad (2)$$

Metal Alloy Product

A picture showing the 10 kg of DyFe metal alloy ingots produced is given in Fig. 4. In all about 16 metal tapping operations were carried out with varying amount of metal per tapping. The variation in tapped metal is a good indication of the effect of varying operational parameters. Table 1 gives a summary of the important operation data collected prior to metal tapping and includes data for current, cell voltage, charge between each tapping, electrolyte temperature, cathode, and anode current densities, tapped metal, and calculated current efficiency. The cathode and anode current densities were calculated assuming there was no change in submersion area in the actual period of the anode and cathode as well as the level of anode immersion.

The results that gave the most metal alloy with the highest current efficiencies were observed to correspond well with relatively low cathode immersion depth, i.e. high cathodic current density and high voltage. Also, higher temperatures seem to have a positive effect on the cathode current efficiency. A decision was made between tapping 9 and 10 to temporarily increase the cathode immersion depth to 11 cm to reduce the cell voltage as can be seen in Fig. 5. The figure shows the variation of the cathode and anode current densities during the trials.

Gas Analysis Results

The gas measurement results are summarised in a separate publication that has also been submitted [12]. The results show the production of two main gases, CO and

Table 1 Summary of data taken prior to metal tapping

Tapping	Amperage (A)	Cell voltage (V)	Total charge passed (Ah)	Electrolyte temp (°C)	Cathode current density (A/cm^2)	Anode current density (A/cm^2)	Metal quantity (g)	Current efficiency (%)
1	450	5.0	1164	1014	3.5	0.5	855	20
2	450	4.2	1092	1013	4.4	0.5	158	4
3	450	4.7	536	1052	3.0	0.5	272	14
4	500	4.9	399	1046	3.4	0.6	107	7
5	500	5.0	938	1039	4.9	0.6	356	10
6	500	5.3	441	1041	4.9	0.6	88	5
7	500	6.5	1354	1058	6.1	0.6	1600	32
8	500	6.0	465	NA	6.1	0.6	175	10
9	500	9.0	979	1110	6.1	0.6	1850	52
10	500	9.2	937	1033	4.5	0.6	905	26
11	450	8.0	675	1074	5.5	0.5	700	28
12	450	7.7	859	1075	5.5	0.5	1400	44
13	450	8.3	950	1079	5.5	0.5	1080	31
14	500	8.5	613	1031	6.1	0.6	365	16
15	500	7.9	284	NA	6.1	0.6	65	6
16	200	8.0	425	1036	2.4	0.2	240	15
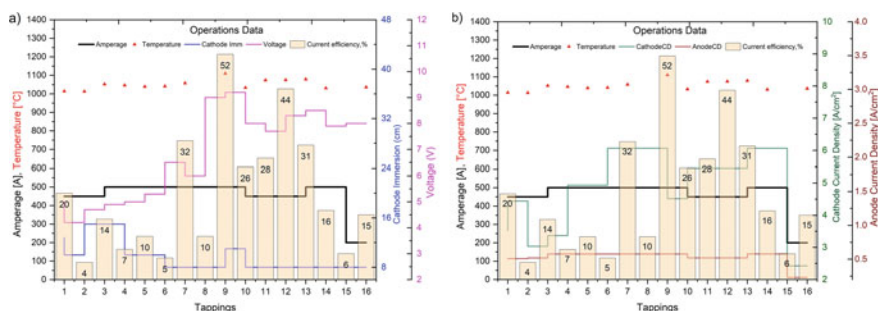
Fig. 5 a Operations data for whole campaign showing the current efficiency, cell voltage, amperage, cathode immersion depth, and electrolyte temperature, **b** operations data for whole campaign showing the current efficiency, anode and cathode current densities, and electrolyte temperature

CO_2, during normal operations of the electrolysis cell. The FTIR instrument showed very high concentrations of CF_4 gases during the trials as illustrated by Fig. 6. When comparing the integrated CF_4 emissions with the integrated CO_2 emissions, and multiplying with the CO_2 equivalent factor for CF_4, we see that the CF_4 emissions contribute to around of 40% of the total CO_2 equivalents in this experiment. We,
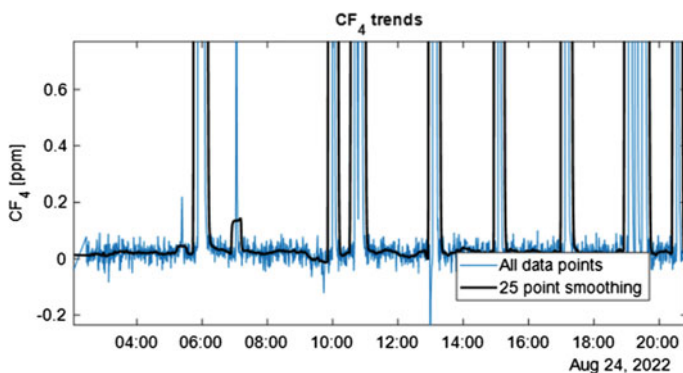
Fig. 6 CF_4 trends, detection level is around 0.03 ppm

however, saw that for long times there were no CF_4, despite the continuous production of metal. Therefore, it can be concluded that DyFe can be produced without CF_4, and avoiding CF_4 is a matter of process control.

Results from Chemical Analysis Using Inert Gas Fusion with LECO

Analysis of the oxide concentration within the electrolyte using electrolyte samples taken during the first and second trials showed varying oxide concentration from ca. 1.5 wt% up to about 4 wt%. The LECO results, as outlined in Fig. 7a, b for the first and second trials, respectively, showed mostly oxide concentration corresponding to expected rare earth oxide solubility in their corresponding rare earth fluorides [9] throughout the experiments albeit some instances where the concentration was low. The highest oxide concentration of ca. 4 wt% was observed for the first electrolyte sample taken prior to electrolysis during the first trial. The high oxide content of this first sample was expected as it was agreed to start with a saturated bath, however, it is worth mentioning that the LECO analysis may include undissolved oxides. Taking samples for LECO analysis from a saturated bath may also end up with some undissolved oxides (oxide slurry) and may return results that are above the saturation limit. The second highest oxide concentration was observed for a sample taken around 08:00 am during the second trial to be ca. 3.5 wt%. Low oxide content of the electrolyte was also observed for both trials. The low oxide content in the electrolyte during the early hours of the first trial gives an indication of the rapid depletion of the oxide during electrolysis considering that the initial electrolyte was saturated with an oxide content of ca. 4 wt%. The lowest oxide content of the electrolyte during the second trial was observed for a sample taken at ca. 10:00 am, just some few hours after measuring the highest oxide content. Carbon content of the produced DyFe metal alloy ingot ranged from 0.06 to 0.16 wt% as shown in Fig. 8.
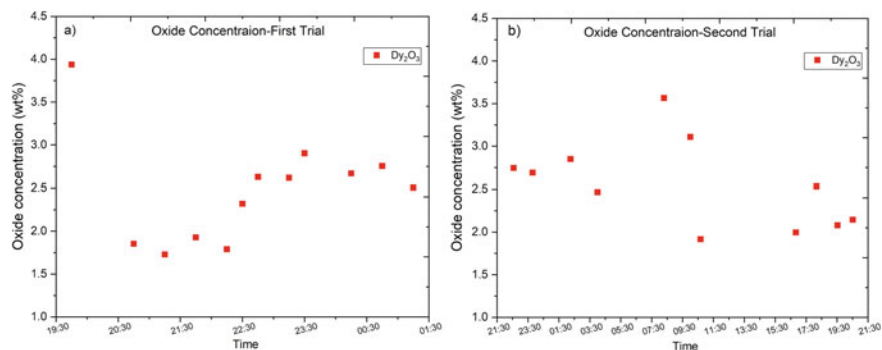
Fig. 7 Oxide concentration of the electrolyte. **a** During first trial (22 August 2022 to 23 August 2022), **b** during second trial (23 August 2022 to 24 August 2022)
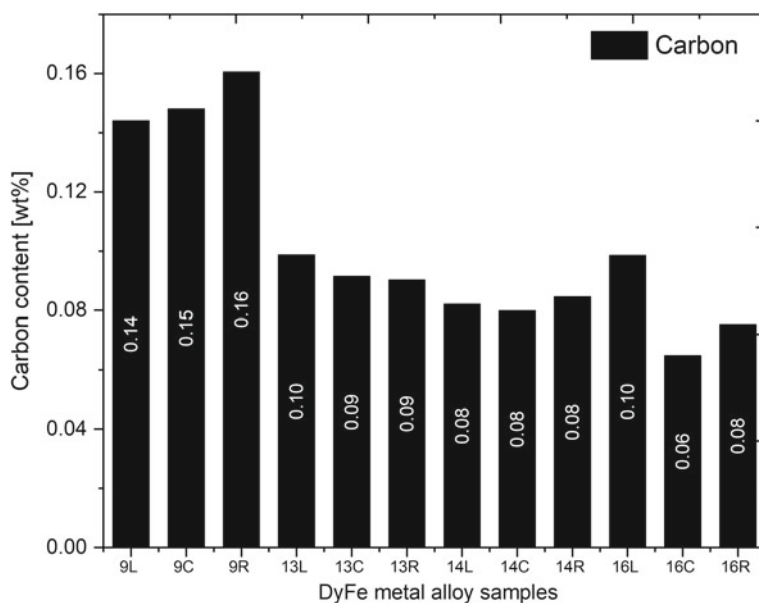
Fig. 8 Carbon content of samples taken from 4 DyFe metal alloy ingots analysed by LECO. Three samples were taken from each metal alloy ingot from different positions labelled as L, C and R where L, C and R stand for left, centre and right positions. The numbers 9, 13, 14, and 16 represent the metal alloy ingot number

Results from Chemical Analysis by ICP

In addition to knowing the different elements present within the DyFe metal alloy ingots produced, ICP made it possible to determine the ratio of Dy to Fe in the DyFe
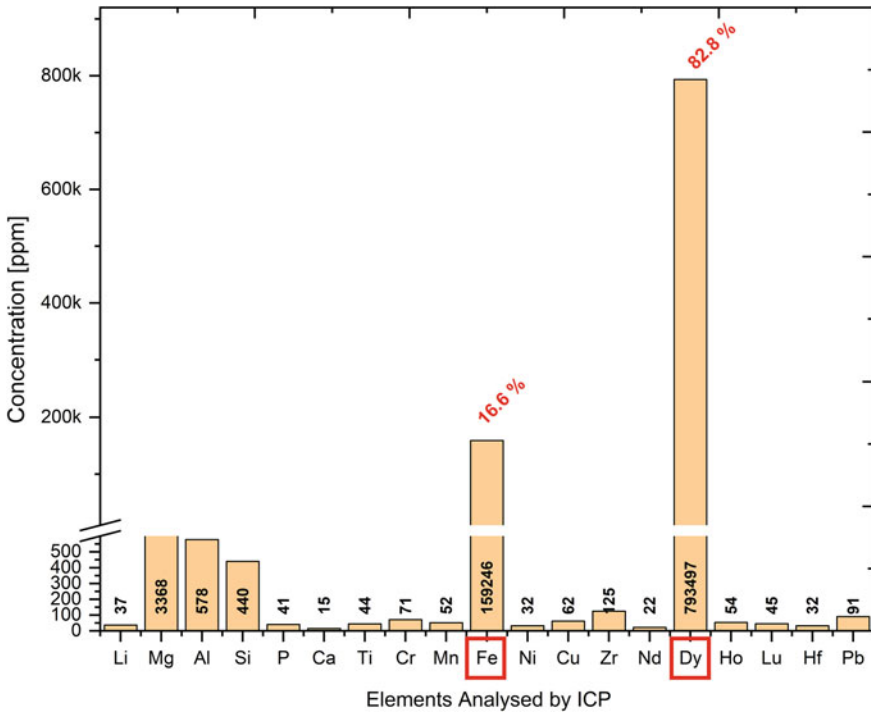
Fig. 9 ICP analysis showing the composition of elements within the DyFe metal alloy ingots in parts per million (ppm) except Fe and Dy which are given in percentage

metal alloy ingots. Figure 9 gives the concentration of the different elements within the alloy in ppm.

Discussion

Table 1 gives a summary of the trials, metal tapping, and operational parameters. It can be seen from this table that the current efficiencies were generally very low with the highest being only 52%. The relatively low current efficiencies have also been reported in earlier works [8]. One reason for this is presumed to be the extensive back reactions arising from the relatively high solubility of the produced alloy in the electrolyte. This is supported by the fact that the highest current efficiencies were obtained when the electrolyte temperature and cathode current density were highest at 1110 °C and 6.1 A/cm^2, respectively. The high electrolyte temperature can be assumed to facilitate a high solubility of the produced metal alloy in electrolyte. Nevertheless, a higher electrolyte temperature and cathode current densities seem

to contribute positively to the production relative to a lower electrolyte temperature and current density.

It can therefore be concluded that despite an assumed negative effect of increased metal solubility at higher electrolyte temperatures, it is more important to avoid too slow formation of metal at the cathode. Several explanations may be valid, one is that higher temperature may better promote the formation of the DyFe alloy since this is closer to the melting point of iron. In addition, more rapid formation of metal, i.e. higher current density (A/cm^2), may promote formation of sufficiently large droplets that drips off the cathode while a slow formation is more likely to cause diffusion into the electrolyte and, hence, contribute to more back reactions.

Also, as mentioned earlier, the higher cathodic current density contributed positively to metal production. Earlier tests have shown that a higher cathode current density may help to counteract back reactions thereby improving the current efficiency, however, there has not been much published work on how high an optimal cathodic current density should be. The work presented here suggests that the cathodic current density could be increased to values well above 6 A/cm^2 as observed during the present tests. Since the anodic current density did not change much during the tests, it is not included in this discussion. Nonetheless, this implies that the cathodic current density plays a more important role than the anodic current density given the current cell design.

As expected, the gas measurements showed the presence of carbon monoxide, CO, and carbon dioxide, CO_2, as the main gases during the electrowinning process of rare earth metals. An interesting observation was an increase in CO concentration relative to CO_2 when the cell was temporarily covered using insulation plates. The CO and CO_2 trends during the trials are presented in [12]. The increased CO concentration observed when the cell was covered could be assumed to result from the Boudouard reaction given by Eq. 3.

$$CO_2 + C \leftrightharpoons 2CO \qquad (3)$$

Figure 6 indicates that the formation of CF_4 only occurs in relation to events such as underfeeding. This points to the importance of having a good feed control during the electrowinning process.

It is already known that the solubility of rare earth oxides in their corresponding fluoride melts is relatively low at ca. 2.5 wt% as compared to other systems such as aluminium oxide in cryolite melts where the solubility is 3–4 times higher. For the experiments presented here, the maximum oxide concentration was measured for the electrolyte prior to electrolysis of the first trial using the inert gas fusion technique with the LECO apparatus to be ca. 4 wt%, although we cannot rule out that this is caused by some undissolved oxides since this is above-reported solubilities. The high oxide content of the electrolyte prior to start of the trials was done to avoid any anode effect during the early stage of the experiments. A relatively high oxide content was also observed for an electrolyte sample taken ca. 2 h after an anode effect that occurred around 06:00 am on 24th August during the second trial (see Fig. 3a). This high oxide content is assumed to result from adding too much oxide after the

anode effect and the hours that followed. Low oxide content of the electrolyte was also observed for both trials, and it is worth mentioning that the lowest oxide content was observed just an hour after the tapping that gave the highest quantity of metal (tapping 9 or T9).

Conclusions

High cathodic current density in the excess of 6 A/cm^2 and high electrolyte temperature above 1060 °C gave the highest production and current efficiencies. At low cathode current densities, the metal yield was lower than expected, indicating that a high current density at the cathode is necessary for avoiding metal dissolution in the electrolyte instead of forming metal droplets that fall into the metal collector below the cathode.

References

1. Binnemans K, Jones PT, Blanpain B et al (2013) Recycling of rare earths: a critical review. J Clean Prod 51:1–22. https://doi.org/10.1016/j.jclepro.2012.12.037
2. Coey JMD (2002) Permanent magnet applications. J Magn Magn Mater 248(3):441–456. https://doi.org/10.1016/S0304-8853(02)00335-9
3. Abbasalizadeh A, Sridar S, Chen Z et al (2018) Experimental investigation and thermodynamic modelling of LiF-NdF3-DyF3 system. J Alloy Compd 753:388–394. https://doi.org/10.1016/j.jallcom.2018.04.013
4. South China Morning Post (2022) How China's rare earth dominance spurs US and its allies to diversify supply chain of critical minerals. Available at https://www.scmp.com/economy/china-economy/article/3185968/how-chinas-rare-earth-dominance-spurs-us-and-its-allies
5. Smith B, Riddle M, Earlam M et al (2022) Rare earth permanent magnets: supply chain deep dive assessment. 1871577. https://doi.org/10.2172/1871577
6. Vogel H, Friedrich B (2015) Development and research trends of the neodymium electrolysis—a literature review. In: The 8th European metallurgical conference (Dusseldorf). https://doi.org/10.13140/RG.2.1.4061.2248
7. Guo X, Sietsma J, Yang Y (2014) Solubility of rare earth oxides in molten fluorides. ERES 2014:149–155
8. Martinez AM, Osen KS, Støre A et al (2018) Manufacturing of dysprosium-iron alloys by electrolysis in fluoride-based electrolytes. Electrolysis in a laboratory-scale cell. Metall Mater Trans B 49(4):2063–2070. https://doi.org/10.1007/s11663-018-1270-3
9. Senanu S, Ratvik AP, Gudbrandsen H et al (2021) Dissolution and online monitoring of Nd and Pr oxides in NdF3–PrF3–LiF electrolytes. Metals 11(2):326. https://doi.org/10.3390/met11020326
10. Martinez AM, Støre A, Osen KS (2018) Manufacturing of dysprosium-iron alloys by electrolysis in fluoride-based electrolytes: oxide solubility determinations. Metall and Mater Trans B 49(2):783–789. https://doi.org/10.1007/s11663-017-1159-6

11. Tenaud PH, Lemaire H, Vial F (1991) Recent improvements in NdFeB sintered magnets. J Magn Magn Mater 101:328–332
12. Kjos OS, Senanu S, Ratvik AP et al (2024) Gas evolution during Nd and DyFe electrowinning. In: Rare Metal Technology 2024

Electrochemical Recovery of Sb, Te, and In in Choline Chloride-Ethylene Glycol DES Electrolyte

Gøril Jahrsengene, Zhaohui Wang, and Ana Maria Martinez

Abstract Choline Chloride-Ethylene Glycol DES mixture (ethaline) is considered a green solvent and is one of the most popular DESs to combine with electrochemical recovery processes due to its superior electrochemical properties compared to other DES systems. In this work, electrochemical behaviour of antimony, tellurium, and indium in the ethaline system has been investigated to evaluate if this electrolyte media is suitable for electrochemical recovery. The metal chlorides $SbCl_3$, $TeCl_4$, and $InCl_3$ were added to model ethaline solutions at 10 mM concentrations. Electrochemical investigations were carried out at 60 °C by cyclic voltammetry (CV), chronoamperometry (CA), and potentiostatic electrolysis using a three-electrode setup. Metal deposits were investigated with SEM–EDS. All three metals were found to deposit within the electrochemical limits of the ethaline electrolyte, the cathodic deposition of the different metals appears in the order Te, then Sb, then In most cathodic.

Introduction

Deep Eutectic Solvents (DESs) have been suggested as a type of green solvent that could be used in metal processing applications instead of aqueous solutions [1]. A DES is a mixture of large, non-symmetric ions with low melting points, mixed around eutectic composition. Lewis or Brønsted acids and bases are mixed and may contain a number of anionic and cationic species (compared to ionic liquids (ILs), where usually one discrete anion and cation is used). This mixture has significantly lower melting point than the singular components, usually less than 100 °C. The most common DES type is denoted type III DES, a eutectic mix of a halide salt (often choline chloride, ChCl) and a hydrogen bond donor (HBD). Type III DESs are able to solvate transition metal species (chlorides, oxides, hydroxides). Many HBDs are very well characterised (amides, carboxylic acids, alcohols), and because of the large

G. Jahrsengene (✉) · Z. Wang · A. M. Martinez
SINTEF Industry, Trondheim, Norway
e-mail: goril.jahrsengene@sintef.no

varieties of HBDs the system is very adaptable. The physical properties of a DES are mainly dependent on the HBD.

DESs are tuneable for variable applications, and easy to prepare (simple mixture of the two components, moderate heating and stirring). The components are cheap, available on large scale and easy to transport on large scale, as they are toxicologically well characterised and non-toxic [2]. DESs are, however, less chemically inert than ILs, most of the DESs themselves are not well characterised for toxicological properties, they tend to have higher viscosity and lower conductivity than most ILs, aqueous electrolytes and molten salts, which limits their use. DESs are also hydroscopic [3].

Key points regarding electrochemical metal processing using DESs are that it avoids the low current efficiency and hydrogen embrittlement that tends to occur in aqueous electrolytes, and it avoids the toxicity issues using, e.g., Cr. Besides metal electrodeposition, metal electropolishing and extraction are other application areas. The applications of DES in metal processing involve incorporating the metal ions in the solution. Directly, this may be used to extract metals from minerals or waste for metal extraction and processing, but the dissolution of metals and metal oxides is also important for several significant processes (e.g., catalysts). When ions are dissolved in the DES, the solution may be used as an electrolyte in metal electrodeposition and electropolishing processes [4].

Ethaline is a mixture of choline chloride (ChCl) and ethylene glycol (EG), most often mixed at a 1:2 molar ratio. This system is known to have superior electrochemical properties compared to other DES type III electrolytes, i.e., lower density, higher viscosity, and higher electrical conductivity. Many metals have been electrochemically characterized in this DES, like Ag [5], Fe [6] and Cu [7, 8], and metal deposition of these metals are possible in the DES.

In this work, the possibility of using electrorecovery to extract the elements Sb, Te, and In in the ethaline DES was investigated. This was done through defining the stable electrochemical species in the system, identifying the redox systems, and obtaining metal deposits if the deposition is possible within the electrochemical limits of the DES.

Experimental

The ethaline DES was prepared by mixing Choline Chloride (Sigma Aldrich, $\geq$ 98%) and ethylene glycol (Acros Organics, 99 + %) in a 1:2 ChCl:EG molar ratio at elevated temperatures (60 °C) until a clear liquid was formed. After cooling, the DES was mixed with $SbCl_3$ (Sigma Aldrich, $\geq$ 99.95%), $TeCl_4$ (Sigma Aldrich, 99%), or $InCl_3$ (Sigma Aldrich, 99.999%) at 60 °C to obtain a 10 mM metal concentration.

The electrochemical experiments were conducted at lab scale using approximately 25 mL of the prepared solutions using a typical three-electrode arrangement: working, counter and reference electrodes. A stable Ag(I)/Ag reference system was constructed using a Pyrex tube closed with a porous glass frit containing AgCl

dissolved in a DES electrolyte and where an Ag wire was immersed, thus establishing the Ag(I)/Ag reference system and also allowing the electrical connection. A Pt spiral was used as counter electrode, also immersed in a Pyrex tube closed with a porous glass frit containing the same electrolyte as in the cell. Different working electrodes were used: glassy (vitreous) carbon (GC, 3 mm rods), Pt wire (0.5 mm wire), and Ag (1 mm wire). GC is known to be as a quite inert material and often results in a nucleation overpotential whereas Pt is less inert and catalyses reactions involving hydrogen evolution.

A number of electrochemical evaluations were done in each of the three solutions. Evaluations of the open circuit potential (OCP) values, cyclic voltammetry (CV), chronoamperometry (CA), and deposition of metals at constant potential were the main methods. The CVs were obtained with scan rates varying in the 10–500 mV/s range, starting from OCP cycling with varying limits depending on electrode material and solution. The CVs all start in the cathodic direction, unless otherwise specified. Short CA measurements were done at a number of potentials around the deposition potential in each solution to obtain results regarding the stationary conditions, and, depending on the results, metal deposition was done by choosing suitable potentials based on the CA results.

The deposits were rinsed in ethanol solution, and subsequently investigated by using a Field Emission Scanning Electron Microscope (FE-SEM, FEI Apreo, Thermo Fisher Scientific) equipped with an Energy Dispersive X-ray Spectroscopy (EDS, Oxford Instruments, UK).

Results and Discussion

Antimony Deposition

Sb(V), Sb(III), and Sb(0) were stable in the DES solution, and the natural state after adding SbCl$_3$ was, as expected, Sb(III). In the CVs (Fig. 1a) both the redox systems Sb(III)/Sb(V) and Sb(III)/Sb(0) are observed. By comparing the voltammograms obtained with the GC and Pt electrodes, the expected nucleation overpotential on GC compared to Pt is observed with a difference of almost 300 mV. In the quasi-stable system (i-E curves from CA measurements), this difference is only 25–50 mV when considering stationary conditions. The stationary results are likely closer to the deposition potential of the metals, and the measured potential of the metalloid formed on the surface of the electrodes was approximately −80 mV versus Ag/AgCl.

Additionally, it can be observed in Fig. 1a that on Pt, a small additional signal is observed before the deposition starts (marked with a *). This signal was found to depend on the state of the Pt wire; although the wire was conditioned at OCP before each scan, this peak disappeared if the scan was obtained on a completely new wire, or when the CV was obtained at very low scan rates (e.g., 10 and 25 mV/s). The peak might be related to moisture in the system, as the DES is hydroscopic. Additionally,
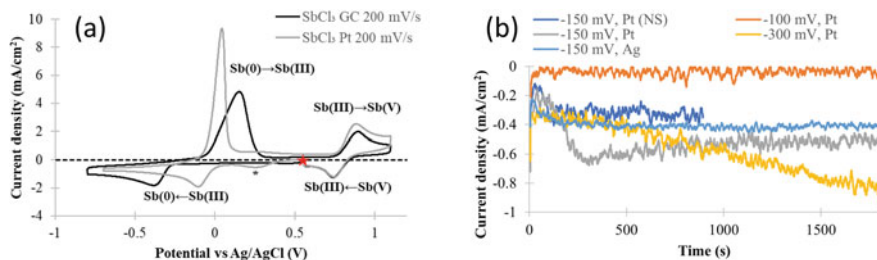
Fig. 1 Electrochemical characterization of model system with Sb(III) in 1ChCl:2EG DES at 60 °C. **a** CVs obtained with a scan rate of 200 mV/s on Pt wire and GC rod and **b** measured CD during the first 1800s of constant potential electrolysis on Pt and Ag wires under stirring (unless marked NS = No Stirring)

further characterization on the Pt wire results in the dissolution peak in the anodic return scan varies a lot more, becoming more anodic. A smaller pre-peak before the deposition was also observed. These observations likely indicate alloying of Sb with the Pt-substrate, as this behavior was not observed on the GC electrode.

Sb deposits were obtained at constant potentials of -100, -150, and -300 mV versus Ag/AgCl on Pt, and -150 mV on Ag. Stirring was used to have better availability of Sb(III) near the wire. The resulting measurements of the current densities (CDs) are presented in Fig. 1b, with NS representing the case with no stirring. As expected, no deposit was observed when running the electrolysis at -100 mV (CD $= 0$). Based on the stationary measurements, at -50 mV, it is expected that the limiting current density of the deposition reaction is not yet reached. This was deliberately chosen to attempt to obtain a dense deposit that adhered well to the substrate. The chronoamperometric measurements (Fig. 1b) at -150 mV show an increase in the measured CD during the first stage of the deposition, indicating nucleation and rapid growth, effectively changing the area. In the second stage (after 200 s), the CD becomes more stable, indicating more constant, macroscopic growth. On Pt and Ag the stable CD obtained in the second stage was -0.50 and -0.41 mA/cm^2 respectively. Both these deposits were then investigated in SEM. Sb-deposition at -300 mV resulted in a deposit did not adhere well to the substrate, signifying dendritic growth. This was also reflected in the measured CD, instead of stabilizing the CD increased during the entire deposition period.

Figure 2 shows the microstructure of the Sb deposit on Pt (top panel) and Ag surface (bottom panel) after 30-min deposition at -150 mV versus Ag/AgCl. Densely packed Sb crystals were observed in both cases. The grain size of Sb deposit on silver surface is slightly larger than that on Pt, both in micrometer and sub-micrometer scale. The morphologies of the two deposits are, however, different. Sb on Pt grows in angular grains, while on Ag forms more flat crystals, reflecting different crystal growth mechanisms on different substrates. EDS point analysis has confirmed the Sb deposits for both cases. The corresponding elemental compositions are listed in Table 1. Besides Sb, the EDS results showed some remains of electrolyte (C, O very
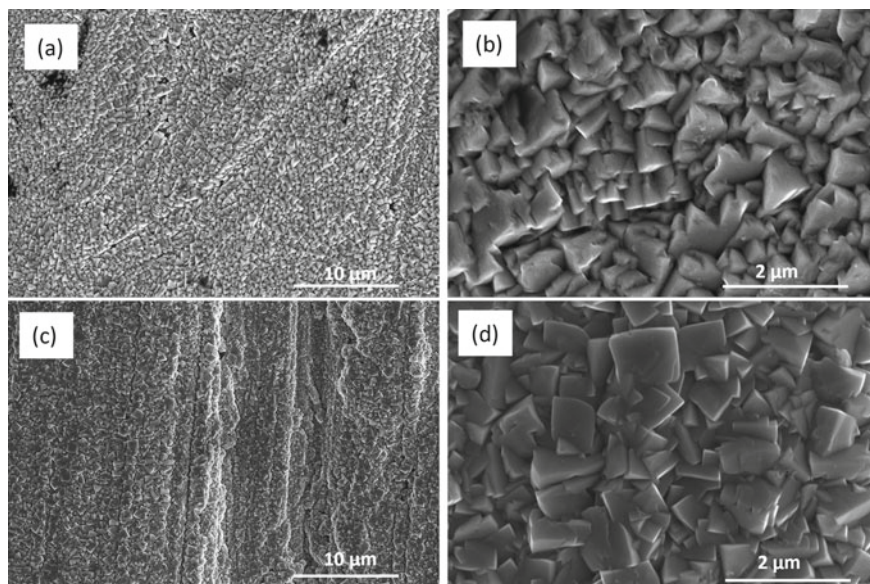
Fig. 2 SEM images of the Sb deposits on **a**, **b** Pt and **c**, **d** Ag electrode, at low (**a**, **c**) and high (**b**, **d**) magnifications, after 30-min deposition at –150 mV

Table 1 Elemental compositions (wt %) of Sb deposits on Pt and Ag surface from EDS point analysis

	C	O	Cl	Sb	Pt	Ag
Sb on Pt	10.64	3.25	0.17	83.19	2.74	N/A
	10.01	3.74	0.27	81.88	4.10	N/A
Sb on Ag	6.58	2.44	0	82.61	N/A	8.37
	7.86	2.49	0	84.30	N/A	5.34

little Cl), caused by the viscous liquid that may be entrapped, and signals from the substrate (quite small amounts), indicating a thick layer of Sb.

Tellurium Deposition

It was difficult to determine all stable species of Te in the DES, as the OCP kept changing over time without any electrochemical measurements occurring. Starting the measurements from the OCP (Fig. 3a), no electrochemical signals were observed when first cycling in the anodic direction. This indicates no stable electrochemical species with Te having a higher oxidation number than IV. A more traditional CV is observed on both substrates when investigating in the cathodic direction, with a
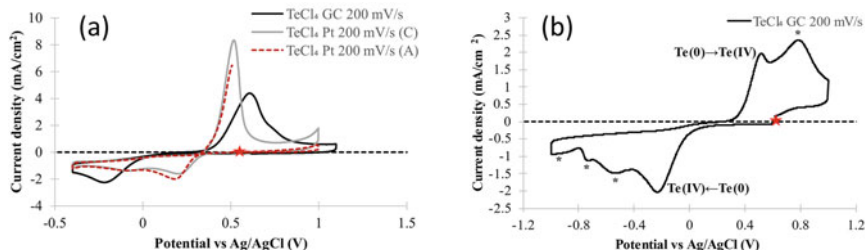
Fig. 3 CVs obtained with a scan rate of 200 mV/s from model system with Te(IV) in 1ChCl:2EG DES at 60 °C. **a** Comparison of CVs on Pt wire and GC rod substrates, cathodic vertex potential −0.4 V versus Ag/AgCl, and **b** GC rod substrate and cathodic vertex potential −1 V versus Ag/AgCl

cathodic deposition peak and anodic dissolution peak, indicating that Te(IV) and Te(0) is stable in the solution. The overpotential of GC compared to Pt is observed similarly as for the Sb-system. However, when cycling sufficiently cathodic, several peaks (marked * in Fig. 3b) were observed during the cathodic scan, indicating stable species with negative oxidation states. Te(-II) has been observed in other DES systems based on ChCl [9], and it likely occurs in the ethaline system as well. A corresponding change in the anodic scan was also observed when these peaks occurred in the cathodic scan.

With similar investigations as for the Sb(III) system, the stationary measurements using the CA measurements showed that for the Te(IV) solution, the first electrochemical reaction starts around + 400–350 mV versus Ag/AgCl, very similar to the range it occurs in the Pt CV (Fig. 3a) with the lowest nucleation overpotential. Based on these results and the measured potential of the substrates covered with metalloid Te, the deposition potential of Te is approximately + 390 mV versus Ag/AgCl.

As the deposition clearly is more anodic than the silver reference system, the deposition on Pt was attempted at + 300 mV versus Ag/AgCl. This potential is relatively close to the start of the deposition and was chosen deliberately to not have the effect of the unknown reactions occurring at more cathodic potentials (* peaks as observed in Fig. 3b). The introduced stirring at this stage resulted in a stable current density of −0.60 mA/cm^2, an increase from −0.33 mA/cm^2 as observed when no stirring occurred. Depositing on Ag at similar cathodic potentials was naturally not possible as that would have resulted in dissolution of Ag. The deposition on Ag at −50 and −150 mV versus Ag/AgCl resulted in current densities of −0.08 and −0.38 mA/cm^2 respectively; compared to the clear two-stage nucleation-growth behavior observed for the Sb-system, this was only observed briefly for the Te system when depositing on Pt (stable CD reached after 20 s). All deposits appeared to adhere well to the substrates.

Considering the standard potentials of electrochemical systems involving a metal substrate and those of the dissolved metal, it is possible to have the substrate covered with other metal(s) without applying current. Any electrochemical system with more anodic standard potential than what is used as a substrate may deposit, while the metal

used as substrate will dissolve in the solution (galvanic cell). As Te-deposition has a more anodic standard potential than Ag, a layer of Te was successfully deposited on an Ag-wire without applying current. This deposit, as well as the ones obtained on Ag with −150 mV and Pt on + 300 mV was investigated further with SEM.

On Pt electrode surface, nano-scale Te crystals could be observed from the SEM image shown in Fig. 4. The crystals are pyramid shaped with tip pointing outwards. The deposit does not fully cover the Pt surface. Pores could be observed. The deposit layer was thin as the signal from the electrode compositions was also shown up in significant amounts in the EDS analysis (Table 2).

Te deposits on Ag have different morphologies compared to those on Pt, in addition to much smaller crystal size (likely caused by the lower CD obtained on Ag). Figure 5 shows Te nanocrystals formed on Ag surface under different deposition conditions, namely after electrolysis at −150 mV versus Ag/AgCl and after electroless deposition. There is no significant difference in the morphology of the two deposits and they both form thin layer on the substrate surfaces and consist of nano-scale crystals. Pores could be observed on both deposits.

Fig. 4 SEM image of Te deposit on Pt electrode after 30-min deposition at + 300 mV versus Ag/AgCl
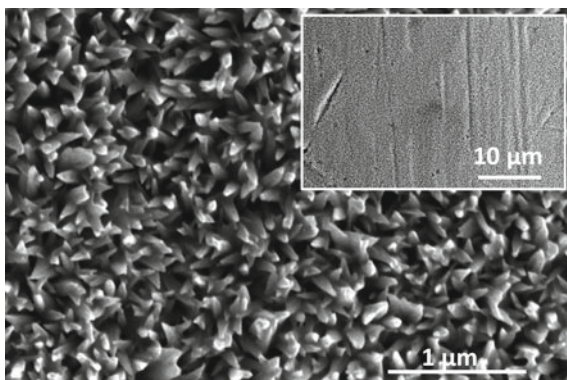
Table 2 Elemental compositions (wt %) of Te deposits on Pt and Ag surface from EDS point analysis

	C	O	Cl	Te	Pt	Ag
Te on Pt	11.85	6.17	0	35.40	46.58	N/A
	12.49	3.45	0.07	34.95	49.03	N/A
Te on Ag	11.23	1.79	0.43	24.87	N/A	61.86
	3.86	0.23	0.29	18.72	N/A	76.90
Electroless Te on Ag	4.81	0	0.27	14.73	N/A	80.13
	9.90	0	0.34	19.99	N/A	69.77
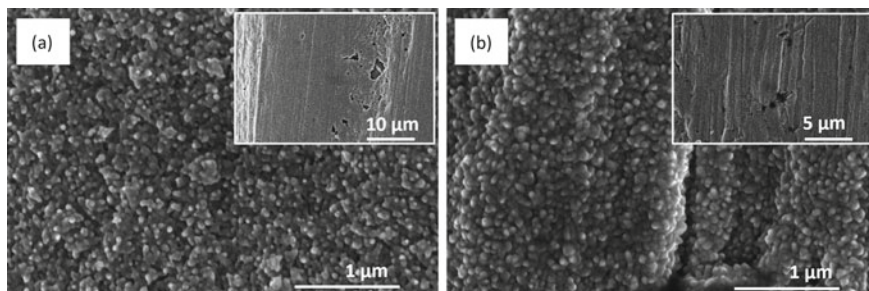
Fig. 5 SEM images of the Te deposits on Ag surface under different conditions, **a** after 15-min deposition at -150 mV versus Ag/AgCl, **b** 60 min electroless deposition

Indium Deposition

In(III) and In(0) were stable in the solution after dissolving $InCl_3$. The electrochemical signal observed on the Pt electrode related to In deposition occurred at the same time as the cathodic deposition reaction (assumed to mainly be hydrogen evolution, as observed by gas bubbles), but no/very small anodic signal could be discerned in the return scan when using a sufficiently slow scan rate. This indicated that the metal may be difficult to extract using electrorecovery methods without also decomposing the electrolyte (although it will depend on substrate chosen). Using CV on the Ag substrate, it was further observed changes in the anodic dissolution peak; in Fig. 6a, the dissolution peak is much more anodic than for GC (Fig. 6b). This might be due to forming an intermetallic phase with Ag stable at room temperature ($AgIn_2$ [10]).

Using the GC electrode, the stable species can be observed within the electrochemical window of the electrolyte (cf. Fig. 6b). The dissolution peak was first observed in the return scan when a potential between -700 and -800 mV was reached on the cathodic scan, while the full deposition and dissolution peaks can be observed going sufficiently cathodic (but still keeping within the limits of the DES electrolyte). These results, as well as the quasi-stable i-E graphs for GC and measured potentials
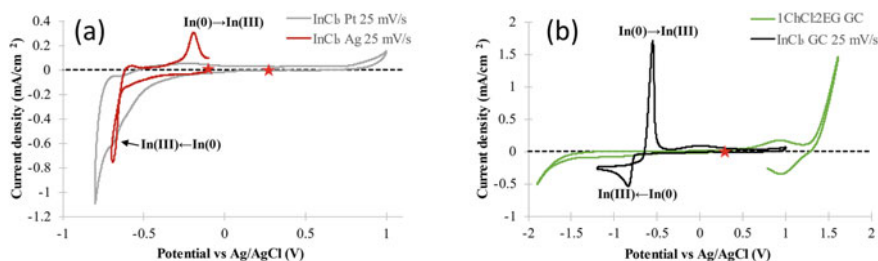
Fig. 6 Electrochemical characterization of model system in 1ChCl:2EG DES at 60 °C using 25 mV/s scan rate. **a** CV curves of a In(III) solution on Pt and Ag, and **b** comparison of CV curves of 1ChCl:2EG with and without In(III) on GC substrate
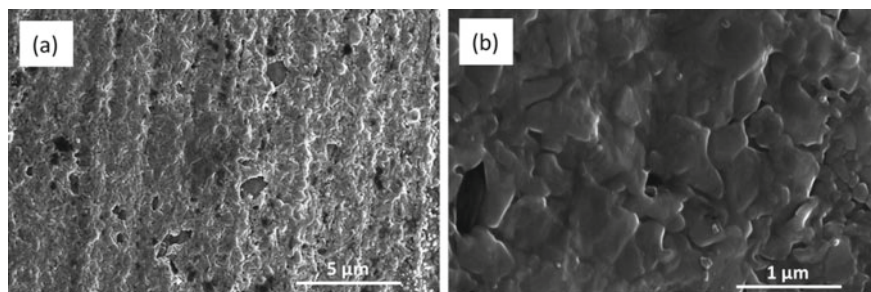
Fig. 7 SEM images of In deposit on Ag surface after 30 min deposition at −700 mV versus Ag/AgCl at **a** low and **b** high magnification, respectively

Table 3 Elemental compositions (wt%) of In deposits on Ag surface from EDS point analysis

	C	O	Cl	In	Ag
In on Ag	5.41	3.06	0.00	16.54	74.99
	5.93	3.98	0.00	17.63	72.46
	5.20	2.59	0.00	19.74	72.47

after deposition, establish the deposition potential for In around −620 mV versus Ag/AgCl.

Deposits obtained after 30 min of constant potential of −700 mV versus Ag/AgCl on the Ag substrate, resulted in a stable current density of −0.22 mA/cm². This deposit was investigated in SEM. Figure 7 shows the morphology of the In deposit on Ag surface. Individual crystals were hardly observed, and they seemed like to be fused together and formed a thin porous layer on the Ag surface. The electrode compositions were also shown up in EDS analysis (Table 3). For the deposit on Ag, although theorized to be the intermetallic phase AgIn₂, this was not possible to confirm due to the thin layer of deposit, as the measured wt % is a reflection of both Ag in the intermetallic phase, and the substrate underneath.

Possibility of Electrorecovery in Single and Multiple Systems

Summarizing the results in the above paragraphs, results reflecting the deposition potentials and other confirmed electroactive species in the DES of Sb, Te, and In, are presented in Fig. 8 compared to the Ag/AgCl system (Ag would deposit at 0 V). Having only the single systems, it appears unproblematic to recover Sb using electrorecovery; the deposition is in the middle of the electroactive window of the DES and a nice, dense layer of Sb was observed. In is likely going to be more problematic to recovery in this way due to the deposition occurring quite cathodic and possibly close to the limit of the DES. More investigations of substrates may yet give
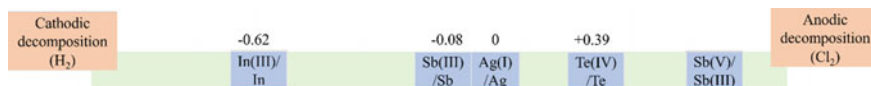
Fig. 8 Deposition potentials of the In, Sb, and Te versus Ag/AgCl (also included) measured in the 1ChCl:2EG DES system

an effective process, and the possibility to use such solutions for other electrochemical processes may exist. Finally, Te was shown to easily deposit electroless on Ag, with the same morphology obtained when using current. Te was also observed to have more stable species with a negative oxidation state, which may result in deposited Te reacting further unless protected by a controlled cathodic current.

The morphologies of the metal deposits on different electrode material were different. In addition to the electrochemical behavior, mass transfer, the properties of the substrate surface likely play an important role. The crystal shape is determined by nucleation and grain growth. Electrochemical investigation may aid in the understanding of nucleation, growth, and morphology (e.g., high-resolution chronoamperometric measurements), but was not attempted in this work as it will strongly depend on the substrate preparations, and ability to have the exact same conditions on the electrode before each measurement.

For optimization purposes, the concentration of metal ions in the electrorecovery process should be as high as possible to achieve the highest possible CD. The solubility of the metal chlorides is very important, as the metal ion most often complexes with the chloride ions in this solution and should be investigated. It is also possible to design processes using other metal salts, oxides or other mineralogical compounds, and although the complexation is often the same, the possibility of dissolving these compounds may differ from that of the pure chloride salts.

The selective electrochemical extraction of single metals from DES solutions containing several metal ions depends on concentration of the relevant metal ions in the DES solution, and the difference in their red-ox potentials. From Fig. 8, the deposition potentials for Sb, Te, and In are sufficiently far apart, and it could be possible to selectively extract the single metals from binary and ternary systems. I.e, first extract Te at applied potentials $-80 < E < 390$ mV versus Ag/AgCl, then Sb at potentials $-620 < E < -80$ mV before extracting In at $E < -620$ mV. In a traditional electrochemical flow cell in galvanostatic mode, this would be challenging, as it requires a relative constant concentration and as such the electrolyte will never be depleted of a single metal. However, a small batch process may be possible. Considering cases where more/other metals than the ones investigated in this work are present, the stable red-ox systems for the relevant metals will also need to be identified and evaluated.

In addition to the above discussions regarding both single, binary, and ternary systems, the anodic reaction needs to be considered. If the electrolyte decomposition reaction is the reaction occurring on the anode, the products may be unwanted chlorinated compounds, which greatly reduces the green credentials of the DES electrolyte.

Conclusions

In this work, it was demonstrated that Sb, Te, and In could be recovered electrochemically using the ethaline DES, with the cathodic deposition occurring in the order of Te $(+390\,\mathrm{mV})$, Sb $(-80\,\mathrm{mV})$, and In $(-620\,\mathrm{mV})$. The relatively high separation in deposition potentials indicates that it may also be possible to electrochemically extract them separately if more than one is present in the electrolyte. Deposits of metals were obtained using constant potential electrolysis. For Sb, different morphologies were observed on Pt and Ag electrodes. For Te, the morphology appeared similar on Pt and Ag substrates, but the lower CD on the Ag substrate likely is what resulted in smaller particles. Te was also demonstrated to deposit without current on Ag. In deposited on Ag likely resulted in an alloy or intermetallic phase, and the possibility of extracting this metal from DES solutions will likely depend on the type of substrate chosen. The possibility of using DESs due to its green credentials is tempting, but it will be necessary to understand the anode reactions, as well as how the low electrical conductivity and possibly low solubility of the metal ions might influence the process and its cost.

References

1. Smith EL, Abbott AP, Ryder KS (2014) Deep eutectic solvents (DESs) and their applications. Chem Rev 114(21):11060–11082
2. Haerens K, Matthijs E, Chmielarz A, Van der Bruggen B (2009) The use of ionic liquids based on choline chloride for metal deposition: a green alternative? J Environ Manage 90(11):3245–3252
3. Chen Y, Yu D, Chen W, Fu L, Mu T (2019) Water absorption by deep eutectic solvents. Phys Chem Chem Phys 21(5):2601–2610
4. Abbott AP, McKenzie KJ (2006) Application of ionic liquids to the electrodeposition of metals. Phys Chem Chem Phys 8(37):4265–4279
5. Abbott AP, Ttaib KE, Frisch G, Ryder KS, Weston D (2012) The electrodeposition of silver composites using deep eutectic solvents. Phys Chem Chem Phys 14(7):2443–2449
6. Miller MA, Wainright JS, Savinell RF (2017) Iron electrodeposition in a deep eutectic solvent for flow batteries. J Electrochem Soc 164(4):A796–A803
7. Abbott AP, Ttaib KE, Frisch G, McKenzie KJ, Ryder KS (2009) Electrodeposition of copper composites from deep eutectic solvents based on choline chloride. Phys Chem Chem Phys 11(21):4269–4277
8. Popescu A, Constantin V, Olteanu M, Demidenko O, Yanushkevich K (2011) Obtaining and structural characterization of the electrodeposited metallic copper from ionic liquids. Rev Chim Buchar Orig Ed 62:626–631

9. Sorgho A, Bougouma M, De Leener G, Vander Steen J, Doneux T (2022) Impact of speciation on the tellurium electrochemistry in choline chloride-based deep eutectic solvents. Electrochem Commun 140:107327
10. Made RI et al (2008) Study of Ag-In solder as low temperature wafer bonding intermediate layer. In: Proceedings of SPIE: reliability, packaging, testing, and characterization of MEMS/MOEMS VII, pp 156–164

YCl$_3$·6H$_2$O Green Electro-metallurgical Preparation of Y$_2$O$_3$

Shengnan Lin, Tingan Zhang, Chengzhen Fuyang, Yingqi Li, and Yifeng Liu

Abstract Rare earth oxides possess exceptional physical and chemical properties, making them extensively utilized in various fields such as new materials, catalysis, and biomedicine. However, the current production process of Y$_2$O$_3$ inevitably results in the emission of pollutants like ammonia and nitrogen oxides. This article aims to address this issue by proposing the preparation of Y$_2$O$_3$ through the YCl$_3$·6H$_2$O electro-metallurgical method. In this method, an aqueous solution of YCl$_3$·6H$_2$O is employed as the raw material, and through cation exchange membrane electrolysis technology, Y(OH)$_3$ precipitate with a layered structure is obtained at the cathode. The thermal decomposition process of yttrium hydroxide was investigated using XRD, FTIR, and DSC-TGA. Furthermore, the microstructure and particle size of the phases were analyzed using SEM and a laser particle size analyzer, demonstrating that the Y$_2$O$_3$ product inherits the precursor's structure. The electro-metallurgical process offers several advantages, including mild reaction conditions, simple equipment, and environmental friendliness.

Keywords YCl$_3$·6H$_2$O · Y$_2$O$_3$ · Electro-metallurgical · Environmental friendliness

Introduction

China possesses one of the world's most abundant rare earth resources. In 1998, China's proven rare earth reserves accounted for approximately 80% of the global total, giving it an undeniable advantage [1]. During the late 1980s, China experienced a remarkable surge in rare earth production, swiftly surpassing the United States to become the largest exporter of rare earths, representing nearly 90% of global trade [2]. However, this development model has undeniably taken a toll on China's rare earth reserves. By 2012, China's total rare earth reserves had dwindled to around 23%

S. Lin · T. Zhang (✉) · C. Fuyang · Y. Li · Y. Liu
Key Laboratory of Ecological Metallurgy, Multi-metal Intergrown Ores of Ministry of Education, School of Metallurgy, Northeastern University, Shenyang 110819, Liaoning, China
e-mail: zta2000@163.net

of the global reserves. To rectify this situation and safeguard the industry's resources, the government has implemented a series of policies aimed at ensuring the sustainable development and competitiveness of the rare earth industry [3]. Leveraging its extensive production chain and vast consumer market, the key to enhancing China's rare earth industry lies in the development of new materials and products based on rare earth elements, which will ultimately bolster its core competitiveness [4].

Y_2O_3 is widely utilized in various industries and daily life due to its exceptional physical and chemical properties. It can enhance the characteristics of ceramics and ceramic-like materials. When incorporated into calcium phosphate bone cement, Y_2O_3 can enhance its biocompatibility, increase final density, and reduce setting time [5]. Even a small quantity of Y_2O_3 can effectively stabilize zirconia ceramic materials, refine the ceramic structure, and enhance refractoriness [6]. Moreover, yttrium oxide exhibits high transparency and excellent physical and chemical stability, particularly in the infrared spectrum where it boasts a transmittance rate exceeding 90% [7]. Consequently, it is employed in the preparation of luminescent material substrates [8] and lenses for infrared devices [9]. There are numerous preparation methods for Y_2O_3, including precipitation [10], sol–gel [11], hydrothermal [12], microemulsion [13], alkoxide [14], ultrasonic [15], spray pyrolysis [16], and more.

Y_2O_3 can be directly prepared by calcining yttrium hydroxide, which serves as a precursor, at high temperatures. During this direct preparation, $Y(OH)_3$ is precipitated in colloidal form, making it difficult to separate them from the preparation system. The use of the precipitant not only pollutes the environment but also increases the cost. The preparation of yttrium hydroxide and yttrium carbonate has not utilized ion-exchange membrane electrolysis technology. In this study, cation membrane electrolysis technology was employed to synthesize $Y(OH)_3$ with good purity and morphology using yttrium chloride aqueous solution and carbon dioxide gas as raw materials under different process conditions. Subsequently, $Y(OH)_3$ powder with an inherited structure was prepared through high-temperature calcination.

The innovation and significance of this study are as follows: The application of ionic membrane electrolysis technology from the chloralkali industry to the preparation process of yttrium hydroxide and yttrium carbonate allows for the realization of high-purity yttrium hydroxide without the need for additional additives. This achievement provides a fresh approach to the preparation of rare earth oxide precursors.

Experiment

Synthesis

In the experiment, the stainless steel sheet mentioned earlier was utilized as the cathode, while the ruthenium-plated titanium sheet served as the anode. The electrolyte volume was 250 mL, and the pole piece had an effective area of 4×4 cm^2.

Table 1 Experimental single factor parameters

Factor	Level
Initial concentration	0.1, 0.15, 0.20, 0.25 mol/L
Current density	15.625, 31.25, 46.875, 62.5 mA/cm^2
Temperature	35, 45, 55, 65 °C

The polar distance was set at 3.5 cm, and the stirring rate was maintained at 150 r/min. To ensure the solution's conductivity, NaCl was added to both the anode and cathode, maintaining the same cation concentration (Table 1).

Material Characterization

The electrolytic and calcined samples' phase structures were analyzed by X'Pert Powder X-ray diffractometer (XRD). The thermal decomposition process of electrolytic samples was analyzed by Swiss Mettler TG-DSC thermogravimetric differential analyzer. The surface morphologies of the electrolytic and calcined samples were observed by Zeiss-$\sum$IGMA-HD high-resolution field emission scanning electron microscopy (FESEM). The molecular functional groups were analyzed by Nicolet IS 50 Fourier infrared analyzer.

Results and Discussion

Effect of Initial Concentration of Anodic Electrolyte

The XRD results of the products with different anode concentrations are presented in Fig. 1 It can be observed that the diffraction peak intensity of the product with an anode concentration of 0.1 mol/L is higher. Moreover, when the concentration exceeds its optimal level, the product only exhibits a peak at the main position, resembling steamed bread. The grain size at the main peak position is calculated to be 4–5 nm. This phenomenon can be attributed to the higher concentration of Y^{3+} at the anode, which facilitates its passage through the cation membrane and results in a shorter binding time with OH$^-$. The main peak of the diffraction pattern of the precipitated product matches the standard card PDF #30-1445, indicating a crystal structure corresponding to Y$_2$(OH)$_{4.86}$Cl$_{1.14}$·1.07H$_2$O.

The SEM images in Fig. 2 depict the SEM of the products at various anode concentrations. From Fig. 2a, b, it is evident that the sediments consist of flakes with a diameter ranging from 100 to 200 nm. Notably, in Fig. 2b, d, some flakes exhibit a relatively larger diameter and thickness, appearing thinner and larger in diameter
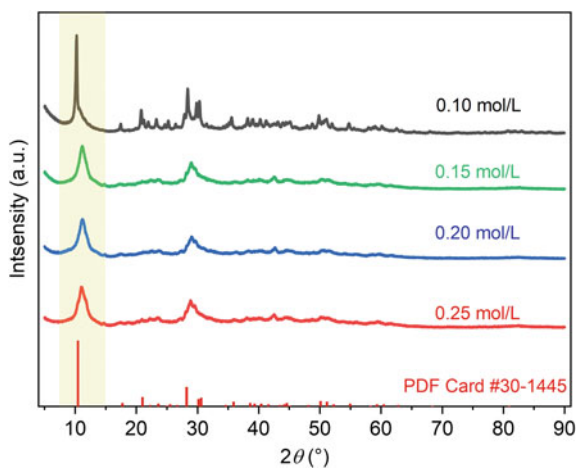
Fig. 1 XRD curves at different anode concentrations

compared to the products at other concentrations. Overall, the alteration in anode concentration does not significantly impact the microstructure of the sediment.
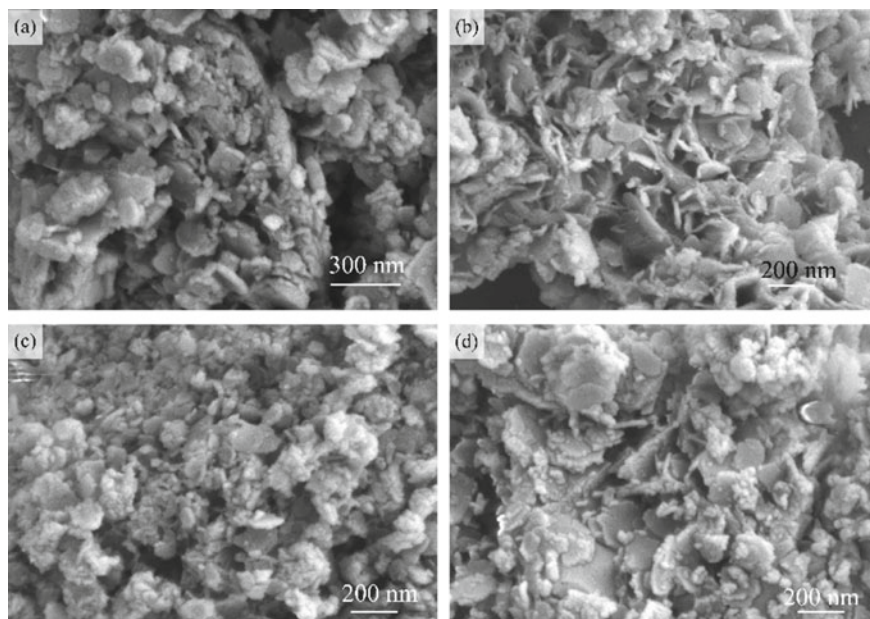
Fig. 2 SEM images at different anode concentrations: **a** 0.10 mol/L, **b** 0.15 mol/L, **c** 0.20 mol/L, **d** 0.25 mol/L

Fig. 3 Particle size distribution of products at different anode concentrations
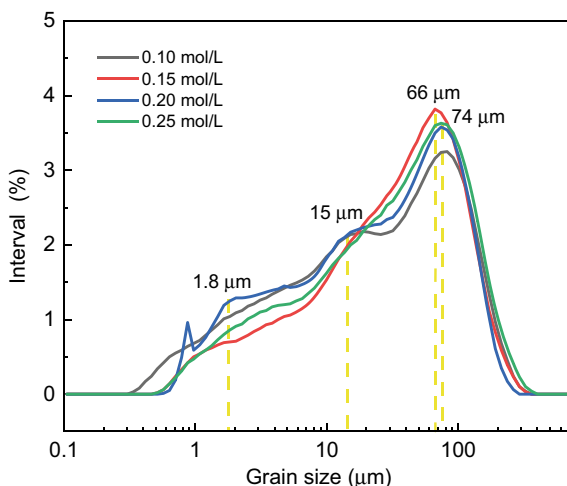
The particle size distribution of the product at different anode concentrations is illustrated in Fig. 3. The peak position of the particle size distribution interval remains relatively constant, indicating a similarity in particle size across different concentrations. Overall, the particle size ranges from 0.5 to 100 µm, with peaks observed around 1.8, 15, and 66–74 µm, which represent the major portion of the particle size distribution. For anode concentrations ranging from 0.10 to 0.25 mol/L, the D$_{50}$ values of the product particle size were 25.58, 37.56, 27.15, and 34.83 µm, respectively. This aligns with the observation that the particle diameter of certain products is larger at concentrations of 0.15 and 0.25 mol/L compared to other concentrations, suggesting that the anode concentration has a limited impact on the particle size of the product.

Effect of Current Density

The XRD patterns at various current densities are presented in Fig. 4. As the current density increases, the peak height of the XRD image decreases while the peak width increases. This observation suggests that the number of grains in the deposit increases with higher current density. The current density is directly related to the electron exchange rate at the interface between the electrode and the liquid phase. A higher current density leads to a faster electrochemical reaction rate, resulting in accelerated generation and consumption of related ions. At a current density of 31.25 mA/cm^2, the peak intensity is high, the peak intervals are distinct, the peak shape is complete, and the signal-to-noise ratio is high.

The SEM images depicting different current densities are presented in Fig. 5. In Fig. 5, the crystals exhibit a strong bond. The images in Fig. 5b–d display stacked
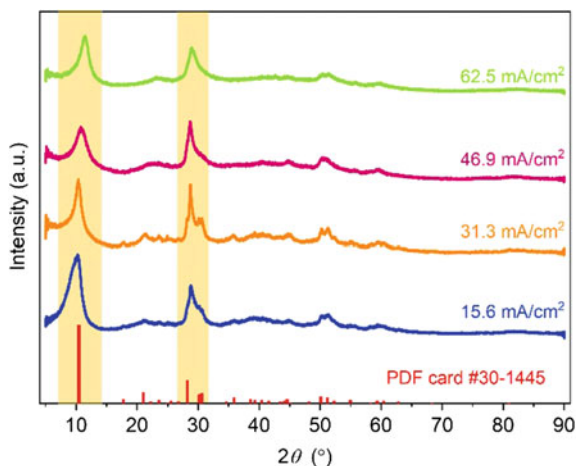
Fig. 4 XRD curves at different current densities

flakes, with the size of the flakes decreasing as the current increases. The results indicate that an increase in current density can lead to a reduction in crystal size and sheet thickness. In Fig. 5b, at a current density of 31.3 mA/cm^2, the sediment consists of intact flakes, and the overall structure appears loose, suggesting good dispersibility. This balance between development and nucleation processes is favorable.

The particle size distribution of the product under different current densities is illustrated in Fig. 6. As the current density increases, the particle size distribution becomes broader. The maximum particle size of the product decreases from 90 to 19 μm, resulting in finer particles. The D_{50} values of the product are 48.27, 21.00, 21.10, 23.94 μm. The particle size decreases with increasing current density and reaches its optimum when the current density exceeds 31.25 mA/cm^2. This suggests that increasing the current density of the electrode leads to an increase in nucleation sites and accelerates the production rate of hydroxide, thereby promoting faster particle growth. In terms of particle size, a wider range is observed.

Effect of Temperature

As depicted in Fig. 7, the products were prepared at temperatures of 35, 45, 55, and 65 °C, respectively, followed by XRD detection. The characteristic peaks of the products were found to be consistent with the standard card PDF #30-1445. Notably, the XRD image of the product exhibited a noticeable increase in peak intensity with temperature, accompanied by a decrease in peak width. This observation suggests that as the temperature rises, the grain development of the cathode sediment becomes more refined and the crystal size becomes more uniform. The
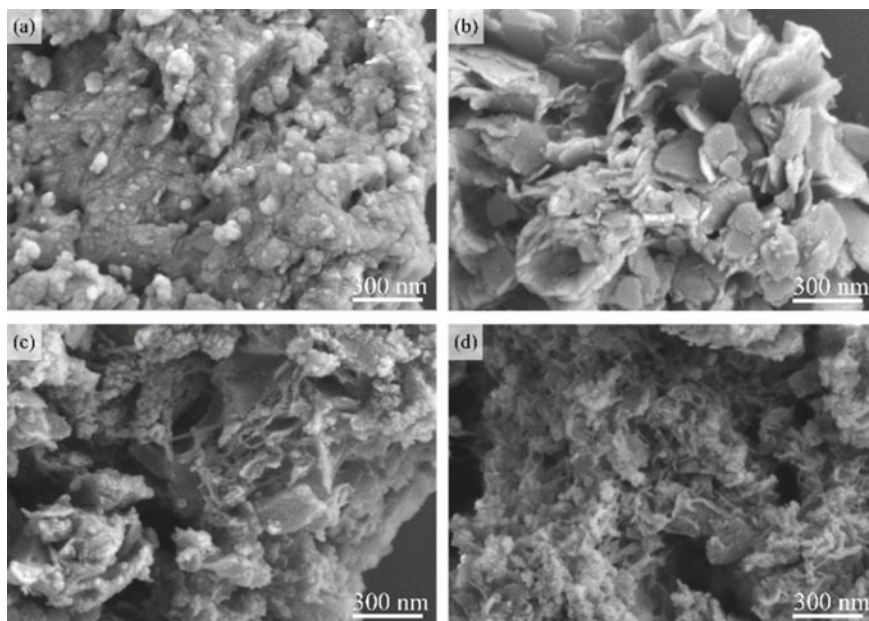
Fig. 5 SEM plot at different current densities: **a** 15.6 mA/cm^2, **b** 31.3 mA/cm^2, **c** 46.9 mA/cm^2, **d** 62.5 mA/cm^2

Fig. 6 Particle size distribution of products at different current densities
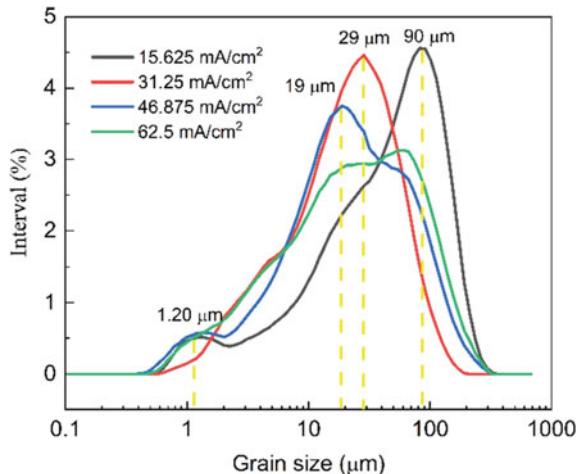
improved crystal development conditions at higher temperatures can be attributed to the enhanced ion activity and ion exchange rate.

The (a), (b), (c), and (d) in Fig. 8 correspond to the SEM images of the products at 35, 45, 55 and 65 °C, respectively. The boundary between the flakes in Fig. 8a is not clear, indicating poor dispersion of the sediment prepared at 35 °C and small flake
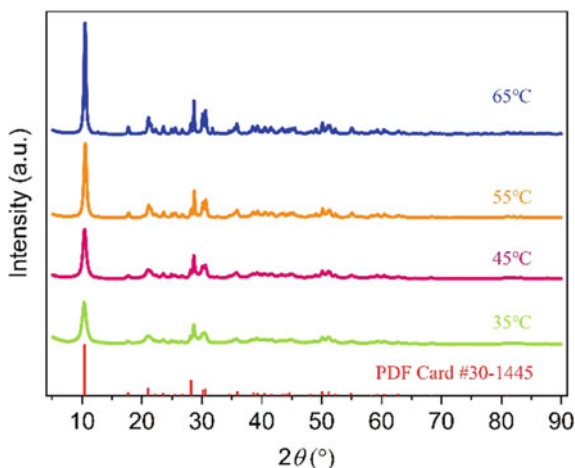
Fig. 7 XRD curve at different temperatures

thickness. In Fig. 8b, the sheet structure becomes clear, the sheet is well dispersed, and an independent sheet is visible. In Fig. 8c, the dispersion of the sheet is further improved. In Fig. 8d, the sheet has the highest degree of looseness, and the edges are rounded, which is noticeably different from the conditions under low temperatures. These results demonstrate that higher temperature promotes the generation of highly dispersed sediments.

The particle size distribution of the product is illustrated in Fig. 9. The D_{50} values of the product within the temperature range of 35–65 °C are as follows: 30.74, 28.94, 14.47, and 9.257 μm. As the electrolysis temperature increases, the overall particle size of the product decreases. This is because, with the temperature rise, there is a higher likelihood of nucleation for Y^{3+} and OH^- [17]. Consequently, the number of nucleation centers increases, leading to a reduction in particle size. The particle size curve also reveals that as the temperature increases, the highest particle size range of the product shifts to 4.73 μm. Simultaneously, the original maximum range gradually transitions from 53.8 to 12.3 μm, with an intermediate value of 28.6 μm. Furthermore, the range of 4.73 μm expands, indicating that the particle size reduction caused by temperature change is a gradual process. Based on these findings, it can be predicted that increasing the temperature will result in a final D_{50} value of approximately 4.7 μm for the product. Overall, the results demonstrate that elevating the temperature is advantageous for producing finer particles and reducing the maximum size of larger particles.
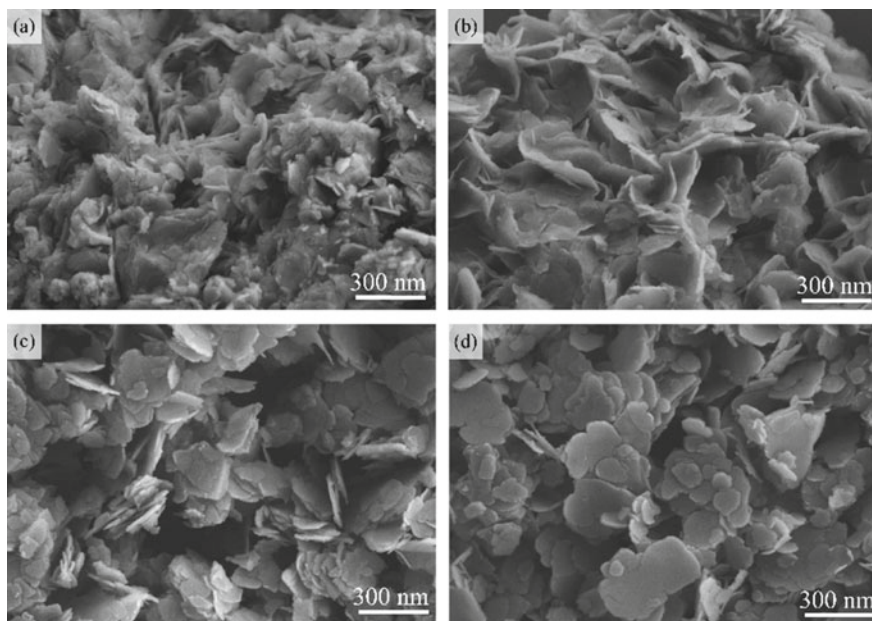
Fig. 8 SEM plot at different temperatures: **a** 35 °C, **b** 45 °C, **c** 55 °C, **d** 65 °C
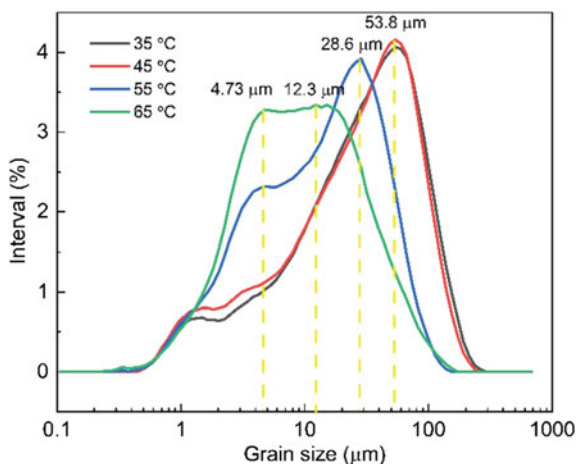
Fig. 9 Particle size distribution of products at different temperatures

Yttrium Hydroxide Calcination

The product was prepared under optimal experimental conditions: electrode distance of 5 cm, current density of 31.3 mA/cm^2, cathode concentration of 0.025 mol/L,

anode concentration of 0.15 mol/L, electrolysis time of 150 min, stirring rate of 150 r/min, temperature of 65 °C, and NH_4Cl supplement ion concentration balance. The product was analyzed, and a suitable temperature for calcination treatment was chosen to obtain the oxide.

Yttrium oxide products were obtained by calcining cathode deposits at temperatures of 320 and 700 °C for 2 h, with a heating rate of 10 °C/min. The resulting products were then tested using XRD. Figure 10 shows that the peak shape of the calcined sample is identical to that of the cubic Y_2O_3 (JCPDS no. 25-1200). After calcination, the XRD main peak intensity of the sample is remarkably high, indicating a high degree of crystallization and fewer defects in the crystal. The signal-to-noise ratio is also large. By applying the Scherrer equation, the average crystallite size of the calcined product was calculated to be 50 nm using the peak width (222) at $2\theta = 29.1°$. No impurity peaks were observed in the entire image, and the XRD test did not detect any other impurities.

The SEM images of the calcined products are presented in Fig. 11. Figure 11a–c depict the morphologies of the products calcined at 900, 700, and 320 °C, respectively. Figure 11d displays the uncalcined SEM image of the same sample. In Fig. 11a, b, the lamellar dehydration transforms into a granular form during the calcination process, resulting in smaller particle sizes.

The DSC-TGA spectra of the calcination process are presented in Fig. 12, displaying three endothermic peaks at 122, 318, and 629 °C. The endothermic peak at 122 °C is likely associated with the elimination of crystal water in the $Y_2(OH)_{4.86}Cl_{1.14} \cdot 1.07H_2O$ molecule. The intensity of the endothermic peak at 220 °C is relatively low, accompanied by a slight increase in mass loss. This could be attributed to the endothermic decomposition of other bound water forms or sediment molecules' surface binding. It may also explain why the weight loss ratio during the
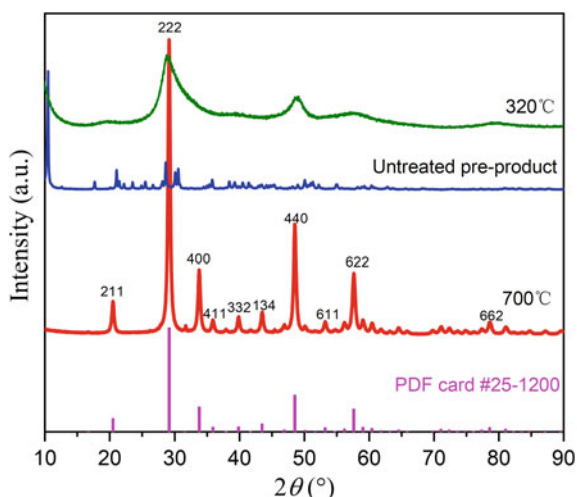
Fig. 10 XRD diagram of cathode product after calcination
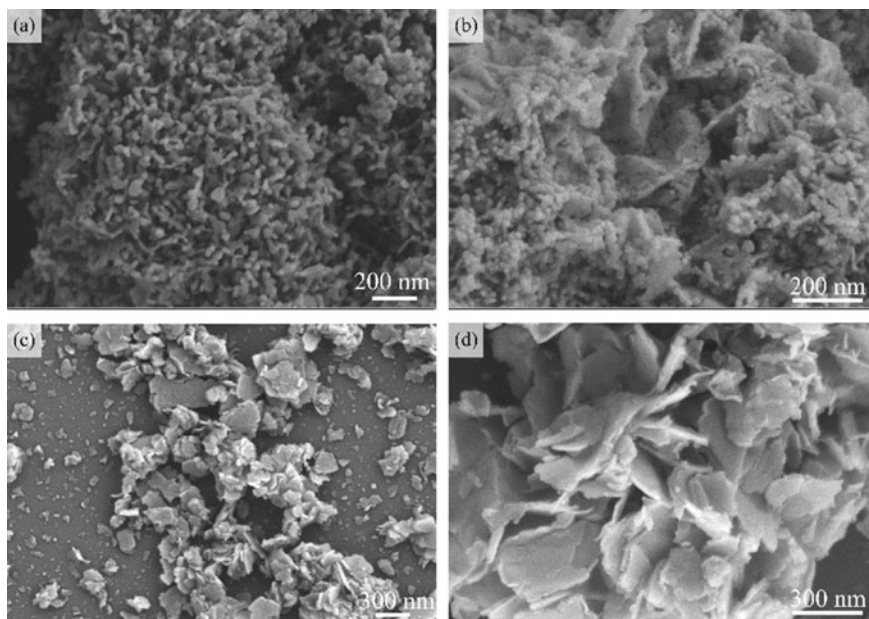
Fig. 11 SEM diagram of products after calcination and before calcination

water loss stage exceeds the theoretical value. The mass of the endothermic peak at 318 °C decreases by 14%, indicating the primary decomposition process of the cathode sediment molecules. At 318 °C, the Y$_2$(OH)$_{4.86}$Cl$_{1.14} \cdot$1.07H$_2$O molecule undergoes a transition from hydroxide to oxide, converting into Y$_2$O$_3$Cl$_x$ molecules within this temperature range. The theoretical mass change of 13.2% aligns with the actual value. Furthermore, the endothermic curve exhibits a strong and broad peak at 629 °C, accompanied by a 6% decrease in mass. This phenomenon may be attributed to the continuous removal of chlorine in the molecule.
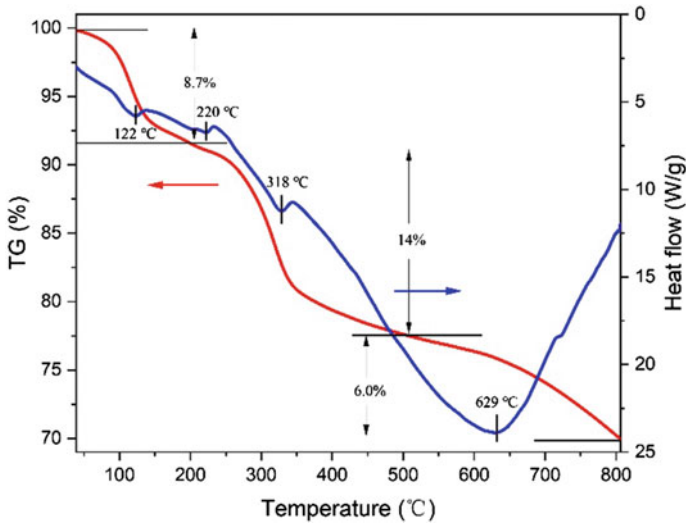
Fig. 12 Hydroxide DSC-TG analysis diagram

Conclusion

In this paper, a new idea is proposed for the preparation of yttrium oxide through electrometallurgy. Yttrium hydroxide is obtained by electrolyzing yttrium chloride in a cation exchange membrane cell, and then the resulting yttrium hydroxide is calcined to obtain yttrium oxide. The current efficiency, phase structure, and microstructure of the products were analyzed using an X-ray diffractometer, scanning electron microscope, and laser particle size analyzer. The overall distribution of cathode sediments does not vary significantly with changes in anode concentration, and the impact of anode concentration on cathode products is limited. The number of grains in the deposit increases as the current density increases. Increasing the temperature during the electrolysis process enhances crystal development, reduces crystal defects, and produces deposits with a high degree of dispersion. After calcination at 70 °C, the diameter of yttrium hydroxide is approximately 20–50 nm. The structure of the deposit transforms into fine particles, and the influence of higher temperature on the product is not significant.

References

1. Gavin B (2015) Sustainable development of China's rare earth industry within and without the WTO. J World Trade 49(3):495–515
2. Morrison WM, Tang R (2012) China's rare earth industry and export regime: economic and trade implications for the United States
3. Mancheri NA (2015) World trade in rare earths, Chinese export restrictions, and implications. Resour Policy 46:262–271
4. Kalantzakos S (2017) China and the geopolitics of rare earths. Oxford University Press
5. Adzila S, Murad M, Sopyan I (2012) Doping metal into calcium phosphate phase for better performance of bone implant materials. Recent Patents Mater Sci 5(1):18–47
6. Akinribide OJ, Mekgwe GN, Akinwamide SO et al (2022) A review on optical properties and application of transparent ceramics. J Mater Res Technol 21:712–738
7. Jiang DT, Mukherjee AK (2010) Spark plasma sintering of an infrared-transparent Y$_2$O$_3$–MgO nanocomposite. J Am Ceram Soc 93(3):769–773
8. Kim SS, Moon JH, Lee BT et al (2004) Microstructures of pulsed laser deposited Eu doped Y$_2$O$_3$ luminescent films on Si (0 0 1) substrates. Appl Surf Sci 221(1–4):231–236
9. Faiza SH, Nowsherwan GA, Khan M et al (2022) Spectral splitting optimization for highly efficient hybrid photovoltaic devices by using Na$_3$AlF$_6$, Y$_2$O$_3$ and TiO$_2$ beam splitter. Adv Sci Technol 119:3–11
10. Hou X, Zhou S, Li Y et al (2010) Luminescent properties of nano-sized Y$_2$O$_3$: Eu fabricated by co-precipitation method. J Alloy Compd 494(1–2):382–385
11. Dupont A, Parent C, Le Garrec B et al (2003) Size and morphology control of Y$_2$O$_3$ nanopowders via a sol–gel route. J Solid State Chem 171(1–2):152–160
12. Dell'Agli G, Mascolo G (2000) Hydrothermal synthesis of ZrO$_2$–Y$_2$O$_3$ solid solutions at low temperature. J Eur Ceram Soc 20(2):139–145
13. Pang Q, Shi J, Liu Y et al (2003) A novel approach for preparation of Y$_2$O$_3$: Eu^{3+} nanoparticles by microemulsion–microwave heating. Mater Sci Eng: B 103(1):57–61
14. Winnubst AJA, Zevert WFMG, Theunissen G et al (1989) Microstructure characteristics of ultra-fine ZrO2·Y2O3 ceramic powders. Mater Sci Eng: A 109:215–219
15. Bi J, Sun L, Wei Q et al (2020) Rapid ultrasonic-microwave assisted synthesis of Eu^{3+} doped Y$_2$O$_3$ nanophosphors with enhanced luminescence properties. J Mater Res Technol 9(5):9523–9530
16. Kang YC, Park SB, Lenggoro IW et al (1999) Preparation of nonaggregated Y$_2$O$_3$: Eu phosphor particles by spray pyrolysis method. J Mater Res 14(6):2611–2615
17. Lin S, Pan X, Meng D et al (2021) Electric conversion treatment of cobalt-containing wastewater. Water Sci Technol 83(8):1973–1986

Recovery of Antimony from Refinery Slag of Unified Mining Company (EMUSA)

Christian Álvaro Mendoza Ramos

Abstract The process of obtaining antimony trioxide from Unified Mining Company S.A. (EMUSA) has two production lines. The refining slag from the second production line was stored since the plant started operations, registering high antimony contents which is the reason for this research project. To recover antimony from the slag, it was necessary to carry out a reducing fusion with slag using pyrometallurgical methods with ternary diagrams; $FeO:Na_2O:SiO_2$ and $FeO:SiO_2:CaO$ the Sb recovery was done in two parts; the first part consisted of melting in a flame furnace and the second a melting in the IIMETMAT thermobalance. The flow of oxygen necessary for antimony recovery was 0.1 l/min higher flows oxidize antimony and lower recovery. The experiments showed that the reaction that controls the process is $PbSb_2O_6 + 6C = 2Sb + Pb + 6CO$. For the melting in the flame furnace, the best slag ratio used was 35:15:50 with the system and with the system, the best ratio was 35:15:50, with Sb recoveries of 98% in both cases.

Keywords Refining slag · Melting in the thermobalance · Antimony recovery

Introduction

Bolivia is one of the largest producers of antimony worldwide, in 2022, it ranked fifth with 2500 t according to es.statisca.com [1] and www.mineria.gob.bo [2]. Bolivian production comes mainly from the mining centers of Caracota province Quijarro, Chilcobija province Sud Chichas in the Department of Potosí. Unified Mining Company S.A. (EMUSA) recovers antimony from an antimonite concentrate with antimony trioxide volatilization systems, the flowchart in Fig. 1 shows the antimony production lines of EMUSA.

In line 1 of antimony oxide production shown in Fig. 1, the operating temperature is 1000 °C for the removal of sulfur and obtaining the volatile "crude oxide" from

C. Á. Mendoza Ramos (✉)

Instituto de Investigaciones en Metalurgia y Materiales IIMETMAT, Universidad Mayor de San Andrés, La Paz, Bolivia

e-mail: chrismr23@hotmail.com
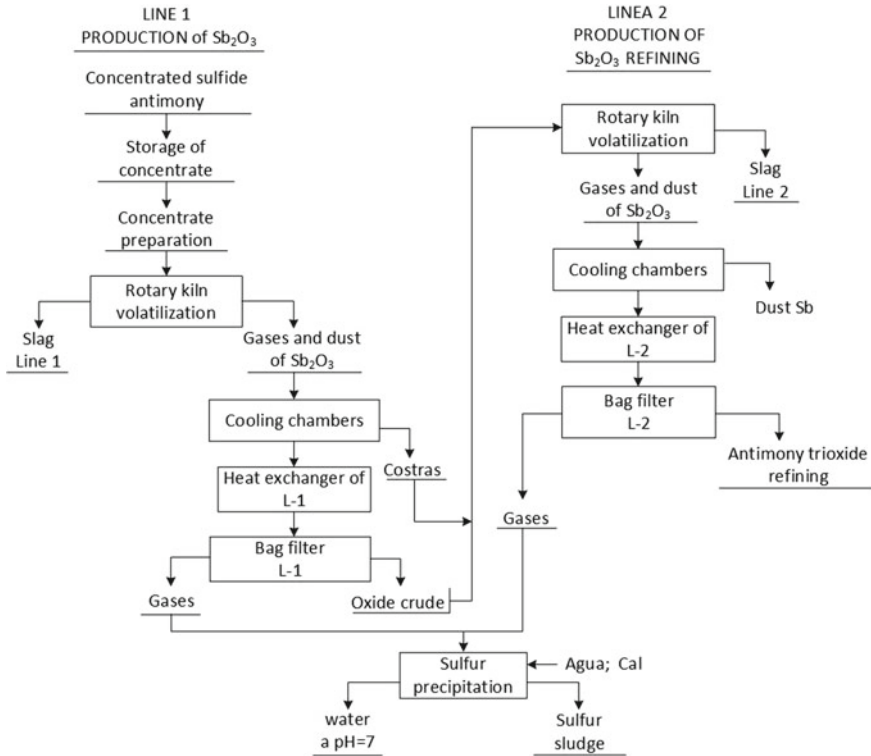
Fig. 1 Flowchart of production from Line 1 to Line 2 and slag with high contents of Sb and Pb

a concentrate with an average grade of 55% Sb that avoids a higher frequency of slag bleeding. Line 2, is called the refining line, is intended for the production of high-quality antimony trioxide. In this line, approximately 3 t/day of "crude oxide" with an average grade of 80% Sb (Ref. EMUSA production data) is fed from the baghouse filter of line 1 production, the slag discharge is carried out every 2 months.

The excess oxygen insufflated in the metallurgical operation leads to increased production of non-volatile oxides. The non-volatile oxides that remain lodged in the slag of line 2; for this reason, the amount of antimony in the final slag is 20–30% antimony according to EMUSA production data. Likewise, a high lead content of 15–25% is recorded in the refining line slag, this component complicates Sb recovery as Sb_2O_3. For this reason, studying and suggesting an alternative for the treatment of the line 2 refining slag to recover antimony is the objective of this research work.

Bibliographic Review

The major compound in the line 2 production slag is bindheimite, which is an alteration of antimony sulfides and oxides, and its crystal structure is of the pyrochlore type, (antimony associated with large cations) the stable structure is $[A^{3+}]_2[B^{4+}]_2[O]_7$. [3]. In the case of the sample of the refining slag of line 2, the atom [A] is Sb^{3+} and [B] is Pb^{4+}. According to Mason and Vitaliano [4] its crystal structure would be found with defects in its networks (empty spaces) that lead to formulating bindheimite in more than one way with great variability in chemical composition and physical properties, assigning a chemical formula to bindheimite is not an easy task due to the above conditions and according to the same researchers, bindheimite can be formulated as $Pb_x Sb_{2-z}(O, OH, H_2O)_{6\,or\,7}$ where "x" varies up to 2 and "z" cannot be greater than 1 and the species (O, OH, H₂O) correspond to the results of X-ray diffraction analyses.

Figure 2 shows the free energies of Sb and Pb oxides that come from volatilization, as well as their interaction with carbon, monoxide, and carbon dioxide with their linearized Gibbs free energies, which were determined from Barin et al. [5] thermodynamic data, the diagram shows the stability of Pb and Sb oxides.

In Fig. 2, the reduction reactions of PbO, Sb_2O_4, and Sb_2O_5 with $CO_{(g)}$ and $CO_{2(g)}$ are shown, where it is observed that the reduction of these oxides to Sb and Pb with the formation of de $CO_{(g)}$, at 700°C their Gibbs free energies are more negative compared to when metallic are formed with $CO_{2(g)}$. The composition must also be controlled, for this reason, the composition versus diagram is analyzed in Fig. 3.
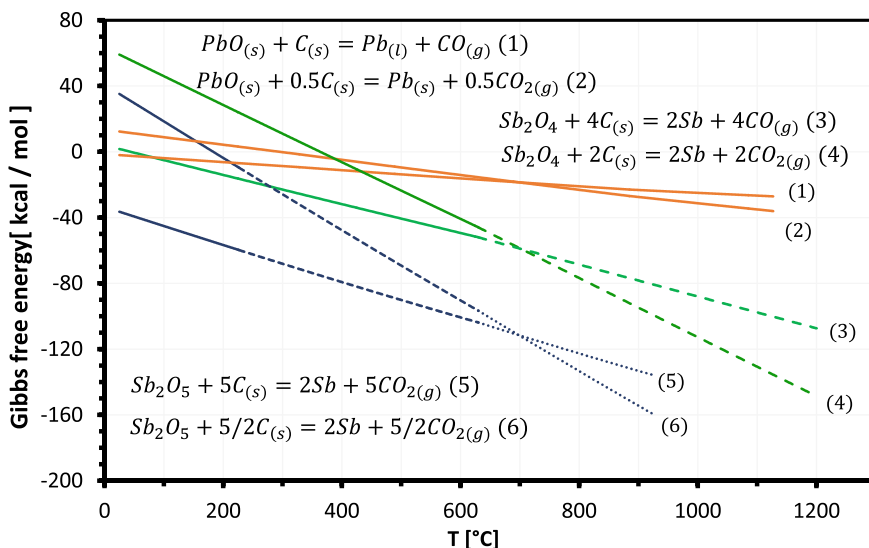
Fig. 2 Ellingham diagram for reduction of antimony and lead oxides [5]

Fig. 3 Diagram of the Sb–S–O system as a function of oxygen at 900 [6]
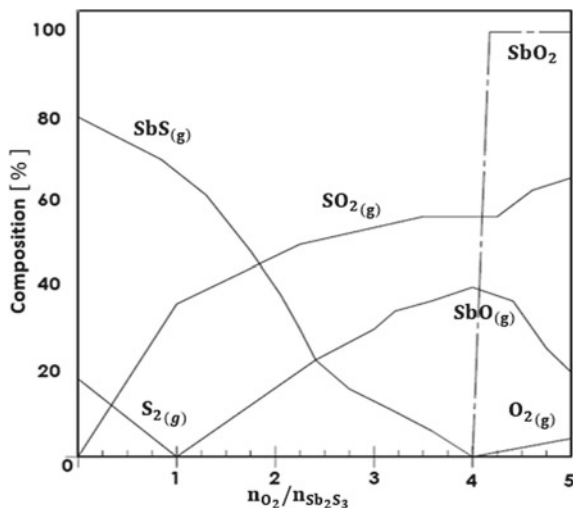
Figure 3 shows the diagram composition % versus $n_{O_2}/n_{Sb_2S_3}$ [6] which says, the less oxygen there is in the medium, the more will be formed $SbS_{(g)}$ volatile from $Sb_2S_{3(s)}$. This effect improves when the ratio of $n_{O_2}/n_{Sb_2S_3}$ is increased in a range of 3–4, more oxygen favors the formation of and will form SbO_2 a stable non-volatile solid phase that will remain in the antimony volatilization furnace.

With the corresponding chemical analyses, XRD analysis results, and thermodynamic aspects, the most suitable compound for the refining slag sample is $PbSb_2O_6$ o ($PbO \cdot Sb_2O_5$).

Experimental Work

Refining Slag Sample

The preparation consisted of crushing, grinding to a − 65 mesh grain size of the Tyler series, homogenized, and quartered to obtain a representative sample. The chemical analysis report of the EMUSA line 2 refining slag sample is shown in Table 1.

Table 1 Chemical composition, EMUSA refining slag (Lab. NOSTERTEC)

%Sb	%Pb	%Fe	%SiO2	%S	%Al	%Zn	%As	%Cu	%K	%Sn	%Mg	%Other
21.59	24.68	3.05	6.01	11.23	1.39	2.7	1.32	0.11	0.43	0.07	1.69	25.73

Table 2 Chemical composition of fluxes

Flux	%Na$_2$O	%CaO	%SiO$_2$	%Fe	%S	%MgO
Caustic soda	30.51	0.518	6.84	0.08	11.03	
Sand		0.07	83.48	0.22	0.04	
Limestone		51.38	0.48			0.83

Fluxes and Reducer

The fluxes and reducer used are shown in Table 2, and their respective compositions were determined in the Nostertec and Conde Morales laboratories.

The vegetable coal has the composition $C_f = 85.94\%$, $V = 10.07\%$, $H = 3.07\%$, $C_z = 0.927\%$ and the air flow insufflated in the tests was 0.1 l/min.

Experimental Procedure

The project was developed in two parts; the first was worked on in a flame furnace where a reducing fusion was made with ternary diagrams FeO:Na$_2$O:SiO$_2$ and CaO; SiO$_2$:FeO. In the second part, in a thermobalance, the variables were established such as; reducer effect, flux effect, and temperature effect.

Results and Discussion

Fusion Tests in a Flame Furnace

Figure 4 shows one of the slag systems used. This figure shows the ternary FeO:Na$_2$O:SiO$_2$ diagram where a fusible slag can be obtained since 800 °C. The system CaO; SiO$_2$:FeO was also analyzed. Based on the selected points, the fusion tests were carried out in a flame furnace with both slag systems considering the reduction reaction (1) of bindheimite with the formation of CO$_{(g)}$.

$$PbSb_2O_6 + 6C = 2Sb + Pb + 6CO \tag{1}$$

The results with the system FeO:Na$_2$O:SiO$_2$ are indicated in Table 3 with the addition of sand, Caustic soda and vegetable coal, and the results with the system are in Table 4 with sand, limestone, and vegetable coal as additives.

In Tables 3 and 4, in addition to the slag ratios and their quantities, the metallic and slag phases are indicated, in these tests, the registered performance was from 96.22 to 98.32% for the system and for the system, the achieved performances vary from

Fig. 4 Ternary diagram for
melting in a flame furnace
[7, p. 148]

Table 3 Results of the melting tests with the system from 800 to 1000 °C

Test	FeO	Na2O	SiO$_2$	Sand	Caustic soda	Coal	Metallic	Slag	Recovery
	%	%	%	(g)	(g)	(g)	(g)	(g)	%
CPT-01	30	15	55	0	5.60	11.45	56.44	20.45	98.03
CPT-02R	30	15	55	0	5.70	11.47	56.49	21.06	96.22
CPT-03	30	15	55	2.96	5.50	11.45	55.89	31.37	97.31
CPT-04	35	15	50	0.80	5.23	10.81	58.94	20.06	98.32
CPT-05	30	25	45	1.75	8.15	10.80	59.35	24.71	97.08
CPT-06	28	22	50	0.59	10.08	10.80	55.49	20.25	97.81
CPT-07	28	22	50	1.70	9.51	10.80	59.80	30.31	97.54

Test FeO

Table 4 Results of the melting tests with the system from 1100 to 1250 °C

Test	FeO	SiO2	CaO	Sand	Limestone	Coal	Metallic	Slag	Recovery
	%	%	%	(g)	(g)	(g)	(g)	(g)	%
CP-01	47	38	15	0	2.86	11.50	60.60	46.86	98.16
CP-02	37	38	25	0	6.02	12.50	61.76	20.41	98.24
CP-03R	33	37	30	0	8.11	12.56	62.78	19.86	97.89
CP-04	32	37	31	0.60	8.68	10.80	58.41	8.73	98.17
CP-05R	40	45	15	0	3.18	10.78	58.01	17.95	98.33
CP-06	35	38	27	0	6.50	10.80	63.50	19.69	98.42
CP-07R	30	48	22	1.16	6.18	10.80	58.75	18.95	96.45

96.45 to 98.42%, these performances are similar; however, the difference consists of the temperature from 800 to 1000 °C in 30 min of melting for the first system and from 1100 to 1250 °C in 50 min of melting for the second system.

Tests on the Thermobalance

Determination of the reaction. These tests have the purpose of determining the type of reaction that governs the process, being necessary to propose the following reactions (2) and (3).

$$PbSb_2O_{6(s)} + 6C_{(s)} = 2Sb_{(M)} + Pb_{(M)} + 6CO_{(g)} \tag{2}$$

$$PbSb_2O_{6(s)} + 3C_{(s)} = 2Sb_{(M)} + Pb_{(M)} + 3CO_{2(g)} \tag{3}$$
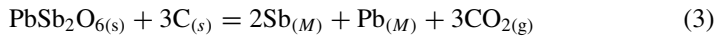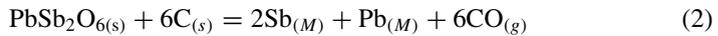
It is necessary to determine the following relationships.

$$R = (W_o - W_t)/W_{teo} = \Delta W/W_{teo} \tag{4}$$

Equation (4) is not sufficient due to the high content of volatiles such as sulfur or other volatile materials. For this reason, Eqs. (5) and (6) are proposed.

$$R = (\Delta W - W_{VT})/W_{teo} \tag{5}$$

$$W_{VT} = W_S + W_{VC} \tag{6}$$

where:

R   experimental weight loss fraction and theoretical weight
ΔW Difference of the initial weight and the final weight recorded on the thermobalance
W_{VT} weight of total volatiles
W_S weight of sulfur in the sample
W_{VC} weight of the charcoal volatiles

From Table 5, the $W_{C_{teo}} = 4.15\%$, $W_S = 9.32\%$ and $W_{VC} = 0.49\%$ and with the masses recorded in the thermobalance in real time ΔW every 5 s the conversion factor R calculates the recovery of the metal, a diagram for the P-50 test is shown in Fig. 5 where $W_{Esc\ Ref} = 2.8906$ g, $W_{Met} = 5.096$ g and the limits of the reactions (2) and (3) are $W_{teo} = 0.476$ g $CO_{(g)}$ and $W_{teo} = 0.374$ g $CO_{2(g)}$.

Figure 5, indicates the limits determined by the W_{teo} where 0.4757 g corresponds to the formation of CO and 0.3737 g corresponds to the formation of CO_2, the experimental values of the test approach the limit of 0.4757 g of CO determined according

Table 5 Distribution of reactants and products in the thermobalance

Reactants	%	Products	%
Sample slag refining	57.02	Metal (Sb, Pb)	26.39
Coal	4.83	Slag	58.17
Caustic soda	21.97	Cz	0.004
Exc Caustic soda 20%	4.4	C_{teo}	4.15
Sand	9.8	Volátil C	0.49
Exc Sand 20%	1.96	S	9.32
		H_2O	1.44
Total	100		100
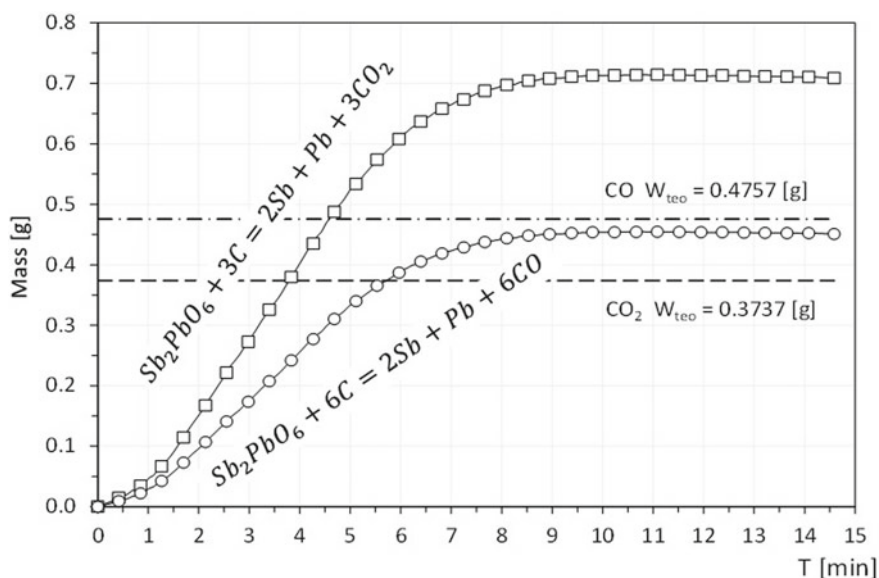
Fig. 5 Experimental weight loss fraction compared to the theoretical weights according to reactions (2) and (3)

to the reaction (2) and the relationship between the experimental weight and the theoretical weight is of 95.56% and according to the reaction (3) with formation CO_2 goes far away from the established limit of 0.3737 g. For this reason, the reaction that controls the reduction process to metallic Sb-Pb is the reaction (2) with CO formation, these results agree with the thermodynamic information analyzed in Fig. 2.

Effect of the Amount of Reducer

For the effect of the reducer on the refining slag sample, the $FeO:Na_2O:SiO_2$ system was used with the slag ratio 30:15:55 based on reaction (2) where $PbSb_2O_6:C = 1:6$ is the stoichiometry ratio, it was considered to vary the amount of carbon in the following percentages: 20%, (r = 1:7.2), 30%, (r = 1:7.8), 50%, (r = 1:9) and 80%,(r = 1:10.8) The results of this series of tests are shown in Fig. 6 for 900 °C.

Figure 6 shows time performance with excesses of 20, 30, 50, and 80% coal. 0.1 l/min and 900 °C oxygen flow. The performance of the stoichiometric test (r 1:6) gave a value of 88.24% in 15 min, this result is due to the impurities of the bindheimite that affected its performance. When performed with carbon excesses of 20, 30, and 50% performance improves to 93.80% in 20 min of process time. However, when excess coal is 80% yield is 75.43% in 20 min, this low result is probably due to insufficient oxygen flow which does not allow the refining slag sample particle to react completely. To corroborate the result of 80% excess carbon, a test was carried out with oxygen flows of 0.3 l/min, 900 °C and the same slag ratio used in the previous tests. The result is shown in Fig. 7.

Figure 7 shows that the yield is 77.5% in time of 50 min, at higher processing times it is observed that the yield decreases with the recording of an increase in weight due to the formation of volatile antimony oxides or compounds with higher degree of oxidation.
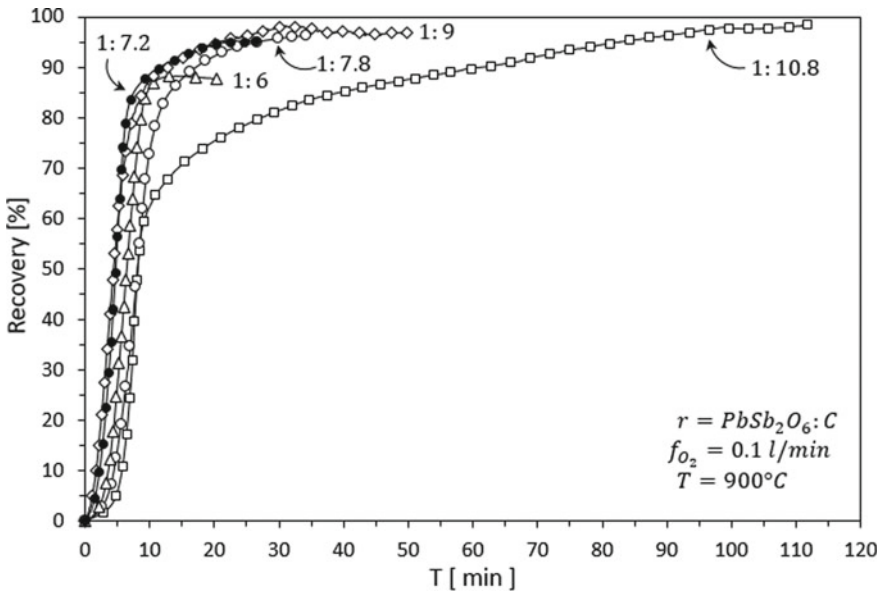
Fig. 6 Effect of coal on bindheimite reduction with excesses of 20, 30, 50, and 80% C
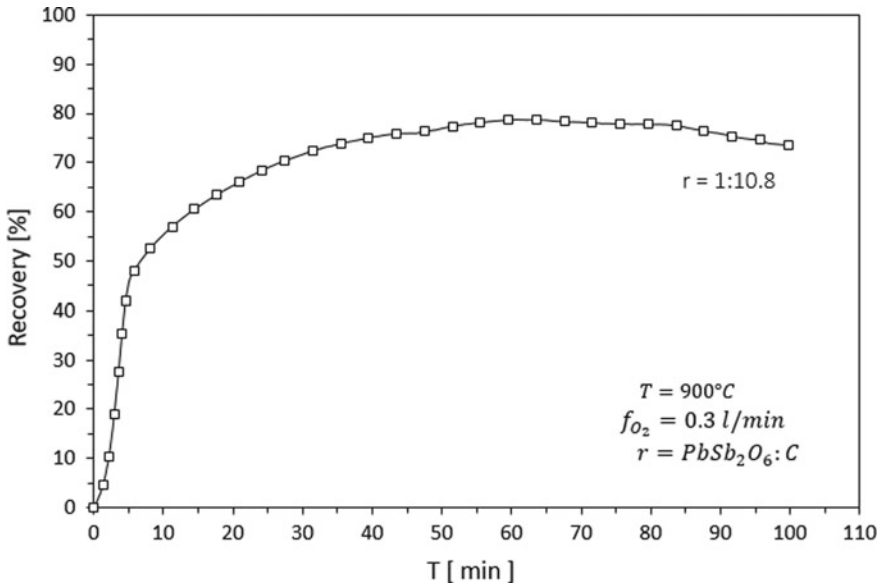
Fig. 7 Effect of excess carbon 80% r = 1:10.8, reduction of bindheimite to 0.3 l/min

Effect of the Composition of the Slag

The temperature and composition of the slag are related, according to the system $FeO:Na_2O:SiO_2$ for obtaining a molten and fluid slag, in the diagram in Fig. 4 several types of slag were analyzed and with the addition of Na_2O decreases the fusing temperature of slag to 800 °C. The results of these tests to 800 °C and $FeO:Na_2O:SiO_2$=10:30:60 show themselves in the Fig. 8.

Figure 8 shows the effect on the reduction of bindheimite without excess fluxes R 0:0, the yield achieved is 85.62% in a time of 10 min, when working at R 10:10 the yield increases up to 89.16% in a time of 10 min, when the R 20:20 ratio was used, the maximum performance of 93.65% was reached in a time of 15 min and when working with the R 50:50 ratios, the test ended in 12 min. With a yield of 71.43%, this effect is due to the fact that in the ternary diagram the position in the type A slag moves towards the vertex of Na_2O with the initial phase of sodium disilicate and 800 °C of melting temperature to the phase of sodium metasilicate approaching the 874 °C melting point isotherm. The combination of several tests to observe the effect of the type of slag is shown in Fig. 9.

Figure 9 shows the effect of the type of slag where the excesses of sand and caustic soda are R = 20:20 do not have a significant effect because in all these experiments a yield of approximately 91.06% is achieved in a time of 10 min; however, the excess of any of the overdubs adversely affects the yield of obtaining Sb-Pb metal as indicated in Fig. 8 with the ratio R = 50:50. A clear advantage of using slag $FeO:Na_2O:SiO_2$
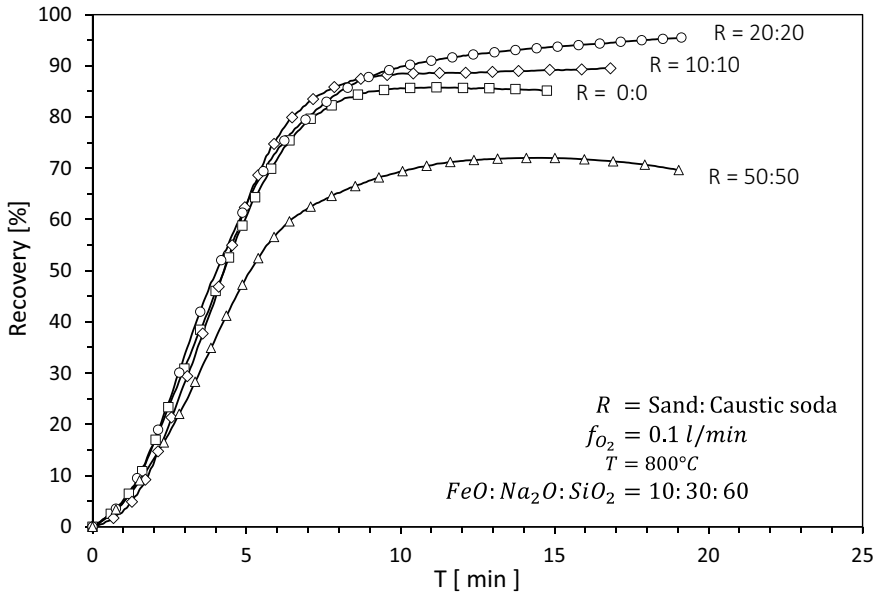
Fig. 8 Effect of slag ratio FeO:Na$_2$O:SiO$_2$ = 10:30:60 at 800 °C and 0.1 l/min on bindheimite reduction
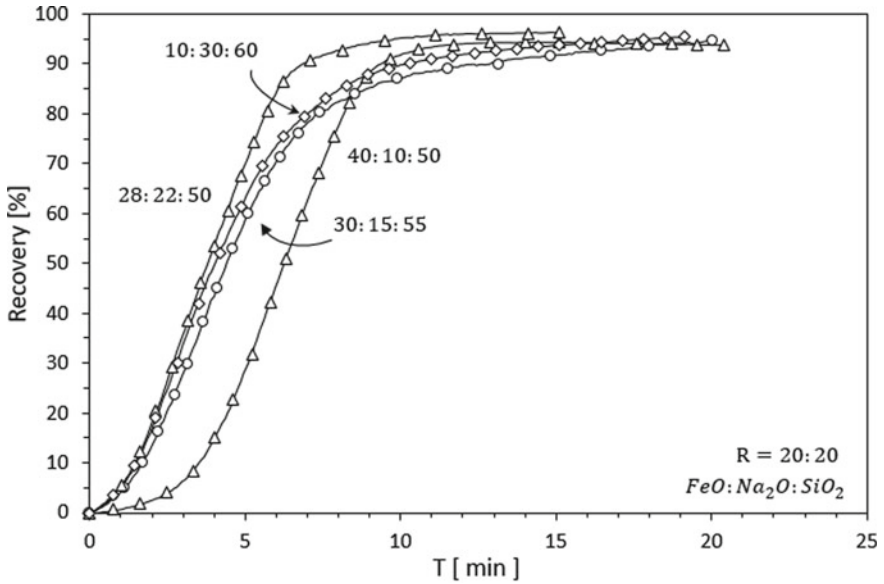
Fig. 9 Effect of slag type FeO:Na$_2$O:SiO$_2$ with excess R = Sand: Caustic soda = 20% in bindheimite reduction

of 10:30:60 is the low temperature of fusibility of 800 °C, however, the balance of mass was made based on the amount of Fe of 3.05% of the refining slag for which more sand and dosing caustic soda are required.

Effect of Temperature

Figure 10 shows the effect of temperature on the bindheimite reduction of the refining slag sample where the system slag $FeO:Na_2O:SiO_2$ has been considered from 10:30:60 to an oxygen flow of 0.1 l/min and excess melt ratio R = 0:0 (no excess).

As shown in Fig. 10 to 800 °C with type A slag (10:30:60) a yield of 79.96% is achieved in a time of 20 min, 850 °C the performance achieved is 80.53% in a time of 20 min, 900 °C performance is 82.63% in a time of 20 min and when working to 1000 °C the performance increases up to 87.50% in a time of 17 min. The effect of temperature is evident when the same is raised whereas the melting temperature of the slag of the ratio $FeO:Na_2O:SiO_2 = 10:30:60$ is 800 °C; also, at higher temperatures, the yield curve moves to the left with faster melting times.
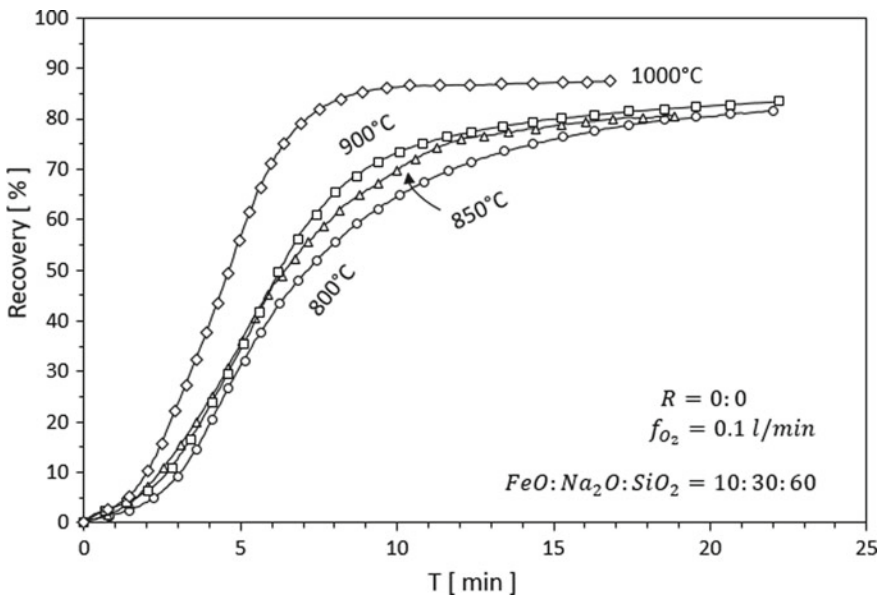
Fig. 10 Effect of temperature on system $FeO:Na_2O:SiO_2 = 10:30:60$ and $f_{O2} = 0.1$ l/min without excess R = 0:0

Conclusions

Based on the obtained results and the set objectives, antimony was successfully recovered from refining slag with values of 98%. The most suitable compound for line 2 slag is $PbSb_2O_6(PbO \cdot Sb_2O_5)$. Experimental tests on a thermobalance identified the controlling reaction in the process ($PbSb_2O_6 + 6C = Pb + 2Sb + 6CO$), which is supported by thermodynamic information. In the thermobalance tests, it was determined that an excess of 20% charcoal as the reducing agent achieved yields greater than 96%, and an excessive amount of this reagent is unnecessary. When the oxygen flow is increased above 0.1 l/min, antimony begins to volatilize, leading to a decrease in its recovery.

With a slag composition of $FeO:Na_2O:SiO_2$ at 10:30:60, a recovery of metallic antimony of 85.62% was achieved. This recovery increased to 93.65% when the amount of fluxes (sand and Na_2CO_3) was increased to 20%. However, the recovery decreased to 71.43% when the amount of fluxes was increased to 50%. Varying the slag composition while simultaneously adjusting the amount of added fluxes resulted in similar recoveries of around 93%, indicating that this result depends more on the slag's fusibility temperature than its composition. Experimental tests on the effect of temperature showed that working at temperatures higher than the slag's fusibility temperature slightly increased yields and accelerated the test kinetics. With a slag composition of $FeO:Na_2O:SiO_2$ at 10:30:60, a recovery of 81% was achieved at 800 °C, which increased to 87.50% when the temperature was raised to 1000 °C.

References

1. es.statista.com (2021) Ranking de los principales países productores de antimonio a nivel mundial en 2020. https://es.statista.com/estadisticas/635358/paises-lideres-en-la-produccion-de-antimonio-a-nivel-mundial/
2. Ministerio de Minería y Metalurgia (2019) Anuario Estadístico. https://www.mineria.gob.bo/revista/pdf/boletin3t2019.pdf
3. Callister WD, Rethwisch DG (1995) Ciencia e ingeniería de los materiales, 2da edn. The University of Utah, Salt Lake City
4. Mason B, Vitaliano ChJ (1952) The mineralogy of the antimony oxides and antimonates. Indiana University, Bloomington. https://rruff.info/uploads/MM30_100.pdf
5. Barin I, Knacke O, Kubaschewski O (1977) Thermochemical properties of inorganic substances. Springer, Berlin
6. Velasco HC (2002) Equilibrio en el sistema Sb-S-O a temperatura elevadas. Universidad Técnica de Oruro Facultad de tecnología, Oruro
7. Springorum D (1995) Slag atlas edited by Verein Deutscher Eisenhuttenleute, 2da edn. https://dokumen.tips/documents/slag-atlas-55d475ae27209.html?page=1
8. Zeballos VM, Velasco HC (2013) Obtención de antimonio por reducción de trióxido de antimonio gaseoso. Universidad Técnica de Oruro, Bolivia
9. Anderson CG (2018) Antimony production and commodities. https://www.researchgate.net/publication/29913334_Antimony_Production_and_Commodites
10. Webmineral.com. Bindheimite. https://www.webmineral.com/data/Bindheimite.shtml

Studies of Layer Growth During the Disintegration of Cemented Carbides with Vaporous Zinc

Lea Luznik, Eva Gerold, Thomas Weirather, Christoph Czettl, Teemu Karhumaa, and Helmut Antrekowitsch

Abstract The recycling of cemented carbides (CC) is an indispensable facet of resource conservation, especially for critical raw materials, signifying its profound environmental, economic, and strategic importance. These complex materials, consisting of refractory carbides embedded in a metallic binder, mainly tungsten carbide and cobalt, offer versatile recycling options. Among these methods, the zinc process is emerging as the most promising with significant potential regarding energy consumption and quality of products. In this method, zinc reacts with cobalt binder to form intermetallic phases, resulting in a breakdown of the material's composite structure due to the higher volume of these phases. In the second step, Zn evaporates at high temperatures under vacuum, leaving behind a porous cemented carbide skeleton. By means of crushing, grinding, and sifting, these can be processed into a powder mixture suitable for direct use in the manufacture of new products. While previous research has focused on the formation of Co-Zn phases during the decomposition step, there is a gap in understanding the growth rate of the disintegration layer. Therefore, this study aims to investigate the layer growth and the kinetics of the disintegration stage of the zinc process. By examining these aspects, a deeper understanding of the fundamental mechanisms at play in this method is gained, contributing to further advancements in the recycling of cemented carbides.

Keywords Cemented carbide disintegration · Layer growth · Zinc process

L. Luznik (✉) · E. Gerold · H. Antrekowitsch
Chair of Nonferrous Metallurgy, Montanuniversitaet Leoben, Franz-Josef-Straße 18, 8700 Leoben, Austria
e-mail: lea.luznik@unileoben.ac.at

T. Weirather · C. Czettl
CERATIZIT Austria GmbH, Metallwerk-Plansee-Straße 71, 6600 Breitenwang, Austria

T. Karhumaa
Tikomet Oy, Iskutie 9, 40320 Jyväskylä, Finland

Introduction

The excellent properties of cemented carbides, such as high hardness, toughness, and wear resistance, make them indispensable in the manufacturing and mining industry. Their versatility extends to applications as cutting tools, wear-resistant components, and chipless forming tools. The desirable properties can be achieved by combining a hard, high-melting carbide phase with a metallic binder. Commonly, tungsten carbide (WC) performs as the hard, wear-resistant phase, while cobalt functions as ductile binder material. The two main components, W and Co, are classified as critical raw materials in the European Union in terms of their potential supply risk and commercial relevance. Thus, the recycling of cemented carbides not only contributes to the conservation of these critical resources, but is also of ecological, economical, and strategical importance. The global recycling scenario for tungsten carbides shows an overall recycling rate of 46%. For cutting tools, the average share of recycling is 55%, with the potential to reach an impressive 80%. This is facilitated by the implementation of localized accumulation strategies at major manufacturing companies. A significant amount of tungsten, approximately 2/3, is used in the production of cemented carbides, highlighting the critical role of recycling strategies in this industry [1–3].

The so-called zinc process is a direct recycling method for the recovery of CC scrap. In the first step, the scrap is loaded with zinc on top into sealed graphite containers. The containers are then heated to around 1000 °C in an inert atmosphere. Zn diffuses into the CC and reacts with cobalt to form intermetallic phases in the binary Co-Zn system. Compared to pure cobalt, these phases display a greater volume, resulting in expansion of the binder material and spalling of WC grains in the form of lamellae. Due to the high temperature which exceeds the evaporation point of 907 °C [4], Zn is not only in a liquid but gaseous state or a mixture of both. Therefore, no reaction with only liquid or gaseous zinc is ensured during this process although the aggregate state has a significant impact on both disintegration rates and the formation of intermetallic phases. In the second stage, the zinc is distilled from the CC under vacuum at high temperatures. The remaining porous matrix is then mechanically processed by crushing, milling, and sifting to generate zinc reclaim powder. The resulting Co-WC powder is ready for use in the production of new cemented carbides [2, 3, 5, 6].

Typical disintegration rates in liquid zinc are in the range of 1 mm per hour, while significantly higher rates are reported in the gaseous aggregate stage. This indicates that reactions using zinc vapor are more promising in terms of duration and energy savings [7–9]. However, there is limited knowledge about the disintegration step using gaseous zinc, which evaporates at 907 °C. In particular, the growth of the layer and the progress of the disintegration during the process. The aim of this study is to identify a suitable rate law in order to comprehend the kinetics of disintegration during the zinc process better.

Experimental

For the investigation of the influence of zinc vapor on the decomposition of cemented carbides in the first stage of the zinc process, cuboidal WC–Co samples were provided by CERATIZIT Austria GmbH. This allows a kinetic study of the decomposition and layer growth during the disintegration. The experiments conducted include durations in the range of interest from 10 to 240 min and three replicate experiments, which allow the check of reproducibility. Therefore, to ensure contact of the cemented carbide with the gaseous zinc, the cuboids were placed in a closed graphite crucible next to another smaller crucible, which is filled with zinc (99.95% purity), next to the specimen. The Zn:CC ratio used is one, which provides an excess of zinc vapor. Subsequently, the crucibles are kept in a resistance furnace at a constant temperature of 950 °C for a defined duration. Throughout the treatment, the formation of the intermetallic Co–Zn phases occurs, resulting in a chipping of WC lamellae and a partial decomposition of the cemented carbides. After the cooling a metallographic preparation was carried out, followed by an analysis under a light optical microscope (LOM).

The yield of each specimen was determined as a percentage by dividing the remaining unreacted CC area, measured by LOM, by the cross-sectional area of the original cemented carbide cuboid. Figure 1 presents examples of the calculated yields, showing two significant zones classified as the unreacted zone (1) of the cemented carbide core and the disintegrated zone (2). The latter comprises the disintegration layer, consisting of detached tungsten carbide grains between the formed Co–Zn phases. The results of the measurements were applied for the evaluation of the disintegration kinetics.

(a) (b)
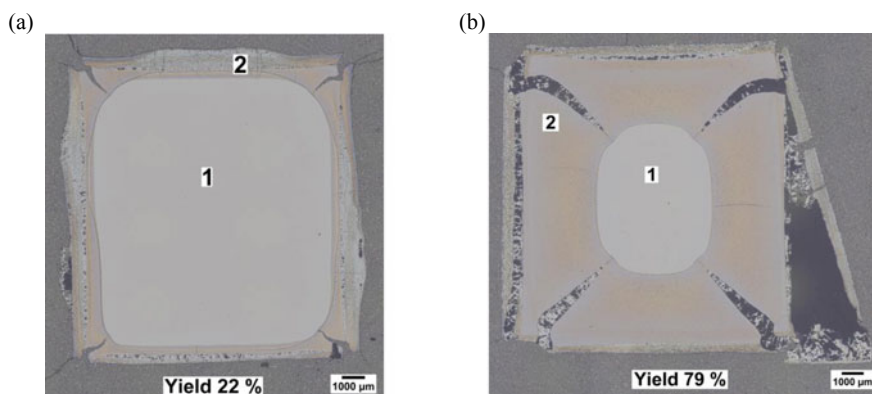
Fig. 1 LOM images and calculated yield for two selected samples with different durations including associated zones: **a** 60 min and **b** 240 min

Results and Discussion

To evaluate disintegration kinetics, the following graphs display the results of the experimental investigations. The generated plots serve to illustrate the estimated yield as a function of the experiment's duration. The standard deviation for the calculated yields was determined by replicating three experiments, thus achieving a high reproducibility of 93.8%. This underscores the overall reliability of the conducted experiments. Figure 2a depicts a linear regression fit. Equation 1 describes the linear function, which exhibits a high degree of conformity with an R^2 value of 97%. Thereby, Y indicates the yield including the footnote representing the applied model and t denotes the duration.

$$Y_{\text{lin}} = 0.31 \pm 0.02 \cdot t \tag{1}$$

A closer look at the data reveals a noticeable deviation within the results. In the first half of the plot, the calculated yields exceed the values predicted by the linear regression fit. Conversely, in the second half, there is a distinct decline in the results, with values falling below those predicted by the linear model. This suggests an alternative model that holds a more accurate alignment. Conversely, Fig. 2b displays a polynomial regression fit, which achieves a remarkable 99% goodness of fit. The polynomial of third degree is given in Eq. 2.

$$Y_{\text{poly}} = 0.64 \pm 0.06 \cdot t - 0.00 \pm 8.56\text{E} - 04 \cdot t^2 + 1.37\text{E} - 05 \pm 2.61\text{E} - 06 \cdot t^3 \tag{2}$$

This finding suggests that while the linear regression model provides a reasonably good fit, a closer examination reveals that the polynomial fit emerges as the more suitable model for characterizing the kinetics of disintegration of cemented carbides.
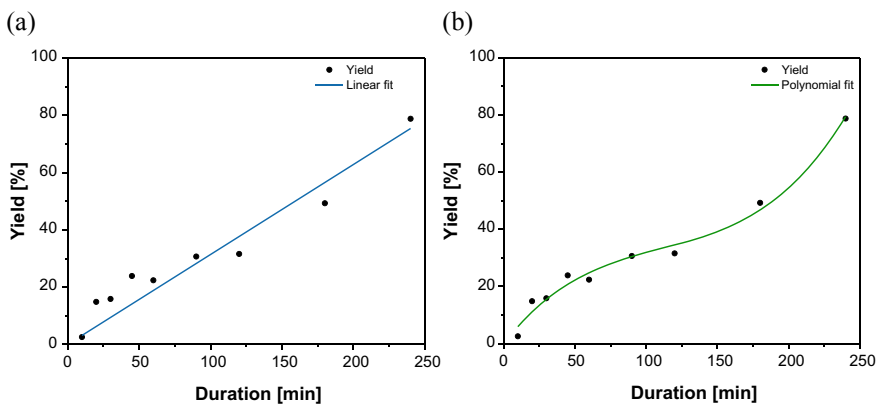
Fig. 2 Determinate kinetic fits with respect of the achieved yields over the duration of the disintegration step: **a** linear regression, **b** polynomial model
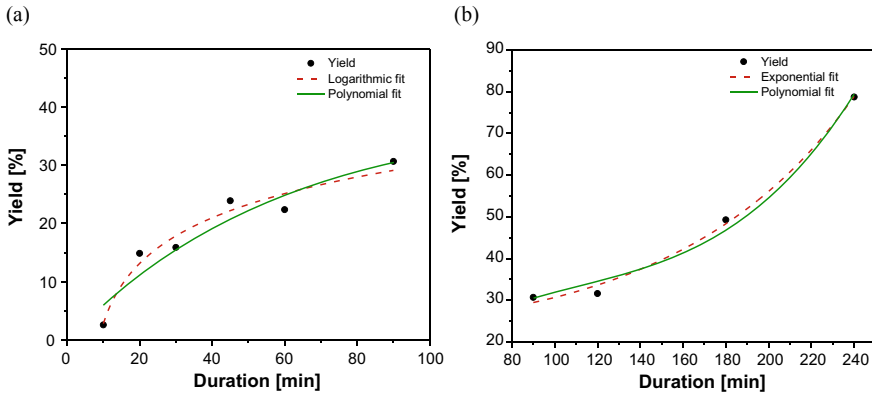
Fig. 3 Identified rate laws in comparison with the particular sections of the determined polynomial fit: **a** logarithmic rate law, **b** exponential rate law

Upon further examination of the deviation within the linear model fit, it is apparent that the experimental results can be separated into two distinct sections, each displaying different rate laws. This phenomenon is prominently illustrated in Fig. 3a, where the graph portrays a logarithmic rate law in comparison to the first half of the polynomial model, characterized by a robust goodness of fit (R^2) of 93%. The logarithmic model is described in Eq. 3.

$$Y_{\log} = -11.53 \pm 12.46 + 9.16 \pm 3.05 \cdot \ln(t - 5.23 \pm 4.59) \tag{3}$$

In Fig. 3b, an exponential rate law is plotted next to the second half of the polynomial model, showing a distinct resemblance. In particular, the exponential model exhibits an exceptional goodness of fit, with an R^2 value of 99%, which is represented by Eq. 4.

$$Y_{\exp} = \exp(3.17 \pm 0.35 + 7.20\mathrm{E} - 04 \pm 0.00 \cdot t + 1.78\mathrm{E} - 05 \pm 1.23\mathrm{E} - 05 \cdot t^2) \tag{4}$$

The transition from a logarithmic to an exponential rate law significantly impacts the kinetics of the disintegration process. The logarithmic rate law in the initial stages of disintegration represents a diffusion-controlled process. As a result, the early stage demonstrates high disintegration rates due to the short diffusion paths. However, as the disintegration evolves, the diffusion paths grow, resulting in a deceleration of the rate. In particular, a key transition point, occurring at around 90 min, marks the beginning of a kinetic shift from a logarithmic to an exponential rate law.

This progression to the exponential rate law is indicative of a transformative phase in the disintegration process. It proposes that the decomposition experiences exponential growth once a specific disintegration layer forms. This occurrence can be ascribed to the emergence of cracks within the decomposition layer. These develop over time, likely due to the differences in volume between the binder material and

the Co–Zn phases among the WC grains. Eventually, the fissures disrupt the structural integrity and create fissures. These accelerate the possible reaction between zinc and the pure binder material without requiring diffusion throughout the entire disintegration layer.

Figure 4 provides a visual representation of the evolving disintegration process through LOM images at various durations. After 10 min, a small but noticeable disintegration layer can be observed in Fig. 4a. First, small cracks begin to appear at the corners of the specimen. Upon closer observation of the lower right corner, it is evident that there are no fissures, and the unreacted cemented carbide core has a more pronounced edge compared to other corners marked by the presence of cracks. Figure 4b illustrates an increase in the thickness of the disintegration layer after 60 min. This stage also depicts the appearance of more pronounced cracks at the corners of the specimen. Notably, the disintegration layer displays fine fissures, indicating increased zinc reactivity with the CC core, which extends beyond the corner regions. A more advanced stage of cracking can be seen in Fig. 4c, which depicts the disintegration after 90 min. Notably, disintegration occurs at an accelerated rate in the corner regions, as evidenced by the more distinct rounding of the unreacted core. There is an effective path for zinc transport through a fine fissure on the lower left side, as evidenced by the localized bulging of the disintegration layer into the CC core in this area. Furthermore, the bigger cracks in the corner regions start to fill with zinc, ensuring a continuous supply to these areas. Figure 4d illustrates the disintegration state after 240 min, which is characterized by large cracks that have grown over time. These cracks act as the primary conduits for zinc infiltration towards the unreacted core. The image highlights the dominant pathways of zinc migration, emphasizing the dynamic nature of the disintegration process and the significant role played by crack formation and zinc transport mechanisms.

Conclusion

Recycling cemented carbides at the end of their product life cycle offers not only economic and ecological but also strategic benefits, while at the same time enhancing the resource efficiency of critical raw materials such as tungsten and cobalt. The zinc process, as the main direct recycling method for cemented carbides, is of particular importance due to its low energy consumption, high tungsten recovery rates, and environmentally sustainable characteristics. The disintegration process is a well-established procedure that operates at temperatures around 1000 °C to form intermetallic Co–Zn phases, which break the bond between the metallic binder and the hard phase. It is crucial to understand how the disintegration progresses, in order to further improve the process and ensure high yields. However, limited knowledge of the underlying kinetics is available up until now. Therefore, this study focuses on a suitable model for a better understanding. The disintegration kinetics are profoundly impacted by the transition from a logarithmic to an exponential rate law. The initial logarithmic regime is driven by diffusion, leading to rapid early-stage disintegration

(a)

10 min

(b)

60 min

(c)

90 min

(d)
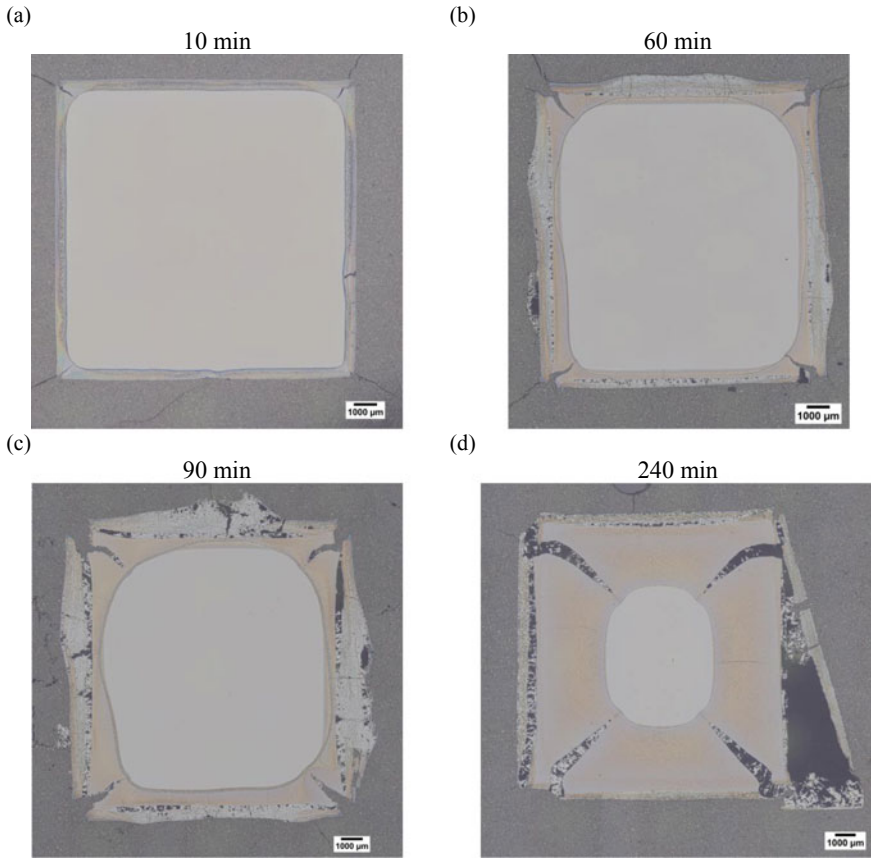
240 min

Fig. 4 LOM images of selected samples with particular duration, representing the progress of disintegration and the occurrence of cracks: **a** 10 min, **b** 60 min, **c** 90 min, **d** 240 min

due to short diffusion paths. As the process evolves, longer diffusion paths lead to a gradual slowing of the rate. The turning point marks the shift to an exponential rate law, indicating accelerated disintegration once a specific layer thickness has formed. This acceleration is related to the development of fissures within the layer, likely due to volume differences between the binder material and the formed Co-Zn phases between the WC grains. These cracks improve reaction kinetics and eliminate the need for complete layer diffusion. The results of this study provide a basic understanding of the disintegration kinetics with gaseous zinc. Further investigation of appropriate rate laws, the turning point, and the behavior of different cemented carbide grades will be conducted.

References

1. Zeiler B, Bartl A, Schubert W (2021) Recycling of tungsten: current share, economic limitations, technologies and future potential. Int J Refract Metals Hard Mater 105546
2. Lassner E, Schubert W (1999) Tungsten. Kluwer Academic/Plenum Publishers, New York
3. Ebner T et al (2021) Influence of the Cemented carbides composition on the disintegration in liquid zinc. In: Anderson C et al (eds) Ni-Co 2021: the 5th international symposium on nickel and cobalt, the minerals, metals & materials series, pp. 329–343
4. Meyer R, Pietsch E (1956) Gmelins Handbuch der anorganischen Chemie. In: 32. Verlag Chemie, GmbH., Weinheim
5. Leitner M et al (2022) Studies on the phase formation of cobalt contacted with zinc vapour. Int J Refract Metal Hard Mater 107:105877
6. Ebner T et al (2020) Studies on the formation of intermetallic compound layers in Co(W)–Zn diffusion couples. In: PbZn 2020: 9th international symposium on lead and zinc processing, the minerals, metals & materials series, pp. 661–672
7. Luznik L et al (2023) Recycling of cemented carbides with gaseous zinc including particular consideration of GGI. In: Proceedings of EMC (2023) online proceedings
8. Ebner T et al (2017) Ausgangsbedingungen und Verfahren für das Recycling von Wolframkarbid-Verbundwerkstoffen. Oesterr Wasser Abfallwirtsch 69:482–494
9. Alkatsev MI, Svistunov NV, Trotsenko IG (2008) Regeneration of the WC-Co hard alloy with the use of gaseous zinc. Russ J Non-Ferrous Met 49:156–159

Rare-Earth Partitioning with Liquid Iron During Sulfidized Magnets Vacuum Treatment

Zachary K. Adams and Antoine Allanore

Abstract An effect previously observed in magnet recycling experiments is further investigated in this work. At high temperatures (1800 °C) and moderate vacuum (0.01 bar) certain heavy rare earth elements are found to selectively partition into a metallic iron phase produced by thermal decomposition from a molten sulfide phase. Works in the literature have established that rare earth elements suppress the concentration of sulfur strongly in liquid iron at 1600 °C, but the behavior of heavy rare earth elements in this context remains uncertain. Herein, experimental results using magnet simulants with heavy rare earth elements – terbium, dysprosium, and erbium – are reported, using concentrations $10 \times$ higher than in magnets, in order to investigate the possible saturation of the iron phase. SEM/EDS analysis showed that terbium and dysprosium partitioned to the metal at low concentrations, approximately 0.50% by weight.

Introduction

The rare earth elements (REEs) are a collection of fourteen elements ranging from lanthanum (57) to lutetium (71), as well as, conditionally, scandium and yttrium. While these elements are not as rare as the name would suggest, it is rare to find the minerals from which they are extracted in high enough concentrations to effectively mine [1]. The natural minerals typically contain the 14 REEs, and supporting their "rare" status, the separation, isolation, and reduction to metal of individual REEs from such natural minerals is a significant challenge. Due to the electronic structure of the REEs, their reactivities are all very similar, which can make isolation difficult

Z. K. Adams
Department of Materials Science, Massachusetts Institute of Technology, Cambridge, MA, USA
e-mail: zadams@mit.edu

A. Allanore (✉)
Department of Materials Science, Massachusetts Institute of Technology, Cambridge, MA, USA
e-mail: allanore@mit.edu

[2]. A critical use of REEs is in high-strength permanent magnets. Praseodymium, neodymium, dysprosium, erbium and terbium are the primary REE for this application. The REE magnets are, approximately, 65% (by weight) iron, 25% neodymium, 5% praseodymium, and 1–2% dysprosium, erbium or terbium [3].

When these REE magnets reach the end of life, they may or may not be recycled. Magnets that are recycled are generally placed back into the supply line of rare earth minerals concentrates, at the solvent extraction stage. The original energy and cost put into the production of the original magnet, in particular, the work to separate the REEs is completely lost in such a process. In order to better recycle magnets, previous work in our group investigated using a pyrothermal process involving sulfur gas to partition and recover rare earth elements. Called sulfidation, this technique has been used for high success in separating difficult-to-separate elements [4]. The product of such sulfidation was then treated using a thermal process, this time under vacuum, where the iron sulfide decomposed into iron metal, while leaving the REEs as a sulfide. Analysis found that the sulfide had very low iron content, while the iron had very low amounts of neodymium and praseodymium. However, the iron metal contained heavy REEs (HREEs) such as dysprosium, terbium, and erbium, at concentrations higher than expected. Very little of these elements were left behind in the sulfide, contrary to neodymium and praseodymium. In different experiments, the distribution of these elements varied slightly [5, 6], but the trends for HREE partitioning remained.

The effect of REEs on sulfur in liquid iron has been investigated before, in the context of industrial desulfurization of steels. Sulfur and certain REEs were studied in the dilute limit, which while this work is certainly not, the desulfurization results provide crucial context. Ejima et al. [8] used controlled additions of La and Ce to liquid iron with a predetermined concentration of dissolved sulfur. They found that the interaction coefficient [7] of the cerium and lanthanum with sulfur in the liquid iron were as follows:

$$e_S^{Ce} = -9.1, \quad e_S^{La} = -18.3$$

showing that cerium decreases the activity of sulfur in liquid iron relatively strongly [8]. Further work by Han et al. [9] found lower values for these coefficients [9]:

$$e_S^{Ce} = -1.88, \quad e_S^{La} = -1.51$$

More recent measurements tend to values closer to the lower values by Han et al. but do not necessarily agree with these values [10, 11]. This likely is a result of the high reactivity of the rare earth metals used in these experiments, which can make controlling all conditions quite challenging. A desulfurization chart is shown as Fig. 1, using literature values from different works.

Similar to the desulfurization, the equilibrium of REEs in liquid iron with sulfur and other elements was also investigated. Primarily, this involved investigating the role of carbon and oxygen. Wu et al. [12] investigated the interaction coefficient between REEs and carbon, and then between REEs and sulfur, with carbon saturated
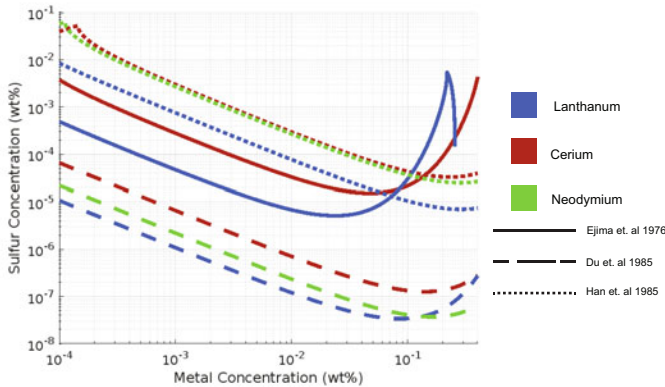
Fig. 1 The desulfurization of liquid iron using cerium, lanthanum and neodymium from 3 sources at 1600°C under 1 bar. These sources looked specifically at RE-S equilibrium with no other elements considered. The red, green and blue curves use data from Ejima et al. [8], Han et al. [9] and Du et al. [10], respectively

iron. The values for the interaction coefficients between REEs and carbon were much lower than for sulfur, between –0.5 and –0.1 at 1600 °C. For REEs-sulfur, reported values were in the range of –3 to –2 [12]. Han et al. [13] and Dong and Han [14] investigated interactions between REEs, primarily cerium, sulfur, and oxygen. The REE-sulfur interaction coefficients reported were in a similar range despite the different systems [13, 14]. Interaction coefficients in the ternary between REEs, oxygen, and sulfur were not reported, but in the work by Han et al., the Gibbs energies of formation for rare earth oxysulfide compounds were reported, which were strongly negative, indicating a large driving force for oxysulfide formation [13]. The desulfurization of steels with REEs forms an important starting point, but only the dilute limits of both sulfur and REE content were investigated. Of note, no heavy REEs were investigated.

Methods and Materials

As an extension of our prior study using REE magnet products, where complete sulfidation of the metallic elements to sulfide was confirmed, a simulant of mixed sulfides was used here instead. This allows better control of the relative amount of each REE and the study of new compositions. In particular, we ultimately aim to evaluate the possible "saturation" of a sulfide or metal phase with certain REE as their concentration is overall increased.

The simulant here was made of iron sulfide, neodymium sulfide and three different heavy REE sulfides: dysprosium, erbium and terbium. The iron (II) sulfide was purchased from Strem Chemicals, had a purity of 99.9% Fe, was a powder, and was

used as purchased. The neodymium, dysprosium, erbium, and terbium sulfides were synthesized from chemical grade oxides (Nd, Dy: Strem Chemicals, 99.9% REO, powder; Tb: ThermoFischer, 99.9% REO, powder; Er: ThermoFischer, 99.9% REO, 3-12mm chunks). All of the oxide feedstock except for terbium were sesquioxides (e.g., Nd_2O_3) whereas the purchased terbium oxide has the formula Tb_4O_7. The synthesis process of sulfidation is described in depth in a prior publication [4]. In brief, the REE oxides were sulfidized at 1500°C in a graphite tray for 60 min, using elemental sulfur vapor carried by an argon gas flow rate of approximately 1500sccm. The success of the procedure was quantified by percent conversion of the oxide to sulfide, determined by mass change for the reaction:

$$RE_2O_{3(s)} + 3S_{2(g)} \rightleftarrows RE_2S_{3(s)} + \frac{3}{2}SO_{2(g)}$$
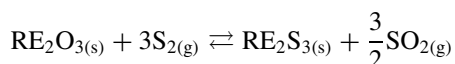
In this reaction, the conversion was 98.6% for all the REE, quantified by the mass change before and after the synthesis. After synthesis, the rare earth sulfide products were placed and handled in a glove box to reduce contamination from air or moisture.

The three different magnet simulant compositions studied herein are presented in Table 1. Ratios are calculated on a metal content basis, assuming the stoichiometry of the sulfides given in the table. The iron sulfide and neodymium sulfide were added in a ratio of 2.8 Fe to 1 Nd (metals basis), as found for the sulfidation of common REE magnet products, while the heavy REEs are added in excess of $10 \times$ of their normal ratios iron in a REE magnet, which typically has a ratio in the range of 2.5–2.7 [3]. This was done so that the saturation of the heavy REEs within the liquid iron could possibly be investigated. Three different mixtures of each composition were made from the sulfides, as shown in Table 1, and the powders mixed for each were coarsely combined inside a glass vial via shaking.

The thermal vacuum decomposition was conducted in an induction furnace fitted with a quartz tube (88.9mm OD, 1.2m length). The furnace used in these experiments is an Ultra Flex Power Technologies induction furnace with a 25kW maximum power output. A schematic of the overall induction furnace setup is shown as Fig. 2b. An alumina rod was used as a lower support rod for the susceptor, but graphite was used

Table 1 Masses, in grams, of sulfide powders mixed together for each composition and each experiment

	Composition 1			Composition 2			Composition 3		
Experiment #	1	2	3	1	2	3	1	2	3
FeS (g)	1.480	1.486	1.490	1.475	1.481	1.491	1.488	1.473	1.484
Nd2S3 (g)	0.880	0.887	0.885	0.885	0.893	0.873	0.882	0.885	0.875
Tb2S3 (g)	0.271	0.325	0.304	–	–	–	–	–	–
Dy2S3 (g)	–	–	–	0.251	0.265	0.360	–	–	–
Er2S3 (g)	–	–	–	–	–	–	0.276	0.266	0.276
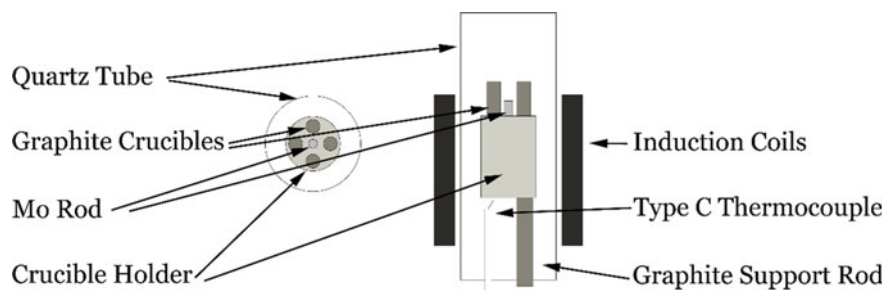
Fig. 2 Two schematics of the induction furnace setup. **a** (left) Top view of the setup, with the crucible holder at the center with graphite crucibles and molybdenum rods above and the quartz tube surrounding. **b** (right) A vertical cross-section view of the induction furnace, showing how the crucible holder is held up by a graphite support rod. There is a type C thermocouple underneath as well, and the placement of the setup relative to the coils of the induction furnace is also shown

as the upper support rod, as under the conditions of the experiment, carbothermic reduction of the alumina is possible.

A total of three experiments were run in this induction furnace, with one sample from each composition being tested. Figure 2a shows a schematic of the crucible setup for the induction furnace. The crucible holder (50 mm diameter) was constructed to accommodate four individual crucibles with 8.4mm outer diameters. A molybdenum rod (McMaster, 99.95%, 76.4 mm long, 8.25 mm diameter) was inserted in the middle hole to provide extra heat for the experiment. The three crucibles (2.25 mm wall thickness, 24.1 mm ID) were constructed of EDM grade graphite and were bored out from a rod using a lathe. Post-machining, the crucibles were sonicated in acetone to remove excess graphite powder. The crucibles were then heated with a heat gun to remove any excess acetone. All parts of this setup were individually weighted before their use in the furnace. Once the empty masses were recorded, the crucibles were filled in a fume hood with the pre-mixed powdered samples retrieved from the vacuum chamber, trying to minimize exposure to ambient conditions.

Setting up the crucibles in the furnace involved securing the support rods and placing the filled crucible holder in the support rods such that the holder was centered. An image of the setup at this point can be seen in Fig. 3a. Then, the fused quartz tube was placed in. This quartz tube served as the primary containment for the furnace. The tube was secured on both top and bottom using custom-made metal fittings with O-rings. Once the furnace was fully secured, vacuum was pulled. The setup was purged with argon, and then subjected to vacuum three times, before leaving it under vacuum. The vacuum level was approximately – 29.5 inHg (0.01 bar).

To start the experiment, the induction furnace power was switched on to 10%. Power was increased quickly, at a rate of approximately 5% every 2 min. Target temperature was 1800 °C, and temperature was measured by a thermocouple underneath the crucible holder, as can be seen in Fig. 2b. At 60% power, or approximately 16 kW, approximately this temperature was reached. Due to the sharp thermal gradients of the furnace and since the thermocouple was below the crucible holder, the
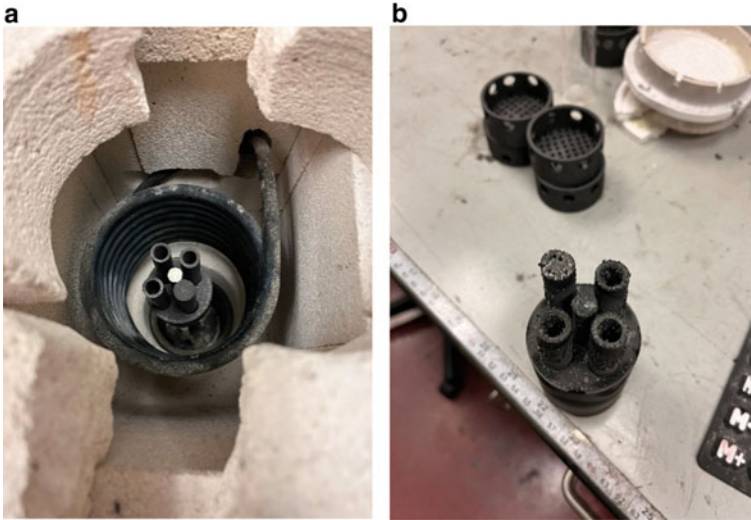
Fig. 3 **a** (left) An image of the induction furnace setup before running an experiment, showing the crucible holder in the center. The holder is loaded with three crucibles, one empty crucible (which is solid through), and the Mo rod is in the middle. Quartz tube has not yet been loaded in. **b** (right). An image of the crucible holder after an experiment was run, showing crucibles within the holder. Important to note material on the tops of the crucibles, the result of splattering during the experiment

thermocouple plateaued at around 1400 °C in each experiment. Once the temperature leveled out, a 1 h timer was started. For this hour, the power was maintained, and after, the power was slowly decreased back down to 10% before powering down. After the furnace completely cooled off, the setup was deconstructed in reverse fashion until the crucible holder was removed and each crucible recovered and weighed. A picture of one such crucible is shown in Fig. 3b. After weighting, the crucibles were broken open in a fume hood and the solidified charge at the bottom of the crucible was removed and cast in epoxy. A total of three runs are discussed herein, for a total of 9 crucibles.

The samples were sectioned and polished for both optical microscopy observation, and scanning electron microscopy characterization. Samples were sectioned vertically with a diamond saw lubricated with kerosene. Grinding occurred using sandpaper grits from 120 to 2400, increasing by approximately 200 grit with each pass. The samples were polished at 6 μm and 1 μm for 5 min each. Elemental analysis of the observed phase was conducted via EDS while performing SEM. The SEM used for analysis was a JEOL 6610-LV. Accelerating voltages used were 20 kV, and imaging was done using the backscatter detector. EDS was performed via point scans, with ten scans per phase per sample.

Results

The three experiments were run to procedural success. The parameters of the induction furnace changed slightly from experiment to experiment, but the level of power reached overall was around 60%. A cross-sectional view using the SEM from a sample of composition 2 from experiment 3 is shown in Fig. 3. Micrographs from the eight other samples all look very similar. In the center of the image, Fig. 3a, metallic iron can be seen, with cracks and voids present throughout. Slightly harder to see are inclusions of iron sulfide, which are visible as darker gray spots in the iron. The brighter phase on the outside, Fig. 4b, is a rare earth sulfide, with small amounts of iron-rich sulfide embedded within. Figure 5 shows a chart depicting the partitioning of the elements, minus oxygen and carbon, between the metal and sulfide phases. It can be seen that iron content in the metallic phase remained high, no less than 97%, but its content in the sulfide had some large variance. The sulfur partitioning had a similar, but inverse relation, being relatively similar in the sulfide across all experiments, but with varying concentrations in the metal. For the heavy REE's terbium and dysprosium partitioned to the metal with about 0.50–60%, while a large amount remained behind in the sulfide phase.

In all three experiments, erbium did not exhibit any partitioning to the metallic phase, while terbium and dysprosium exhibited limited partitioning only. In the case of the terbium and dysprosium, approximately 0.005 g of the heavy REE would have been present in the iron, only 4.4% of the total amount added as a sulfide. This
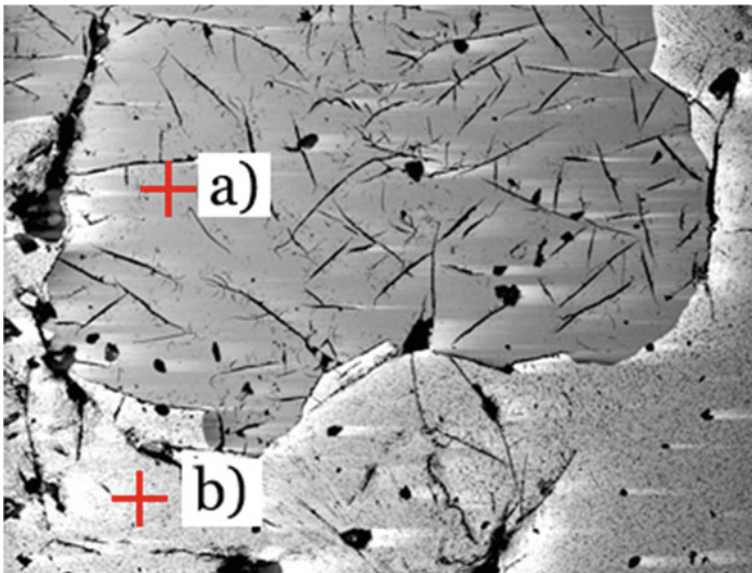
Fig. 4 Micrograph of a sample of Composition 2, from Experiment 3. Metallic iron **a** is the smooth phase top and center, sulfide **b** is the rough phase along the bottom
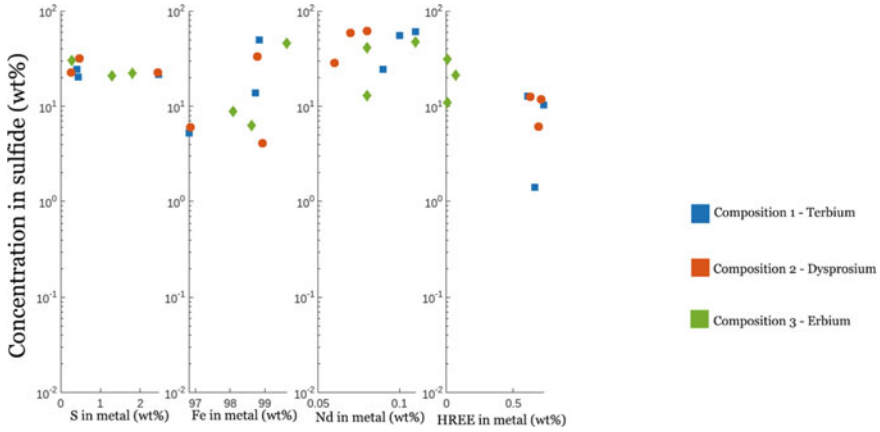
Fig. 5 A side-by-side chart showing the partitioning of the various elements between the metallic and sulfide phases. The y-axis is shared, but x-axes are separate. Heavy REEs are shown in the far-right chart, and is labelled 'HREE'

number is obtained by assuming all of the iron sulfide converted to iron metal and HREE content was determined by the EDS results. This mass of HREE produced was then compared to the total mass of the HREE present in the sulfide.

Discussion

The partitioning effect, when examining the SEM results, is both lower than expected and hoped from previous work and higher than what would normally be expected for REEs in liquid iron when sulfur is present in large amounts. There are several potential explanations for this partitioning effect. One possibility could be that it is driven by the alloying between iron and the heavy REE under vacuum. This effect would be governed by the reaction:

$$RE_2S_3 \rightleftarrows 2\underline{RE} + \frac{3}{2}S_{2(g)}$$
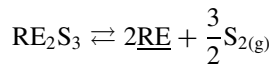
where 'RE' is a heavy REE, and the underbar indicates the REE dissolving in liquid iron. According to solution data for the Fe-REE systems at 1 atm, this alloying reaction is spontaneous, but has an energy change for terbium, dysprosium, and erbium of − 0.69 kJ/mol, − 0.62 kJ/mol, − 0.61 per mole of metal, respectively [16]. These numbers are also calculated at an REE concentration of 0.005 by weight. According to the reaction, the standard state free energy of the above reaction can be expressed:

$$\Delta G^\circ = -\text{RT} \ln\left(\frac{a_{\text{RE}}^2 a_{\text{S}_2}^{3/2}}{a_{\text{RE}_2\text{S}_3}} \right)$$

To match with observations, $X_{\text{RE}} = 0.005$, assuming an ideal solution, the standard state free energy change would have to be in the range of 100 kJ/mol. This may be able to provide some explanation for differences in observation, as erbium does technically have the weakest alloying at these low concentrations. This could be further investigated by measuring the activity of the heavy REE's in the liquid iron and measuring how they interact with sulfur at low concentrations.

One factor competing with the partitioning of the elements may be the volatility of the metallic REEs. At 1800°C under vacuum, the vapor pressure of terbium, dysprosium, and erbium cannot be neglected. Depending on the precise mechanism by which this effect may occur, this volatility may have more or less of an effect. For instance, if the REE metal partitions directly into the metallic iron, the volatility may not have as much of an effect as if the REE sulfide disassociated on its own, and then partitioned into the metallic iron. It is also possible that the heavy REE can vaporize directly from the liquid iron. Of the three elements tested, erbium has the lowest boiling point, which may help to explain why it was not observed partitioning. To further investigate this specific avenue, running this experiment at a range of different pressures would be essential.

Finally, it is, at the moment, difficult to ascertain whether these results represent steady-state thermodynamic partitioning. Previous experiments, where larger masses were involved, saw a more pronounced partitioning effect. If, potentially, the dissociation of dysprosium sulfide and terbium sulfide in the presence of iron metal is faster than the re-sulfidation of those metals while in the iron metal, an hour-long experiment would find a higher amount than thermodynamically possible. It would also have to be the case that for the erbium, these kinetic limitations do not exist to the same degree. Further investigations with varrying the length of time for the experiment, including for a long time, several hours, are now warranted. Additionally, the experiment could use a much higher mass for the lowest partitioning element, erbium in this case, and run for the same amount of time.

Conclusions

This investigation set out to determine the saturation of three different heavy rare earth elements in liquid iron during a reactive vacuum thermal treatment. Previous work had observed a peculiar effect where certain heavy rare earth elements preferentially migrate away from a sulfide phase into a metallic phase under the effect of high temperatures and low pressures. Literature investigating the desulfurization of steel found that rare earth elements have a strong effect on decreasing the maximum solubility of sulfur in liquid iron. For the heavy REEs to partition as observed, desulfurization would have to be radically different for the heavy REEs than for the

REEs investigated in the literature. The experiments were procedurally successful, with minor issues of thermal control between runs. It was found that terbium and dysprosium partitioned into the metallic iron phase, at concentrations between 0.50 and 0.60% by weight, while erbium did not partition into the metal at all. Three potential mechanisms are discussed, and further work to rule out these mechanisms is proposed.

References

1. Gschneidner KA, Pecharsky VK (2022) Rare-earth elements. Encyclopedia Britannica
2. Gschneidner KA, Beaudry BJ, Capellen J (1990) Rare earth metals. In: Properties and selection: nonferrous alloys and special-purpose materials 720–732 ASM international
3. Wagner ME, Allanore A (2020) Chemical thermodynamic insights on rare-earth magnet sludge recycling. ISIJ Int 60:2339–2349
4. Stinn C, Allanore A (2022) Selective sulfidation of metal compounds. Nature 602:78–83
5. Stinn CR (2023) Pyrometallurgical oxide-sulfide anion exchange for improved material separation and metal production. Massachusetts Institute of Technology
6. Allanore A, Stinn C (2023) Sulfide reactive vacuum distillation, absorption, stripping, and extraction for metal alloy production
7. Lupis CHP (1983) Chemical thermodynamics of materials. Elsevier Science Publishing Co., Inc., 581
8. Ejima A, Suzuki KI, Harada N, Sanbongi K (1977) Sulfur equilibria in molten Fe-Ce-S, Fe-La-S, Fe-Ti-S and Fe-Zr-S systems
9. Han Q, Dong Y, Feng X, Xiang C, Yang S (1985) Equilibria between rare earth elements and sulfur in molten iron. Metall Trans B 16:785–792
10. Du T, Wang L, Wu Y, Zhang Y, Liu A (1993) Thermodynamic behavior of Fe-S-RE, Fe-Csat-S-RE, Ni-S-RE, Cu-S-RE solutions. J Mater Sci Technol 9:68–70
11. Vahed A, Kay DAR (1976) Thermodynamics of rare earths in steelmaking. Metall Trans B 7:375–383
12. Wu Y, Wang L, Du T (1985) Thermodynamics of rare earth elements in liquid iron. J Less Common Metals 110:187–193
13. Han Q, Xiang C, Dong Y, Yang S, Chen D (1988) Equilibria between the rare earth elements, oxygen and sulfur, in molten iron. Metall Trans B 19:409–418
14. Dong Y, Han Q (1997) The precipitation diagram of [Ce]-[O]-[S] in liquid iron and its application. Steel Res Int 68:388–391
15. Daehn KE et al (2022) Liquid copper and iron production from chalcopyrite, in the absence of oxygen. Metals 12:1440
16. Konar B, Kim J, Jung I-H (2017) Critical systematic evaluation and thermodynamic optimization of the Fe-RE system: RE = Gd, Tb, Dy, Ho, Er, Tm, Lu, and Y. J Phase Equilib Diffus 38:509–542

Effect of Ce Substitution with La and Nd on Microstructure and Mechanical Properties of Al$_{11}$Ce$_3$

Jie Qi and David C. Dunand

Abstract The study investigates the microstructure and mechanical properties of five cast, coarse-grained intermetallic alloys: binary Al$_{11}$Ce$_3$ and Al$_{11}$La$_3$, ternary Al$_{11}$(Ce$_{0.75}$La$_{0.25}$)$_3$ and Al$_{11}$(Ce$_{0.5}$La$_{0.5}$)$_3$, and quaternary Al$_{11}$(Ce$_{0.54}$La$_{0.27}$Nd$_{0.19}$)$_3$ with mischmetal composition. All compounds exhibit a single phase indicating a solid solution among the rare-earth elements (RE = Ce, La, and Nd) on the Ce sublattice of Al$_{11}$RE$_3$, contrary to Thermo-Calc prediction of segregation of Ce and (La, Nd) into two insoluble compounds. The orthorhombic Immm-structured α-Al$_{11}$RE$_3$ phase's lattice parameters increase with increasing La concentration, while the α-β phase transformation temperature decreases. The mechanical properties, encompassing high hardness (4.1–4.3 GPa), low indentation fracture toughness (0.48–0.65 MPa m$^{1/2}$), together with the high twinning propensity among these five Al$_{11}$RE$_3$ compounds are remarkably similar. This similarity suggests that these Al$_{11}$RE$_3$ compounds will exhibit comparable strengthening in Al-RE-based eutectic alloys, while also positioning them as economically and environmentally favorable alternatives to the well-developed binary Al$_{11}$Ce$_3$ compound formed in current eutectic Al-Ce alloys.

Keywords Ce substitution · Al-Ce-based alloys · Microstructure and mechanical properties of Al$_{11}$RE$_3$ compounds

Introduction

Al-Ce-based alloys demonstrate excellent castability, allowing both traditional casting [1–7] and laser powder-bed fusion (LPBF) [8–13]. Concurrently, these alloys show good mechanical properties at room temperatures, coupled with exceptional creep resistance and coarsening resistance at high temperatures. The binary Al-Ce alloys with composition close to Al-10Ce (wt%) exhibit a eutectic microstructure,

J. Qi · D. C. Dunand (✉)

Department of Materials Science and Engineering, Northwestern University, Evanston, IL 60208, USA

e-mail: dunand@northwestern.edu

characterized by the fine lamellar $Al_{11}Ce_3$ phase in a pure Al matrix. Strengthening of this alloy is predominantly influenced by two mechanisms: (i) the effective load transfer from the weak Al matrix onto the stronger $Al_{11}Ce_3$ intermetallic (IM) phase [7] enabled by the strong $Al-Al_{11}Ce_3$ interface [14], and (ii) the Orowan strengthening mechanism by $Al_{11}Ce_3$ platelets with submicron spacing [4, 15]. Al-Ce-based alloys can be further strengthened through the addition of solid-solution strengtheners such as Mg [3, 6, 7, 10, 16–19], precipitation strengtheners including Sc and Zr [10, 11], or another eutectic former such as Ni [5, 20, 21].

The crystallographic, thermal, and mechanical characteristics of the $Al_{11}Ce_3$ strengthening phase are critical for finite element models (FEM) development to predict the cast or LPBF-printed Al-Ce alloys' properties, such as stiffness, strength, toughness, creep resistance, and thermal expansion. The binary $Al_{11}Ce_3$ compound was experimentally investigated in terms of the microstructure, hardness, thermal expansion, oxidization, and compressive creep behavior by Wu and Dunand [22]. A density functional theory (DFT) study from Ding et al. [23] predicts the lattice constant, elastic properties, and electronic structure of $Al_{11}Ce_3$ (along with Al_2Ce and Al_4Ce). More recently, DFT was also applied to various $Al_{11}RE_3$ IM compounds, where RE stands for the rare-earth elements La, Ce, Pr, and Nd, for the prediction of structural, mechanical, and thermodynamic properties by Fan et al. [24] and Liu et al. [25].

Recently, research efforts have focused on replacing Ce with mischmetal (MM) in Al- and Mg-based alloys [26, 27]. MM is a mixture of RE elements primarily composed of Ce and La with lower amounts of Nd and Pr. The Al-La, Al-Ce, Al-Pr, and Al-Nd phase diagrams [26] are analogous in terms of the $Al_{11}RE_3$ phase crystal structure (Immm), $Al-Al_{11}RE_3$ eutectic composition (9–13 wt% RE), and eutectic temperature (630–640 °C). Replacing $Al_{11}Ce_3$ with $Al_{11}MM_3$ as the strengthening phase [26] in Al-RE-based alloys thus appears feasible and desirable, as MM offers a more cost-effective and environmentally sustainable alternative to the use of pure Ce in Al- or Mg-based alloys [28–30], establishing a compelling motivation for such substitution.

While the technical feasibility of substituting Ce with MM is evident, accompanied by potential economic and environmental advantages, there has been limited research on the effects of replacing Ce with La and MM, fully or partially, upon the structure, properties, and strengthening behavior of the $Al_{11}RE_3$ phase. In this study, we primarily focus on how Ce substitution by RE elements influences the $Al_{11}RE_3$ phase formation, lattice parameters, and mechanical properties including hardness and indentation fracture toughness. Because of the variability in MM compositions from distinct sources, particularly with differing Ce/La ratios, our exploration encompasses five $Al_{11}RE_3$ compounds:

(i) binary $Al_{11}Ce_3$ and $Al_{11}La_3$, serving as control compounds with individual RE elements.

(ii) ternary $Al_{11}(Ce_{0.5}La_{0.5})_3$ and $Al_{11}(Ce_{0.75}La_{0.25})_3$, which typify lower and upper limits of Ce/La ratios in recycled MM [29] and in MM depleted of the economically valuable Nd and Pr.

(iii) quaternary $Al_{11}(Ce_{0.54}La_{0.27}Nd_{0.19})_3$, denoted as $Al_{11}MM_3$, which employs an average MM composition including Nd, as directly obtained from the mining process and as used in prior research [26, 27, 31], Notably, Pr is excluded due to its minimal occurrence in most MM.

Experimental Methods

High-purity Al (99.99% pure, sourced from C-KOE Metals, Euless, TX, USA) with Ce, La, and Nd (each with a purity level of no less than 99.9%, procured from Luciteria Science, Olympia, WA, USA) were arc-melted into 30 g ingots. This procedure was conducted under an argon cover gas within a water-cooled copper crucible. The melting was repeated five times, with the alloy maintained in a liquid state for approximately 30 s during each melting. The ingot was flipped after each melt. The as-cast samples were then sectioned along the solidification direction, mounted, and polished to a 1 μm finish (using diamond suspensions) with a final 0.06 μm finish (using colloidal silica). Post-preparation, the specimens were analyzed using a scanning electron microscope (SEM) and measured for microhardness. For further X-ray diffraction (XRD) and differential scanning calorimetry (DSC) evaluations, the samples underwent a grinding process to yield fine powders.

Microstructural assessments and compositional analyses were undertaken using a Quanta 650 SEM, equipped with an Energy Dispersive X-ray Spectroscopy (EDS) detector. XRD measurements were conducted using a SmartLab diffractometer with Cu-Kα radiation. The scanning rate was approximately 1.5 deg/s. The scanning angle (2θ) was from 10 to 70 deg.

Hardness measurements were conducted with a Buehler Wilson VH3100 indenter, which applied a 5 N load onto the specimen's surface for 5 s. Both Vickers microhardness (HV) and indentation fracture toughness (K_{IC}) were determined from the indent dimensions and observed crack length, with these parameters being determined by the instrument's integrated software. Measurements for HV and K_{IC} were performed at twenty random points on each cross-section, and the resultant data are presented as mean values accompanied by standard deviations.

DSC was performed utilizing a Mettler Toledo TGA/DSC 3+ apparatus. Specimens, each weighing approximately 20 mg, were heated to 850 °C and held for 10 min. Subsequently, the samples underwent two heating–cooling procedures between 850 and 1150 °C, with a consistent temperature change rate of 10 °C/min. Nitrogen cover gas was used throughout to inhibit oxidation. The onset of heat release or absorption peak was used to determine the allotropic temperature for phase transformation.

Results and Discussion

Thermodynamic Analysis

Figure 1a, b illustrates the Thermo-Calc-simulated phase transitions for the $Al_{11}(Ce_{0.5}La_{0.5})_3$ and $Al_{11}MM_3$ IM compounds. It is predicted that, during congruent solidification, Ce segregates into the $Al_{11}Ce_3$ compound, while La and Nd form a separate $Al_{11}(La, Nd)_3$ compound. However, the validity of this dual-phase prediction, comprising both $Al_{11}Ce_3$ and $Al_{11}(La, Nd)_3$ phases, is debatable. Previous research has identified the single-phase $Al_{11}(Ce, La, Nd)_3$ formation in various Al alloys [26, 32] and Mg alloys [27, 31]. In this study, we will experimentally demonstrate the complete solubility of Ce, La, and Nd in the pure $Al_{11}RE_3$ compounds, for various Ce/La ratios.

$Al_{11}RE_3$ compounds exhibit phase transformations between a high-temperature tetragonal phase (β-$Al_{11}RE_3$, I4/mmm) and a low-temperature orthorhombic phase (α-$Al_{11}RE_3$, Immm). The transformation temperatures (T_{trans}) from the literature are 1006 °C for $Al_{11}Ce_3$ [33], 915 °C for $Al_{11}La_3$ [34, 35], and 950 °C for $Al_{11}Nd_3$ [36]. The reported allotropic temperatures align well with our DSC measurements for $Al_{11}Ce_3$ and $Al_{11}La_3$. For other compounds ($Al_{11}(Ce_{0.75}La_{0.25})_3$, $Al_{11}MM_3$, and $Al_{11}(Ce_{0.5}La_{0.5})_3$), our T_{trans} measurements are also shown in Fig. 1c. $Al_{11}Ce_3$ displays the highest T_{trans} at 1006 °C. As La is substituted in, T_{trans} drops consistently, reaching 918 °C for $Al_{11}La_3$. As these transformation temperatures are notably higher than the eutectic temperatures for Al-MM alloys, the low-temperature α-$Al_{11}RE_3$ phase is anticipated to form directly during the solidification of these alloys.
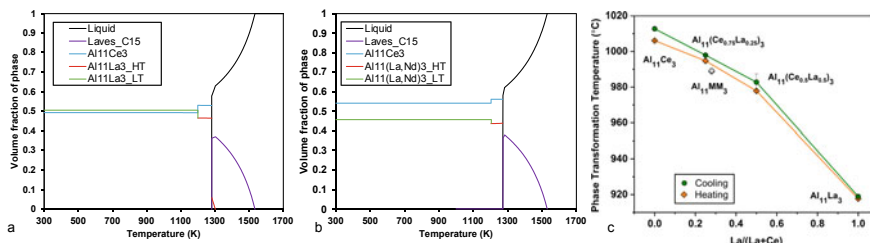
Fig. 1 a, **b** Thermo-Calc simulation results (with TCAL8: Al-Alloys V8.1 database) showing volume fractions of equilibrium phases at various temperatures for **a** $Al_{11}(Ce_{0.5}La_{0.5})_3$ and **b** $Al_{11}MM_3$. Mischmetal (MM) composition is Ce-27La-19Nd (at.%). **c** Allotropic phase transformation temperatures (between high-temperature β-$Al_{11}RE_3$ phase and low-temperature α-$Al_{11}RE_3$ phase) for $Al_{11}Ce_3$, $Al_{11}(Ce_{0.75}La_{0.25})_3$, $Al_{11}MM_3$, $Al_{11}(Ce_{0.5}La_{0.5})_3$, and $Al_{11}La_3$ compounds, as measured by DSC. The horizontal axis represents the La/(Ce + La) atomic ratio. Onset transformation temperatures during cooling and heating are plotted

Microstructures and Phase Formation

Microstructures

The microstructures of binary $Al_{11}La_3$ and $Al_{11}Ce_3$ compounds are shown in Fig. 2. In Fig. 2a, e, both compounds have coarse (mm-scale) grains elongated along the solidification direction with aligned dendrites. Examples of grain boundaries are highlighted by dashed yellow lines. Frequently observed cracks, marked by red arrows, likely result from internal stresses during cooling, which could arise from: (i) solidification, given the volumetric contraction transitioning from a low-density liquid to a high-density solid phase, and (ii) allotropic transformation, attributed to the volume change from the denser β phase to the less dense α phase. The rapid cooling after arc melting might not allow for sufficient creep relaxation of the internal stresses, leading to crack formation.

Examples of the inter-dendritic areas are highlighted by red dashed lines in Fig. 2a, b, e, f. Aluminum enrichment in some inter-dendritic areas can be observed in the EDS elemental distribution maps in Fig. 2c, g. According to phase diagrams, these
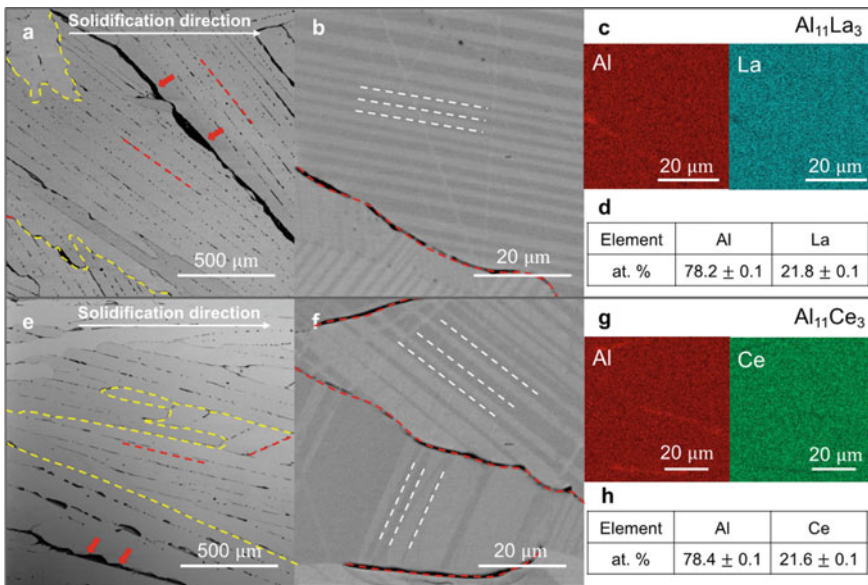
Fig. 2 **a**, **b**, **e**, **f** SEM images showing the microstructures of the $Al_{11}La_3$ and $Al_{11}Ce_3$ compounds. **a**, **e** low-magnification micrographs showing coarse and elongated grain with cracks formed during the solidification process (as indicated by red arrows); red dashed lines indicate inter-dendritic areas while yellow dashed lines provide examples of grain boundaries; **b**, **f** high-magnification micrographs showing twins (highlighted by white dashed lines as examples) and inter-dendritic areas marked by red dashed lines; **c**, **g** EDS map scans showing the elemental distributions for images **b**, **f**, with the inter-dendritic areas rich in Al. **d**, **h** Overall compositions of the $Al_{11}La_3$ and $Al_{11}Ce_3$ samples as measured by EDS

thin regions are pure Al, due to a locally slight Al excess in these line-compound alloys. Twins, highlighted by the white dashed lines in Fig. 2b, f, are prominent in both samples. They likely emerge post-solidification during the allotropic transition from β to α phase, in agreement with previous observations in arc-melted $Al_{11}Ce_3$ [22]. Such twinning was also observed in Al_4Ca (close to the $Al_{11}MM_3$ stoichiometry) due to a phase transformation at 130 °C from a tetragonal $D1_3$ to a monoclinic phase [37]. Figure 2d, h displays the alloy compositions as measured by EDS, which are both aligning closely to the nominal stoichiometric composition of Al-21.4Ce/La (at%).

Figure 3 shows the microstructure of ternary $Al_{11}(Ce_{0.75}La_{0.25})_3$, with elongated grains similar to the $Al_{11}La_3$ and $Al_{11}Ce_3$ compounds. In Fig. 3a, grain boundaries, major cracks, and inter-dendritic areas are highlighted with yellow dashed lines, red arrows, and red dashed lines, respectively. In the higher-magnification SEM image in Fig. 3b, examples of twins are marked by the yellow dashed box. The inter-dendritic areas are highlighted by red dashed lines. The EDS maps in Fig. 3d show that these inter-dendritic areas as Al-rich and Ce- and La-deficient. Notably, Ce and La are uniformly distributed within the $Al_{11}(Ce_{0.75}La_{0.25})_3$ cross-section, which contradicts the Thermo-Calc-predicted phase separation into $Al_{11}Ce_3$ and $Al_{11}La_3$ in Fig. 1a, b. Figure 3c shows the EDS-determined composition, which closely aligns with the nominal composition of Al-16.0Ce-5.4La (at%), albeit slightly enriched in Al and depleted in Ce.

Figure 4 shows the microstructure of $Al_{11}(Ce_{0.5}La_{0.5})_3$. In Fig. 4a, two distinct phases are visible: a darker primary phase with elongated grains (examples of grain boundaries are indicated by yellow dashed lines), and a secondary, lighter-contrast phase within inter-dendritic areas (red dashed lines). A magnified SEM image (Fig. 4b) shows the secondary phase (region 2) with the primary phase (regions 1 and 3). Twins are evident in the primary phase (region 3). The EDS maps in Fig. 4d show Ce and La's concurrent presence, in disagreement with the phase separation predicted by Thermo-Calc in Fig. 1a, b. There is a noticeable Al deficiency in region 2 (white outline). Figure 4c lists the compound compositions determined by EDS. The overall composition is Al-lean versus the nominal composition of Al-10.7Ce-10.7La (at%). The secondary phase composition aligns with $Al_3(Ce_{0.5}La_{0.5})$'s nominal composition (Al-12.5Ce-12.5La, at%). This is consistent with Al_3RE, a line-compound phase adjacent to $Al_{11}RE_3$ in Al-RE phase diagrams [26], emerging due to a slight Al deficiency during casting. The presence of $Al_3(Ce_{0.5}La_{0.5})$ is further validated by XRD patterns discussed in Sect. 3.2.2. Crucially, there is no Ce and La separation in the $Al_{11}RE_3$ phase from Fig. 4d, indicating full solid solubility for Ce/La atomic ratios between 3 and 1. Considering binary Ce-La alloys possess negative mixing enthalpies [38] and exhibit full solid solubility [39], the absence of a driving force separating Ce and La in the $Al_{11}RE_3$ compound's RE sublattice is anticipated.

Figure 5 presents the microstructures of $Al_{11}MM_3$. Figure 5a displays coarse, elongated grains, similar to those observed in the previous compounds. Red arrows mark long cracks, while examples of grain boundaries and inter-dendritic regions are highlighted by yellow and red dashed lines, respectively. Twins, indicated by white dashed lines, are seen in Fig. 5b. Figure 5d shows EDS elemental maps for Fig. 5a,
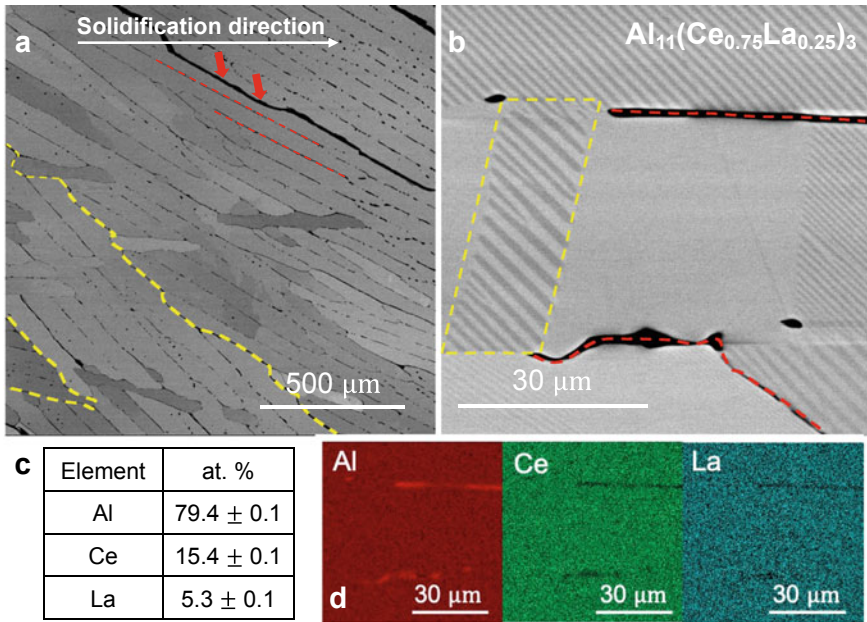
Fig. 3 **a**, **b** SEM images showing the microstructure of the $Al_{11}(Ce_{0.75}La_{0.25})_3$ compound: **a** the low-magnification image displaying the elongated $Al_{11}(Ce_{0.75}La_{0.25})_3$ dendrites with cracks formed during solidification (red arrows); red dashed lines indicate inter-dendritic regions, while yellow dashed lines provide examples of grain boundaries; **b** the high-magnification image showing twins (examples are highlighted within the yellow dashed box) with inter-dendritic area rich in Al (marked by red dashed lines). **c** The overall composition of the sample as measured by EDS. **d** EDS map scans showing the elemental distributions for image **b**, with inter-dendritic areas having an enrichment in Al and the depletion in Ce and La
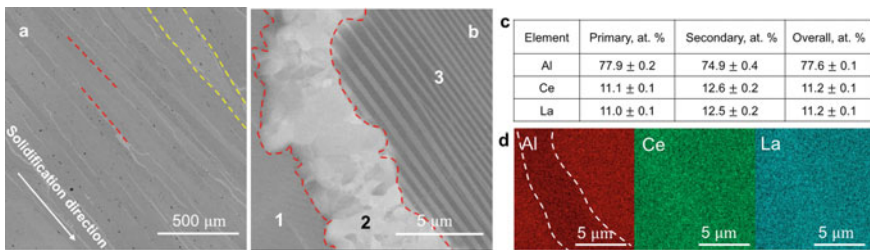
Fig. 4 **a**, **b** SEM images showing the microstructure of the $Al_{11}(Ce_{0.5}La_{0.5})_3$ compound: **a** the low-magnification image displaying the elongated $Al_{11}(Ce_{0.5}La_{0.5})_3$ dendrites and the inter-dendritic areas with lighter-contrast phase (red dashed lines); the yellow dashed lines provide examples of grain boundaries; **b** the high-magnification image showing the primary phase (in darker contrast, labeled as region 1 and 3), a secondary phase emerging in the inter-dendritic region (in white contrast, labeled as region 2), and the appearance of twins within the primary phase (in region 3). **c** Overall sample composition, and the compositions of the primary and secondary phases, as determined by EDS analysis. **d** EDS map scans displaying the elemental distributions for image (**b**). The secondary phase, outlined by white dashed lines, is slightly depleted in Al

Element	Al	Ce	La	Nd
at. %	78.6 ± 0.1	11.7 ± 0.1	5.9 ± 0.1	3.8 ± 0.1
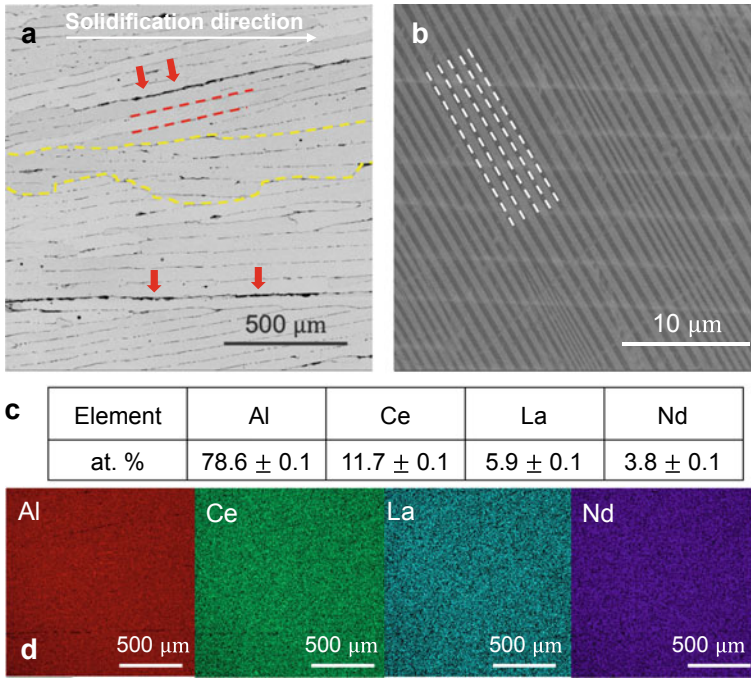
Fig. 5 **a**, **b** SEM images showing the microstructure of the $Al_{11}MM_3$ compound (where MM = $Ce_{0.54}La_{0.27}Nd_{0.19}$): **a** the low-magnification image displays elongated dendrites with cracks that formed during the solidification process, indicated by red arrows. The red dashed lines indicate inter-dendritic areas, while yellow dashed lines provide examples of grain boundaries; **b** the high-magnification image showing twins (highlighted by the white dashed lines as examples). **c** The overall composition of the sample as measured via EDS. **d** EDS map scans displaying the elemental distributions for image (**a**)

revealing Ce, La, and Nd's concurrent presence, and complete solid solubility on the RE sublattice, in the $Al_{11}RE_3$ phase. This indicates that $Al_{11}MM_3$ can act as a single strengthening phase in Al-MM eutectic alloys. The EDS-determined composition in Fig. 5c closely matches the nominal composition of $Al_{11}(Ce_{0.54}La_{0.27}Nd_{0.19})_3$, or Al-11.6Ce-5.8La-4.0Nd (at%).

Phase Formation and Lattice Mismatch Analysis

Figure 6a shows the XRD patterns of the as-cast $Al_{11}Ce_3$, $Al_{11}(Ce_{0.75}La_{0.25})_3$, $Al_{11}MM_3$, $Al_{11}(Ce_{0.5}La_{0.5})_3$, and $Al_{11}La_3$ compounds. All compounds exhibit the orthorhombic (Immm) low-temperature α-$Al_{11}RE_3$ phase, except for $Al_{11}(Ce_{0.5}La_{0.5})_3$, where a secondary phase with hexagonal $P6_3/mmc$ structure is observed. According to (PDF00-054-0358) [40], this hexagonal $P6_3/mmc$ structure corresponds to the secondary $Al_3(Ce_{0.5}La_{0.5})$ phase with light contrast in Fig. 4.
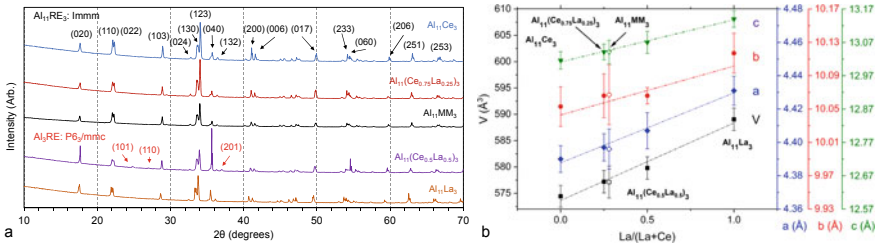
Fig. 6 a X-ray diffraction patterns for the $Al_{11}Ce_3$, $Al_{11}(Ce_{0.75}La_{0.25})_3$, $Al_{11}MM_3$, $Al_{11}(Ce_{0.5}La_{0.5})_3$, and $Al_{11}La_3$ compounds (where MM = $Ce_{0.54}La_{0.27}Nd_{0.19}$). All compounds form the orthorhombic α-phase (Immm space group No. 71), except for the $Al_{11}(Ce_{0.5}La_{0.5})_3$ compound, which also exhibits a minor presence of the $Al_3(Ce_{0.5}La_{0.5})$ phase (hexagonal, P63/mmc space group No.194) due to a slight Al deficiency during alloy synthesis. **b** Plot showing the effect of the La/(La + Ce) ratio on the lattice unit cell volume (left y-axis) and individual lattice parameters (right y-axis) for the five compounds. For the $Al_{11}MM_3$ compound (represented by hollow markers), the x-axis value corresponds to the La/(Ce + La + Nd) ratio

Figure 6b displays the lattice parameters and unit cell volumes for the five $Al_{11}RE_3$ phases, exhibiting systematic variations with RE compositions. Considering that the ionic atomic radii of Nd, Ce, and La with coordinate number 6 in the Orthorhombic structure are 98.3, 101, and 103.2 pm [41], respectively, the incorporation of the larger La atom results in increased lattice parameters. However, these variations across the compounds are relatively subtle, remaining within a 1% difference.

Mechanical Properties

Figure 7 compares the hardness and indentation fracture toughness of the $Al_{11}Ce_3$, $Al_{11}(Ce_{0.75}La_{0.25})_3$, $Al_{11}MM_3$, $Al_{11}(Ce_{0.5}La_{0.5})_3$, and $Al_{11}La_3$ compounds. They are brittle, with low toughness values spanning 0.48–0.65 MPa m$^{1/2}$. They exhibit high hardness, with values within the range of 4.1 to 4.3 GPa (the hardness value of $Al_{11}Ce_3$ agrees with a prior measurement [22]). Given the similar hardness values within the experimental error, it can be concluded that the mixture of Ce and La in the $Al_{11}RE_3$ sublattice has a negligible solid-solution strengthening effect. It is thus inferred that the strengthening from the $Al_{11}RE_3$ phases in Al-RE alloys is likely to be comparable.

Figure 7 also compares the hardness values for various Al_3X trialuminides (which also form eutectic or peritectic phases with Al in Al-X alloys), including Al_3Sc (L1$_2$) [42], Al_3V (D0$_{22}$) [42], Al_3Ti (D0$_{22}$) [42], Al_3Zr (D0$_{23}$) [42], and Al_3Ni (D0$_{11}$) [43]. $Al_{11}RE_3$ compounds have higher hardness (i.e., strength) in comparison to the Al_3Sc phase with the cubic FCC-like L1$_2$ structure, which is known to exhibit plasticity [44, 45]. In contrast, the lower crystallographic symmetry phases, including the tetragonal D0$_{22}$-Al_3V and -Al_3Ti, D0$_{23}$-Al_3Zr, and orthorhombic D0$_{11}$-Al_3Ni phases, exhibit
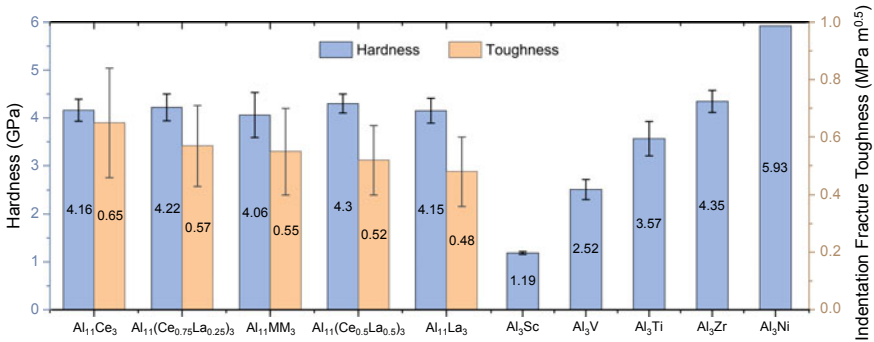
Fig. 7 The hardness and indentation fracture toughness for $Al_{11}Ce_3$, $Al_{11}(Ce_{0.75}La_{0.25})_3$, $Al_{11}MM_3$, $Al_{11}(Ce_{0.5}La_{0.5})_3$, and $Al_{11}La_3$ compounds are displayed on left and right axes. Hardness data for trialuminide compounds (Al_3Sc, Al_3V, Al_3Ti, Al_3Zr, and Al_3Ni) from the literature are plotted for comparison

a range of hardness values below (for Al_3V), similar (for Al_3Ti and Al_3Zr) or even above (for Al_3Ni) those measured here for $Al_{11}RE_3$.

Conclusions

We investigated the microstructure and mechanical properties of $Al_{11}RE_3$ compounds – binary $Al_{11}Ce_3$ and $Al_{11}La_3$, ternary $Al_{11}(Ce_{0.75}La_{0.25})_3$ and $Al_{11}(Ce_{0.5}La_{0.5})_3$ and quaternary $Al_{11}(Ce_{0.54}La_{0.27}Nd_{0.19})_3$ which is represented as $Al_{11}MM_3$. This research, which is also reported in a peer-reviewed journal [46], yields the following key conclusions:

1. All five $Al_{11}RE_3$ compounds undergo a phase transformation from a high-temperature β phase to a low-temperature α phase with an orthorhombic structure (Immm). A decrease in allotropic temperatures, as measured by DSC, is observed with rising La content, ranging from 1006 °C in $Al_{11}Ce_3$ to 918 °C in $Al_{11}La_3$.
2. The arc-melted $Al_{11}RE_3$ compounds display elongated grains on the millimeter scale, coupled with a high density of twins. The twins might form during cooling post-solidification, e.g., during the allotropic phase transformation.
3. The lattice parameters of the α-$Al_{11}RE_3$ compounds increase with increasing La content.
4. The α-$Al_{11}RE_3$ compounds exhibit, at ambient temperature, a narrow range of high microhardness values (4.1–4.3 GPa) and low indentation fracture toughness (0.48 to 0.65 MPa $m^{1/2}$).
5. The similarities among the five α-$Al_{11}RE_3$ compounds, in terms of crystal structure, lattice parameters, hardness, and indentation fracture toughness, indicate that their strengthening capability in Al-RE eutectic alloys could be similar. Consequently, the partial or complete replacement of Ce with La or MM in

Al-Ce eutectic alloys, leading to the formation of the α-Al$_{11}$RE$_3$ phase upon solidification, appears to be a feasible path toward creating cost-effective alloys with reduced energy consumption and CO$_2$ emissions.

References

1. Liu Y, Michi RA, Dunand DC (2019) Cast near-eutectic Al-12.5 wt.% Ce alloy with high coarsening and creep resistance. Mater Sci Eng, A 767:138440. https://doi.org/10.1016/J.MSEA.2019.138440
2. Czerwinski F (2019) Cerium in aluminum alloys. J Mater Sci 55(1):24–72. https://doi.org/10.1007/S10853-019-03892-Z
3. Weiss D (2019) Improved high-temperature aluminum alloys containing cerium. J Mater Eng Perform 28:1903–1908. https://doi.org/10.1007/S11665-019-3884-2
4. Czerwinski F, Amirkhiz BS (2020) On the Al–Al11Ce3 eutectic transformation in aluminum-cerium binary alloys. Materials 13:1–27. https://doi.org/10.3390/MA13204549
5. Wu T, Plotkowski A, Shyam A, Dunand DC (2022) Microstructure and creep properties of cast near-eutectic Al–Ce–Ni alloys. Mater Sci Eng, A 833:142551. https://doi.org/10.1016/J.MSEA.2021.142551
6. Ng DS, Dunand DC (2020) Aging- and creep-resistance of a cast hypoeutectic Al-6.9Ce-9.3Mg (wt.%) alloy. Mater Sci Eng, A 786:139398. https://doi.org/10.1016/J.MSEA.2020.139398
7. Sims ZC, Rios OR, Weiss D, Turchi PEA, Perron A, Lee JRI, Li TT, Hammons JA, Bagge-Hansen M, Willey TM, An K, Chen Y, King AH, McCall SK (2017) High performance aluminum–cerium alloys for high-temperature applications. Mater Horiz 4:1070–1078. https://doi.org/10.1039/C7MH00391A
8. Plotkowski O, Rios N, Sridharan Z, Sims K, Unocic RT, Ott RR, Dehoff SS (2017) Babu, evaluation of an Al-Ce alloy for laser additive manufacturing. Acta Mater 126:507–519. https://doi.org/10.1016/J.ACTAMAT.2016.12.065
9. Zhou L, Huynh T, Park S, Hyer H, Mehta A, Song S, Bai Y, McWilliams B, Cho K, Sohn Y (2020) Laser powder bed fusion of Al–10 wt% Ce alloys: microstructure and tensile property. J Mater Sci 55:14611–14625. https://doi.org/10.1007/S10853-020-05037-Z

10. Ekaputra CN, Weiss D, Mogonye JE, Dunand DC (2023) Eutectic, precipitation-strengthened alloy via laser fusion of blends of Al-7Ce-10Mg (wt.%), Zr, and Sc powders. Acta Mater 246:118676. https://doi.org/10.1016/J.ACTAMAT.2023.118676

11. Ekaputra CN, Rakhmonov JU, Weiss D, Mogonye JE, Dunand DC (2022) Microstructure and mechanical properties of cast Al-Ce-Sc-Zr-(Er) alloys strengthened by Al11Ce3 microplatelets and L12 Al3(Sc, Zr, Er) nano-precipitates. Acta Mater 240:118354. https://doi.org/10.1016/J.ACTAMAT.2022.118354

12. Sisco K, Plotkowski A, Yang Y, Leonard D, Stump B, Nandwana P, Dehoff RR, Babu SS (2021) Microstructure and properties of additively manufactured Al–Ce–Mg alloys. Sci Rep 11(1):1–14. https://doi.org/10.1038/s41598-021-86370-4

13. Henderson HB, Hammons JA, Baker AA, McCall SK, Li TT, Perron A, Sims ZC, Ott RT, Meng F, Thompson MJ, Weiss D, Rios O (2021) Enhanced thermal coarsening resistance in a nanostructured aluminum-cerium alloy produced by additive manufacturing. Mater Des 209:109988. https://doi.org/10.1016/J.MATDES.2021.109988

14. Zhang, Peng P, Lv H, Gao H, Wang Y, Wang J, Sun B (2022) Orientation relationships and interface structure between Al11Ce3 and Al in Al–Ce eutectic. J Mater Res Technol 18:693–704. https://doi.org/10.1016/J.JMRT.2022.02.132

15. Sun Y, Hung C, Hebert RJ, Fennessy C, Tulyani S, Aindow M (2019) Eutectic microstructures in dilute Al-Ce and Al-Co alloys. Mater Charact 154:269–276. https://doi.org/10.1016/J.MATCHAR.2019.06.010

16. Sims ZC, Weiss D, McCall SK, McGuire MA, Ott RT, Geer T, Rios O, Turchi PAE (2016) Cerium-based, intermetallic-strengthened aluminum casting alloy: high-volume co-product development. JOM 68:1940–1947. https://doi.org/10.1007/S11837-016-1943-9

17. Lane RJ, Momen AM, Kesler MS, Brechtl J, Rios O, Nawaz K, Mirzaeifar R (2021) Developing an experimental-computational framework to investigate the deformation mechanisms and mechanical properties of Al-8Ce-10Mg alloys at micro and macroscales. Mater Today Commun 28:102674. https://doi.org/10.1016/J.MTCOMM.2021.102674

18. Hu, Quan B, Li D, Wang X, Li Z, Zeng X (2021) Solid solution strengthening mechanism in high pressure die casting Al–Ce–Mg alloys. Mater Sci Eng, A 812:141109. https://doi.org/10.1016/J.MSEA.2021.141109

19. Stromme ET, Henderson HB, Sims ZC, Kesler MS, Weiss D, Ott RT, Meng F, Kassoumeh S, Evangelista J, Begley G, Rios O (2018) Ageless aluminum-cerium-based alloys in high-volume die casting for improved energy efficiency. JOM 70:866–871. https://doi.org/10.1007/S11837-018-2861-9

20. Belov NA, Naumova EA, Eskin DG (1999) Casting alloys of the Al–Ce–Ni system: microstructural approach to alloy design. Mater Sci Eng, A 271:134–142. https://doi.org/10.1016/S0921-5093(99)00343-3

21. Wu T, Plotkowski A, Shyam A, Dunand DC (2023) Microstructure and mechanical properties of hypoeutectic Al–6Ce–3Ni-0.7Fe (wt.%) alloy. Mater Sci Eng, A 875:145072. https://doi.org/10.1016/J.MSEA.2023.145072

22. Wu T, Dunand DC (2022) Microstructure and thermomechanical properties of Al11Ce3. Intermetallics (Barking) 148:107636. https://doi.org/10.1016/J.INTERMET.2022.107636

23. Ding WJ, Yi JX, Chen P, Li DL, Peng LM, Tang BY (2012) Elastic properties and electronic structures of typical Al–Ce structures from first-principles calculations. Solid State Sci 14:555–561. https://doi.org/10.1016/J.SOLIDSTATESCIENCES.2012.02.006

24. Fan T, Lin L, Liang H, Ma Y, Tang Y, Hu T, Ruan Z, Chen D, Wu Y (2023) First-principles study of the structural, mechanical and thermodynamic properties of Al11RE3 in aluminum alloys. Crystals 13:347. https://doi.org/10.3390/CRYST13020347

25. Liu T, Ma T, Li Y, Ren Y, Liu W (2022) Stabilities, mechanical and thermodynamic properties of Al–RE intermetallics: a first-principles study. J Rare Earths 40:345–352. https://doi.org/10.1016/J.JRE.2020.11.009

26. Sims ZC, Weiss D, Rios O, Henderson HB, Kesler MS, McCall SK, Thompson MJ, Perron A, Moore EE (2020) The efficacy of replacing metallic cerium in aluminum–cerium alloys with LREE mischmetal. Miner Metals Mater Ser 216–221. https://doi.org/10.1007/978-3-030-36408-3_30

27. Zhang J, Liu S, Leng Z, Zhang M, Meng J, Wu R (2011) Microstructures and mechanical properties of heat-resistant HPDC Mg–4Al-based alloys containing cheap misch metal. Mater Sci Eng, A 528:2670–2677. https://doi.org/10.1016/J.MSEA.2010.12.031

28. Talens Peiró L, Villalba Méndez G (2013) Material and energy requirement for rare earth production, JOM 65:1327–1340. https://doi.org/10.1007/S11837-013-0719-8/TABLES/9

29. Yurramendi L, Gijsemans L, Forte F, Aldana JL, del Río C, Binnemans K (2019) Enhancing rare-earth recovery from lamp phosphor waste. Hydrometallurgy 187:38–44. https://doi.org/10.1016/J.HYDROMET.2019.04.030

30. Vargas SJR, Schaeffer N, Souza JC, da Silva LHM, Hespanhol MC (2021) Green separation of lanthanum, cerium and nickel from waste nickel metal hydride battery. Waste Manage 125:154–162. https://doi.org/10.1016/J.WASMAN.2021.02.038

31. Zhang J, Yu P, Liu K, Fang D, Tang D, Meng J (2009) Effect of substituting cerium-rich mischmetal with lanthanum on microstructure and mechanical properties of die-cast Mg–Al– RE alloys. Mater Des 30:2372–2378. https://doi.org/10.1016/J.MATDES.2008.10.028

32. Medvedev AE, Murashkin MY, Enikeev NA, Bikmukhametov I, Valiev RZ, Hodgson PD, Lapovok R (2019) Effect of the eutectic Al-(Ce,La) phase morphology on microstructure, mechanical properties, electrical conductivity and heat resistance of Al-4.5(Ce,La) alloy after SPD and subsequent annealing. J Alloys Compd 796:321–330. https://doi.org/10.1016/J.JALLCOM.2019.05.006

33. Okamoto H (2011) Al-Ce (aluminum-cerium). J Phase Equilibria Diffus. 32:392–393. https://doi.org/10.1007/S11669-011-9914-X

34. Okamoto H (2007) Al-La (aluminum-lanthanum). J Phase Equilib Diffus 28:581. https://doi.org/10.1007/S11669-007-9178-7

35. Eckerlin P, Kandler H (n.d.) Structure data of elements and intermetallic phases. In: AlLa— AlNiZr: datasheet from Landolt-Börnstein—Group III Condensed Matter, vol 6: "Structure data of elements and intermetallic phases". Springer. https://doi.org/10.1007/10201454_23

36. Gschneidener KA, Calderwood FW (1989) The Al-Nd (Aluminum-Neodymium) system. Bull Alloy Phase Diagrams 10:28–30. https://doi.org/10.1007/BF02882168

37. Zogg H, Schwellinger P (1979) Phase transformation of the intermetallic compound Al4Ca. J Mater Sci 14:1923–1932. https://doi.org/10.1007/BF00551033

38. Takeuchi A (2010) Inoue, Mixing enthalpy of liquid phase calculated by miedema's scheme and approximated with sub-regular solution model for assessing forming ability of amorphous and glassy alloys. Intermetallics (Barking) 18:1779–1789. https://doi.org/10.1016/J.INTERMET.2010.06.003

39. Gschneidner KA, Calderwood FW (1982) The Ce-La (cerium-lanthanum) system. Bull Alloy Phase Diagrams 2:445–447. https://doi.org/10.1007/BF02876156

40. Zanicchi G, Riani P, Mazzone D, Marazza R, Rossi D, Ferro R (1994) On some ternary alloys R'-R''-Al with rare earths. J Alloys Compd 215:181–186. https://doi.org/10.1016/0925-8388(94)90838-9

41. Rollinson H, Adetunji J (2018) Ionic radii, pp 738–743. https://doi.org/10.1007/978-3-319-39312-4_340

42. Harada Y, Dunand DC (2002) Microstructure of Al3Sc with ternary transition-metal additions. Mater Sci Eng, A 329–331:686–695. https://doi.org/10.1016/S0921-5093(01)01608-2

43. Mu J, Sha P, Zhu Z, Wang Y, Zhang H, Hu Z (2014) Synthesis of high strength aluminum alloys in the Al–Ni–La system. J Mater Res 29:708–717. https://doi.org/10.1557/JMR.2014.35

44. Fukunaga K, Shouji T, Miura Y (1997) Temperature dependence of dislocation structure of L12–Al3Sc. Mater Sci Eng, A 239–240:202–205. https://doi.org/10.1016/S0921-5093(97)00582-0

45. Harada Y, Dunand DC (2000) Creep properties of Al3Sc and Al3(Sc, X) intermetallics. Acta Mater 48:3477–3487. https://doi.org/10.1016/S1359-6454(00)00142-7

46. Qi J, Dunand DC (2023) Substituting Ce with La and Nd in Al11Ce3: Effect on microstructure and mechanical properties. Acta Mater 261:119357. https://doi.org/10.1016/J.ACTAMAT.2023.119357

Part VI
Poster Session

Effect of MgO, MnO, and Al$_2$O$_3$ on Vanadium Extraction in Sodium Roasting-Water Leaching Process of Vanadium Slag

Liyuan Jiang, Jiang Diao, Hao Qin, Quan Zhang, Wenfeng Tan, Hong-Yi Li, and Bing Xie

Abstract The effect of different oxides in vanadium slag, such as MgO, MnO, and Al$_2$O$_3$ on vanadium extraction in the sodium roasting-water leaching process has been investigated. The results show that the increase of these oxides has a positive influence on the conversion rate of vanadium. At the condition of sodium roasting, with the increase of MgO, MnO, and Al$_2$O$_3$ contents to 11.49%, 14.22%, and 11.13%, the conversion rates of vanadium increased from 89.9% to 97.3%, 98.0% and 95.8%, respectively. With increasing MgO content, more vanadium transformed into spinel phase. The roasting and leaching parameters have also been optimized. 97.3% of vanadium could be extracted from high MgO vanadium slag at the following conditions: roasting temperature of 800 °C, V/Na molar ratio 0.2; leaching time of 60 min, liquid/solid ratio of 10:1. The results can provide a fundamental basis to the modification of vanadium slag based on slag splashing in vanadium extraction converter.

Keywords Vanadium slag · High MgO content · Extraction · Conversion rate

Introduction

Vanadium is a valuable nonferrous element widely applied in numerous fields, such as steel, aerospace, automobile, and new energy industries due to its special chemical and physical properties [1–3]. Because of this, worldwide demand for vanadium has skyrocketed [4]. According to statistics, 76.2% of the world's vanadium products are extracted from vanadium slag [5]. In China, the grade evaluation of vanadium slag is determined by the chemical composition of vanadium slag. According to the technological requirements for extracting V$_2$O$_5$ from vanadium slag through the sodium roasting-water leaching process, the lower the content of SiO$_2$, P, and CaO,

L. Jiang · J. Diao (✉) · H. Qin · Q. Zhang · W. Tan · H.-Y. Li · B. Xie
College of Materials Science and Engineering, Chongqing University, Chongqing 400044, China
e-mail: diaojiang@163.com

the higher the grade of vanadium slag. In addition, the grade of vanadium slag is also determined by the concentration of V_2O_5 (actually V_2O_3) in the slag. Generally, the higher the content of V_2O_5 in the slag, the higher the conversion rate of vanadium element in the sodium roasting process [6].

The concentration of CaO in vanadium slag is strictly limited as CaO would react with vanadium oxides to generate water-insoluble calcium vanadates such as $Ca(V_2O_3)_2$ and $CaV_{12}O_{30}$ etc. [7, 8]. It is reported that for every 1% increase in the mass fraction of CaO in vanadium slag, the loss of V_2O_5 will be 4.7–9.0% [9]. CaO also affects the existing form of vanadium element in vanadium slag. When CaO content is higher than 12.89%, vanadium may exist simultaneously as (Mn, Fe, Mg)V_2O_4 in dendritic-like spinels and $Ca_3V_2(SiO_4)_3$ in the matrix phase [10–13]. SiO_2 mainly exists as olivine in vanadium slag, which is a low melting point phase in vanadium slag [14]. The olivine often encapsulates the spinel and hinders the oxidation and decomposition of vanadium spinel. SiO_2 is also easy to produce soluble vitreous body in sodium roasting. In the water leaching process, the hydrolysis reaction precipitates glial SiO_2, which causes the filter screen to be blocked and the leaching efficiency to be reduced [15]. Phosphorus would generate soluble phosphate during the sodium roasting process, which has a great influence on the precipitation of vanadium, and it seriously affects the grade of vanadium products [16].

However, in addition to the above components, there is no systematic study on the effect of other components in vanadium slag on the quality of vanadium slag. For instance, there are different views on the influence of MnO in vanadium slag. Some people believe that MnO is a useful component, which can catalyze the oxidation of vanadium spinel [17]. However, there are also studies suggesting that MnO has a negative impact on the filtration process and the grade of vanadium slag [18]. Al_2O_3, TiO_2, Cr_2O_3, and other components in vanadium slag would displace V_2O_3 as a solid solution in spinel. MgO can exist both in the spinel and silicate phases. Sometimes, the content of these components may be adjusted. For example, the slag splashing operation needs to increase the MgO content in vanadium slag. The increase of this oxide content may affect the conversion of vanadium during the sodium roasting process. Therefore, the purpose of this work is to explore the effect of MgO, MnO, and Al_2O_3 on vanadium extraction in the sodium roasting-water leaching process of vanadium slag, and provide a reference for the composition adjustment of vanadium slag based on process needs.

Experimental

Materials

The original vanadium slag (M0) used in the experiments was collected from Pan Steel in China. Analytical reagents were added to the original vanadium slag to prepare the pre-melted vanadium slag with different MgO, MnO, and Al_2O_3 content.

Table 1 Chemical composition of slag samples, wt %

No.	FeO	CaO	SiO$_2$	TiO$_2$	V$_2$O$_3$	MnO	Cr$_2$O$_3$	P$_2$O$_5$	Al$_2$O$_3$	MgO
M0	39.12	1.63	12.45	16.9	13.05	8.01	2.07	0.12	3.13	3.52
M1	37.98	1.58	12.09	16.41	12.67	7.78	2.01	0.12	3.04	6.33
M2	36.91	1.54	11.75	15.94	12.31	7.56	1.95	0.11	2.95	8.98
M3	35.89	1.5	11.42	15.5	11.97	7.35	1.9	0.11	2.87	11.49
M4	36.47	1.53	11.61	15.76	12.17	14.22	1.93	0.11	2.92	3.28
M5	35.89	1.5	11.42	15.5	11.97	7.35	1.9	0.11	11.13	3.23

The chemical compositions of the slag samples are shown in Table 1. The deionized water used in the leaching process was produced by a water purifier (Millipore Aquelix 5).

Experimental Procedure

The vanadium slag samples were ground to less than 74 µm in particle size. 3 g powder of slag sample was mixed with 0.63–2.54 g Na$_2$CO$_3$. The mixture was charged in a ceramic evaporation dish and heated in a muffle furnace at 600–800 °C for 2 h. In the roasting process, the mixture was stirred occasionally to prevent agglomeration of materials. The furnace door was half opened to maintain the constant oxidizing atmosphere. After the roasting was finished, the roasted clinker was naturally cooled to room temperature. Then, the roasted clinker was ground to less than 74 µm in particle size. 0.2 g powder of roasted clinker was leached with 2–10 ml deionized water to extract soluble vanadate in the water bath with a rotary magnet rotor at a speed of 200 r/min. The leaching time was between 5 and 120 min. The leaching temperature was 20 °C. After the leaching was finished, the slurry was filtrated using a syringe filter (< 0.40 µm). The leaching liquid was diluted to 500 mL in a volumetric flask. 0.5 g powder of slag sample was leached with 80 ml aqua regia for 2 h at 25 °C. The suspension liquid was diluted to 1 L in the volumetric flask. The concentrations of vanadium in the leaching liquid and aqua regia were determined by inductively coupled plasma-atomic emission spectrometry (ICP-AES, ICAP6300 DUO, ThermoFisher Scientific).

Calculation of Conversion Rate

The conversion rate of vanadium in the sodium roasting-water leaching process can be calculated through Eq. (1).

$$\text{Conversion rate} = \frac{5N}{M} \tag{1}$$

where N denotes the concentration of vanadium in the leaching liquid; M is the concentration of vanadium in the aqua regia.

Results and Discussion

Effect of Different Oxides on the Conversion Rate of Vanadium

Figure 1 shows the conversion rates of vanadium in slag samples with different oxides. All the conversion rates were measured under the same experimental conditions. In the roasting step, the roasting temperature and holding time were controlled at 800 °C and 120 min, respectively. In the leaching step, the liquid/solid ratio and leaching time were controlled at 10:1 (mL/g) and 60 min, respectively. At the condition of direct roasting, the conversion rates of vanadium increased from 54.3% to 63.9%, 85.4%, and 89.9%, respectively, with the increase of MgO, MnO, and Al_2O_3 contents to 11.49%, 14.22% and 11.13%, respectively. At the condition of sodium roasting (the V/Na molar ratio is controlled at 0.2), the conversion rates of vanadium increased from 89.9% to 94.6%, 98.0%, and 95.8%, respectively. It can be concluded that these oxides not only do not impede the conversion of vanadium but increase the conversion rate of vanadium.

Fig. 1 Conversion rates of vanadium in slag samples with different oxides. Roasting step: 800 °C, 120 min, V/Na molar ratio 0.2 (for sodium roasting); leaching step: 60 min, liquid/solid 10:1 (mL/g)
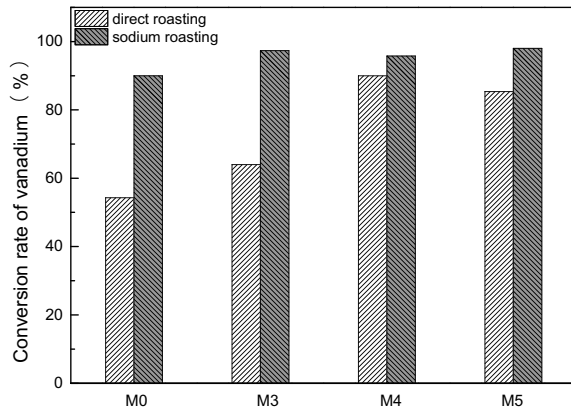
Effect of MgO Concentration on the Conversion Rate of Vanadium

The slag composition of vanadium slag and ordinary converter steel slag is completely different. As the content of CaO is strictly limited in the vanadium slag, lime cannot be added to the vanadium extraction converter in the slag splashing operation. Therefore, the content of MgO in vanadium slag must be increased in the slag splashing operation. Figure 2 shows the conversion rates of vanadium in slag samples with different MgO concentrations. With the MgO concentration increasing from 3.52% to 8.98%, the conversion rate of vanadium increases from 88.9% to 97.3%. After that, the conversion rate of vanadium no longer increases.

In order to further explore the role of MgO, the mineral phases of vanadium slags with different MgO concentrations were characterized by XRD. As Fig. 3 shows, the V-bearing phase in the vanadium slag is $(Fe, Mg, Mn)(V, Cr)_2O_4$ spinel. In addition, accompanied by olivine phase $(Fe, Mg)_2SiO_4$ and pyroxene phase $(Ca, Fe, Mg)SiO_3$. With MgO concentration increases, the intensities of diffraction peaks of the spinel phases enhance together with Fe_2SiO_4 and Mg_2SiO_4. There are not any new phases generated. The XRD result indicates that more vanadium transformed into a spinel phase with increasing MgO concentration. This can be explained by the following two aspects. On the one hand, MgO can react with V_2O_3 to form MgV_2O_4 spinel; on the other hand, a certain amount of MgO can reduce the viscosity of slag, and promote the diffusion of vanadium into the spinel phase (Fig. 3).
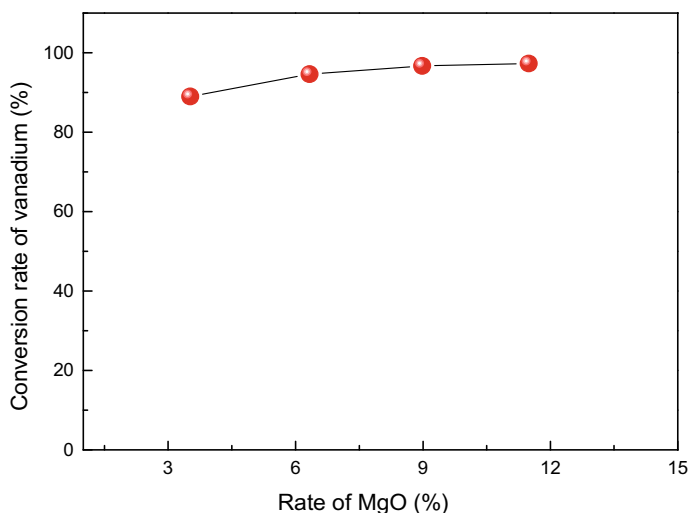
Fig. 2 Conversion rates of vanadium in slag samples with different MgO concentrations. Roasting step: 800 °C, 120 min, V/Na molar ratio 0.2; leaching step: 60 min, liquid/solid 10:1 (mL/g)
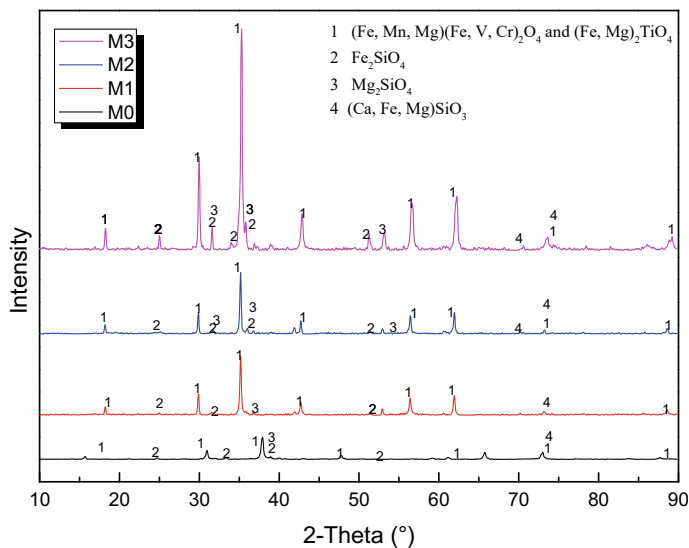
Fig. 3 XRD patterns of the slag samples with different MgO concentrations

Effect of Roasting Parameters on the Conversion Rate of High MgO Vanadium Slag

Roasting temperature is a key parameter for the transition of the vanadium phase. It has an important influence on the extraction of vanadium. Figure 4 shows the conversion rates of high MgO vanadium slag at different roasting temperatures. It can be found that the maximum conversion rate of vanadium reached 97.3%. The optimal roasting temperature of 800 °C is in good agreement with previous studies [8, 19, 20]. This is also similar to the conventional vanadium slag. Further increase in the roasting temperature would lead to a decrease in the conversion rate of vanadium. Because, a large amount of newly generated $NaVO_3$ (melting point: 630 °C) melted at high temperatures and covered on the surface of unreacted spinels, which thus hinders further oxidation of spinels [8]. On the contrary, the low temperature makes it difficult to ensure that vanadium is completely converted from spinel to soluble vanadate.

Figure 5 shows the conversion rates of high MgO vanadium slag at different V/Na molar ratios. When the V/Na molar ratio exceeds 0.2, the conversion rate of vanadium decreases from 97.3% to 79.8%. A high V/Na molar ratio makes it difficult to guarantee the complete transformation of vanadium spinel. However, when the V/Na molar ratio is lower than 0.2, the conversion rate of vanadium also decreases. This is due to the excessive Na_2CO_3 combined with V_2O_5 to form liquid vanadates, which leads to agglomeration of roasted clinker. Therefore, the optimal V/Na molar ratio is considered as 0.2. The corresponding addition of soda is more than the
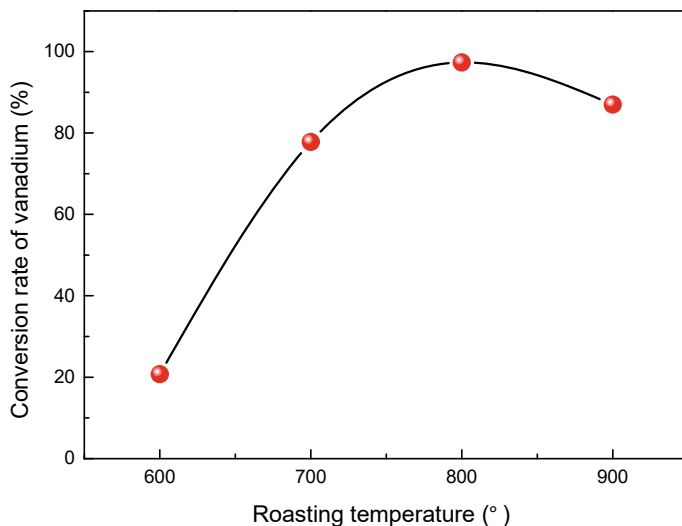
Fig. 4 Influence of roasting temperature on the conversion rate of high MgO vanadium slag. Roasting step: 120 min, V/Na molar ratio 0.2; leaching step: 60 min, liquid/solid 10:1 (mL/g)

stoichiometric one. That is due to other components, such as SiO_2 and Al_2O_3 also consuming considerable amounts of soda during roasting.
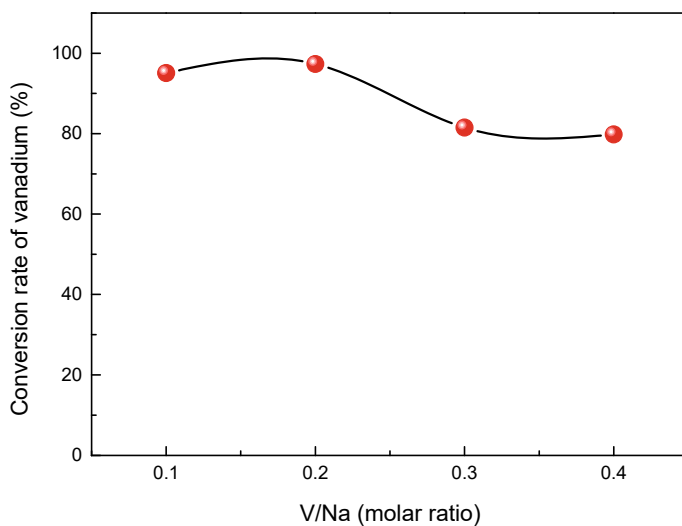
Fig. 5 Influence of V/Na molar ratio on the conversion rate of high MgO vanadium slag. Roasting step: 120 min, 800 °C; leaching step: 60 min, liquid/solid 10:1 (mL/g)
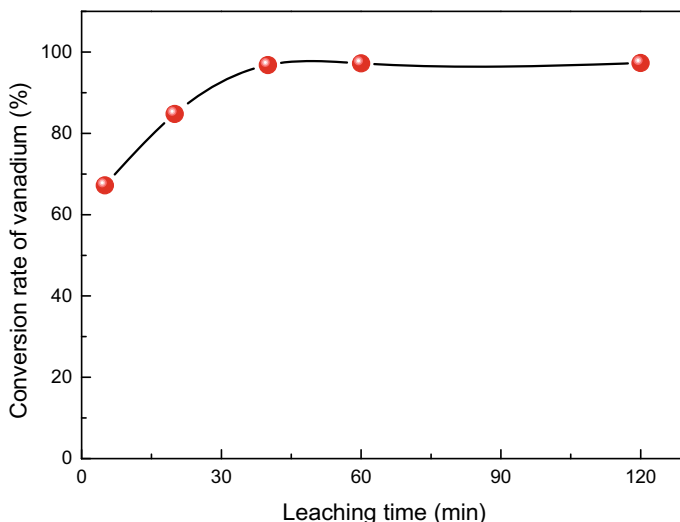
Fig. 6 Influence of leaching time on the conversion rate of high MgO vanadium slag. Roasting step: 120 min, 800 °C, V/Na molar ratio 0.2; leaching step: liquid/solid 10:1 (mL/g)

Effect of Leaching Parameters on the Conversion Rate of High MgO Vanadium Slag

As shown in Fig. 6, two distinct stages are observed during the leaching process. In the initial stage of leaching (0–40 min), the conversion rate of vanadium increases rapidly with increasing the leaching time. In the later stage of leaching (40–120 min), the conversion rate of vanadium is growing very slowly, almost invariable. The optimal leaching time is believed to be 60 min, at which the maximal conversion rate of 97.3% is obtained.

Figure 7 shows the conversion rates of high MgO vanadium slag at different liquid/solid ratios. When the liquid/solid ratio is lower than 5:1, the conversion rate of vanadium is no more than 84.6%. More than 90% of vanadium can be recovered at the liquid/solid ratio in the range of 10:1 to 20:1. However, too much liquid will lower the vanadium concentration, which is detrimental to vanadium extraction as well as wasteful [21]. Therefore, in consideration of the high extraction of vanadium and economy, the optimal liquid/solid ratio is thought to be 10:1.

Conclusions

The effect of MgO, MnO, and Al_2O_3 on vanadium extraction in the sodium roasting-water leaching process of vanadium slag was investigated in the present paper. In summary, we found that both at the condition of direct roasting and sodium roasting,
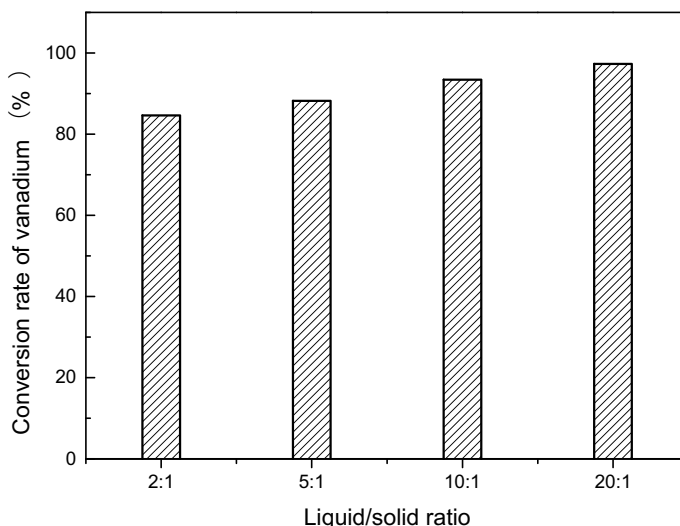
Fig. 7 Influence of liquid/solid ratio on the conversion rate of high MgO vanadium slag. Roasting step: 120 min, 800 °C, V/Na molar ratio 0.2; leaching step: 60 min

MgO, MnO, and Al$_2$O$_3$ can promote the extraction of vanadium from vanadium slag. At the condition of sodium roasting, with the increase of MgO, MnO, and Al$_2$O$_3$ contents to 11.49%, 14.22%, and 11.13%, the conversion rates of vanadium increased from 89.9% to 97.3%, 98.0% and 95.8%, respectively. More vanadium transformed into a spinel phase with increasing MgO concentration in vanadium slag. With the MgO concentration increasing from 3.52% to 8.98%, the conversion rate of vanadium increases from 88.9% to 97.3%. After that, the conversion rate of vanadium no longer increases. Effects of roasting parameters and leaching parameters on the conversion rate of high MgO vanadium slag were also investigated. The optimal condition is as follows: roasting temperature 800 °C, V/Na molar ratio 0.2; leaching time 60 min, liquid/solid ratio 10:1. The maximal conversion rate of vanadium is as high as 97.3%. The results can provide a reference for the modification of vanadium slag based on slag splashing in the vanadium extraction converter.

References

1. Gilligan R, Nikoloski AN (2020) The extraction of vanadium from titanomagnetites and other sources. Miner Eng 14(6):106106–106123
2. Gupta CK, Krishnamurthy N (1992) Extractive metallurgy of vanadium. Elsevier, Amsterdam

3. Moskalyk RR, Alfantazi AM (2003) Processing of vanadium: a review. Miner Eng 16(9):793–805

4. Hu YB, Ye GH, Zuo Q, Xie Y, Tong X (2020) The research progress and prospect of extractants for vanadium from acid leaching solution of stone coal vanadium ore. Multipurpose Utilization Mineral Resour 1:10–15

5. Chen DH (2022) Annual Evaluation of vanadium industry in 2021. Hebei Metallurgy 12:19–30

6. NDRC, 2006. YB/T 008-2006. GB of Vanadium slag

7. Li XJ, Zhang RP, Xie B (2012) Effects of calcified roasting parameters of vanadium slag on vanadium leaching rate. Chin J Process Eng 12(1):54–58

8. Li HY, Fang HX, Wang K, Zhou W, Yang Z, Yan XM, Ge WS, Li QW, Xie B (2015) Asynchronous extraction of vanadium and chromium from vanadium slag by stepwise sodium roasting–water leaching. Hydrometallurgy 15(6):124–135

9. Wang JC (2004) Effect of calcium on vanadium content of vanadium. Sichuan Nonferrous Metals 4:27–29

10. Diao J, Xie B, Wang Y, Ji CQ (2009) Mineralogical characterisation of vanadium slag under different treatment conditions. Ironmak Steelmak 36(6):476–480

11. Huang DX (2000) Vanadium extraction and steelmaking. Metallurgical Industry Press, Beijing

12. Fang HX, Li HY, Zhang T, Liu BS, Xie B (2015) Influence of CaO on existence form of vanadium-containing phase in vanadium slag. ISIJ Int 55(1):200–206

13. Zhang X, Xie B, Diao J, Li XJ (2012) Nucleation and growth kinetics of spinel crystals in vanadium slag. Ironmak Steelmak 39(2):147–154

14. Wang Y, Guan T, Cao HL, Zhang SQ, Xi B, Wei ZW (2010) The study of SiO_2-V_2O_5 binary phase diagram. National conference on metallurgical physics and chemistry, pp 24–27

15. Yu L, Dong YC, Ye GZ, Du S (2007) Concentrating of vanadium oxide in vanadium rich phase(s) by addition of SiO_2 in converter slag. Ironmaking Steelmaking 34(2):131–137

16. Li HY, Wang K, Hua WH, Yang Z, Zhou W, Xie B (2016) Selective leaching of vanadium in calcification-roasted vanadium slag by ammonium carbonate. Hydrometallurgy 160(2):18–25

17. Yang ZQ, Chen XQ, Gao GJ, Li QW (2014) A method of extracting vanadium from a manganese roasting vanadium slag

18. Zhao XW (1993) Study on the preparation and generic properties of manganese vanadium slag and magnesium vanadium slag. Iron Steel Vanadium Titanium 1:16–19

19. Meng LP, Wang SN, Du H, Zheng SL (2016) The mechanism of roasting process of vanadium slag roasting—alkali leaching process. Chin J Process Eng 16(3):445–451

20. Xi ZH, Tan XM, Zhao JF (2005) The control of calcining temperature in the process of sodium roasting vanadium slag. Ferro-Alloys 36(4):19–20

21. Li C, Li HY, Tu CB, Zhang T, Fang HX, Xie B (2013) Selective extraction of vanadium from the APV-precipitated wastewater. TMS 2013 Annual Meeting. REWAS 2013 Enabling Mater Resour Sustain pp 302–308

Efficient Extraction of Cd in Zn Recovery Process by Wet Leaching of Zn-Rich Dust

Yan Li, Xuefeng She, Jingsong Wang, Zeming Wang, and Qingguo Xue

Abstract This study develops a green and efficient hydrometallurgical process for the recovery of Zn and Cd from Zn-rich dust after pyrometallurgical treatment of iron and steel metallurgical dust. The feasibility of separating Zn, Cd, and Fe in the leaching system was confirmed by thermodynamic analysis. In the acid leaching process, dilute H_2SO_4 is used as the leaching agent, Zn and Cd are leached and recovered in the liquid in the form of Zn_2SO_4 and Cd_2SO_4. This article studies the leaching behavior of Cd and Bi under different experimental conditions (such as H_2SO_4 concentration, liquid-to-solid ratio, temperature, and reaction time). Under the optimal conditions, the leaching rates of Cd and Bi are 93.15% and 0.78% respectively. In the second step, the Cd in the leaching solution is extracted through the replacement process to prepare Cd products to realize resource utilization.

Keywords Zinc-rich dust · Cd · Hydrometallurgical leaching · Resourceful recycling

Introduction

The dust and sludge produced in the metal smelting process contain various heavy metals such as Cd and Zn, which are the main industrial pollutants that pollute the air, poison water sources, and harm the soil [1–3]. Cadmium and its compounds are highly toxic and were included in the list of Class 1 carcinogens by the World Health Organization in 2017 [4]. The air and food polluted by cadmium are seriously harmful to the human body. The representative chronic cadmium poisoning disease is "Itai-itai disease" that first occurred in Toyama Prefecture, Japan in 1950 [5]. After 2000, a number of cadmium rice incidents occurred in China, which aroused widespread public concern [6, 7]. It can be seen that if metallurgical dust containing

Y. Li · X. She · J. Wang (✉) · Z. Wang · Q. Xue
State Key Laboratory of Advanced Metallurgy, University of Science and Technology Beijing, Beijing 100083, China
e-mail: wangjingsong@ustb.edu.cn

toxic heavy metals is not properly disposed of, it will eventually threaten human health and survival.

Cadmium is a rare and precious non-ferrous metal with good corrosion resistance, wear resistance, and ductility [8, 9]. It is widely used in cadmium-nickel batteries [10], pigments [11], coatings [12], alloy [13], electroplating [14] and other fields. Cadmium is mainly associated with various minerals in nature. At present, about 95% of cadmium is recovered from copper cadmium slag and cadmium fume in the zinc production process [15, 16]. Another source of secondary resources of Cd is the iron and steel industry. Cd is found in the metallurgical dust generated in the iron and steel smelting production process [17, 18]. After iron and steel metallurgical dust is treated by pyrotechnics, Cd and Zn will be enriched in the Zn-rich dust for the second time, which creates good conditions for the effective recovery of Cd [19, 20].

The treatment process of metallurgical dust has been very mature, such as rotary kiln process, rotary hearth furnace process, wet treatment process, etc. [21]. However, they often focus on the recovery of elements with high content such as Zn and Pb, and the recovery of Cd has not attracted enough attention. With the increasingly stringent environmental protection regulations and industrial policies, the resource utilization of metallurgical dust has begun to turn to increasingly important associated metals [22]. In view of this, a hydrometallurgical process for recovering Zn from Zn-rich dust in conjunction with recovering Cd was proposed. Firstly, H_2SO_4 is used as leaching agent, Zn and Cd are simultaneously leached and recovered in the leaching solution in the form of $ZnSO_4$ and $CdSO_4$. Then replace the Cd in the leaching solution with zinc powder to prepare a sponge cadmium product. The selective separation of Zn and Cd can be achieved by replacing the cadmium-producing unit. The Zn-enriched leaching solution is used in subsequent processes to prepare zinc sulfate, zinc oxide and other products, and the sponge cadmium can be sold to non-ferrous metallurgical enterprises. This process realizes the efficient resource utilization of Zn-rich dust, and the recovered Cd can become an important support for national strategic resources.

Experimental

Materials

The raw material is Zn-rich dust collected by a pyroprocessing plant of an environmental protection technology company in China, as shown in Fig. 1a. Figure 1b shows the particle size distribution of Zn-rich dust. The average particle size (D50) was 3.73 µm, and 80% of the particles were in the range of 1.13–9.86 µm. It is concluded that the Zn-rich dust used in the experiment is fine particles with a concentrated size distribution and relatively stable properties. Table 1 shows the chemical composition of Zn-rich dust, which contains approximately 47.73% Zn, 0.21% Cd, 6.27% Potassium, 5.32% Pb, 4.22% Na, 1.42% Fe, 0.18% Sn, 0.15% Bi and 0.03% In. The zinc-rich dust in this experiment is obtained from metallurgical dust such
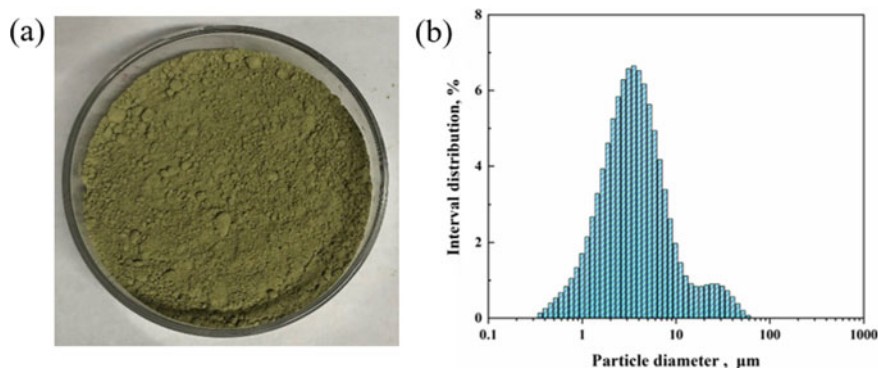
Fig. 1 Characteristics of zinc-rich dust: **a** physical drawing; **b** particle size distribution

Table 1 Chemical composition of zinc-rich dust

Element	Zn	Cd	K	Pb	Na	Fe	Sn	Bi	In
Weight (%)	47.73	0.21	6.27	5.32	4.22	1.42	0.18	0.23	0.03

as blast furnace dust after the rotary kiln fire method. Most of the metal elements such as Zn, Cd, Pb, and Fe in the zinc-rich dust exist in the form of oxides, and a small part exists in the form of chlorides. K and Na elements in dust mainly exist in the form of KCl and NaCl. The reagents H_2SO_4, H_2O_2, ZnO, and Zn powder used in the experiments were of analytical grade, and deionized water was used in all experiments.

Experimental Procedure

The process flow of zinc-rich dust wet synergistic recovery of zinc and cadmium is shown in Fig. 2. KCl and NaCl in the zinc-rich dust are removed in the three-stage rinsing process, and the leaching solution enriched in K and Na is sent to a multi-effect evaporation device to extract KCl and NaCl products through evaporation and crystallization. Dilute H_2SO_4 is used as a leaching agent to selectively dissolve Cd and Zn in the water-washed cake to obtain an acid leaching solution rich in $ZnSO_4$ and $CdSO_4$. The main components of acid leaching residue are lead sulfate, oxides of scattered metals (Bi, In, Sn), and a small part of complex zinc oxides. The acid leaching residue is sent to the scattered element recovery unit to recover Zn, Bi, Pb, In, and Sn. The acid leaching solution is sent to the two-stage replacement cadmium production unit to prepare sponge cadmium products after the iron removal unit removes iron, and the iron removal filter residue is returned to the rotary kiln for resource utilization.
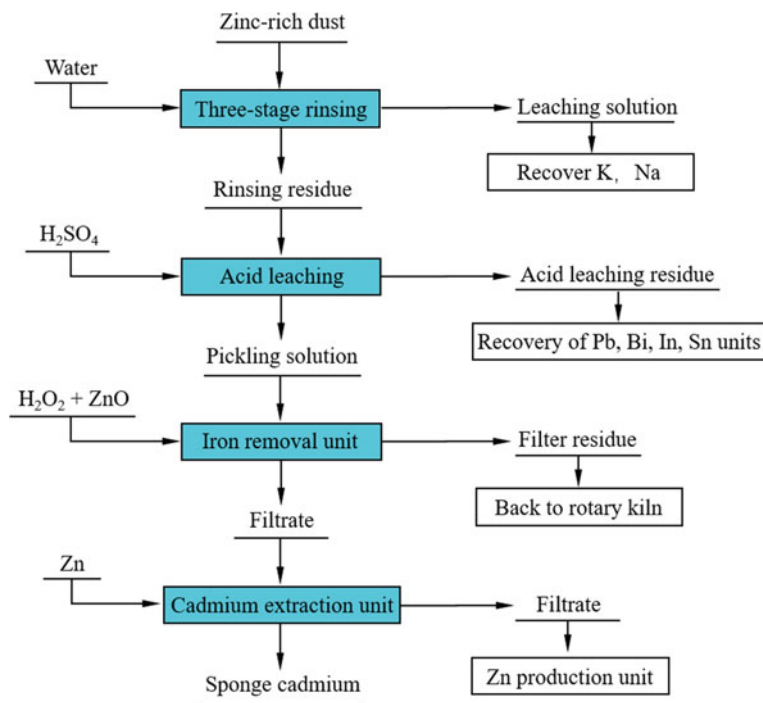
Fig. 2 Schematic diagram of the process for recovering Zn and Cd from Zn-rich dust

The three-stage rinsing experiment and the oxidation iron removal experiment were carried out in a 1000 ml beaker. The acid leaching experiments were carried out in a 250 ml three-necked flask equipped with an overhead stirrer. The three-neck beaker was placed in a constant temperature water bath to control the reaction temperature, and the stirring speed of each test was fixed at 200 rpm. The reactor is also equipped with a condenser to prevent evaporation losses.

The zinc-rich dust was added to a beaker with a liquid–solid ratio of 3 (ml/g), leached in a water bath at 25 °C, and separated from solid and liquid by a vacuum filter. The water-leached filter cake is put into the three-necked flask in the acid leaching process, and dilute H_2SO_4 is used as the leaching agent. After the leaching is completed, the slurry is immediately vacuum-filtered. The diluted pickling solution was sent to ICP analysis to calculate the leaching rate of Cd and Bi. Zinc powder is added to the iron removal filtrate, and the solid–liquid separation is realized through a vacuum filter after the reaction is completed. The filtrate rich in zinc sulfate is sent to the zinc production unit, and the main component of the filter residue is metal Cd. The sponge cadmium samples were washed with deionized water and dried at 80 °C for 12 h, and then the cadmium content was detected by ICP.
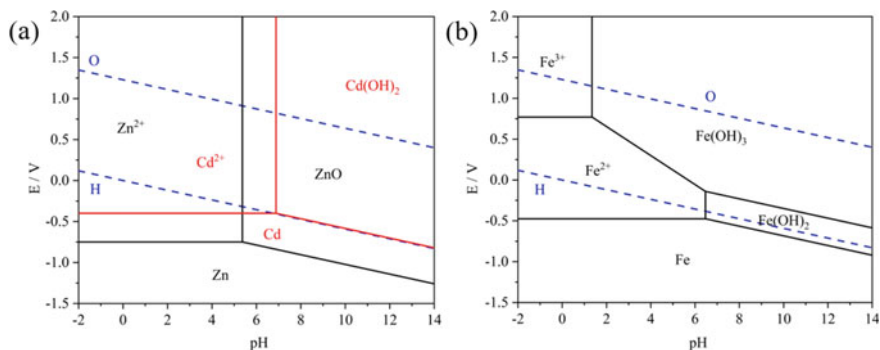
Fig. 3 E-pH of different systems at 298 K: **a** Zn-H$_2$O, Cd-H$_2$O; **b** Fe-H$_2$O

Results and Discussion

Thermodynamic Analysis

The E-pH diagrams of Cd–H$_2$O, Zn–H$_2$O, and Fe–H$_2$O systems at 298 K were calculated by HSC Chemistry 9.0, and the results are shown in Fig. 3. The dashed line indicates the stable region of water. It can be seen from Fig. 3a that both Zn^{2+} and Cd^{2+} can exist stably in a strong acidic solution, and the range of Cd^{2+} in the pH direction is larger than that of Zn^{2+}. Therefore, the leaching of Zn and Cd can be achieved by controlling the Ph value of the sulfuric acid leaching process to be less than the critical value of Zn during the experiment. Through experimental research, it is found that in the initial stage of acid leaching experiment, the reaction rate and leaching rate of Cd are higher than that of Zn. PbO in the water leaching residue will react with H$_2$SO$_4$ to form PbSO$_4$. Since the PbSO$_4$ solubility product (1.6 × 10^{-8}, 18 °C) is small and there is a large amount of SO$_{4-}$ in the solution, Pb remains in the acid leaching residue in the form of PbSO$_4$ precipitation. Production practice shows that the end point pH of the acid leaching process is about 5. As can be seen from Fig. 3b, Fe^{2+} in the acid leach solution cannot be precipitated off at this time. The oxidant is used to oxidize Fe^{2+} into Fe^{3+}, and Fe^{3+} will undergo a hydrolysis reaction to generate Fe(OH)$_3$ precipitation, and finally achieve the goal of purifying and removing iron in the acid leaching solution. The reactions that may occur during the process are shown in Table 2.

Sulfuric Acid Leaching to Recover Zn and Cd

H$_2$SO$_4$ has been demonstrated for its effectiveness, low cost, and general availability in dissolving compounds of valuable elements [23]. Therefore, the recovery of Zn from Zn-bearing dust and zinc ore using H$_2$SO$_4$ as a leaching agent has been widely

Table 2 Possible reactions during the process

Element	Reaction	No.
Cd	$CdO + H_2SO_4 = CdSO_{4\,(aq)} + H_2O$	(1)
	$CdSO_{4(aq)} + Zn = ZnSO_{4(aq)} + Cd$	(2)
Zn	$ZnO + H_2SO_4 = ZnSO_{4(aq)} + H_2O$	(3)
	$ZnFe_2O_4 + 4\,H_2SO_4 = ZnSO_{4(aq)} + Fe_2(SO_4)_{3(aq)} + 4\,H_2O$	(4)
	$ZnFe_2O_4 + H_2SO_4 + 2\,H_2O = ZnSO_{4(aq)} + 2\,Fe(OH)_3$	(5)
Pb	$PbO + H_2SO_4 = PbSO_4 + H_2O$	(6)
Fe	$Fe_2O_3 + 3\,H_2SO_4 = Fe_2(SO_4)_{3(aq)} + 3\,H_2O$	(7)
	$Fe_3O_4 + 4\,H_2SO_4 = FeSO_{4(aq)} + Fe_2(SO_4)_{3(aq)} + 4\,H_2O$	(8)
	$2\,Fe^{2+} + H_2O_2 + 2\,H^+ = 2\,Fe^{3+} + 2\,H_2O$	(9)
	$Fe^{3+} + 3\,H_2O = Fe(OH)_3 + 3\,H^+$	(10)

studied and has been put into commercial operation [24]. In the acid leaching process, dilute sulfuric acid is selected as the leaching agent in order to achieve the leaching of Zn and Cd without leaching of scattered elements such as Pb and Bi. Since there are many articles about the leaching behavior of Zn in sulfuric acid system [25, 26], this article will not repeat them. The separation of elements (Cd and Bi) in zinc-rich dust by sulfuric acid leaching was studied by single factor conditional test method. The leaching behavior of Cd and Bi under different experimental conditions (such as: H_2SO_4 concentration, liquid–solid ratio, temperature, and reaction time) was systematically studied. The aim was to find the optimal conditions on a laboratory scale for maximum Cd leaching efficiency and minimum amount of Bi in the aqueous phase.

Effect of H_2SO_4 Concentration

Under the conditions of liquid–solid ratio of 5 mL/g, leaching time of 40 min, and leaching temperature of 70 °C, the effect of sulfuric acid concentration on the leaching rate of Cd and Bi is shown in Fig. 4. When the concentration range of H_2SO_4 is 70–140 g/L, the leaching of Cd is mainly affected by the concentration of H_2SO_4. With the increase of H_2SO_4 concentration, the leaching rate of Cd increases from 49.77% to 93.15%. When the concentration interval of H_2SO_4 was 140–160 g/L, the leaching rate of Cd increased from 93.15% to 97.06%, and the leaching rate increased slowly. Sensitivity to Cd leaching efficiency suggests that Cd may exist in the dust as an oxide phase [27]. The H_2SO_4 concentration increased from 140 g/L to 160 g/L, and the Bi leaching rate increased from 0.78% to 3.12%. Considering that too high H_2SO_4 concentration will increase the acid consumption, it is considered most appropriate to select the H_2SO_4 concentration of the leaching agent as 140 g/L.

Fig. 4 Effect of H$_2$SO$_4$ concentration on the leaching efficiency of Cd and Bi
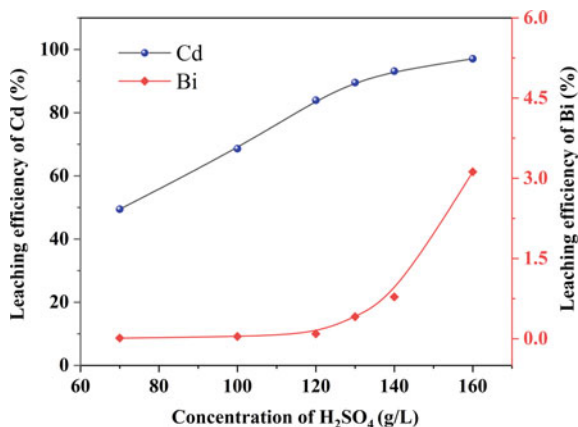
Effect of Liquid-to-Solid Ratio

Under the conditions of H$_2$SO$_4$ concentration of 140 g/L, leaching time of 40 min, and leaching temperature of 70 °C, the effect of liquid–solid ratio on the leaching rates of Cd and Bi is shown in Fig. 5. When the liquid–solid ratio increased from 2 mL/g to 5 mL/g, the leaching rate of Cd was significantly increased from 42.56% to 93.15%. This is due to the improvement of the surface contact between the solution and the dust due to the increase of the liquid–solid ratio, which facilitates the dissolution of Cd [28]. As the liquid-to-solid ratio increased from 5 mL/g to 6 mL/g, the Cd leaching rate slowly increased from 93.15% to 94.83%. When the liquid-to-solid ratio increased from 5 mL/g to 6 mL/g, the leaching rate of Bi increased from 0.78% to 2.18%. Increasing the liquid–solid ratio usually accelerates mass transfer and promotes the reaction, but it also increases equipment volume and energy consumption and reduces production efficiency. Therefore, from the perspectives of economy, operability, and leaching rate, it is considered appropriate to select a liquid–solid ratio of 5 mL/g.

Effect of Temperature

The leaching temperature is an important thermodynamic parameter. Under the conditions of H$_2$SO$_4$ concentration of 140 g/L, leaching time of 40 min, and liquid-to-solid ratio of 5 mL/g, the effect of reaction temperature (25–80 °C) on the leaching rate of Cd and Bi is shown in Fig. 6. As the temperature increases from 25 to 70 °C, the Cd leaching rate increases from 77.46% to 93.15%. This can be attributed to the fact that the relatively high temperature will improve the atomic/molecular collision and mass transfer rate [29], thereby speeding up the reaction rate to a certain extent and increasing the leaching rate of Cd. As the temperature increases from 70 to 90 °C, the Cd leaching rate remains around 93%. As the temperature increases from 25 to 90 °C, the leaching rate of Bi element is less than 0.9%, which shows that

Fig. 5 Effect of liquid-to-solid ratio on the leaching efficiency of Cd and Bi
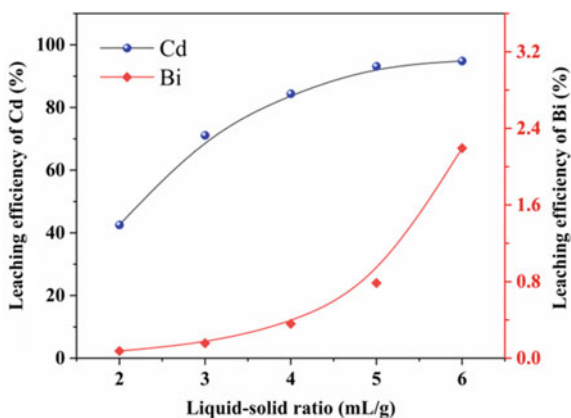
Fig. 6 Effect of temperature on the leaching efficiency of Cd and Bi
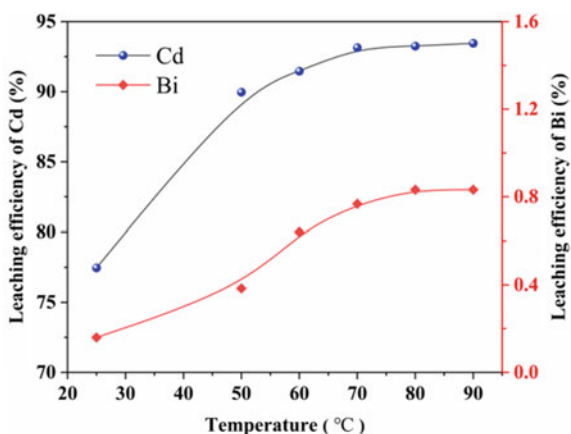
temperature has no significant effect on the leaching rate of Bi element. Excessively high reaction temperature has limited contribution to improving the leaching rate of Cd, but may lead to an increase in the leaching rate of other impurity ions. Therefore, in order to obtain a high reaction rate and avoid energy waste, 50 °C was selected as the appropriate experimental leaching temperature.

Effect of Reaction Time

Under the conditions of H_2SO_4 concentration of 140 g/L, liquid-to-solid ratio of 5 mL/g, and leaching temperature of 70 °C, the effect of reaction time on the leaching rate of Cd and Bi is shown in Fig. 7. As the leaching time increased from 5 to 40 min, the leaching efficiency of Cd increased from 79.28% to 93.15%. When the leaching time exceeds 40 min, the leaching efficiency does not increase significantly. As

Fig. 7 Effect of reaction time on the leaching efficiency of Cd and Bi
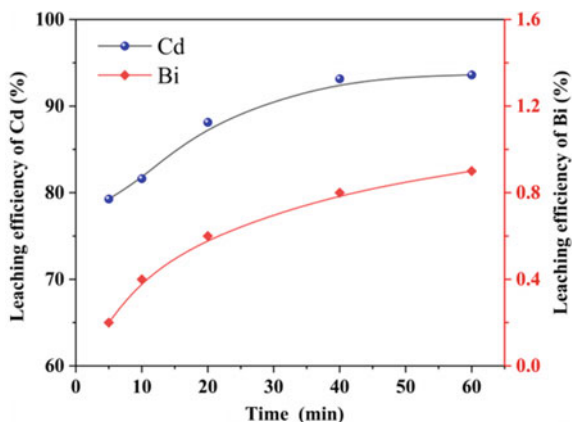
the leaching time increases, the leaching rate of Bi is less than 1%. Considering that excessively increasing the reaction time will reduce production efficiency, a leaching time of 40 min was determined as the optimal reaction time.

Zinc Powder Replacement to Produce Cadmium

The sulfuric acid leaching process completed the preliminary extraction of Cd, the replacement iron removal process completed the removal of impurity Fe in the acid leaching solution, and the replacement cadmium production unit completed the conversion of Cd^{2+} in the iron removal filtrate to sponge cadmium. In order to improve the cadmium production effect, the replacement cadmium production unit adopts a two-stage replacement. An appropriate amount of zinc powder is added to the oxidized iron removal filtrate, and after the reaction is completed, filter to obtain the primary cadmium removal filtrate and sponge cadmium. Excessive zinc powder is added to the primary cadmium removal filtrate for secondary replacement to produce cadmium. After the reaction is completed, filter to obtain the secondary cadmium removal filtrate and filter residue. The main components of the filter residue are metal Cd and Zn, and the filter residue is returned to the primary replacement cadmium production process. The reaction equation between zinc and cadmium sulfate in the cadmium production process. The main component of the secondary cadmium removal filtrate is zinc sulfate, which is sent to the zinc production unit to prepare zinc products. The cadmium sponge was washed with deionized water and dried at 80 °C for 12 h. The ICP test results showed that the cadmium content in the cadmium sponge was 70.3%, and the calculated cadmium recovery rate was 87.56%. The resulting sponge cadmium can be sold to non-ferrous smelters as a raw material for producing high-purity Cd (Fig. 8).
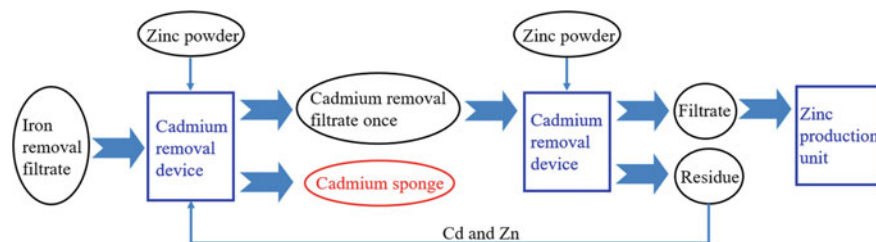
Fig. 8 Two-stage replacement cadmium production process

Conclusions

A two-stage displacement hydrometallurgical process was proposed for the recovery of Zn and Cd from Zn-rich dust. The feasibility of separating Zn, Cd, and Fe in the leaching system was confirmed by thermodynamic analysis. Zn and Cd are firstly leached and recovered in the leach solution in the form of sulfate, and the leached residue enriched with scattered elements such as Pb and Bi can be further processed to recover Pb and Bi. The results show that H_2SO_4 concentration, liquid–solid ratio, and leaching temperature are the main factors affecting the leaching rate of Cd. Under optimal conditions, the leaching rates of Cd and Bi were 93.15% and 0.78% respectively. Using zinc powder as a reducing agent, a sponge cadmium product with a purity of 70.3% was prepared through a two-stage replacement cadmium production process.

References

1. Wu G, Kang H, Zhang X et al (2010) A critical review on the bio-removal of hazardous heavy metals from contaminated soils: issues, progress, eco-environmental concerns and opportunities. J Hazard Mater 174:1–8. https://doi.org/10.1016/j.jhazmat.2009.09.113
2. Gunarathne V, Rajapaksha AU, Vithanage M et al (2022) Hydrometallurgical processes for heavy metals recovery from industrial sludges. Crit Rev Environ Sci Technol 52:1022–1062. https://doi.org/10.1080/10643389.2020.1847949
3. Li Y, Feng H, Wang J et al (2022) Current status of the technology for utilizing difficult-to-treat dust and sludge produced from the steel industry. J Clean Prod 367:132909. https://doi.org/10.1016/j.jclepro.2022.132909
4. Rahman Z, Singh VP (2019) The relative impact of toxic heavy metals (THMs) (arsenic (As), cadmium (Cd), chromium (Cr)(VI), mercury (Hg), and lead (Pb)) on the total environment: an overview. Environ Monit Assess 191:419. https://doi.org/10.1007/s10661-019-7528-7
5. Kikuchi T, Okazaki M, Toyota K et al (2007) The input–output balance of cadmium in a paddy field of Tokyo. Chemosphere 67:920–927. https://doi.org/10.1016/j.chemosphere.2006.11.018

6. Rafiq MT, Aziz R, Yang X et al (2014) Cadmium phytoavailability to rice (*Oryza sativa L.*) grown in representative Chinese soils. A model to improve soil environmental quality guidelines for food safety. Ecotoxicol Environ Saf 103:101–107. https://doi.org/10.1016/j.ecoenv.2013.10.016

7. Wang P, Chen H, Kopittke PM et al (2019) Cadmium contamination in agricultural soils of China and the impact on food safety. Environ Pollut 249:1038–1048. https://doi.org/10.1016/j.envpol.2019.03.063

8. Kanthiah A, Manimaran EI, Pactulingam R (2020) Microstructural and magnetic properties of cadmium incorporated magnetic alloys as monolayer and multilayer coatings. J Mater Sci Mater Electron 31:19332–19342. https://doi.org/10.1007/s10854-020-04467-4

9. Ganesan P, Kumaraguru SP, Popov BN (2006) Development of Zn–Ni–Cd coatings by pulse electrodeposition process. Surf Coatings Technol 201:3658–3669. https://doi.org/10.1016/j.surfcoat.2006.08.143

10. Rana M, Ishtiaq Hossain Khan M, Nshizirungu T et al (2023) Green and sustainable route for the efficient leaching and recovery of valuable metals from spent Ni−Cd batteries. Chem Eng J 455:140626. https://doi.org/10.1016/j.cej.2022.140626

11. Turner A (2019) Cadmium pigments in consumer products and their health risks. Sci Total Environ 657:1409–1418. https://doi.org/10.1016/j.scitotenv.2018.12.096

12. Rayner G, Costello SD, McClelland A et al (2021) Preliminary investigations into the alteration of cadmium orange restoration paint on an ancient greek terracotta krater. Heritage 4:1497–1510. https://doi.org/10.3390/heritage4030082

13. Paramanik S, Chatterjee S, Pal AJ (2021) Reverse bandgap-bowing in nickel-cadmium sulfide alloys ($Ni_{1-x} Cd_x S$) and its origin. J Phys Condens Matter 33:245703. https://doi.org/10.1088/1361-648X/abe9d8

14. Kruglikov SS, Nekrasova NE, Kuznetsov VV et al (2019) An electromembrane process for cadmium recovery from dilute cadmium electroplating dragout solutions. Membr Membr Technol 1:120–126. https://doi.org/10.1134/S2517751619020057

15. Kubier A, Wilkin RT, Pichler T (2019) Cadmium in soils and groundwater: a review. Appl Geochemistry 108:104388. https://doi.org/10.1016/j.apgeochem.2019.104388

16. Zhang H, Reynolds M (2019) Cadmium exposure in living organisms: a short review. Sci Total Environ 678:761–767. https://doi.org/10.1016/j.scitotenv.2019.04.395

17. Chang F, Wu S, Zhang F et al (2015) Characterization of sintering dust, blast furnace dust and carbon steel electric arc furnace dust. Charact Miner Met Mater 2015:83–90. https://doi.org/10.1007/978-3-319-48191-3_10

18. Xiao X, Zhang S, Sher F et al (2021) A review on recycling and reutilization of blast furnace dust as a secondary resource. J Sustain Metall 7:340–357. https://doi.org/10.1007/s40831-021-00377-9

19. Wang J, Li Y, Feng H et al (2021) Progress in treating difficult-to-handle dust and sludge and full-scale resource utilization in an iron and steel industry cluster. Chin J Eng 43:1737–1746. https://doi.org/10.13374/j.issn2095-9389.2021.09.15.004

20. Wang J, Zhang Y, Cui K et al (2021) Pyrometallurgical recovery of zinc and valuable metals from electric arc furnace dust—A review. J Clean Prod 298:126788. https://doi.org/10.1016/j.jclepro.2021.126788

21. Li Y, Zhao Z, Feng H et al (2022) Technology of treating zinc-containing dust and mud in iron and steel plant by rotary hearth furnace. Sinter Pelletizing 47:106–114. https://doi.org/10.13403/j.sjqt.2022.06.091

22. Li Y, Feng H, Wang J et al (2023) Efficient extraction of Bismuth in a two-stage leaching process for the recovery of zinc and lead from zinc-rich dust. Miner Met Mater Ser 297–309. https://doi.org/10.1007/978-3-031-22765-3_27

23. Jha MK, Kumar V, Singh RJ (2001) Review of hydrometallurgical recovery of zinc from industrial wastes. Resour Conserv Recycl 33:1–22. https://doi.org/10.1016/S0921-3449(00)00095-1

24. Kukurugya F, Vindt T, Havlík T (2015) Behavior of zinc, iron and calcium from electric arc furnace (EAF) dust in hydrometallurgical processing in sulfuric acid solutions: thermodynamic and kinetic aspects. Hydrometallurgy 154:20–32. https://doi.org/10.1016/j.hydromet.2015.03.008

25. Halli P, Hamuyuni J, Revitzer H et al (2017) Selection of leaching media for metal dissolution from electric arc furnace dust. J Clean Prod 164:265–276. https://doi.org/10.1016/j.jclepro.2017.06.212

26. Kaya M, Hussaini S, Kursunoglu S (2020) Critical review on secondary zinc resources and their recycling technologies. Hydrometallurgy 195:105362. https://doi.org/10.1016/j.hydromet.2020.105362

27. Trinkel V, Mallow O, Thaler C et al (2015) Behavior of chromium, nickel, lead, zinc, cadmium, and mercury in the blast furnace—a critical review of literature data and plant investigations. Ind Eng Chem Res 54:11759–11771. https://doi.org/10.1021/acs.iecr.5b03442

28. Qiang L, Pinto ISS, Youcai Z (2014) Sequential stepwise recovery of selected metals from flue dusts of secondary copper smelting. J Clean Prod 84:663–670. https://doi.org/10.1016/j.jclepro.2014.03.085

29. Trung ZH, Kukurugya F, Takacova Z et al (2011) Acidic leaching both of zinc and iron from basic oxygen furnace sludge. J Hazard Mater 192:1100–1107. https://doi.org/10.1016/j.jhazmat.2011.06.016

Extraction of Vanadium from High Calcium and High Phosphorus Vanadium Slag by Magnesiation Roasting-Acid Leaching

Xin-Mian Chen, Hong-Yi Li, Jing Tan, Jie Cheng, Jiang Diao, and Bing Xie

Abstract Magnesiation roasting-acid leaching is carried out to extract vanadium from high calcium and high phosphorus vanadium slag (HCPVS). The effects of roasting and leaching conditions on vanadium and phosphorus extraction are studied. In optimal conditions, the extraction efficiency of vanadium reaches 79.7%, and only 35.6% of phosphorus is leached owing to Mg^{2+} inhibiting the leaching of phosphorus. The roasting mechanism is analyzed by XRD and BSE-EDS systematically, best of the vanadium in V-spinel is converted into vanadate, and a small part of vanadium is dissolved into Ca_2SiO_4–$Ca_3(PO_4)_2$ and $CaTiO_3$ phase. This work reveals the influence mechanism of Ca_2SiO_4–$Ca_3(PO_4)_2$ and $CaTiO_3$ phase on vanadium extraction, providing new insights for vanadium extraction from HCPVS.

Keywords High calcium and high phosphorus vanadium slag · $CaTiO_3$ · Ca_2SiO_4 · Magnesiation roasting

Introduction

Vanadium, as an important strategic resource, is widely used in steel, chemical, and battery fields [1]. In China, V-Ti magnetite is reduced in a blast furnace to obtain vanadium-containing hot metal, which is blown in a converter to obtain semi-steel and vanadium slag [2]. Vanadium slag is first subjected to sodium salt roasting or calcification roasting, then leached to obtain a vanadium solution. The ammonium salt is used to precipitate vanadium from the vanadium solution, and the deposit is then calcined to obtain V_2O_5, which is the main industrial process for the production of V_2O_5 from V-Ti magnetite.

However, the low basicity vanadium slag obtained from the existing converter vanadium extraction process has no dephosphorization potential, and the phosphorus of the molten iron hardly enters the vanadium slag, coupled with massive oxidation of

X.-M. Chen · H.-Y. Li (✉) · J. Tan · J. Cheng · J. Diao · B. Xie
College of Materials Science and Engineering, Chongqing University, Chongqing 400044, China
e-mail: hongyi.li@cqu.edu.cn

Si and Mn in the hot iron leads to the difficulty of dephosphorization of the subsequent semi-steel [3]. Therefore, scholars propose to add CaO in the process of vanadium extraction in the converter to realize the simultaneous extraction of vanadium and dephosphorization in order to meet the half-steel smelting process, vanadium and phosphorus are simultaneously enriched to the vanadium slag in the formation of high calcium and high phosphorus vanadium slag(HCPVS) [4].

The mature sodium salt roasting-water leaching process is suitable for slags with very low calcium and phosphorus content. When vanadium slag with high Ca content is used as raw material for vanadium extraction, the slag will generate insoluble calcium vanadate after roasting, which will reduce vanadium recovery efficiency [5]. Considering the high calcium content in HCPVS, some scholars propose the vanadium extraction methods of calcinated roasting-alkaline leaching, blank roasting-alkaline leaching, calcinated roasting-acidic leaching, and blank roasting-acidic leaching, which inevitably form the $CaCO_3$ and $CaSO_4$ precipitates deteriorating the vanadium leaching environment [6–8]. And a zero discharge green vanadium extraction method (Magnesiation roasting vanadium—acid leaching), MgO as roasting additives, not only without forming precipitation with acid, but also additives through the precipitation to achieve the recovery, which is a promising new method of vanadium extraction [9].

In this work, HCPVS as the raw material for vanadium extraction based on the method, and the effects of different roasting conditions and leaching conditions on the vanadium leaching efficiency are investigated, and the evolution of the phase and microscopic morphology of the process are analyzed. The aim of this work is to provide a new view of the use of HCPVS as raw material for vanadium extraction.

Experimental

Materials

The HCPVS used herein is obtained from Pan Steel, China, with the main chemical compositions of HCPVS shown in Table 1. All chemicals in the experiments are purchased from the Chengdu Chron Chemicals Company, China. MgO is calcined in a muffle furnace at 1000 °C for 1 h before use. All the aqueous solutions are prepared using deionized water produced by Millipore Aquelix 5 apparatus (USA).

Table 1 Chemical composition of HCPVS (wt%)

CaO	FeO	V_2O_3	SiO_2	TiO_2	Al_2O_3	MnO	MgO	Cr_2O_3	P_2O_5
25.77	22.91	9.31	10.89	6.82	6.52	5.72	4.32	1.17	1.10

Experimental Procedure

Magnesiation Roasting

Prior to roasting, the HCPVS is milled and sieved through a 74 μm sieve and dried at 90 °C for 12 h in a drying oven. Mixing 10 g of HCPVS with MgO for each roasting, with a Mg/V molar ratio of 0–2.0, and the mixture is placed in a muffle furnace at 700–1000 °C for 10–120 min, with the furnace door slightly open to ensure an oxidizing atmosphere. After roasting, the roasted slag is taken out and air-cooled to room temperature.

Sulfuric Acid Leaching

The roasted slag is milled and sieved through a 74 μm sieve, 5 g of slag is placed in a three-necked flask, and deionized water is added with the leaching liquid–solid ratio at 8:1. The leaching process is carried out in a magnetic stirring water bath, with a temperature of 25–90 °C, and the leaching time for 2–60 min at 200 rpm, and sulfuric acid is used to adjust the pH value of the leaching at 2.0–4.0. At the end of the leaching, the solid–liquid separation is done by vacuum filtration. The elemental leaching efficiency is calculated as follows:

Leaching efficiency (%) = $(C_L V_L/m) \times 100\%$

Where C_L and V_L represent the concentration of elements in the leaching solution and the volume of the leaching solution, respectively, and m_2 represents the mass of elements in the roasted slag.

Characterization

The elemental compositions of HCPVS are determined by X-ray fluorescence (XRF, ARL Performance'X, Thermo Fisher Scientific CD Ltd, Switzerland). The concentration of elements is determined using an inductively coupled plasma optical emission spectrometer (ICP-OES, PerkinElmer Optima 8000). The phases of the samples in this work are determined by X-ray diffraction using Cu Kα radiation from 5° to 90° (XRD, Panalytical X'Pert Powder, Panalystic B.V., Netherlands). The microstructures and element distribution of slags are analyzed by BSE (TESCAN MIRA LMS, Czech) along with an EDS spectrometer (Xplore 30).

Results and Discussion

Magnesiation Roasting

In this section, the effects of roasting agent MgO addition, roasting temperature, and roasting time on the leaching efficiency of vanadium and phosphorus are investigated. The leaching conditions are sulfuric acid as the leaching agent along with a pH value of 2.5, leaching time 30 min, and leaching temperature 40 °C. The results are shown in Fig. 1a–c.

Effect of Mg/V Molar Ratio

The vanadium and phosphorus leaching efficiency with different additives varying from Mg/V = 0 to 2.0 at a roasting temperature of 850 °C for 60 min are shown in Fig. 1a. The vanadium leaching efficiency increases from 64.5% to 79.7% with the increase of MgO addition from Mg/V = 0 to 1.0, and the vanadium leaching efficiency is maintained at the same level with the increase of MgO addition. The phosphorus leaching efficiency is significantly reduced from 53.2% at Mg/V = 0 to 35.6% at Mg/V = 1.0 and then almost unchanged. The optimum amount of MgO can be selected as Mg/V = 1.0.

Effect of Roasting Temperature

The vanadium and phosphorus leaching efficiency at different roasting temperatures with Mg/V = 1.0 for 60 min are shown in Fig. 1b. With the increase of roasting temperature from 700 °C to 850 °C, the vanadium leaching efficiency increased significantly from 33.8% to 79.7%. However, the vanadium leaching efficiency decreases when with roasting temperature exceeds 850 °C. At lower temperatures, the oxidation rates of V-spinel and Ca–Fe olivine are low, which is not conducive to the generation
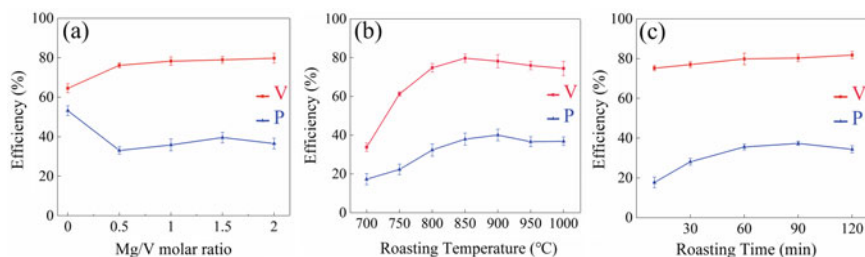
Fig. 1 Effect of roasting conditions on the leaching efficiency of vanadium and phosphorus. **a** Mg/V molar ratio. **b** roasting temperature. **c** roasting time

of vanadate, resulting in a poor vanadium leaching efficiency, whereas excessive temperature will lead to the melting of vanadate, which is not conducive to oxygen diffusion and promotes the generation of side reactions, resulting in a lower leaching efficiency. The optimal roasting temperature is 850 °C.

Effect of Roasting Time

The vanadium and phosphorus leaching efficiency for a roasting time in the range of 10–120 min at a roasting temperature of 850 °C and the MgO addition of Mg/V = 1.0 are shown in Fig. 1c. The vanadium leaching efficiency reaches 75.2% after only 10 min of roasting, and the vanadium leaching efficiency reaches a maximum value of 79.7% by extending the roasting time to 60 min, and the vanadium leaching efficiency is unchanged with continuing to increase the roasting time. Because of the existence of $CaTiO_3$ and free CaO in HCPVS, which can be directly involved in the generation of vanadate, coupled with the small ionic radius of Mg^{2+}, diffusion kinetic conditions are better. During roasting, vanadate can be synchronously formed inside and outside the slag, unlike vanadium slag first the oxidation of the olivine phase exposes the spinel and then reacts to generate vanadate, thus exhibiting a faster roasting efficiency. The phosphorus leaching efficiency increased from 17.7% at 10 min to 35.6% at 60 min and then did not increase anymore. It can also be inferred that the roasting of HCPVS was almost completed at around 60 min. The optimum roasting time is determined to be 60 min.

Acid Leaching

Dilute sulfuric acid is used as a leaching agent to maximize the leaching of vanadium from roasted slag. The leaching behaviors of vanadium and phosphorus under different leaching conditions (pH, temperature, and time) are investigated as shown in Fig. 2.
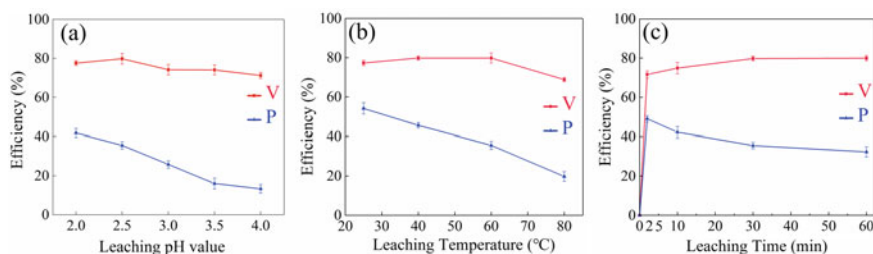
Fig. 2 Effect of leaching conditions on the leaching efficiency of vanadium and phosphorus. **a** pH value of leaching solution. **b** leaching temperature. **c** leaching time

Effect of Leaching pH

Figure 2a shows the leaching efficiency of vanadium and phosphorus at leaching pH values of 2.0–4.5. The vanadium leaching efficiency shows a decreasing trend with increasing leaching pH, which is due to the difference in the solubility of vanadate at different pH. The solubility of vanadate decreases at a high pH solution, resulting in vanadate being less soluble. The significant decrease in the leaching efficiency of phosphorus with increasing pH value is due to the fact that phosphorus forms more stable precipitates with calcium and magnesium. The optimum leaching pH condition is pH = 2.5.

Effect of Leaching Temperature

Figure 2b shows the leaching efficiency of vanadium and phosphorus at different leaching temperatures.

As the leaching temperature increases, the vanadium leaching efficiency changes slightly and then decreases. This is because the leaching solution at room temperature compared to 40 °C, the former with a greater viscosity of the solution, which is not conducive to the mass transfer of the leaching process. Whereas, the vanadium may occur a small amount of hydrolysis, and the silicate colloid is more likely to be precipitated and adsorbed by a certain degree of poly vanadium anion with an excessive temperature, resulting in a reduction of the leaching efficiency of vanadium. As for phosphorus, with the increase of leaching temperature, the leaching efficiency shows a significant decrease trend, indicating that increasing the temperature is more favorable to the precipitation of phosphorus. It could be because increasing the temperature promotes the irregular thermal movement of PO_4^{3-} with Mg^{2+}, Ca^{2+}, and other ions, and facilitates the occurrence of precipitation reaction. The optimum leaching temperature is 40 °C.

Effect of Leaching Time

Figure 2c shows the leaching efficiency of vanadium and phosphorus at different leaching times. The vanadium leaching efficiency reached 71.6% within 2 min after the leaching started, and the vanadium leaching efficiency increased slowly and remained about 80% with increasing the leaching time. Phosphorus reaches the maximum in 2 min at the beginning of leaching, and leaching efficiency gradually decreases as leaching continues, which is presumed to be due to the increase in the concentration of ions such as Ca^{2+} and Mg^{2+} obtained from vanadate dissolution, which causes the precipitation of phosphorus, resulting in a decrease in the phosphorus leaching efficiency. The optimum leaching time is 30 min.

Characterization of Roasted HCPVS and Leaching Residue

The XRD patterns of HCPVS after roasting at 850 °C for 60 min with Mg/V = 1.0 and leaching residue are shown in Fig. 3. The XRD pattern with Mg/V = 1 shows that the disappearance of V-spinel diffraction peaks is accompanied by the appearance of Fe_2O_3 and $Ca_5Mg_4V_6O_{24}$ peaks. The significant attenuation of the intensity of the diffraction peaks $CaTiO_3$, which suggests that $CaTiO_3$ is an important source of calcium for the generation of calcium vanadate, indicating that after the addition of MgO, it reacts with the calcium such as $CaTiO_3$ and free CaO to generate $Ca_5Mg_4V_6O_{24}$. The Ca_2SiO_4–$Ca_3(PO_4)_2$ phase remains stable after roasting, while the diffraction peaks of the Ca-Fe olivine phase disappear. Similarly, XRD analysis is conducted on the leaching residue. The main phases in the residue are Fe_2TiO_5, Ca_2SiO_4-$Ca_3(PO_4)_2$, $CaTiO_3$, Fe_2O_3, and $CaSO_4·2H_2O$. The diffraction peaks of $Ca_5Mg_4V_6O_{24}$ completely disappear after leaching.

The microscopic image of the roasted slag is shown in Fig. 4, and the corresponding EDS results are shown in Table 2. There is still unreacted Ca_2SiO_4–$Ca_3(PO_4)_2$ solution in roasted slag as point A. From the point analysis results, it can be seen that P is still mainly distributed in this solid solution, which is consistent with the original slag. The difference is that the vanadium content in the Ca_2SiO_4–$Ca_3(PO_4)_2$ solid solution increases, probably because the oxidized pentavalent vanadium replaces the position of Si in the silicate phase [10–12]. Point B is known to be the $CaTiO_3$ phase according to the EDS results and XRD analysis, and part of the vanadium is solidly dissolved in this phase as well. The phenomenon of secondary distribution of vanadium also explains the result that the vanadium leaching efficiency of HCPVS in this work is only 79.7%.
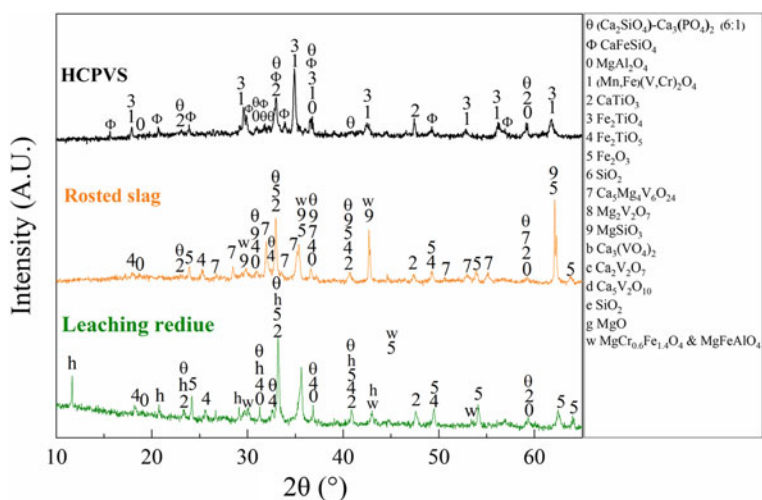
Fig. 3 XRD patterns of roasted slag and leaching residue
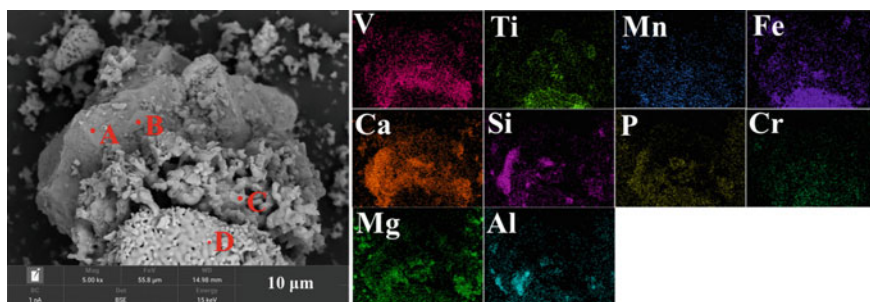
Fig. 4 BSE images of roasted slag with Mg/V = 1.0 at 850 °C for 60 min

Table 2 EDS analysis results of roasted slag

No.	O	Mg	Al	Si	P	Ca	Ti	V	Cr	Mn	Fe
A	27.21	4.53	0.71	11.86	2.84	33.61	0.18	4.06	0.58	4.44	9.98
B	28.11	2.17	0.43	0.62	0.12	29.76	24.77	9.20	1.07	0.74	3.00
C	37.32	3.18	0.50	1.54	2.59	28.38	0.97	20.83	0.05	2.26	2.38
D	48.04	4.54	1.48	0.05	0.42	0.32	5.41	0.37	2.81	3.24	33.34

Conclusions

In this work, the leaching behaviors of vanadium and phosphorus based on Magnesiation roasting-acid leaching of HCPVS are investigated. The effects of roasting and leaching conditions on the leaching efficiency of vanadium and phosphorus are explored. The leaching efficiency of 79.7% and 35.6% for vanadium and phosphorus under roasting conditions of Mg/V = 1.0, 850 °C for 2 h, and leaching conditions of leaching pH value of 2.5, 40 °C for 30 min. $CaTiO_3$ is involved in vanadate formation as a calcium source, and Ca_2SiO_4–$Ca_3(PO_4)_2$ remains stable as an inert phase after roasting. The secondary distribution of vanadium between Ca_2SiO_4–$Ca_3(PO_4)_2$ and $CaTiO_3$ limits vanadium efficient recycling.

References

1. Petranikova M, Tkaczyk AH, Bartl A, Amato A, Lapkovskis V, Tunsu C (2020) Vanadium sustainability in the context of innovative recycling and sourcing development. Waste Manag 113:521–544

2. Zhang J-H, Zhang W, Zhang L, Gu S-Q (2014) A critical review of technology for selective recovery of vanadium from leaching solution in V2O5Production. Solvent Extr Ion Exch 32:221–248
3. Puqiao D (1997) Current situation of the converter semi-steel steelmaking technology in China. Steelmaking 2:62–64
4. Wang YN, Song WC, Li H (2015) Vanadium extraction from molten vanadium slag with high Ca and P contents by direct oxidation-acid leaching method. In: International conference on industrial technology and management science, pp 375–380
5. Li H-Y, Wang N, Xie B (2012) Vanadium extraction from high calcium-content vanadium slag by calcification roasting. In: T.T. Chen honorary symposium on hydrometallurgy, electrometallurgy and materials characterization, pp 621–627
6. (2015) Roasting and leaching of high calcium and high phosphorus vanadium slag. Chin J Rare Metals 11:1039–1042
7. Yu T, Jiang T, Wen J, Sun H, Li M, Peng Y (2022) Effect of chemical composition on the element distribution, phase composition and calcification roasting process of vanadium slag. Int J Miner Metall Mater 29:2144–2151
8. Li H-Y, Wang K, Hua W-H, Yang Z, Zhou W, Xie B (2016) Selective leaching of vanadium in calcification-roasted vanadium slag by ammonium carbonate. Hydrometallurgy 160:18–25
9. Li H-Y, Wang CJ, Yuan YH, Guo Y, Diao J, Xie B (2020) Magnesiation roasting-acid leaching: a zero-discharge method for vanadium extraction from vanadium slag. J Cleaner Prod 260
10. Wu L, Gao W, Xie D, Li L, Dong Y (2015) Thermodynamic analysis of V-concentrating phase formation in V-bearing steelmaking slag modified by MgO. High Temp Mater Processes 34
11. Stewart DI, Bray AW, Udoma G, Hobson AJ, Mayes WM, Rogerson M, Burke IT (2018) Hydration of dicalcium silicate and diffusion through neo-formed calcium-silicate-hydrates at weathered surfaces control the long-term leaching behaviour of basic oxygen furnace (BOF) steelmaking slag. Environ Sci Pollut Res Int 25:9861–9872
12. Wu LS, Zhou Y, Dong YC (2013) Precipitation behavior of V-enrichment mineral in steelmaking slag bearing vanadium modified by SiO2. Appl Mech Mater 295–298:1729–1734

Theoretical Study on the Separation of Impurity Tellurium from Crude Selenium by Vacuum Distillation

Xin Yu, Guozheng Zha, and Wenlong Jiang

Abstract Theoretical research on the separation of tellurium by vacuum distillation from crude selenium could provide further key data support for industrial production. In this work, theoretical and experimental studies on the separation of tellurium impurities from crude selenium by vacuum distillation were systematically carried out. The saturated vapor pressure, separation coefficient, vapor–liquid equilibrium composition, average molecular free path, and evaporation rate characteristics of selenium and tellurium under different distillation conditions were calculated theoretically. We conducted research on the volatilization characteristics of crude selenium and measured the volatilization rate of crude selenium under pressures of 498–573 K and 10–500 Pa using the vacuum differential method. The volatilization rate values of crude selenium under different conditions were obtained, and the influences of distillation temperature and system pressure on the volatilization rate of crude selenium were uncovered.

Keywords Crude selenium · Separation of impurity tellurium · Vacuum distillation · Thermodynamic analysis · Volatilization kinetics

Introduction

Selenium is a typical dispersed metal, and due to its unique properties, it has become an indispensable material for high-tech development. In particular, the excellent optical properties of selenium make it widely used in the preparation of solar photovoltaic cells, LEDs, optical detectors, and other materials. Selenium has great application potential [1–3]. However, the complex state of impurities in crude selenium

X. Yu · G. Zha (✉) · W. Jiang
National Engineering Research Center of Vacuum Metallurgy, Kunming University of Science and Technology, Kunming 650093, Yunnan, China
e-mail: gz_zha@kust.edu.cn

Faculty of Metallurgical and Energy Engineering, Kunming University of Science and Technology, Kunming 650093, China

limits their separation ability, especially regarding the removal of tellurium impurities. In some previous studies, the main methods for removing tellurium from crude selenium were hydrometallurgical processes, including the oxidation method, hydrogen selenide thermal decomposition method [4], and selective dissolution method. Vacuum distillation is a physical metallurgical process in a closed vessel under negative pressure conditions. Based on the advantages of low energy consumption, green environmental protection, and high efficiency, vacuum distillation is widely used to separate impurities from crude metals [5–10]. Some scholars have focused on the purification method and effects of selenium and tellurium by vacuum distillation. For example, Luo [2] found that the volatilization of impurity tellurium would lead to low-purity selenium and proposed a preoxidation vacuum distillation process. The results showed that through this process, the purity of crude selenium was purified from 89.24 to 99.98%, and the tellurium content was reduced from 22.300 to 24.19 ppm. Zha et al. [11] purified crude selenium recovered from copper anode slime from a purity of 99.4–99.992% through three consecutive vacuum distillation steps, and the total impurity content was reduced from 2997.38 to 79.08 ppm. Some recent scholars have studied the evaporation characteristics of metals during vacuum distillation. For example, You et al. [12] measured the evaporation rate of pure lead at 1173, 1273, and 1373 K, studied the evaporation rules of Pb-Ag alloys and obtained the rate control step for liquid transfer Quality; additionally, the apparent activation energy metallurgical mass transfer coefficient of Pb during the evaporation process of the Pb-Ag alloy was obtained. Huang et al. [13] studied the volatilization rate of tellurium under different temperature and system pressure conditions. The results showed that when the system pressure was constant, the natural logarithm of the tellurium evaporation rate had a linear relationship with the reciprocal of temperature.

In the vacuum distillation process of crude selenium, the thermodynamic and volatilization kinetics are of great significance for vacuum distillation, but few reports are available. In this work, the saturated vapor pressure, molecular mean free path, gas–liquid equilibrium composition, and actual volatilization rate characteristics at different pressures and temperatures are theoretically analyzed. We aim to provide theoretical guidance for the separation of tellurium impurities from crude selenium by vacuum distillation.

Theoretical Analyses

Saturated Vapor Pressure

During the vacuum distillation process, the saturation vapor pressure of the metal changes with changing temperature. The relationship between saturated vapor pressure and temperature can be expressed as follows:
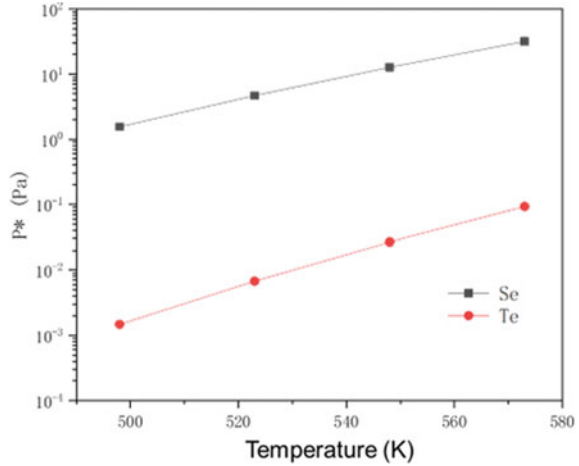
$$lgp* = AT^{-1} + BlgT + CT + D \tag{1}$$

where p^* is the saturated vapor pressure, Pa; T is the system temperature, K; and A, B, C, and D are evaporation constants. According to Eq. (1) and the values of A, B, C, and D, the saturated vapor pressure can be calculated. Figure 1 shows the saturation vapor pressures of Se and Te at temperatures from 500 to 580 K. Figure 1 shows that when the temperature is the same, there is a certain difference in the saturated vapor pressures of Se and Te.

Separation Coefficient B

In the vacuum distillation process of the Se–Te binary alloy, the vapor pressures of the two components in the gas phase are the same. The separation coefficient β can be calculated by Eq. (2)

$$\beta_{Se-Te} = \frac{\gamma_{Se} P^*_{Se}}{\gamma_{Te} P^*_{Te}} \tag{2}$$

Figure 2 shows the β_{Se-Te} values at temperatures of 573 K, 623 K, and 673 K. Under the three temperature conditions, β_{Se-Te} gradually approaches unity with increasing selenium content in the Se–Te binary alloy. This trend suggests that it is difficult to separate tellurium from crude selenium using vacuum distillation. Especially when the tellurium content is low, deep separation of tellurium cannot be achieved.

Fig. 2 Separation coefficient of the Se–Te binary alloy
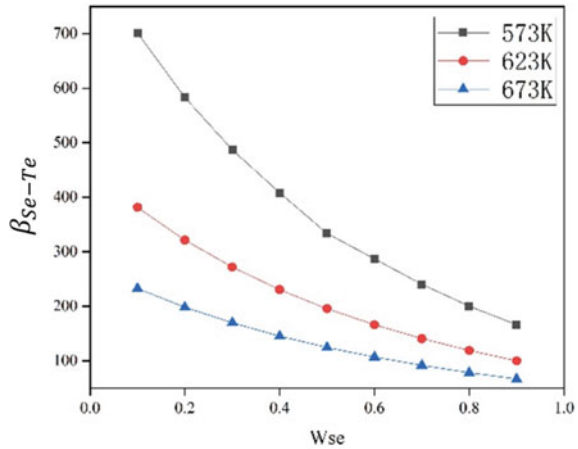
Vapor–Liquid Equilibrium Composition

In the vacuum distillation process of the Se–Te binary alloy, $w_{Se,g}$, $w_{Te,g}$ and $w_{Se,1}$, $w_{Te,1}$ are used to represent the components of the gas and liquid phases.

In the gas phase: $w_{Se,g} + w_{Te,g} = 1$.

In the liquid phase: $w_{Se,1} + w_{Te,1} = 1$.

The following analysis is obtained:

$$w_{Se,\ g} = \left[1 + \frac{x_{Te}}{x_{Se}} \cdot \frac{\gamma_{Te}}{\gamma_{Se}} \cdot \frac{P_{Te}^*}{P_{Se}^*}\right]^{-1} \tag{3}$$

$$w_{Te,g} = \left[1 + \frac{x_{Se}}{x_{Te}} \frac{\gamma_{Se}}{\gamma_{Te}} \frac{P_{Se}^*}{P_{Te}^*}\right]^{-1} \tag{4}$$

The calculation results are plotted as gas–liquid phase composition diagrams, as shown in Fig. 3. Figure 3 shows that the gas-phase tellurium content increases with increasing liquid-phase tellurium content. With the same composition, the higher the temperature is, the greater the gas phase tellurium content.

Mean Molecular Free Path

The distance traveled by a gas molecule between two consecutive collisions is the free path, and its average value is the mean free path ($\bar{\lambda}$). The mean free path of similar gas molecules is a function of temperature and pressure. The calculation formula is shown in Eq. (5).

Fig. 3 Vapor–liquid phase composition diagram of Te content from 0.001 to 0.1
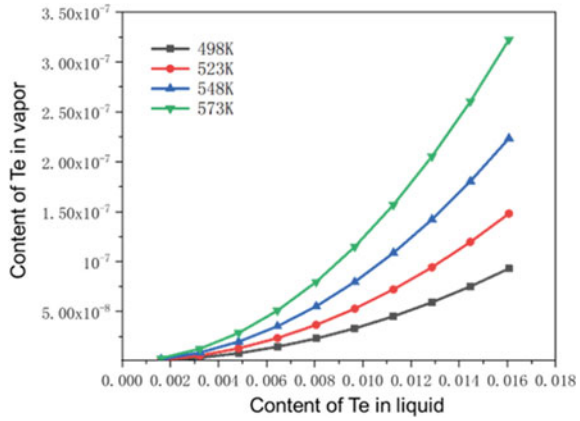
$$\bar{\lambda} = \frac{kT}{\sqrt{2}\pi d^2 p} \tag{5}$$

where k is the Boltzmann constant, 1.38×10^{-23} J/K; $\bar{\lambda}$ is the molecular mean free path, cm; T is the temperature, K; d is the atomic diameter, cm; and p is the system pressure, Pa. The calculated results of the molecular mean free path of Se and Te are shown in Figs. 4 and 5.

As shown in Figs. 4 and 5, under the same conditions, $\lambda_{Se} < \lambda_{Te}$ can theoretically achieve the separation and purification of selenium and tellurium by controlling the condensation height.

Fig. 4 Relationship between the Se molecule free path and temperature
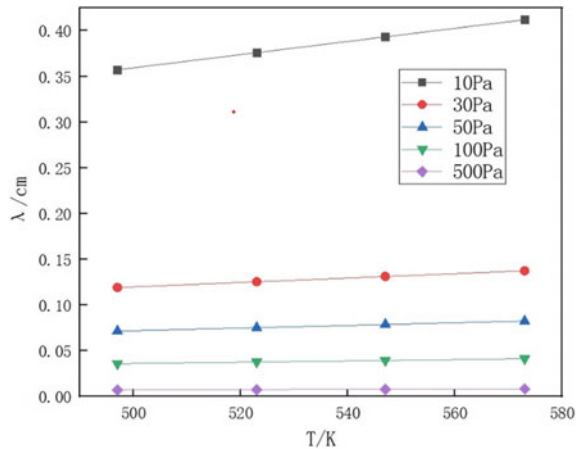
Fig. 5 Relationship between
the Te molecule free path
and temperature
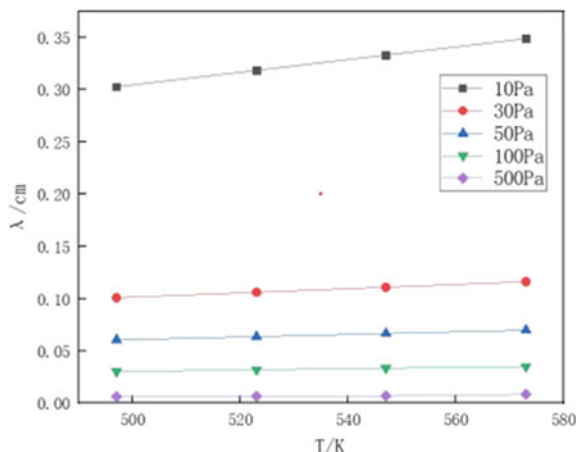
Maximum Theoretical Evaporation Rate

The maximum theoretical evaporation rate of metal under vacuum can be obtained.
P is calculated by Clausius' formula.

$$\omega_{max} = 4.376 \times 10^{-4} \times \alpha \times p^* \sqrt{\frac{M}{T}} \quad \left(g\, s^{-1}\, cm^{-2} \right) \tag{6}$$

where p^* is the saturated vapor pressure, Pa, and T is the temperature, K. The
maximum theoretical evaporation rates of Se and Te are plotted in Fig. 6. The theo-
retical maximum volatilization rates of metallic selenium and tellurium are positively
correlated with temperature, and ω_{max}, Se > ω_{max}, Te. While pure theoretical research
can guide production, measurement and research on actual evaporation rates are of
great significance. The actual evaporation rate is related to experimental conditions
and is described by an empirical relationship between actual production and control-
lable parameters. The guiding significance of the evaporation rate for production is
even greater than that of pure theory.

Experimental Study on the Volatilization Characteristics
of Impurity Tellurium

Experimental Method

The vacuum distillation experiment of crude selenium under the conditions of a
distillation time of 30 min, a pressure of 10–500 Pa and a temperature of 498–
573 K was performed to explore the volatilization characteristics of impurity Te.
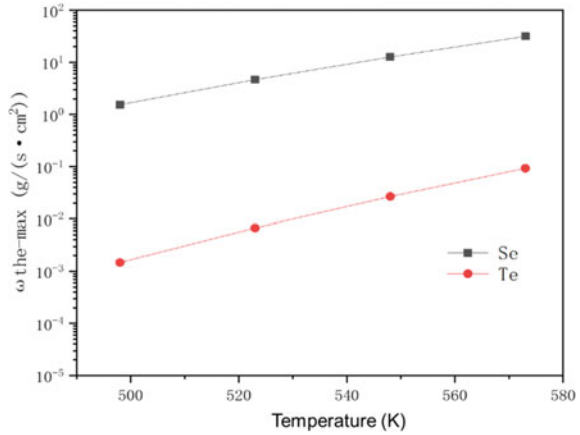
The experimental equipment was a vacuum differential furnace. Based on the raw data ($m \sim t$), the metal weight changes with time under the experimental conditions of the vacuum differential gravity furnace.

Experimental Results

The curves of the mass of crude selenium over time under temperature conditions of 498, 523, 548, and 573 K and pressures of 10, 30, 50 Pa, 100, and 500 Pa were measured, as shown in Fig. 7.

Figure 7 shows that the mass of crude selenium decreases uniformly with time; that is, the volatilization rate of crude selenium is constant over a period under certain temperature and pressure conditions. Under the same temperature conditions, the mass change curve tends to be flat as the pressure increases; that is, the volatilization rate of crude selenium decreases when the pressure increases. Straight line fitting was performed on the corresponding data to obtain the slope. The evaporation rate under this condition could be calculated, and a program could be used to solve and filter the slope at different times to obtain the slope and calculate the evaporation rate.

$$\omega = \frac{\Delta m}{\Delta t \cdot S} \tag{7}$$

The volatilization rates of crude selenium under different conditions are shown in Table 1.
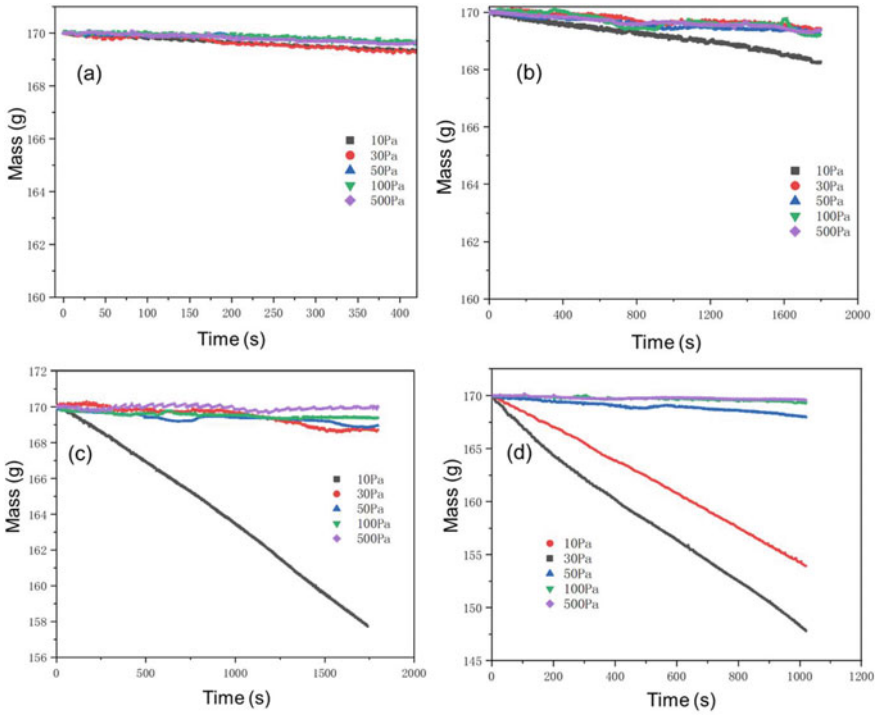
Fig. 7 Relationship between mass and time of crude selenium at different temperatures: **a** 498 K, **b** 523 K, **c** 548 K, and **d** 573 K

Relationship Between Crude Selenium Evaporation Rate and Temperature

The relationship between the evaporation rate and temperature of crude selenium at different pressures and temperatures is shown in Fig. 8. Figure 8 shows that when the system pressure is 10 and 30 Pa, the volatilization rate of crude selenium increases significantly with increasing temperature. When the temperature is 573 K, the maximum value is 2.90×10^{-3} g/(cm^2·s) at a pressure of 10 Pa.

Relationship Between Crude Selenium Evaporation Rate and Pressure

The relationship between the evaporation rate and the pressure of crude selenium is shown in Fig. 9. Figure 9 shows that the volatilization rate of crude selenium decreases as the system pressure increases, and the obvious decrease section is between 10 and 50 Pa. That is, when the pressure changes from 10 to 50 Pa, the volatilization rate of crude selenium decreases rapidly and remains at a low level thereafter. It can be

Table 1 The volatilization rates of crude selenium under different conditions

Temperature (K)	Pressure (Pa)	Volatilization rate (g/cm^{-2}·s^{-1})
498	10	2.14×10^{-4}
	30	2.53×10^{-4}
	50	1.26×10^{-4}
	100	1.33×10^{-4}
	500	1.56×10^{-4}
523	10	1.25×10^{-4}
	30	4.71×10^{-5}
	50	5.42×10^{-5}
	100	5.42×10^{-5}
	500	4.65×10^{-5}
548	10	1.02×10^{-3}
	30	1.26×10^{-4}
	50	6.01×10^{-5}
	100	3.49×10^{-5}
	500	6.98×10^{-6}
573	10	2.90×10^{-3}
	30	2.23×10^{-3}
	50	2.28×10^{-4}
	100	7.79×10^{-5}
	500	4.49×10^{-5}
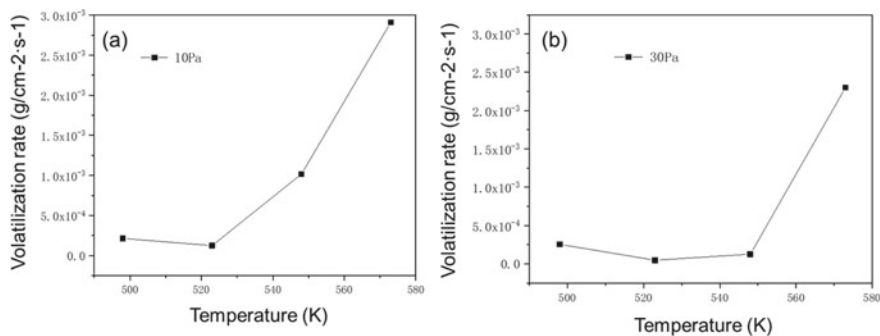
Fig. 8 Relationships between the evaporation rate and temperature at pressures of 10 Pa and 30 Pa

preliminarily determined that the critical pressure of crude selenium is between 10 and 50 Pa.
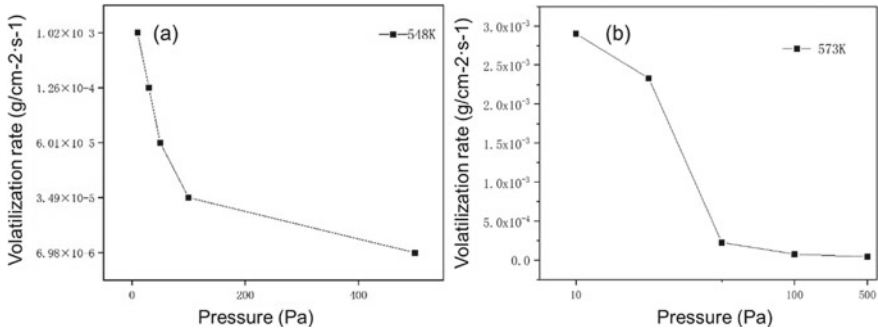
Fig. 9 Relationships between evaporation rate and pressure at temperatures of 548 K and 573 K

Conclusion

(1) The saturated vapor pressure, separation coefficient, gas–liquid equilibrium composition, mean molecular free path, and volatilization rate characteristics of selenium and tellurium were theoretically calculated, and the feasibility of separating selenium and tellurium by vacuum distillation was analyzed.

(2) The evaporation rates of selenium at temperatures of 498–573 K and pressures of 10–500 Pa were measured by vacuum differential gravimetry; the maximum evaporation rate was 2.90×10^{-3} g/(cm^2·s) under the conditions of 10 Pa and 573 K.

(3) The volatilization rate of crude selenium increased with increasing temperature. The volatilization rate of crude selenium increased gradually when the pressure decreased.

References

1. Zhao-Karger Z, Lin X, Minella BC et al (2016) Selenium and selenium-sulfur cathode materials for high-energy rechargeable magnesium batteries. J Power Sources 323
2. Luo H, Jiang et al (2022) Selective separation of tellurium and copper from crude selenium by pre-oxidation and vacuum distillation. Metall Mater Trans B 53(2)
3. Jorge P, Marie J, Angélique B et al (2017) Investigations of temperature and power effects on Cu(In,Ga)Se2 thin-film formation during a 3-stage hybrid co-sputtering/evaporation process. Prog Photovoltaics Res Appl 26(1)
4. Pearson RK, Haugen GR (1981) Kinetics of the thermal decomposition of H2Se. Int J Hydrogen Energy 6(5):509–519

5. Lu Z, Zhenming X (2011) Separating and recovering Pb from copper-rich particles of crushed waste printed circuit boards by evaporation and condensation. Environ Sci Technol 45(12)
6. Guo X, Zhou Y, Zha G et al (2020) A novel method for extracting metal Ag and Cu from high value-added secondary resources by vacuum distillation. Sep Purif Technol 242
7. Zhang X, Liu D, Jiang W et al (2020) Application of multi-stage vacuum distillation for secondary resource recovery: potential recovery method of cadmium telluride photovoltaic waste. J Mater Res Technol 9(4)
8. Zha G, Yang B, Yang C, et al (2019) Selective separation and recovery of valuable metals by vacuum distillation of copper anode slime flotation tailings. JOM 71(7)
9. Huan L, WenLong J, GuoZheng Z et al (2022) Removal of impurity Pb during crude selenium purification by controlling potential oxidation and vacuum distillation. Vacuum 195
10. Yuan T, Xiaopan Z, Tao Q et al (2021) Technical research on vacuum distillation to purify magnesium to 99.99% purity. Mater Rese Express 8(5)
11. Zha G, Wang Y, Cheng M et al (2020) Purification of crude selenium by vacuum distillation and analysis. J Mater Res Technol 9(3)
12. Yanjun Y, Junjie X, Lingxin K et al (2021) Kinetics study of Pb evaporation from pure Pb and Pb–Ag alloy in vacuum evaporation process. J Mater Res Technol 15
13. Daxin H, Wenlong J, Baoqiang X et al (2023) Evaporation characteristics of elemental tellurium in the vacuum distillation process based on differential weight method measurement. Vacuum 208

Author Index

Subject Index

A

Adsorption, 76, 79–81, 84, 85, 97, 98, 100, 101, 103, 165–169, 181–185, 208, 216, 262, 281, 316
Al-Ce-based alloys, 415, 416
Aluminum-vanadium alloy, 323
Amine extractants, 251, 253
Ammoniacal leach liquor, 263
Anode effect, 336, 339, 344, 346, 347, 353, 354
Antagonistic extraction, 265, 271
Antimony, 357, 359, 383–386, 391, 395
Antimony recovery, 383
Antisolvent, 55–61, 87–89, 93, 95
A-Spodumene, 141–144, 152, 157

B

Bacteriophage, 161, 162
Bauxite ore, 74, 87, 88
Bauxite residue, 73–78, 84, 88
Bayer liquor, 87, 88, 95
Biomaterials, 185
Biosorption, 161

C

Ca_2SiO_4, 453, 459, 460
Calcification roasted vanadium slag, 114
Capacitor, 3–6, 9, 10, 181
Cathodic Current Density, 343, 348, 353, 354
$CaTiO_3$, 453, 457, 459, 460
Cd, 14, 240, 241, 441–450
Cemented carbide disintegration, 400
Ce substitution, 416
CF_4, 334–338, 340–342, 344, 349, 350, 353

Cobalt

Cobalt, 97, 102, 104, 131, 171, 172, 175–177, 188, 189, 262, 397, 398, 402
Concentrated solar power, 188
Conversion rate, 17, 431–439
Crude selenium, 463–465, 468–472
Crystallization, 55, 56, 58, 59, 61, 87–89, 91, 92, 95, 97, 281, 378, 443
Current density, 127, 128, 323–331, 334, 336, 339–341, 345, 348, 349, 352–354, 360, 362, 365, 371, 373–375, 377, 380

D

D2EHPA, 36, 41–43, 45–49, 51, 52, 81, 131–138, 239, 241, 242, 246–248, 316, 319
Deep Eutectic Solvents (DES), 357
Degradation, 6, 122, 123, 125
Dense Medium Separation (DMS), 201–205, 207, 211
Distillation, 63, 463, 468
DyFe Electrowinning, 333, 343

E

Effluent, 4, 172, 181–185
Electric vehicles, 33, 34, 42, 63, 65, 121–123, 128, 141, 162, 171, 187, 188, 201, 273
Electro-metallurgical, 369
Electrometallurgy, 380
Electrorecovery, 358, 364–366
Environmental friendliness, 369
Ethaline DES, 358, 367
Extraction chromatography, 41–43, 52